

Probing Iron-Ligand Interactions by combining Modern
High-resolution Hard X-ray Spectroscopy and Density
Functional Theory: A Powerful Methodology in Cases
where Conventional Methods Fail

Dissertation

zur Erlangung des Doktorgrades
des Fachbereichs Naturwissenschaften
der Universität Paderborn

vorgelegt von

Lukas Burkhardt

Paderborn 2019

Promotionskommission

Prof. Dr.-Ing. Hans-Joachim Warnecke

Kommissionsvorsitz

Prof. Dr. Matthias Bauer

Erstgutachter

Prof. Dr. Thomas Kühne

Zweitgutachter

Jun. Prof. Dr. Stephan Hohloch

Drittprüfer

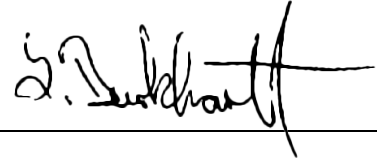
I like my photons to be as high-energetic as my personality.

Jason Shearer, XAFS 2018

Eidesstaatliche Erklärung

Hiermit versichere ich, dass alle Bestandteile der vorliegenden Arbeit selbständig durchgeführt und keinerlei, außer der von mir angegeben Hilfsmittel verwendet wurden. Alle Genehmigungen bezüglich der erneuten Veröffentlichung urheberrechtlich geschützter Veröffentlichungen wurden eingeholt. Vor jeder Publikation wurde angegeben welche Arbeiten von welchem Kooperationspartner in welchem Umfang durchgeführt wurden. Alle wörtlichen - sowie sinngemäße Zitate wurden als solche gekennzeichnet.

Paderborn, den 29.04.2019

A handwritten signature in black ink, appearing to read 'L. Burkhardt', written over a horizontal line.

Lukas Burkhardt

Abstract

A detailed investigation of the sensitivity of modern high-resolution hard X-ray spectroscopy towards transition metal (TM)-ligand interactions is carried out in the framework of this thesis. Valence-to-core X-ray emission spectroscopy (VtC-XES) combined with density functional theory (DFT) to probe occupied TM-ligand interactions and high energy resolution X-ray absorption near edge structure (HERFD-XANES) in combination with time-dependent DFT (TDDFT) to probe unoccupied TM-ligand interactions are introduced as powerful tools to investigate transition metal compounds where standard spectroscopic or scattering techniques fail. The combination of both is ideally suited to characterize the electronic and geometric structure of Fe hydride complexes, Fe nitrosyl complexes and Fe polypyridyl-NHC (N-heterocyclic carbene) complexes.

Two low-valent, terminal iron hydride complexes and a dinuclear, bridged poly-hydride are investigated in comparison to their non-hydride analogues. Bonding and antibonding TM-H interactions lead to significant spectral changes in the VtC-XES and XANES region. Both methods show to be highly sensitive to the hydride coordination mode (terminal or bridged) and the TM-H distance and therefore are highly suited to study reactions in situ where hydride species are involved.

The electronic structure of the well-known Hieber anion, $[\text{Fe}(\text{CO})_3(\text{NO})]^-$ is revisited by modern high-resolution hard X-ray spectroscopy in combination with theoretical spectroscopy. Nitrosyl coordination isomers of the Hieber anion are obtained by accessing the singlet and triplet potential energy surfaces by a simple DFT scanning approach. These isomers are utilized further as a case study to investigate the strength of VtC-XES and HERFD-XANES to probe and discriminate structural nitrosyl isomers by theoretical spectroscopy. Both methods show a great sensitivity to structural and electronical changes of the Fe-NO motif. This work presents the possibility to follow the fate of the non-incent nitrosyl ligand during e.g. catalytic reactions or photophysical applications.

The electronic structure of a series of potential iron-based photosensitizers is investigated and compared by modern hard X-ray spectroscopy in combination with (TD)DFT. Obtained distinctions of ground state valence levels are correlated with excited state characteristics, probed by ultrafast transient absorption spectroscopy. The number of coordinating σ -donating N-heterocyclic carbene (NHC) ligands per complex is correlated to observed shifts in the core-to-core (CtC) XES spectrum, caused by changes in TM-ligand covalency.

Kurzzusammenfassung

Eine detaillierte Untersuchung der Empfindlichkeit moderner, synchrotronbasierter harter Röntgenspektroskopie hinsichtlich Übergangsmetall (TM)-Ligand Wechselwirkungen, wird im Rahmen dieser Arbeit durchgeführt. *Valence-to-core* Röntgenemissionsspektroskopie (VtC-XES) in Kombination mit Dichtefunktionaltheorie (DFT) zur Abfrage besetzter TM-Ligand Wechselwirkungen und hoch energieaufgelöste, fluoreszenzdetektierte Röntgen-Nahkanten-Absorptions-Spektroskopie (HERFD-XANES) in Kombination mit zeitabhängiger Dichtefunktionaltheorie (TDDFT) zur Abfrage unbesetzter TM-Ligand Wechselwirkungen werden als leistungsstarke Hilfsmittel vorgestellt um Übergangsmetallverbindungen in Fällen zu charakterisieren, in denen herkömmliche Spektroskopie- oder Streuungsmethoden versagen. Es wird gezeigt, dass die Kombination beider Methoden ideal geeignet ist um die elektronische sowie geometrische Struktur von Fe-Hydrid-Komplexen, Fe-Nitrosyl-Komplexen und Fe-Polypyridyl-NHC-Komplexen zu charakterisieren.

Zwei niedervalente, terminale Eisenhydride und ein dinukleares, verbrückendes Polyhydrid werden im Vergleich mit ihren hydridfreien Analogon untersucht. Bindende und antibindende TM-Ligand-Wechselwirkungen führen zu signifikanten spektralen Änderungen im VtC-XES- und XANES-Bereich. Beide Methoden zeigen sich höchst sensitiv hinsichtlich der Koordinationsgeometrie des Hydridliganden (terminal, verbrückend) sowie der TM-H Bindungslänge und eignen sich somit in hohem Maße, um Reaktionen in situ zu untersuchen, in denen Hydridspezies involviert sind.

Die elektronische Struktur des altbekannten Hierberanions, $[\text{Fe}(\text{CO})_3(\text{NO})]^-$ wird mittels moderner, hochauflösender, harter Röntgenspektroskopie in Kombination mit theoretischer Spektroskopie neubetrachtet. Durch eine simple, DFT-basierte *scanning* Methode wurden strukturelle Nitrosyl-Koordinationsisomere des Hieberanions im singlet und triplet Spinzustand erhalten. Diese Strukturen werden als Fallstudie genutzt, um die Stärke von VtC-XES und HERFD-XANES hinsichtlich der Fähigkeit zur Charakterisierung und Unterscheidung dieser zu untersuchen. Beide Methoden zeigen eine hohe Empfindlichkeit hinsichtlich struktureller sowie elektronischer Änderungen des Fe-NO-Motivs. Diese Arbeit verdeutlicht die Möglichkeit dem Schicksal des redoxaktiven Nitrosylliganden z.B. während Reaktionen oder photophysikalischen Anwendungen zu folgen.

Mit Hilfe moderner, hochauflösender, harter Röntgenspektroskopie kombiniert mit (TD)DFT-Rechnungen wird die elektronische Struktur des Grundzustandes einer Serie potenzieller eisenbasierter Photosensibilisatoren charakterisiert und miteinander verglichen. Gefundene Abweichungen werden mit Eigenschaften der angeregten Zustände dieser Verbindungen korreliert, welche durch transiente Ultrakurzzeitabsorptionsspektroskopie erhalten wurden. Des Weiteren wird gezeigt, dass die Anzahl N-heterozyklischer-Carben-Liganden (NHC) pro Eisenkomplex mit experimentell beobachteten Verschiebungen des *Core-to-core* Röntgenemissionsspektrums (CtC-XES) korrelieren.

Danksagung

An dieser Stelle möchte ich allen Personen, die mich in den letzten viereinhalb Jahren unterstützt und begleitet haben danken.

Als Erstes möchte ich mich bei Matthias Bauer für die Aufnahme in seinen Arbeitskreis, die Vergabe meines Promotionsthemas, das entgegengebrachte Vertrauen sowie der Finanzierung meiner Promotion bedanken. Er nahm sich immer Zeit für meine Anliegen, auch wenn diese nicht immer nur von fachlicher Natur waren und stand mit Rat und Tat zur Seite. Ich danke allen ehemaligen, sowie aktuellen Mitgliedern des Arbeitskreises für viele lustige Momente im L-Raum, Labor oder auf Messzeit. Bis auf wenige Ausnahmen, herrschte immer eine gute Stimmung und ein sehr angenehmes Arbeitsklima. Bei Patrick Müller möchte ich mich für viele fruchtbare Diskussionen über unsere Forschung und der stetigen Hilfestellung bei auftretenden Problemen mit Rechnungen danken. Yannik Vukadinovic, Tim Frühling, Tanja Hirschhausen, Oliver Groß und Peter Zimmer möchte ich für die Synthese von benötigten Modelverbindungen sowie der Unterstützung bei synthetischen Problemen danken. Roland Schoch und Kai Stührenberg danke ich für die stetige Hilfe bei Problemen und dafür, dass Sie immer ein offenes Ohr für mich hatten. Vor allem möchte ich meiner Freundin Milina für all die Unterstützung und Kraft danken, die Sie mir in den letzten Jahren gegeben hat, ohne Sie wäre diese Arbeit nicht entstanden. Zu guter Letzt danke ich meiner Familie und Freunden für Ablenkung, Motivation und Unterstützung.

List of Beamtimes

European Synchrotron Radiation Facility (ESRF):

- ID26 Beamline
 - June 13 - 19, 2018
 - February 21 - 27, 2018
 - November 16 - 22 2016
 - April 14 - 21, 2015

Deutsches Elektronensynchrotron (DESY) Petra III:

- P65 Beamline
 - April 2 - 9, 2018
 - August 31 - September 5, 2017
 - June 2 - 7, 2017
 - April 20 - 25, 2017
 - October 28 - November 2, 2016
 - September 15 - 20, 2016
 - July 25 - August 2, 2016
- P64 Beamline
 - October 5 - 10, 2017
 - October 25 - November 1, 2018
 - April 11- 17, 2019

Ångströmquelle Karlsruhe (ANKA):

- XAS Beamline
 - November 12 - 14, 2015

List of Publications

- (1) Burkhardt, L.; Holzwarth, M.; Plietker, B.; Bauer, M. Detection and Characterization of Hydride Ligands in Iron Complexes by High-Resolution Hard X-ray Spectroscopy and Implications for Catalytic Processes. *Inorg. Chem.* **2017**, 56, 13300-13310.
- (2) Burkhardt, L.; Mueller, C.; Groß, O. A.; Sun, Y.; Sitzmann, H.; Bauer, M. The Bonding Situation in the Dinuclear Tetra-Hydrido Complex $[\{^5\text{CpFe}\}_2(\mu\text{-H})_4]$ Revisited by Hard X-Ray Spectroscopy. *Inorg. Chem.* **2018**, DOI: 10.1021/acs.inorgchem.8b03032.
- (3) Zimmer, P. ; Burkhardt, L. ; Friedrich, A.; Steube, J.; Neuba, A.; Schepper, R.; Müller, P.; Flörke, U.; Huber, M.; Lochbrunner, S; Bauer, M. The Connection between NHC Ligand Count and Photophysical Properties in Fe(II) Photosensitizers: An Experimental Study. *Inorg. Chem.* **2018**, 57, 360-373;
- (4) Burkhardt, L.; Vukadinovic, Y; Kalinko A.; .Rudolph, J.; Carlsson, P.; Jacob, C.; Bauer, M. Revival of the formal description: Fe(-II) identified in the Hieber anion by hard X-ray emission and absorption spectroscopy. *Angew. Chem.* **2019**, *in preperation*.
- (5) Zimmer, P.; Müller, P.; Burkhardt, L.; Schepper, R.; Neuba, A.; Steube, J.; Dietrich, F.; Flörke, U.; Mangold, S.; Gerhards, M.; Bauer, M. N-Heterocyclic Carbene Complexes of Iron as Photosensitizers for Light-Induced Water Reduction. *Eur. J. Inorg. Chem.* **2017**, 1504-1509.
- (6) Zimmer, P.; Burkhardt, L.; Schepper, R.; Zheng, K.; Gosztola, D.; Neuba, A.; Flörke, U.; Wölper, C.; Schoch, R.; Gawelda, W, Canton, S. E.; Bauer, M. Towards Noble-Metal-Free Dyads: Ground and Excited State Tuning by a Cobalt Dimethylglyoxime Motif Connected to an Iron N-Heterocyclic Carbene Photosensitizer. *Eur. J. Inorg. Chem.* **2018**, 5203-5214.
- (7) Preiß, S.; Pöpcke, A.; Burkhardt, L.; Großmann, L.; Lochbrunner, S.; Bauer, M.; Opatz, T.; Heinze, K. Gold(II) Porphyrins in Photoinduced Electron Transfer Reactions. *Chem. Eur. J.* **2019**, 25, 5940.
- (8) Steube, J.; Burkhardt, L.; Pöpcke, A.; Moll, J.; Zimmer, P.; Schoch, R.; Wölper, C.; Heinze, K.; Lochbrunner, S.; Bauer, M. Excited state kinetics of an air-stable cyclometalated iron(II) complex. *Angew. Chem.* **2019**, *submitted*.
- (9) Soyler, H.; Burkhardt, L.; Bauer M. Directing WNA Activity in Ru-bda Type Water Oxidation Catalysts: An Experimental and Computational Study. *Inorg. Chem.* **2019**, *in preparation*.
- (10) Burkhardt, L.; Chakraborty, U.; von Wangelin, A. J.; Bauer, M. Exploring the Electronic Structure of Hydride and HMDS stabilized Iron Clusters by High-Resolution Hard X-ray Spectroscopy. *Inorg. Chem.* **2019**, *in preparation*.

List of Oral Presentations

- (1) Burkhardt, L.; Bauer, M. Bridging catalytic Disciplines - X-ray Absorption Spectroscopy; 24th North American Catalysis Society Meeting, NAM 2015, Pittsburgh (PA, USA), June 16, **2015**
- (2) Burkhardt, L.; Bauer, M. X-ray Emission Based Spectroscopy and Its Relevance for Cu K-edge Measurements, Bioanorganisches Symposium 2016, Aachen (Germany), September 2, **2016**
- (3) Burkhardt, L.; Bauer, M. Exploring the Sensitivity of HERFD-XANES and VtC-XES to Probe Hydride Interactions in Transition Metal Complexes, 17th International conference on X-ray Absorption Fine Structure, XAFS 2018, Kraków (Poland), July 23, **2018**
- (4) Burkhardt, L.; Gregori, B.; von Wangelin, A. J.; Bauer, M. Synthesis and X-ray Spectroscopy of Iron Nanocluster Catalysts and Their Application as Semihydrogenation Catalysts, SPP 1708 Zwischenberichtskolloquium, Dresden (Germany), September 12, **2018**

List of Poster Presentations

- (1) Burkhardt, L.; Bauer, M. Hard X-ray Spectroscopy: A Probe for the Iron Hydride Bond, 115th General Assembly of the German Bunsen Society for Physical Chemistry, Bunsentagung 2016, Rostock (Germany), May 6, **2016**
- (2) Burkhardt, L.; Bauer, M. X-ray Emission Based Spectroscopy and Its Relevance for Cu K-edge Measurements, Bioanorganisches Symposium 2016, Aachen (Germany), September 2, **2016**
- (3) Burkhardt, L.; Bauer, M. Visualize Hydrides Hard X-rays, 13. Koordinationschemie-Treffen; KCT 2017, Potsdam (Germany), March 6, **2017**
- (4) Burkhardt, L.; Bauer, M. Exploring the Sensitivity of Hard X-ray Spectroscopy to probe Transition Metal - Hydride Interaction, Meeting of the Paderborn Center for Parallel Computing, PC2 user meeting 2018, Paderborn (Germany), December 10, **2018**

Table of Contents

1. Introduction	2
2. Theory	4
2.1. Fundamentals of X-ray absorption and emission	4
2.2. Selection rules	5
2.3. X-ray Emission spectroscopy	5
2.3.1. Core-to-core XES	6
2.3.2. Valence-to-core XES	8
2.4 K-edge X-ray Absorption Spectroscopy	10
2.4.1. HERFD-XANES	12
2.5. Simulating X-ray absorption and emission spectra	13
2.6. X-ray sources	14
2.6.1 X-ray tubes	15
2.6.2 Synchrotron and X-ray free electron laser radiation	15
2.6.2.1 Moving Charges: Bending Magnets and Insertion devices	17
2.7. Spectrometer types	19
3. References	22
4. Publications	28
4.1 Detection and Characterization of Hydride Ligands in Iron Complexes by High-Resolution Hard X-ray Spectroscopy and Implications for Catalytic Processes	28
4.2 The Bonding Situation in the Dinuclear Tetra-Hydrido Complex [$\{^5\text{CpFe}\}_2(\mu\text{-H})_4$] Revisited by Hard X-ray Spectroscopy	42
4.3 Revival of the formal description: Fe(-II) identified in the Hieber anion by hard X-ray emission and absorption spectroscopy	54
4.4 The Connection Between NHC Ligand Count and Photophysical Properties in Fe(II) Photosensitizers: An Experimental Study	72
5. Summary and Outlook	88
6. Supporting Information	90
6.1 Detection and Characterization of Hydride Ligands in Iron Complexes by High-Resolution Hard X-ray Spectroscopy and Implications for Catalytic Processes	90
6.2 The Bonding Situation in the Dinuclear Tetra-Hydrido Complex [$\{^5\text{CpFe}\}_2(\mu\text{-H})_4$] Revisited by Hard X-ray Spectroscopy	158
6.3 Revival of the formal description: Fe(-II) identified in the Hieber anion by hard X-ray emission and absorption spectroscopy	178
6.4 The connection between NHC ligand count and photophysical properties in Fe(II) photosensitizers: An experimental study	190

1. Introduction

In order to understand or improve the working principles of transition metal (TM) complexes or materials like e.g. catalysts in chemical reactions, enzymes in bioinorganic processes or compounds in photophysical applications, knowledge about the geometric and electronic structure of these compounds is indispensable. Many TM complexes or materials are successfully characterized by standard spectroscopic or scattering techniques, but there are many key compounds of the above-mentioned fields where characterization via readily accessible standard techniques is not straight forward. For this reason, a substituting method is needed that is able to probe both, the electronic and geometric structure of these compounds, while being not affected by any restriction of conventional analytical methods.

The investigation of TM hydride compounds is highly restricted, especially structural characterization or even the detection of present hydrides itself can be challenging. The working horses concerning geometric structure determination, namely elastic X-ray scattering, Nuclear magnetic resonance (NMR) spectroscopy and vibrational spectroscopy are not able to locate the hydride ligand in many hydride compounds. It is hard or almost impossible in some cases to observe hydrides by elastic scattering techniques due to the small X-ray scattering cross-section of hydrogen, which is often submerged by the electron density of the bonded transition metal, especially in case of bridged hydrides.¹ NMR spectroscopy is a key analytical method to study diamagnetic transition metal (TM) hydrides. Nevertheless, in case of paramagnetic compounds, standard NMR spectroscopy is not able to directly detect spectral signals of hydride ligands.^{2,3} Vibrational spectroscopy combined with *ab initio* calculations is an important methodology to probe the geometric structure. However, hydride associated vibrations are often superimposed by overlapping ligand, solvent or co-reactant vibrations and in case of bridged hydrides TM-hydride stretching vibrations are often too weak to be detected.³ Modern high-resolution hard X-ray spectroscopy at TM K-edges is able to overcome the above mentioned limitations by probing occupied TM-H interactions via TM K-edge valence-to-core X-ray emission spectroscopy (VtC-XES) combined with density functional theory (DFT) and unoccupied TM-H interactions via TM K-edge high energy resolution fluorescence detected X-ray absorption near-edge structure (HERFD-XANES) combined with time-dependent DFT (TDDFT). So far there were only preliminary studies on hydrogenases and hydrogenase mimics indicating the possibility of both methods to probe hydride interactions.⁴⁻⁶ These findings will be improved in this work by further accessing the possibilities of this methodology by studying well-defined terminal and bridged molecular Fe hydride catalysts in comparison to their non-hydride references.

Another example of challenging compounds are TM nitrosyl (NO) complexes and materials. Especially the characterization of the valence configuration of the bonded TM and the nitrosyl ligand itself is a great challenge, since NO is known to be a non-innocent ligand with nitrosyl π^* occupations ranging from zero (NO^+) to two (NO^-). For this reason, Enemark and Feltham suggested to characterize

TM nitrosyls only via the total occupation number n in TM 3d and nitrosyl π^* orbitals together via $\{\text{TM}(\text{NO})\}^n$, instead of determining separately the TM and nitrosyl valence composition.⁷ Determination of the geometric structure of TM nitrosyl complexes is less challenging for pure compounds in the electronic ground state, however as mentioned above due to the non-innocence of the nitrosyl ligand it is hard to extract the exact valence configuration. Since, nitrosyl ligands in TM nitrosyl compounds are often involved in redox and electronic excitations processes, it would be highly desired to follow the fate of nitrosyl ligands in situ in catalytic reactions or via transient spectroscopy after electronic excitation. Typically, vibrational spectroscopy is used to probe TM nitrosyls but especially in case of catalytic reactions, vibrations of the nitrosyl ligand are often superimposed by vibrations of the solvent, ligands, reactants or co-reactants. Modern high-resolution hard X-ray spectroscopy combined with computational methods is able to overcome the above-mentioned limitations by probing the present TM-NO interaction of such compounds, while being element specific and independent of the state of aggregation and reaction conditions.⁸ VtC-XES combined with DFT calculations is able to probe nitrosyl bond orbitals and occupied TM-NO interactions,⁹ whereas pre-edge HERFD-XANES combined with TDDFT calculations is in principle able to probe unoccupied TM-NO interactions and therefore it is possible to access both, TM 3d and nitrosyl π^* occupation. The well-known Hieber anion $[\text{Fe}(\text{CO})_3(\text{NO})]^-$ serves as a case study to establish this methodology to investigate the coordination chemistry of nitric oxide.

Octahedral $\text{Fe}^{\text{II/III}}$ polypyridyl complexes have a great potential to substitute noble metals as photosensitizers in the new future.¹⁰ Nevertheless, Fe^{II} polypyridyl are known to populate low-lying metal centered triplet (^3MC) and quintet states (^5MC) after optical excitation¹⁰ which are not favorable to interact with electron donors (reductive) or acceptors (oxidative) in electron transfer reactions. For this reason, many efforts are going into tuning the excited state order by either stabilizing the desired singlet and triplet metal-to-ligand charge transfer states ($^1/^3\text{MLCT}$) or by destabilizing the undesired ^3MC and ^5MC states.¹⁰ It has been shown that the substitution of pyridyl functions by strong σ -donating NHC (N-hetero cyclic carbene) functions is able to significantly destabilize unoccupied Fe e_g^* levels and consequently destabilize ^3MC and ^5MC states.¹⁰ In order to understand the influence of the number of NHC-functions per Fe atom and geometric assembly of these groups (symmetric or asymmetric ligands, homoleptic or heteroleptic complexes) a series of four different complexes with varying NHC numbers and positions are investigated by core-to-core XES (CtC-XES), VtC-XES and HERFD-XANES combined with (TD)DFT to probe the influence of these groups on occupied Fe t_{2g} , unoccupied Fe e_g^* and ligand π^* levels. Furthermore, these changes of the electronic ground state structure induced by incorporation of NHC donor functions is correlated to changes in the electronic excited state structure by comparison with excited state characteristics of these complexes probed by ultrafast transient absorption spectroscopy.¹¹

2. Theory

2.1. Fundamentals of X-ray absorption and emission

In the X-ray absorption process, inner- or core-levels are excited to unoccupied states, as illustrated in figure 1. These excitations are observed as sharp absorption edges with decaying tails to higher energies over several keV in the X-ray absorption spectrum.

Following the Siegbahn notation each edge is defined by the excited shell,^{12,13} which is defined by the principal quantum number of a given occupied state. For example, 1s excitations occur at K-edges (K-shell, $n = 0$), while 2s excitations cause L_1 -edges (L-shell, $n = 1$) and 2p excitations evoke L_2 - and L_3 -edges etc. (see Scheme 1).

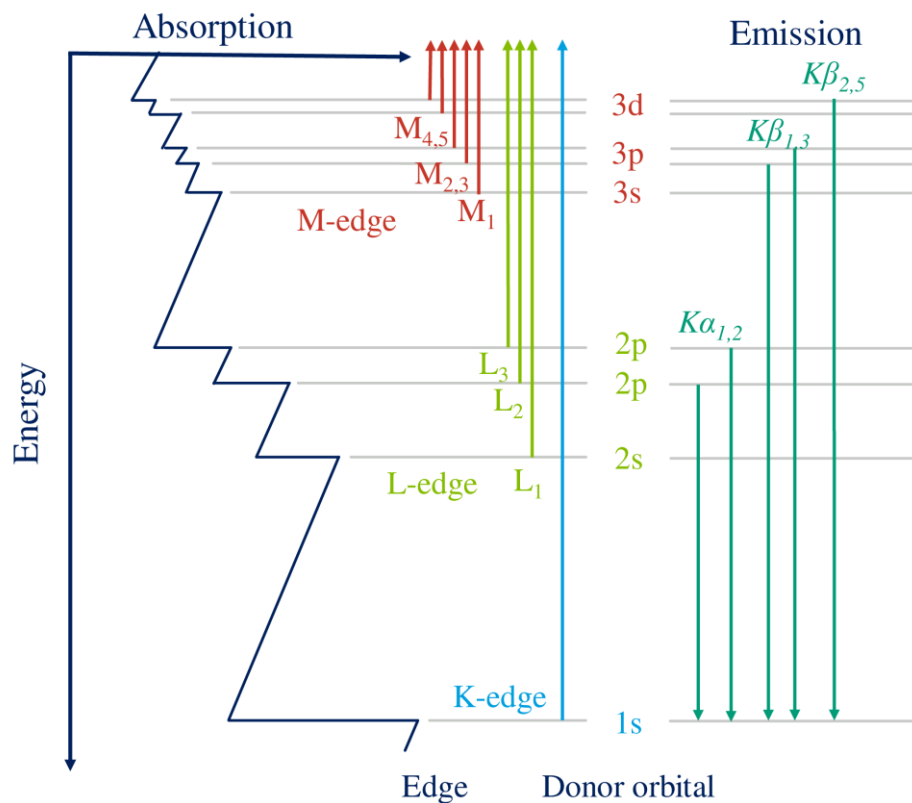


Figure 1. Overview of absorption M-, L- and K-edges of a given 3d TM (left) and K-edge emission lines of a given 3d TM (right).

Each inner- or core-shell excitation process is followed by a decay of an electron of higher (energy) occupied levels to the core-hole, either under emission of a photon or non-radiative by emission

of an electron. Scheme 1 (right) illustrates all possible radiative relaxation pathways following 1s excitations of a given 3d TM. In case of a 3d TMs, emissive relaxations of 2p, 3p and 3d levels to the 1s levels are observed. Each emission line is defined by the capital letter of its acceptor shell which has been excited previously at a given absorption edge and a Greek letter with indices that are not clearly defined, which is why the International Union of Pure and Applied Chemistry (IUPAC) recommends to define emission lines by their donor and acceptor shell, e.g. using K - L2 instead of $K\alpha_1$ in case of $2p \rightarrow 1s$ relaxation.¹⁴

The energy range where given absorption edges or emission lines occur is element specific, since stabilization of core-levels, e.g. the 1s level is increasing with increasing nuclear charge. The stabilization of core-levels through nuclear charge is significantly stronger than the stabilization of valence levels, due to charge compensation by levels in between, leading to a decrease or vanishing of the effective charge Z_{eff} felt by the valence. For this reason, the energy of a given absorption edge or emission line is increasing with nuclear charge, since the energy gap between core-levels and the valence-levels is increasing.¹⁵

2.2. Selection rules

X-ray absorption and emission follow the identical electric dipole selection rules as optical absorption or emission. In general, electric dipole transitions are limited by the following selection rules:

Where l is the azimuthal quantum number and m is the magnetic quantum number. Equation (2.2.1) illustrates, that with every emission or absorption of a photon, angular momentum must be transferred. Since each photon has its own spin, angular momentum conservation must be fulfilled. Spin flips are also forbidden, which is given by equation (2.2.4). Additionally, for centrosymmetric complexes or molecules, the Laporte rule must be fulfilled, which forbids parity conversion (g , *gerade* or u , *ungerade*), with respect to the inversion center. Only transitions that involve a change in parity like $u \rightarrow g$ or $g \rightarrow u$ are allowed. However, this selection rule is abolished, if the center of symmetry is distorted by reasons like Jahn-Teller distortion or asymmetric vibrations.^{16,17}

The transition probability of electric quadrupole transitions is negligible in relation to dipole transitions, but especially in the pre-edge region of 3d TM K-edge spectra, where $1s \rightarrow 3d$ transitions occur ($\Delta l = \pm 2$), electric quadrupole transitions play an important role.^{16,17} The selection rule of the azimuthal quantum number for electronic quadrupole transitions is given by:

$$\Delta l = 0, \pm 2 \quad (2.2.5)$$

2.3. X-ray Emission spectroscopy

As given in section 2.1, after X-ray absorption an excited core-hole final state is created, which will decay, either radiative, under emission of a photon or non-radiative, under emission of an electron.

X-ray emission spectroscopy is recording the radiative decay in the range of the core-hole lifetime broadening as a function of the emission energy.^{17,18}

2.3.1. Core-to-core XES

Core-to-core (CtC) XES studies the $3p \rightarrow 1s$ relaxation after $1s$ excitation ($K\beta_{1,3}$ emission). In general, a $1s$ electron is excited non-resonantly to the continuum, approximately 100 - 500 eV above a given 3d TM K -edge, followed by a $3p \rightarrow 1s$ relaxation (see Scheme 1, Chapter 2.1), which is monitored as a function of the emission energy. The CtC-XES spectrum consist of mainly two features, the weak low-energy $K\beta'$ feature or $K\beta$ satellite and the intense, high-energy $K\beta_{1,3}$ feature or $K\beta$ mainline (see figure 2).^{17,18}

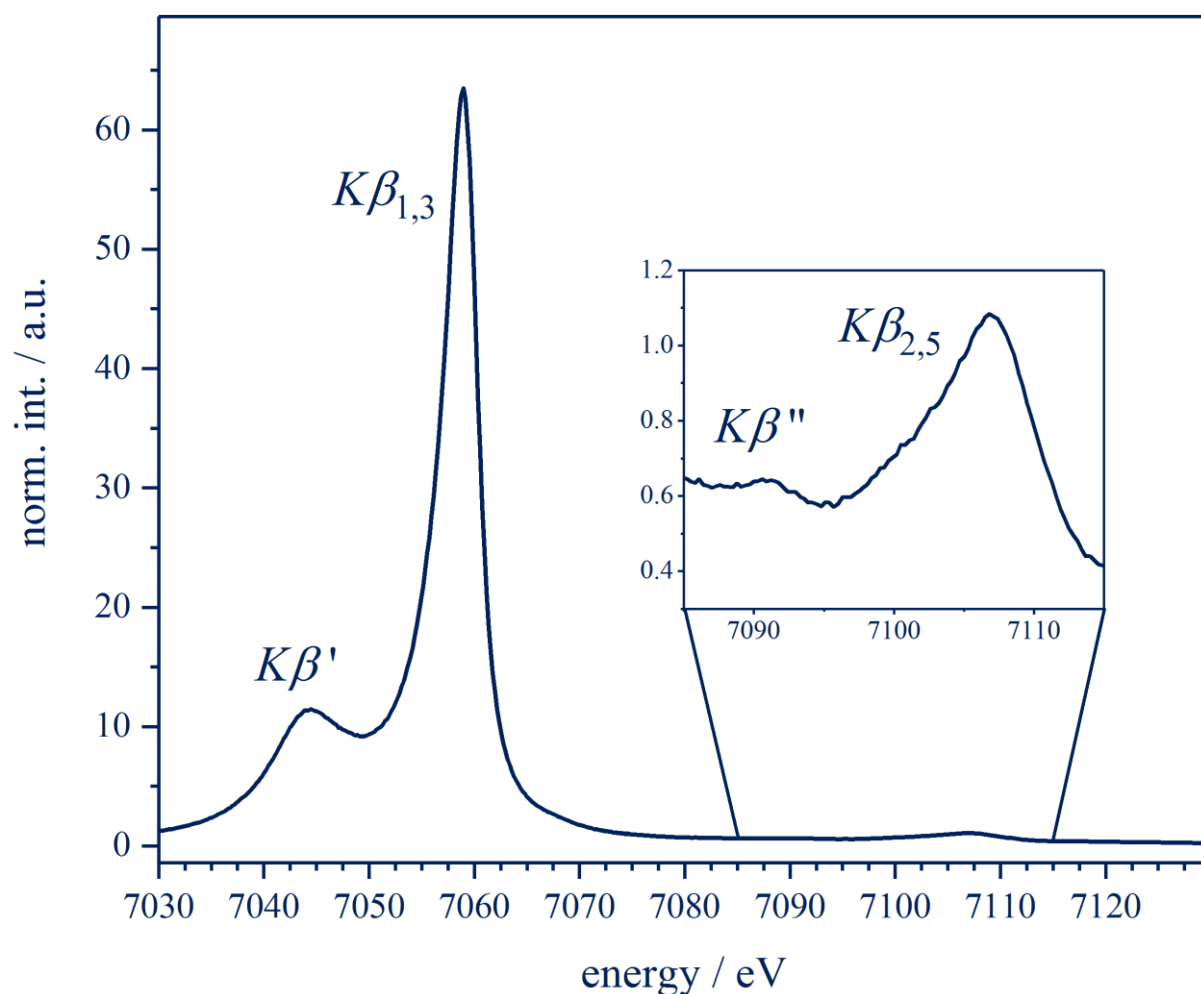


Figure 2. Fe $K\beta$ emission spectrum of Fe_2O_3 .¹⁹

In the final state (after $3p \rightarrow 1s$ relaxation) an unpaired $3p$ electron is created, which is able to interact with unpaired $3d$ electrons via $3p$ - $3d$ exchange interaction, causing the splitting between $K\beta$ mainline and satellite. The higher the spin state of a given system, the higher is the observed $K\beta$ splitting and the smaller is the $I_{K\beta_{1,3}}:I_{K\beta'}$ intensity ratio.¹⁸ Figure 3a shows CtC-XES spectra of an octahedral Fe^{II} (d^8) spin-crossover complex in the low-spin (LS) and high-spin (HS) state. LS compounds are

characterized by a small splitting between the mainline and the $K\beta'$ feature ($\Delta E(E_{K\beta_{1,3}} - E_{K\beta'})$) and high intensity ratio between both ($I_{K\beta_{1,3}}:I_{K\beta'}$), whereas HS compounds exhibit a significantly increased splitting and a small intensity ratio of both. For this reason, CtC-XES is highly sensitive to the spin state of a given system and allows to discriminate different spin states.¹⁷

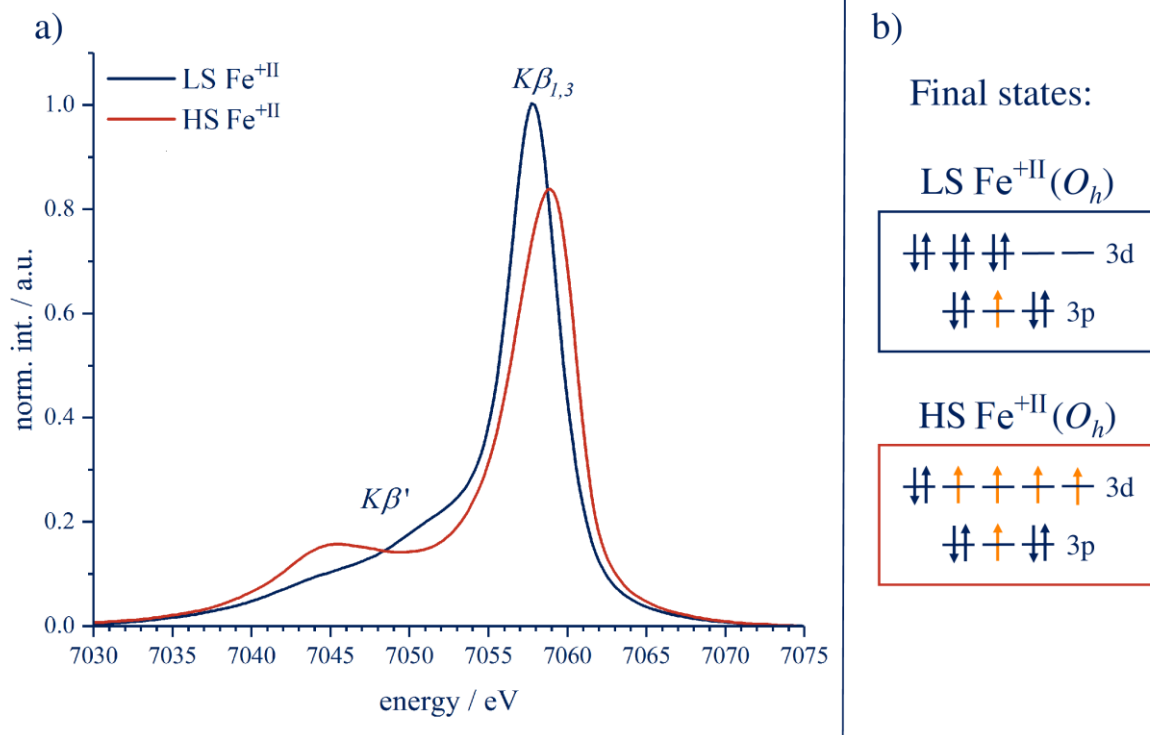


Figure 3. a) CtC-XES spectrum of an octahedral coordinated Fe^{+II} ion in low-spin (LS) configuration (blue) and high-spin (HS) configuration (red). b) present 3d and 3p occupation of both spin states in the CtC final state.²⁰

There are many examples, where mainline shifts were assigned to the oxidation state of the excited TM atom. Lowering the oxidation state means lowering the effective spin in the 3d shell and therefore decreasing the 3p-3d exchange interaction, shifting the mainline maximum to lower-energies. However, assigning mainline shifts to changes of the oxidation state, leads often to misinterpretations, due to superposition with covalency effects. Since covalency is also inducing a formal decrease of the 3d occupation and therefore lowering the effective 3d spin. It has been shown experimentally and computationally by Glatzel and Bergmann with a series of LS Ni^{2+} complexes¹⁷ and by Atanasov, Neese and Debeer for a series of HS Fe^{3+} complexes²¹ that the mainline is shifting significantly to lower energies with increasing TM-ligand covalency. To avoid a misassignment of covalency induced mainline shifts, proper reference compounds, with similar coordination sphere are required.

2.3.2. Valence-to-core XES

In general valence-to-core XES (VtC-XES) studies the relaxation of valence levels to a core level of a given atom after core excitation, as illustrated in figure 4 (for Fe K-edge VtC-XES). In case of a 3d TM, the $K\beta_{2,5}$ emission line is the VtC-XES signal (valence \rightarrow 1s relaxation, see figure 3) or in case of a main group, third row element like phosphorous, the $K\beta_{1,3}$ emission line is the VtC-XES signal etc., depending on the valence configuration of a given element.²²

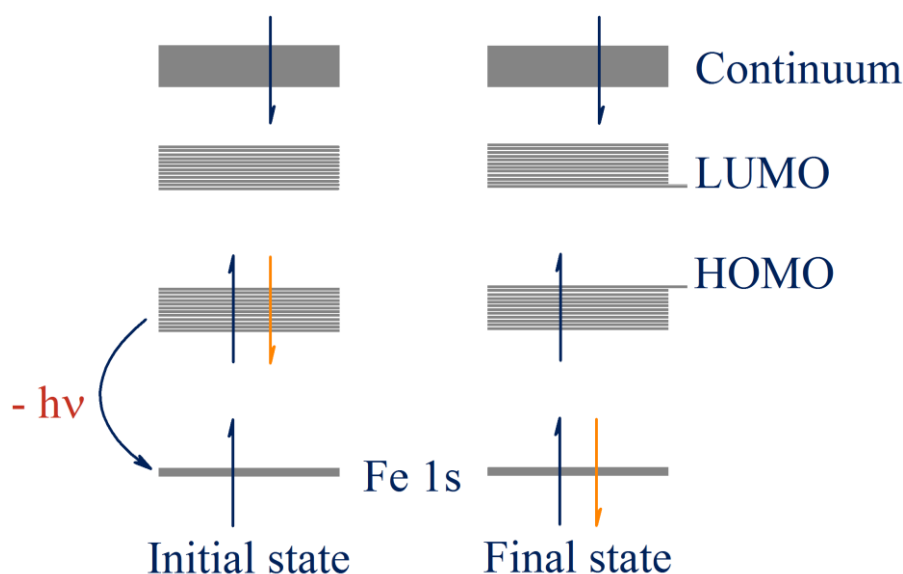


Figure 4. Illustration of the X-ray emission initial state (left) and final (state) after 1s excitation.

The $K\beta_{2,5}$ emission line and its low-energy $K\beta''$ satellite are located at the high-energy slope of the $K\beta_{1,3}$ emission line (see figure 2). In contrast to $K\beta_{1,3}$ emission, $K\beta_{2,5}$ emission is not allowed by means of dipole selection rules, since it is formally a 3d (valence) \rightarrow 1s relaxation. Similar to 1s \rightarrow 3d pre-edge transitions in the XANES region, only quadrupole transitions are allowed for 3d \rightarrow 1s transitions ($\Delta l = -2$), which are much weaker in intensity in relation to electric dipole transitions (factor ~ 100 weaker than $K\beta_{1,3}$ line).²³ Nevertheless, it has been shown, that 3d \rightarrow 1s transitions gain dipole transition probability by hybridization with TM np orbitals.²⁴ The amount of np hybridization depends on the coordination geometry of the central 3d TM. In centrosymmetric coordination geometries, e.g. octahedral, no np hybridization is observed (depending on the order of the distortion of the overall structure), whereas e.g. tetrahedral coordinated TM complexes exhibit high TM np hybridization and therefore high transition probabilities due to the increased dipole character of the connected transition.²⁵ In TM coordination compounds, 3d \rightarrow 1s transitions are typically located at the high-energy slope or high-energy feature of the VtC-XES spectrum.²³ The intensity of this region (see figure 5, 7107 - 7112 eV) in VtC-XES spectra is therefore sensitive to the coordination geometry of an TM ion, similar to the pre-peak intensity in XANES spectra.^{26,27}

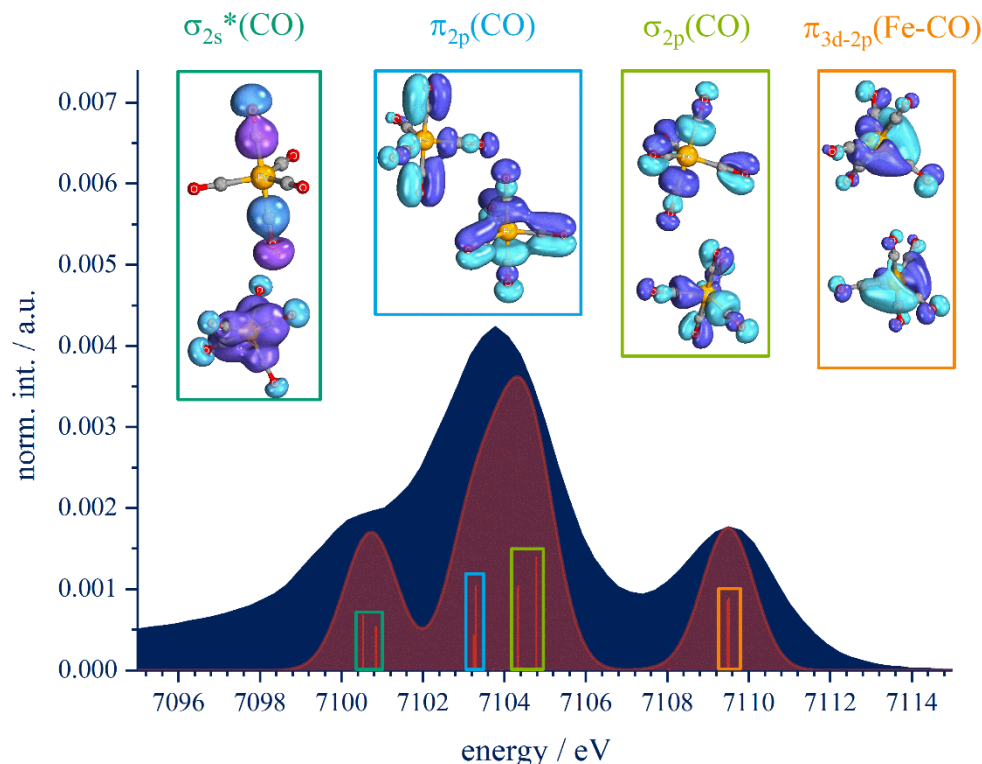


Figure 5. Experimental (blue) and theoretical (red; def2-TZVP, TPSS) VtC-XES spectra of $\text{Fe}(\text{CO})_5$.¹⁹

Lower-energy VtC-XES features (see figure 5, 7098 - 7106 eV) are typically evoked by ligand localized valence orbitals,²⁸ which gain also transition probability due to minor TM np hybridization. The observed intensity of these transitions is therefore highly sensitive to the ligand-TM distance, due to a decreasing overlap of TM np and ligand np orbitals with increasing distance (as will be shown in chapter 4.1).⁴ In combination with DFT calculations, detailed information about these levels can be extracted.²⁹⁻³² To illustrate the possibilities of this method the Fe K-edge VtC-XES spectrum of $\text{Fe}(\text{CO})_5$ and predominant donor orbitals are shown in figure 5. The observed donor orbitals (see inset figure 9) reflect the σ_{2s}^* , π_{2p} and σ_{2p} orbitals of the carbonyl ligand and their bonding interactions with Fe 3d orbitals.

The low-energy $K\beta''$ satellite (see figure 2) of the $K\beta_{2.5}$ emission line of TM K-edge emission spectra is typically evoked by ligand 2s (second row main group elements) or 3s (third row main group elements) orbitals.²⁹ There are only few examples, where the $K\beta''$ satellite gives valuable or unknown information. Nevertheless, in particular cases, the $K\beta''$ satellite has been shown to be a sensitive probe for the identity of coordinating atoms. E.g. in solving the for decades ongoing discussion about the identity of the central atom in the nitrogenase FeMoco and FeVco clusters. Even though, the crystal structures were known for decades, the ion radii of C, N and O are too similar to be distinguished by scattering techniques. Debeer et al showed that the $K\beta''$ satellite is shifting significantly for different central atoms, due to the element specific energies of given 2s levels. In combination with frozen-core DFT calculations, they were able to characterize the central atom as a carbon atom.^{33,34}

2.4 K-edge X-ray Absorption Spectroscopy

TM K-edge absorption spectra are divided in three regions: the low-energy pre-edge region, the X-ray absorption near-edge structure (XANES) region and the extended X-ray absorption fine structure (EXAFS) region as illustrated in figure 6.

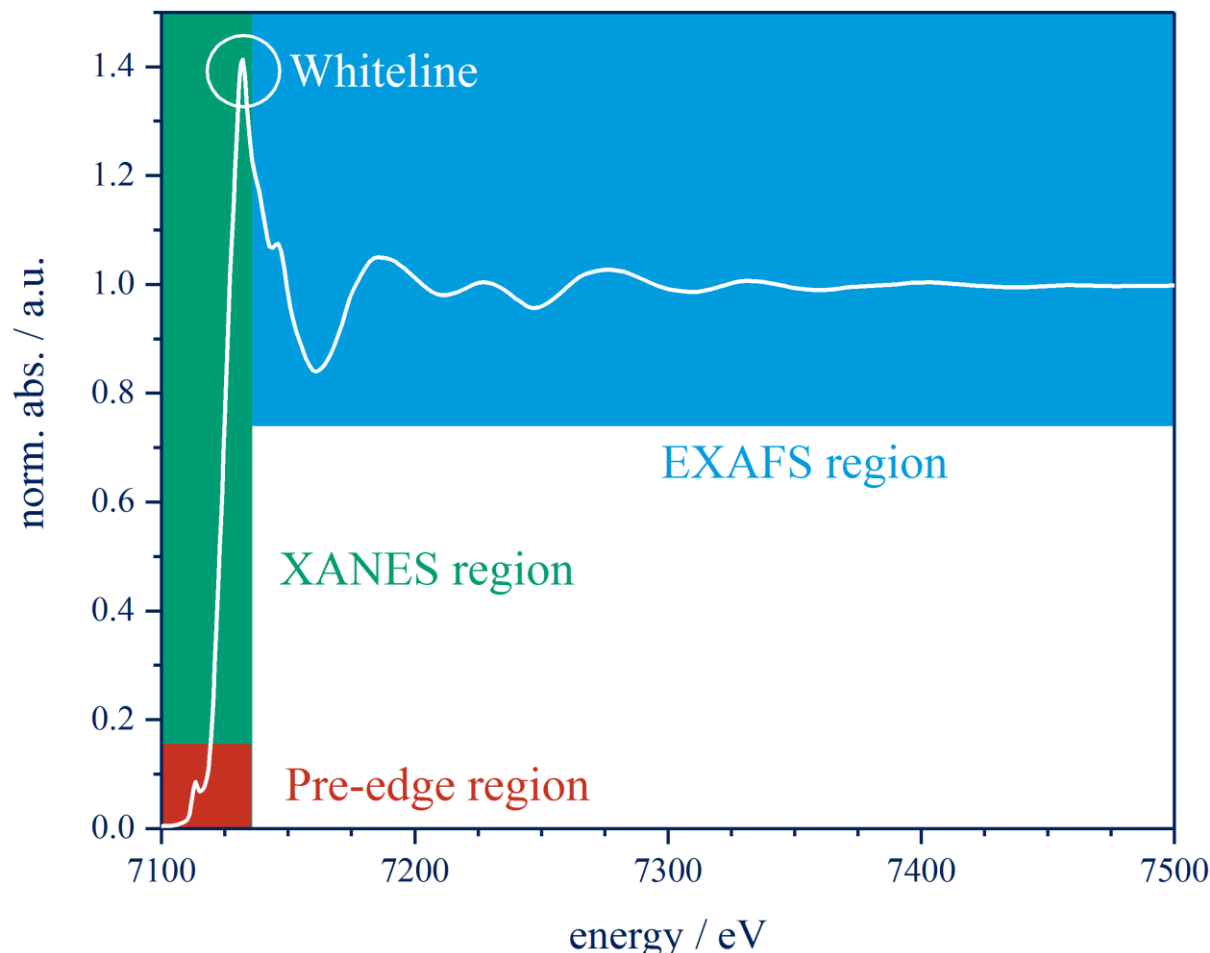


Figure 6. XAS spectrum of Fe_2O_3 , characteristic regions are highlighted.

Pre-peaks in the pre-edge region (see figure 6) are caused by $1s \rightarrow 3d$ / LUMO (or combinations of 3d and ligand localized orbitals) transitions (see figure 7). For this reason pre-peaks are only observed in TM ions with non- or partial occupied d-shells ($3d^0 - 3d^9$).³⁵ Similar to $3d \rightarrow 1s$ transition in the VtC-XES region, $1s \rightarrow 3d$ transitions are formally forbidden by dipole selection rules and therefore only quadrupole transition are allowed to occur in the pre-edge region.²⁴ Depending on the coordination geometry, TM 4p hybridization of 3d levels is observed, increasing the dipole character of given transitions and leading to an increased transition probability.²⁵

For this reason, the pre-edge region of TM K-edges is often utilized to discriminate different possible coordination numbers or geometries. In centrosymmetric coordination geometries, e.g. octahedral coordinated 3d TMs, no 4p hybridization of 3d orbitals is possible by symmetry and therefore

only a very weak pre-peak is observed. In contrast, tetrahedral coordinated 3d ions observe great 4p hybridization, leading to intense pre-peaks.^{36,37} For the same reason it is also possible to determine the order of distortion of centrosymmetric coordination compounds, by comparison with pre-peak intensities of suited reference compounds.³⁸ Since the pre-edge is highly sensitive to unoccupied 3d levels, it is often utilized to probe 3d occupation. For example, pre-peak spectra of octahedral coordinated d^6 LS ions will only observe $1s \rightarrow t_{2g}$ transitions, whereas an octahedral coordinated d^6 HS ion will show both $1s \rightarrow t_{2g}$ and $1s \rightarrow e_g$ transitions, leading to a second or broadened pre-peak feature, depending on the t_{2g} - e_g splitting and experimental resolution (see figure 8).

In the XANES region $1s \rightarrow 4p$ transitions occur, since these are allowed electronic dipole transitions, the near-edge intensity is rising sharply to the white line (figure 6), where the $1s$ electron is excited to continuum states. Beyond the white line, in the extended X-ray absorption fine structure region, the $1s$ electron is finally ejected as a photoelectron wave in the EXAFS region.

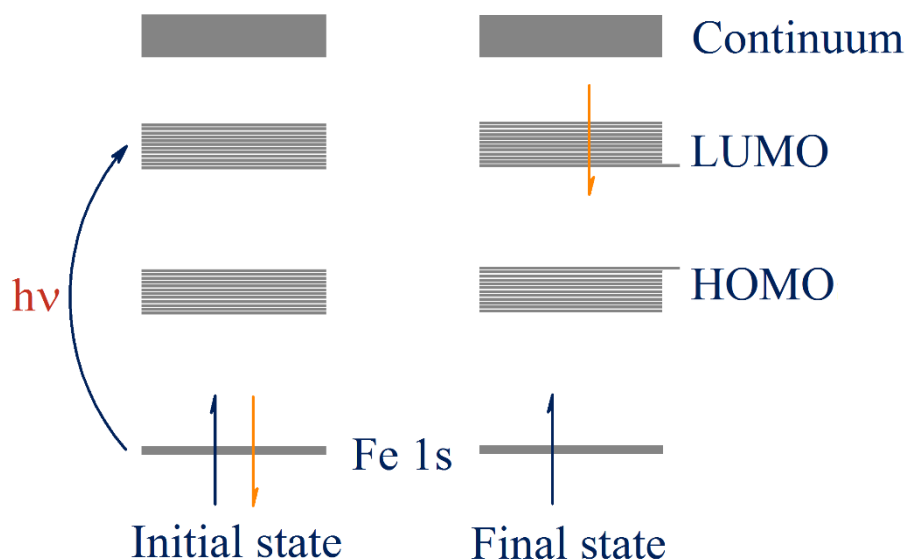


Figure 7. Illustration of the X-ray absorption K-edge initial state (left) and final state (right).

The majority of publications applying conventional XANES utilize the sensitivity of the edge-position to the oxidation state of an excited TM ion as a probe for oxidation states.¹⁵ The increase of the oxidation state of an given TM ion leads to an greater increase of the effective charge felt by the $1s$ level in relation to the increase felt by valence levels of this ion or in other words, the $1s$ level is stabilized stronger than valence levels and therefore an increase of the energy gap between $1s$ and LUMO / LUMO+1 ... / LUMO+X etc. levels is observed. For this reason, TM ions in higher oxidation states exhibit blue-shifted edge positions in relation to TM ions in lower oxidation states. Nevertheless, depending on the TM element studied, this approach is only applicable if compared compounds possess a similar coordination sphere with similar type of ligands.³⁹

2.4.1. HERFD-XANES

As illustrated in the previous section, TM K-edge pre-peaks of coordination compounds are highly sensitive to TM-ligand interactions of a given compound, since these are evoked by combinations of unoccupied 3d orbitals and unoccupied ligand localized orbitals. Nevertheless, fine structure in the pre-edge region is often masked by the poor intrinsic resolution of conventional XAS, caused by the short lifetime of core-excited final states in relation to valence excited final states.¹⁸

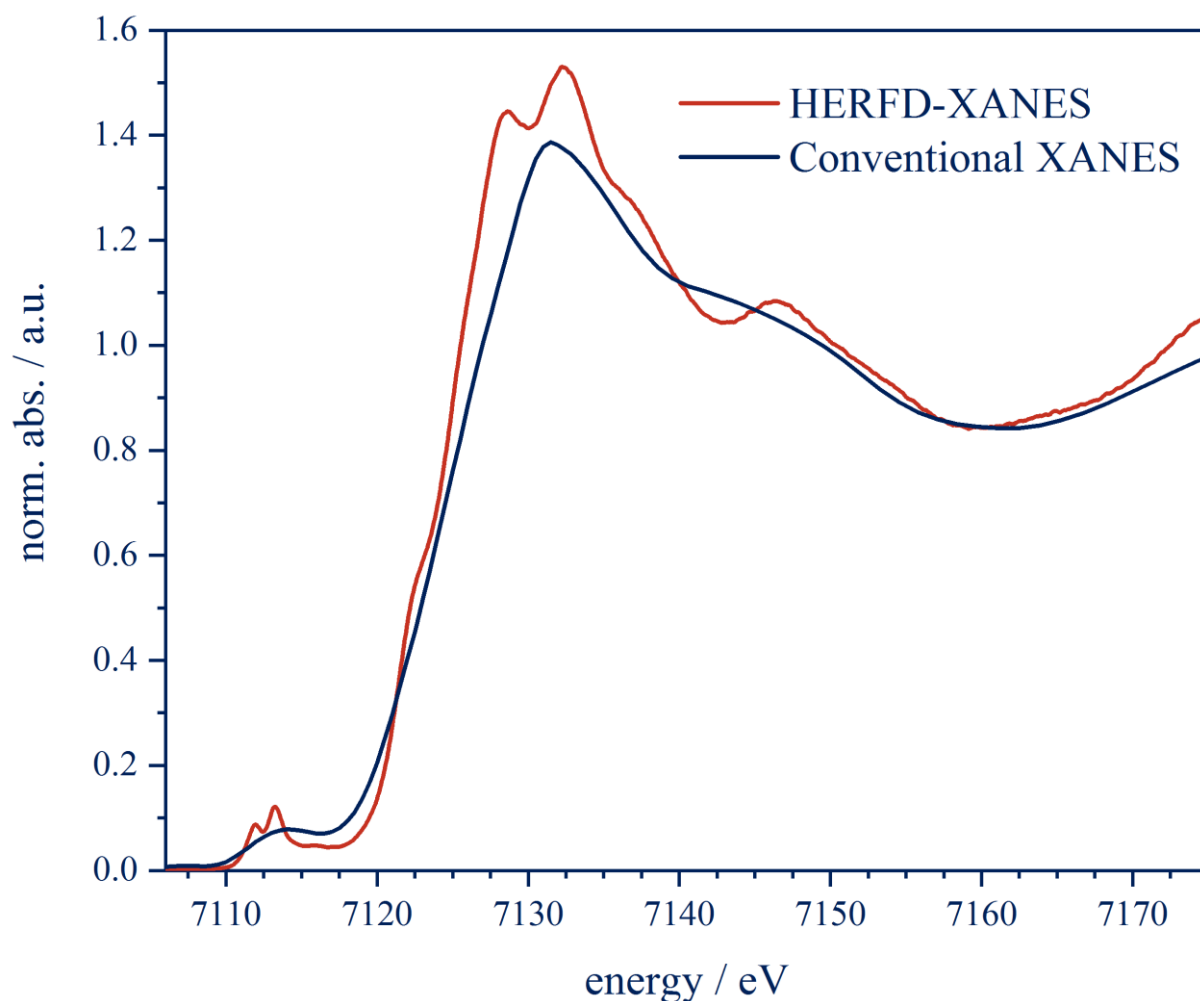


Figure 8. Comparison of HERFD-XANES and conventional XANES at the Fe K-edge of Fe_2O_3 .¹⁹

High energy resolution fluorescence detected XANES (HERFD-XANES) is able to overcome the core-hole lifetime broadening by detecting an emissive final state with an increased lifetime (in relation to the core-hole lifetime) in a narrow bandwidth (in the range of the core-hole lifetime broadening),³⁵ since the minimal linewidth of a transition is inversely proportional to the lifetime of its final state, as can be simply understood by the time-energy uncertainty relation and described by the Kramers-Heisenberg theory.⁴⁰

This sharpening effect has been demonstrated by the groups of Hämäläinen⁴¹ and de Groot.⁴² Especially in the pre-edge and near-edge region, HERFD-XANES shows a drastically increased resolution as illustrated in figure 8 by a comparison of conventional XANES and HERFD-XANES of Fe₂O₃.

In combination with time-dependent DFT (TDDFT) calculations, pre-edge HERFD-XANES is able to probe unoccupied TM-ligand interactions by accessing core-excited state compositions, as will be shown in chapter 4.^{43,44}

2.5. Simulating X-ray absorption and emission spectra

Calculations of TM K-edge XAS spectra need to be segmented into calculating EXAFS, XANES and pre-edge spectra. Calculating EXAFS data is well understood and is based on a semi-empirical methods,^{45,46} whereas the analysis of XAS edge data is more sophisticated.

Since core-hole excitations need to be described, the application of pseudopotential methods is not straightforward, whereas all-electron calculations demand a disproportionate computational cost compared to pseudopotential methods. There are examples where ground state DFT has been applied to study pre-edges but DFT is not able to treat the quasiparticle character of electrons and the core-hole attraction. By applying the Bethe-Salpeter equation (BSE) method,⁴⁷ electron-hole pairs can be described but the computational cost is increasing significantly. Of course, coupled cluster methods⁴⁸⁻⁵⁴ are able to describe core-hole excited states accurately, nevertheless again the computational cost is too high to be applied as a standard tool to analyze pre- and near-edges.

Time-dependent DFT (TDDFT) is the most frequently used method to describe charge-neutral excitations and it has been shown that TDDFT is able to accurately describe TM K-edge pre- to near-edge spectra (see chapter 4).^{55,56} Depending on the investigated compound (materials or molecular compounds) molecular orbital⁵⁷⁻⁵⁹ or plane wave⁴³ basis sets are applied.

It is known that the transition energy of a charge-transfer transition in the UV/VIS region described by TDDFT crucially depends on the amount of Hartree-Fock-exchange (HF-exchange) of an applied hybrid-functional. The same effect occurs in the pre-edge to near-edge region as shown by Roemelt et al.⁶⁰ and illustrated in figure 9.

Compared to XANES calculations, a reasonable theoretical description of TM K-edge VtC-XES spectra is rather fast and convenient. As shown for many TM compounds, in most cases a ground state DFT description is more than sufficient.^{28,62} There are only a few exceptions where an excited state description was needed to obtain a sufficient description of the experiments.⁶³

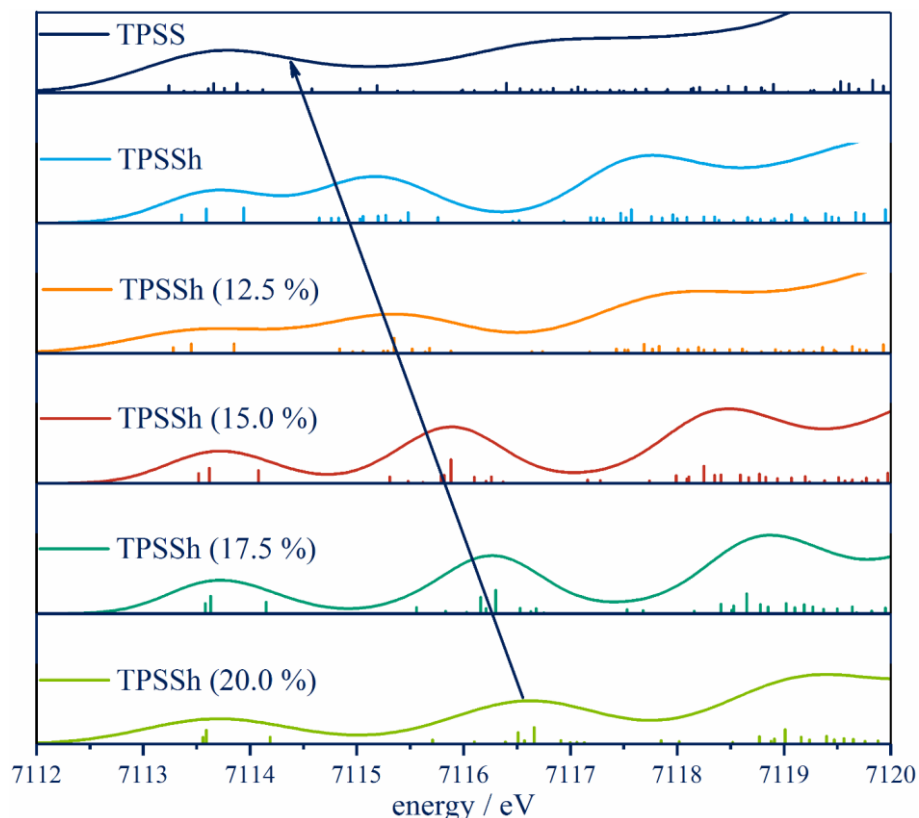


Figure 9. Theoretical Fe K-edge pre-edge spectra including varying percentages of HF-exchange, to illustrate the connection between the charge-transfer energy and the amount of HF-exchange applied in a hybrid functional.⁶¹

2.6. X-ray sources

There are two main methods to produce X-rays: particle accelerators, like synchrotrons or free electron lasers (FELs) and X-ray tubes. The main difference here is the brightness of these sources. X-ray tubes are able to perform in XES and XAS experiments, with the serious restriction of the very low flux compared to synchrotron and XFEL sources. The low flux leads to much longer acquisition times to obtain useful statistics.

However, in the 1970s and 80s, laboratory / table top spectrometer utilizing X-ray tubes as a radiation source were established,⁶⁴ but the large majority of publications in the field of X-ray spectroscopy were conducted on synchrotron-based radiation sources. In the last years more and more publications on table-top spectrometers using X-ray tubes occurred. This is due to the fact, that the brilliance of X-ray tubes has been greatly increased over the last decades and XAS, especially EXAFS (which was the working horse at synchrotrons for many decades) becomes more and more a standard analytic method and therefore the demand on building conventional XAS beamlines or to keep existing ones in service is decreasing.⁶⁵

2.6.1 X-ray tubes

In X-ray tubes, an electron gun or a hot tungsten cathode is used to produce high kinetic energy electrons. This electron beam is guided by a focusing cup (see figure 10) with an applied high potential (25 - 600 kV) towards an anode.²³ The electrons of the electron beam are inelastically scattered by the anode material, where core- or inner-electrons are ejected. The created vacancies, in e.g. the 1s level, are refilled by higher levels and the energy difference between both levels is emitted as an X-ray photon, leading to element specific emission lines as described in chapter 2.1.²³ Additionally, an underground over a wide energy range (1 keV) is observed due to bremsstrahlung, which is naturally occurring when a charged particle (in this case the electron) is decelerated.²³

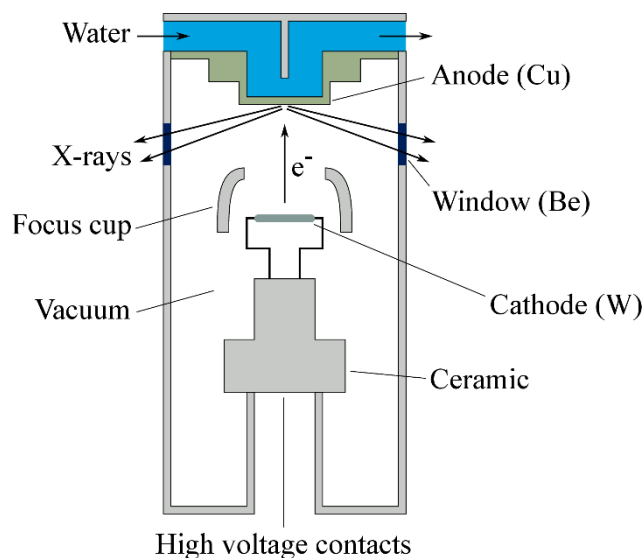


Figure 10. Schematic construction of an X-ray tube.⁶⁶

Since the mean free path of electrons in the gas phase under atmospheric pressure is only 68 nm in air, X-ray tubes need to be operated in vacuum, to increase the mean free path of the electron beam. The steady electron impact is generating great heat on the anode surface, leading to melting of the anode material. Therefore, the anode material needs to be cooled, by e.g. direct cooling via conduction or convection and water cooling.²³

2.6.2 Synchrotron and X-ray free electron laser radiation

As mentioned above, to achieve suitable statistics and signal to noise ratios, high X-ray flux is demanded. The best X-ray sources regarding flux, have been for decades based on the relativistic properties of fast-moving charged particles like electrons, positrons or protons.²³ Synchrotrons and X-ray free electron laser (XFELs) are able to produce high photon flux over a wide energy range, going from the infrared (IR) up to Γ -ray regime of the electromagnetic spectrum.²³ Both synchrotrons and XFELs accelerate charged particles to relativistic velocities. Radiations is produced by deflecting these charged particles under the effect of magnetic fields. The deflections result in a change of the velocity vector and

therefore synchrotron radiation can be understood as a special case of *Bremsstrahlung*. Synchrotrons are ring shaped, whereas XFELs are linear accelerators.²³

Each synchrotron consists of linear and bent sections. In linear sections, electrons are either guided by quadrupoles or led through wigglers or undulators to produce synchrotron radiation, whereas bend sections are realized by bending magnets. To increase the mean free path of the charged particles, the whole ring needs to be hold at a high vacuum. The charged particles are first pre-accelerated with a linear accelerator (LINAC) to several millions of electron volts (MeV), which transfers the particles to a booster ring. In the booster ring, the particles are further accelerated up to several Giga electron volts (GeV) and are guided to the storage ring.²³ If needed, it is possible to further accelerate the particles by radio frequency (RF) electric fields, which are applied in cavities of linear sections. The particles are forced to follow the circular path by bending magnets, where they lose kinetic energy during each turn, emitting synchrotron radiation. The lost kinetic energy is fully recovered, when passing through the RF electric fields in the linear sections.²³

There are four different generations of synchrotron sources that need to be distinguished. The main difference is found in terms of brilliance between each generation.²³ Brilliance B is defined as the quantity of photons ΔN per time t , area A and solid angle $\Delta\Omega$ within a small bandwidth $\frac{\Delta\lambda}{\lambda}$:

$$B = \frac{\Delta N}{t \cdot A \cdot \Delta\Omega \cdot \frac{\Delta\lambda}{\lambda}} \quad (2.6.1)$$

In the first generation, synchrotrons were not built to use synchrotron radiation to conduct experiments. Synchrotron radiation was only a side product of the particle accelerator and has been used in a parasitic way, during high-energy physic experiments. In the second generation, synchrotrons were built exclusively to use the synchrotron radiation, which was mainly produced by bending magnets. The development of Wiggler devices allowed the production of radiation in linear sections for the first time. Afterwards, development of undulators and optimization of wigglers took place, leading to third generation sources. Improvements of third generation sources are still possible, but fourth generation sources are already being developed and built based on free electron lasers (FELs). The characteristics of FELs and fourth generation are very short coherent pulses of very high peak intensity and brilliance.²³

As mentioned above bending magnets, wiggler and undulators are designed to produce synchrotron radiation by deflecting charged particles at relativistic velocities. The following section will cover the fundamentals and working principle of these devices.

2.6.2.1 Moving Charges: Bending Magnets and Insertion devices

An accelerated charge is emitting electromagnetic dipole radiation, as given by numerical solutions of Maxwell equations.⁶⁷ The emitted intensity is proportional to the square of the charge acceleration: $x_0^2 \omega^4$. With the frequency ω of the oscillating charge in the direction x :

$$x = x_0 \cdot \sin(\omega t) \quad (2.6.2)$$

The oscillation amplitude x_0 is decreasing with increasing mass of the charged particle. For this reason, a more intense emission is observed for massive particles like protons than for small-mass electrons.²³ The emitted wavelength λ defined as:

$$\lambda = \frac{2\pi c}{\omega} \quad (2.6.3)$$

, where c is the speed of light. The dipole emission is disappearing along the oscillation and is maximum perpendicular towards the direction x . Therefore, the time-dependent electric field, caused by the oscillation of the charged particle is parallel to the x -axis and the emission is linearly polarized.²³

By considering only the classical mechanisms and typical electron oscillator frequencies present in atoms, the emitted photon energy would correspond to infrared, visible and near-ultraviolet wavelengths. With help of the Doppler Effect it is possible to shift the emission maximum to smaller wavelength into the hard X-ray regime. Therefore, the electron has to move with a constant speed v along the z -direction perpendicular (longitudinal) to the oscillation in x -direction.²³

$$\lambda = \frac{2\pi c}{\omega} \sqrt{\frac{1 - \beta}{1 + \beta}} \quad (2.6.4)$$

, with $\beta = \frac{v^2}{c^2}$.

The resulting wavelength is decreasing extreme (Γ -ray regime) for relativistic electrons. When $v \approx c$, it is given:

$$\frac{1 - \beta}{1 + \beta} = \frac{1 - \beta^2}{(1 + \beta)^2} \approx \frac{1}{4\gamma^2} \quad (2.6.5)$$

, where $\gamma = \frac{1}{\sqrt{1 - \beta^2}}$ is the relativistic γ -factor, i.e. the electron energy in $m_0 c^2$ units.

Therefore equation (4) can be written as:

$$\lambda = \frac{2\pi c}{\omega} \frac{1}{2\gamma} \quad (2.6.6)$$

the γ -factor ranges typically from 10^2 to 10^4 in electron accelerators:

Relativistic longitudinal motion of the electron (motion in z -direction), leads to projection of the dipole radiation in forward direction, with a “torchlight” like emission in z -direction and an extreme narrow emission cone. Furthermore, the brightness (equation (2.6.1)) is greatly enhanced, due to a decrease of the “source size” Σ and angular spread Ω . To realize the combination of transverse electron oscillation and relativistic longitudinal speed additional devices are required. Relativistic speed is automatically produced in particle accelerators like synchrotron storage rings and linear accelerators (LIN-ACs). Only, the transverse oscillation must be added by magnetic devices.²³

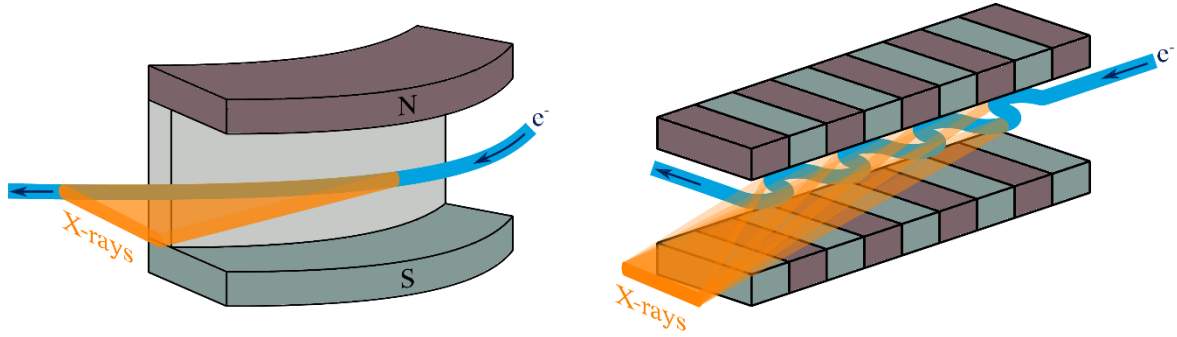


Figure 11. Schematic view of a bending magnet (left) and an insertion device (right).⁶⁶

One typical device to induce transverse oscillation is the insertion device, as illustrated in figure 11. An insertion device consists of two parallel series of dipole magnets, where both series are arranged south opposite to north and vice versa. The charged particle is guided in between both magnet series and the magnetic field applies a periodic Lorentz force, which causes the particle to oscillate. Since the applied Lorentz force does not perform any work, it is not possible to change the overall magnitude of the velocity. Therefore, the induced transverse oscillation goes along with a slower longitudinal motion, which has to be recovered by radiofrequency cavities.²³

There are mainly two different types of insertion devices, undulators and wigglers. Main difference here is the applied magnetic field, undulators are weak field devices whereas wigglers are strong field devices. The stronger field in wigglers leads to a much stronger oscillation of the charged particle, leading to a broad superimposed emission spectrum, whereas the weak field in undulators is characterized by narrow emission lines of given harmonics.²³ To keep the particles in a closed-loop, bending magnets (see figure 11) are used to deflect them in a circular motion, producing synchrotron radiation as a byproduct of the deflection. Similar to Wigglers, bending magnets produce a broadband emission spectrum. Wigglers can be regarded as a series of bending magnets in opposite directions.²³

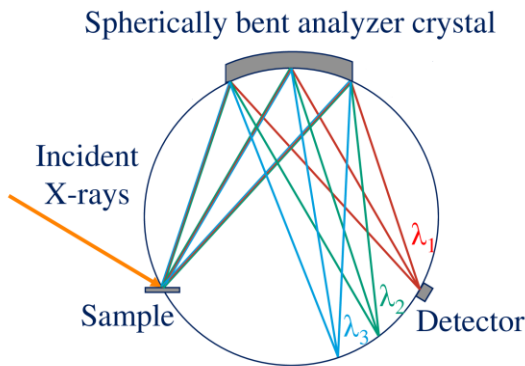
2.7. Spectrometer types

After the excitation of a sample at a given absorption edge by a monochromatized X-ray beam, radiative relaxation of occupied states to the created core-hole occurs as derived in section 2.1. In order to scan the resulting emission energy with high efficiency and energy-resolution an analyzer is needed. All possible high-resolution X-ray detection schemes are based on diffraction of X-rays over crystallographic planes (Bragg) and lattices (Laue)²³ as given by the Bragg equation:

$$n\lambda = 2d \cdot \sin\theta \quad (2.6.7)$$

, where n is the diffraction order, λ the X-ray photon wavelength, d the lattice constant and θ is the Bragg angle. The Bragg equations illustrates that an incident photon with a given photon energy ($h \cdot \nu$) is diffracted by a Bragg crystal at a given angle and vice versa. The use of a reflection (Bragg) or transmission (Laue) geometry, depends on the energy range, where the experiment will be operated. Bragg geometries are typically applied below 20 keV and Laue geometries above 20 keV, where typically larger Bragg angles become inevitable due to the limited choice of appropriate crystals. Bragg geometries are the most common for X-ray emission spectroscopy. In principle there are two different Bragg geometries: focusing and dispersive geometries (see figure 12).²³

Focusing (scanning) geometry



Dispersive geometry

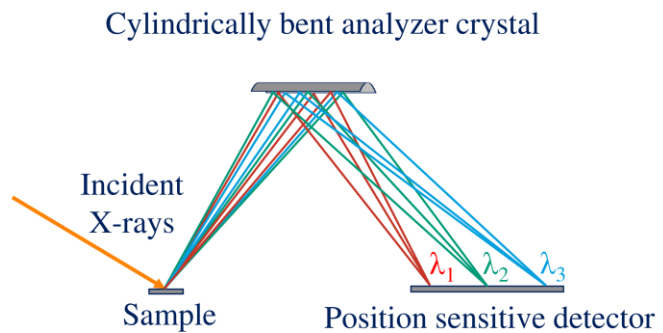


Figure 12. Schematic construction of a spectrometer in scanning geometry (left) and dispersive geometry (right).

In dispersive geometries (see figure 12, right) like the von Hamos geometry, there is no need to scan the emission energy, since cylindrically bent crystals in combination with a position sensitive detector are used.⁶⁸ The cylindrically bent analyzers diffract simultaneously X-rays over a range of Bragg angles, each photon energy is focused on a different spot of the position sensitive detector. Therefore, it is possible to record the whole emission spectrum within a single pulse (in theory, at high flux and high sample concentrations), leading to an outstanding data acquisition time. For this reason, von Hamos

spectrometers are often applied in time-depending experiments, like pump-probe or in-situ experiments.²³

In focusing geometries (see figure 12), the sample, a spherically bent analyzer crystal with a curvature of twice the Rowland circle radius $2R$ and a solid-state detector are arranged in a so-called Rowland circle. The resulting polychromatic emission of the previous excited sample is collected by a spherically bent analyzer, which diffracts the photon depending on its energy at a given resulting Bragg angle (depending on the X-ray photon energy). Each photon energy is therefore focused on a different spot of the Rowland circle and can be independently recorded by moving the crystals and or the detector in the Rowland circle, while the sample stays fixed. To increase the captured solid angle, multiple crystals are used, located on overlapping Rowland circles. There are mainly two different types of scanning spectrometers, the Johann and Johansson type (see figure 13).²³

In the traditional Johann approach, proposed in 1931, cylindrically bent crystals were used.⁶⁹ Nowadays Johann and Johansson are using spherically bent analyzer crystals, where the crystallographic planes are bent to a curvature with twice the radius of the Rowland circle $2R$, leading to a pencil-shaped focus. The main difference between both types is that the crystals in the Johansson spectrometer are ground to the same curvature as the Rowland circle with the radius R (see figure 14).⁷⁰ For this reason, Johansson spectrometers are exactly focusing and are able to solve the incremental variation of incident angles transverses to the crystal of a Johann-type spectrometer, which enables the use of near backscattering geometries. Therefore Johansson-type spectrometers are very powerful in the low-energy tender X-ray regime (1.4 - 4.5 eV) where typically smaller Bragg angles become inevitable due to the limited choice of appropriate crystals.²³

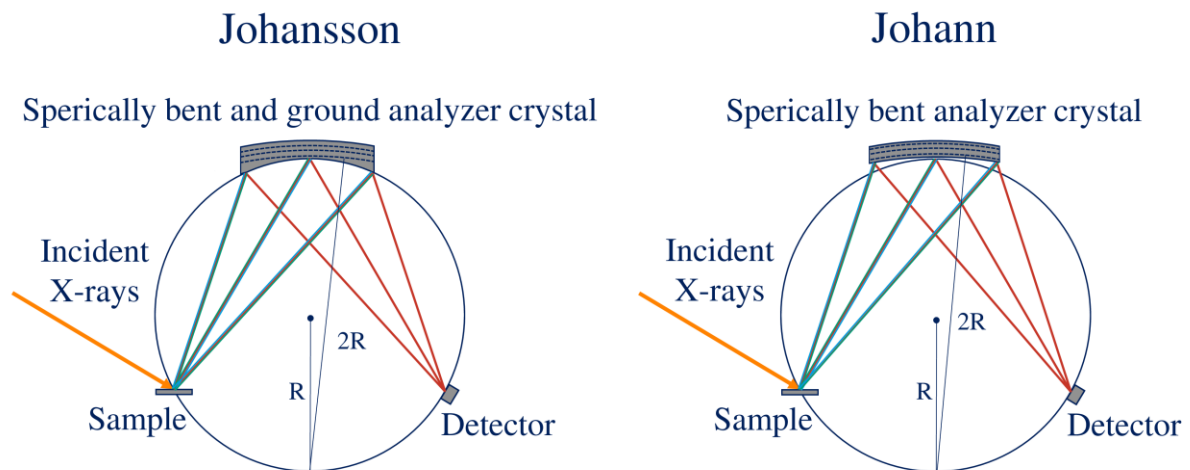


Figure 13. Schematic construction of a spectrometer in Johansson geometry (left) and Johann geometry (right).

3. References

- (1) Bau, R.; Teller, R. G.; Kirtley, S. W.; Koetzle, T. F. Structures of transition-metal hydride complexes. *Acc. Chem. Res.* **2002**, *12*, 176-183.
- (2) Ott, J. C.; Wadehohl, H.; Enders, M.; Gade, L. H. Taking Solution Proton NMR to Its Extreme: Prediction and Detection of a Hydride Resonance in an Intermediate-Spin Iron Complex. *J. Am. Chem. Soc.* **2018**, DOI: 10.1021/jacs.8b11330.
- (3) Pelmenchikov, V.; Gee, L. B.; Wang, H.; MacLeod, K. C.; McWilliams, S. F.; Skubi, K. L.; Cramer, S. P.; Holland, P. L. High-Frequency Fe-H Vibrations in a Bridging Hydride Complex Characterized by NRVS and DFT. *Angew. Chem.* **2018**, *130*, 9511-9515.
- (4) Hugenbruch, S.; Shafaat, H. S.; Krämer, T.; Delgado-Jaime, M. U.; Weber, K.; Neese, F.; Lubitz, W.; DeBeer, S. In search of metal hydrides: An X-ray absorption and emission study of NiFe hydrogenase model complexes. *Phys. Chem. Chem. Phys.* **2016**, *18*, 10688-10699.
- (5) Leidel, N.; Hsieh, C.-H.; Chernev, P.; Sigfridsson, K. G. V.; Darensbourg, M. Y.; Haumann, M. Bridging-hydride influence on the electronic structure of an FeFe hydrogenase active-site model complex revealed by XAES-DFT. *Dalton Trans.* **2013**, *42*, 7539-7554.
- (6) Chernev, P.; Lambertz, C.; Brünje, A.; Leidel, N.; Sigfridsson, K. G. V.; Kositzki, R.; Hsieh, C.-H.; Yao, S.; Schiwon, R.; Driess, M. *et al.* Hydride binding to the active site of FeFe-hydrogenase. *Inorg. Chem.* **2014**, *53*, 12164-12177.
- (7) Enemark, J. H.; Feltham, R. D. Principles of structure, bonding, and reactivity for metal nitrosyl complexes. *Coord. Chem. Rev.* **1974**, *13*, 339-406.
- (8) Bauer, M. HERFD-XAS and valence-to-core-XES: New tools to push the limits in research with hard X-rays? *Phys. Chem. Chem. Phys.* **2014**, *16*, 13827-13837.
- (9) Lu, T.-T.; Weng, T.-C.; Liaw, W.-F. X-Ray Emission Spectroscopy: A Spectroscopic Measure for the Determination of NO Oxidation States in Fe-NO Complexes. *Angew. Chem.* **2014**, *126*, 11746-11750.
- (10) Wenger, O. S. Is Iron the New Ruthenium? *Chemistry* **2019**, DOI: 10.1002/chem.201806148.
- (11) Berera, R.; van Grondelle, R.; Kennis, J. T. M. Ultrafast transient absorption spectroscopy: Principles and application to photosynthetic systems. *Photosynth Res.* **2009**, *101*, 105-118.
- (12) Barkla, C. G. XXXIX. The spectra of the fluorescent Röntgen radiations. *Philos. Mag.* **2009**, *22*, 396-412.
- (13) SIEGBAHN, M. Relations between the K and L Series of the High-Frequency Spectra. *Nature* **1916**, *96*, 676.
- (14) Jenkins, R.; Manne, R.; Robin, R.; Senemaud, C. IUPAC—nomenclature system for x-ray spectroscopy. *X-Ray Spectrom.* **1991**, *20*, 149-155.

- (15) Sarode, P. R.; Ramasesha, S.; Madhusudan, W. H.; Rao, C. N. R. Relation between effective atomic charge and chemical shifts in X-ray absorption spectra of transition-metal compounds. *J. Phys. C: Solid State Phys.* **1979**, *12*, 2439-2445.
- (16) Evans, R. D. *The atomic nucleus*, Repr. d. Ausg. 1955; Malabar, Fla., 1985.
- (17) Glatzel, P.; Bergmann, U. High resolution 1s core hole X-ray spectroscopy in 3d transition metal complexes—electronic and structural information. *Coord. Chem. Rev.* **2005**, *249*, 65-95.
- (18) Glatzel, P.; Weng, T.-C.; Kvashnina, K.; Swarbrick, J.; Sikora, M.; Gallo, E.; Smolentsev, N.; Mori, R. A. Reflections on hard X-ray photon-in/photon-out spectroscopy for electronic structure studies. *J. Electron Spectrosc. Relat. Phenom.* **2013**, *188*, 17-25.
- (19) Burkhardt, L.; Bauer, M. unpublished results.
- (20) Schepper, R.; Bauer, M. unpublished results.
- (21) Pollock, C. J.; Delgado-Jaime, M. U.; Atanasov, M.; Neese, F.; DeBeer, S. K β mainline X-ray emission spectroscopy as an experimental probe of metal-ligand covalency. *J. Am. Chem. Soc.* **2014**, *136*, 9453-9463.
- (22) Petric, M.; Bohinc, R.; Bučar, K.; Nowak, S. H.; Žitnik, M.; Kavčič, M. Electronic Structure of Third-Row Elements in Different Local Symmetries Studied by Valence-to-Core X-ray Emission Spectroscopy. *Inorg. Chem.* **2016**, *55*, 5328-5336.
- (23) van Bokhoven, J. A.; Lamberti, C. *X-Ray Absorption and X-Ray Emission Spectroscopy*; John Wiley & Sons, Ltd: Chichester, UK, **2016**.
- (24) Arrio, M.-A.; Rossano, S.; Brouder, C.; Galois, L.; Calas, G. Calculation of multipole transitions at the Fe K pre-edge through p - d hybridization in the Ligand Field Multiplet model. *Europhys. Lett.* **2000**, *51*, 454-460.
- (25) Yamamoto, T. Assignment of pre-edge peaks in K-edge x-ray absorption spectra of 3d transition metal compounds: Electric dipole or quadrupole? *X-Ray Spectrom.* **2008**, *37*, 572-584.
- (26) Martin-Diaconescu, V.; Chacón, K. N.; Delgado-Jaime, M. U.; Sokaras, D.; Weng, T.-C.; DeBeer, S.; Blackburn, N. J. K β Valence to Core X-ray Emission Studies of Cu(I) Binding Proteins with Mixed Methionine - Histidine Coordination. Relevance to the Reactivity of the M- and H-sites of Peptidylglycine Monooxygenase. *Inorg. Chem.* **2016**, *55*, 3431-3439.
- (27) Pollock, C. J.; Lancaster, K. M.; Finkelstein, K. D.; DeBeer, S. Study of iron dimers reveals angular dependence of valence-to-core X-ray emission spectra. *Inorg. Chem.* **2014**, *53*, 10378-10385.
- (28) Lee, N.; Petrenko, T.; Bergmann, U.; Neese, F.; DeBeer, S. Probing valence orbital composition with iron K β X-ray emission spectroscopy. *J. Am. Chem. Soc.* **2010**, *132*, 9715-9727.
- (29) Pollock, C. J.; DeBeer, S. Insights into the geometric and electronic structure of transition metal centers from valence-to-core X-ray emission spectroscopy. *Acc. Chem. Res.* **2015**, *48*, 2967-2975.
- (30) Pollock, C. J.; DeBeer, S. Valence-to-core X-ray emission spectroscopy: A sensitive probe of the nature of a bound ligand. *J. Am. Chem. Soc.* **2011**, *133*, 5594-5601.

- (31) Chandrasekaran, P.; Chiang, K. P.; Nordlund, D.; Bergmann, U.; Holland, P. L.; DeBeer, S. Sensitivity of X-ray core spectroscopy to changes in metal ligation: A systematic study of low-coordinate, high-spin ferrous complexes. *Inorg. Chem.* **2013**, *52*, 6286-6298.
- (32) Lancaster, K. M.; Finkelstein, K. D.; DeBeer, S. K β X-ray emission spectroscopy offers unique chemical bonding insights: Revisiting the electronic structure of ferrocene. *Inorg. Chem.* **2011**, *50*, 6767-6774.
- (33) Kowalska, J.; DeBeer, S. The role of X-ray spectroscopy in understanding the geometric and electronic structure of nitrogenase. *Biochim. Biophys. Acta* **2015**, *1853*, 1406-1415.
- (34) Rees, J. A.; Bjornsson, R.; Schlesier, J.; Sippel, D.; Einsle, O.; DeBeer, S. The Fe-V Cofactor of Vanadium Nitrogenase Contains an Interstitial Carbon Atom. *Angew. Chem., Int. Ed. Engl.* **2015**, *54*, 13249-13252.
- (35) Groot, F. de; Vankó, G.; Glatzel, P. The 1s x-ray absorption pre-edge structures in transition metal oxides. *J. Phys. Condens. Matter* **2009**, *21*, 104207.
- (36) Shimizu, K.-i.; Maeshima, H.; Yoshida, H.; Satsuma, A.; Hattori, T. Ligand field effect on the chemical shift in XANES spectra of Cu(II) compounds. *Phys. Chem. Chem. Phys.* **2001**, *3*, 862-866.
- (37) Kau, L. S.; Spira-Solomon, D. J.; Penner-Hahn, J. E.; Hodgson, K. O.; Solomon, E. I. X-ray absorption edge determination of the oxidation state and coordination number of copper. Application to the type 3 site in *Rhus vernicifera* laccase and its reaction with oxygen. *J. Am. Chem. Soc.* **1987**, *109*, 6433-6442.
- (38) Uozumi, T.; Okada, K.; Kotani, A.; Durmeyer, O.; Kappler, J. P.; Beaurepaire, E.; Parlebas, J. C. Experimental and Theoretical Investigation of the Pre-Peaks at the Ti K -Edge Absorption Spectra in TiO₂. *Europhys. Lett.* **1992**, *18*, 85-90.
- (39) Tromp, M.; Moulin, J.; Reid, G.; Evans, J. Cr K-Edge XANES Spectroscopy: Ligand and Oxidation State Dependence — What is Oxidation State? In *AIP Conference Proceedings*; AIP, **2007**; pp 699-701.
- (40) Kramers, H. A.; Heisenberg, W. Über die Streuung von Strahlung durch Atome. *Z. Physik* **1925**, *31*, 681-708.
- (41) Härmäläinen; Siddons; Hastings; Berman. Elimination of the inner-shell lifetime broadening in x-ray-absorption spectroscopy. *Phys. Rev. Lett.* **1991**, *67*, 2850-2853.
- (42) Groot, F. M. F. de; Krisch, M. H.; Vogel, J. Spectral sharpening of the Pt L edges by high-resolution x-ray emission. *Phys. Rev. B* **2002**, *66*, 621.
- (43) Vollmers, N. J.; Müller, P.; Hoffmann, A.; Herres-Pawlis, S.; Rohrmüller, M.; Schmidt, W. G.; Gerstmann, U.; Bauer, M. Experimental and Theoretical High-Energy-Resolution X-ray Absorption Spectroscopy: Implications for the Investigation of the Entatic State. *Inorg. Chem.* **2016**, *55*, 11694-11706.
- (44) Atkins, A. J.; Bauer, M.; Jacob, C. R. High-resolution X-ray absorption spectroscopy of iron carbonyl complexes. *Phys. Chem. Chem. Phys.* **2015**, *17*, 13937-13948.

- (45) Zhang, H. H., B. Hedman, and K. O. Hodgson. X-ray absorption spectroscopy and EXAFS analysis: the multiple-scattering method and applications in inorganic and bioinorganic chemistry. *Inorg. Electron. Struct. Spectrosc.*, 1999, 513-554.
- (46) Levina, A.; Armstrong, R. S.; Lay, P. A. Three-dimensional structure determination using multiple-scattering analysis of XAFS: Applications to metalloproteins and coordination chemistry. *Coord. Chem. Rev.* **2005**, 249, 141-160.
- (47) Shirley, E. L. Ab Initio Inclusion of Electron-Hole Attraction: Application to X-Ray Absorption and Resonant Inelastic X-Ray Scattering. *Phys. Rev. Lett.* **1998**, 80, 794-797.
- (48) Coriani, S.; Fransson, T.; Christiansen, O.; Norman, P. Asymmetric-Lanczos-Chain-Driven Implementation of Electronic Resonance Convergent Coupled-Cluster Linear Response Theory. *J. Chem. Theory Comput.* **2012**, 8, 1616-1628.
- (49) Peng, B.; Lestrang, P. J.; Goings, J. J.; Caricato, M.; Li, X. Energy-Specific Equation-of-Motion Coupled-Cluster Methods for High-Energy Excited States: Application to K-edge X-ray Absorption Spectroscopy. *J. Chem. Theory Comput.* **2015**, 11, 4146-4153.
- (50) List, N. H.; Coriani, S.; Christiansen, O.; Kongsted, J. Identifying the Hamiltonian structure in linear response theory. *J. Chem. Phys.* **2014**, 140, 224103.
- (51) Sassi, M.; Pearce, C. I.; Bagus, P. S.; Arenholz, E.; Rosso, K. M. First-Principles Fe L_{2,3}-Edge and O K-Edge XANES and XMCD Spectra for Iron Oxides. *J. Phys. Chem. A* **2017**, 121, 7613-7618.
- (52) Rehr, J. J.; Ankudinov, A. L. Progress in the theory and interpretation of XANES. *Coord. Chem. Rev.* **2005**, 249, 131-140.
- (53) Dutta, A. K.; Gupta, J.; Vaval, N.; Pal, S. Intermediate Hamiltonian Fock Space Multireference Coupled Cluster Approach to Core Excitation Spectra. *J. Chem. Theory Comput.* **2014**, 10, 3656-3668.
- (54) Brabec, J.; Bhaskaran-Nair, K.; Govind, N.; Pittner, J.; Kowalski, K. Communication: Application of state-specific multireference coupled cluster methods to core-level excitations. *J. Chem. Phys.* **2012**, 137, 171101.
- (55) DeBeer George, S.; Petrenko, T.; Neese, F. Prediction of iron K-edge absorption spectra using time-dependent density functional theory. *J. Phys. Chem. A* **2008**, 112, 12936-12943.
- (56) Besley, N. A. Fast Time-Dependent Density Functional Theory Calculations of the X-ray Absorption Spectroscopy of Large Systems. *J. Chem. Theory Comput.* **2016**, 12, 5018-5025.
- (57) Westre, T. E.; Kennepohl, P.; DeWitt, J. G.; Hedman, B.; Hodgson, K. O.; Solomon, E. I. A Multiplet Analysis of Fe K-Edge 1s \rightarrow 3d Pre-Edge Features of Iron Complexes. *J. Am. Chem. Soc.* **1997**, 119, 6297-6314.
- (58) DuBois, J. L.; Mukherjee, P.; Stack, T. D. P.; Hedman, B.; Solomon, E. I.; Hodgson, K. O. A Systematic K-edge X-ray Absorption Spectroscopic Study of Cu(III) Sites. *J. Am. Chem. Soc.* **2000**, 122, 5775-5787.

- (59) George, S. D.; Brant, P.; Solomon, E. I. Metal and ligand K-edge XAS of organotitanium complexes: Metal 4p and 3d contributions to pre-edge intensity and their contributions to bonding. *J. Am. Chem. Soc.* **2005**, *127*, 667-674.
- (60) Roemelt, M.; Beckwith, M. A.; Duboc, C.; Collomb, M.-N.; Neese, F.; DeBeer, S. Manganese K-edge X-ray absorption spectroscopy as a probe of the metal-ligand interactions in coordination compounds. *Inorg. Chem.* **2012**, *51*, 680-687.
- (61) Burkhardt, L.; Holzwarth, M.; Plietker, B.; Bauer, M. Detection and Characterization of Hydride Ligands in Iron Complexes by High-Resolution Hard X-ray Spectroscopy and Implications for Catalytic Processes. *Inorg. Chem.* **2017**, *56*, 13300-13310.
- (62) Beckwith, M. A.; Roemelt, M.; Collomb, M.-N.; Duboc, C.; Weng, T.-C.; Bergmann, U.; Glatzel, P.; Neese, F.; DeBeer, S. Manganese K β X-ray emission spectroscopy as a probe of metal-ligand interactions. *Inorg. Chem.* **2011**, *50*, 8397-8409.
- (63) Zhang, Y.; Mukamel, S.; Khalil, M.; Govind, N. Simulating Valence-to-Core X-ray Emission Spectroscopy of Transition Metal Complexes with Time-Dependent Density Functional Theory. *J. Chem. Theory Comput.* **2015**, *11*, 5804-5809.
- (64) Williams, A. Laboratory x-ray spectrometer for EXAFS and XANES measurements. *Rev. Sci. Instrum.* **1983**, *54*, 193-197.
- (65) Jahrman, E. P.; Holden, W. M.; Ditter, A. S.; Mortensen, D. R.; Seidler, G. T.; Fister, T. T.; Kozimor, S. A.; Piper, L. F. J.; Rana, J.; Hyatt, N. C., et al. An Improved Laboratory-Based XAFS and XES Spectrometer for Analytical Applications in Materials Chemistry Research. *Rev. Sci. Instrum.* **2019**, *90*, 024106, DOI: 10.1063/1.5049383.
- (66) Schoch, R. *Active species identification of iron-based homogeneously and heterogeneously catalyzed reactions*. Disstertation, **2017**.
- (67) Yee, K. Numerical solution of initial boundary value problems involving maxwell's equations in isotropic media. *IEEE Trans. Antennas Propagat.* **1966**, *14*, 302-307.
- (68) Hámos, L. v. Röntgenspektroskopie und Abbildung mittels gekrümmter Kristallreflektoren. *Naturwissenschaften* **1932**, *20*, 705-706.
- (69) Johann, H. H. Die Erzeugung lichtstarker Röntgenspektren mit Hilfe von Konkavkristallen. *Z. Physik* **1931**, *69*, 185-206.
- (70) Johansson, T. ber ein neuartiges, genau fokussierendes Röntgenspektrometer. *Z. Physik* **1933**, *82*, 507-528.

4. Publications

4.1 Detection and Characterization of Hydride Ligands in Iron Complexes by High-Resolution Hard X-ray Spectroscopy and Implications for Catalytic Processes

Burkhardt, L.; Holzwarth, M.; Plietker, B.; Bauer, M. *Inorg. Chem.* **2017**, *56*, 13300-13310.

Two low-valent iron hydride complexes and their non-hydride analogues are investigated by VtC-XES and HERFD-XANES combined with (TD)DFT. These complexes serve as model compounds to investigate the strength of modern hard X-ray spectroscopy to probe TM-hydride interactions of terminal hydride complexes. Bonding Fe-hydride interactions contribute significantly to Fe K-edge VtC-XES features, whereas antibonding Fe-hydride interactions show only minor contributions to pre-edge features.

Participation in this Publication

L. Burkhardt: X-ray spectroscopy, simulation of VtC-XES and HERFD-XANES spectra, manuscript preparation

M. Holzwarth and B. Plietker: synthesis of all investigated compounds

M. Bauer: corresponding author

Detection and Characterization of Hydride Ligands in Iron Complexes by High-Resolution Hard X-ray Spectroscopy and Implications for Catalytic Processes

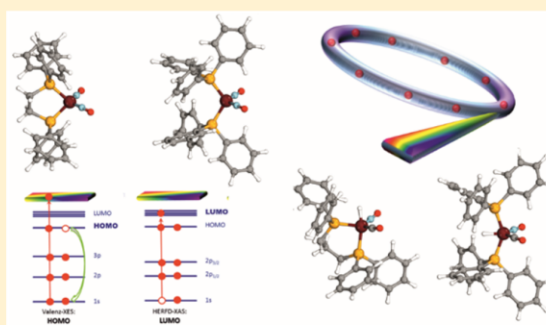
Lukas Burkhardt,[†] Michael Holzwarth,[‡] Bernd Plietker,[‡] and Matthias Bauer^{*,†,§}

[†]Department Chemie, Universität Paderborn, Warburger Straße 100, D-33098 Paderborn, Germany

[‡]Institut für Organische Chemie, Universität Stuttgart, Pfaffenwaldring 55, D-70569 Stuttgart, Germany

S Supporting Information

ABSTRACT: Two hydride catalysts $[\text{Fe}(\text{CO})(\text{dppp})\text{H}(\text{NO})]$ (dppp = 1,3-bis(diphenylphosphino)propane) and $[\text{Fe}(\text{CO})\text{H}(\text{NO})(\text{PPh}_3)_2]$ in comparison with nonhydride analogues $[\text{Fe}(\text{dppe})(\text{NO})_2]$ (dppe = 1,3-bis(diphenylphosphino)ethane) and $[\text{Fe}(\text{NO})_2(\text{PPh}_3)_2]$ are investigated with a combination of valence-to-core X-ray emission spectroscopy (VtC-XES) and high-energy resolution fluorescence detected X-ray absorption near-edge structure (HERFD-XANES). To fully understand the experiments and to obtain precise information about molecular levels being involved in the spectral signals, time-dependent density functional theory (TD-DFT) calculations and ground state density functional theory (DFT) calculations are necessary. An excellent agreement between experiment and theory allows the identification of particular spectral signals of the Fe–H group. Antibonding Fe–H interactions clearly contribute to pre-edge signals in HERFD-XANES spectra, while bonding Fe–H interactions cause characteristic signatures in the VtC-XES spectra. The sensitivity of both methods with respect to the Fe–H distance is demonstrated by a scanning simulation approach. The results open the way to study metal hydride complexes in situ, their formation, and their fate during catalytic reactions, using high-resolution XANES and valence-to-core X-ray emission spectroscopy.



INTRODUCTION

Transition metal hydrides are of great importance in biological and chemical catalysis. They are known as active compounds or intermediates^{1–9} for many chemical transformations, for hydrogen storage,¹⁰ or in renewable energy¹¹ applications like water reduction.¹² In nature enzymes like FeFe- and/or NiFe-hydrogenases^{13–16} catalyze hydrogen formation via transition metal hydrides with very high rates.¹⁶ Since this process works only under anaerobic conditions, a transfer to industrial H_2 production requires more oxygen tolerant catalysts. Such catalysts could be mononuclear iron hydride complexes coordinated by nitrosyl, carbonyl, or bidentate phosphine ligands, which for example catalyze hydrogen formation via dehydrogenative silylation of alcohols.¹⁷

To understand the working principle of hydrogenases, their related biomimetic complexes, or metal complexes catalyzing hydrogen formation and hydrogen transfer, experimental methods to access their geometric and electronic structure in the corresponding in situ environment are required. Basically, spectroscopic or scattering methods usually provide either of the two parameters. However, most of these methods have more or fewer limitations: Vibrational spectroscopy is a powerful tool to determine both the electronic and geometric structure if combined with theoretical calculations.^{18,19} None-

theless, it can be very challenging if not impossible if the oscillator strength of the investigated vibration is weak or overlapped by ligand, solvent, or co-reactant frequencies. Mössbauer spectroscopy is mostly sensitive to the electronic structure,^{20,21} but usually requires enrichment of the sample with ^{57}Fe and can only be applied in the solid state or under certain conditions in frozen solution.²² In contrast EPR spectroscopy requires unpaired electrons to be present. Finally, neutron diffraction could be a powerful technique due to the large scattering length of ^2H , but of course it requires selective deuteration.²³ X-ray scattering fails for hydride species due to the small scattering amplitude of hydrogen;²³ even with high-quality data it is challenging to distinguish hydrogen atoms from the background noise.

X-ray absorption spectroscopy (XAS)²⁴ and X-ray emission spectroscopy (XES)²⁵ using hard X-rays at metal K-edges are promising methods to overcome these limitations without being subject to any experimental restrictions: Since hard X-ray are used, practically any experimental or in situ environment can be tolerated. While XAS can be roughly divided into a XANES (X-ray absorption near-edge structure)²⁶ region

Received: August 13, 2017

Published: October 23, 2017

including the pre-edge signal²⁷ and the EXAFS (extended X-ray absorption fine structure) region,²⁸ XES can be divided into core-to-core (CtC) and valence-to-core (VtC) emission.^{25,29}

Although few attempts exist to identify hydrogen ligands using EXAFS,^{30–33} the method is rather unsuited, since the physical origin of EXAFS is the backscattering of an outgoing photoelectron from the X-ray absorbing atom at neighboring ligands.³⁴ Consequently, the backscattering signal of a neighbor atom depends on its form factor, which is minimal in the case of hydrogen. Similarly, core-to-core XES is not suited to detect hydrogen ligands, as it is sensitive to the p–d exchange interaction and thus mainly reflects the total d-spin at an X-ray absorbing metal center.^{35,36}

In contrast, both XANES spectroscopy and valence-to-core XES should in principle be able to structurally characterize complexes containing hydrogen ligands and to identify and investigate the metal–hydrogen interaction, as these techniques probe electronic structure details of the HOMO and LUMO states.³⁷ It is particularly the pre-edge signal in transition metal K-edge XANES spectra which carries the main information about the unoccupied 3d levels and LUMO states, respectively. This is due to the fact that this prepeaks originate from $1s \rightarrow M$ 3d/LUMOs transitions.²⁴ The energetic order of the LUMO states is strongly influenced by the coordination symmetry and the oxidation state of the central atom. Unfortunately, many of these details are masked by the lifetime broadening of the $1s$ electron hole in the final state.²⁵ In order to overcome this reduced resolution, Eisenberger et al. proposed in the mid-80s of the 20th century a technique currently called high-energy resolution fluorescence detected XANES (HERFD-XANES) that reduces the lifetime broadening by detection of the XAS spectrum using the intensity of the emitted fluorescence in a narrow energy bandwidth.³⁸

On the other hand, K-edge VtC-XES^{39,40} offers a unique probe of the HOMO levels.⁴¹ In this technique the $1s$ electron is excited nonresonantly into the continuum, and the radiative HOMOs $\rightarrow 1s$ relaxation channel is monitored. Consequently, VtC-XES is highly sensitive to different ligand types, their distance, and their coordination details.^{42–48} Since, of course also hydrogen ligands are involved in HOMO states of hydride complexes, this technique can be applied complementarily to HERFD-XANES for investigations of such compounds.

The combination of both methods is thus anticipated to be a powerful tool to follow changes of transition metal complexes in general and at the metal hydride bond in particular, during catalytic reactions. However, both methods have so far not been applied to study reactions with metal–hydride species as active catalysts or key intermediates. To the best of our knowledge, only hydrides bound to the metal center of hydrogenase model complexes were investigated with X-ray absorption spectroscopy and VtC-XES by the work groups of DeBeer and Haumann.^{49–51} We therefore chose the two hydride complexes $[\text{Fe}(\text{CO})(\text{dppp})\text{H}(\text{NO})]$ and $[\text{Fe}(\text{CO})\text{H}(\text{NO})(\text{PPh}_3)_2]$ as effective catalysts for hydrogen formation via dehydrogenative silylation of alcohols¹⁷ to establish the methodological combination of HERFD-XANES and VtC-XES for the investigation of hydride complexes and especially of the Fe–H bond using hard X-rays. These methods will allow to follow the fate of Fe–H groups in catalytic reactions *in situ* and *in operando*, since it will be also proven that the application of both methods can detect changing bond details in the course of catalytic reactions.

EXPERIMENTAL SECTION

Materials. Compounds **(1)** $[\text{Fe}(\text{dppe})(\text{NO})_2]$ and **(2)** $[\text{Fe}(\text{NO})_2(\text{PPh}_3)_2]$, and **(1H)** $[\text{Fe}(\text{CO})(\text{dppp})\text{H}(\text{NO})]$ and **(2H)** $[\text{Fe}(\text{CO})\text{H}(\text{NO})(\text{PPh}_3)_2]$, were synthesized according to reported procedures.^{17,52,53} For XES and HERFD-XANES measurements, solid samples of all investigated compounds were diluted with BN in a ratio of approximately 1:4 and sealed with Kapton tape. Handling of all samples was performed under an inert atmosphere in a glovebox.

HERFD-XANES and VtC-XES measurements were carried out at beamline ID26 of the European Synchrotron Radiation Facility ESRF (Grenoble, France). For the measurements, two u35 undulators were used. The incident X-ray beam had a flux of approximately 2×10^{13} photons s^{-1} on the sample position. All measurements were conducted at 15 K using a He cryostat under vacuum conditions. Measurements were conducted with a Johann-type X-ray emission spectrometer in the horizontal plane, where the sample, crystal analyzers, and photon detector (avalanche photodiode) were arranged in a vertical Rowland geometry. Calibration of the emission spectrometer was performed using the elastic scattering line. The incident energy was selected using the $\langle 311 \rangle$ reflection from a double Si crystal monochromator. The HERFD-XANES spectra at the Fe K-edge were obtained by recording the intensity of the Fe $K\beta_{1,3}$ emission line as a function of the incident energy. The emission energy was selected using the $\langle 620 \rangle$ reflection of five spherically bent Ge crystal analyzers (with $R = 1$ m) aligned at 80° Bragg angle. The total fluorescence yield (TFY) was monitored by a photodiode installed at about 90° scattering angle and at 45° to the sample surface. The spectral features in the conventional XANES experiments are broadened by 5.3 eV at the Fe K-edge due to the $1s$ core-hole lifetime. The HERFD signal exhibits a better signal-to-noise ratio and shows a sharpening of the absorption features.^{54,55} During the XANES scans, the undulators were kept at a fixed gap, and only the monochromator angle was changed. Each HERFD-XANES measurement was carried out in 60 s, with four spectra, each measured at a different spot of the homogeneous sample, averaged. To exclude radiation damage, fast measurements over the prepeak with a scan-time of 4 s were carried out before and after each long HERFD-XANES measurement. Within these time frames, no radiation damage could be detected.

For the VtC-XES data collection, an incident energy of 7.2 keV was chosen. VtC-XES energy scans were carried out in the range from 7080 to 7130 eV. Four 60 s scans were measured, utilizing a different sample spot for each scan. Care was taken that all spectra were of identical intensity. The four spectra were averaged and then merged with a spectrum of the $K\beta_{1,3}$ main line. Furthermore, to exclude radiation damage, fast measurements over the energy region 7110–7146 eV with a scan-time of 4 s were carried out before and after each long VtC-XES measurement. Within these time frames, no radiation damage was detected.

Since the VtC-XES region is superimposed with the slope of the $K\beta$ main line, all four VtC-XES spectra had to be background corrected. For this purpose, the $K\beta$ main line slope was fitted by a pseudo-Voigt function, and the experiments were subtracted by the resulting fit. Normalization of VtC-XES and HERFD-XANES spectra was achieved by dividing each point by the sum of all intensity values.

Theoretical Calculations. All calculations were performed with the ORCA quantum chemistry package (version 3.0.3).⁵⁶ Unconstrained geometry optimization was performed on all compounds using the TPSSH^{57,58} functional in conjunction with the RIJCOSX approximation⁵⁹ and the def2-TZVP basis set⁶⁰ on all atoms, combined with the def2-TZVP/J auxiliary basis set.^{61,62} Crystal structures of the components were used as a starting point for the gas phase structure optimization of complexes **1**, **2**, and **2H**.^{63–65}

TD-DFT^{66,67} XANES calculations were accomplished using a modified TPSSH functional, with an adjusted Hartree–Fock exchange⁶⁸ of 12.5% (ScalHFX = 0.125) in conjunction with the RIJCOSX approximation and the def2-TZVP basis set, combined with the def2-TZVP/J auxiliary basis set (with a special integration accuracy of 5) on all atoms except Fe, for which the expanded CP(PPP) basis set⁶⁹ (with a special integration accuracy of 7) was used. VtC-XES

spectra were calculated with a one electron approach,⁴² in which the nonhybrid TPSS functional⁷⁰ in conjunction with the RI-J approximation instead of TPSSh was used. Although it was shown in previous studies that calculated VtC-XES intensities exhibit reduced errors utilizing optimized structures compared to crystal structures,⁴² both approaches were performed with a single point protocol on optimized structures.

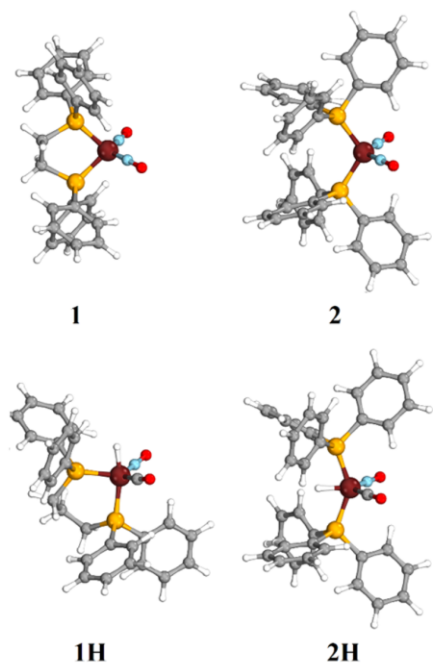
The calculated TD-DFT XANES transitions were broadened by a 1.5 eV Gaussian (fwhm) and DFT VtC-XES transitions by a 2.5 eV Gaussian (fwhm). Calculated TD-DFT XANES spectra were shifted by 151.3 eV. DFT VtC-XES spectra were shifted by 169.5 eV.

Fragment population projections from these calculations for VtC-XES spectra were performed using MOAnalyzer (version 1.3).⁷¹ Intrinsic bond orbitals⁷² were generated with the IBO-View program (version 20150427).⁷³ Orbital populations were extracted via Löwdin reduced orbital population analysis (LROP).^{74,75} Individual fragment projections of VtC-XES spectra were performed by selecting only donor orbitals with significant density values of a given element via LROP.

RESULTS

Experimental Results. Scheme 1 shows the geometry optimized structures of the compounds under investigation, the

Scheme 1. Gas Phase Structures of Complexes 1, 2, 1H, and 2H



{Fe(NO)₂}¹⁰ reference complexes [Fe(dppe)(NO)₂] (**1**) and [Fe(NO)₂(PPh₃)₂] (**2**) and the catalytically relevant {Fe(NO)}⁸ hydride complexes [Fe(CO)(dppe)H(NO)] (**1H**) and [Fe(CO)H(NO)(PPh₃)₂] (**2H**). The reference complexes were chosen because of their chemical relation to the hydride complexes. Since differences in the formal charge of the complexes would cause a shift in the spectra, the [NO]⁺ ligands in references **1** and **2** needed to be exchanged by CO in the hydride complexes **1H** and **2H**. Although the usual nomenclature of hydrides for Fe–H groups in transition metal complexes is used throughout this work, it has to be mentioned that the synthesis of the hydride complexes **1H** and

2H is achieved via protonation of an anionic precursor complex.^{17,52}

In order to provide a structural basis for the following discussion of the spectroscopic results, we start with a short discussion of the geometry optimization outcome (structural parameters are given in Table S1 in the [Supporting Information](#)) for the four complexes **1**, **1H**, **2**, and **2H**. The nonhydride complexes (**1**, **2**) exhibit a distorted tetrahedral coordination geometry. Upon exchange of one nitrosyl ligand against one carbonyl ligand and one hydride ligand, the coordination geometry changes to distorted trigonal bipyramidal. Interestingly, the hydride ligand is located in the axial position with the bidentate diphosphine ligand dppe in **1H**, while with the monodentate PPh₃ ligand in **2H** the equatorial position is preferred, leading to an enlarged P–Fe–P dihedral angle. Moreover, in **1H** the iron center is located slightly below the equatorial plane, while in **2H** the axial ligands are dislocated toward the hydride ligand, indicating a phosphine–hydride interaction. Independently of the structural differences in the hydride complexes, it will be shown that general signatures of Fe–H groups exist in both VtC-XES and HERFD-XANES spectra that allow identification and investigation of coordinating hydrogen ligands.

In order to investigate the impact of Fe–H contributions on the LUMO states, the spectral signatures of the experimental HERFD-XANES spectra shown in [Figure 1](#) will now be discussed. In general, two pre-edge features are observed in all four complexes. The associated energies of the features are listed in [Table 1](#). Signal A is found at an energy of around 7114 eV. Its intensity decreases when going from the nonhydride complexes **1** and **2** to the hydride complexes **1H** and **2H**. At the same time a slight blue-shift is observed, which changes the appearance of signal A to a shoulder.

The opposite is observed for signal B at around 7116 eV. Here the complexes lacking a hydride show a shift to higher energies, overlapping with the other edge signals, leading to a shoulder-like form, while **1H** and **2H** are characterized by a peak signal. Thus, the hydride complexes are characterized by a reduced splitting between signals A and B and a different intensity ratio compared to those of the nonhydride references.

While the HERFD-XANES data already shows promising differences in the spectra that point toward a sensitivity for Fe–H groups, the VtC-XES spectra exhibit even more distinct features, as demonstrated in [Figure 1](#). The spectral signal A at 7097.5 eV is known to be a fingerprint for NO σ_{2s}* orbitals.⁷⁷ Accordingly the intensity ratio of 2:1 reflects nicely the di- and mononitrosyl character of **1**, **2** and **1H**, **2H**, respectively. In contrast, feature B around 7103 eV exhibits a more complex behavior depending on the compound and present ligands. This is due to the fact that, on one hand, it has been identified as a fingerprint of CO ligands.⁴⁰ On the other hand, in the absence of coordinating CO, as in **1** and **2**, this feature is also a fingerprint for NO σ_{2p} orbitals in nitrosyl complexes.⁷⁶ Consequently, in **1H** and **2H** it is tentatively assigned to a superposition of CO → Fe 1s and NO → Fe 1s transitions, which is in line with an asymmetric shape of this feature and an increase in intensity compared to the nonhydride complexes **1** and **2**. The high-energy feature D at around 7109 eV is typical for transitions from occupied Fe 3d states, mostly independent of the coordinating ligands, which is in line with the identical intensity in all four complexes.⁴⁰

This preceding assignment of the VtC-XES signals, based on literature reports,⁵¹ leaves signal C at an energy of roughly 7106

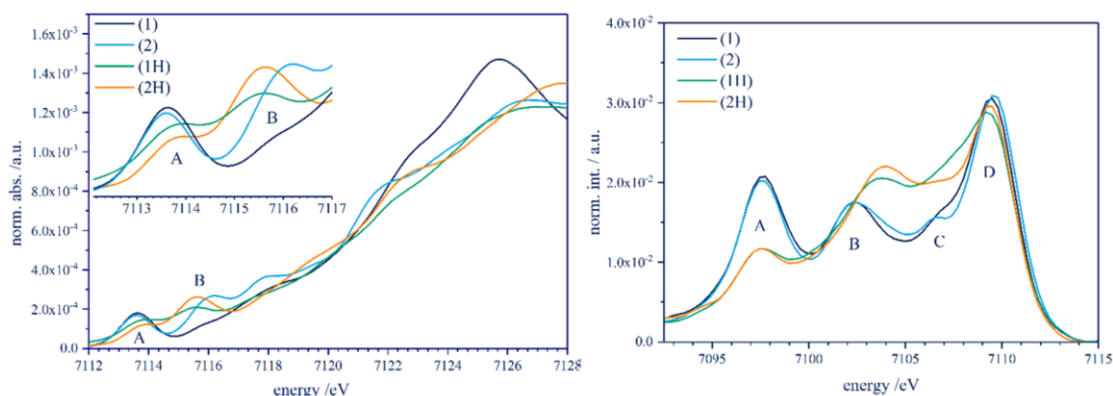


Figure 1. Left: experimental Fe K-edge HERFD-XANES spectra of **1**, **2**, **1H**, and **2H**. Right: experimental VtC-XES spectra of **1**, **2**, **1H**, and **2H**.

Table 1. Characteristic Signal Energies for VtC-XES and HERFD-XANES Spectra of Complexes **1**, **2**, **1H**, and **2H**

compd	HERFD-XANES prepeak energies/eV (norm int/au)		VtC-XES peak energies/eV (norm int/au)			
	A	B	A	B	C	D
Fe(NO) ₂ dppe (1)	7113.6 (1.8×10^{-4})	7116.1 (1.4×10^{-4})	7097.7 (2.0×10^{-2})	7102.5 (1.7×10^{-2})	7106.7 (1.6×10^{-2})	7109.4 (3.0×10^{-2})
Fe(NO) ₂ (PPh ₃) ₂ (2)	7113.6 (1.7×10^{-4})	7116.2 (2.7×10^{-4})	7097.7 (2.0×10^{-2})	7102.5 (1.7×10^{-2})	7106.4 (1.5×10^{-2})	7109.6 (3.0×10^{-2})
HFe(CO)(NO)dppp (1H)	7114.0 (1.5×10^{-4})	7115.6 (2.1×10^{-4})	7097.7 (1.1×10^{-2})	7103.8 (2.1×10^{-2})		7109.2 (2.8×10^{-2})
HFe(CO)(NO)(PPh ₃) ₂ (2H)	7113.9 (1.2×10^{-4})	7115.6 (2.6×10^{-4})	7097.7 (1.1×10^{-2})	7104.1 (2.1×10^{-2})		7109.1 (2.9×10^{-2})

eV as a potential unique fingerprint for coordinating hydride ligands with emission from the Fe–H motif. In the experimental spectra of the hydride complexes **1H** and **2H**, the signal intensity is increased compared to the nonhydride complexes **1** and **2**. Although this might be caused partially by the blue-shifted signal B in the hydride complexes, the following DFT analysis will prove underlying Fe–H contributions as the origin of the increased intensity in signal C.

Theoretical Results. The presented experimental spectra were so far only discussed on the basis of literature reports. Although such a fingerprinting approach is very valid in catalysis research, detailed knowledge about the molecular orbital origin of the observed spectral signatures is of utmost importance. This aim can only be achieved here by application of theoretical methods, providing precise information about molecular levels being responsible for the spectral signals. The results of such calculations will be given in the same order here as in the discussion of the experimental results.

Previous studies have shown that TD-DFT calculated core-excited charge-transfer transitions are shifting toward higher energies with a higher amount of HF-exchange of a hybrid functional (see SI Figure S4).^{68,77} For all four investigated complexes a TPSSH functional with an adjusted HF-exchange to 12.5% showed the best overall agreement with the experiment concerning the energy ratio of both prepeaks A and B. The TD-DFT XANES spectra are compared with the experimental data in Figure S1 in the Supporting Information. As evidenced with this comparison, a very good overall agreement between theory and experiment is achieved. Not only are the prepeaks precisely modeled, but also the signatures on the high-energy side of the prepeaks above 7117 eV are

modeled, due to an adjustment of the HF-exchange of the applied TPSSH functional. Usually, such quasi-continuum near-edge states are hard to reproduce by DFT due to the localized character of the method.⁷⁷

On the basis of this very good agreement, detailed information relevant for the aim of identifying Fe–H bonds in catalytically active complexes and the investigation of their properties can be extracted. The HERFD-spectra in Figures 2 and 3 compare the two sets of nonhydride and hydride complexes **1**, **1H** and **2**, **2H**. Each calculated transition corresponds to a core-excited state, which consists of the initial Fe 1s donor orbital and the originally unoccupied acceptor orbital.^{66,67} Normally, an excited state is described as an orbital excitation of an occupied donor orbital (in the case of metal K-edges always the 1s) to an unoccupied acceptor orbital; however, sometimes the core-excited state has a more complicated nature and must be described as a combination of many different orbitals pairs. In this case only acceptor orbitals are shown here (and in the Supporting Information) that contribute of more than 20% to the different core-excited states.

Starting with the complexes containing bidentate diphosphine ligands [Fe(dppe)(NO)₂] (**1**) and [Fe(CO)(dppp)H-(NO)] (**1H**), it was realized in the Experimental Results section that prepeak A shifts to higher energies in the hydride complex **1H**. As can be deduced from Figure 2, this shift for **1H** is caused by a contribution at 7114.0 eV at the high-energy side of the otherwise very similar main contributions in both **1** and **1H** in the range from 7113.5 to 7113.8 eV. The final states that cause these low-energy contributions are mainly formed by acceptor orbitals, which reflect the doubly degenerated NO π^*

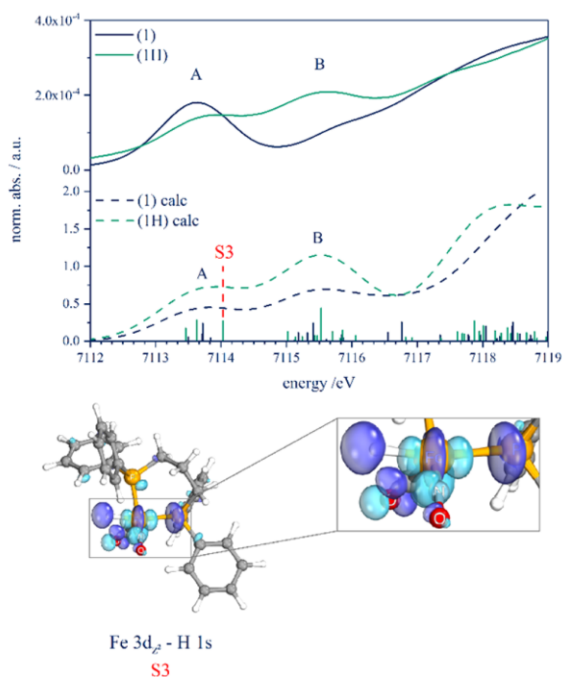


Figure 2. Detailed comparison of experimental (top —) and theoretical (bottom ---) Fe K-edge HERFD-XANES spectra of complexes **1** and **1H**. The acceptor orbital (IBO) of mainly Fe–H character is shown below the spectra.

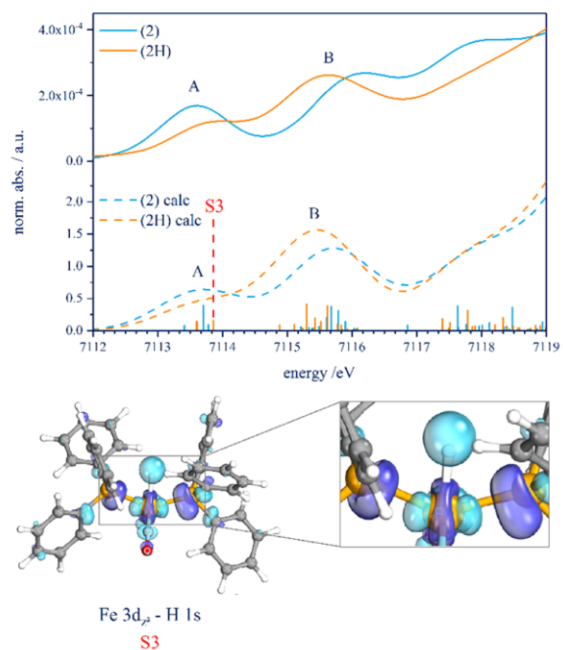


Figure 3. Detailed comparison of experimental (—) and theoretical (---) Fe K-edge HERFD-XANES spectra of complexes **2** and **2H**. The acceptor orbital (IBO) of mainly Fe–H character is shown below the spectra.

orbitals in antibonding combination with Fe 3d orbitals. Four underlying transitions are observed in the dinitrosyl complex **1**,

while the mononitrosyl complex **1H** exhibits only two transitions (for details see Tables S8 and S9 of the [Supporting Information](#)). The number of transitions and the resulting intensity of A therefore reflect nicely the mono- and dinitrosyl characters of **1** and **1H**, respectively. In contrast, the newly appearing high-energy contribution at 7114.0 eV in [Figure 2](#) of the hydride complex $[\text{Fe}(\text{CO})(\text{dppp})\text{H}(\text{NO})]$ (**1H**) is a transition to the antibonding combination of the Fe $3d_{z^2}$ (23.4% Löwdin reduced orbital population LROP) and H 1s orbital (5.8% LROP), corresponding to the LUMO + 10 (for details of core-excited state compositions see [Tables S9 and S14](#)).

For signal B, the opposite trend to signal A was observed; i.e., in the hydride complex **1H** a red-shift and intensity increase are observed compared to the signal for **1**. This signal is overall composed of transitions to phenyl π^* based acceptor orbitals of the phosphine ligands. The intensity increase in complex $[\text{Fe}(\text{CO})(\text{dppp})\text{H}(\text{NO})]$ (**1H**) compared to $[\text{Fe}(\text{dppe})(\text{NO})_2]$ (**1**) is, however, caused by additional transitions into doubly degenerated CO π^* orbitals in antibonding combination with Fe 3d orbitals at 7115.53 and 7116.06 eV (for details see [Table S9](#) of the [Supporting Information](#)).

A very similar situation is found in the monophosphine complexes $[\text{Fe}(\text{NO})_2(\text{PPh}_3)_2]$ (**2**) and $[\text{Fe}(\text{CO})\text{H}(\text{NO})(\text{PPh}_3)_2]$ (**2H**) in [Figure 3](#). Also here, the shift of prepeak A to higher energies in the hydride complex **2H** is caused by an additional transition ([Supporting Information S3](#), [Figure 3](#)) to the antibonding combination of the Fe $3d_{z^2}$ (26.4% LROP), the H 1s orbital (5.3% LROP), and additionally both P $3p_z$ orbitals (3.2/2.3% LROP) corresponding to the LUMO + 14 (for details of core-excited state compositions see [Table S9](#)). As in **1** and **1H**, the transitions at lower energies are mainly formed by acceptor orbitals, which reflect the doubly degenerated NO π^* orbitals in antibonding combination with Fe 3d orbitals, resulting in four underlying transitions in the dinitrosyl complex **2**, while the mononitrosyl complex **2H** exhibits only two transitions (for details see [Tables S8 and S9](#) of the [Supporting Information](#)).

Also as seen in the diphosphine complexes (**1**, **1H**), signal B is composed by transitions to phenyl π^* based acceptor orbitals of the phosphine ligands. The intensity increase in complex $[\text{Fe}(\text{CO})\text{H}(\text{NO})(\text{PPh}_3)_2]$ (**2H**) compared to $[\text{Fe}(\text{NO})_2(\text{PPh}_3)_2]$ (**2**) is however caused by additional transitions into doubly degenerated CO π^* orbitals in antibonding combination with Fe 3d orbitals at 7116.01 and 7117.40 eV (for details see [Tables S9 and S14](#) of the [Supporting Information](#)). Since complexes **2** and **2H** of monodentate PPh_3 contain in total six phenyl groups, while the bidentate diphosphine complexes **1** and **1H** carry only four, the preceding assignment is supported by the experimentally observed intensity differences of prepeak B for (**1**, **1H**) and (**2**, **2H**).

The full VtC-XES spectra are calculated using a TPSS functional and are compared with the experimental data in [Figure S2](#) in the [Supporting Information](#). As in the case of HERFD-XANES, the agreement between theory and experiment is impressively high. In this computational approach every transition is a single electron transition from a particular occupied molecular orbital to the Fe 1s orbital.⁴² It is therefore sufficient to discuss only the donor orbitals instead of the full excited state as in the case of HERFD-XANES. In order to account for the ligand selective nature of VtC-XES, the ligand projected spectra are shown in the following [Figure 4](#) for (**1**, **1H**) and (**2**, **2H**).

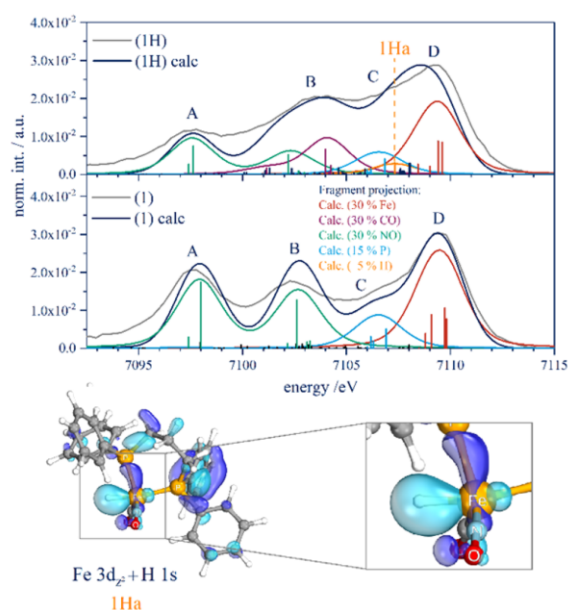


Figure 4. Comparison of experimental (gray) and theoretical (blue) Fe K-edge VtC-XES spectra for **1** (bottom) and **1H** (top). Contributions of individual fragment projections to the VtC-XES spectra are also shown.

Starting again with complexes $[\text{Fe}(\text{dppe})(\text{NO})_2]$ (**1**) and $[\text{Fe}(\text{CO})(\text{dppp})\text{H}(\text{NO})]$ (**1H**), Figure 4 shows by looking at the orbital projections that signal A at around 7097.5 eV is caused solely by nitrosyl σ_{2s}^* donor orbitals. The intensity of A is reduced in the hydride complex **1H**, which reflects the reduced number of NO ligands in **1H** (for details see Tables S2 and S3 of the Supporting Information). In the nonhydride compound **1** feature B at around 7102.8 eV is as well only caused by nitrosyl donor orbitals, here nitrosyl σ_{2p} states. As stated in the discussion of the experimental spectra above, the presence of CO in the hydride complex **1H** causes a shift of feature B to higher energy and an increased intensity. The theoretical calculations in Figure 4 prove the suspected origin of this effect by superposition of transitions from both NO σ_{2p} and CO $\sigma_{2s}^*/\sigma_{2p}$ orbitals. This superposition results in a broad, asymmetric, and more intense signal B (for details see Tables S2 and S3 of the Supporting Information).

The following signal C is suspected to be a signature of the hydride ligand in the discussion of the experimental data. In the nonhydride complex $[\text{Fe}(\text{dppe})(\text{NO})_2]$ (**1**), signal C is solely attributable to the bonding interaction of P 3p and Fe 3d orbitals (for details of the donor orbitals see Supporting Information). Although such contributions are also present in the hydride complex $[\text{Fe}(\text{CO})(\text{dppp})\text{H}(\text{NO})]$ (**1H**), they are superimposed by transitions of a donor orbital with significant hydride density. This superposition together with contributions from the CO ligand as discussed above leads to the increased intensity of feature C. As demonstrated in Figure 4, the main contribution **1Ha** is characterized by transitions from the bonding interaction between the Fe $3d_{z^2}$ (10.1% LROP) and the H 1s (10.1% LROP) at 7107.9 eV (for details see Tables S2, S3, and S14 of the Supporting Information).

Finally, signal D is caused by Fe 3d donor orbitals and their bonding combinations with the double degenerated nitrosyl π^*

orbitals (**1**, **1H**) and carbonyl π^* orbitals, respectively (**1H**). The broadening to lower energies in the hydride complex **1H** can be attributed to the above-mentioned transition of **1Ha** \rightarrow Fe 1s (Figure 4).

For signals A and B, a very similar situation is found in the monodentate phosphine complexes $[\text{Fe}(\text{NO})_2(\text{PPh}_3)_2]$ (**2**) and $[\text{Fe}(\text{CO})\text{H}(\text{NO})(\text{PPh}_3)_2]$ (**2H**). The transitions underlying signals A and B are basically identical. The most significant difference can be found in signal C, where **2H** in contrast to **1H** exhibits two instead of one contribution characteristic for the Fe–H motif. The donor orbital **2Ha** (Figure 5) relating closely

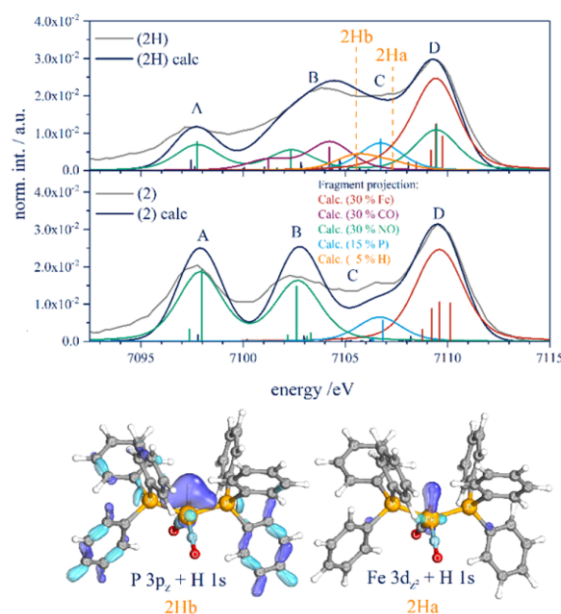


Figure 5. Comparison of experimental (gray) and theoretical (blue) Fe K-edge VtC-XES spectra for **2** (bottom) and **2H** (top). Contributions of individual fragment projections to the VtC-XES spectra are also shown.

to **1Ha** (Figure 4) is formed by the bonding interaction between the Fe $3d_{z^2}$ (23.6% LROP) and the H 1s (14.4% LROP); the transition from this state to the Fe 1s is found at 7107.3 eV. Additionally the transition from orbital **2Hb** appears at 7105.6 eV, which resembles the interaction of both P 3p_z (4.7/4.5% LROP) and H 1s (8.8% LROP).

As seen in the diphosphine complexes (**1**, **1H**), signal D is assigned to Fe 3d donor orbitals or their bonding combinations with the double degenerated nitrosyl π^* orbitals (**2**, **2H**) and carbonyl π^* orbitals (**2H**), respectively. Nevertheless, **2H** exhibits a higher nitrosyl population of this contribution, which can be seen in the ligand projection of signal D (Figure 5). While in **1**, **1H**, and **2** all contributions of D are assigned to the iron fragment (red line, Figure 4), **2H** also exhibits a significant nitrosyl proportion (green line, Figure 5, for details see Tables S2 and S3 of the Supporting Information).

The slight difference in the spectra of **1H** and **2H** can be basically explained by the different spectral contributions of the Fe–H group: Since the **1Ha** \rightarrow Fe 1s transition exhibits twice the transition probability of the **2Ha** \rightarrow Fe 1s transition, feature D is broadened to lower energies in **1H**. On the contrary, a broadening of feature B instead of D is observed in **2H**, which

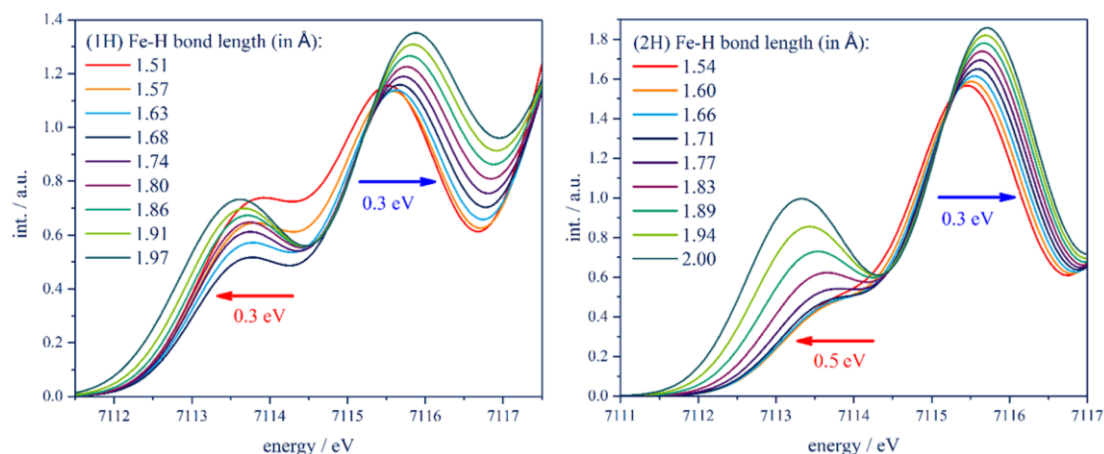


Figure 6. Left: simulated TD-DFT Fe K-edge spectra of **1H** at different Fe–H bond lengths. Right: simulated TD-DFT Fe K-edge spectra of **2H** at different Fe–H bond lengths.

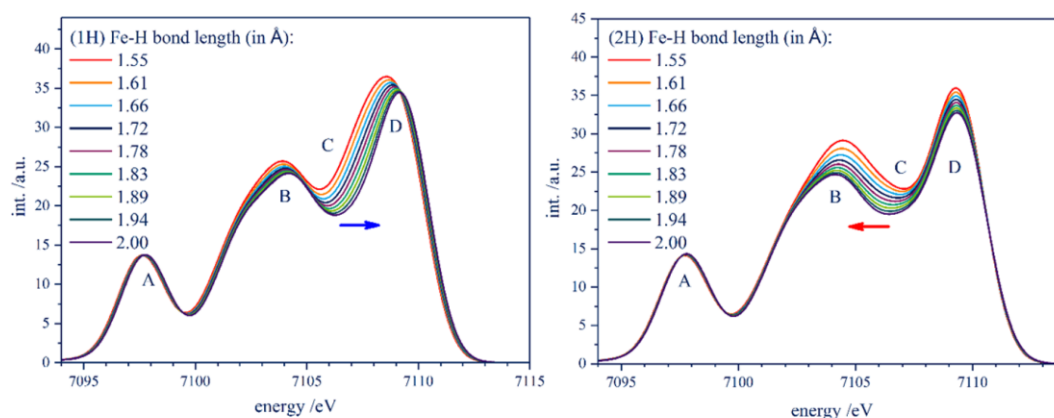


Figure 7. Left: simulated Fe K-edge VtC-XES spectra of **1H** at different Fe–H bond lengths. Right: simulated Fe K-edge VtC-XES spectra of **2H** at different Fe–H bond lengths.

can be explained with the additional hydride–phosphine interaction. Since in **1H** the hydride ligand cannot occupy the position between both phosphorus atoms due to the narrow bite angle of the dppp ligand, the H–P distance is significantly increased. Therefore, the strength of the hydride–phosphine interaction is drastically reduced compared to that of **2H**.

As an intermediate summary, the increased intensity in the area of C in both hydride complexes (**1H**, **2H**) can unequivocally be assigned to the bonding interaction of the Fe $3d_{z^2}$ orbital (**1Ha**, **2Ha**) and the H $1s$ orbital, the Fe–H σ molecular orbital. This presents a spectral signature that allows unequivocal detection of the presence of a hydride ligand, but moreover, it offers a tool to study the behavior of Fe–H groups in chemical reactions as will be explored in the following paragraphs.

As shown in the Theoretical Results section, the bonding and antibonding Fe–H interaction is naturally influencing the HOMO and LUMO levels, thus leading to characteristic structures in the VtC-XES and HERFD-XANES spectra of the hydride complexes **1H** and **2H**. In order to demonstrate the potential of the following reactions involving bond formation and dissociation of hydride ligands by VtC-XES and HERFD-XANES, the Fe–H bond length in complexes **1H** and **2H** is

incremented between the actual bound state with a length of 1.52 Å (**1H**) or 1.55 Å (**2H**) and 2.0 Å, while the remaining structure was kept fixed. At each step, DFT VtC-XES spectra and TD-DFT HERFD-XANES spectra are calculated to explore the changes in the spectra that have to be significant enough to be detected experimentally. In the case of hydrogenase model complexes, this bond length scan approach has already been successfully applied to VtC-XES and HERFD-XANES by the work group of Debeer.⁵¹

The calculated XANES spectra with increasing Fe–H distance in Figure 6 reflect nicely the transition from the hydride to the nonhydride complexes. Accordingly, at extended bond length (2.0 Å), a calculated red-shift of 0.3 eV for **1H** and 0.5 eV for **2H**, respectively, is observed. On the other hand, feature B blue-shifts by 0.3 eV for both complexes. The red-shift of feature A with increasing Fe–H distance is explained by the decreasing overlap between H $1s$ and Fe $3d_{z^2}$, which leads to a stabilization of the antibonding combination.

Since feature B was assigned to a combination of Fe $1s \rightarrow$ phenyl π^* and Fe $1s \rightarrow$ CO π^* transitions, changing the Fe–H distance should not directly affect this signal, and the observed theoretical blue-shift is thus explained by changes of the overall electron density distribution.

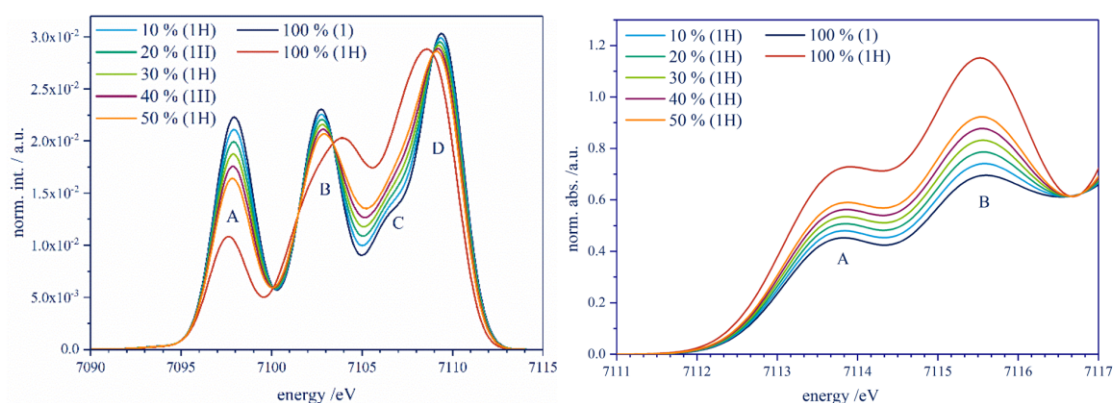


Figure 8. Mixtures of calculated VtC-XES (left) and HERFD-XANES spectra (right) of **1H** in **1**.

Using the same approach as that for the XANES spectra, the influence of occupied hydride orbitals on the HOMO levels can be investigated by simulation of the VtC-XES spectra for incrementing Fe–H bond lengths. As already observed for the simulated XANES spectra, the calculated VtC-XES in Figure 7 (**1H**, **2H**) resembles the trend according to a transition from the hydride (**1H**, **2H**) to the nonhydride (**1**, **2**) complexes quite closely. The scan also reflects the experimental and theoretical observed differences between both hydride complexes: The bond length scan of **1H** in Figure 7 underlines the assignment of signal B to the Fe–H motif and reflects the sharpening and blue-shift of feature D in the nonhydride complex. The reduced overlap of H 1s and Fe 3d_{z²} with increasing bond lengths leads to a destabilization of the relevant orbital **1Ha**. The **1Ha** → Fe 1s transition is therefore blue-shifted, and furthermore, the transition probability decreases significantly. Complex **2H** also shows a similar destabilization of **2Ha** with increasing bond length caused again by the reduced overlap of the H 1s and Fe 3d_{z²} and a drastically reduced transition probability of the **2Ha** → Fe 1s transition at extended bond length.

As mentioned above, the hydride bonding situation in **2H** is not described only by the interaction of the H 1s with the Fe 3d_{z²} orbitals, which would mainly influence the D feature (as seen in **1H**). Instead, the H 1s also interacts with P 3p_z orbitals (**2Hb**, Figure 5), which leads to the rise in intensity at the high-energy side of B compared to complex **1H**. This effect is also clearly reproduced by the bond length scan shown in Figure 7. It is caused by the diminishing overlap of H 1s and P 3p_z, leading to a destabilization of orbital **2Hb** (cf. Figure 5). The **2Hb** → Fe 1s transition is therefore blue-shifted, and furthermore, the transition probability of the **2Hb** → Fe 1s transition decreases drastically which leads to the sharpening of B.

The bond length scan approach clearly illustrates that the observed main differences between the hydride (**1H**, **2H**) and nonhydride complexes (**1**, **2**) in the VtC-XES spectra can be reduced to the interaction of the H 1s with the Fe 3d_{z²} (**1H**, **2H**) and P 3p_z orbital (**2H**), respectively. Consequently, VtC-XES is able to probe details of the Fe–H interactions in any case directly and in selected cases where the geometric assembly allows the possibility of a hydride coordination in close proximity to the phosphine ligand, via the spectator P–H interaction in complexes with phosphine ligands.

Finally, the potential of both VtC-XES and HERFD-XANES to study catalytic reactions depends crucially on the specificity of both methods to detect Fe–H bonds in a reaction mixture. Although this issue cannot be accessed fully here, Figure 8 compares mixtures of the calculated spectra of 50% to 10% **1H** in **1**. Both the intensity of signals A and C and the energy of signal D in the VtC-XES spectra allow the detection of hydride ligands even in the presented mixtures. The HERFD-XANES spectra are unfortunately less specific. VtC-XES is therefore superior to HERFD-XANES for catalytic investigations. However, we have to admit that these mixtures present the undiluted case. To further verify the specificity of the method, solution measurements on mixtures need to be carried out in the future.

CONCLUSION

A detailed investigation of different hydride complexes [Fe(CO)(dppp)H(NO)] and [Fe(CO)H(NO)(PPh₃)₂] (**1H**, **2H**) and their nonhydride analogues [Fe(dppe)(NO)₂] and [Fe(NO)₂(PPh₃)₂] (**1**, **2**) has been carried out using VtC-XES and HERFD-XANES in combination with DFT and TD-DFT, respectively.

It has been demonstrated for this type of complex that the antibonding Fe–H interaction indeed contributes in a characteristic way to the pre-edge features in the XANES region. At around 7114 eV, a particular signal resulting from a final state formed by the antibonding interaction of the Fe 3d_{z²} and the H 1s could be unequivocally assigned by TD-DFT calculations using a combination of a TPSSH functional with an adjusted Hartree–Fock exchange of 12.5% and the def2-TZVP basis set.^{56,66} This important finding was supported by theoretical scans of the Fe–H bond length, where a Fe–H elongation resulted in a transition of the spectra toward the nonhydride reference.

The VtC-XES analogue of this approach offers an even increased sensitivity to Fe–H interactions. It has been shown that both complexes (**1H**, **2H**) exhibit a characteristic hydride signal at 7107.3 eV, which is caused by the bonding interaction of the Fe 3d_{z²} and the H 1s (**1H**, **2H**). With the hydride ligand in close proximity to phosphine ligands, an additional signal at 7105.6 eV was observed in **2H**. This signal is caused by the bonding interaction of the P 3p_z and the H 1s orbitals as could be shown by DFT calculations using a combination of the TPSS functional and the def2-TZVP basis set.^{42,56} The theoretical Fe–H bond length scan procedure also applied

here showed that elongation of the Fe–H bond transforms all features influenced by the Fe–H motif to similar energies and intensities of both non-hydride references (**1**, **2**). This clearly demonstrates the sensibility of VtC-XES regarding the Fe–H bond length, as previously shown for hydrogenase model complexes.⁵¹

In summary, the presented results provide two key results for the investigation of iron hydride compounds with relevance for catalytic reactions: First, it could be shown that a combination of iron K-edge HERFD-XANES and VtC-XES and (TD-)DFT calculations is highly suited to detect hydride coordination and to investigate the HOMO and LUMO details of hydride complexes. Second, the possibility to follow the fate of Fe–H groups in the course of catalytic reactions was evaluated by theoretical spectroscopy. With this result, the high potential of hard X-ray spectroscopy to investigate even hydrogen compounds is further substantiated, and the basis for in situ and in operando experiments on hydrogenation or hydrosilylation reactions is set.

■ ASSOCIATED CONTENT

■ Supporting Information

The Supporting Information is available free of charge on the ACS Publications website at DOI: 10.1021/acs.inorgchem.7b02063.

Comparison of experimental and calculations; comparison of all relevant VtC-XES transitions concerning ligand/element populations (donor orbital), energies, and normalized intensities; comparison of all relevant TD-DFT XANES states concerning relevant orbital pairs, energies, and normalized intensities; relevant donor orbitals; and relevant acceptor orbitals (PDF)

■ AUTHOR INFORMATION

Corresponding Author

*E-mail: matthias.bauer@uni-paderborn.de.

ORCID

Matthias Bauer: 0000-0002-9294-6076

Notes

The authors declare no competing financial interest.

■ ACKNOWLEDGMENTS

The ESRF is acknowledged for a provision of beamtime. We thank the staff of beamline ID26 for support during the measurements. The German BMBF is acknowledged for funding in frame of project “SusChEmX” (FKZ 05K14PP1).

■ REFERENCES

- (1) Chaplin, A. B.; Weller, A. S. B-H activation at a rhodium(I) center: isolation of a bimetallic complex relevant to the transition-metal-catalyzed dehydrocoupling of amine-boranes. *Angew. Chem., Int. Ed.* **2010**, *49*, 581–584.
- (2) Ding, B.; Zhang, Z.; Liu, Y.; Sugiyama, M.; Imamoto, T.; Zhang, W. Chemoselective transfer hydrogenation of α,β -unsaturated ketones catalyzed by pincer-Pd complexes using alcohol as a hydrogen source. *Org. Lett.* **2013**, *15*, 3690–3693.
- (3) Felton, G. A. N.; Vannucci, A. K.; Okumura, N.; Lockett, L. T.; Evans, D. H.; Glass, R. S.; Lichtenberger, D. L. Hydrogen Generation from Weak Acids: Electrochemical and Computational Studies in the $[(\eta^5\text{-C}_5\text{H}_5)\text{Fe}(\text{CO})_2]_2$ System. *Organometallics* **2008**, *27*, 4671–4679.
- (4) Hills, I. D.; Fu, G. C. Elucidating reactivity differences in palladium-catalyzed coupling processes: the chemistry of palladium hydrides. *J. Am. Chem. Soc.* **2004**, *126*, 13178–13179.
- (5) Ito, H.; Saito, T.; Miyahara, T.; Zhong, C.; Sawamura, M. Gold(I) Hydride Intermediate in Catalysis: Dehydrogenative Alcohol Silylation Catalyzed by Gold(I) Complex. *Organometallics* **2009**, *28*, 4829–4840.
- (6) Nolin, K. A.; Krumper, J. R.; Pluth, M. D.; Bergman, R. G.; Toste, F. D. Analysis of an unprecedented mechanism for the catalytic hydrosilylation of carbonyl compounds. *J. Am. Chem. Soc.* **2007**, *129*, 14684–14696.
- (7) Ozawa, F.; Okamoto, H.; Kawagishi, S.; Yamamoto, S.; Minami, T.; Yoshifuji, M. (π -Allyl)palladium Complexes Bearing Diphosphinodienecyclobutene Ligands (DPCB): Highly Active Catalysts for Direct Conversion of Allylic Alcohols. *J. Am. Chem. Soc.* **2002**, *124*, 10968–10969.
- (8) Mai, V. H.; Nikonov, G. I. Transfer Hydrogenation of Nitriles, Olefins, and N-Heterocycles Catalyzed by an N-Heterocyclic Carbene-Supported Half-Sandwich Complex of Ruthenium. *Organometallics* **2016**, *35*, 943–949.
- (9) Zhang, G.; Hanson, S. K. Cobalt-catalyzed acceptorless alcohol dehydrogenation: synthesis of imines from alcohols and amines. *Org. Lett.* **2013**, *15*, 650–653.
- (10) Armaroli, N.; Balzani, V. The hydrogen issue. *ChemSusChem* **2011**, *4*, 21–36.
- (11) Abbasi, T.; Abbasi, S. A. ‘Renewable’ hydrogen: Prospects and challenges. *Renewable Sustainable Energy Rev.* **2011**, *15*, 3034–3040.
- (12) Hollmann, D.; Gartner, F.; Ludwig, R.; Barsch, E.; Junge, H.; Blug, M.; Hoch, S.; Beller, M.; Bruckner, A. Insights into the mechanism of photocatalytic water reduction by DFT-supported in situ EPR/Raman spectroscopy. *Angew. Chem., Int. Ed.* **2011**, *50*, 10246–10250.
- (13) Mulder, D. W.; Shepard, E. M.; Meuser, J. E.; Joshi, N.; King, P. W.; Posewitz, M. C.; Broderick, J. B.; Peters, J. W. Insights into FeFe-Hydrogenase structure, mechanism, and maturation. *Structure* **2011**, *19*, 1038–1052.
- (14) Ogata, H.; Kramer, T.; Wang, H.; Schilter, D.; Pelmenchikov, V.; van Gastel, M.; Neese, F.; Rauchfuss, T. B.; Gee, L. B.; Scott, A. D.; Yoda, Y.; Tanaka, Y.; Lubitz, W.; Cramer, S. P. Hydride bridge in NiFe-Hydrogenase observed by nuclear resonance vibrational spectroscopy. *Nat. Commun.* **2015**, *6*, 7890.
- (15) Peters, J. W.; Schut, G. J.; Boyd, E. S.; Mulder, D. W.; Shepard, E. M.; Broderick, J. B.; King, P. W.; Adams, M. W. W. FeFe- and NiFe-Hydrogenase diversity, mechanism, and maturation. *Biochim. Biophys. Acta, Mol. Cell Res.* **2015**, *1853*, 1350–1369.
- (16) Stripp, S. T.; Happe, T. How algae produce hydrogen—news from the photosynthetic hydrogenase. *Dalton Trans.* **2009**, *45*, 9960–9969.
- (17) Rommel, S.; Hettmanczyk, L.; Klein, J. E. M. N.; Plietker, B. Cooperative catalysis: electron-rich Fe-H complexes and DMAP, a successful “joint venture” for ultrafast hydrogen production. *Chem. - Asian J.* **2014**, *9*, 2140–2147.
- (18) Andrews, L. Matrix infrared spectra and density functional calculations of transition metal hydrides and dihydrogen complexes. *Chem. Soc. Rev.* **2004**, *33*, 123–132.
- (19) *Spectroscopic Properties of Inorganic and Organometallic Compounds*; Yarwood, J., Douthwaite, R., Duckett, S., Eds.; Royal Society of Chemistry: Cambridge, 2012.
- (20) Gütlisch, P.; Bill, E.; Trautwein, A. X. *Mössbauer Spectroscopy and Transition Metal Chemistry*; Springer: Berlin, 2011.
- (21) Kajcsos, Z.; Sauer, C.; Zinn, W.; Meisel, W.; Spiering, H.; Alflen, M.; Gütlisch, P. High-performance Mössbauer spectroscopy: Criteria, possibilities, limitations. *Hyperfine Interact.* **1992**, *71*, 1469–1477.
- (22) Weckhuysen, B. M. Snapshots of a working catalyst: Possibilities and limitations of in situ spectroscopy in the field of heterogeneous catalysis. *Chem. Commun.* **2002**, 97–110.
- (23) Bau, R.; Teller, R. G.; Kirtley, S. W.; Koetzle, T. F. Structures of transition-metal hydride complexes. *Acc. Chem. Res.* **1979**, *12*, 176–183.
- (24) Bauer, M.; Bertagnolli, H. X-ray Absorption Spectroscopy—The Method and Its Applications. In *Methods in Physical Chemistry*; Schäfer, R., Schmidt, P. C., Eds.; Wiley-VCH Verlag GmbH & Co. KGaA: Weinheim, Germany, 2012; pp 231–269.

- (25) Glatzel, P.; Bergmann, U. High resolution 1s core hole X-ray spectroscopy in 3d transition metal complexes—electronic and structural information. *Coord. Chem. Rev.* **2005**, *249*, 65–95.
- (26) Arčon, I.; Kolar, J.; Kodre, A.; Hanžel, D.; Strlič, M. XANES analysis of Fe valence in iron gall inks. *X-Ray Spectrom.* **2007**, *36*, 199–205.
- (27) Westre, T. E.; Kennepohl, P.; DeWitt, J. G.; Hedman, B.; Hodgson, K. O.; Solomon, E. I. A Multiplet Analysis of Fe K-Edge 1s → 3d Pre-Edge Features of Iron Complexes. *J. Am. Chem. Soc.* **1997**, *119*, 6297–6314.
- (28) Bunker, G. *Introduction to XAFS: A Practical Guide to X-ray Absorption Fine Structure Spectroscopy*; Cambridge University Press: Cambridge, UK, 2010.
- (29) de Groot, F. High-Resolution X-ray Emission and X-ray Absorption Spectroscopy. *Chem. Rev.* **2001**, *101*, 1779–1808.
- (30) D'Angelo, P.; Barone, V.; Chillemi, G.; Sanna, N.; Meyer-Klaucke, W.; Pavel, N. V. Hydrogen and Higher Shell Contributions in Zn²⁺, Ni²⁺, and Co²⁺ Aqueous Solutions: An X-ray Absorption Fine Structure and Molecular Dynamics Study. *J. Am. Chem. Soc.* **2002**, *124*, 1958–1967.
- (31) Koningsberger, D. C.; Oudenhuijzen, M. K.; Bitter, J. H.; Ramaker, D. E. Study of geometrical and electronic effects induced by hydrogen chemisorption on supported Pt particles. Analysis of Pt-H EXAFS and Pt-H anti-bonding state shape resonances. *Top. Catal.* **2000**, *10*, 167–177.
- (32) Oudenhuijzen, M. K.; Bitter, J. H.; Koningsberger, D. C. The Nature of the Pt–H Bonding for Strongly and Weakly Bonded Hydrogen on Platinum. A XAFS Spectroscopy Study of the Pt–H Antibonding Shaperesonance and Pt–H EXAFS. *J. Phys. Chem. B* **2001**, *105*, 4616–4622.
- (33) Prešeren, R.; Kodre, A.; Arčon, I.; Borowski, M. Atomic background and EXAFS of gaseous hydrides of Ge, As, Se and Br. *J. Synchrotron Radiat.* **2001**, *8*, 279–281.
- (34) Koningsberger, D. C.; Prins, R. X-ray Absorption: Principles, Applications, Techniques of EXAFS, SEXAFS and XANES. *Chemical Analysis 92*; Wiley: New York, 1988.
- (35) Vanko, G.; Glatzel, P.; Pham, V.-T.; Abela, R.; Grolimund, D.; Borca, C. N.; Johnson, S. L.; Milne, C. J.; Bressler, C. Picosecond time-resolved X-ray emission spectroscopy: ultrafast spin-state determination in an iron complex. *Angew. Chem., Int. Ed.* **2010**, *49*, 5910–5912.
- (36) Vanko, G.; Neisius, T.; Molnar, G.; Renz, F.; Karpati, S.; Shukla, A.; de Groot, F. M. F. Probing the 3d spin momentum with X-ray emission spectroscopy: the case of molecular-spin transitions. *J. Phys. Chem. B* **2006**, *110*, 11647–11653.
- (37) Bauer, M. HERFD-XAS and valence-to-core-XES: new tools to push the limits in research with hard X-rays? *Phys. Chem. Chem. Phys.* **2014**, *16*, 13827–13837.
- (38) Eisenberger, P.; Platzman, P. M.; Winick, H. X-Ray Resonant Raman Scattering: Observation of Characteristic Radiation Narrower than the Lifetime Width. *Phys. Rev. Lett.* **1976**, *36*, 623–626.
- (39) Atkins, A. J.; Bauer, M.; Jacob, C. R. The chemical sensitivity of X-ray spectroscopy: high energy resolution XANES versus X-ray emission spectroscopy of substituted ferrocenes. *Phys. Chem. Chem. Phys.* **2013**, *15*, 8095–8105.
- (40) Delgado-Jaime, M. U.; DeBeer, S.; Bauer, M. Valence-to-core X-ray emission spectroscopy of iron-carbonyl complexes: implications for the examination of catalytic intermediates. *Chem. - Eur. J.* **2013**, *19*, 15888–15897.
- (41) Smolentsev, G.; Soldatov, A. V.; Messenger, J.; Merz, K.; Weyhermüller, T.; Bergmann, U.; Pushkar, Y.; Yano, J.; Yachandra, V. K.; Glatzel, P. X-ray emission spectroscopy to study ligand valence orbitals in Mn coordination complexes. *J. Am. Chem. Soc.* **2009**, *131*, 13161–13167.
- (42) Lee, N.; Petrenko, T.; Bergmann, U.; Neese, F.; DeBeer, S. Probing valence orbital composition with iron Kβ X-ray emission spectroscopy. *J. Am. Chem. Soc.* **2010**, *132*, 9715–9727.
- (43) Pollock, C. J.; DeBeer, S. Insights into the geometric and electronic structure of transition metal centers from valence-to-core X-ray emission spectroscopy. *Acc. Chem. Res.* **2015**, *48*, 2967–2975.
- (44) Chandrasekaran, P.; Chiang, K. P.; Nordlund, D.; Bergmann, U.; Holland, P. L.; DeBeer, S. Sensitivity of X-ray core spectroscopy to changes in metal ligation: a systematic study of low-coordinate, high-spin ferrous complexes. *Inorg. Chem.* **2013**, *52*, 6286–6298.
- (45) Lancaster, K. M.; Roemelt, M.; Ettenhuber, P.; Hu, Y.; Ribbe, M. W.; Neese, F.; Bergmann, U.; DeBeer, S. X-ray emission spectroscopy evidences a central carbon in the nitrogenase iron-molybdenum cofactor. *Science* **2011**, *334*, 974–977.
- (46) Martin-Diaconescu, V.; Chacon, K. N.; Delgado-Jaime, M. U.; Sokaras, D.; Weng, T.-C.; DeBeer, S.; Blackburn, N. J. Kβ Valence to Core X-ray Emission Studies of Cu(I) Binding Proteins with Mixed Methionine - Histidine Coordination. Relevance to the Reactivity of the M- and H-sites of Peptidylglycine Monooxygenase. *Inorg. Chem.* **2016**, *55*, 3431–3439.
- (47) Pollock, C. J.; DeBeer, S. Valence-to-core X-ray emission spectroscopy: a sensitive probe of the nature of a bound ligand. *J. Am. Chem. Soc.* **2011**, *133*, 5594–5601.
- (48) Pollock, C. J.; Lancaster, K. M.; Finkelstein, K. D.; DeBeer, S. Study of iron dimers reveals angular dependence of valence-to-core X-ray emission spectra. *Inorg. Chem.* **2014**, *53*, 10378–10385.
- (49) Chernev, P.; Lambert, C.; Brunje, A.; Leidel, N.; Sigfridsson, K. G. V.; Kositzki, R.; Hsieh, C.-H.; Yao, S.; Schiwoon, R.; Driess, M.; Limberg, C.; Happe, T.; Haumann, M. Hydride binding to the active site of FeFe-Hydrogenase. *Inorg. Chem.* **2014**, *53*, 12164–12177.
- (50) Leidel, N.; Hsieh, C.-H.; Chernev, P.; Sigfridsson, K. G. V.; Darensbourg, M. Y.; Haumann, M. Bridging-hydride influence on the electronic structure of an FeFe hydrogenase active-site model complex revealed by XAES-DFT. *Dalton Trans.* **2013**, *42*, 7539–7554.
- (51) Hugenbruch, S.; Shafaat, H. S.; Kramer, T.; Delgado-Jaime, M. U.; Weber, K.; Neese, F.; Lubitz, W.; DeBeer, S. In search of metal hydrides: an X-ray absorption and emission study of NiFe hydrogenase model complexes. *Phys. Chem. Chem. Phys.* **2016**, *18*, 10688–10699.
- (52) Belger, C.; Plietker, B. Aryl-aryl interactions as directing motifs in the stereodivergent iron-catalyzed hydrosilylation of internal alkynes. *Chem. Commun.* **2012**, *48* (44), 5419–5421.
- (53) Bitterwolf, T. E.; Steele, B. Facile synthesis of Fe(NO)₂L₂ compounds, where L = phosphines and phosphites. *Inorg. Chem. Commun.* **2006**, *9*, 512–513.
- (54) de Groot, F. M. F.; Krisch, M. H.; Vogel, J. Spectral sharpening of the Pt L edges by high-resolution x-ray emission. *Phys. Rev. B: Condens. Matter Mater. Phys.* **2002**, *66*, 195112-1–195112-7.
- (55) Swarbrick, J. C.; Skyllberg, U.; Karlsson, T.; Glatzel, P. High energy resolution X-ray absorption spectroscopy of environmentally relevant lead(II) compounds. *Inorg. Chem.* **2009**, *48*, 10748–10756.
- (56) Neese, F. The ORCA program system. *WIREs Comput. Mol. Sci.* **2012**, *2*, 73–78.
- (57) Staroverov, V. N.; Scuseria, G. E.; Tao, J.; Perdew, J. P. Comparative assessment of a new nonempirical density functional: Molecules and hydrogen-bonded complexes. *J. Chem. Phys.* **2003**, *119*, 12129.
- (58) Staroverov, V. N.; Scuseria, G. E.; Tao, J.; Perdew, J. P. Erratum: “Comparative assessment of a new nonempirical density functional: Molecules and hydrogen-bonded complexes” [J. Chem. Phys. 119, 12129 (2003)]. *J. Chem. Phys.* **2004**, *121*, 11507.
- (59) Neese, F.; Wennmohs, F.; Hansen, A.; Becker, U. Efficient, approximate and parallel Hartree-Fock and hybrid DFT calculations. A ‘chain-of-spheres’ algorithm for the Hartree-Fock exchange. *Chem. Phys.* **2009**, *356*, 98–109.
- (60) Weigend, F.; Ahlrichs, R. Balanced basis sets of split valence, triple zeta valence and quadruple zeta valence quality for H to Rn: Design and assessment of accuracy. *Phys. Chem. Chem. Phys.* **2005**, *7*, 3297–3305.
- (61) Eichkorn, K.; Weigend, F.; Treutler, O.; Ahlrichs, R. Auxiliary basis sets for main row atoms and transition metals and their use to approximate Coulomb potentials. *Theor. Chem. Acc.* **1997**, *97*, 119–124.

- (62) Weigend, F. Accurate Coulomb-fitting basis sets for H to Rn. *Phys. Chem. Chem. Phys.* **2006**, *8*, 1057–1065.
- (63) Albano, V. G.; Araneo, A.; Bellon, P. L.; Ciani, G.; Manassero, M. Stereochemistry of tetrahedral complexes of group VIII metals. Crystal and molecular structures of dinitrosylcarbonyltriphenylphosphineiron, $\text{Fe}(\text{NO})_2(\text{CO})(\text{PPh}_3)$, and of dinitrosylbis(triphenylphosphine)iron, $\text{Fe}(\text{NO})_2(\text{PPh}_3)_2$. *J. Organomet. Chem.* **1974**, *67*, 413–422.
- (64) Cygler, M.; Ahmed, F. R.; Forgues, A.; Roustan, J. L. A. Synthesis and crystal structure of an iron nitrosyl carbonyl hydride. *Inorg. Chem.* **1983**, *22*, 1026–1030.
- (65) Li Kam Wah, H.; Postel, M.; Pierrot, M. Structure-activity correlation in iron nitrosyl complexes: Crystal structures of $[\text{Fe}(\text{NO})_2(\text{Cl})]_2(\mu\text{-dppe})$ and $\text{Fe}(\text{NO})_2(\text{dppe})$. *Inorg. Chim. Acta* **1989**, *165*, 215–220.
- (66) DeBeer George, S.; Petrenko, T.; Neese, F. Prediction of iron K-edge absorption spectra using time-dependent density functional theory. *J. Phys. Chem. A* **2008**, *112*, 12936–12943.
- (67) DeBeer George, S.; Petrenko, T.; Neese, F. Time-dependent density functional calculations of ligand K-edge X-ray absorption spectra. *Inorg. Chim. Acta* **2008**, *361*, 965–972.
- (68) Roemelt, M.; Beckwith, M. A.; Duboc, C.; Collomb, M.-N.; Neese, F.; DeBeer, S. Manganese K-edge X-ray absorption spectroscopy as a probe of the metal-ligand interactions in coordination compounds. *Inorg. Chem.* **2012**, *51*, 680–687.
- (69) Neese, F. Prediction and interpretation of the ^{57}Fe isomer shift in Mössbauer spectra by density functional theory. *Inorg. Chim. Acta* **2002**, *337*, 181–192.
- (70) Tao, J.; Perdew, J. P.; Staroverov, V. N.; Scuseria, G. E. Climbing the density functional ladder: nonempirical meta-generalized gradient approximation designed for molecules and solids. *Phys. Rev. Lett.* **2003**, *91*, 146401-1–146401-4.
- (71) Delgado-Jaime, M. U.; DeBeer, S. Expedited analysis of DFT outputs: introducing MOAnalyzer. *J. Comput. Chem.* **2012**, *33*, 2180–2185.
- (72) (a) Knizia, G. Intrinsic Atomic Orbitals: An Unbiased Bridge between Quantum Theory and Chemical Concepts. *J. Chem. Theory Comput.* **2013**, *9*, 4834–4843. (b) Knizia, G.; Klein, J. E. M. N. Electron flow in reaction mechanisms-revealed from first principles. *Angew. Chem., Int. Ed.* **2015**, *54*, 5518–5522.
- (73) Knizia, G. IboView; <http://www.iboview.org>.
- (74) *Reviews in Computational Chemistry*; John Wiley & Sons, Wiley-VCH: New York, 2001; Vol. 17.
- (75) Atkins, P. W.; Friedman, R. S. *Molecular Quantum Mechanics*, 5th ed.; Oxford University Press: Oxford, 2011.
- (76) Lu, T.-T.; Weng, T.-C.; Liaw, W.-F. X-ray emission spectroscopy: a spectroscopic measure for the determination of NO oxidation states in Fe-NO complexes. *Angew. Chem., Int. Ed.* **2014**, *53*, 11562–11566.
- (77) Vollmers, N. J.; Muller, P.; Hoffmann, A.; Herres-Pawlis, S.; Rohrmüller, M.; Schmidt, W. G.; Gerstmann, U.; Bauer, M. Experimental and Theoretical High-Energy-Resolution X-ray Absorption Spectroscopy: Implications for the Investigation of the Entatic State. *Inorg. Chem.* **2016**, *55*, 11694–11706.

4.2 The Bonding Situation in the Dinuclear Tetra-Hydrido Complex $[\{^5\text{CpFe}\}_2(\mu\text{-H})_4]$ Revisited by Hard X-ray Spectroscopy

Burkhardt, L.; Mueller, C.; Groß, O. A.; Sun, Y.; Sitzmann, H.; Bauer, M. *Inorg. Chem.* **2018**, DOI: 10.1021/acs.inorgchem.8b03032.

The publication has been accepted and will be published as the cover of Issue 11 (Volume 58) of ACS Inorganic Chemistry.

The dinuclear bridged polyhydride $[\{^5\text{CpFe}\}_2(\mu\text{-H})_4]$ and its non-hydride reference $[\text{CpCpFe}]$ are investigated by VtC-XES and HERFD-XANES combined with (TD)DFT. These compounds serve as model complexes to investigate the strength of modern hard X-ray spectroscopy to investigate Fe-Fe, Fe-H interaction and spin states in dinuclear bridged hydride complexes. Bonding Fe-hydride interactions contribute essentially to Fe K-edge VtC-XES features, whereas antibonding Fe-hydride interactions evoke an additional well-pronounced pre-edge feature in the XANES region.

Participation in this Publication

L. Burkhardt: HERFD-XANES and VtC-XES; geometry optimizations, simulation of VtC-XES spectra, XANES spectra, theoretical spectroscopy, manuscript preparation

C. Mueller, O. A. Groß: synthesis of all investigated compounds, NMR spectroscopy

Y. Sun: single crystal diffraction

H. Sitzmann: manuscript preparation

M. Bauer: corresponding author

The Bonding Situation in the Dinuclear Tetra-Hydrido Complex $[\text{CpFe}_2(\mu\text{-H})_4]$ Revisited by Hard X-Ray Spectroscopy

Lukas Burkhardt,[†] Carsten Mueller,[§] Oliver A. Groß,[†] Yu Sun,[§] Helmut Sitzmann,[§] and Matthias Bauer^{*,†,‡,§}

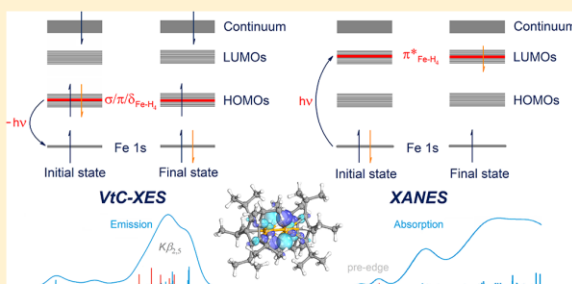
[†]Faculty of Science, Paderborn University, Warburger Straße 100, 33098 Paderborn, Germany

[‡]Center for Sustainable Systems Design (CSSD), Paderborn University, Warburger Straße 100, 33098 Paderborn, Germany

[§]Department of Chemistry, University of Kaiserslautern, Erwin-Schrödinger-Straße 54, 67663 Kaiserslautern, Germany

Supporting Information

ABSTRACT: High energy resolution fluorescence detected XANES (HERFD-XANES) and valence-to-core X-ray emission spectroscopy (VtC-XES) are introduced as powerful tools to investigate hydride–iron interaction, the possible iron–iron bond, and iron spin state of the dinuclear tetra-hydrido complex $[\text{CpFe}_2(\mu\text{-H})_4]$ (**1H**, $\text{Cp} = \eta^5\text{-C}_5\text{H}_5$) by thoroughly accessing the geometric and electronic structure of this complex in comparison to the nonhydride reference $[\text{CpCpFe}]$ (**1**, $\text{Cp} = \text{C}_5\text{H}_5$). The so far observed most intense hydride induced signals in the pre-edge feature of the HERFD-XANES and in the VtC-XES spectra at the iron K-edge allow a precise analysis of the LUMO and HOMO states, respectively, by application of time-dependent density function theory (TD-DFT) and density functional theory (DFT) calculations. The results of these calculations are further employed to understand the oxidation state, spin states, and potential Fe–Fe bonds in this complex.



INTRODUCTION

Transition metal (TM) hydrides gain increasing importance in chemistry and biology as active compounds or intermediates^{1–9} for many chemical transformations or hydrogen storage¹⁰ or in renewable energy¹¹ applications like water reduction.¹² In order to understand the working principle of applied catalysts, enzymes, and materials, determination of the electronic and geometric structure is indispensable, which can create major challenges if determined under in situ and in operando conditions.

The structure is usually accessed by standard spectroscopic and scattering methods. However, many methods are limited for several reasons. For example, due to the small scattering amplitude of hydrogen, X-ray scattering can only be applied under ideal conditions.¹³ In contrast, due to the large scattering length of ^2H , neutron diffraction is a powerful technique but requires selective deuteration. In the same sense, Mössbauer spectroscopy may require enrichment of the sample with ^{57}Fe .^{14,15} ^1H NMR spectroscopy is well suited only for the investigation of diamagnetic transition metal hydrides. Finally, vibrational spectroscopy can be powerful to determine both the electronic and geometric structure, if combined with theoretical calculations.^{16,17} But it can be challenging if the bands of the investigated compounds are forbidden or overlapping with ligand, solvent, or coreactant vibrations. ^{57}Fe nuclear resonance vibrational spectroscopy (NRVS) is

able to overcome the limitations of conventional vibrational spectroscopy. The intensity of NRVS spectra is only sensitive to ^{57}Fe nuclear motion and is therefore able to detect signals in spectral regions that would be otherwise superimposed by other vibrational modes in conventional vibrational spectroscopy.¹⁸

To complement these methods, an element specific method, delivering a spectroscopic signal not interfered with by any factors, and applicable in situ and even in operando, would be highly desired. Hard X-ray absorption near edge spectroscopy (XANES)^{19,20} and X-ray emission spectroscopy (XES)²¹ at metal K-edges can overcome the aforementioned limitations.

In the pre-edge signal of K-edge XANES spectra, a 1s electron of a given element is excited to empty states and thus contains unique information about the unoccupied transition metal 3d levels and LUMO levels.²² Unfortunately, many of these details are masked by signal broadening induced by the core-hole lifetime. Since the minimal line width of a transition is inversely proportional to the lifetime of its final state, the experimental resolution can be enhanced by detecting an emissive final state with a longer lifetime, as can be simply understood by the time-energy uncertainty relation and has been described by the Kramers–Heisenberg formula.²³ This

Received: October 26, 2018



ACS Publications

© XXXX American Chemical Society

A

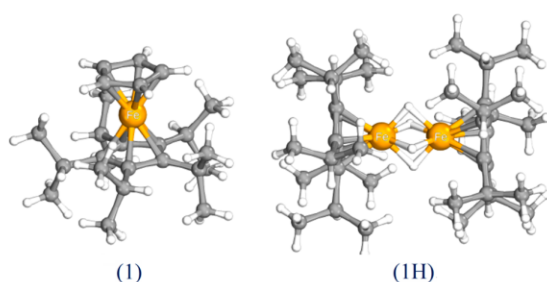
DOI: 10.1021/acs.inorgchem.8b03032
Inorg. Chem. XXXX, XXX, XXX–XXX

sharpening effect has been named high energy resolution fluorescence detected XANES (HERFD-XANES).^{19,24,20}

In K-edge valence-to-core (VtC)-XES,^{25,26} a 1s electron is excited nonresonantly above the continuum, and the emissive valence state \rightarrow Fe 1s relaxation channel is monitored. Thus, VtC-XES offers a unique probe of HOMO levels and therefore is able to probe occupied 3d levels, ligand localized orbitals, and their bonding interactions.^{27–34} We have proven in our previous study that the methodological combination of HERFD-XANES and VtC-XES is a powerful tool to investigate Fe–H interactions in great detail.³⁵

We will therefore use the established methodology plus the additional application of core-to-core (CtC)-XES as a precise measure of the oxidation state in terms of localized spin density to revisit the electronic structure of the tetrahydrido complex $[\{\text{CpFe}\}_2(\mu\text{-H})_4]$ (**1H**, $^5\text{Cp} = \eta^5\text{-C}_5\text{iPr}_5$) by hard X-rays, which is shown in Chart 1. By classical description of the

Chart 1. Crystal Structures of Complexes **1** and **1H**^a



^a**1H**: dinuclear molecule on a crystallographic inversion centre, Fe– $^5\text{Cp}_{\text{cent}}$ 167.3 pm, Fe–Fe 221.45(6) pm. **1**: three independent molecules, Fe1– $^5\text{Cp}_{\text{cent}}$ 166.1 pm, Fe1–Cp_{cent} 167.3; Fe2– $^5\text{Cp}_{\text{cent}}$ 166.2 pm, Fe2–Cp_{cent} 166.9; Fe3– $^5\text{Cp}_{\text{cent}}$ 166.6 pm, Fe3–Cp_{cent} 166.7 (thermal ellipsoids of **1** and **1H** are shown in the Supporting Information, Charts S2 and S3).

hydride ligand and the 18 valence electron rule, one might describe the bonding situation as two Fe^{III} ions connected via an Fe–Fe triple bond.³⁶ In contrast, the bonding situation in the ruthenium analogue, $[\{\text{CpRu}\}_2(\mu\text{-H})_4]$, has been described solely based on ab initio methods by Morokuma and Koga as two Ru^{II} centers coordinated to a $[\text{H}_4]^{2-}$ cluster, with no additional Ru–Ru bonding interaction.³⁶ To date, there has been no experimental proof for this description, especially not for the iron tetrahydrido complex investigated here. It will be shown in the following that HERFD-XANES and VtC-XES in combination with (TD-)DFT calculations can determine the oxidation state of the iron centers unambiguously, resolve details of the hydride coordination, and determine the presence of an Fe–Fe bond. These important issues are complemented by theoretical X-ray spectroscopy, demonstrating that HERFD-XANES and VtC-XES are powerful tools to identify spin states and that the methodic combination of VtC-XES and HERFD-XANES can resolve hydride species even in reaction mixtures.

EXPERIMENTAL SECTION

X-Ray Spectroscopy. High-resolution X-ray absorption and emission experiments were carried out at beamline ID26 of the European Synchrotron Radiation Facility ESRF (Grenoble, France). Two u35 undulators were used, yielding an incident X-ray flux of approximately 2×10^{13} photons s^{-1} . Experiments were conducted

with a Johann-type X-ray emission spectrometer in the horizontal plane, where the sample, crystal analyzers, and photon detector (avalanche photodiode) were arranged in a vertical Rowland geometry. The emission spectrometer was calibrated using the elastic scattering line. The incident energy was selected using the (111) reflection from a double Si crystal monochromator, and the emission energy was selected using the (620) reflection of five spherically bent Ge crystal analyzers (with $R = 1$ m) of the Johann spectrometer. All Fe K-edge HERFD-XANES spectra were obtained by recording the intensity of the Fe $K\beta_{1,3}$ emission line as a function of the incident energy. The total fluorescence yield (TFY) was monitored by a photodiode installed at about a 90° scattering angle and at 45° to the sample surface. During the HERFD-XANES scans, the undulators gaps were kept fixed, and only the monochromator angle was changed. Each HERFD-XANES scan was carried out in 10 s, recording three spectra per point of the homogeneous sample. Thirty spectra were averaged to yield an adequate signal-to-noise ratio. To decrease the radiation damage, all measurements were conducted at 50 K using a He cryostat under vacuum conditions. Each sample was tested for radiation damage in the beginning by 10 fast measurements with a scan-time of 10 s on one spot. Within these time frames, no radiation damage could be detected (no decrease/increase/shift for all observed pre-edge/near-edge/white-line features).

For the VtC-XES data collection, an incident energy of 7.2 keV was chosen. VtC-XES energy scans were carried out in the range from 7065 to 7140 eV. To observe reasonable data, 30 spectra (50 s per scan) were recorded, utilizing a different sample spot for each scan. Detailed information about the treatment of experimental data is given in the Supporting Information.

X-Ray Structure Analyses. The single-crystal X-ray diffraction data were recorded on a Rigaku Oxford Xcalibur, Sapphire3, Gemini ultra diffractometer with Cu $K\alpha$ radiation ($\lambda = 1.54184$ Å). Crystal data and refinement parameters for compounds **1** and **1H** are collected in Table S5 of the Supporting Information. Both structures were solved using direct methods (SIR92),³⁷ completed by subsequent difference Fourier syntheses, and refined by full-matrix least-squares procedures.³⁸ Analytical numeric absorption corrections were applied on both complexes.³⁹ All non-hydrogen atoms were refined with anisotropic displacement parameters. In the structure of compound **1**, the hydrogen atoms H1 and H2, which are bound to Fe1, were observed in the following difference Fourier synthesis and then were allowed to be refined freely. All the other hydrogen atoms were placed in calculated positions and refined by using a riding model. CCDC 1875499–1875500 contain the supplementary crystallographic data for this paper. These data can be obtained free of charge from The Cambridge Crystallographic Data Centre via www.ccdc.cam.ac.uk/data_request/cif.

Theoretical Calculations. All computations presented in this article were performed using the ORCA package (version 4.0.1).⁴⁰ Unconstrained geometry optimizations were conducted utilizing the PBEh-3c method of the Grimme group.⁴¹ All presented optimized structures were confirmed to be minima structures by numerical frequency calculations and the absence of negative frequencies.

Theoretical VtC-XES (DFT) and XANES (TD-DFT)^{42,43} spectra were calculated using a modified TPSSH functional, with an adjusted Hartree–Fock exchange⁴⁴ to 5% in conjunction with the RJCOSX approximation and the def2-TZVP⁴⁵ basis set, combined with the def2-TZVP/J⁴⁶ auxiliary basis set (with a special integration accuracy of 5) on all atoms except Fe, for which the expanded CP(PPP) basis set⁴⁷ (with a special integration accuracy of 7) was used. Dispersion correction was included via Becke–Johnson damping scheme (D3BJ).^{48,49}

XANES (TD-DFT) transitions were broadened by a 1.5 eV Gaussian (fwhm) and shifted by 162.6 eV. VtC-XES (DFT) transitions were broadened by a 2.5 eV Gaussian (fwhm) and shifted by 163.6 eV. All calculated spectra were normalized on the number of Fe atoms per complex. Kohn–Sham orbitals were visualized with the IboView program (version 20150427).⁵⁰ Orbital populations were extracted via Löwdin reduced orbital population analysis.

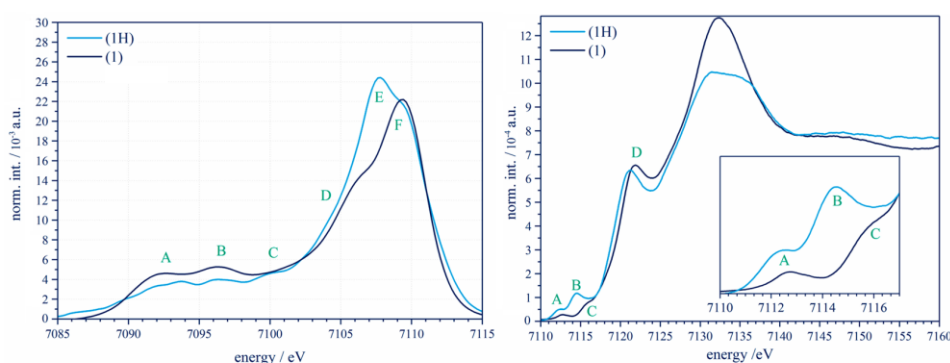


Figure 1. Left: experimental Fe K-edge VtC-XES spectra of **1** and **1H**. Right: experimental Fe K-edge HERFD-XANES spectra of **1** and **1H**.

Table 1. Characteristic Signal Energies of VtC-XES and HERFD-XANES Spectra of Complexes **1** and **1H**

compound	VtC-XES peak energies/eV (norm. int./a.u.)					
	A	B	C	D	E	F
[⁵ CpCpFe] (1)	7092.4 (0.005)	7096.4 (0.005)	7101.1 (0.005)	7103.6 (0.008)	7106.5 (0.015)	7109.4 (0.022)
[⁵ CpFe] ₂ (μ-H) ₄ (1H)	7092.9 (0.003)	7096.5 (0.004)	7100.0 (0.005)	7104.2 (0.010)	7107.8 (0.024)	7109.3 (0.021)
	HERFD-XANES prepeak energies/eV (norm. abs./a.u.)					
	A	B	C	D		
[⁵ CpCpFe] (1)	7112.7 (2.9 × 10 ⁻⁵)	7114.5 (1.2 × 10 ⁻⁵)	superimposed	7121.9 (6.5 × 10 ⁻⁵)		
[⁵ CpFe] ₂ (μ-H) ₄ (1H)	7112.5 (5.0 × 10 ⁻⁵)	not detected	7116.0 (8.1 × 10 ⁻⁵)	7121.2 (6.3 × 10 ⁻⁴)		

Synthesis. Reactions were carried out under argon atmosphere using standard Schlenk techniques or a glovebox. Solvents were distilled over potassium (THF) or sodium/potassium (pentane). Solvents were degassed prior to use by standard procedures. Penta-isopropylcyclopentadienyl (dimethoxyethane) iron(II) bromide⁵¹ was synthesized according to the literature cited; other chemicals were purchased from Sigma-Aldrich, ABCR, or ACROS. Lithium aluminum hydride was dissolved in diethyl ether, and pure material for synthetic use was recovered by evaporation of the solution after removal of insoluble impurities by filtration. NMR spectra (shown in the Supporting Information, Figures S7 and S8) were recorded using either a Bruker AC 200 or AMX 400 device.

Synthesis of 1. Penta-isopropylcyclopentadienyl (dimethoxyethane) iron(II) bromide (100 mg, 0.17 mmol) and sodium cyclopentadienide (16.0 mg, 0.18 mmol) were initially charged, and tetrahydrofuran (20 mL), cooled to 0 °C, was added causing the solution to turn yellow. After stirring at room temperature for 18 h, the solvent was removed under reduced pressure. The obtained residue was extracted with pentane (15 mL). The insolubles were removed, and the solvent was evaporated under vacuo to give a yellow solid. The crude product was taken up in diethyl ether (5 mL), and acetonitrile (25 mL) was added. A yellow solid precipitated, which was isolated by centrifugation and dried in vacuo. The product was obtained as a yellow solid (43.0 mg, 0.12 mmol 71%). ¹H NMR (200 MHz, C₆D₆): δ (ppm) 1.16 (d, *J* = 7.3 Hz, 15 H, ⁵Cp-CH(CH₃)₂), 1.50 (d, *J* = 7.3 Hz, 15 H, ⁵Cp-CH(CH₃)₂), 2.87 (sept, *J* = 7.3 Hz, 5 H, ⁵Cp-CH(CH₃)₂), 4.21 (s, 5H Cp-H). Anal. Calcd for **1** (396.43): C, 75.74; H, 10.17. Found: C, 75.79; H, 10.28.

Synthesis of 1H. **1H** was prepared using a modified version of the [⁵Cp*Fe]₂(μ-H)₄ synthesis procedure by Suzuki and Ohki.⁵² Penta-isopropylcyclopentadienyl (dimethoxyethane) iron(II) bromide (200 mg, 0.40 mmol) was dissolved in THF (20 mL), and the yellow solution was cooled to -78 °C. To this solution, a suspension of lithium aluminum hydride (120 mg, 3.2 mmol) in THF (20 mL) was added, while the mixture turned red. The reaction mixture was allowed to thaw to room temperature and was stirred overnight. The solvent was evaporated, and the brown residue was extracted with pentane. The insolubles were removed, and the solution was evaporated to give a yellow solid, which was dissolved in THF (10

mL). The resulting red solution was cooled to -78 °C, and a solution of water in THF (V/V = 1:1000, 18.5 mL, 1.03 mmol H₂O) was added slowly with a color change from red to yellow. The resulting mixture was allowed to slowly thaw to room temperature and stirred overnight, while the color changed from yellow to purple. The solvent was evaporated, and the purple residue was extracted with pentane (20 mL). Insolubles were separated from the product mixture by centrifugation, and the deep purple solution was evaporated to dryness. The crude product was obtained as a brown-violet solid, which after several pentane washings afforded a violet solid (55 mg, 0.08 mmol, 41%). ¹H NMR (400 MHz, C₆D₆): δ (ppm) -22.31 (4 H, hydride bridges of one diastereomer⁵³), -22.37 (4 H, hydride bridges of other diastereomer), 1.13 (d, *J* = 7.1 Hz, 30 H, ⁵Cp-CH(CH₃)₂), 1.96 (d, *J* = 7.1 Hz, 15 H, ⁵Cp-CH(CH₃)₂), 1.97 (d, *J* = 7.1 Hz, 15 H, ⁵Cp-CH(CH₃)₂), 2.78 (sept, *J* = 7.1 Hz, 10 H, ⁵Cp-CH(CH₃)₂). Anal. Calcd for **1H** (666.73): C, 72.06; H, 11.19. Found: C, 72.76; H, 11.20.

RESULTS

Experimental Results. Chart 1 shows the structure of [⁵CpFe]₂(μ-H)₄ (**1H**) and [⁵Cp₂Fe] (**1**) as a hydride free reference. [⁵CpFe]₂(μ-H)₄ (**1H**) is more tolerant toward air compared to the highly reactive and rather unstable complexes [⁵Cp*Fe]₂(μ-H)₄⁵⁴ or [⁵Cp'''Fe]₂(μ-H)₄,⁵⁵ with Cp = η⁵-C₅H₅, ⁵Cp = η⁵-C₅iPr₅, Cp* = η⁵-C₅Me₅, and Cp''' = 1,2,4-C₅H₂(CMe₃)₃. These dinuclear tetra-hydrido complexes are known for C(sp²)-H,⁵⁶ Si-H,⁵⁶ P-H, B-H,^{57,58} and P₄ activation⁵⁵ and were described as diamagnetic, classical metal hydrides with a short Fe-Fe distance of 2.20 Å.⁵⁴ Since **1H** is a 30 e⁻ species, the noble gas rule would require an Fe-Fe triple bond between both Fe atoms, which is contradicted by Morokuma and Koga for the Ru analogue, where they claim a missing direct M-M bond.³⁶

Reference **1** is coordinated in a typical sandwich structure, while **1H** exhibits a triple-decker structure with a planar H₄ cluster ({H₄}) bridging both iron atoms, with an Fe-Fe

distance of 2.21 Å (for detailed information, see Supporting Information [Charts S2 and S3](#)). The diamagnetic character of both **1** and **1H** and the almost identical Fe–⁵Cp distances (see Supporting Information, [Table S1](#)) agree with low spin Fe^{+II} central atoms for both complexes. Due to the alignment of the *i*Pr substituents in the ⁵Cp ligand, **1H** is obtained as a mixture of diastereomers.⁵³ Both stereoisomers are present in solution as well as in the crystalline state as illustrated by ¹H NMR and diffraction data (see [Experimental Section](#)). The {H₄} plane of **1H** is slightly tilted by 4.75° against both ⁵Cp planes (see Supporting Information [Chart S1 and Table S1](#)).

As mentioned above, details of the HOMO states are probed in VtC-XES spectra, which are shown in [Figure 1](#) (left). They exhibit characteristic features for both **1** and **1H**, which are summarized in [Table 1](#). On the low energy side, two rather weak Kβ'' signals A and B are located, followed by C and D that appear as low energy shoulders to the emission maximum, which is composed of E and F. Both low-energy features A and B show a smaller intensity for **1H** compared to **1**. Shoulder C is equal in intensity and energy for both **1** and **1H**, while D is again characterized by a reduced intensity and smaller energy in the tetra-hydrido complex (**1H**). In contrast, feature E is slightly blue-shifted and drastically more intense for **1H**, while feature F shows an opposite behavior. Furthermore, this signal appears to be broadened in the hydride **1H**.

Since Kβ'' features are caused by ligand 2s → Fe 1s transitions, the decrease in intensity of A and B for **1H** is attributed to reduction of the total number of ligand donor orbitals⁵⁹ per iron atom in relation to **1**.^{25,60,61} The most significant changes induced by the {H₄} fragment found for features D and E at around 7107 eV can be qualitatively assigned to the bonding interaction between Fe 3d and the H 1s orbital according to previous studies.³⁵ Accordingly, the spectral differences between **1** and **1H** are suspected to originate from bonding Fe–H₄–Fe interactions, since the energy and quantity of remaining ligand donor orbitals⁵⁹ should be almost identical for both complexes **1** and **1H**. Further analysis of the bonding situation from the VtC-XES is only possible by application of DFT calculations. The results will be given after discussion of the experimental HERFD-XANES data.

Complementary to VtC-XES, HERFD-XANES allows probing of the LUMO states of **1** and **1H**. The experimental spectra are shown in [Figure 1](#) (right); the assigned features are again summarized in [Table 1](#). In both complexes **1** and **1H**, an intense near-edge feature D and two pre-edge features A and C are observed. Pre-edge feature B is only observed for **1H**. The low-energy pre-edge feature A is higher in intensity and red-shifted in the tetra-hydrido complex **1H** compared to reference **1**. On the basis of literature reports,^{25,60,61} this feature is assigned to Fe 1s → Fe 3d transitions.

As mentioned above, feature B is only observed in the tetra-hydrido complex **1H**. Investigations of ferrocenium complexes also observed a second prepeak feature,^{25,60,61} due to semioccupation of the Fe 3d_z² in case of a central Fe^{+III} ion.

Both complexes (**1**, **1H**) exhibit an intense near-edge feature D, which is well-known for ferrocene compounds.^{25,60,61} Such a feature in Cu^{+I}/Cu^{+II} compounds is assigned to 1s → 4p transitions.^{62,63} Accordingly, feature D is in both cases of **1** and **1H** assigned to Fe 4p acceptor orbitals or combinations of 4p and ligand orbitals.

Although the formal Fe oxidation state is +II in **1** [⁵Cp^{−1}Cp^{−1}Fe^{+II}] and +III in **1H**[(⁵Cp^{−1}Fe^{+III})₂(μ-H^{−1})₄], the

edge positions indicate an oxidation state of +II for both complexes, whereas an oxidation state of +III for **1H** can be excluded. The edge position of **1H** is even slightly red-shifted in comparison with spectra of the ferrocene **1**. That means **1H** displays an Fe oxidation state of +II or lower, since the redshift of the edge position in relation to **1** can be either explained by even further reduced Fe^{±0/+1} ions or by the strong donor characteristics of the hydride ligands. From the experimental CtC-XES spectra, which are given in the Supporting Information ([Figure S1](#)), a similar spin state, i.e., oxidation state, must be present in both complexes. Since no Kβ' satellite is observed, a high spin-state can be excluded. The only difference observed between **1H** and **1** is a slight blue-shift of the main line in **1H**, interpreted by a higher Fe 3d density due to the strongly donating hydride ligands. The origin of the red-shifted edge position in **1H** in relation to **1** can only be addressed with the help of TD-DFT calculations in the next section.

Theoretical Results. Although the fingerprint approach applied so far and outlined above is suitable for shedding some light on the experimental results, the atomic and quantum mechanical origin of the spectral features in **1H** can only be understood on the basis of theoretical calculations. Details of the calculations are given in the [Experimental Section](#) and [Supporting Information](#).

The crystal structure of **1H** exhibits a tilted {H₄} plane in relation to both ⁵Cp planes, while the DFT gas phase structure shows a parallel orientation, which does not reflect reality in the measured solid samples (see [Supporting Information Chart S1](#)). In the DFT structure of **1H**, four identical Fe–H bond lengths of 1.62 Å and four identical H–H distances of 1.71 Å are observed, while in the crystal structure different Fe–H distances of 1.64/1.66 Å and 1.54/1.55 Å and two different H–H bond lengths of 1.73 and 1.52 Å are present (for further information, see [Supporting Information Table S1](#)). For this reason, all calculations shown here were performed on the nonoptimized crystal structures.

Theoretical and experimental VtC-XES spectra are compared in [Figure S3](#) in the Supporting Information. Using an adjusted TPSSH functional, an impressive degree of agreement between experiment and theory is obtained in both complexes **1** and **1H**, which justifies the extraction of detailed information about the involved molecular orbitals and their chemical nature. Ligand projected spectra were generated to assign particular spectral features to different coordinating ligands. The deconvoluted spectra of **1** and **1H** are shown in [Figure 2](#).

As already extensively investigated in the case of ferrocene and the ferrocenium cation by DeBeer et al.⁶⁰ and functionalized ferrocene derivatives by Bauer et al.,⁶¹ Cp (or ⁵Cp) localized donor orbitals and their bonding combinations are naturally involved in all observed emission features A to D, as also illustrated by the Cp (or ⁵Cp) projections in [Figure 2](#). In the following discussion, we will focus on the tetra-hydrido part of the ligands, since detailed investigations of the Cp (⁵Cp) coordination have been communicated earlier.^{25,60,61}

The hydride projected VtC-XES contribution highlighted in [Figure 2](#) appears as a broad band with a maximum at 7105.8 eV and a shoulder at around 7107.9 eV. This projection clearly shows that the experimentally observed differences between **1** and **1H** in the region of signals D and E are caused by hydride donor orbitals, which is further stressed in [Figure S6](#) of the Supporting Information.

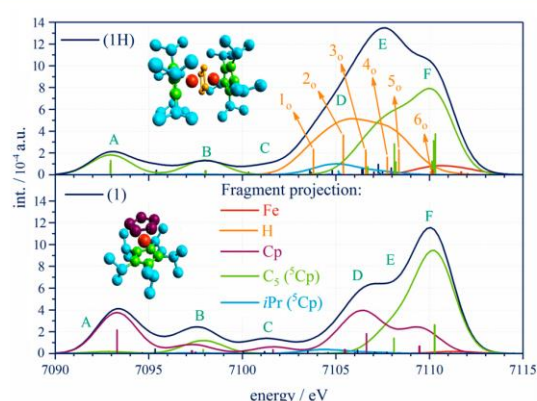


Figure 2. Comparison of theoretical ligand/fragment projected Fe K-edge VtC-XES spectra of complexes **1** (bottom) and **1H** (top). Hydride localized donor orbitals are highlighted (N_o denotes occupied, see Figure 3).

All donor orbitals with significant hydride density (1_o to 6_o , occupied) are presented and described in Figure 3 (atomic orbital populations are given in Supporting Information Table S2). These hydride donor orbitals reflect the bonding combination of the a_{1g} , the doubly degenerated e_u and the b_{2g} orbital of $\{H_4\}$ (D_{4h}) with mainly Fe 3d orbitals (Figure 3). This is in line with the conclusions of Koga and Morokuma⁴⁰ for the ruthenium analogue. The δ -bond type orbital 6_o is entirely described by interaction of Fe 3d and H 1s orbitals;

almost no Fe 4p hybridization could be observed, leading to a very weak transition probability of the $6_o \rightarrow$ Fe 1s transition (Figure 2). Morokuma and Koga proposed no interaction of the metal orbitals and the a_{1g} orbital of $\{H_4\}$ for the analog ruthenium complex. In contrast, we observe weak bonding interactions of the a_{1g} orbital of $\{H_4\}$ with Fe 4s and Fe 4p orbitals here, and therefore hydride orbitals $1_o/2_o$ are described as σ -bond orbitals by symmetry (atom orbital populations are given in Supporting Information Table S3).

Experimental and calculated HERFD-XANES spectra of **1** and **1H** are compared in Figure S4 in the Supporting Information. The agreement of experiment and theory is remarkably good, since not only the prepeak but also the edge fine structure and white line features are entirely described (see also Supporting Information Figure S2). Such good agreement using TD-DFT is usually not expected but was recently observed in other cases as well.^{35,64} These observations suggest that the nature of the underlying transitions is rather localized. Ligand projected XANES spectra were created to facilitate the assignment of spectral features to involved ligands (Figure 4), in the same manner as performed for the VtC-XES spectra. In both complexes **1** and **1H**, feature A is solely caused by a Fe 1s \rightarrow Fe 3d_{xz/yz} (LUMO/LUMO+1) transition as suspected in the Experimental Section (acceptor orbitals are presented in Supporting Information Chart S4). The ligand projected XANES spectra (Figure 4) clearly illustrate that near-edge feature C possesses no significant contribution of Fe 3d (**1**, **1H**) or H 1s/2p orbitals (**1H**) and solely originates from Cp (**1**) and 5Cp (**1**, **1H**) localized acceptor orbitals, respectively.

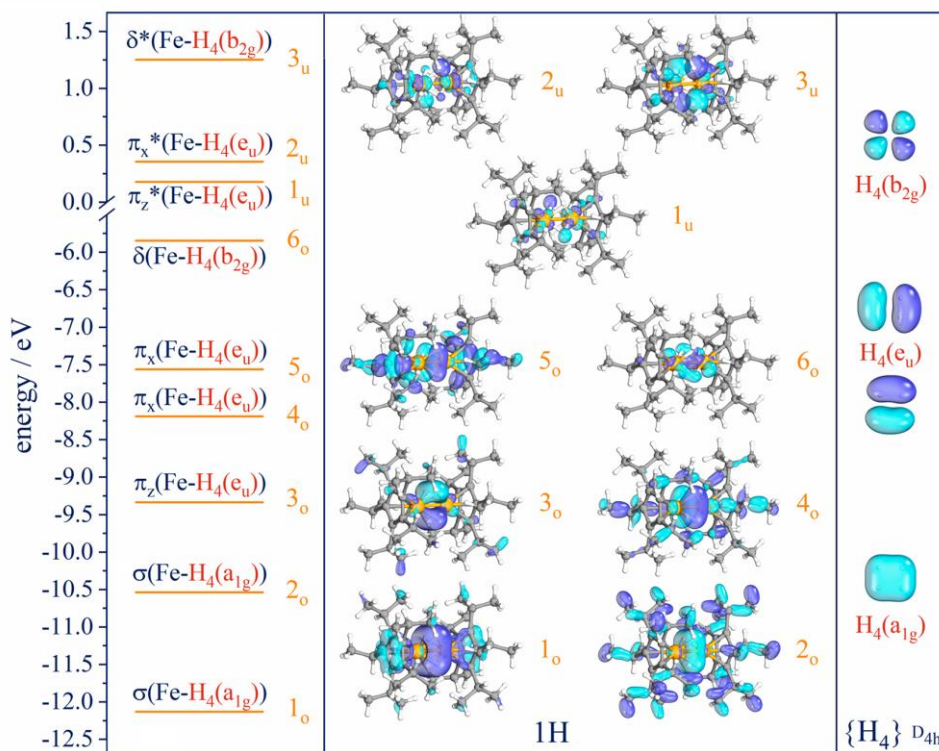


Figure 3. Energetic order of hydride localized donor (N_o , occupied, VtC-XES) and acceptor orbitals (N_u , unoccupied, XANES) of **1H** according to the analysis of the VtC-XES and XANES.

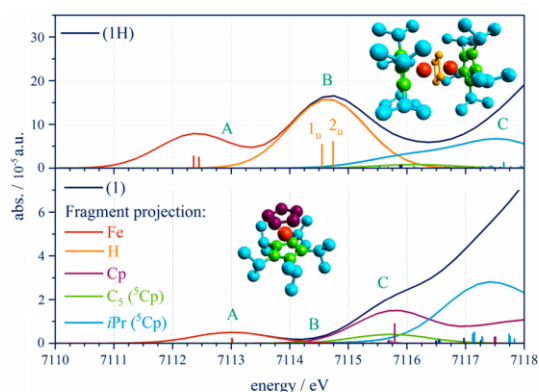


Figure 4. Comparison of XANES ligand/fragment projected spectra of **1** (bottom) and **1H** (top). Hydride localized acceptor orbitals are highlighted (N_u , unoccupied, see Figure 3).

The calculated pre-edge feature B is caused by transitions of Fe 1s to acceptor orbitals with significant hydride density, as proven from the acceptor orbitals presented in Figure 3 as 1_u and 2_u , which reflect the antibonding interactions of Fe $3d_{xz/yz}$ with the e_u orbital of $\{H_4\}$ (AO populations are given in Supporting Information Table S2). Consequently, feature B is not a result of a higher oxidation state in **1H** as seen for the ferrocenium cation.^{25,60,61} Instead, it is caused by antibonding interactions of Fe 3d orbitals and the e_u orbital of $\{H_4\}$. No transition with significant intensity is observed for the antibonding δ^* -type hydride orbital 3_u (Figure 3), since 3_u is entirely described by antibonding interactions of Fe 3d and H 1s orbitals and almost no Fe 4p hybridization could be observed, leading to a very weak transition probability of the Fe $1s \rightarrow 3_u$ transition (AO populations are given in Supporting Information Table S2).

Summarizing, signal B is unequivocally assigned to the $\{H_4\}$ fragment and is a very pronounced spectroscopic signature of hydrogen ligands in X-ray absorption spectra, proving the high power of HERFD-XANES to detect hydrogen in transition metal complexes.

DISCUSSION

All calculations on **1H** presented above were conducted in the singlet ground state according to the low-spin Fe^{+II} configuration. Nevertheless, there are more possible hypothetical spin states that could be considered for the electronic ground state in **1H**. In order to figure out which spin state is present in **1H** and to illustrate the sensitivity of VtC-XES and HERFD-XANES to the spin of an investigated compound, spectra of **1H** in the singlet, triplet, nonet, and $M_S = 11$ were calculated. To allow a meaningful comparison of all states, the nonoptimized crystal structure of **1H** is utilized.

The following states were taken into account: a singlet state, reflecting two low-spin (LS) Fe^{+II} ions, two antiferromagnetically coupled LS Fe^{+III} centers, two antiferromagnetically coupled high-spin (HS) Fe^{+II} ions, or two antiferromagnetically coupled HS Fe^{+III} ions. Two ferromagnetic coupled LS Fe^{+III} ions lead to a triplet state. The ferromagnetic coupling of two HS Fe^{+II} ions results in a nonet state, and finally, two ferromagnetically coupled HS Fe^{+III} ions result in multiplicity $M_S = 11$.

Figure 5 compares VtC-XES- (left) and XANES spectra (right) of the singlet, triplet, nonet, and $M_S = 11$ spin state of **1H**. The intensity ratio $I(E)/I(F)$ and energy splitting $\Delta E(E-F)$ of the peak features E and F are well described by the singlet and triplet state, while both ratios are too low in the nonet and the $M_S = 11$ state (Figure 2). The triplet, nonet, and $M_S = 11$ states exhibit a new high-energy feature H, which is caused by a partial occupation of higher 3d levels. Unfortunately, feature H is only weakly pronounced in the triplet state, and therefore we cannot exclude the triplet state by means of the experimental resolution and signal-to-noise ratio. Thus, theoretical VtC-XES excludes all spin states except the singlet and triplet state as the electronic ground state of **1H**.

HERFD-XANES exhibits a similar ability to distinguish the different spin states. Distinct spectral changes in the pre-edge region are predicted. In contrast to the VtC-XES, only the singlet state is able to describe the experimentally observed pre-edge features A and B (see Supporting Information Figure S4) in terms of intensity ratio $I(A)/I(B)$ and energy splitting $\Delta E(B-A)$. Pre-edge feature A is significantly blue-shifted and increases in intensity in the triplet state, while B is not affected in energy but decreases in intensity. In the nonet state, an

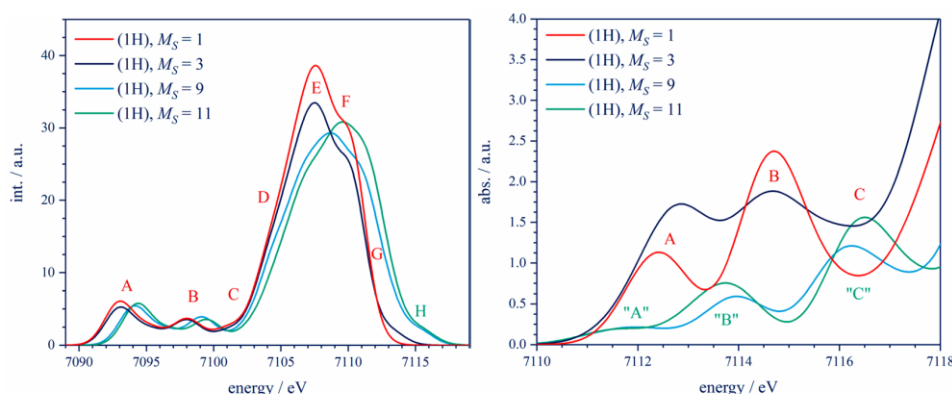


Figure 5. Left: Comparison of theoretical Fe K-edge VtC-XES spectra of the singlet, triplet, nonet, and $M_S = 11$ spin state of **1H**. Right: Comparison of theoretical Fe K-edge XANES spectra of the singlet, triplet, nonet, and $M_S = 11$ spin state of **1H**.

F

DOI: 10.1021/acs.inorgchem.8b03032
Inorg. Chem. XXXX, XXX, XXX–XXX

additional pre-edge feature “C” is appearing at an energy similar to C, while features A (“A”) and B (“B”) are shifting to lower energies and are decreased in intensity. A similar spectrum is observed in the spin state $M_S = 11$, with “B” further red-shifted and increased in intensity, while “C” is blue-shifted and also increases in intensity compared to $M_S = 9$. Consequently, the singlet state is confirmed as the present electronic ground state in **1H** by comparison of experimental and calculated HERFD-XANES spectra.

Fe–Fe Interaction. Finally, the Fe–Fe interaction in **1H** will be discussed in light of the X-ray spectroscopic results. To the best of our knowledge, to date there is no published theoretical or experimental investigation of the Fe–Fe interaction of related dinuclear iron tetrahydrido complexes.⁵³ As mentioned above, Morokuma and Koga proposed no M–M bond for the ruthenium analogue $[\{\text{Cp}^*\text{Ru}\}_2(\mu\text{-H})_4]$.⁴⁰ In order to investigate the Fe–Fe interaction in **1H**, all occupied and unoccupied orbitals with significant Fe density are compared to those of **1** in Figure 6 (AO populations are given in Supporting Information Table S3). The $\text{Fe } 3d_{x^2-y^2}$, $\text{Fe } 3d_{xy}$, and $\text{Fe } 3d_z$ of both Fe ions in **1H** are interacting with their counterparts and splitting up into bonding ($\text{Fe}^1 3d_{xy} + \text{Fe}^2 3d_{xy}$), ($\text{Fe}^1 3d_z + \text{Fe}^2 3d_z$), and ($\text{Fe}^1 3d_{x^2-y^2} + \text{Fe}^2 3d_{x^2-y^2}$) and antibonding ($\text{Fe}^1 3d_{x^2-y^2} - \text{Fe}^2 3d_{x^2-y^2}$), ($\text{Fe}^1 3d_z - \text{Fe}^2 3d_z$), and ($\text{Fe}^1 3d_{xy} - \text{Fe}^2 3d_{xy}$) combinations. In sum, six iron localized orbitals are fully occupied with 12 electrons of two $3d^6 \text{Fe}^{II}$ ions, consistent with our interpretation of the experimental results. Since the number of fully occupied bonding combinations is equal to the number of fully occupied antibonding combinations, no Fe–Fe bond is present in **1H**.

Outlook. As an outlook, the potential of the methods VtC-XES and HERFD-XANES to investigate hydride species in situ or in operando is presented in the following section. In such measurements, hydride complexes might be present in mixtures with nonhydride species. Thus, theoretical combinations of hydride (**1H**) and nonhydride (**1**) species were simulated with **1H** fractions of 2–90%. The resulting VtC-XES and HERFD-XANES data are shown on the left side of Figure 7. Both the intensity and energy position of signals D and E in the VtC-XES region allow a detection of hydride species from a mole fraction of around 10%.

For HERFD-XANES, a similar situation is found. In the case of **1H**, hydride pre-edge feature B is very pronounced, and the specificity of HERFD-XANES toward Fe–H species is similar to VtC-XES here. Consequently, the detection limit in these HERFD-XANES for hydride compounds is the same as found in VtC-XES with around 10%. This observation is in contrast to our last study, where only a weak hydride signal could be observed in the XANES region, and VtC-XES was by far more sensitive to the Fe–H interaction.³⁵

We have to admit that in situ measurements suffer from low absorber (in this case, Fe) concentrations, which are typically much less concentrated than solid samples. However, in contrast to conventional XANES, HERFD-XANES is filtering background photons with great efficiency and therefore HERFD-XANES is able to study ultradiluted elements as shown, for example, for metalloids in environmental biogeochemistry.⁶⁵ Furthermore, it has been shown in many studies that a characterization of diluted active species in situ or in operando is feasible with HERFD-XANES and VtC-XES.^{66–74}

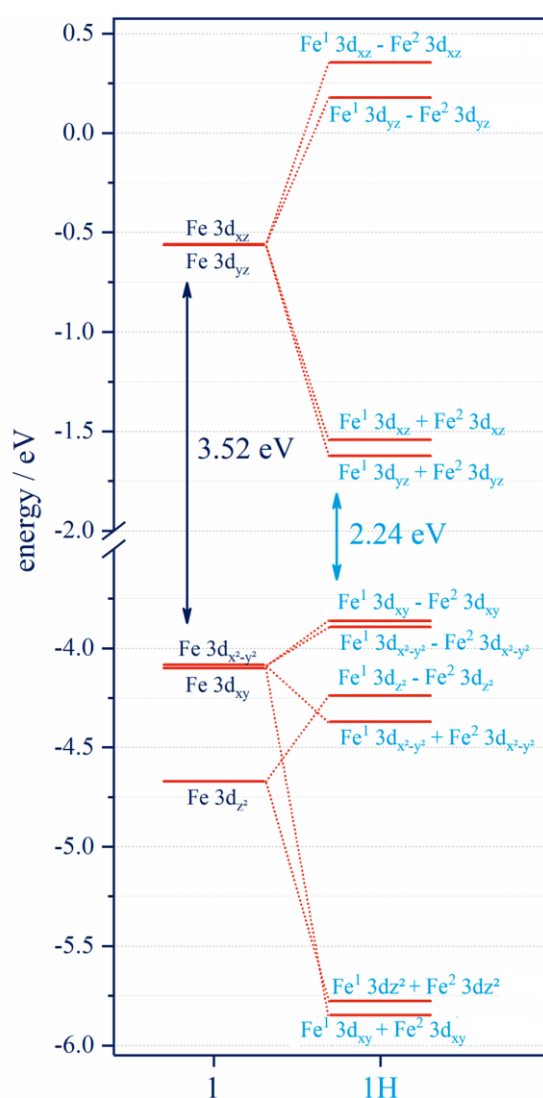


Figure 6. Energetic order of Fe 3d localized orbitals of **1** (dark blue) and their resulting bonding or antibonding combinations in **1H** (light blue).

SUMMARY

The dinuclear tetra-hydrido complex $[\{\text{Cp}^*\text{Fe}\}_2(\mu\text{-H})_4]$ (**1H**) in comparison to the hydride-free ferrocene reference $[\text{Cp}^*\text{Cp}^*\text{Fe}]$ (**1**) has been investigated in detail by VtC-XES and HERFD-XANES in combination with DFT and TD-DFT, respectively.

An outstanding agreement between theory and experiment has been achieved, and therefore detailed information about the occupied (VtC-XES) and unoccupied molecular orbital levels (HERFD-XANES) could be extracted. It has been demonstrated that the antibonding Fe–H interaction contributes unequivocally to HERFD-XANES pre-edge features. A distinct pre-edge feature at around 7114.5 eV has been detected, which could be clearly assigned by TD-DFT to a final state caused by π^* -type acceptor orbitals, which reflect the

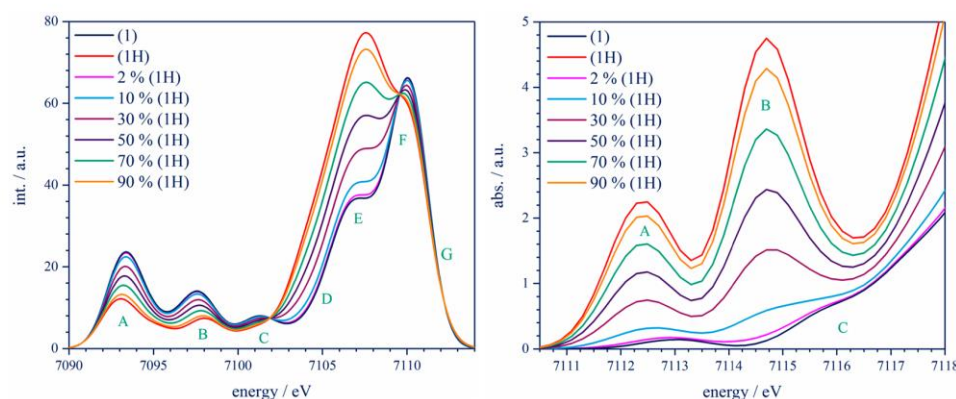


Figure 7. Composite spectra of calculated VtC-XES (left) and HERFD-XANES spectra (right) of **1H** diluted in **1**.

antibonding interaction of the bridged H_4 -cluster $\{H_4\}$ with Fe $3d_{xz}$ and $3d_{yz}$ orbitals of both Fe ions. Due to the presence of four hydride ligands within the complex, the HERFD-XANES hydride signal is the most intense observed so far.

In contrast to the HERFD-XANES and in agreement with the physical origin, bonding Fe–H interactions contribute significantly to the VtC-XES spectrum. A noticeable, broad increase in intensity for **1H** (relative to **1**) at around 7106 eV has been detected, which is caused by donor orbitals reflecting the bonding interactions of the bridged H_4 cluster with Fe $3d_{xz}$, $3d_{yz}$, and $3d_{xy}$ orbitals.

Due to the very high agreement between experiment and theory, further details of the bonding situation and oxidation state of the iron centers could be extracted from the DFT analysis in combination with CtC-XES. With this approach, it is evidenced that both Fe ions of **1H** are in a low-spin configuration of a +II oxidation state, contrary to the formally expected +III state. Finally, it could be shown that no Fe–Fe bond exists in **1H**.

These results further substantiate the high potential of hard X-ray spectroscopy to investigate oxidation states, spin states, TM–TM interactions, and hydride coordination in TM complexes. A solid foundation for in operando investigations of catalytic reactions where hydrides and spin state changes are present is set.

■ ASSOCIATED CONTENT

■ Supporting Information

The Supporting Information is available free of charge on the ACS Publications website at DOI: 10.1021/acs.inorgchem.8b03032.

Treatment of experimental data; comparison of structural parameters of DFT and crystal structures; crystal structures; DFT structures; core-to-core XES spectra; NMR spectra; comparison of experimental and calculations; comparison of all relevant VtC-XES transitions concerning ligand/element populations (donor orbital), energies, and normalized intensities; comparison of all relevant TD-DFT XANES states concerning relevant orbital pairs, energies, and normalized intensities; relevant donor orbitals; relevant acceptor orbitals; xyz coordinates of optimized structures; crystallographic data, data collection, and refinement (PDF)

■ Accession Codes

CCDC 1875499–1875500 contain the supplementary crystallographic data for this paper. These data can be obtained free of charge via www.ccdc.cam.ac.uk/data_request/cif, or by emailing data_request@ccdc.cam.ac.uk, or by contacting The Cambridge Crystallographic Data Centre, 12 Union Road, Cambridge CB2 1EZ, UK; fax: +44 1223 336033.

■ AUTHOR INFORMATION

■ Corresponding Author

*E-mail: matthias.bauer@uni-paderborn.de.

■ ORCID

Matthias Bauer: 0000-0002-9294-6076

■ Funding

Deutsche Forschungsgemeinschaft (DFG, FKZ BA 4467/4-1; SPP 1708, FKZ BA 4467/6-1) Bundesministerium für Bildung und Forschung (BMBF; TrEXHigh, FKZ 05K16PP1)

■ Notes

The authors declare no competing financial interest.

■ ACKNOWLEDGMENTS

The ESRF (beamline ID26: Pieter Glatzel) is acknowledged for a provision of beamtime. We thank Blanka Detlefs and Sara Lafuerza for assistance during the measurements. The Deutsche Forschungsgemeinschaft (DFG, FKZ BA 4467/4-1; SPP 1708, FKZ BA 4467/6-1) and the Bundesministerium für Bildung und Forschung (BMBF; TrEXHigh, FKZ 05K16PP1) are kindly acknowledged for financial support. Generous grants of computing time at the Paderborn Center for Parallel Computing PC² are gratefully acknowledged.

■ REFERENCES

- (1) Chaplin, A. B.; Weller, A. S. B-H activation at a rhodium(I) center: isolation of a bimetallic complex relevant to the transition-metal-catalyzed dehydrocoupling of amine-boranes. *Angew. Chem., Int. Ed.* **2010**, *49*, 581–584.
- (2) Ding, B.; Zhang, Z.; Liu, Y.; Sugiya, M.; Imamoto, T.; Zhang, W. Chemoselective transfer hydrogenation of α,β -unsaturated ketones catalyzed by pincer-Pd complexes using alcohol as a hydrogen source. *Org. Lett.* **2013**, *15*, 3690–3693.
- (3) Felton, G. A. N.; Vannucci, A. K.; Okumura, N.; Lockett, L. T.; Evans, D. H.; Glass, R. S.; Lichtenberger, D. L. Hydrogen Generation from Weak Acids: Electrochemical and Computational Studies in the $[(\eta^5-C_5H_5)Fe(CO)_2]_2$ System. *Organometallics* **2008**, *27*, 4671–4679.

- (4) Hills, I. D.; Fu, G. C. Elucidating reactivity differences in palladium-catalyzed coupling processes: the chemistry of palladium hydrides. *J. Am. Chem. Soc.* **2004**, *126*, 13178–13179.
- (5) Ito, H.; Saito, T.; Miyahara, T.; Zhong, C.; Sawamura, M. Gold(I) Hydride Intermediate in Catalysis: Dehydrogenative Alcohol Silylation Catalyzed by Gold(I) Complex. *Organometallics* **2009**, *28*, 4829–4840.
- (6) Nolin, K. A.; Krumper, J. R.; Pluth, M. D.; Bergman, R. G.; Toste, F. D. Analysis of an unprecedented mechanism for the catalytic hydrosilylation of carbonyl compounds. *J. Am. Chem. Soc.* **2007**, *129*, 14684–14696.
- (7) Ozawa, F.; Okamoto, H.; Kawagishi, S.; Yamamoto, S.; Minami, T.; Yoshifuji, M. (π -Allyl)palladium Complexes Bearing Diphosphinidenecyclobutene Ligands (DPCB): Highly Active Catalysts for Direct Conversion of Allylic Alcohols. *J. Am. Chem. Soc.* **2002**, *124*, 10968–10969.
- (8) Mai, V. H.; Nikonov, G. I. Transfer Hydrogenation of Nitriles, Olefins, and N-Heterocycles Catalyzed by an N-Heterocyclic Carbene-Supported Half-Sandwich Complex of Ruthenium. *Organometallics* **2016**, *35*, 943–949.
- (9) Zhang, G.; Hanson, S. K. Cobalt-catalyzed acceptorless alcohol dehydrogenation: synthesis of imines from alcohols and amines. *Org. Lett.* **2013**, *15*, 650–653.
- (10) Armadori, N.; Balzani, V. The hydrogen issue. *ChemSusChem* **2011**, *4*, 21–36.
- (11) Abbasi, T.; Abbasi, S. A. 'Renewable' hydrogen: Prospects and challenges. *Renewable Sustainable Energy Rev.* **2011**, *15*, 3034–3040.
- (12) Hollmann, D.; Gartner, F.; Ludwig, R.; Barsch, E.; Junge, H.; Blug, M.; Hoch, S.; Beller, M.; Bruckner, A. Insights into the mechanism of photocatalytic water reduction by DFT-supported in situ EPR/Raman spectroscopy. *Angew. Chem., Int. Ed.* **2011**, *50*, 10246–10250.
- (13) Bau, R.; Teller, R. G.; Kirtley, S. W.; Koetzle, T. F. Structures of transition-metal hydride complexes. *Acc. Chem. Res.* **1979**, *12*, 176–183.
- (14) Gütllich, P.; Bill, E.; Trautwein, A. X. *Mössbauer Spectroscopy and Transition Metal Chemistry*; Springer: Berlin, 2011.
- (15) Kajcsos, Z.; Sauer, C.; Zinn, W.; Meisel, W.; Spiering, H.; Alflen, M.; Gütllich, P. High-performance Mössbauer spectroscopy: Criteria, possibilities, limitations. *Hyperfine Interact.* **1992**, *71*, 1469–1477.
- (16) Andrews, L. Matrix infrared spectra and density functional calculations of transition metal hydrides and dihydrogen complexes. *Chem. Soc. Rev.* **2004**, *33*, 123–132.
- (17) *Spectroscopic Properties of Inorganic and Organometallic Compounds*; Yarwood, J., Douthwaite, R., Duckett, S., Eds.; Royal Society of Chemistry: Cambridge, 2012.
- (18) Pelmentschikov, V.; Gee, L. B.; Wang, H.; MacLeod, K. C.; McWilliams, S. F.; Skubi, K. L.; Cramer, S. P.; Holland, P. L. High-Frequency Fe-H Vibrations in a Bridging Hydride Complex Characterized by NRVs and DFT. *Angew. Chem., Int. Ed.* **2018**, *57*, 9367–9371.
- (19) Hämäläinen, K.; Siddons, D. P.; Hastings, K. B.; Berman, L. E. Elimination of the inner-shell lifetime broadening in x-ray-absorption spectroscopy. *Phys. Rev. Lett.* **1991**, *67*, 2850–2853.
- (20) Bauer, M. HERFD-XAS and valence-to-core-XES: New tools to push the limits in research with hard X-rays? *Phys. Chem. Chem. Phys.* **2014**, *16*, 13827–13837.
- (21) Glatzel, P.; Bergmann, U. High resolution 1s core hole X-ray spectroscopy in 3d transition metal complexes—electronic and structural information. *Coord. Chem. Rev.* **2005**, *249*, 65–95.
- (22) *Methods in Physical Chemistry: X-ray Absorption Spectroscopy—The Method and Its Applications*; Bauer, M., Bertagnolli, H., Eds.; Wiley-VCH Verlag GmbH & Co. KGaA: Weinheim, Germany, 2012.
- (23) Kramers, H. A.; Heisenberg, W. Über die Streuung von Strahlung durch Atome. *Z. Phys.* **1925**, *31*, 681–708.
- (24) de Groot, F. M. F.; Krisch, M. H.; Vogel, J. Spectral sharpening of the Pt L edges by high-resolution x-ray emission. *Phys. Rev. B: Condens. Matter Mater. Phys.* **2002**, *66*, 621.
- (25) Atkins, A. J.; Bauer, M.; Jacob, C. R. The chemical sensitivity of X-ray spectroscopy: High energy resolution XANES versus X-ray emission spectroscopy of substituted ferrocenes. *Phys. Chem. Chem. Phys.* **2013**, *15*, 8095–8105.
- (26) Delgado-Jaime, M. U.; DeBeer, S.; Bauer, M. Valence-to-core X-ray emission spectroscopy of iron-carbonyl complexes: Implications for the examination of catalytic intermediates. *Chem. - Eur. J.* **2013**, *19*, 15888–15897.
- (27) Chandrasekaran, P.; Chiang, K. P.; Nordlund, D.; Bergmann, U.; Holland, P. L.; DeBeer, S. Sensitivity of X-ray core spectroscopy to changes in metal ligation: A systematic study of low-coordinate, high-spin ferrous complexes. *Inorg. Chem.* **2013**, *52*, 6286–6298.
- (28) Lancaster, K. M.; Roemelt, M.; Ettenhuber, P.; Hu, Y.; Ribbe, M. W.; Neese, F.; Bergmann, U.; DeBeer, S. X-ray emission spectroscopy evidences a central carbon in the nitrogenase iron-molybdenum cofactor. *Science (Washington, DC, U. S.)* **2011**, *334*, 974–977.
- (29) Lee, N.; Petrenko, T.; Bergmann, U.; Neese, F.; DeBeer, S. Probing valence orbital composition with iron K β X-ray emission spectroscopy. *J. Am. Chem. Soc.* **2010**, *132*, 9715–9727.
- (30) Martin-Diaconescu, V.; Chacón, K. N.; Delgado-Jaime, M. U.; Sokaras, D.; Weng, T.-C.; DeBeer, S.; Blackburn, N. J. K β Valence to Core X-ray Emission Studies of Cu(I) Binding Proteins with Mixed Methionine - Histidine Coordination. Relevance to the Reactivity of the M- and H-sites of Peptidylglycine Monooxygenase. *Inorg. Chem.* **2016**, *55*, 3431–3439.
- (31) Pollock, C. J.; DeBeer, S. Valence-to-core X-ray emission spectroscopy: A sensitive probe of the nature of a bound ligand. *J. Am. Chem. Soc.* **2011**, *133*, 5594–5601.
- (32) Pollock, C. J.; DeBeer, S. Insights into the geometric and electronic structure of transition metal centers from valence-to-core X-ray emission spectroscopy. *Acc. Chem. Res.* **2015**, *48*, 2967–2975.
- (33) Pollock, C. J.; Lancaster, K. M.; Finkelstein, K. D.; DeBeer, S. Study of iron dimers reveals angular dependence of valence-to-core X-ray emission spectra. *Inorg. Chem.* **2014**, *53*, 10378–10385.
- (34) Smolentsev, G.; Soldatov, A. V.; Messinger, J.; Merz, K.; Weyhermüller, T.; Bergmann, U.; Pushkar, Y.; Yano, J.; Yachandra, V. K.; Glatzel, P. X-ray emission spectroscopy to study ligand valence orbitals in Mn coordination complexes. *J. Am. Chem. Soc.* **2009**, *131*, 13161–13167.
- (35) Burkhardt, L.; Holzwarth, M.; Plietker, B.; Bauer, M. Detection and Characterization of Hydride Ligands in Iron Complexes by High-Resolution Hard X-ray Spectroscopy and Implications for Catalytic Processes. *Inorg. Chem.* **2017**, *56*, 13300–13310.
- (36) Koga, N.; Morokuma, K. Ab initio study on the structure and H₂ dissociation reaction of a tetrahydride-bridged dinuclear Ru complex, (C₅H₅)Ru(μ -H)₄Ru(C₅H₅). *J. Mol. Struct.* **1993**, *300*, 181–189.
- (37) Altomare, A.; Cascarano, G.; Giacovazzo, C.; Guagliardi, A.; Burla, M. C.; Polidori, G.; Camalli, M. SIR 92—a program for automatic solution of crystal structures by direct methods. *J. Appl. Crystallogr.* **1994**, *27*, 435.
- (38) Sheldrick, G. M. A short history of SHELX. *Acta Crystallogr., Sect. A: Found. Crystallogr.* **2008**, *64*, 112–122.
- (39) CrysAlisPro, version 1.171.37.35; Agilent Technologies, 2014. CrysAlisPro, Version 1.171.38.46; Rigaku Oxford Diffraction, 2015.
- (40) Neese, F. Software update: The ORCA program system, version 4.0. *WIREs Comput. Mol. Sci.* **2018**, *8*, No. e1327.
- (41) Hostaš, J.; Řezáč, J. Accurate DFT-D3 Calculations in a Small Basis Set. *J. Chem. Theory Comput.* **2017**, *13*, 3575–3585.
- (42) DeBeer George, S.; Petrenko, T.; Neese, F. Prediction of iron K-edge absorption spectra using time-dependent density functional theory. *J. Phys. Chem. A* **2008**, *112*, 12936–12943.
- (43) DeBeer George, S.; Petrenko, T.; Neese, F. Time-dependent density functional calculations of ligand K-edge X-ray absorption spectra. *Inorg. Chim. Acta* **2008**, *361*, 965–972.
- (44) Roemelt, M.; Beckwith, M. A.; Duboc, C.; Collomb, M.-N.; Neese, F.; DeBeer, S. Manganese K-edge X-ray absorption spectroscopy.

copy as a probe of the metal-ligand interactions in coordination compounds. *Inorg. Chem.* **2012**, *51*, 680–687.

(45) Weigend, F.; Ahlrichs, R. Balanced basis sets of split valence, triple zeta valence and quadruple zeta valence quality for H to Rn: Design and assessment of accuracy. *Phys. Chem. Chem. Phys.* **2005**, *7*, 3297–3305.

(46) Weigend, F. Accurate Coulomb-fitting basis sets for H to Rn. *Phys. Chem. Chem. Phys.* **2006**, *8*, 1057–1065.

(47) Neese, F. Prediction and interpretation of the 57Fe isomer shift in Mössbauer spectra by density functional theory. *Inorg. Chim. Acta* **2002**, *337*, 181–192.

(48) Grimme, S.; Antony, J.; Ehrlich, S.; Krieg, H. A consistent and accurate ab initio parametrization of density functional dispersion correction (DFT-D) for the 94 elements H–Pu. *J. Chem. Phys.* **2010**, *132*, 154104.

(49) Grimme, S.; Ehrlich, S.; Goerigk, L. Effect of the damping function in dispersion corrected density functional theory. *J. Comput. Chem.* **2011**, *32*, 1456–1465.

(50) Knizia, G. *IboView*; Pennsylvania State University.

(51) Weismann, D.; Sun, Y.; Lan, Y.; Wolmershäuser, G.; Powell, A. K.; Sitzmann, H. High-Spin Cyclopentadienyl Complexes: A Single-Molecule Magnet Based on the Aryl-Iron(II) Cyclopentadienyl Type. *Chem. - Eur. J.* **2011**, *17*, 4700–4704.

(52) Ohki, Y.; Suzuki, H. $[(\eta^5\text{-CSMeS})\text{Fe}]_2(\mu\text{-H})_4$: A Novel Dinuclear Iron Tetrahydrido Complex. *Angew. Chem.* **2000**, *112*, 3250–3252.

(53) Sitzmann, H.; Boese, R.; Stellberg, P. Meso- und Rac-Decaisopropylstannocen: Stereoisomerie bedingt durch parallele Anordnung zweier Pentaaisopropylcyclopentadienyl-Liganden in Schaufelrad-Konformation. *Z. Anorg. Allg. Chem.* **1996**, *622*, 751–755.

(54) Ohki, Y.; Suzuki, H. $[(\eta^5\text{-CSMeS})\text{Fe}]_2(\mu\text{-H})_4$: A Novel Dinuclear Iron Tetrahydrido Complex. *Angew. Chem., Int. Ed.* **2000**, *39*, 3120–3122.

(55) Walter, M. D.; Grunenberg, J.; White, P. S. Reactivity studies on $[\text{Cp}^*\text{Fe}]_2$: From iron hydrides to P4-activation. *Chem. Sci.* **2011**, *2*, 2120.

(56) Ohki, Y.; Kojima, T.; Oshima, M.; Suzuki, H. $\{(\eta^5\text{-C}_5\text{Me}_5\text{Fe})_2(\mu\text{-H})_2(\mu\text{-}\eta^2\text{-H}_2\text{-H}_2\text{Si t Bu}_2)\}$, a Versatile Precursor for Bimetallic Active Species. *Organometallics* **2001**, *20*, 2654–2656.

(57) Peldo, M. A.; Beatty, A. M.; Fehner, T. P. Routes to Compounds Containing M–B Bonds. Reaction of $[\text{Cp}^*\text{FeH}_2]_2$ with $\text{BH}_3 \cdot \text{THF}$, Yielding the Hydrogen-Rich arachno- η^5 -Ferrapentaborane $1\text{-Cp}^*\text{FeB}_4\text{H}_{11}$ ($\text{Cp}^* = \eta^5\text{-C}_5\text{Me}_5$). *Organometallics* **2002**, *21*, 2821–2823.

(58) Peldo, M. A.; Beatty, A. M.; Fehner, T. P. Reaction of the Transition Metal Hydrides $[\text{Cp}^*\text{MH}_2]_2$ ($\text{Cp}^* = \eta^5\text{-C}_5\text{Me}_5$; M = Fe, Ru) with $\text{BH}_3 \cdot \text{THF}$ to Yield Metallaboranes. Improved Kinetic Control Leads to Novel Ferraboranes. *Organometallics* **2003**, *22*, 3698–3702.

(59) Excluding iPr substituents.

(60) Lancaster, K. M.; Finkelstein, K. D.; DeBeer, S. $K\beta$ X-ray emission spectroscopy offers unique chemical bonding insights: Revisiting the electronic structure of ferrocene. *Inorg. Chem.* **2011**, *50*, 6767–6774.

(61) Atkins, A. J.; Jacob, C. R.; Bauer, M. Probing the electronic structure of substituted ferrocenes with high-resolution XANES spectroscopy. *Chem. - Eur. J.* **2012**, *18*, 7021–7025.

(62) Kau, L. S.; Spira-Solomon, D. J.; Penner-Hahn, J. E.; Hodgson, K. O.; Solomon, E. I. X-ray absorption edge determination of the oxidation state and coordination number of copper. Application to the type 3 site in Rhus vernicifera laccase and its reaction with oxygen. *J. Am. Chem. Soc.* **1987**, *109*, 6433–6442.

(63) Kosugi, N.; Yokoyama, T.; Asakura, K.; Kuroda, H. Polarized Cu K-edge XANES of square planar CuCl_4^{2-} ion. Experimental and theoretical evidence for shake-down phenomena. *Chem. Phys.* **1984**, *91*, 249–256.

(64) Vollmers, N. J.; Müller, P.; Hoffmann, A.; Herres-Pawlis, S.; Rohrmüller, M.; Schmidt, W. G.; Gerstmann, U.; Bauer, M. Experimental and Theoretical High-Energy-Resolution X-ray Absorp-

tion Spectroscopy: Implications for the Investigation of the Entatic State. *Inorg. Chem.* **2016**, *55*, 11694–11706.

(65) Proux, O.; Lahera, E.; Del Net, W.; Kieffer, I.; Rovezzi, M.; Testemale, D.; Irar, M.; Thomas, S.; Aguilar-Tapia, A.; Bazarkina, E. F.; et al. High-Energy Resolution Fluorescence Detected X-Ray Absorption Spectroscopy: A Powerful New Structural Tool in Environmental Biogeochemistry Sciences. *J. Environ. Qual.* **2017**, *46*, 1146–1157.

(66) Boubnov, A.; Carvalho, H. W. P.; Doronkin, D. E.; Günter, T.; Gallo, E.; Atkins, A. J.; Jacob, C. R.; Grunwaldt, J.-D. Selective catalytic reduction of NO over Fe-ZSM-5: Mechanistic insights by operando HERFD-XANES and valence-to-core X-ray emission spectroscopy. *J. Am. Chem. Soc.* **2014**, *136*, 13006–13015.

(67) Frenkel, A. I.; Small, M. W.; Smith, J. G.; Nuzzo, R. G.; Kvashina, K. O.; Tromp, M. An in Situ Study of Bond Strains in 1 nm Pt Catalysts and Their Sensitivities to Cluster-Support and Cluster-Adsorbate Interactions. *J. Phys. Chem. C* **2013**, *117*, 23286–23294.

(68) Friebe, D.; Miller, D. J.; O'Grady, C. P.; Anniyev, T.; Bargar, J.; Bergmann, U.; Ogasawara, H.; Wikfeldt, K. T.; Pettersson, L. G. M.; Nilsson, A. In situ X-ray probing reveals fingerprints of surface platinum oxide. *Phys. Chem. Chem. Phys.* **2011**, *13*, 262–266.

(69) Gorczyca, A.; Moizan, V.; Chizallet, C.; Proux, O.; Del Net, W.; Lahera, E.; Hazemann, J.-L.; Raybaud, P.; Joly, Y. Monitoring Morphology and Hydrogen Coverage of Nanometric Pt/ $\gamma\text{-Al}_2\text{O}_3$ Particles by In Situ HERFD-XANES and Quantum Simulations. *Angew. Chem.* **2014**, *126*, 12634–12637.

(70) Manyar, H. G.; Morgan, R.; Morgan, K.; Yang, B.; Hu, P.; Szlachetko, J.; Sá, J.; Hardacre, C. High energy resolution fluorescence detection XANES—an in situ method to study the interaction of adsorbed molecules with metal catalysts in the liquid phase. *Catal. Sci. Technol.* **2013**, *3*, 1497.

(71) Safonova, O. V.; Florea, M.; Bilde, J.; Delichere, P.; Millet, J. M. M. Local environment of vanadium in V/Al/O-mixed oxide catalyst for propane ammoxidation: Characterization by in situ valence-to-core X-ray emission spectroscopy and X-ray absorption spectroscopy. *J. Catal.* **2009**, *268*, 156–164.

(72) Singh, J.; Lamberti, C.; van Bokhoven, J. A. Advanced X-ray absorption and emission spectroscopy: In situ catalytic studies. *Chem. Soc. Rev.* **2010**, *39*, 4754–4766.

(73) Singh, J.; van Bokhoven, J. A. Structure of alumina supported platinum catalysts of different particle size during CO oxidation using in situ IR and HERFD XAS. *Catal. Today* **2010**, *155*, 199–205.

(74) van Bokhoven, J. A.; Louis, C.; Miller, J. T.; Tromp, M.; Safonova, O. V.; Glatzel, P. Activation of Oxygen on Gold/Alumina Catalysts: In Situ High-Energy-Resolution Fluorescence and Time-Resolved X-ray Spectroscopy. *Angew. Chem.* **2006**, *118*, 4767–4770.

4.3 Revival of the formal description: Fe(-II) identified in the Hieber anion by hard X-ray emission and absorption spectroscopy

Burkhardt, L.; Vukadinovic, Y; Kalinko A.; Rudolph, J.; Carlsson, P.; Jacob, C.; Bauer, M. *Angew. Chem.* **2019**, *in preparation*.

This publication will be submitted to *Angewandte Chemie* between the 29th of April and 24th of June.

The Hieber anion is examined by high-resolution hard X-ray spectroscopy, (TD)DFT and theoretical spectroscopy. In great contrast to a recent study, our experimental and computational results are in very good agreement with the former well-known description of a 3d¹⁰ Fe^{-II} ion bound to a linear NO⁺ ligand. The triplet and singlet potential energy surfaces of the Hieber anion are examined and all computational observed nitrosyl coordination isomers are utilized further and studied by theoretical VtC-XES and HERFD-XANES spectroscopy. Both methods show a great sensitivity to changes in the nitrosyl coordination mode and spin state.

Participation in this Publication

L. Burkhardt: HERFD-XANES and VtC-XES, geometry optimizations, simulation of VtC-XES and XANES spectra, theoretical spectroscopy, manuscript preparation

Y. Vukadinovic: Synthesis of investigated compounds

A. Kalinko: Assisted during the XES and XAS measurements

M. Bauer: corresponding author

J. Rudolph, C. Jacob: Preliminary calculations and preliminary analysis of XANES and VtC-XES

RESEARCH ARTICLE

Revival of the formal description: Fe(-II) identified in the Hieber anion by hard X-ray emission and absorption spectroscopy

Lukas Burkhardt,^[a] Yannik Vukadinovic,^[a] Aleksandr Kalinko,^[a] Julian Rudolph,^[b] Per-Anders Carlsson,^[c] Christoph R. Jacob,^[b] Matthias Bauer*,^[a]

Abstract: The Hieber anion $[\text{Fe}(\text{CO})_3(\text{NO})]^-$ has been reincarnated in the last years as an active catalyst in organic synthesis, yet there is a great deal of discussion about the oxidation state of the central iron and the resulting charge of the NO ligand. New experimental light is shed on this question by a combined valence-to-core X-ray emission spectroscopy (VtC-XES), X-ray absorption near edge structure spectroscopy (XANES) and high-energy resolution fluorescence detected XANES (HERFD-XANES) investigation within the context of the Fe-3d⁸ compound $\text{Fe}(\text{CO})_5$ and the Fe-3d¹⁰ complex $[\text{Fe}(\text{CO})_4]^{2-}$. In order to extract precise information about the electronic structure, (time-dependent) density functional theory are applied. This combination of experimental and computational methods reveals that the electron density at the Fe center of the Hieber anion is highly related to the 3d¹⁰ reference $[\text{Fe}(\text{CO})_4]^{2-}$ and significantly increased compared to $\text{Fe}(\text{CO})_5$. These observations are in agreement with the textbook description of a Fe(-II) center in combination with a linear NO⁺ ligand, thus contributing in an important way to the ongoing debate about the present iron oxidation state and nitrosyl charge in the Hieber anion. The aspects of nitrosyl coordination are further elucidated by theoretical spectroscopy of six different structural nitrosyl isomers in the singlet and triplet state. A great sensitivity of both methods towards the Fe-NO interaction is observed, paving the way for future isomerization studies.

Introduction

Transition metal nitrosyl complexes are a subject of continuous interest in inorganic or bioinorganic chemistry, photophysics or catalysis. Nitric oxide (NO) ligands plays an important role in physiological processes like neurotransmission, blood pressure regulation or immune system response.^[1] Many iron and ruthenium nitrosyl complexes are known to release nitric oxide and have been employed in photodynamic therapy to deliver targeted NO to biological tissues.^[2] Additionally, complexes like $[\text{Fe}(\text{CN})_5(\text{NO})]^{2-}$ are promising candidates for optical data storage because of long-living metastable states.^[3-6]

The nitrosyl ligand is a well-known non-innocent ligand in coordination chemistry^[7] and the M-NO fragment is usually characterized by a strong delocalized electron density and a strong metal-ligand covalency. By this definition, it is not less than challenging task to determine the distribution of valence electrons in the M-NO bond over metal d and nitrosyl π^* orbitals, respectively. Consequently, Enemark and Feltham suggested to define M-NO complexes by $\{\text{M}(\text{NO})\}^n$, where n is the total number of electrons in the metal d orbitals and nitrosyl π^* orbitals.^[8]

The textbook description of NO coordinating to metal centers is based on the consideration of linear or bent configurations, according to a formal NO⁺ and NO⁻ ligand. The difference between both modes is an electron pair at the NO ligand, and therefore different reactions are possible in the two cases.^[9] Accordingly, NO donates or withdraws an electron pair to or from the metal center, changing the electronic state and coordination properties at the metal center. Moving from a linear to a bent configuration, a potential coordination site is created at the metal, at which further ligands could coordinate. The identification of the coordination mode of NO is therefore the first step to understand reactions that involve M-NO structure motifs. Beside linear and bent nitrosyl structures, numerous transition metal nitrosyl complexes are known to form metastable oxygen (iso-nitrosyl) and side-on coordinated structures after laser excitation, including $\text{Na}_2[\text{Fe}(\text{CN})_5(\text{NO})]$, $\text{Cp}^*\text{Ni}(\text{NO})$, $\text{K}_2[\text{RuCl}_5(\text{NO})]$ and $[\text{CpRe}(\text{CO})_2(\text{NO})][\text{BF}_4]$.^[3-6,9,10]

- [a] Lukas Burkhardt and Prof. Dr. Matthias Bauer
Department of Chemistry and Center for sustainable systems design (CSSD)
Paderborn University
Warburger Straße 100, 33098 Paderborn, Germany
E-mail: matthias.bauer@uni-paderborn.de
- [b] Julian Rudolph and Prof. Dr. Christoph R. Jacob
Institute of Physical and Theoretical Chemistry
TU Braunschweig
Gaußstraße 17, 38106 Braunschweig, Germany
- [c] Prof. Dr. Per-Anders Carlsson
Department of Chemistry and Chemical Engineering and
Competence Centre for Catalysis
412 96 Gothenburg, Sweden

Supporting information for this article is given via a link at the end of the document.

RESEARCH ARTICLE

Chemical or catalytic reactions involving NO catalysts or intermediates are very often carried out in a complex mixture of active species and solvents, or under harsh experimental conditions, like elevated temperatures or pressure. Especially the most established IR spectroscopy can be less suited under such circumstances. Spectra of complexes with linear and bend NO coordination differ by about 80-100 cm^{-1} around an average value of 1680-1700 cm^{-1} .^[11,12] Since this is also the range where stretching vibrations of homo- and heteroatomic double bonds of esters, aldehydes, etc. appear, band interference in reaction mixtures make the isolation and analysis of the NO band more often than not impossible.

Therefore, a substitute for IR spectroscopy that provides similar information, while being independent of the experimental environment would be highly desired. Hard X-Ray Absorption Spectroscopy (XAS)^[13] and X-Ray Emission Spectroscopy (XES)^[14] at metal K-edges are able to overcome these limitations without being subject to any experimental restrictions.

In the pre-edge region^[15] of iron K-edge XANES (X-ray absorption near edge structure)^[16] spectra a 1s electron is excited to unoccupied states. The pre-peak or pre-edge signal contains the main information about unoccupied 3d levels and/or LUMO states, since pre-peaks originate from 1s \rightarrow TM 3d / LUMOs transitions.^[13,17] Unfortunately, many of these details are masked by the experimental resolution, which is limited by the core-hole lifetime. Since the minimal linewidth of a transition is inversely proportional to the lifetime of its final state, the experimental resolution can be enhanced by detecting an emissive final state with a longer lifetime, as can be simply understood by the time-energy uncertainty relation, and what is described by the Kramers-Heisenberg formula.^[18] This sharpening effect has been demonstrated by the groups of Hämäläinen (1991)^[19] and de Groot (2002).^[20] Accordingly, the method is called high-energy resolution fluorescence detected XANES (HERFD-XANES).

In K-edge valence-to-core X-ray emission spectroscopy (VtC-XES)^[21] a 1s electron is excited non-resonantly to the continuum and the emissive valence \rightarrow Fe 1s relaxation channel is monitored. Thus, VtC-XES offers a unique probe of HOMO levels and therefore is able to probe occupied 3d levels, ligand localized orbitals and their bonding interactions.^[22,23]

Here we want to establish HERFD-XANES and VtC-XES at the iron K-edge as highly sensitive methods to investigate the coordination chemistry of nitric oxide with hard X-rays. The well-known Hieber anion $[\text{Fe}(\text{CO})_3(\text{NO})]^-$ serves as a selected case study for this purpose, since the electronic configuration of the

Hieber anion has been described for decades by a Fe^{II} ion ($3d^6$) bound to a linear NO^+ ligand, due to great resemblance to the tetracarbonylferrate $[\text{Fe}(\text{CO})_4]^{2-}$.^[11,24,25] Contradictory to this, a previous study describes the bonding situation in the Hieber anion as a $\text{Fe}^{\pm 0}$ ($3d^8$) ion bound to a linear NO ligand by a π -double bond.^[26]

Consequently, the aim of this study is twofold:

1. Revisiting the bonding situation in the Hieber anion by hard X-ray spectroscopy.
2. Exploring the sensitivity of VtC-XES and HERFD-XANES to characterize and discriminate structural nitrosyl isomers.

Results

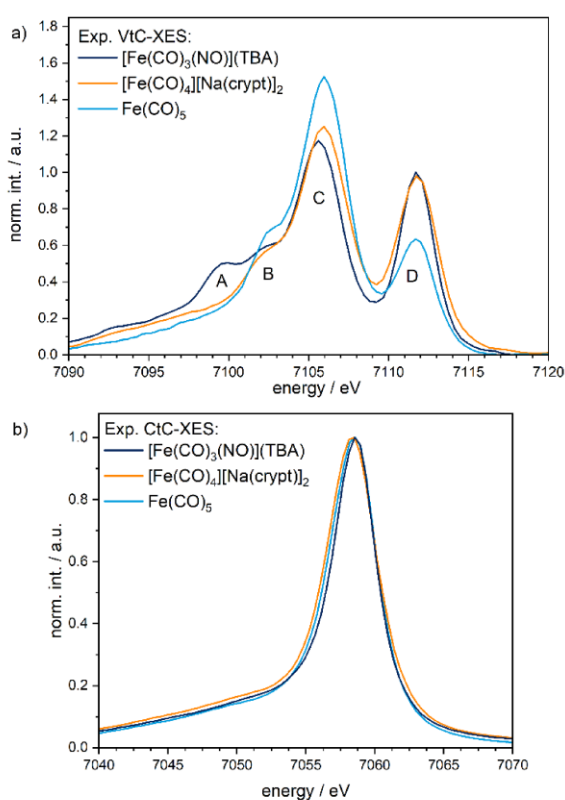
Experimental results

The ground state of $[\text{Fe}(\text{CO})_3(\text{NO})]^-$ is characterized by a C_{3v} symmetry, in which the central iron is coordinated by three linear carbonyl ligands and one linear nitrosyl ligand (Fe-N-O angle at around 180°).^[27] The salt $[\text{Fe}(\text{CO})_3(\text{NO})](\text{TBA})$ (TBA = Tetrabutylammonium) is used as model reference due to the weak interaction between the $[\text{Fe}(\text{CO})_3(\text{NO})]^-$ anion and the $(\text{TBA})^+$ cation. In order to characterize the electronic structure and Fe-NO interactions in the Hieber anion, XANES, HERFD-XANES, CtC and VtC emission of $[\text{Fe}(\text{CO})_3(\text{NO})](\text{TBA})$ are compared to the trigonal bipyramidal $\text{Fe}^{\pm 0}$ reference $\text{Fe}(\text{CO})_5$ and the tetrahedral Fe^{II} reference, $[\text{Fe}(\text{CO})_4][\text{Na}(\text{crypt})]$ (crypt : [2.2.2]Cryptand = 4,7,13,16,21,24-Hexaoxa-1,10-diazabicyclo[8.8.8]hexacosane) in this section, which is followed by a thorough computational analysis in the subsequent section. The local Fe 3d (spin) density of $[\text{Fe}(\text{CO})_3(\text{NO})](\text{TBA})$ is probed by core-to-core X-ray emission spectroscopy (CtC-XES, $K\beta_{1,3}$), the spectrum is compared to $\text{Fe}(\text{CO})_5$ and $[\text{Fe}(\text{CO})_4][\text{Na}(\text{crypt})]_2$ in figure 1 (b). For all three complexes only a small splitting and intensity ratio between the satellite ($K\beta'$) and mainline is observed, consistent with the diamagnetic character of all three complexes.^[26,28] The HOMO probing VtC-XES spectrum of $[\text{Fe}(\text{CO})_3(\text{NO})](\text{TBA})$ is compared to $\text{Fe}(\text{CO})_5$ and $[\text{Fe}(\text{CO})_4][\text{Na}(\text{crypt})]_2$ in figure 1 (a). Four spectral features A-D are observed for $[\text{Fe}(\text{CO})_3(\text{NO})](\text{TBA})$, the according energies and intensities are given in table 1. Based on literature reports, the low-energy feature A is caused by nitrosyl $\text{NO } \sigma_{2s}^* \rightarrow \text{Fe } 1s$ transitions.^[29,30]

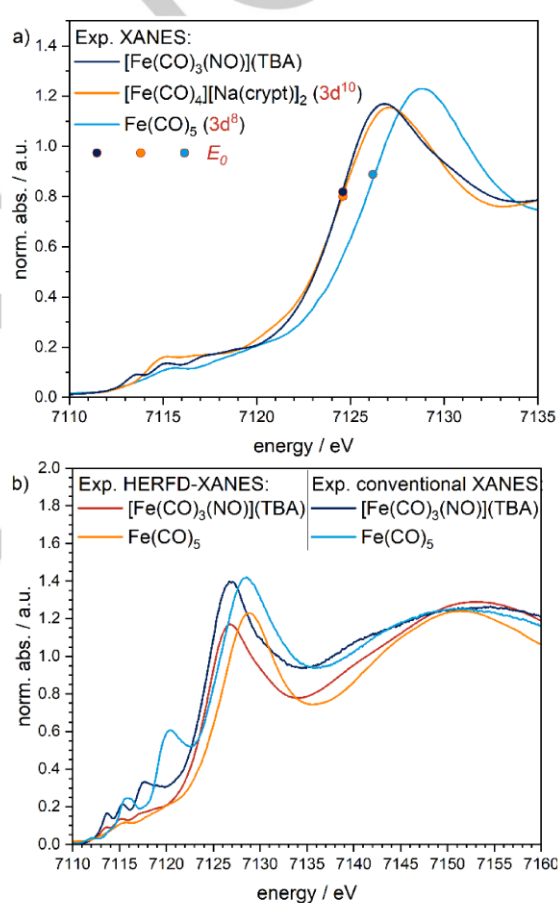
RESEARCH ARTICLE

Table 1: Characteristic VtC-XES and HERFD-XANES signal energies and intensities of $[\text{Fe}(\text{CO})_3(\text{NO})](\text{TBA})$, $[\text{Fe}(\text{CO})_4][\text{Na}_2(\text{crypt})]$ and $\text{Fe}(\text{CO})_5$.

Compound	VtC-XES peak energies / eV (norm. int. / a.u.)				HERFD-XANES pre-peak energies / eV (norm. int. / a.u.)		
	A	B	C	D	A	B	C
$[\text{Fe}(\text{CO})_3(\text{NO})](\text{TBA})$	7099.7 (1.2)	7102.6 (1.6)	7105.6 (1.2)	7111.7 (1.0)	7113.7 (0.17)	7115.3 (0.21)	7117.7 (0.33)
$[\text{Fe}(\text{CO})_4][\text{Na}(\text{crypt})]_2$	- (-)	7102.3 (0.6)	7106 (1.3)	7111.7 (1.0)	- (-)	- (-)	- (-)
$\text{Fe}(\text{CO})_5$	- (-)	7102.6 (0.7)	7106 (1.5)	7111.7 (0.6)	7112.1 (0.03)	7115.9 (0.25)	7120.4 (0.61)

**Figure 1.** a) Experimental VtC-XES spectra of $[\text{Fe}(\text{CO})_3(\text{NO})](\text{TBA})$, $\text{Fe}(\text{CO})_5$ and $[\text{Fe}(\text{CO})_4][\text{Na}_2(\text{crypt})]$. b) Experimental Fe K-edge CtC-XES spectra of $[\text{Fe}(\text{CO})_3(\text{NO})](\text{TBA})$, $\text{Fe}(\text{CO})_5$ and $[\text{Fe}(\text{CO})_4][\text{Na}_2(\text{crypt})]$.

Additionally, a symmetry dependent increase in transition probability by 3d-4p hybridization could cause this intensity increase. Final identification of the origin requires the comparison to quantum-chemical calculations, which will be provided below.

**Figure 2.** a) Experimental Fe K-edge XANES spectra of $[\text{Fe}(\text{CO})_3(\text{NO})](\text{TBA})$, $\text{Fe}(\text{CO})_5$ and $[\text{Fe}(\text{CO})_4][\text{Na}_2(\text{crypt})]$. b) HERFD-XANES spectra of $[\text{Fe}(\text{CO})_3(\text{NO})](\text{TBA})$ and $\text{Fe}(\text{CO})_5$ in comparison to conventional XANES spectra.

To probe the local iron density of the Hieber anion, conventional XANES spectra of all three complexes were

RESEARCH ARTICLE

recorded, which are shown in figure 2 (a). A distinctive redshift of the absorption edge of 1.6 eV is observed for both tetrahedral anions, $[\text{Fe}(\text{CO})_3(\text{NO})](\text{TBA})^-$ and $[\text{Fe}(\text{CO})_4][\text{Na}(\text{crypt})]_2^-$ (7124.6 eV) compared to $\text{Fe}(\text{CO})_5$ (7126.2 eV). This redshift is consistent with a decrease of the iron oxidation state from ± 0 to -II (first derivative XANES spectra are given in figure S3 in the supporting information).

Complementary to VtC-XES, HERFD-XANES probes the local LUMO structure of $[\text{Fe}(\text{CO})_3(\text{NO})](\text{TBA})^-$, of which the spectra are compared to $\text{Fe}(\text{CO})_5$ in figure 2 (right). The pre-edge region of the Hieber anion exhibits 3 features, for which the details are given in table 1. The pre-edge region of iron carbonyl complexes, is typically caused by acceptor orbitals reflecting the antibonding interaction of Fe 3d orbitals with CO σ_{2p} or CO π_{2p}^* orbitals,⁶⁴ while the pre-edge of low-valent nitrosyl complexes with linear NO motifs is typically caused by acceptor orbitals reflecting the antibonding interaction of Fe 3d and NO π^* orbitals.^[29] Further interpretation of observed pre-edge features is not reasonable at this point and will be continued in combination with TD-DFT calculations in the computational section.

Computational results

The presented experimental spectra were so far only discussed based on literature reports. To examine the quantum-mechanical origin of the spectral signatures in the VtC-XES and HERFD-XANES data, quantum-chemical calculations are mandatory. Spectra were calculated via DFT (VtC-XES) or TDDFT (XANES) utilizing the optimized gas phase structure of $[\text{Fe}(\text{CO})_3(\text{NO})]^-$ and $[\text{Fe}(\text{CO})_4]^{2-}$. All observed bond length and bond angles are in high agreement with published values of the crystal structures $\text{Ti}[\text{Fe}(\text{CO})_3(\text{NO})]^{[27]}$ and $[\text{Fe}(\text{CO})_4][\text{Na}(\text{crypt})]_2^{[25]}$ and are given in table 2 and table S3 in the supporting information, respectively. The Ti^+ cation of $\text{Ti}[\text{Fe}(\text{CO})_3(\text{NO})]$ is

located on the C_3 axis along the Fe-N bond and is located in a non-interacting distance to the Fe complex (Ti-Fe: 7.545(1) Å, Ti-O (CO): 6.737(7) Å).

Calculated and experimental VtC-XES and HERFD-XANES spectra are compared in figure 3. The agreement between experiment and calculation regarding spectral signatures, energy and intensity ratios, is very satisfactory. Ligand projected spectra were generated in case of the VtC-XES to assign observed spectral features to the different coordinating ligands (see figure 3, left). In the following, observed donor and acceptor orbitals will be described by the symmetry of the reflected ligand or fragment orbital symmetry (σ , π) to facilitate the direct comparison to the individual fragments. Feature A is caused by nitrosyl $\sigma_{2s}^* \rightarrow \text{Fe } 1s$ transitions, while nitrosyl $\sigma_{2p} \rightarrow \text{Fe } 1s$ transitions are located in between feature B and C at around 7101.9 eV. No significant transition probability is observed for nitrosyl $\pi_{2p} \rightarrow \text{Fe } 1s$ transitions, consistent with previous studies.^[29,30] The high-energy feature D is mainly caused by transitions of the HOMO, HOMO-1 and HOMO-2 to the Fe 1s orbital. The HOMO-2 reflects the Fe $3d_{z^2}$ orbital, while HOMO and HOMO-1 are reflecting the bonding interactions of the unoccupied, doubly degenerated NO π^* orbital and occupied Fe 3d orbitals, which is in line with studies on the isoelectronic $\text{Co}(\text{CO})_3(\text{NO})^{69}$ and other low-valent Fe-NO complexes.^[29,30] No occupation of the antibonding analogues of HOMO and HOMO-1 (with respect to the Fe-N interaction) are observed, which is in-line with the textbook molecular orbital description of a linear NO^+ ligand.^{17,65-67} In agreement with numerous previous studies, signal D is mainly caused by donor orbitals with predominant Fe 3d character^[29,31] (for further details of the elemental contributions to the MOs, see table 3). This feature will be further discussed in the following section with respect to the Fe-NO bonding interaction and the iron oxidation state of the Hieber anion.

Table 2. Comparison of structural parameters of the $\text{Ti}[\text{Fe}(\text{CO})_3(\text{NO})]$ crystal structure and optimized gasphase structure.

Compound	N-O bond length / Å	Fe-N bond length / Å	Fe-N-O bond angle / °	C-O bond length / Å	Fe-C bond length / Å	Fe-C-O bond angle / °
$[\text{Fe}(\text{CO})_3(\text{NO})]^-$ (DFT)	1.19	1.64	179.8	1.16	1.78	178.5
				1.16	1.78	178.5
				1.16	1.78	178.2
$\text{Ti}[\text{Fe}(\text{CO})_3(\text{NO})]^{69}$ (cryst.)	1.212(14)	1.659(11)	180.0(6)	1.150 (9)	1.800(8)	178.3(8)
				1.150 (9)	1.800(8)	178.3(8)
				1.150 (9)	1.800(8)	178.3(8)

RESEARCH ARTICLE

For the calculated XANES of $[\text{Fe}(\text{CO})_3(\text{NO})]^-$ (figure 3 right) ligand projected spectra were also generated to deconvolute the spectral signatures with respect to the coordinating ligands. Feature A is solely caused by Fe $1s \rightarrow \text{LUMO} / \text{LUMO}+1$ transitions. The LUMO and LUMO+1 are reflecting the antibonding combination of the doubly degenerated nitrosyl π^* orbital with Fe $3d_{xz}$ and Fe $3d_{yz}$ orbitals.^[29,30] In contrast, features B and C are attributed to a superposition of transitions to acceptor orbitals with predominant carbonyl and nitrosyl character.

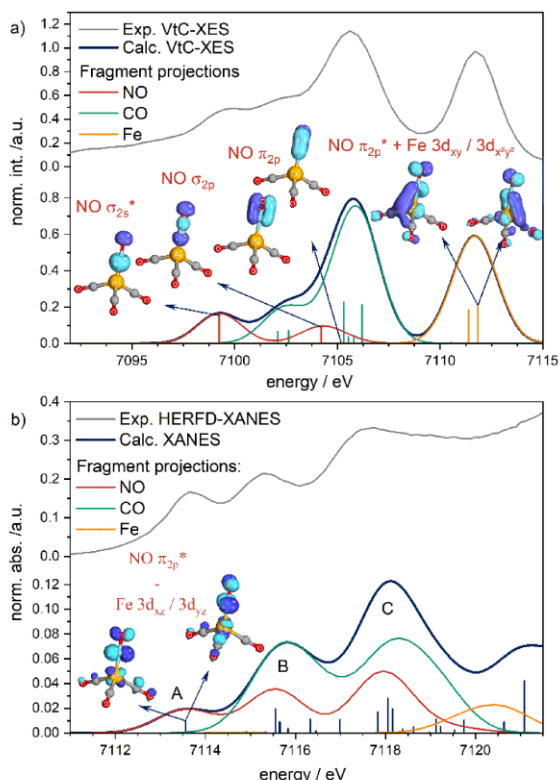


Figure 3: a) Comparison of experimental (top) and calculated (bottom) Fe K-edge VtC-XES. b) Comparison of experimental (top) and calculated (bottom) Fe K-edge HERFD-XANES of $[\text{Fe}(\text{CO})_3(\text{NO})]^-$. Ligand projected spectra and predominant donor- and acceptor orbitals, respectively are also included.

Probing 3d occupation via VtC-XES

It has been demonstrated by the edge-position of $[\text{Fe}(\text{CO})_3(\text{NO})]^-$ (TBA) in relation to $\text{Fe}(\text{CO})_5$ and $[\text{Fe}(\text{CO})_4][\text{Na}(\text{crypt})]_2$ that the Fe center of the Hieber anion is indeed characterized by a significant increased Fe 3d occupation compared to the Fe^0 reference. This evidence is strengthened by the increasing intensity of the “3d feature” D in the VtC-XES region of the Hieber anion compared to those of $\text{Fe}(\text{CO})_5$ (see figure 4). Nevertheless, it must be clarified if discrepancies

concerning the energy position and intensity of feature D are caused by varying 3d occupation or by changes in transition probability of underlying transitions due to e.g. symmetry effects.

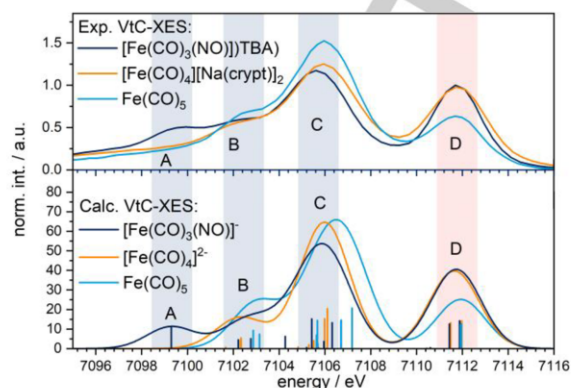


Figure 4: Calculated Fe K-edge VtC-XES (left) of $\text{Fe}(\text{CO})_5$, $[\text{Fe}(\text{CO})_3(\text{NO})]^-$ and $[\text{Fe}(\text{CO})_4]^{2-}$.

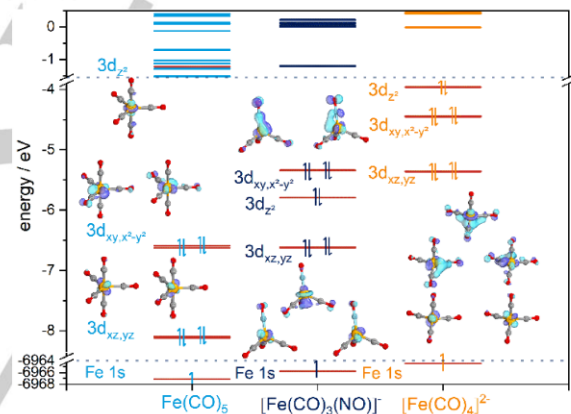


Figure 5: DFT level diagram (right) of $\text{Fe}(\text{CO})_5$, $[\text{Fe}(\text{CO})_3(\text{NO})]^-$ and $[\text{Fe}(\text{CO})_4]^{2-}$.

For this reason, calculated VtC-XES spectra and relevant donor orbitals of $\text{Fe}(\text{CO})_5$, $[\text{Fe}(\text{CO})_3(\text{NO})]^-$ and $[\text{Fe}(\text{CO})_4]^{2-}$ are compared in figure 4. The tetracarbonylferrate has been chosen as an ideal $3d^{10}$ reference. The only difference to the isoelectronic Hieber anion is the substitution of NO^+ against CO. Comparable intensities and energies of feature D are observed for both, $[\text{Fe}(\text{CO})_3(\text{NO})]^-$ and $[\text{Fe}(\text{CO})_4]^{2-}$. In both anions feature D is provoked by five underlying transition, while in $\text{Fe}(\text{CO})_5$ only four transitions are responsible for feature D. The transition probability of the Fe $3d_{xz/yz} \rightarrow \text{Fe } 1s$ channel is negligible in all three compounds, since no significant 4p hybridization of $3d_{xz/yz}$ levels is observed (HOMO-3 / HOMO-4 in case of $[\text{Fe}(\text{CO})_3(\text{NO})]^-$ and $[\text{Fe}(\text{CO})_4]^{2-}$ and HOMO-2 / HOMO-3 in case of $\text{Fe}(\text{CO})_5$, see figure 4 and table 3 for detailed information). Both $3d_{xz/yz}$ orbitals of

RESEARCH ARTICLE

Table 3. Parameter of donor orbitals responsible for VtC-XES high-energy feature D.

Compound	Parameter	Donor orbital				
		HOMO	HOMO-1	HOMO-2	HOMO-3	HOMO-4
Fe(CO) ₅	Orbital energy / eV	-6.6	-6.6	-8.1	-8.1	
	Fe(d) ^a / %	45.6	46.3	64.0	64.1	
	Fe(p) ^b / %	6.6	6.3	0.0	0.0	
	Transition energy ^c / eV	7112.0	7111.9	7110.5	7110.4	
	(int / a.u.)	(12.70)	(12.32)	(0.18)	(0.18)	
[Fe(CO) ₄] ²⁻	Orbital energy / eV	-4.0	-4.4	-4.5	-5.4	-5.4
	Fe(d) ^a / %	32.9	37.1	37.0	62.4	62.3
	Fe(p) ^b / %	11.7	8.3	8.2	0.0	0.0
	Transition energy ^c / eV	7112.0	7111.5	7111.5	7110.6	7110.6
	(int / a.u.)	(14.17)	(13.13)	(13.11)	(0.18)	(0.18)
[Fe(CO) ₃ (NO)] ⁻	Orbital energy / eV	-5.3	-5.3	-5.8	-6.6	-6.6
	Fe(d) ^a / %	31.9	31.9	43.7	61.2	61.1
	Fe(p) ^b / %	8.5	8.5	6.4	0.1	0.1
	Transition energy ^c / eV	7111.9	7111.9	7111.4	7110.6	7110.6
	(int / a.u.)	(14.13)	(14.15)	(12.53)	(0.40)	(0.42)

^a: Löwdin Fe 3d population, ^b: Löwdin Fe 4p population, ^c: energy and intensity of related VtC-XES HOMO-X → Fe 1s transition,

[Fe(CO)₃(NO)]⁻ and [Fe(CO)₄]²⁻ are hybridized by fractions of 3d_{xy/x²-y²} orbitals, leading to a tilt towards the x/y-plane (see figure 4). In contrast, comparably pronounced 4p hybridization of 3d_{xy/x²-y²} orbitals is observed in all three complexes leading to similar transition probabilities of Fe 3d_{xy/x²-y²} → Fe 1s transitions (HOMO / HOMO-1 in case of [Fe(CO)₃(NO)]⁻ and HOMO-1 / HOMO-2 in case of [Fe(CO)₄]²⁻, see figure 4 and table 3 for detailed information). Complementary to the hybridization of 3d_{xz/yz} orbitals through 3d_{xy/x²-y²} orbitals in [Fe(CO)₃(NO)]⁻ and [Fe(CO)₄]²⁻, both 3d_{xy/x²-y²} orbitals are hybridized by fractions of 3d_{xz/yz} leading to a tilting towards the z-axis (see figure 5). So far, similar 4p hybridization of 3d_{xz/yz/xy/x²-y²} levels and thus similar transition probabilities of all three compounds related transition are observed. An intensity increase of D due to an increase of the overall transition probability of Fe 3d → Fe 1s transitions through an increase in 4p hybridization is therefore excluded (see table 3). Consequently, observed intensity differences of high-energy feature D have to be attributed to the aforementioned, additional donor orbital in [Fe(CO)₃(NO)]⁻ and [Fe(CO)₄]²⁻, which is the Fe 3d_{z²} orbital (the HOMO-2 in case of [Fe(CO)₃(NO)]⁻ and the

HOMO in case of [Fe(CO)₄]²⁻, see figure 4 and table 3 for detailed information). While in Fe(CO)₅ the 3d_{z²} orbital remains unoccupied (LUMO+4, see figure 5), in both tetrahedral anions it is occupied and exhibits significant Fe 4p hybridization. The related Fe 3d_{z²} → Fe 1s transition leads to an intensity increase of the D feature by 2/3 in [Fe(CO)₃(NO)]⁻ and [Fe(CO)₄]²⁻.

The Influence of the M-N-O Bond Angle on VtC-XES and XANES

In order to illustrate the strength of HERFD-XANES and VtC-XES to determine M-N-O bond angles in nitrosyl transition metal complexes and to follow the fate of the M-NO group in catalytic reactions, an unrelaxed scan of the Fe-N-O bond angle in the singlet state of the [Fe(CO)₃(NO)]⁻ anion ground state structure has been performed. To judge the sensitivity of the HERFD-XANES and VtC-XES spectra with respect to changes in the structure,^[32] calculations were performed for different Fe-N-O bond angles as shown in figure 6. Only negligible changes are observed for the "ligand bond features" A, B and C, which were shown to be evoked by a superposition of carbonyl (feature A and

RESEARCH ARTICLE

B) and nitrosyl (feature A, B and C) ligand bond orbitals (σ_{2s}^* , σ_{2p} , π_{2p}), with negligible Fe population (see computational results section). Only in the extreme case of 120° (Fe-N-O) a small redshift of these features is observed. Thus, in this range (180°-120°) only negligible electronic changes of the nitrosyl ligand are observed in the singlet state, since reduction or oxidation of the nitrosyl ligand would cause a significant shift of low-energy feature C.^[30] The “3d feature” D decreases significantly in intensity and is shifting to higher energies with decreasing Fe-N-O bond angle. This observation can be explained by a decreasing transition probability of Fe $3d_{xz/yz} \rightarrow$ Fe $1s$ transitions due to a decrease in 4p hybridization of both levels. The observed blueshift is allocated to a reduced overlap of NO $\pi_{x,y}^*$ and Fe $3d_{xy,x^2-y^2}$ orbitals, leading to a significant destabilization of the HOMO, which is a typical effect in bent nitrosyl complexes.^{17,65-67} The reduced overlap is demonstrated by visualization of the HOMO and HOMO-1 at 180° and 140° angle of Fe-N-O in figure 6.

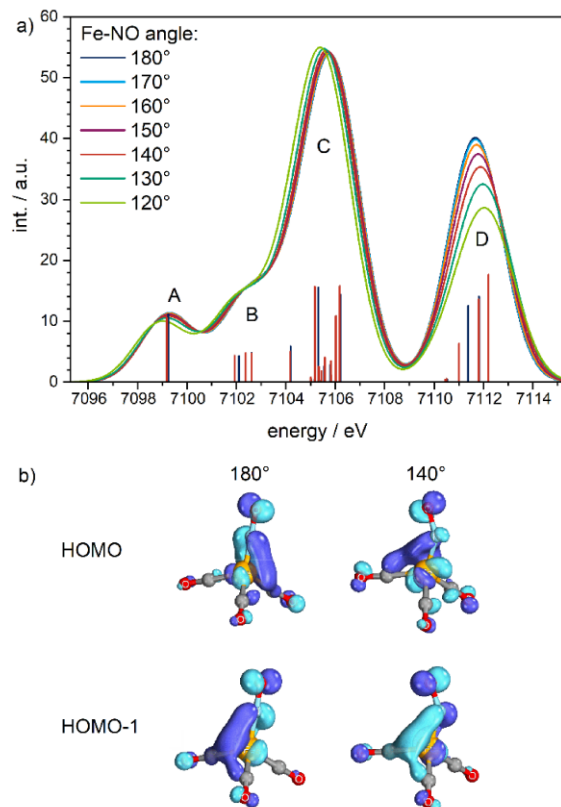


Figure 6: a) Calculated VtC-XES spectra $[\text{Fe}(\text{CO})_3(\text{NO})]^+$ in different coordination modes of the NO ligand (Fe-N-O angle between 120°-180°), transitions are only shown for 180° and 140° structures for clarity. b) HOMO respectively HOMO-1 orbital of the 180° and 140° structures.

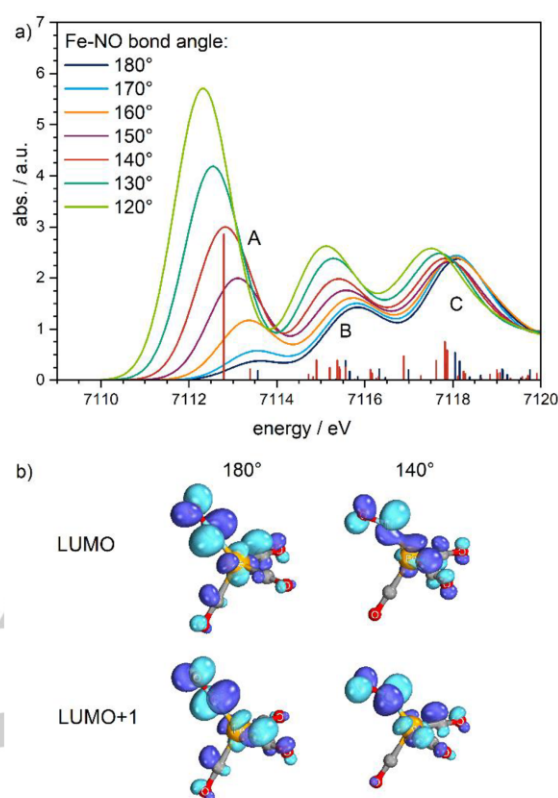


Figure 7: a) Calculated XANES spectra showing the pre-edge region of $[\text{Fe}(\text{CO})_3(\text{NO})]^+$ in different coordination modes of the NO ligand (Fe-N-O angle between 120°-180°), transitions are only shown for 180° and 140° structures for clarity. b) LUMO and LUMO+1 with a Fe-N-O angle of 180° and 140° structures.

The pre-edge region (XANES) shows a more significant influence of the decreasing Fe-N-O angle (see figure 7) compared to VtC-XES (see figure 6). The largest effect is found for feature A, which has been shown to be solely evoked by transitions to the LUMO / LUMO+1, reflecting the antibonding combination of the doubly degenerated nitrosyl π^* orbital with Fe $3d_{xz}$ and Fe $3d_{yz}$ orbitals (see results section). Feature A shows a tremendous increase of the intensity and a redshift correlated to a bond angle reduction. With decreasing Fe-N-O bond angle an overlap of NO $\pi_{x,y}^*$ orbitals and Fe $3d_{xz,yz}$ orbitals is emerging, leading to a successive stabilization of the antibonding combination (LUMO) with decreasing Fe-N-O bond angle, which is a typical effect of bent nitrosyl complexes.^{17,65-67} Due to the stabilization of the LUMO a redshift of the Fe $1s \rightarrow$ LUMO transition is observed. A comparison of the LUMO and LUMO+1 at 180° and 140° Fe-N-O angle is shown in figure 7.

RESEARCH ARTICLE

Discrimination of coordination isomers by VtC-XES and HERFD-XANES

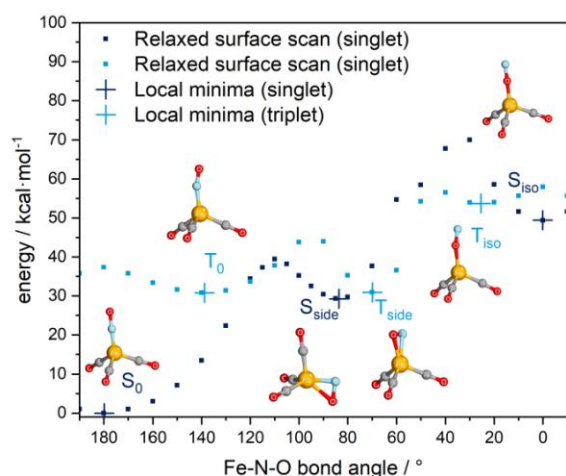


Figure 8: Relaxed surface scan of the Fe-N-O bond angle in singlet and triplet of $[\text{Fe}(\text{CO})_3(\text{NO})]^-$; local minima structures are shown.

The bond angle scan approach clearly illustrates the sensitivity of HERFD-XANES and VtC-XES to the Fe-N-O bond angle. Nevertheless, this approach considers only the structural influence of the M-NO motif in the singlet state on occupied and unoccupied levels, excluding a structural rearrangement of the carbonyl ligands. Since bent nitrosyl complexes with an integer total spin typically occupy a triplet ground state,^{17,65–67} triplets are also be considered. The isoelectronic $\text{Co}(\text{CO})_3(\text{NO})$ is known to occupy low-lying singlet and triplet structural nitrosyl isomers.⁶⁹ For this reason also in the case of the Hieber anion, both possible spin states should be covered to computationally investigate the spectral signatures of “real” nitrosyl coordination isomers.

In order to investigate the potential of HERFD-XANES and VtC-XES to discriminate structural nitrosyl isomers in the singlet and triplet state, minima structures of these structural isomers are required. For this reason, a relaxed Fe-N-O bond-angle scan has been performed in the singlet and triplet state in 10° steps, starting at 180° (linear, nitrosyl) and going to 0° (linear, iso-nitrosyl) to cover all possible structural isomers (figure 8). In both multiplicities three minima are observed: linear (S_0), side-on (S_{side}) and linear iso-nitrosyl (S_{iso}) coordinated structural isomers in the singlet state and bent (T_0), side-on (T_{side}) and bent iso-nitrosyl (T_{iso}) coordinated structural isomers in the triplet state, which is in line with theoretical investigations of the isoelectronic $\text{Co}(\text{CO})_3(\text{NO})$.⁶⁹ All refined structures, parameters and related energies are shown in figure 8 and table 4. VtC-XES and XANES

spectra of all observed structural isomers are calculated and compared in the following.

Table 4. Bond angles and energies (relative to the ground state S_0) of all structural nitrosyl isomers of $[\text{Fe}(\text{CO})_3(\text{NO})]^-$ found in the relaxed surface scans. The corresponding molecular structures are shown in figure 8.

Structural isomer	Fe-N-O bond angle / °	N-O bond length / Å	Fe-N bond length / Å	Fe-O bond length / Å	Energy ^a / kcal·mol ⁻¹
Linear, singlet (S_0)	179.9	1.19	1.64	-	0.0
Side-on, singlet (S_{side})	83.6 (59.0)	1.25	1.76	2.04	29.2
Iso, linear, singlet (S_{iso})	0.1 (179.8)	1.18	-	1.72	49.4
Bent, triplet (T_0)	138.8	1.21	1.79	-	30.8
Side-on, triplet (T_{side})	69.9 (70.9)	1.29	1.93	1.92	30.9
Iso, bent, triplet (T_{iso})	25.5 (138.2)	1.24	-	1.9	53.7

^a: Relative to the ground state S_0 .

The discussion will be first restricted to geometric effects by comparison of the singlet structural isomers S_{side} , S_{iso} to the singlet ground state S_0 . Afterwards the considered triplet structural isomers will be compared to the electronic ground state S_0 .

The linear iso-nitrosyl isomer S_{iso} exhibits a Fe-O-N bond angle of 179.8° , a N-O bond length of 1.18 Å and a Fe-O distance of 1.72 Å. Even though there are only slight structural deviations from S_0 , distinct spectral differences are observed, as shown in figure 9. The largest influence is observed for the low-energy VtC-XES feature A, which is red-shifted by about 1.5 eV in relation to S_0 , caused through a pronounced stabilization of nitrosyl σ_{2s}^* levels in case of the iso-coordination. Additionally, the splitting between shoulder B and feature C is increased, due to a significant redshift and decrease in transition probability of $\text{NO } \sigma_{2p} \rightarrow \text{Fe } 1s$

RESEARCH ARTICLE

transitions at around 7102 eV. The bonding combination of NO $\pi_{x,y}^*$ and Fe 3d levels is destabilized in case of iso- coordination, leading to a blueshift of the high energy feature D. Furthermore, a decrease of the transition probability of Fe 3d \rightarrow Fe 1s transitions is observed, leading to a decrease of the intensity of feature D.

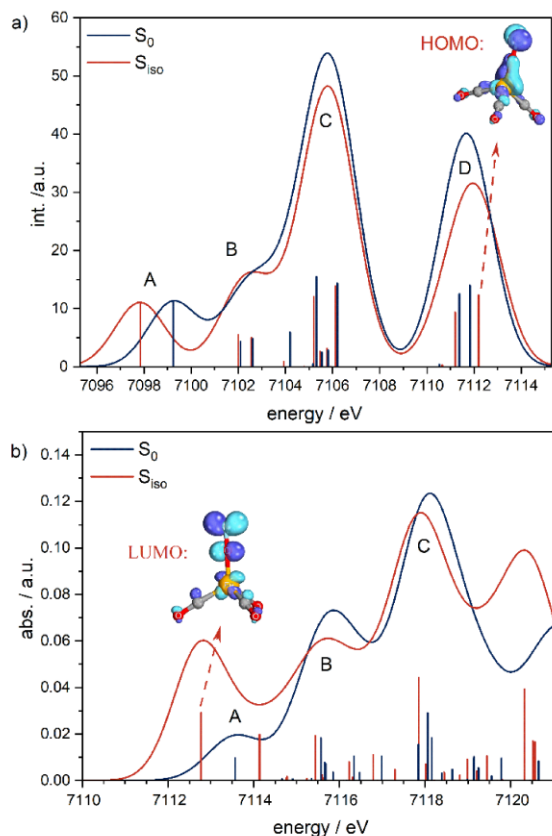


Figure 9: Comparison of calculated VtC-XES (a) and XANES spectra (b) of S_{iso} and S_0 .

Since iso-coordination leads to a destabilization of the bonding combination of NO $\pi_{x,y}^*$ and Fe 3d levels, it in turn leads to a stabilization of the antibonding combination of NO $\pi_{x,y}^*$ and Fe 3d orbitals (LUMO, LUMO+1). This affects the XANES pre-edge feature A, which is redshifted by about 1 eV and increases in intensity compared to S_0 , which is shown in figure 9. The observed intensity is simply explained by an increase in the transition probability of Fe 1s \rightarrow LUMO / LUMO+1 transitions, caused by an increase in Fe 4p hybridization of both antibonding combinations.

The singlet side-on coordinated structural isomer S_{side} occupies a Fe-N-O bond angle of 83.58° and a N-O distance

increased by 0.06 Å (cf. table 4). Calculated VtC-XES and XANES spectra of S_{side} in comparison to S_0 are given in figure 10. Low-energy VtC-XES feature A is blue-shifted for S_{side} , reflecting a destabilization of NO σ_{2s}^* orbitals due to the additional interaction of iron with oxygen. Similar to S_{iso} the transition probability of the NO $\sigma_{2p} \rightarrow$ Fe 1s transition in S_{side} vanishes almost completely (reduction of 97%), leading to a significant decrease in intensity and redshift of B.

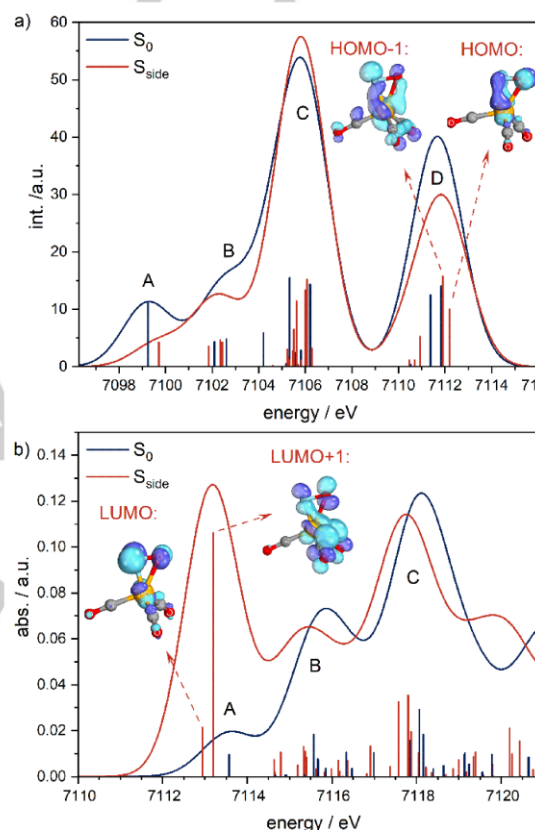


Figure 10: Comparison of calculated VtC-XES spectra (a) and XANES spectra (b) of S_{side} and S_0 .

In the ground state S_0 , HOMO and HOMO-1 are degenerated and reflecting the bonding interaction of NO $\pi_{x,y}^*$ with Fe $3d_{xy,x^2-y^2}$ orbitals, which was earlier indicated in figure 3. The HOMO of S_{side} reflects the bonding interaction of the NO π_x^* and $3d_{xy}$, similar to S_0 and displayed in figure 10. The bonding interaction of the NO π_y^* and the $3d_{x^2-y^2}$ orbital is not possible anymore by symmetry for S_{side} and therefore bonding interaction of the NO π_y^* and the $3d_{z^2}$ orbital is observed, creating the HOMO-1. Both, HOMO and HOMO-1 are energetically destabilized compared to S_0 , leading to a slight blueshift of high-energy feature

RESEARCH ARTICLE

D and additionally an average decrease of the transition probability of Fe 3d \rightarrow Fe 1s transitions is observed due to a decrease in 4p hybridization, leading to a decrease of the intensity of feature D. As shown for S_0 , the LUMO and LUMO+1 are the antibonding equivalents of the HOMO and HOMO-1 also in case of S_{side} . The LUMO of S_{side} reflects the antibonding interaction of NO π_x^* and $3d_{x^2-y^2}$, while LUMO+1 reflects the antibonding interaction of the NO π_y^* and the $3d_{z^2}$ orbital. Since HOMO and HOMO-1 are destabilized in S_{side} in relation to S_0 , the antibonding equivalents LUMO and LUMO+1 are stabilized, shifting pre-edge feature A significantly to lower energies by about 0.5 eV. Furthermore, a six-fold increase in intensity of A is observed due to a significant increased 4p contribution to the LUMO and LUMO+1 in S_{side} .

S_{side} .

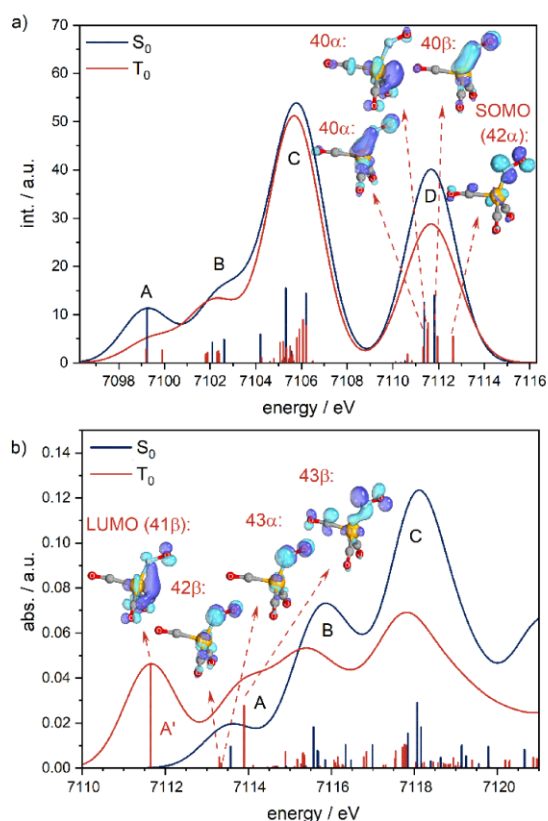


Figure 11: Comparison of calculated VTC-XES spectra (a) and XANES spectra (b) of S_0 and T_0 .

Next, the results of the singlet ground state S_0 are compared to the triplet structural isomers, starting with the triplet ground state T_0 (see figure 11). The triplet ground state adopts a bent nitrosyl conformation with a Fe-N-O bond angle of 139° , a N-O distance of 1.21 Å and a Fe-N distance of 1.79 Å. Comparison of

the spectra to S_0 are given in figure 11. The low-energy VTC-XES feature A is decreasing in intensity and broadened to higher-energies, due to a significant destabilization of the spin down (β) NO σ_{2s}^* orbital, while the spin up (α) equivalent is only slightly stabilized. Similar to S_{iso} and S_{side} , the transition probability of the NO $\sigma_{2p} \rightarrow$ Fe 1s transition in T_0 is drastically reduced, leading to a significant decrease in intensity and redshift of B. Similar to S_{side} , no interaction of NO π_y^* and $3d_{x^2-y^2}$ in T_0 is possible by symmetry due to the bent conformation, and therefore only bonding interaction of the NO π_x^* and $3d_{xy}$ orbital is observed, represented by the molecular orbitals 40α and 40β in figure 11. The remaining NO π_y^* orbital of T_0 is only weakly interacting with the $3d_{xz}$ orbital, leading to the high energy SOMO 42α (figure 11). In contrast to the HOMO or HOMO-1 of S_0 , the SOMO of T_0 occupies only a negligible 3d population of 12.8 % and therefore the SOMO reflects rather a singly occupied NO π_y^* orbital than a $3d_{xz}$ orbital in bonding combination with a NO π_y^* . No equivalent occupied β orbital is found and therefore a single occupied NO π_y^* is observed in T_0 . Complimentary, only a single occupation of the Fe $3d_{z^2}$ is observed, reflected in the 41α orbital. The overall decrease in intensity of high energy feature D in the VTC-XES spectra of the triplet ground state can be therefore traced back to an overall decrease of Fe 4p density of the underlying donor orbitals. The LUMO (41β , figure 11) is the beta equivalent of the semi occupied $3d_{z^2}$ orbital, which has been shown to be fully occupied in all observed singlet structures and therefore does not show up in the XANES region. The related Fe 1s \rightarrow 41β transition causes a new feature A' in the XANES region at around 7111.5 eV. Pre-edge feature A in T_0 originates from transitions to acceptor orbitals reflecting the antibonding combination of NO π_x^* and $3d_{xy}$, 42β and 43α and the unoccupied beta equivalent of the SOMO (NO π_y^* , 42α), 43β . The Fe 1s \rightarrow 43β transition leads to a blueshift and significant intensity increase of feature A.

The iso-nitrosyl bent coordinated structural isomer T_{iso} exhibits a very similar structure to T_0 (see table 4), and therefore also the spectral signatures are very similar to each other as concluded from figure S1 in the supporting information, where also a full discussion of the spectral signatures is given. The most significant difference between T_{iso} and T_0 to be mentioned here is an even further decreasing overlap of NO π^* and Fe 3d orbitals, since the electron-density in NO π^* orbitals is concentrated on the nitrogen atom. Therefore, the SOMO exhibits even less iron density compared to T_0 and bonding interaction of NO π_x^* and $3d_{xy}$ is even more destabilized in relation to T_0 .

RESEARCH ARTICLE

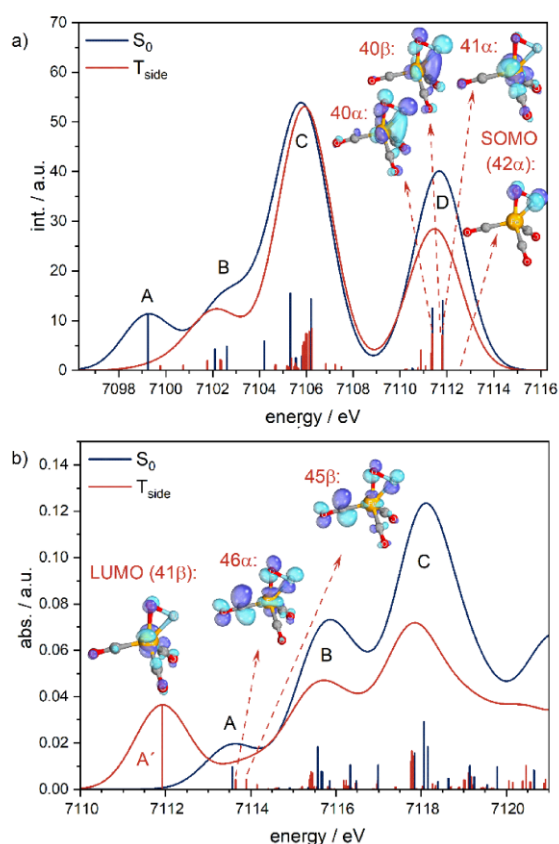


Figure 12: Left: Comparison of calculated VtC-XES spectra (a) and XANES spectra (b) of S_0 and T_{side} .

The triplet structural isomer T_{side} occupies a side-on coordinated nitrosyl ligand. The N-O bond length is elongated by 0.05 Å compared to the singlet analogue S_{side} . T_{side} occupies similar Fe-N and Fe-O distances of 1.93 Å or 1.92 Å, in contrast to S_{side} , possessing a significantly shortened Fe-N bond length of 1.76 Å in relation to its Fe-O bond length of 2.04 Å. The calculated VtC-XES and XANES spectra of T_{side} are shown and compared in figure 12 to the ground state S_0 . The strongest blueshift of the low-energy VtC-XES feature A in relation to the singlet ground state of all investigated structural isomers is observed for T_{side} . Feature A is blueshifting towards feature B by which it is strongly superimposed and thus appears only as a low-energy tail of B caused by significant destabilization of the nitrosyl σ_{2s}^* levels in T_{side} . As observed for all structural isomers except S_0 , the transition probability of nitrosyl $\sigma_{2p} \rightarrow \text{Fe } 1s$ transitions decreases also significantly in T_{side} , leading to a redshift of feature B. The π_x^* is interacting in bonding combination with the Fe $3d_{x^2-y^2}$ orbital, resulting in 40α and 40β (cf. figure 12). The π_y^* orbital (SOMO) of T_{side} shows no significant interaction with Fe 3d orbitals (5.1 %

LROP), resulting in a destabilization of the SOMO level, as seen for T_0 and T_{iso} . For this reason, the SOMO reflects a localized semi-occupied π_y^* orbital. Due to an even further decreasing Fe 4p hybridization of the SOMO in relation to T_0 and T_{iso} , no observable transition probability of the SOMO $\rightarrow \text{Fe } 1s$ transition is present. An overall decrease of 4p hybridization of NO-Fe bonding interactions is observed, leading to a significant decreased intensity of the VtC-XES high-energy feature D. In T_{side} also a semi-occupied Fe 3d orbital is observed but in contrast to T_{iso} and T_0 , it is the Fe $3d_{xz/yz}$ orbital in T_{side} . The Fe $1s \rightarrow \text{Fe } 3d_{xz/yz}$ transition causes also an additional pre-edge feature A' as already seen in T_{iso} and T_0 .

Discussion

In the following the outcome of the computational results section concerning the local iron density and nitrosyl charge will be discussed. The Fe K-edge position of the Hieber anion is significantly redshifted by 1.6 eV in comparison to the $3d^8$ reference $\text{Fe}(\text{CO})_5$ and shows the exact same position as the $3d^{10}$ reference $[\text{Fe}(\text{CO})_4][\text{Na}(\text{crypt})]_2$ (see figure 2, first derivative XANES spectra are shown in figure S3 in the supporting information), illustrating an increased local electron density at the iron center. This observation is in-line with the increase in intensity of the 3d-VtC-XES-feature D of both anions relative to $\text{Fe}(\text{CO})_5$. These experimental evidence clearly agree with the old, well-known description of an Fe^{II} ion bound to a linear NO^+ ligand and therefore we have to disagree with the present description of the Hieber anion, to be a $\text{Fe}^{\pm 0}$ atom bound linear to an NO^- ligand by a double π -bond.

Since the Hieber anion is coordinated by a nitrosyl ligand, we will discuss in the following the observed Fe-NO bonding interaction based on quantum chemical calculations presented here and in preceding publications. DFT calculation presented above illustrate that HOMO and HOMO-1 of $[\text{Fe}(\text{CO})_3(\text{NO})]^-$ are reflecting π bonding interactions between Fe 3d and nitrosyl π^* orbitals, while LUMO and LUMO+1 are reflecting the analogue antibonding interactions, which is in line with observations made in ref. 26. If all four electrons located at the Fe-NO " π -double-bond" would be pure covalently shared, reflecting a NO^- ligand (due to a formal double occupation of nitrosyl π^* orbitals), then both bonding and antibonding interactions should show equal Fe 3d contributions. In case of a cationic NO^+ ligand, significantly increased Fe 3d density for both antibonding interactions in

RESEARCH ARTICLE

comparison to both bonding interactions is present. Independently of the applied functional (BP86, TPSS, TPSSh, adj. TPSSh and B3LYP) we observe a significantly increased Fe 3d density for both bonding interactions (HOMO and HOMO-1) in comparison to both antibonding combination, reflecting a more neutral to positively charged nitrosyl ligand (Loewdin populations of HOMO-4 to LUMO+1 for all tested functionals are shown in supporting information table S2). Nevertheless, we have to test whether DFT methods are justified to draw any conclusions about the Fe-NO bonding interaction, since metal-nitrosyl bonds are well-known to be influenced by static electron correlation. For this reason, the fractional-occupation-number-weighted density (FOD) is analyzed which has been recently introduced by Grimme et al. (details are given in the supporting information).^[33] The FOD analysis gives information about the amount and localization of static electron correlation and reflects therefore a bridge between DFT and wave-function-based methods. Analysis of the FOD density indicates significant static electron correlation for both NO π^* and Fe 3d orbitals, as shown by the FOD density plot in the supporting information figure S2 and by significantly depopulation of the HOMO to HOMO-4 (see supporting information table S1). Therefore, an adequate active space in for example a Complete Active Space Self Consistent Field (CASSCF) calculation should consist of 10 electrons in 10 orbitals. Such a CASSCF (10,10) calculation of the Hieber anion using natural orbitals has been shown in the supporting information of ref. 26. Where a significant depopulation of the bonding Fe-NO π interaction by the antibonding one was observed (0.16:1.85 antibonding/bonding), consistent with values observed by FOD (see supporting information table S1). Both π bonding Fe-NO interactions also exhibit a significant increased Fe 3d density in comparison to both π antibonding Fe-NO interactions (supporting information ref. 26, CASSCF (10,10)), in agreement with the DFT analysis shown above, pointing out to a more neutral to positively charged nitrosyl ligand.

An additional evidence to the nitrosyl charge can be extracted via a method published by Liaw et al. (ref. 30), where the energy gap between the NO $\sigma^*_{2s} \rightarrow$ Fe 1s transition and NO $\sigma_{2p} \rightarrow$ Fe 1s transition probed by VtC-XES is utilized as a measure for the NO ligand charge. Since the agreement of the energy splitting of all experimental and computational observed VtC-XES features is outstanding (figure 3), calculated transition energies of the NO $\sigma^*_{2s} \rightarrow$ Fe 1s transition and NO $\sigma_{2p} \rightarrow$ Fe 1s transitions are utilized. A NO(σ_{2p})-NO(σ^*_{2s}) gap ($\Delta E[\text{NO}(\sigma_{2p})\text{-NO}(\sigma^*_{2s})]$) of 4.95 eV (see figure 3) is observed in case of the Hieber anion,

resulting in a calculated charge of +0.21 (± 0.18) using their method, which is in line with all observations made above.

However, the work of Liaw et al. (ref. 30) only considered the raw effect of the nitrosyl charge on the NO(σ_{2p})-NO(σ^*_{2s}) gap probed by VtC-XES and excludes the effect of the binding mode itself on 3d connected features in the VtC-XES (feature D, figure 3) and the pre-edge region of the Fe K-edge (feature A, figure 3). The analysis of these features is especially important in cases where nitrosyl ligands with similar charges but different coordination modes need to be discriminated or where the extraction of both NO $\sigma^*_{2s} / \sigma_{2p} \rightarrow$ Fe 1s transitions is hindered, as for example in case of nitrosyl complexes coordinated by additional ligands with intense features in the region of NO $\sigma^*_{2s} \rightarrow$ Fe 1s transitions (~ 7099 eV) and NO $\sigma_{2p} \rightarrow$ Fe 1s transitions (~ 7104 eV) or due to bad overlap of NO σ_{2p} and Fe 4p orbitals and therefore a vanishing of the connected transition probability, as observed for both computational explored nitrosyl coordination isomers S_{iso} and S_{side} (figure 9 and 10).

In the following the overall outcome of the structural nitrosyl isomer section will be discussed and the influence of the binding mode and spin state on 3d connected features of both VtC-XES and HERFD-XANES will be reviewed. Both singlet structural nitrosyl isomers S_{iso} and S_{side} show a great similarity to S_0 , with two occupied bonding Fe-NO interactions (HOMO and HOMO-1, figure 9 and 10) and two unoccupied antibonding Fe-NO interactions (LUMO and LUMO+1, figure 9, 10). Both bonding interactions (HOMO and HOMO-1, figure 10) are destabilized, leading to a decrease in intensity, broadening and blueshift of VtC-XES feature D, while both antibonding interactions are significantly stabilized, showing a significantly increase in 4p hybridization (LUMO and LUMO+1, figure 9 and 10). This effect is increasing dramatically the intensity of pre-edge feature A, shifting A to lower energies. The redshift of pre-peak feature A is much more pronounced in case of S_{iso} (~ 0.5 eV), while S_{side} shows almost twice the increase in intensity relative to S_{iso} and therefore the discrimination of both isomers is also possible based on the computational results. For all three computational observed triplet structural nitrosyl isomers T_0 , T_{iso} and T_{side} an additional pre-edge feature A' is observed, which has been shown to be evoked by a semi-occupied acceptor orbital, reflecting the 3d_{z²} orbital in case of T_0 and T_{iso} and the 3d_{xz/yz} orbital for T_{side} . The SOMO in all three triplet isomers reflects a single nitrosyl π^* orbital non-interacting with 3d orbitals. Due to the semi occupation of one 3d orbital in each triplet isomer, a significant decrease in intensity of VtC-XES feature D and the overall occupied 3d

RESEARCH ARTICLE

density is observed. T_{iso} shows the smallest intensity of VtC-XES feature D and the highest intensity of pre-edge feature A', while T_0 shows the most pronounced pre-edge feature A. Consequently, it is possible to discriminate all observed nitrosyl structural isomers (singlet or triplet) due to characteristic variations of 3d connected features, VtC-XES feature D and pre-edge features A' and A.

Conclusion

With the approach of combining high energy resolution X-ray absorption and emission spectroscopy with quantum-chemical calculations, new detailed insights into the electronic and geometric structure of the Hieber anion $[\text{Fe}(\text{CO})_3(\text{NO})]^-$ could be gained. The combination of hard X-ray spectroscopies can be easily transferred now to in-situ investigations of reactions catalyzed by the $[\text{Fe}(\text{CO})_3(\text{NO})]^-$ precatalyst to understand its working principle. By investigation of the XANES edge-position and Valence-to-Core emission it could be experimentally proven that the local electron density at the Fe center of $[\text{Fe}(\text{CO})_3(\text{NO})]^-$ is indeed significantly increased relative to the $3d^8$ reference complex $\text{Fe}(\text{CO})_5$ and shows equal characteristics (edge position and intensity of VtC-XES feature D) as the $3d^{10}$ reference complex $[\text{Fe}(\text{CO})_4][\text{Na}(\text{crypt})]_2$. Furthermore it has been shown that the $\text{NO}(\sigma_{2p})\text{-NO}(\sigma_{2s}^*)$ gap ($\Delta E[\text{NO}(\sigma_{2p})\text{-NO}(\sigma_{2s}^*)]$) (probed by VtC-XES) results in a calculated charge of + 0.21 (± 0.18) using the method of Liaw et al. (ref. 30) for nitrosyl charge determination via VtC-XES. The presented experimental data is clearly substantiating the well-know $3d^{10}$, Fe^{II} description and disagrees with the latest $3d^8$, Fe^{I} description of ref. 26. We suggest therefore to reopen the debate about the present Fe oxidation state and nitrosyl charge in the Hieber anion.

Beside such very fundamental results on the ground state electronic structure, the high potential of the spectroscopic approach can be applied in a much broader manner. The theoretical investigation of six different structural nitrosyl isomers in the singlet and triplet spin state illustrated, that the coordination mode itself shows a dramatic effect on 3d-localised features in both, the VtC-XES region (feature D) and the pre-edge region (feature A and A'). Which even allows to discriminate different nitrosyl binding modes in cases where nitrosyl ligands with similar charges but different coordination modes are present.

Experimental Section

Materials

$[\text{Fe}(\text{CO})_3(\text{NO})](\text{TBA})$ (TBA = Tetrabutylammonium) and $[\text{Fe}(\text{CO})_4][\text{Na}_2(\text{crypt})]$ (crypt : Cryptand 222 = 4,7,13,16,21,24-Hexaoxa-1,10-diazabicyclo[8.8.8]hexacosane) have been synthesized by given procedures.^[25,34,34,35] TBABr, Cryptand 222 and $\text{Fe}(\text{CO})_5$ were purchased from sigma-aldrich and $\text{Fe}(\text{CO})_5$ has been distilled freshly prior usage. For the X-ray absorption and emission measurements, $[\text{Fe}(\text{CO})_3(\text{NO})](\text{TBA})$ and $[\text{Fe}(\text{CO})_4][\text{Na}_2(\text{crypt})]$ were diluted in BN in a mass ratio of 1:4 to avoid self-absorption effects and the liquid $\text{Fe}(\text{CO})_5$ has been prepared by impregnating BN wafers with $\text{Fe}(\text{CO})_5$. All preparation steps were conducted in a glovebox and the samples were sealed by multiple layers of Kapton® tape.

Quantum-chemical calculations

All calculations presented here were conducted with the ORCA quantum chemistry package (version 4.0.1).^[36] Unconstraint geometry optimization and relaxed surface scans were performed using the TPSSh^[37] functional, the atom-pairwise dispersion correction with the Becke-Johnson damping scheme (D3BJ)^[38] and the ma-def2-QZVPP (anions)^[39] or def2-TZVP (neutral complexes) basis set^[40] on all atoms. No symmetry constraints were enforced for any optimization. Plietker et al. have shown that for the ground state structure (S_0) of the Hieber anion no symmetry breaking is observed for the functionals BP86,^[41] TPSS,^[42] TPSSh^[42] and B3LYP.^[43] All presented optimized structures were confirmed to be minima structures by numerical frequency calculations and the absence of negative frequencies.

TD-DFT (XANES)^[44] and DFT (VtC-XES)^[23] calculations were accomplished using a modified TPSSh functional, with an adjusted Hartee-Fock exchange of 12.5 %, which has been applied in previous studies of our group on low-valent iron carbonyl / nitrosyl complexes,^[29] biomimetic copper complexes^[45] and iron poly-pyridyl complexes^[46] and has been shown to achieve a very good agreement between theory and experiment for these type of complexes concerning the splitting of metal-centered (MC) and metal-to-ligand charge transfer (MLCT) transitions in the near-edge to pre-edge region. The ma-def2-QZVPP^[39] basis set (with a special integration accuracy of 5) was applied on all atoms except Fe, for which the expanded CP(PPP) basis set^[47] is used (with a special integration accuracy of 7). All calculations were performed using gas phase optimized structures. Inclusion of polar crystal environment effects for both

RESEARCH ARTICLE

anions via the conductor-like polarizable continuum model (CPCM, $\epsilon = \infty$)^[48] and solvation of $\text{Fe}(\text{CO})_5$ by $\text{Fe}(\text{CO})_5$ (CPCM, $\epsilon = 2.6$) was included for the comparison of theoretical VtC-XES spectra and DFT-levels of $[\text{Fe}(\text{CO})_4]^{2-}$, $[\text{Fe}(\text{CO})_3(\text{NO})]$ and $\text{Fe}(\text{CO})_5$.

All calculated XANES (TD-DFT) transitions were broadened by 1.5 eV (fwhm) and VtC-XES (DFT) transitions by 2.5 eV (fwhm). Calculated XANES and VtC-XES spectra were adjusted to experiment by shifting them by 151.1 eV and 151.4 eV, respectively.

Kohn-Sham orbitals were visualized with IBOView (version 20150427).^[49] Orbital populations were extracted via Löwdin Orbital Population (LROP) Analysis.^[50] Ligand or atom projected VtC-XES spectra are created by taking only a set of donor orbitals with significant population of a given atom or fragment into account (Fe: 30 % LROP, NO: 30% LROP and CO: 60 % LROP) as indicated in the results and discussion section. While for TD-DFT XANES it is necessary to determine which core-excited state is associated with the previous assigned acceptor orbitals of a given atom or fragment (Fe: 30 % LROP, NO: 30% LROP and CO: 60 % LROP). Ligand or atom projected XANES spectra are created by taking only a set of core-excited states of a given atom or fragment into account. A detailed description of the projection approach has been given in previous studies of our group.^[29,31]

Acknowledgements

The ESRF (beamline ID26: Pieter Glatzel) and Petra III (beamline P64: Wolfgang Caliebe) are acknowledged for a provision of beamtime. The Deutsche Forschungsgemeinschaft (DFG; FKZ BA 4467/4-1; SPP 1708, FKZ BA 4467/6-1) and the Bundesministerium für Bildung und Forschung (BMBF; SynXAS, FKZ 05K18PPA; TReXHigh FKZ, 05K16PP1) are kindly acknowledged for financial support. Generous grants of computing time at the Paderborn Center for Parallel Computing PC² are gratefully acknowledged.

Keywords: Hieber Anion • oxidation state • nitrosyl • HERFD-XANES • VtC-XES

- [1] a) L. J. Ignarro, *Angew. Chem. Int. Ed.* **1999**, 38, 1882; b) F. Murad, *Angew. Chem. Int. Ed.* **1999**, 38, 1856; c) E. Culotta, D. Koshland, *Science* **1992**, 258, 1862; d) R. F. Furchgott, *Angew. Chem. Int. Ed.* **1999**, 38, 1870.
- [2] a) A. K. Patra, P. K. Mascharak, *Inorg. Chem.* **2003**, 42, 7363; b) C. F. Works, P. C. Ford, *J. Am. Chem. Soc.* **2000**, 122, 7592; c) C. F. Works, C. J. Jocher, G. D. Bart, X. Bu, P. C. Ford **2002**; d) P. C. Ford, I. M. Lorkovic, *Chem. Rev.* **2002**, 102, 993; e) J. L. Bourassa, P. C. Ford, *Coord. Chem. Rev.* **2000**, 200-202, 887; f) A. R. Butler, I. L. Megson, *Chem. Rev.* **2002**, 102, 1155; g) P. C. Ford, J. Bourassa, K. Miranda, B. Lee, I. Lorkovic, S. Boggs, S. Kudo, L. Laverman, *Coord. Chem. Rev.* **1998**, 171, 185.
- [3] P. Coppens, D. V. Fomitchev, M. D. Carducci, K. Culp, *J. Chem. Soc., Dalton Trans.* **1998**, 865.
- [4] T. E. Bitterwolf, *Coord. Chem. Rev.* **2006**, 250, 1196.
- [5] M. Atanasov, T. Schönherr, *J. Mol. Struct.: THEOCHEM* **2002**, 592, 79.
- [6] P. Boulet, H. Chermette, J. Weber, *Inorg. Chem.* **2001**, 40, 7032.
- [7] W. Kaim, B. Schwederski, *Coord. Chem. Rev.* **2010**, 254, 1580.
- [8] J. H. Enemark, R. D. Feltham, *Coord. Chem. Rev.* **1974**, 13, 339.
- [9] R. Eisenberg, C. D. Meyer, *Acc. Chem. Res.* **2002**, 8, 26.
- [10] a) P. Coppens, I. Novozhilova, A. Kovalevsky, *Chem. Rev.* **2002**, 102, 861; b) D. V. Fomitchev, P. Coppens, *Comments Inorg. Chem.* **1999**, 21, 131; c) M. D. Carducci, M. R. Pressprich, P. Coppens, *J. Am. Chem. Soc.* **1997**, 119, 2669; d) M. Buchs, C. A. Daul, P. T. Manoharan, C. W. Schlöpfer, *Int. J. Quantum Chem.* **2003**, 91, 418.
- [11] K. H. Pannell, Y. S. Chen, K. Belknap, C. C. Wu, I. Bernal, M. W. Creswick, H. N. Huang, *Inorg. Chem.* **1983**, 22, 418.
- [12] C. P. Brock, J. P. Collman, G. Dolcetti, P. H. Farnham, J. A. Ibers, J. E. Lester, C. A. Reed, *Inorg. Chem.* **2002**, 12, 1304.
- [13] M. Bauer, H. Bertagnolli in *Methods in Physical Chemistry* (Eds.: R. Schäfer, P. C. Schmidt), Wiley-VCH Verlag GmbH & Co. KGaA, Weinheim, Germany, **2012**, pp. 231-269.
- [14] P. Glatzel, U. Bergmann, *Coord. Chem. Rev.* **2005**, 249, 65.
- [15] T. E. Westre, P. Kennepohl, J. G. DeWitt, B. Hedman, K. O. Hodgson, E. I. Solomon, *J. Am. Chem. Soc.* **1997**, 119, 6297.
- [16] I. Arčon, J. Kolar, A. Kodre, D. Hanžel, M. Strlič, *X-Ray Spectrom.* **2007**, 36, 199.
- [17] A. J. Atkins, C. R. Jacob, M. Bauer, *Chemistry (Weinheim an der Bergstrasse, Germany)* **2012**, 18, 7021.
- [18] H. A. Kramers, W. Heisenberg, *Z. Physik* **1925**, 31, 681.
- [19] Hämäläinen, Siddons, Hastings, Berman, *Physical review letters* **1991**, 67, 2850.
- [20] F. M. F. de Groot, M. H. Krisch, J. Vogel, *Phys. Rev. B* **2002**, 66, 621.
- [21] a) M. U. Delgado-Jaime, S. DeBeer, M. Bauer, *Chemistry (Weinheim an der Bergstrasse, Germany)* **2013**, 19, 15888; b) A. J. Atkins, M. Bauer, C. R. Jacob, *Phys. Chem. Chem. Phys.* **2013**, 15, 8095.
- [22] a) G. Smolentsev, A. V. Soldatov, J. Messinger, K. Merz, T. Weyhermüller, U. Bergmann, Y. Pushkar, J. Yano, V. K. Yachandra, P. Glatzel, *J. Am. Chem. Soc.* **2009**, 131, 13161; b) C. J. Pollock, S. DeBeer, *Accounts of chemical research* **2015**, 48, 2967.
- [23] N. Lee, T. Petrenko, U. Bergmann, F. Neese, S. DeBeer, *J. Am. Chem. Soc.* **2010**, 132, 9715.
- [24] B. Plietker, A. DIESKAU, *Eur. J. Org. Chem.* **2009**, 2009, 775.
- [25] R. G. Teller, R. G. Finke, J. P. Collman, H. B. Chin, R. Bau, *J. Am. Chem. Soc.* **1977**, 99, 1104.

RESEARCH ARTICLE

- [26] J. E. M. N. Klein, B. Miehl, M. S. Holzwarth, M. Bauer, M. Milek, M. M. Khusniyarov, G. Knizia, H.-J. Werner, B. Plietker, *Angew. Chem., Int. Ed. Engl.* **2014**, *53*, 1790.
- [27] L. M. Clarkson, W. Clegg, D. C. R. Hockless, N. C. Norman, *Acta Crystallogr. C Cryst. Struct. Commun.* **1992**, *48*, 236.
- [28] A. Schwenk, *Physics Letters A* **1970**, *31*, 513.
- [29] L. Burkhardt, M. Holzwarth, B. Plietker, M. Bauer, *Inorg. Chem.* **2017**, *56*, 13300.
- [30] T.-T. Lu, T.-C. Weng, W.-F. Liaw, *Angew. Chem.* **2014**, *126*, 11746.
- [31] L. Burkhardt, C. Mueller, O. A. Groß, Y. Sun, H. Sitzmann, M. Bauer, *Inorg. Chem.* **2018**.
- [32] S. W. Oung, J. Rudolph, C. R. Jacob, *Int. J. Quantum Chem.* **2018**, *118*, e25458.
- [33] C. A. Bauer, A. Hansen, S. Grimme, *Chemistry (Weinheim an der Bergstrasse, Germany)* **2017**, *23*, 6150.
- [34] J. M. Shreeve, *Inorganic Syntheses*, John Wiley & Sons, Inc, Hoboken, NJ, USA, **1986**.
- [35] Y. Xu, B. Zhou, *J. Org. Chem.* **1987**, *52*, 974.
- [36] F. Neese, *WIREs Comput Mol Sci* **2018**, *8*, e1327.
- [37] a) V. N. Staroverov, G. E. Scuseria, J. Tao, J. P. Perdew, *J. Chem. Phys.* **2003**, *119*, 12129; b) V. N. Staroverov, G. E. Scuseria, J. Tao, J. P. Perdew, *J. Chem. Phys.* **2004**, *121*, 11507.
- [38] a) S. Grimme, S. Ehrlich, L. Goerigk, *Journal of computational chemistry* **2011**, *32*, 1456; b) S. Grimme, J. Antony, S. Ehrlich, H. Krieg, *The Journal of chemical physics* **2010**, *132*, 154104.
- [39] J. Zheng, X. Xu, D. G. Truhlar, *Theor Chem Acc* **2011**, *128*, 295.
- [40] F. Weigend, R. Ahlrichs, *Phys. Chem. Chem. Phys.* **2005**, *7*, 3297.
- [41] a) A. D. Becke, *Phys. Rev. A* **1988**, *38*, 3098; b) J. P. Perdew, *Phys. Rev. B* **1986**, *33*, 8822.
- [42] J. Tao, J. P. Perdew, V. N. Staroverov, G. E. Scuseria, *Physical review letters* **2003**, *91*, 146401.
- [43] a) A. D. Becke, *The Journal of chemical physics* **1993**, *98*, 5648; b) C. Lee, W. Yang, R. G. Parr, *Phys. Rev. B* **1988**, *37*, 785.
- [44] a) S. DeBeer George, T. Petrenko, F. Neese, *Inorganica Chimica Acta* **2008**, *361*, 965; b) S. DeBeer George, T. Petrenko, F. Neese, *The journal of physical chemistry. A* **2008**, *112*, 12936.
- [45] N. J. Vollmers, P. Müller, A. Hoffmann, S. Herres-Pawlis, M. Rohrmüller, W. G. Schmidt, U. Gerstmann, M. Bauer, *Inorg. Chem.* **2016**, *55*, 11694.
- [46] a) P. Zimmer, L. Burkhardt, A. Friedrich, J. Steube, A. Neuba, R. Schepper, P. Müller, U. Flörke, M. Huber, S. Lochbrunner et al., *Inorg. Chem.* **2018**, *57*, 360; b) P. Zimmer, L. Burkhardt, R. Schepper, K. Zheng, D. Gosztola, A. Neuba, U. Flörke, C. Wölper, R. Schoch, W. Gawelda et al., *Eur. J. Inorg. Chem.* **2018**, *2018*, 5203.
- [47] F. Neese, *Inorganica Chimica Acta* **2002**, *337*, 181.
- [48] a) V. Barone, M. Cossi, *The journal of physical chemistry. A* **1998**, *102*, 1995; b) Y. Takano, K. N. Houk, *Journal of chemical theory and computation* **2005**, *1*, 70.
- [49] G. Knizia, *iboview*, <http://www.iboview.org>.
- [50] a) *Reviews in computational chemistry. Vol. 17*, Wiley-VCH, New York, **2001**; b) P. W. Atkins, R. S. Friedman, *Molecular quantum mechanics*, Oxford Univ. Press, Oxford, **2011**.

4.4 The Connection Between NHC Ligand Count and Photophysical Properties in Fe(II) Photosensitizers: An Experimental Study

Zimmer, P.; Burkhardt, L.; Friedrich, A.; Steube, J.; Neuba, A.; Schepper, R.; Müller, P.; Flörke, U.; Huber, M.; Lochbrunner, S; Bauer, M. *Inorg. Chem.* **2018**, *57*, 360-373;

P. Zimmer and L. Burkhardt contributed equally to this publication.

Homoleptic and heteroleptic Fe^{+II} photosensitizers coordinated by tridentate (poly)pyridine-NHC ligands with varying NHC / pyridine ratios are investigated by modern hard X-ray spectroscopy combined with (TD)DFT. The CtC-XES mainline is shifting significant to lower energies with increasing number of σ -donating NHC functions, due to an increasing ligand-iron covalency. A similar effect is observed for the HERFD-XANES pre-peak feature which shows a distinct blue-shift with increasing number NHC functions due to an increasing destabilization of underlying e_g^* levels. Obtained distinctions of ground state valence levels are correlated with excited state characteristics, probed by ultrafast transient absorption spectroscopy

Participation in this Publication

P. Zimmer and L. Burkhardt contributed equally to this publication.

P. Zimmer: Synthesis of investigated compounds, NMR spectroscopy, cyclic voltammetry, UV-Vis spectroscopy, manuscript preparation

L. Burkhardt: HERFD-XANES and VtC-XES; geometry optimizations; simulation of VtC-XES spectra, XANES spectra, redox potentials and molecular levels; manuscript preparation

M. Bauer: corresponding author

A. Friedrich and S. Lochbrunner: transient absorption spectroscopy, manuscript preparation

R. Schepper: EXAFS analysis

P. Müller: preliminary computational studies

J. Steube: synthesis of investigated compounds

The Connection between NHC Ligand Count and Photophysical Properties in Fe(II) Photosensitizers: An Experimental Study

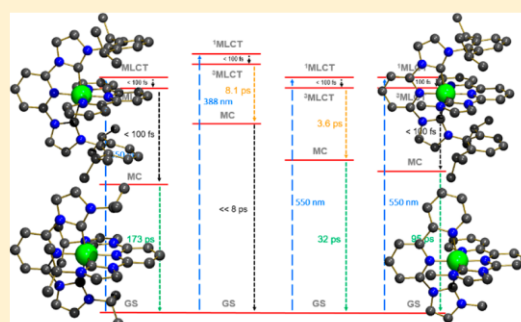
Peter Zimmer,^{†,§} Lukas Burkhardt,^{†,§} Aleksej Friedrich,[‡] Jakob Steube,[†] Adam Neuba,[†] Rahel Schepper,[†] Patrick Müller,^{†,§} Ulrich Flörke,[†] Marina Huber,[†] Stefan Lochbrunner,[‡] and Matthias Bauer^{*,†,§}

[†]Department Chemie, Universität Paderborn, Warburger Straße 100, 33098 Paderborn, Germany

[‡]Institute of Physics, University of Rostock, Albert-Einstein-Str. 23, 18059 Rostock, Germany

S Supporting Information

ABSTRACT: Four homo- and heteroleptic complexes bearing both polypyridyl units and N-heterocyclic carbene (NHC) donor functions are studied as potential noble metal-free photosensitizers. The complexes $[\text{Fe}^{\text{II}}(\text{L1})(\text{terpy})][\text{PF}_6]_2$, $[\text{Fe}^{\text{II}}(\text{L2})_2][\text{PF}_6]_2$, $[\text{Fe}^{\text{II}}(\text{L1})(\text{L3})][\text{PF}_6]_2$, and $[\text{Fe}^{\text{II}}(\text{L3})_2][\text{PF}_6]_2$ (terpy = 2,2':6',2''-terpyridine, L1 = 2,6-bis[3-(2,6-diisopropylphenyl)imidazol-2-ylidene]pyridine, L2 = 2,6-bis[3-isopropylimidazol-2-ylidene]pyridine, L3 = 1-(2,2'-bipyridyl)-3-methylimidazol-2-ylidene) contain tridentate ligands of the C[∧]N[∧]C and N[∧]N[∧]C type, respectively, resulting in a Fe-NHC number between two and four. Thorough ground state characterization by single crystal diffraction, electrochemistry, valence-to-core X-ray emission spectroscopy (VtC-XES), and high energy resolution fluorescence detected X-ray absorption near edge structure (HERFD-XANES) in combination with ab initio calculations show a correlation between the geometric and electronic structure of these new compounds and the number of the NHC donor functions. These results serve as a basis for the investigation of the excited states by ultrafast transient absorption spectroscopy, where the lifetime of the ³MLCT states is found to increase with the NHC donor count. The results demonstrate for the first time the close interplay between the number of NHC functionalities in Fe(II) complexes and their photochemical properties, as revealed in a comparison of the activity as photosensitizers in photocatalytic proton reduction.



INTRODUCTION

Light-driven reactions received considerable attention in the last years, not least because sunlight is an attractive source for green and sustainable energy. A prominent example is homogeneous photocatalytic water or proton reduction, which produces hydrogen as an important synthesis building block and future energy source. For this task, many model systems have been developed during the last decades.^{1,2} They typically include metal complexes based on ruthenium, iridium, or platinum as a photosensitizing component.^{3–10} Replacing these noble metals by inexpensive, earth abundant, and potentially nontoxic metals would make these systems more attractive for the use on a larger scale.^{11,12}

One highly attractive candidate for this purpose is iron, if several specific disadvantages typically related to 3d transition metals can be circumvented. Polypyridyl ligands like bipyridine, which are used in many complexes for photosensitizing applications, suffer typically from kinetic lability.¹³ An even more serious problem are the short lifetimes of the metal-to-ligand charge transfer (MLCT) states. With the catalytically active excited electron located at the complex periphery on the ligand, these excited states are mandatory for photocatalytic applications. An efficient electron transfer to the catalytic center requires therefore a sufficient lifetime of such states.

In the case of 6-fold coordinated polypyridyl based iron(II) photosensitizers, the unfavored short lifetime of the MLCT states is caused by low-lying metal-centered (MC) high spin states. The reduced energy of the MC states is a consequence of the small ligand field splitting of iron in comparison to corresponding ruthenium or iridium complexes.^{14,15} These MC states with their nonradiative decay into the ground state act as spin traps and hinder both MLCT based luminescence and photocatalytic transfer of the electron excited in the MLCT state (Figure 1).¹⁶

Therefore, several strategies were applied in recent years to extend the lifetime of the photochemical relevant MLCT states.¹⁴ Replacing the outer pyridine rings of terpyridine complexes by strong sigma-donating NHC ligands like imidazolylidene^{17,18} or benzimidazolylidene functions¹⁹ in homoleptic complexes destabilizes the e_g^* orbitals, which correspond to the excited MC states. In addition, electron-accepting substituents like carboxyl groups at the pyridine ring of the NHC ligands in homoleptic complexes were found to further prolong the ³MLCT lifetime: NHC σ -donor functions destabilize the MC states, while the electron withdrawing

Received: October 12, 2017

Published: December 13, 2017



ACS Publications

© 2017 American Chemical Society

360

DOI: 10.1021/acs.inorgchem.7b02624
Inorg. Chem. 2018, 57, 360–373

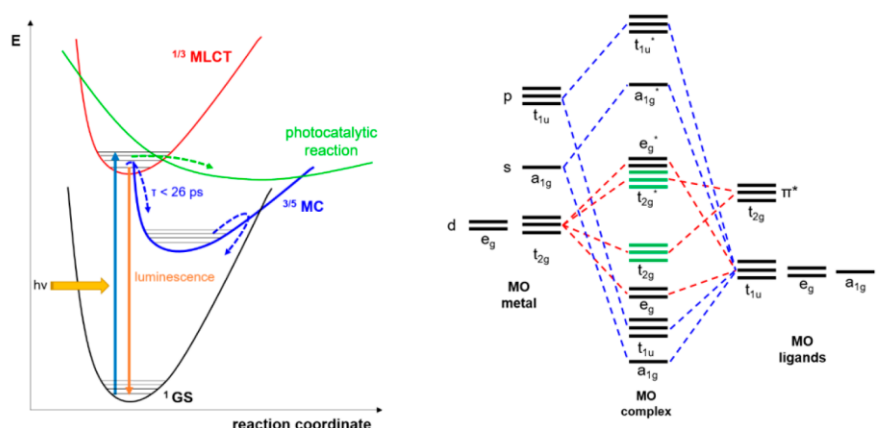
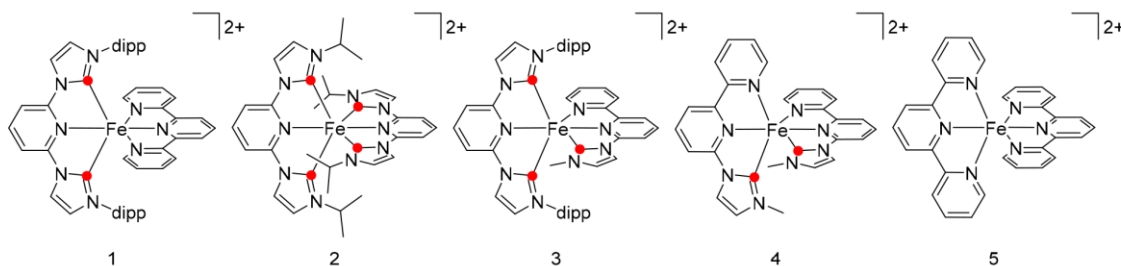


Figure 1. Simplified potential energy curves of a typical iron-based photosensitizer with pathways for excitation, emission, and deactivation, respectively (left), and basic MO scheme for an octahedral coordinated metal center (right).

Scheme 1. Complexes Investigated within This Work (with dipp = Diisopropylphenyl)^a



^aRed dots mark the NHC donor positions.

carboxyl groups stabilize the MLCT states (cf. Figure 1).^{19,20} In this way, ³MLCT lifetimes up to 26 ps are possible up to now.^{14,19} Unfortunately, since the π^* -orbitals of NHC ligands exhibit low π -accepting properties, the energy of the MLCT transition is enlarged.¹⁴ This leads to a hypsochromic shift of the MLCT bands in homoleptic iron(II)–NHC complexes.¹⁷

By combining NHC ligands with polypyridyl moieties in heteroleptic complexes, this disadvantageous blue-shift can be compensated.^{21–23} In a recent study, we compared the activity of homo- and heteroleptic complexes of the type $[\text{Fe}(\text{L1})\text{-terpy}][\text{PF}_6]_2$ (1, terpy = 2,2':6',2''-terpyridine, L1 = 2,6-bis[3-(2,6-diisopropylphenyl)imidazol-2-ylidene]pyridine, 2,6-diisopropylphenyl = dipp) and $[\text{Fe}(\text{L2})][\text{PF}_6]_2$ (2, L2 = 2,6-bis[3-isopropylimidazol-2-ylidene]pyridine), respectively, as photosensitizers in photocatalytic proton reduction.²³ The NHC functionality could be identified as mandatory for photocatalytic activity. However, the results indicate also an influence of the number of NHC donor functions: With the homoleptic complex bearing four carbene donors, a higher activity could be achieved than with two carbene groups in the heteroleptic complex.

Despite the fact that NHC ligands were suggested and investigated as potential ligands leading to increased MLCT lifetimes, no attempts to correlate the photophysical properties—with focus on the MLCT lifetimes—with the number of NHC functionalities exist so far. With respect to the evaluation of the potential of the concept, this step remains mandatory.

We therefore will present a thorough comparison of complexes containing different numbers of NHC groups

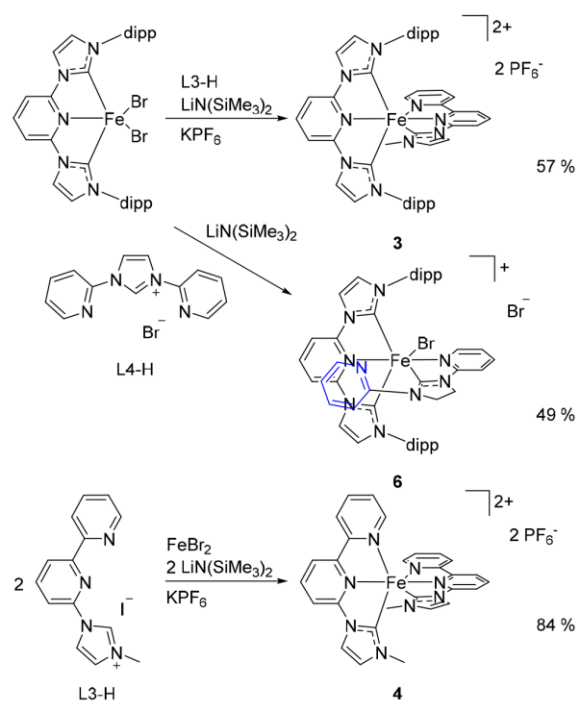
regarding their photophysical properties. For this purpose, the above-mentioned complexes are extended by new compounds, combining polypyridyl and NHC functions in a single ligand L3 (=1-(2,2'-bipyridyl)-3-methylimidazol-2-ylidene) of the N⁺N⁺C type.²⁴ Using this ligand, the two complexes $[\text{Fe}(\text{L1})[\text{L3}]][\text{PF}_6]_2$ (3) and $[\text{Fe}(\text{L3})_2][\text{PF}_6]_2$ (4) are obtained. The well-known bis-terpy complex $[\text{Fe}(\text{terpy})_2][\text{PF}_6]_2$ (5) is used in this study as a reference (Scheme 1). Solid state HERFD-XANES and VtC-XES in combination with DFT and TD-DFT calculations give detailed insights into the electronic ground state. Electrochemistry, UV–vis spectroscopy, and spectroelectrochemistry as a combination of both methods characterize 1–5 in solution. Transient absorption spectroscopy on the complexes finally indicates the beneficial effect of NHC groups on the photophysics of NHC iron complexes.

RESULTS AND DISCUSSION

Synthesis and Ground State Characterization. Synthesis of complexes 1 and 2 is carried out according to our previous work.²³ The heteroleptic complex 3 was also prepared by methods published before (Scheme 2).²³ The homoleptic complex 4 was synthesized by treating FeBr_2 with the free carbene ligand L3, which was obtained after deprotonation of L3-H with $\text{LiN}(\text{SiMe}_3)_2$. In all cases, air and water stable complexes were obtained in fair to very good yields.

Unfortunately, the similar coordination of deprotonated 1,3-bis-2-pyridyl-imidazoliumbromide L4-H ligand to the iron center proceeded in a undesired manner due to the small

Scheme 2. Route of Synthesis for Complexes **3**, **4**, and **6** (with dipp = Diisopropylphenyl)



bite angle in the ligand L4. The second pyridine ring in complex **6** is noncoordinating and therefore disordered over two positions in the crystal structure (see below). Hence, in the following physicochemical discussion, this complex has been neglected.

By diffusion of diethyl ether in a dichloromethane solution, single crystals of **3** and **6** were obtained. In **3**, the outer pyridine and imidazole ring, respectively, of ligand L3 are disordered with a one-to-one-ratio (the molecular structure of **3** pictures only one orientation (Figure 2)). Diffusion of chloroform into an acetone solution of **4** also yielded crystals suitable for X-ray

measurements. Both **3** and **4** cations show a slightly distorted octahedral geometry around the Fe center. A common structural feature of **3** and **6** is the coplanar arrangement of the outer phenyl rings and the central pyridine ring; the relevant dihedral angles for **3** measure $9.1(4)$ and $5.8(4)^\circ$ for (ring-C1)/(ring-N7) and (ring-N7)/(ring-C24). For **6**, the values are $6.2(4)$ and $7.5(4)^\circ$ as well. In **6**, the coordination geometry at the Fe center is also a slightly distorted octahedron but with a terminal bromido ligand. The pyridine ring attached at N8 as well as the Br^- anion are disordered over two positions each with site occupation factors of $0.526(7)$ (N11-ring)/ $0.474(7)$ (N22) for the pyridine and $0.58(1)$ ($\text{Br}21$)/ $0.42(1)$ ($\text{Br}22$) for the anion, respectively.

It is interesting to compare **2** with complexes with methyl and tert-butyl substituents at the imidazolyldiene moieties as they are discussed by Wärnmark et al.,¹⁷ in terms of the iron–carbon bond length (which is expected to correlate with the NHC donor strength) and the C–Fe–C bite angles. It turns out that isopropyl leads to similar bonding properties as in the methyl derivative (Table S1b in the Supporting Information). In contrast, the tert-butyl substituent by Wärnmark exhibits an enlarged geometric demand. This results in a significantly increased bond length. In Table S1b of the Supporting Information, we consider also a heteroleptic complex with four NHC donors bearing both L1 and L2.²⁵ Again, the geometry and the bond length are comparable to **2**. The donor properties of the bis-NHC ligand are therefore similar with dipp (L1) and isopropyl (L2) substituents. In contrast, in complexes with L3, the iron–carbon bond is shortened in comparison to the discussed bis-NHC ligand.

As in the case of **1** and **2**, the structure of **3** and **4** was also proven by analysis of XANES and EXAFS measurements (cf. Figures S12 and S13 in the Supporting Information). The weak prepeaks verify the distorted octahedral geometry, and the edge position is consistent with other iron(II)–NHC complexes.^{23,26} To gain deeper information about the electronic structure of the investigated photosensitizers using hard X-ray methods and to provide the basis for future ultrafast X-ray measurements, core-to-core X-ray emission spectroscopy (CtC-XES, $K\beta_{1,3}$ emission),^{27–31} valence-to-core X-ray emission spectroscopy (VtC-XES, $K\beta_{2,5}$ emission),^{32–36} and high energy resolution

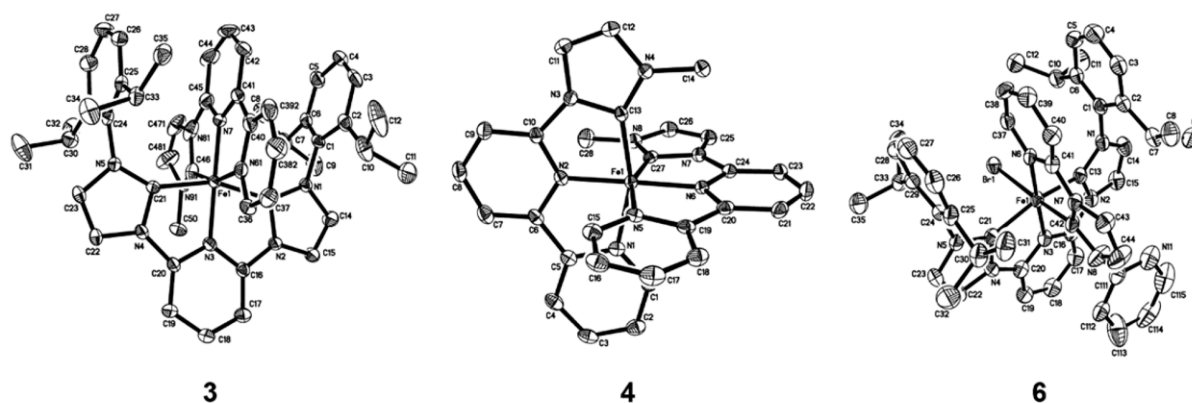


Figure 2. Molecular structures of **3**, **4**, and **6** with anisotropic displacement ellipsoids drawn at the 50% probability level. Hydrogen atoms, anions, and solvent molecules are omitted for clarity. Also, for **3** and **6**, only one position of their disordered moieties is shown. Selected geometric parameters: **3** Fe–N3 1.900(3), Fe–N7 1.886(3), Fe–N61 1.948(4) Å, N3–Fe–N7 178.28(14) $^\circ$; **4** Fe–N1 1.995(2), Fe–N2 1.892(2), Fe–N5 1.990(2), Fe–N6 1.895(2) Å, N2–Fe–N6 178.54(9) $^\circ$; **6** Fe–N3 1.907(3), Fe–N6 1.988(3), Fe–Br 2.5158(7) Å, N3–Fe–N6 177.77(15) $^\circ$.

fluorescence detected XANES (HERFD-XANES)^{37–40} were conducted with the solid compounds 1–4.

Starting with the spin state, which is effectively probed by CtC-XES,²⁸ Figure 3 shows the corresponding spectra.

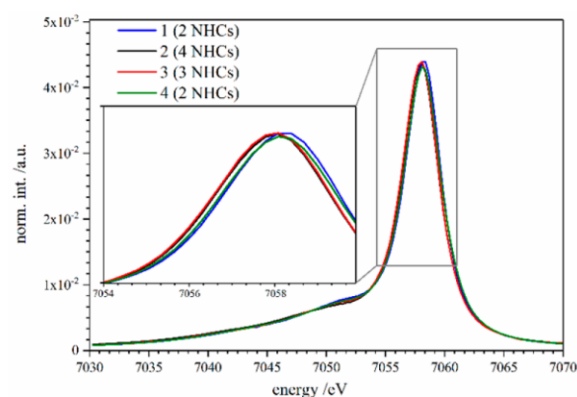


Figure 3. Experimental CtC-XES spectra of complexes 1–4.

Complexes 1–4 are clearly in a low-spin configuration (LS, $S = 0$), since the satellite ($K\beta'$) is not separated from the mainline ($K\beta_{1,3}$) and the intensity ratio between both signals ($K\beta':K\beta_{1,3}$) is small.²⁸ This observation is confirmed by the high resolution of the ^1H NMR features of 1–4, which excludes paramagnetism (see the Supporting Information for details).

Nevertheless, the mainline is redshifting from complexes 1 and 4 to 2 and 3. Since all complexes are in the Fe $3d^6$ LS configuration, this shift is interpreted following the known literature by alterations in metal–ligand covalency.^{27,28,31} Higher covalency leads to a lower energy position of the mainline as the $3d$ spin density is lowered.

According to the strong σ -donating properties of NHC ligands, an increasing number of such functionalities should have the same effect on the CtC-XES spectra. A corresponding

trend is indeed observed in Figure 3. The highest energy is found for 1 at 7058.3 eV, followed by 4 at 7058.2 eV. Both complexes are coordinated by two NHC donors. The redshift by 0.1 eV in 4 is a result of the decreased NHC bond length by 0.06 Å (cf. Table 1), causing a higher degree of metal–ligand covalency. The same effect causes the nearly identical main line energy of 2 (four Fe–carbene bonds) and 3 (three Fe–carbene bonds). In complex 3, one of the three Fe–carbene bonds is shortened by 0.05 Å compared to complex 2 (cf. Table 1).

The LUMO states of the complexes can be directly probed by iron K-edge HERFD-XANES spectroscopy (Figure 4).³⁹ In general, a well-resolved pre-edge feature A at around 7113.5 eV and two near-edge features B (at around 7119 eV) and C (at around 7123 eV) are observed. The lowest energy of pre-edge feature A is detected for 4 and the highest energy for 2. The prepeaks of 1 and 3 are found in between with the same energy. Near-edge feature B gains resolution and shifts to lower energies with increasing quantity of NHC functions. On the contrary, feature C shifts and evolves to lower energies with increasing quantity of pyridyl functions in the order $2 > 3 > 4 \geq 1$.

To understand the quantum mechanical origin of the HERFD-XANES features, TD-DFT XANES calculations using the TPSSH functional with an adjusted Hartree–Fock exchange of 12.5% were performed.⁴¹ With this approach, a very satisfactory agreement between experiment and theory is achieved for all compounds 1–4 (see Figure S14 in the Supporting Information). Especially for the features overlapping with the rising edge, this is very surprising, as such quasi-continuum states are typically not well described by local density approaches.⁴¹ In order to visualize the origin of the experimental observed features, ligand/element projected spectra were generated (see Figure S15 and Tables S4–S7 in the Supporting Information).⁴² In general, selection of localized ligand orbitals is demanding due to the delocalized character of the involved orbitals. Furthermore, due to the varying number of pyridyl and NHC functions, it is difficult to select defined Löwdin population values for all complexes (for details, see

Table 1. Physicochemical Properties of Complexes 1–5

#	HOMO (DFT) ^a (eV)	LUMO (DFT) ^a (eV)	$\Delta E_{\text{HOMO-LUMO}}$ (eV)	$\lambda_{\text{MLCT,abs.}}^b$ [e $\times 10^{-4}$] nm [cm ⁻¹ M ⁻¹]	E_{red} (ligand based) (V)	E_{ox} (Fe ^{II} /Fe ^{III}) (V)	number of NHC donors and their bond length by XRD [DFT] (nm)	$E_{\text{prepeak (XANES)}}$ (eV)	ΔE_{ox} [ΔE_{red}] ^f (eV)
1 ^c	-10.40	-7.43	2.97	379 [0.84] 503 [0.98] 538 [0.86]	-1.89 ^c	0.56 ^c	2 \times 1.995 [1.987]	7113.5	5.16 [-2.59]
2 ^c	-10.30	-7.04	3.26	392 [0.83] 458 [1.45]	-2.31 ^d	0.43 ^c	4 \times 1.952 [1.972]	7113.9	5.02 [-2.08]
3	-10.26	-7.37	2.89	376 [0.55] 409 [0.64] 466 [0.52] 506 [0.50] 538 [0.53]	-1.93 ^c	0.46 ^c	1 \times 1.939 [1.920] 2 \times 1.972 [1.973]	7113.5	5.04 [-2.52]
4	-10.76	-7.91	2.85	419 [0.41] 508 [0.47] 557 [0.70]	-1.74 ^c -2.02 ^c	0.44 ^c	2 \times 1.919 [1.932]	7113.3	5.04 [-2.71]
5 ^c	-11.07	-8.06	3.01	551 [1.14]	-1.64 ^c -1.80 ^c	0.72 ^c			5.31 [-2.86]

^adef2-TZVP with CP(PPP) on Fe, TPSSH (HF-exchange adjusted to 12.5%); for details, see the Supporting Information. ^bMost intensive MLCT absorptions. ^cReversible. ^dIrreversible. ^eSee ref 23 for details. ^fEnergy change by oxidation (ΔE_{ox}) and reduction (ΔE_{red}), respectively (DFT, def2-TZVP, TPSSH, SMD (acetonitrile)).

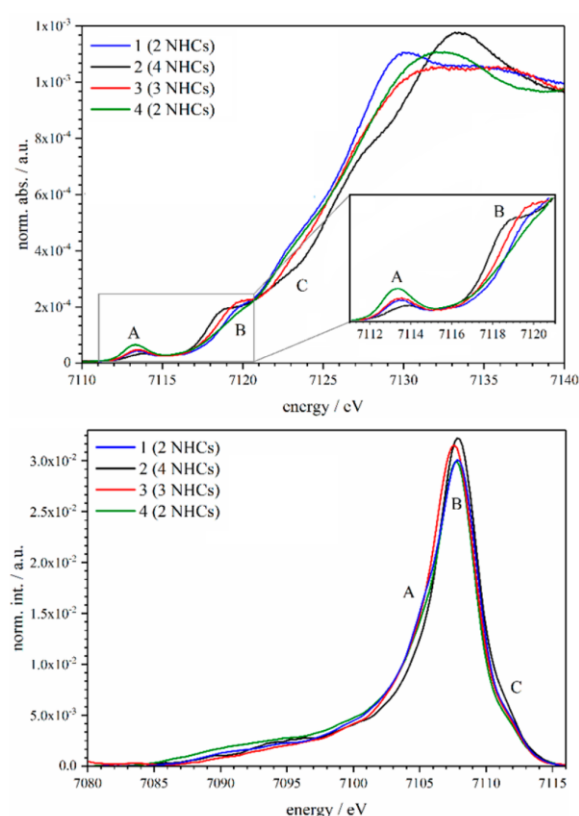


Figure 4. Experimental Fe K-edge HERFD-XANES spectra of complexes 1–4 (top) and experimental VtC-XES spectra of complexes 1–4 (bottom).

the Supporting Information). Nevertheless, the ligand/element projected spectra allow one to visualize the origin of the discussed spectral features.

For all compounds, pre-edge feature A consists mainly of Fe $1s \rightarrow e_g^*$ transitions located at the iron center (see the Supporting Information, Tables S4–S7, Figures S15 and S22). Additionally, transitions of Fe $1s$ to pyridyl/polypyridyl dominated acceptor orbitals contribute to the high energy side of A. Near-edge feature B is caused by a superposition of transitions to acceptor orbitals with NHC and pyridyl/polypyridyl character. Feature C is solely caused by transitions to acceptor orbitals with pyridyl/polypyridyl character. In order to substantiate the experimental XANES spectra (i.e., feature B is evolving with increasing quantity of NHC functions, and feature C is evolving with increasing quantity of pyridyl functions), the spectrum of the bis-terpy complex 5 was also calculated (see Figure S19 in the Supporting Information). The obtained features B and C clearly follow the postulated trends, since 5 exhibits the lowest calculated intensity of B and highest intensity of C.

Complementary to the LUMO states, the HOMO states can be investigated by VtC-XES. The experimental spectra are given in Figure 4 (bottom).³⁹ They are dominated by a main signal, which can be divided into three spectral regions A, B, and C. The maximum energy of main feature B is 7107.9 eV for 1 and 2 and shifts to 7107.7 eV for 4 and further to 7107.5 eV for 3. Feature B increases in intensity with increasing number of

NHC donors in the order $1 \leq 4 < 3 < 2$. The low energy shoulder A at around 7105.3 eV is least pronounced in complex 2 and rises with increasing amount of pyridyl functions in the order $2 < 3 < 4 < 1$. The high-energy feature C at around 7112 eV is typical for transitions from occupied Fe $3d$ states. These transitions are mostly independent of the coordinating ligands, which is in line with the identical intensity in all four complexes.³²

The full DFT VtC-XES spectra were calculated using the TPSSH functional with an adjusted Hartree–Fock exchange of 12.5%.⁴¹ As in the case of HERFD-XANES, theory and experiment agree very well (see Figure S14 in the Supporting Information). In order to account for the ligand selective nature of VtC-XES, element/ligand projected spectra were generated similar to the XANES part (for details, see Figure S15 and Tables S8–S11 in the Supporting Information).

Transitions from pyridyl/polypyridyl σ donor orbitals to Fe $1s$ mainly contribute to the low energy shoulder A, while main feature B originates from a superposition of NHC and pyridyl/polypyridyl σ/π donor orbitals (as an example, representative orbitals of 4 are shown in Figure 5 and representative orbitals of

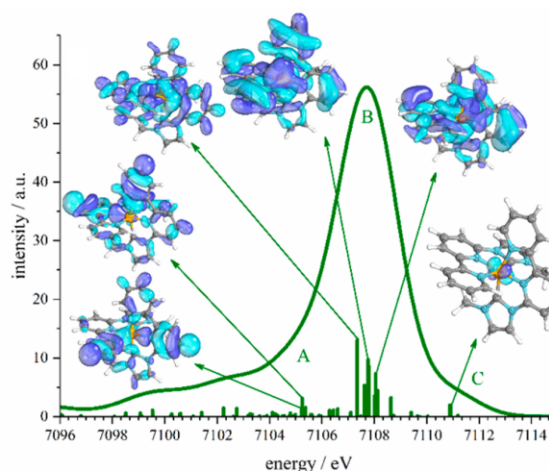


Figure 5. Calculated VtC-XES spectra of complex 4 and predominant molecular orbitals that contribute to the observed features A, B, and C.

1–3 are shown in Figures S16–S18 in the Supporting Information). For all complexes 1–4, the high energy feature C is solely caused by transitions of the iron centered ligand field t_{2g} orbitals (Fe $3d_{xy}$, $3d_{xz}$, and $3d_{yz}$ corresponding to the HOMO, HOMO–1, and HOMO–2 states in Figure S21 in the Supporting Information) to the Fe $1s$. In order to reinforce the findings of the experimental part (i.e., that feature A is evolving with increasing quantity of pyridyl functions and feature B is evolving with increasing quantity of NHC functions), the VtC-XES spectrum of the bis-terpy complex 5 was calculated. The comparison of calculated VtC-XES spectra of 1–5 is shown in Figure S19 in the Supporting Information. The calculated features A and B of complex 5 clearly follow the postulated trends: 5 exhibits the highest calculated intensity of feature A and lowest intensity of feature B.

DFT HOMO and LUMO levels, which were obtained via calculating theoretical X-ray spectra as described above, are depicted in Figure 6. In addition, Figure 6 as well as Table 1

contain in addition physicochemical parameters, relevant for further ground state characterization in the following sections.

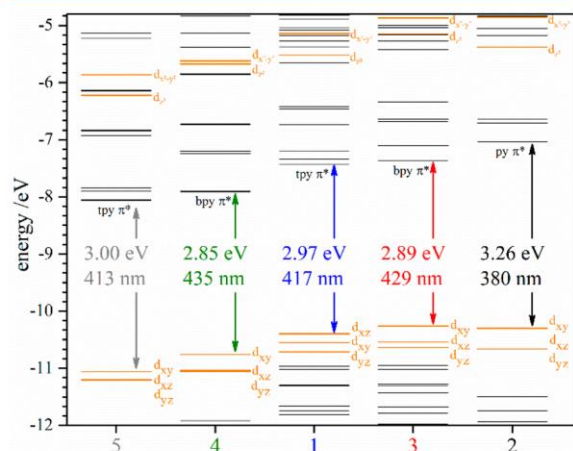


Figure 6. Molecular orbital levels of complexes 1–5 (def2-TZVP with CP(PPP) on Fe, TPSSh (HF-exchange adjusted to 12.5%; for details, see the [Supporting Information](#)). Theoretical HOMO–LUMO gaps are given in between the HOMO and LUMO of each complex. Levels with significant Fe 3d contribution are shown in orange. The predominant characters of LUMOs are given below each LUMO.

These gas phase DFT results based on the X-ray experiments allow several statements: (1) The theoretical LUMOs of complexes 1–5 are π^* type orbitals of the polypyridyl ligands and reflect their π -acceptor abilities, whereas the e_g^* levels (Fe $3d_{z^2}/Fe\ 3d_{x^2-y^2}$) are located at higher energies. Consequently, the LUMO of 2 has the highest energy, since the bis-NHC ligands are known for their poor π -acceptor properties (Figure 6 and Table 1). Both 1 with a terpy function and 3 with a bipyridine (bipy) function in L3, respectively, show nearly the same LUMO energy, which is about 0.4 eV lower in comparison to 2. Here, the enlarged π -system of terpy in comparison to L3 results in a decreased LUMO energy. The homoleptic complex 4 shows a further decrease of the LUMO energy by about 0.5 eV, since the delocalization of the MO involves both ligands (see Figure S22 in the [Supporting Information](#)). Hence, for 5, the lowest LUMO can be expected, which was confirmed by the calculations. (2) Following the VtC-XES results, the HOMO states are metal based and of t_{2g} character, in line with the predictions of the simplified MO model in Figure 1. These levels are both influenced by the π -accepting abilities of the polypyridyl functions and the σ -donor abilities of the NHC ligands. The polypyridyl ligands decrease the energy of the HOMO levels due to more efficient π -backbonding interactions,⁴³ whereas the NHC ligands intuitively increase the HOMO energies by enhancing the electron density on the metal center.^{14,17} Indeed, HOMO energies of 1–5 increase with increasing number of NHC donor functions. Nevertheless, by comparing 1 and 4, which both have two NHC donors, the lower HOMO energy of 4 is likely the result of the better π -accepting capability of two ligands L3 compared to one terpy in 1.

Whereas VtC-XES and HERFD-XANES are excellent tools to investigate the electronic structure in the solid state, the solution electronic structure of the complexes was proven by electrochemical measurements. The redox potentials are

expected to represent the energies of the HOMO and LUMO levels, respectively, since the ionization potential is related to the HOMO energy corresponding to the Koopmans theorem, whereas the LUMO energy is a measure for the electron affinity.⁴⁴ The electrochemical measurements for 1–5 dissolved in acetonitrile show two separated transitions (Figure 7). At positive potentials, one-electron iron based oxidations

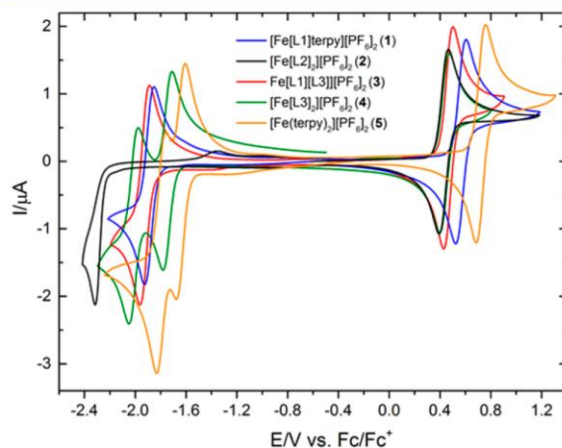


Figure 7. Cyclic voltammograms of complexes 1–5 in acetonitrile (scan rate: 100 mV/s).

were found (Fe(II) \rightarrow Fe(III)). Their fully reversible behavior was proved by diagnostic criteria proposed by Nicholson^{45,46} and the Randles–Sevcik equation.^{47,48} (for details, see Tables S13–S17 in the [Supporting Information](#)). Chronoamperometric investigations being fully reversible for this redox couple confirms this assumption.

At negative potentials, ligand based reductions occur. In the case of 4, it is assigned to L3, since two sets of waves were detected with one reversible transition for each ligand.⁴⁹ Consequently, in the case of 1, only one wave was recorded and two waves for complex 5, which can be attributed to the terpyridine majorities. Since 3 only bears one bipy function with ligand L3, a single one-electron transition with reversible behavior was detected. The tetra-NHC complex 2 instead shows no reversible transition. Due to the poor π -accepting properties of the NHC ligands, one irreversible transition at -2.3 V was found, which is in line with previous publications.¹⁷ The potentials of these reductions correlate with the energy of the LUMO levels, which are responsible for accepting an electron during reduction. For 4, the LUMO energy is much lower in comparison to 1 and 3 having nearly the same energy. In contrast, the LUMO level of 2 is much higher and the absence of a delocalized polypyridyl majority results in an irreversible reduction well separated from the other waves (Figure 7).

Comparison of the gas phase HOMO energy obtained by DFT calculations and applied in the X-ray spectra interpretation shows a particular discrepancy with the oxidation waves found in cyclic voltammetry measurements (cf. also Figure 6), as for example demonstrated by comparison of complexes 4 and 2: Both complexes show an identical oxidation potential of 0.47 V, but the gas phase DFT HOMO level of 4 is about 0.46 eV lower than that of 2. Actually, 4 should have a more positive redox potential compared to 2, as it was found for analogous

ruthenium complexes.²⁴ This issue is attributed to the solvation of the complexes, and can thus be compensated by inclusion of solvent effects into the calculations. The SMD solvation model was applied here,⁵⁰ which leads to shifted and less differentiated energy levels, while the relative HOMO–LUMO gaps stay almost unchanged (for details, see Figure S20 in the Supporting Information).

On the basis of DFT calculations with the SMD solvation model, the oxidation and reduction transition states were simulated by subtracting the energy of each low-spin Fe(II) complex from the corresponding energy of the oxidized low-spin Fe(III) ($S = 2$) and reduced Fe(I) ($S = 2$) complex, respectively, while the solvated ground state geometry was retained (ΔE_{ox} and ΔE_{red} , cf. Table 1). In this approach, the experimental redox potentials can be correlated with these calculated energy differences. Both ΔE_{ox} (black) and ΔE_{red} (orange) are plotted in Figure 8. The corresponding redox

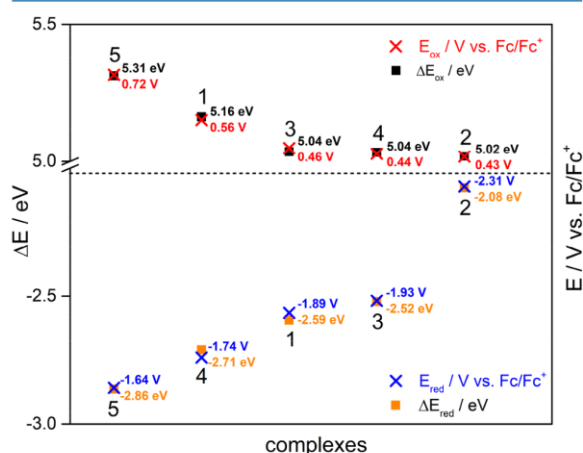


Figure 8. Energy changes by one-electron oxidation (top) and reduction (bottom) of complexes 1–5 (DFT, def2-TZVP, TPSSH, SMD (acetonitrile), retained ground state geometry of Fe(II)). The potentials obtained from electrochemistry are also shown (crosses). For each pair of values, the corresponding complex is indicated.

potentials by cyclic voltammetry are added for comparison (red and blue). These calculations indeed represent the experimental redox potentials very well (cf. Figure 8). Especially both 2 and 4 (top right) show the lowest energy change during oxidation, whereas 5 exhibits the highest ionization energy (cf. top left). In the same way, ΔE_{red} corresponds to the energetic order of the first reduction waves. Here, 2 shows the lowest energy gain due to reduction (bottom right) and 5 obviously has the highest electron affinity (bottom left).

Ground and Excited State Optical Spectroscopy. The optical ground state spectra of complexes 1–5 in acetonitrile represent the basis for the excited state characterization and photosensitizing properties. They are displayed in Figure 9.

All spectra show broad absorption bands from about 350 to 700 nm, which typically can be assigned to MLCT transitions. At smaller wavelengths below 350 nm, $\pi \rightarrow \pi^*$ transitions occur.^{17,21,23} As a first approximation, the bathochromic shift of the lowest energy MLCT transitions in the order $5 \approx 4 > 1 \approx 3 > 2$ is a result of the decreasing energy of the LUMO levels.⁴⁹ As expected, for all complexes with polypyridyl functions, an enlarged integral absorption was found in the visible spectral

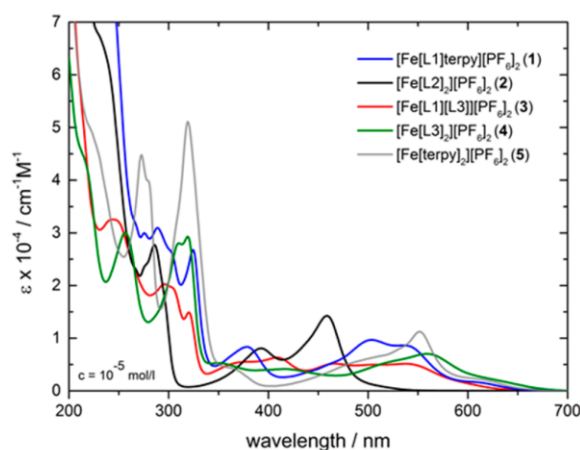


Figure 9. UV-vis spectra of complexes 1–5 measured in acetonitrile.

range in comparison to 2. This trend was also observed by Chung et al., who investigated a series of ruthenium complexes.²⁴ It is remarkable that 3 and 4 with the NHC ligand L3 also exhibit extended absorption bands from 400 to 650 nm. Their MLCT bands show a similar redshift as both terpy complexes 1 and 5 and are advantageous for the absorption of sun light.

In preparation for transient absorption measurements, spectroelectrochemical measurements of complexes 1–4 were performed for both the oxidation and reduction transitions. Detailed results of these experiments are shown in the Supporting Information. In all cases, several isosbestic points were involved in the spectral changes. In the case of complex 2, only the oxidation was accessible due to the absence of a reversible reduction wave (cf. Figure 7). In Figure 10, the resulting differential spectra are shown, which were obtained by subtracting the initial UV-vis spectrum from the corresponding spectrum at the reductive or oxidative end of the electrolysis. At the isosbestic points, the differential curves intersect the y-axis at zero. In accordance with the CV measurements, all oxidations were fully reversible after bulk electrolysis. In contrast, the reduced species of 1 and 3 with the bis-NHC ligand L1 were found to be unstable on a longer time scale. Here the formation of a consecutive product is likely, whereas reoxidation of double reduced 4 was possible with only slight amounts of byproducts (see the Supporting Information for details). Nevertheless, the isosbestic behavior during reduction of 1, 3, and 4 was taken as an indicator for the initial absence of side product formation.^{51,52} In all cases, both reduction and oxidation of the neutral complexes weakens the MLCT intensity due to a partial or respectively complete degradation of the appropriate chromophore.⁵² Instead, at wavelengths larger than around 580 nm, in both cases, new absorption bands appear. These are expected to have ligand-to-metal charge transfer (LMCT) character in the oxidized complex and ligand based $\pi^* \rightarrow \pi^*$ character in the reduced complex.^{51–53}

Excited state characterization typically starts with luminescence spectroscopy. Unfortunately, no MLCT emission is observed for complexes 1–5, which is in line with low-lying MC states acting as spin-traps providing an efficient non-radiative decay route (Figure 1). Therefore, the lifetime of the photophysical relevant MLCT states as the most prominent

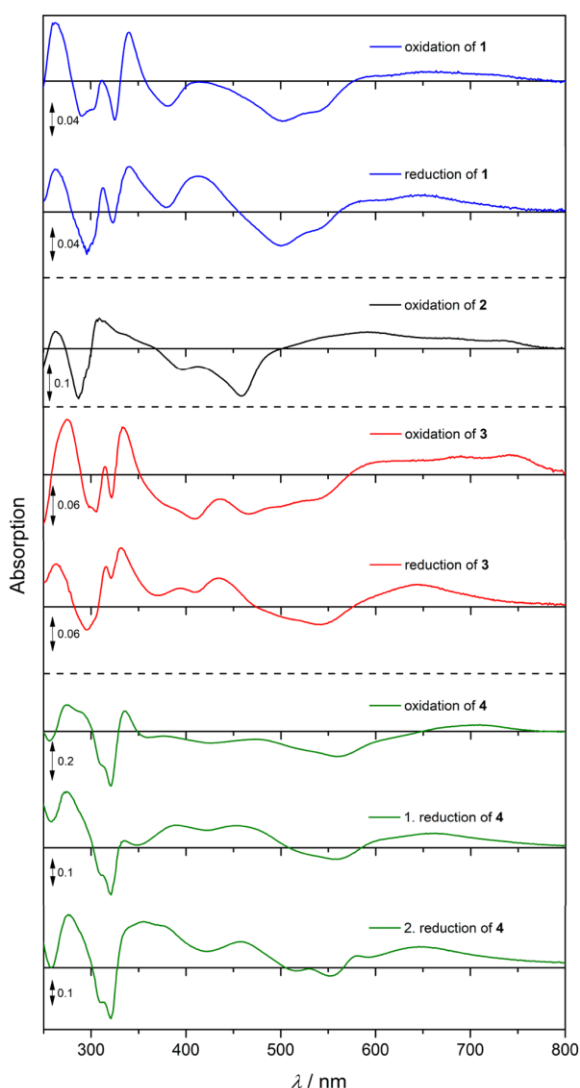


Figure 10. Spectroelectrochemical investigations of 1–4 measured in acetonitrile. Differential UV–vis spectra are shown (blue, 1; black, 2; red, 3; green, 4).

parameter of photosensitizing organometallic complexes could not be measured by time correlated single photon counting (TCSPC). Consequently, the photoinduced dynamics of the complexes $[\text{Fe}(\text{L1})\text{terpy}][\text{BPh}_4]_2$ (**1'**) and $[\text{Fe}(\text{L2})_2][\text{BPh}_4]_2$ (**2'**)³⁴ as well as of **3** and **4** are accessed by ultrafast pump–probe spectroscopy. The following discussion of the transient absorption spectra is ordered with respect to the number of NHC functionalities. Complexes **1** and **4** containing two NHC groups will be first considered, followed by complex **3** with three Fe–NHC groups and finally complex **2** with four carbene donors.

Starting with complex **4**, Figure 11 shows the evolution of the absorption change ΔA in acetonitrile after optical excitation at 550 nm.

The transient spectra are dominated by a negative band with a spectral shape similar to the original absorption of the complex (cf. Figure 9), indicating that bleach of the ground

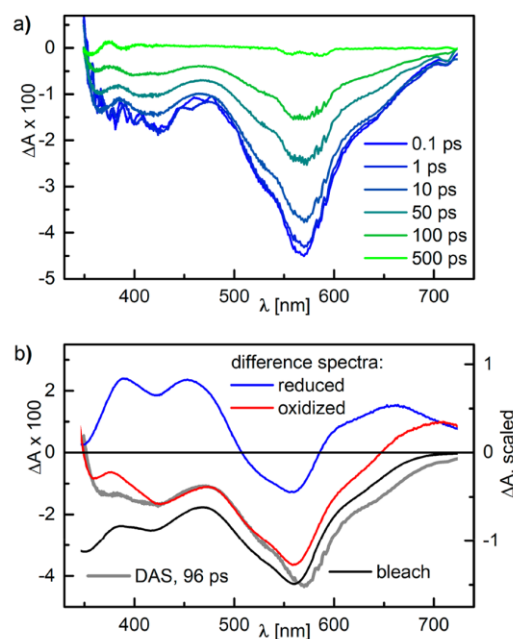


Figure 11. (a) Transient absorption spectra of **4** in acetonitrile at the specified delay times after optical excitation at 550 nm. (b) Decay associated amplitude spectrum (DAS, gray line, left scale) of the exponential decay with a time constant of 96 ps. The DAS is compared to the inverted ground state absorption reflecting the excitation induced bleach (black line) and to the difference spectra between the reduced respectively oxidized form and the original ground state. Bleach and difference spectra are scaled for optimal comparison.

state is responsible for most of the signal. The observed dynamics can be well fitted by a monoexponential decay with a time constant of 96 ps for the return to the electronic ground state. The decay associated spectrum (DAS) which is shown in the lower graph of Figure 11 corresponds to the difference between the spectra of the excited and ground state species. It is compared to the pure bleach and the difference spectra of the reduced and oxidized form with respect to the original form, as they are obtained from the spectroelectrochemical measurements (cf. Figure 10).

While the difference spectrum of the reduced species disagrees strongly with the DAS, the oxidized form seems to resemble the DAS at least in the green and blue spectral regions. However, it exhibits an absorption component in the red region, which is missing in the DAS. The similarities between the DAS and the difference spectrum of the oxidized form reflect the fact that in both cases an electron is removed from the metal based HOMO. Optical excitation of the Fe complexes should populate a MLCT state, since the LUMO is located at the ligands according to the ab initio calculations and X-ray measurements presented above. Transient absorption studies on other iron complexes found that population of MLCT states but also of MC states results in an absorption band in the spectral region around 350 nm.^{19,22} This fits to the absorption increase appearing at wavelengths below 380 nm (see Figure 11). MLCT states, however, exhibit typically also an excited state absorption (ESA) on the red side of the ground state bleach, which is missing here. This points to the population of a MC state and to the following relaxation scenario: After optical excitation of the singlet ¹MLCT state,

very fast intersystem crossing (ISC) to the $^3\text{MLCT}$ state and internal conversion to the MC high spin state occur within the time resolution of our pump–probe measurements. Then, the MC state relaxes back to the ground state with a lifetime of 96 ps. This kind of scenario was already reported for similar Fe complexes.^{14,17}

We observed this behavior also for the heteroleptic $[\text{Fe}(\text{C}^{\wedge}\text{N}^{\wedge}\text{C})(\text{N}^{\wedge}\text{N}^{\wedge}\text{N})]^{2+}$ complex **1'** containing two NHC groups as well. However, the MC state lifetime of 173 ps is nearly twice the value found in **4** (see Figure S39 in the Supporting Information). For the homoleptic complex **5** containing no NHC groups, Liu et al. found, again by transient absorption measurements, that the MC state is populated within 145 fs after optical excitation and exhibits a lifetime of 4 ns.¹⁷ In another work, a MC lifetime of even 5.3 ns was reported.⁴³ This is in line with the expectation that a destabilization of the MC state by NHC groups shortens its lifetime.

The transient absorption spectra of complex **3** containing three Fe-carbene groups are shown in Figure 12. They reveal

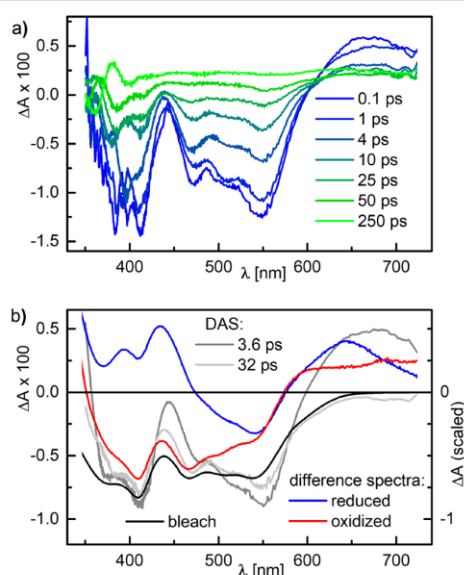


Figure 12. (a) Transient absorption spectra of **3** in acetonitrile at the specified delay times after optical excitation at 550 nm. (b) Decay associated amplitude spectra (DAS) of the two exponential components with decay times of 3.6 and 32 ps, respectively (left scale), in comparison to the bleach and the difference spectra between the reduced respectively oxidized form and the original ground state form (right scale). Bleach and difference spectra are scaled for optimal comparison.

photoinduced dynamics different from **1'** and **4**. The transient absorption is again dominated by the ground state bleach and its recovery. However, the recovery is substantially faster and an additional ESA component is observed at wavelengths above 620 nm, i.e., at the red side of the bleach. The ESA band has some similarities with the difference spectrum of the reduced form in this spectral region. This might indicate that the ESA band is related to an excess electron on the ligand and the involvement of charge transfer states. The absorption increase below 380 nm points again to population of MLCT and MC states.^{17,19} The dynamics can be fitted with a biexponential

decay, with the time constants being 3.6 and 32 ps. The DAS of the 32 ps decay resembles the inverse of the original absorption spectrum and reflects the return to the electronic ground state. The 3.6 ps component is similar to the bleach in the blue and green spectral regions with some extra absorption below 380 nm but contains the ESA band in the red. This points to charge transfer contributions, and such features have been already assigned to MLCT states in other Fe complexes.¹⁴ The 3.6 ps component therefore reflects the depopulation of the $^3\text{MLCT}$ state to the $^3/5\text{MC}$ state which relaxes subsequently back to the electronic ground state within 32 ps. The ISC from the optically populated $^1\text{MLCT}$ to the $^3\text{MLCT}$ state is again faster than our time resolution. The lifetime of 3.6 ps for the $^3\text{MLCT}$ state of **3** indicates that the coupling to the MC state is less efficient than in **1'** and **4**.

The relaxation dynamics of **3** discussed above is to some degree special, since for **3** the two sequential steps leading from the $^3\text{MLCT}$ to the MC state and from the latter to the ground state have both been observed. Thus, it provides strong evidence for the proposed sequential pathways.

The transient spectra of the tetra-carbene complex **2'** show also an ESA at the red side of the ground state bleach (see Figure S40 in the Supporting Information). The absorption change decays monoexponentially with a time constant of 8.1 ps, and the DAS represents a superposition of the ground state bleach and the ESA band. Because of the ESA feature, we attribute the observed dynamics to the depopulation of the $^3\text{MLCT}$ state, which has accordingly a lifetime of 8.1 ps. The $^3\text{MLCT}$ state relaxes most probably to the MC state. Since no features related to the MC state appear in the transient spectra, we assume that its lifetime is shorter than 8.1 ps. In this case, the population in the MC state is negligible and the observed dynamics seem to lead directly back to the electronic ground state. Such relaxation scenarios were already proposed for other Fe complexes with NHC ligands, which exhibit lifetimes between some and a few tens of picoseconds.^{19,20,22}

The results of these investigations are summarized in Figure 13. A clear correlation between the lifetime of the MLCT state and the number of the NHC donor functions was found: **2'** with four NHC donors exhibits a lifetime about twice as long compared to **3** with only three NHC donors. Furthermore, the lifetime of the MC state decreases with prolonged MLCT lifetime. This behavior is also known for other Fe complexes.¹⁷ Regardless of the unresolved MLCT relaxation in **1'** and **4** (both with two NHC donors), a shorter MLCT lifetime for **1'** in comparison to **4** can therefore be expected. This is in line with the faster MC relaxation for **4** due to the shorter bond length of the Fe-carbene bond (cf. Table 1) and the resulting increased ligand field splitting.

The discussed results also explain the catalytic experiments for complexes **1** and **2**, which have previously been reported.²³ Both complexes were found to be active photosensitizers in the photocatalytic water splitting with Pt nanoparticles as catalyst. The higher activity of **2** is caused by the longer MLCT lifetime, whereas the improved integral absorption of **1** seems to play a minor role. For further development, photoactive complexes should therefore combine these two factors, as was shown with complex **3** within this work.

CONCLUSIONS

The four homo- and heteroleptic complexes **1–4** (cf. Scheme 1) of Fe(II) containing both a polypyridyl unit and a NHC

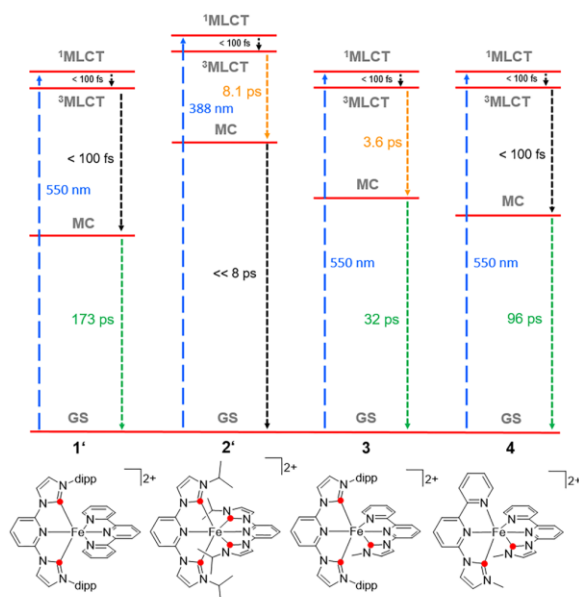


Figure 13. Photoinduced dynamics of **1'**, **2'**, **3**, and **4** (GS = ground state, blue: excitation wavelength).

donor function and with a total NHC number between two and four were investigated with respect to their structural, electronic, and excited state properties, as they could act as potential photosensitizers substituting noble metals.

Ground state characterization revealed an increased degree of iron–ligand covalency with a higher number of NHC functionalities by CtC-XES. The LUMO states were identified as mainly ligand π^* -pyridyl/polypyridyl states via HERFD-XANES spectroscopy in combination with TD-DFT calculations, while the HOMO states as probed by VtC-XES and DFT are built up by the metal $3d_{xy}$, $3d_{xz}$, and $3d_{yz}$ states.

Following the approach of destabilizing MC, i.e., ligand field states by NHC donor ligands, a rising energy of the HOMO level energy was observed with an increasing number of Fe–carbene bonds. Unfortunately, the LUMO states follow this trend as well due to the reduced number of polypyridyl groups in the complexes with higher NHC count. Nonetheless, a redshift of the MLCT bands similar to complexes with polypyridyl ligands like terpy could be achieved in complexes **3** and **4**, which is important for sunlight harvesting applications.

In addition, electrochemical properties and electronic structure in solution have been proven by cyclic voltammetry and spectroelectrochemistry. Both methods were necessary to understand the investigations of the excited state properties by transient absorption spectroscopy. A clear correlation of the $^3\text{MLCT}$ lifetime with the number of NHC ligands was found. While with two NHC donors the $^3\text{MLCT}$ lifetime was below 100 fs (complexes **1** and **4**), it could be increased to 3.6 ps with three NHC functionalities (complex **3**). For the tetra-carbene complex **2**, the maximum $^3\text{MLCT}$ lifetime of 8.1 ps was observed, which is in agreement with the values for a similar complex published recently.¹⁷

Summarizing, with the present study, the concept of using NHC donors to avoid low-lying MLCT states in iron complexes was put on a systematic basis by investigating a row of NHC-polypyridyl-Fe(II) complexes with a variable

count of NHC donors. A clear increase of the $^3\text{MLCT}$ lifetime with the number of NHC donors was found. Further trends of the physicochemical parameters could also be linked to the NHC number, and especially a thorough X-ray spectroscopic analysis could be provided that will serve as a basis for ultrafast X-ray measurements.⁵⁵

Future work has to focus on concepts to increase the number of carbene functions on the one hand. On the other, factors like octahedral symmetry optimization were not treated here, which are known to have a large impact.⁵⁶ Combining both aspects could potentially enable much higher $^3\text{MLCT}$ lifetimes.

EXPERIMENTAL SECTION

Synthesis. Reactions were carried out under an argon atmosphere using standard Schlenk techniques. Solvents were dried over molecular sieves in a MBraun Solvent Purification System or distilled over sodium with benzophenone as an indicator in the case of THF, respectively. Solvents were degassed prior to use by standard procedures. All chemicals were purchased from Sigma-Aldrich, TCI, or ACROS and used without further purification. NMR spectra were recorded using either a Bruker Avance 500 or Avance 300 device. IR spectra were recorded using a Bruker Vertex 70 with ATR equipment. Mass spectra (ESI) were recorded with a Waters Synapt G2 quadrupole – time-of-flight spectrometer. The solvent used is denoted for every substance.

The five-coordinated Fe(II) precursor $[\text{Fe}(\text{L1})\text{Br}_2]$ with **L1** = 2,6-bis[3-(2,6-diisopropylphenyl)-imidazol-2-ylidene]pyridine was synthesized according to literature procedures.^{23,57} **L1-H** was synthesized by a procedure described elsewhere,⁵⁸ the synthesis of 1-(2,2'-bipyridyl)-3-methyl-imidazolium iodide **L3-H**²⁴ and **L4-H**³⁹ has been reported previously. Generation of free carbene ligands was performed by a literature method.⁶⁰

Synthesis of 3. **L3-H** (0.5 mmol, 182 mg) was suspended in THF (10 mL) at -37°C . To this slightly yellow suspension, a solution of lithium bis(trimethylsilyl)amide (1 mol/L in THF, 0.5 mmol, 0.5 mL) was added dropwise. The suspension immediately cleared up while intensifying the yellow color. After 30 min, the cooling bath was removed. After another hour of stirring, the intensely red solution was added to a solution of $[\text{Fe}(\text{L1})\text{Br}_2]$ (0.5 mmol in THF, 20 mL). After 24 h, the solvent was removed in vacuo. The dark red residue was dissolved in water (50 mL). After filtration, potassium hexafluorophosphate (4 equiv, 370 mg, 2.01 mmol) dissolved in a small amount of water was added to precipitate a purple powder. The precipitate was filtered off and washed with water. The solid was dissolved in DCM. After infusion of diethyl ether into this solution, purple crystals of **3** (316.7 mg, 0.284 mmol, 57%) were obtained. ^1H NMR (500 MHz, methylene chloride- d_2) δ = 8.51 (t, J = 8.2, 1H), 8.24 (d, J = 2.2, 2H), 8.09 (t, J = 8.7, 3H), 7.95 (td, J = 7.7, 1.5, 1H), 7.76 (d, J = 2.2, 1H), 7.49–7.45 (m, 2H), 7.41 (dd, J = 8.0, 0.9, 1H), 7.38 (ddd, J = 7.1, 5.5, 1.3, 1H), 7.12 (t, J = 7.8, 2H), 7.05 (dd, J = 8.0, 0.9, 1H), 6.98 (dd, J = 6.9, 2.2, 3H), 6.87 (dd, J = 7.9, 1.4, 2H), 6.77 (dd, J = 7.9, 1.4, 2H), 2.79 (s, 3H), 1.24 (dt, J = 13.3, 7.1, 2H), 0.94 (d, J = 6.7, 6H), 0.80 (p, J = 6.6, 2H), 0.75 (d, J = 6.7, 6H), 0.60 (dd, J = 6.6, 2.1, 12H). ^{13}C NMR (126 MHz, methylene chloride- d_2) δ (ppm) = 198.66, 197.46, 156.81, 155.22, 155.08, 153.68, 151.32, 145.23, 145.13, 141.68, 137.46, 137.02, 133.70, 131.25, 131.16, 127.80, 126.60, 125.18, 124.25, 124.09, 119.38, 117.18, 116.99, 108.63, 107.92, 66.22, 35.86, 28.49, 27.95, 27.04, 26.84, 24.16, 23.50, 15.66. HRMS (ESI) m/z 411.6906 0.5 [$\text{M} - 2\text{PF}_6$] $^{2+}$ (calcd for $\text{C}_{49}\text{H}_{53}\text{FeN}_9$ 823.3813).

Synthesis of 4. **L3-H** (0.91 mmol, 348 mg) was suspended in THF (15 mL) at -18°C . Then, a lithium bis(trimethylsilyl)amide solution (1 mol/L in THF, 0.91 mmol, 0.91 mL) was added dropwise. The mixture was stirred for 45 min until the cooling bath was removed. Afterward, the mixture was stirred for another hour. The green/brownish solution was then filtered and added to a suspension of iron(II) bromide (0.445 mmol, 96 mg) in THF (30 mL). Upon addition, the color changed to purple. The reaction mixture was stirred for 17 h before removing the solvent under reduced pressure. The

purple residue was dissolved in water (20 mL) and filtered off. Potassium hexafluorophosphate (4 equiv, 1.78 mmol, 327 mg) was dissolved in a small amount of water and added to the purple solution. A purple solid precipitated, which was filtered off and was washed with water. The precipitate was recrystallized from acetone/chloroform to give purple crystals of **4** (305 mg, 0.373 mmol, 84%). ^1H NMR (500 MHz, acetone- d_6) δ (ppm) = 8.79 (dd, J = 8.0, 0.8, 2H), 8.74–8.72 (m, 2H), 8.58 (t, J = 8.1, 2H), 8.49–8.47 (m, 4H), 8.07 (ddd, J = 8.1, 7.6, 1.5, 2H), 7.47 (ddd, J = 5.5, 1.4, 0.8, 2H), 7.33 (ddd, J = 7.5, 5.6, 1.3, 2H), 7.24 (d, J = 2.2, 2H), 2.81 (s, 6H). ^{13}C NMR (126 MHz, acetone- d_6) δ (ppm) = 196.23, 159.44, 156.58, 156.39, 151.65, 139.54, 139.01, 128.26, 128.06, 124.68, 119.90, 118.93, 111.74, 79.21, 35.40. HRMS (ESI) m/z 264.0740 0.5 $[\text{M} - 2\text{PF}_6]^{2+}$ (calcd for $\text{C}_{28}\text{H}_{24}\text{FeN}_8$ 528.1473).

Synthesis of 6. The synthesis of **6** was carried out similar to the synthesis of **3**. The raw product was dissolved in dichloromethane and was crystallized by diffusion diethyl ether into the deep red solution. Red crystals were obtained (yield: 49%). ^1H NMR (500 MHz, acetone- d_6) δ (ppm) = 8.86 (ddd, J = 5.8, 1.6, 0.7 Hz, 1H), 8.55 (d, J = 2.2 Hz, 2H), 8.37 (d, J = 2.3 Hz, 1H), 8.27 (ddd, J = 4.9, 1.9, 0.8 Hz, 1H), 7.84–7.74 (m, 2H), 7.58 (d, J = 8.1 Hz, 2H), 7.50 (d, J = 2.1 Hz, 2H), 7.42 (dt, J = 8.2, 1.0 Hz, 1H), 7.36 (ddd, J = 7.6, 4.9, 1.0 Hz, 1H), 7.32 (d, J = 2.3 Hz, 1H), 7.26 (ddd, J = 8.2, 7.4, 1.6 Hz, 1H), 7.06 (t, J = 7.8 Hz, 2H), 6.99 (dd, J = 7.9, 1.5 Hz, 2H), 6.78 (dd, J = 7.7, 1.5 Hz, 2H), 6.74 (dt, J = 7.8, 0.9 Hz, 1H), 6.30 (ddd, J = 7.3, 5.8, 1.3 Hz, 1H), 3.46 (h, 2H), 1.91 (h, 2H), 1.23 (d, J = 6.6 Hz, 6H), 0.98 (d, J = 6.7 Hz, 6H), 0.92 (dd, J = 7.6, 6.8 Hz, 12H). HRMS (ESI) m/z 404.6818 0.5 $[\text{M} - 2\text{Br}]^{2+}$, 888.2813 $[\text{M} - \text{Br}]^+$ (calcd for $\text{C}_{48}\text{H}_{51}\text{FeN}_9\text{Br}$ 888.2800).

X-ray Crystallography. Pertinent crystallographic data for **3**, **4**, and **6** are summarized in Table S1a in the Supporting Information. All structures suffer from severe disorder of some or all solvent molecules; accordingly, these were treated with SQUEEZE.⁶¹ All data were collected on a Bruker AXS SMART APEX CCD diffractometer, graphite monochromator, $\lambda(\text{MoK}\alpha) = 0.71073 \text{ \AA}$, $T = 130(2) \text{ K}$. Data collection $1.5^\circ < \theta < 27.9^\circ$, data reduction, and absorption correction were performed with SAINT and SADABS.⁶² Full-matrix least-squares refinement⁶³ was based on F^2 . All non-hydrogen atoms were refined anisotropically. All H atom positions were clearly derived from difference Fourier maps and then refined on idealized positions with $U_{\text{iso}} = 1.2U_{\text{eq}}(\text{C})$ or $1.5U_{\text{eq}}(\text{C}_{\text{methyl}})$ and C–H 0.95–1.00 \AA .

3. ($\text{C}_{49}\text{H}_{53}\text{FeN}_9$)(PF_6)₂, x Solv. 53557 reflections collected, 13594 independent, $R_{\text{int}} = 0.082$, 696 parameters, refinement converged at R_1 ($I > 2\sigma(I)$) = 0.080; $wR_2(\text{all data}) = 0.221$, $\text{Goof} = 1.07$, min/max. ΔF $-0.51/0.84 \text{ e/\AA}^3$. The pyridine and imidazole moieties with N81 and N61 are disordered over two sites with occupation factors of 0.5. There are 8 very severely disordered Et_2O and/or CH_2Cl_2 solvent molecules per sum formula that the type of solvent could not be determined unequivocally and thus no refinement with a reasonable model was possible. Accordingly, these structure parts were treated with SQUEEZE.⁶¹

4. ($\text{C}_{28}\text{H}_{24}\text{FeN}_8$)(PF_6)₂, acetone. 35923 reflections collected, 9023 independent, $R_{\text{int}} = 0.059$. The acetone solvent was severely disordered and treated with SQUEEZE. 500 parameters, refinement converged at R_1 ($I > 2\sigma(I)$) = 0.054; $wR_2(\text{all data}) = 0.136$, $\text{Goof} = 1.043$, min/max. ΔF $-0.52/0.67 \text{ e/\AA}^3$.

6. ($\text{C}_{48}\text{H}_{51}\text{BrFeN}_9$)(Br), 2.57 H_2O , 1.5 CH_2Cl_2 . 98413 reflections collected, 12803 independent, $R_{\text{int}} = 0.117$. The CH_2Cl_2 solvent molecules were severely disordered and treated with SQUEEZE. The pyridine ring at N(8) is disordered over two sites with occupation factors of 0.525(6) (C111 ring) and 0.475(6) (C121 ring), respectively. The bromide anion is disordered over two positions Br21 and Br22 with occupation 0.58(1) and 0.42(1). Water O1 and O2 positions have occupation of 0.24(1) and 0.325(9). 634 parameters, refinement converged at R_1 ($I > 2\sigma(I)$) = 0.069; $wR_2(\text{all data}) = 0.174$, $\text{Goof} = 0.975$, min/max. ΔF $-0.42/0.96 \text{ e/\AA}^3$.

CCDC-1548839, 1548838, and 1548837 contain the supplementary crystallographic data for **3**, **4**, and **6**, respectively.

Electrochemistry. Cyclic and square-wave voltammograms at room temperature were performed with the PAR101 potentiostat from

Metrohm in MeCN/0.1 M $[(n\text{-Bu})_4\text{N}]\text{PF}_6$ ($c_{\text{analyt}} = 0.001 \text{ mol/L}$) with the following three-electrode arrangement: Pt working electrode (1 mm diameter), Ag/0.01 M AgNO_3 , 0.1 M $[(n\text{-Bu})_4\text{N}]\text{PF}_6$ in MeCN as reference and Pt wire counter electrode. Ferrocene was added as internal standard after the measurements, and all potentials are referenced relative to the Fc/Fc^+ couple. The cyclic and square-wave voltammograms were analyzed with the software NOVA version 1.10.5 from Metrohm. The interpretation of the voltammetric response was performed on the basis of the diagnostic criteria proposed by Nicholson^{45,46} and the Randles–Sevcik equation.^{47,48} In the case of **3**, it was not possible to determine the currents I_{pc} and I_{pa} with common baseline methods in an adequate manner. The ratio $I_{\text{pa}}/I_{\text{pc}}$ was also conveniently calculated using the empirical method by Nicholson.⁶⁴

Spectroelectrochemical and coulometric experiments at room temperature were performed in an optically transparent electrochemical cell ($d = 4 \text{ mm}$, MeCN/0.1 M $[(n\text{-Bu})_4\text{N}]\text{PF}_6$ as supporting electrolyte) with a Pt gauze working electrode. During oxidations/reductions, spectral changes were recorded on a Varian Cary 50 spectrophotometer in the range 200–1100 nm. All measurements were carried out under argon atmosphere, with absolute and deoxygenated acetonitrile. Note: Diagnostic criteria slightly deviate from perfect reversible behavior, because solution resistances are not completely compensated by the electrochemical instrumentation.

UV–vis Spectroscopy. For all measurements, spectroscopy grade solvents from VWR were used. All measured solutions had a concentration of 10^{-5} mol/L . The absorption spectra were recorded with a PerkinElmer Lambda 45 double beam UV spectrophotometer. Quartz cuvettes by Hellma with a path length of 1 cm were used.

Ultrafast Pump–Probe Spectroscopy. Transient absorption spectra were recorded with a time resolution of 100 fs by a pump–probe setup based on a noncollinear optical parametric amplifier (NOPA) tuned to 550 nm for excitation and a white light continuum for probing.⁶⁵ The NOPA as well as the continuum generation are pumped by a Ti:sapphire laser system providing 160 fs long laser pulses at a repetition rate of 1 kHz and a center wavelength of 775 nm. The polarizations of the pump and the white light probe were set to magic angle, and the two beams were focused onto the sample to overlapping spots with diameters of approximately 300 and 100 μm , respectively. As sample served a degassed acetonitrile solution of the compounds filled in a fused silica cell with a thickness of 1 mm.

X-ray Spectroscopy. Extended X-ray absorption fine structure (EXAFS) measurements were performed at beamline BM25A at the European Synchrotron Radiation Facility (ESRF, Grenoble, France). A Si(111) double crystal monochromator was used for the measurements at the Fe K-edge (7.112 keV). Energy calibration was performed with an iron foil. The experiments were carried out under ambient conditions. The solid samples were diluted in boron nitride as matrix and pressed into pellets. The spectra were recorded in transmission mode with ionization chambers filled with nitrogen. Several spectra were collected and merged to obtain a better signal-to-noise ratio. Details of the data analysis are given in the Supporting Information.

High-energy-resolution X-ray absorption and valence-to-core X-ray emission experiments were performed at beamline ID26 at the European Synchrotron Radiation Facility. All measurements were performed at 20 K in a He cryostat under vacuum conditions. The electron energy was 6.0 GeV, and the ring current varied between 180 and 200 mA. The measurements were carried out using two u35 undulators. The incident energy was selected using the $\langle 111 \rangle$ reflection from a double Si crystal monochromator. The energy calibration was performed using a Fe foil. The incident X-ray beam had a flux of approximately $2 \times 10^{13} \text{ photons s}^{-1}$ on the sample position. HERFD spectra were measured with an X-ray emission spectrometer in the horizontal plane.^{66,67} Sample, analyzer crystal, and photon detector (avalanche photodiode) were arranged in a vertical Rowland geometry. The Fe HERFD spectra at the K-edge were obtained by recording the intensity of the Fe $K\beta_{1,3}$ emission line as a function of the incident energy. The emission energy was selected using the $\langle 620 \rangle$ reflection of five spherically bent Ge crystal analyzers (with $R = 1 \text{ m}$) aligned at 80° Bragg angle. The total fluorescence yield (TFY) was

monitored by a photodiode installed at about 90° scattering angle and at 45° to the sample surface. During the XANES scans, the undulators were kept at a fixed gap and only the monochromator angle was changed.

Valence-to-core XES spectra were recorded off resonance at an excitation energy of 7300 eV in the range 7020–7130 eV, with a step width of 0.3 eV over the $K\beta_{2,5}$ emission line (7080–7130 eV). Spectra were normalized to the incident flux measured with an ionization chamber. The spectrometer energy was calibrated using the elastic line. Further details can be found in the [Supporting Information](#).

DFT Calculations. All gas phase calculations presented in this work were performed with the ORCA quantum chemistry package (version 3.0.3).⁶⁸ Unconstrained geometry optimization was performed using the TPSSH^{69,70} functional in conjunction with the RJCOSX approximation,⁷¹ the def2-TZVP basis set⁷² on all atoms, combined with the def2-TZVP/J auxiliary basis set^{73,74} and the atom-pairwise dispersion correction with the Becke–Johnson damping scheme (D3BJ).^{75,76} Crystal structures of the components were used as a starting point for complexes 1–4.

XAS TD-DFT^{77,78} XES DFT,³⁴ and molecular orbital calculations were accomplished using a modified TPSSH functional, with an adjusted Hartree–Fock exchange⁴¹ of 12.5% (ScalHFX = 0.125) in conjunction with the RJCOSX approximation and the def2-TZVP basis set, combined with the def2-TZVP/J auxiliary basis set (with a special integration accuracy of 5) on all atoms except Fe, for which the expanded CP(PPP) basis set⁷⁹ (with a special integration accuracy of 7) was chosen. Dispersion corrections were taken into account via the atom-pairwise dispersion correction with the Becke–Johnson damping scheme (D3BJ). Both simulations were performed with a single point protocol on optimized structures, concerning significantly reduced errors in calculated VtC intensities, compared to crystal structures.³⁴

Optimized structures, single point energies, and MO levels in solution were calculated via the SMD module⁵⁰ on optimized structures using the TPSSH^{69,70} functional with the def2-TZVP basis set and the atom-pairwise dispersion correction with the Becke–Johnson damping scheme (D3BJ) with the ORCA quantum chemistry package (version 4.0.1).⁸⁰

All calculated TD-DFT XANES transitions were broadened by a 1.5 eV Gaussian (fwhm) and DFT VtC-XES transitions a 2.5 eV Gaussian (fwhm). Calculated TD-DFT XANES spectra were shifted by 151.5 eV. DFT VtC-XES spectra were shifted by 150.9 eV. Intrinsic bond orbitals⁸¹ were generated with the IBO-View program (version 20150427).⁸² Orbital populations were extracted via Löwdin reduced orbital population analysis (LROP).^{83,84}

■ ASSOCIATED CONTENT

■ Supporting Information

The Supporting Information is available free of charge on the [ACS Publications website](#) at DOI: [10.1021/acs.inorgchem.7b02624](https://doi.org/10.1021/acs.inorgchem.7b02624).

NMR spectra; details concerning spectroelectrochemistry, cyclic voltammetry, X-ray, and pump–probe measurements; information on computational studies ([PDF](#))

Accession Codes

CCDC 1548837–1548839 contain the supplementary crystallographic data for this paper. These data can be obtained free of charge via www.ccdc.cam.ac.uk/data_request/cif, or by emailing data_request@ccdc.cam.ac.uk, or by contacting The Cambridge Crystallographic Data Centre, 12 Union Road, Cambridge CB2 1EZ, UK; fax: +44 1223 336033.

■ AUTHOR INFORMATION

Corresponding Author

*E-mail: matthias.bauer@uni-paderborn.de.

ORCID

Patrick Müller: [0000-0003-1103-4073](https://orcid.org/0000-0003-1103-4073)

Matthias Bauer: [0000-0002-9294-6076](https://orcid.org/0000-0002-9294-6076)

Author Contributions

[§]P.Z., L.B.: These authors contributed equally to the paper.

Notes

The authors declare no competing financial interest.

■ ACKNOWLEDGMENTS

The ESRF (beamline ID26: Pieter Glatzel, Rafal Baran; beamline 25A: Germán Castro, Aida Serrano) is acknowledged for a provision of beamtime. Generous grants of computer time at the Paderborn Center for Parallel Computing PC2 is gratefully acknowledged. The German ministry Bundesministerium für Bildung und Forschung (BMBF) is kindly acknowledged for funding in the frame of the German–Swedish project SusChEmX (F-Kz. 05K14PP1). Financial support by the Deutsche Forschungsgemeinschaft (DFG) via the research unit FOR1405 (project TP5) and the collaborative research center SFB 652 is gratefully acknowledged. P.Z. thanks the Fonds der Chemischen Industrie for a Kekulé grant.

■ REFERENCES

- (1) Tinker, L. L.; McDaniel, N. D.; Bernhard, S. Progress towards solar-powered homogeneous water photolysis. *J. Mater. Chem.* **2009**, *19*, 3328–3337.
- (2) Wang, M.; Na, Y.; Gorlov, M.; Sun, L. Light-driven hydrogen production catalysed by transition metal complexes in homogeneous systems. *Dalton Trans.* **2009**, 6458.
- (3) Gärtner, F.; Denurra, S.; Losse, S.; Neubauer, A.; Boddien, A.; Gopinathan, A.; Spannenberg, A.; Junge, H.; Lochbrunner, S.; Blug, M.; et al. Synthesis and Characterization of New Iridium Photosensitizers for Catalytic Hydrogen Generation from Water. *Chem. - Eur. J.* **2012**, *18*, 3220–3225.
- (4) Goldsmith, J. I.; Hudson, W. R.; Lowry, M. S.; Anderson, T. H.; Bernhard, S. Discovery and High-Throughput Screening of Heteroleptic Iridium Complexes for Photoinduced Hydrogen Production. *J. Am. Chem. Soc.* **2005**, *127*, 7502–7510.
- (5) Tinker, L. L.; McDaniel, N. D.; Curtin, P. N.; Smith, C. K.; Ireland, M. J.; Bernhard, S. Visible Light Induced Catalytic Water Reduction without an Electron Relay. *Chem. - Eur. J.* **2007**, *13*, 8726–8732.
- (6) Ajayakumar, G.; Kobayashi, M.; Masaoka, S.; Sakai, K. Light-induced charge separation and photocatalytic hydrogen evolution from water using RuIIpTII-based molecular devices: Effects of introducing additional donor and/or acceptor sites. *Dalton Trans.* **2011**, 40, 3955–3966.
- (7) Na, Y.; Wei, P.; Zhou, L. Photochemical Hydrogen Generation Initiated by Oxidative Quenching of the Excited Ru(bpy)₃(2+) * by a Bio-Inspired 2Fe2S Complex. *Chem. - Eur. J.* **2016**, *22*, 10365–10368.
- (8) Tschierlei, S.; Karnahl, M.; Presselt, M.; Dietzek, B.; Guthmüller, J.; González, L.; Schmitt, M.; Rau, S.; Popp, J. Photochemical Fate: The First Step Determines Efficiency of H₂ Formation with a Supramolecular Photocatalyst. *Angew. Chem., Int. Ed.* **2010**, *49*, 3981–3984.
- (9) Du, P.; Schneider, J.; Jarosz, P.; Eisenberg, R. Photocatalytic Generation of Hydrogen from Water Using a Platinum(II) Terpyridyl Acetylide Chromophore. *J. Am. Chem. Soc.* **2006**, *128*, 7726–7727.
- (10) Du, P.; Schneider, J.; Jarosz, P.; Zhang, J.; Brennessel, W. W.; Eisenberg, R. Photoinduced electron transfer in platinum(II) terpyridyl acetylide chromophores: reductive and oxidative quenching and hydrogen production. *J. Phys. Chem. B* **2007**, *111*, 6887–6894.
- (11) Sun, Y.-Y.; Wang, H.; Chen, N.-Y.; Lennox, A. J. J.; Friedrich, A.; Xia, L.-M.; Lochbrunner, S.; Junge, H.; Beller, M.; Zhou, S.; et al. Efficient Photocatalytic Water Reduction Using In Situ Generated Knölker's Iron Complexes. *ChemCatChem* **2016**, *8*, 2340–2344.

- (12) Luo, S.-P.; Mejía, E.; Friedrich, A.; Pazidis, A.; Junge, H.; Surkus, A.-E.; Jackstell, R.; Denurra, S.; Gladiali, S.; Lochbrunner, S.; et al. Photocatalytic Water Reduction with Copper-Based Photosensitizers: A Noble-Metal-Free System. *Angew. Chem., Int. Ed.* **2013**, *52*, 419–423.
- (13) Dixon, I. M.; Alary, F.; Boggio-Pasqua, M.; Heully, J.-L. The (N 4 C 2) 2– Donor Set as Promising Motif for Bis(tridentate) Iron(II) Photoactive Compounds. *Inorg. Chem.* **2013**, *52*, 13369–13374.
- (14) Liu, Y.; Persson, P.; Sundström, V.; Wärnmark, K. Fe N-Heterocyclic Carbene Complexes as Promising Photosensitizers. *Acc. Chem. Res.* **2016**, *49*, 1477–1485.
- (15) Pápai, M.; Vankó, G.; Rozgonyi, T.; Penfold, T. J. High-Efficiency Iron Photosensitizer Explained with Quantum Wavepacket Dynamics. *J. Phys. Chem. Lett.* **2016**, *7*, 2009–2014.
- (16) Dixon, I. M.; Khan, S.; Alary, F.; Boggio-Pasqua, M.; Heully, J.-L. Probing the photophysical capability of mono and bis-(cyclometallated) Fe(II) polypyridine complexes using inexpensive ground state DFT. *Dalton Trans.* **2014**, *43*, 15898–15905.
- (17) Liu, Y.; Harlang, T.; Canton, S. E.; Chábera, P.; Suárez-Alcántara, K.; Fleckhaus, A.; Vithanage, D. A.; Göransson, E.; Corani, A.; Lomoth, R.; et al. Towards longer-lived metal-to-ligand charge transfer states of iron(II) complexes: an N-heterocyclic carbene approach. *Chem. Commun.* **2013**, *49*, 6412.
- (18) Fredin, L. A.; Pápai, M.; Rozsályi, E.; Vankó, G.; Wärnmark, K.; Sundström, V.; Persson, P. Exceptional Excited-State Lifetime of an Iron(II)–N-Heterocyclic Carbene Complex Explained. *J. Phys. Chem. Lett.* **2014**, *5*, 2066–2071.
- (19) Liu, L.; Duchanois, T.; Etienne, T.; Monari, A.; Beley, M.; Assfeld, X.; Haacke, S.; Gros, P. C. A new record excited state (3)MLCT lifetime for metalorganic iron(II) complexes. *Phys. Chem. Chem. Phys.* **2016**, *18*, 12550–12556.
- (20) Duchanois, T.; Etienne, T.; Cebrián, C.; Liu, L.; Monari, A.; Beley, M.; Assfeld, X.; Haacke, S.; Gros, P. C. An Iron-Based Photosensitizer with Extended Excited-State Lifetime: Photophysical and Photovoltaic Properties. *Eur. J. Inorg. Chem.* **2015**, *2015*, 2469–2477.
- (21) Duchanois, T.; Etienne, T.; Beley, M.; Assfeld, X.; Perpète, E. A.; Monari, A.; Gros, P. C. Heteroleptic Pyridyl-Carbene Iron Complexes with Tuneable Electronic Properties. *Eur. J. Inorg. Chem.* **2014**, *2014*, 3747–3753.
- (22) Liu, Y.; Kjaer, K. S.; Fredin, L. A.; Chábera, P.; Harlang, T.; Canton, S. E.; Lidin, S.; Zhang, J.; Lomoth, R.; Bergquist, K.-E.; et al. A heteroleptic ferrous complex with mesoionic bis(1,2,3-triazol-5-ylidene) ligands: taming the MLCT excited state of iron(II). *Chem. - Eur. J.* **2015**, *21*, 3628–3639.
- (23) Zimmer, P.; Müller, P.; Burkhardt, L.; Schepper, R.; Neuba, A.; Steube, J.; Dietrich, F.; Flörke, U.; Mangold, S.; Gerhards, M.; et al. N-Heterocyclic Carbene Complexes of Iron as Photosensitizers for Light-Induced Water Reduction. *Eur. J. Inorg. Chem.* **2017**, *2017*, 1504–1509.
- (24) Kim, H.-M.; Jeong, D.; Noh, H. C.; Kang, Y. K.; Chung, Y. K. Manipulation of Absorption Maxima by Controlling Oxidation Potentials in Bis(tridentate) Ru(II) N-Heterocyclic Carbene Complexes. *Bull. Korean Chem. Soc.* **2014**, *35*, 448–456.
- (25) Flörke, U.; Zimmer, P.; Bauer, M. CCDC 1584659: Experimental Crystal Structure Determination. DOI: [10.5517/ccdc.csd.cclq5z1x](https://doi.org/10.5517/ccdc.csd.cclq5z1x).
- (26) Ericson, F.; Honarfar, A.; Prakash, O.; Tatsuno, H.; Fredin, L. A.; Handrup, K.; Chabera, P.; Gordivska, O.; Kjaer, K. S.; Liu, Y.; et al. Electronic structure and excited state properties of iron carbene photosensitizers – A combined X-ray absorption and quantum chemical investigation. *Chem. Phys. Lett.* **2017**, *683*, 559–566.
- (27) Gamblin, S. D.; Urch, D. S. Metal K β X-ray emission spectra of first row transition metal compounds. *J. Electron Spectrosc. Relat. Phenom.* **2001**, *113*, 179–192.
- (28) Glatzel, P.; Bergmann, U. High resolution 1s core hole X-ray spectroscopy in 3d transition metal complexes—electronic and structural information. *Coord. Chem. Rev.* **2005**, *249*, 65–95.
- (29) Bergmann, U.; Glatzel, P. X-ray emission spectroscopy. *Photosynth. Res.* **2009**, *102*, 255–266.
- (30) Vankó, G.; Neisius, T.; Molnar, G.; Renz, F.; Karpati, S.; Shukla, A.; Groot, F. M. F. de. Probing the 3d spin momentum with X-ray emission spectroscopy: The case of molecular-spin transitions. *J. Phys. Chem. B* **2006**, *110*, 11647–11653.
- (31) Pollock, C. J.; Delgado-Jaime, M. U.; Atanasov, M.; Neese, F.; DeBeer, S. K β mainline X-ray emission spectroscopy as an experimental probe of metal-ligand covalency. *J. Am. Chem. Soc.* **2014**, *136*, 9453–9463.
- (32) Delgado-Jaime, M. U.; DeBeer, S.; Bauer, M. Valence-to-core X-ray emission spectroscopy of iron-carbonyl complexes: Implications for the examination of catalytic intermediates. *Chem. - Eur. J.* **2013**, *19*, 15888–15897.
- (33) Smolentsev, G.; Soldatov, A. V.; Messenger, J.; Merz, K.; Weyhermüller, T.; Bergmann, U.; Pushkar, Y.; Yano, J.; Yachandra, V. K.; Glatzel, P. X-ray emission spectroscopy to study ligand valence orbitals in Mn coordination complexes. *J. Am. Chem. Soc.* **2009**, *131*, 13161–13167.
- (34) Lee, N.; Petrenko, T.; Bergmann, U.; Neese, F.; DeBeer, S. Probing valence orbital composition with iron K β X-ray emission spectroscopy. *J. Am. Chem. Soc.* **2010**, *132*, 9715–9727.
- (35) Pollock, C. J.; DeBeer, S. Insights into the geometric and electronic structure of transition metal centers from valence-to-core X-ray emission spectroscopy. *Acc. Chem. Res.* **2015**, *48*, 2967–2975.
- (36) Pollock, C. J.; DeBeer, S. Valence-to-core X-ray emission spectroscopy: A sensitive probe of the nature of a bound ligand. *J. Am. Chem. Soc.* **2011**, *133*, 5594–5601.
- (37) Westre, T. E.; Kennepohl, P.; DeWitt, J. G.; Hedman, B.; Hodgson, K. O.; Solomon, E. I. A Multiplet Analysis of Fe K-Edge 1s \rightarrow 3d Pre-Edge Features of Iron Complexes. *J. Am. Chem. Soc.* **1997**, *119*, 6297–6314.
- (38) de Groot, F. High-Resolution X-ray Emission and X-ray Absorption Spectroscopy. *Chem. Rev.* **2001**, *101*, 1779–1808.
- (39) Bauer, M. HERFD-XAS and valence-to-core-XES: New tools to push the limits in research with hard X-rays? *Phys. Chem. Chem. Phys.* **2014**, *16*, 13827–13837.
- (40) Atkins, A. J.; Bauer, M.; Jacob, C. R. The chemical sensitivity of X-ray spectroscopy: High energy resolution XANES versus X-ray emission spectroscopy of substituted ferrocenes. *Phys. Chem. Chem. Phys.* **2013**, *15*, 8095–8105.
- (41) Roemelt, M.; Beckwith, M. A.; Duboc, C.; Collomb, M.-N.; Neese, F.; DeBeer, S. Manganese K-edge X-ray absorption spectroscopy as a probe of the metal-ligand interactions in coordination compounds. *Inorg. Chem.* **2012**, *51*, 680–687.
- (42) Delgado-Jaime, M. U.; DeBeer, S. Expedited analysis of DFT outputs: Introducing MOAnalyzer. *J. Comput. Chem.* **2012**, *33*, 2180–2185.
- (43) Jamula, L. L.; Brown, A. M.; Guo, D.; McCusker, J. K. Synthesis and characterization of a high-symmetry ferrous polypyridyl complex: Approaching the ST2/3T1 crossing point for Fe(II). *Inorg. Chem.* **2014**, *53*, 15–17.
- (44) Zhan, C.-G.; Nichols, J. A.; Dixon, D. A. Ionization Potential, Electron Affinity, Electronegativity, Hardness, and Electron Excitation Energy: ? Molecular Properties from Density Functional Theory Orbital Energies. *J. Phys. Chem. A* **2003**, *107*, 4184–4195.
- (45) Nicholson, R. S.; Shain, I. Theory of Stationary Electrode Polarography. Single Scan and Cyclic Methods Applied to Reversible, Irreversible, and Kinetic Systems. *Anal. Chem.* **1964**, *36*, 706–723.
- (46) Heinze, J. Cyclovoltammetrie — die “Spektroskopie” des Elektrochemikers. *Angew. Chem.* **1984**, *96*, 823–840.
- (47) Randles, J. E. B. A cathode ray polarograph. Part II: The current-voltage curves. *Trans. Faraday Soc.* **1948**, *44*, 327–338.
- (48) Scholz, F. *Electroanalytical methods: Guide to experiments and applications*, 2, rev. and extended ed.; Springer: Berlin, 2010.
- (49) Braterman, P. S.; Song, J. I.; Peacock, R. D. Electronic absorption spectra of the iron(II) complexes of 2,2'-bipyridine, 2,2'-bipyrimidine, 1,10-phenanthroline, and 2,2': 6',2'-terpyridine and their reduction products. *Inorg. Chem.* **1992**, *31*, 555–559.

- (50) Marenich, A. V.; Cramer, C. J.; Truhlar, D. G. Universal solvation model based on solute electron density and on a continuum model of the solvent defined by the bulk dielectric constant and atomic surface tensions. *J. Phys. Chem. B* **2009**, *113*, 6378–6396.
- (51) Damrauer, N. H.; McCusker, J. K. Ultrafast Dynamics in the Metal-to-Ligand Charge Transfer Excited-State Evolution of [Ru(4,4'-diphenyl-2,2'-bipyridine) 3^{+}]. *J. Phys. Chem. A* **1999**, *103*, 8440–8446.
- (52) Monat, J. E.; McCusker, J. K. Femtosecond Excited-State Dynamics of an Iron(II) Polypyridyl Solar Cell Sensitizer Model. *J. Am. Chem. Soc.* **2000**, *122*, 4092–4097.
- (53) Nazeeruddin, M. K.; Zakeeruddin, S. M.; Kalyanasundaram, K. Enhanced intensities of the ligand-to-metal charge-transfer transitions in ruthenium(III) and osmium(III) complexes of substituted bipyridines. *J. Phys. Chem.* **1993**, *97*, 9607–9612.
- (54) **1'** and **2'** differ from **1** and **2**, respectively, only by the counterion.
- (55) Lemke, H. T.; Bressler, C.; Chen, L. X.; Fritz, D. M.; Gaffney, K. J.; Galler, A.; Gawelda, W.; Haldrup, K.; Hartsock, R. W.; Ihee, H.; et al. Femtosecond X-ray absorption spectroscopy at a hard X-ray free electron laser: Application to spin crossover dynamics. *J. Phys. Chem. A* **2013**, *117*, 735–740.
- (56) Mengel, A. K. C.; Förster, C.; Breivogel, A.; Mack, K.; Ochsmann, J. R.; Laquai, F.; Ksenofontov, V.; Heinze, K. A heteroleptic push-pull substituted iron(II) bis(tridentate) complex with low-energy charge-transfer states. *Chem. - Eur. J.* **2015**, *21*, 704–714.
- (57) Danopoulos, A. A.; Tsoureas, N.; Wright, J. A.; Light, M. E. N-Heterocyclic Pincer Dicarbene Complexes of Iron(II): C-2 and C-5 Metalated Carbenes on the Same Metal Center. *Organometallics* **2004**, *23*, 166–168.
- (58) Danopoulos, A. A.; Tulloch, A. A. D.; Winston, S.; Eastham, G.; Hursthouse, M. B. Chelating and 'pincer' dicarbene complexes of palladium; synthesis and structural studies. *Dalton Trans.* **2003**, 1009–1015.
- (59) Chen, J. C. C.; Lin, I. J. B. Palladium Complexes Containing a Hemilabile Pyridylcarbene Ligand. *Organometallics* **2000**, *19*, 5113–5121.
- (60) McGuinness, D. S.; Gibson, V. C.; Steed, J. W. Bis(carbene)-pyridine Complexes of the Early to Middle Transition Metals: Survey of Ethylene Oligomerization and Polymerization Capability. *Organometallics* **2004**, *23*, 6288–6292.
- (61) Spek, A. L. Single-crystal structure validation with the program PLATON. *J. Appl. Crystallogr.* **2003**, *36*, 7–13.
- (62) SMART (version 5.63), SAINT (version 6.02); Bruker AXS Inc.: Madison, WI, 2002.
- (63) Sheldrick, G. M. A short history of SHELX. *Acta Crystallogr., Sect. A: Found. Crystallogr.* **2008**, *64*, 112–122.
- (64) Nicholson, R. S. Semiempirical Procedure for Measuring with Stationary Electrode Polarography Rates of Chemical Reactions Involving the Product of Electron Transfer. *Anal. Chem.* **1966**, *38*, 1406.
- (65) Riedle, E.; Beutter, M.; Lochbrunner, S.; Piel, J.; Schenkl, S.; Spörlein, S.; Zinth, W. Generation of 10 to 50 fs pulses tunable through all of the visible and the NIR. *Appl. Phys. B: Lasers Opt.* **2000**, *71*, 457–465.
- (66) Swarbrick, J. C.; Skyllberg, U.; Karlsson, T.; Glatzel, P. High energy resolution X-ray absorption spectroscopy of environmentally relevant lead(II) compounds. *Inorg. Chem.* **2009**, *48*, 10748–10756.
- (67) de Groot, F. M. F.; Krisch, M. H.; Vogel, J. Spectral sharpening of the Pt L edges by high-resolution x-ray emission. *Phys. Rev. B: Condens. Matter Mater. Phys.* **2002**, *66*, 621.
- (68) Neese, F. The ORCA program system. *Wiley Interdiscip. Rev. Comput. Mol. Sci.* **2012**, *2*, 73–78.
- (69) Staroverov, V. N.; Scuseria, G. E.; Tao, J.; Perdew, J. P. Comparative assessment of a new nonempirical density functional: Molecules and hydrogen-bonded complexes. *J. Chem. Phys.* **2003**, *119*, 12129.
- (70) Staroverov, V. N.; Scuseria, G. E.; Tao, J.; Perdew, J. P. Comparative assessment of a new nonempirical density functional: Molecules and hydrogen-bonded complexes. *J. Chem. Phys.* **2003**, *119*, 12129–12137.
- (71) Neese, F.; Wennmohs, F.; Hansen, A.; Becker, U. Efficient, approximate and parallel Hartree–Fock and hybrid DFT calculations. A 'chain-of-spheres' algorithm for the Hartree–Fock exchange. *Chem. Phys.* **2009**, *356*, 98–109.
- (72) Weigend, F.; Ahlrichs, R. Balanced basis sets of split valence, triple zeta valence and quadruple zeta valence quality for H to Rn: Design and assessment of accuracy. *Phys. Chem. Chem. Phys.* **2005**, *7*, 3297–3305.
- (73) Eichkorn, K.; Weigend, F.; Treutler, O.; Ahlrichs, R. Auxiliary basis sets for main row atoms and transition metals and their use to approximate Coulomb potentials. *Theor. Chem. Acc.* **1997**, *97*, 119–124.
- (74) Weigend, F. Accurate Coulomb-fitting basis sets for H to Rn. *Phys. Chem. Chem. Phys.* **2006**, *8*, 1057–1065.
- (75) Grimme, S.; Ehrlich, S.; Goerigk, L. Effect of the damping function in dispersion corrected density functional theory. *J. Comput. Chem.* **2011**, *32*, 1456–1465.
- (76) Grimme, S.; Antony, J.; Ehrlich, S.; Krieg, H. A consistent and accurate ab initio parametrization of density functional dispersion correction (DFT-D) for the 94 elements H–Pu. *J. Chem. Phys.* **2010**, *132*, 154104.
- (77) DeBeer George, S.; Petrenko, T.; Neese, F. Prediction of iron K-edge absorption spectra using time-dependent density functional theory. *J. Phys. Chem. A* **2008**, *112*, 12936–12943.
- (78) DeBeer George, S.; Petrenko, T.; Neese, F. Time-dependent density functional calculations of ligand K-edge X-ray absorption spectra. *Inorg. Chim. Acta* **2008**, *361*, 965–972.
- (79) Neese, F. Prediction and interpretation of the 57Fe isomer shift in Mössbauer spectra by density functional theory. *Inorg. Chim. Acta* **2002**, *337*, 181–192.
- (80) Neese, F. Software update: The ORCA program system, version 4.0. *Wiley Interdiscip. Rev. Comput. Mol. Sci.* **2017**, *2*, e1327.
- (81) Knizia, G. Intrinsic Atomic Orbitals: An Unbiased Bridge between Quantum Theory and Chemical Concepts. *J. Chem. Theory Comput.* **2013**, *9*, 4834–4843.
- (82) Knizia, G. *iboview*; <http://www.iboview.org>.
- (83) Atkins, P. W.; Friedman, R. S. *Molecular quantum mechanics*, 5th ed.; Oxford Univ. Press: Oxford, U.K., 2011.
- (84) *Reviews in computational chemistry*; John Wiley & Sons; WILEY-VCH: New York, 2001; Vol. 17.

5. Summary and Outlook

The methodological combination of VtC-XES, HERFD-XANES and (TD)DFT calculations has been shown to be an excellent tool to probe the geometric and electronic structure of TM compounds in cases where conventional scattering or spectroscopic techniques fail, with a set of Fe hydride, nitrosyl and polypyridyl-NHC complexes in comparison to their non-hydride, non-nitrosyl and polypyridyl analogues.

It has been shown for all investigated hydride compounds that bonding Fe-hydride interactions contribute essentially to Fe K-edge VtC-XES features around 7107 eV. Furthermore, we have shown that even hydride-phosphine interactions resulting from proximity of adjacent phosphine and hydride ligands contribute significantly to the VtC-XES spectrum around 7105 eV. Moreover, we have shown that antibonding Fe-hydride interactions of bridged poly-hydrides evoke an additional well-pronounced pre-edge feature around 7115 eV in the XANES region. In contrast to terminal Fe hydrides, which show only minor contributions to pre-edge features around 7114 eV. However, for both terminal and bridged poly-hydrides it has been demonstrated by theoretical spectroscopy that modern high-resolution hard X-ray spectroscopy is able to detect even diluted hydride species down to a mole fraction of 5 % and therefore high-resolution hard X-ray spectroscopy combined with (TD)DFT is a promising tool to study reaction mechanisms in-situ where hydrides are present.

The Hieber anion has been examined by high-resolution hard X-ray spectroscopy, (TD)DFT and theoretical spectroscopy. In great contrast to a recent study, our experimental and computational results are in very good agreement with the former well-known description of a $3d^{10}$ Fe^{II} ion bound to a linear NO^+ ligand. The ability of VtC-XES and HERFD-XANES to probe nitrosyl localized orbitals and their interactions with Fe 3d orbitals has further been strengthened and explored. The triplet and singlet potential energy surfaces of the Hieber anion were examined and all computational observed nitrosyl coordination isomers (six) were utilized further and studied by theoretical hard X-ray spectroscopy. It has been shown that changes of the nitrosyl bonding mode are inducing significant spectral variations of VtC-XES and HERFD-XANES spectra and therefore the above-mentioned methodology is indeed able to probe and discriminate structural nitrosyl isomers. This opens the path to study transient nitrosyl species on ultrafast timescales and to investigate reactions in-situ where nitrosyl ligands are involved.

Homoleptic and heteroleptic Fe^{II} photosensitizers coordinated by tridentate (poly)pyridine-NHC ligands with varying NHC / pyridine ratios were studied by high-resolution hard X-ray spectroscopy combined with (TD)DFT. It has been shown, that the CtC-XES mainline is shifting significantly to lower energies with increasing number of σ -donating NHC functions, due to an increasing ligand-iron covalency. A similar effect was found for the HERFD-XANES pre-peak feature which shows a

distinct blue-shift with increasing number NHC functions due to an increasing destabilization of underlying e_g^* levels. An unexpected sensitivity of the HERFD-XANES near-edge to the nature of the coordinating ligand (NHC or pyridine) has been observed. NHC-rich (three and four NHC functions per complex) structures exhibit a well-pronounced near-edge feature around 7119 eV which is significantly blue-shifting into the absorption-edge with a decreasing number of NHC functions, whereas pyridine-rich structures show a distinct near-edge feature around 7124 eV which is blue-shifting into the absorption-edge with decreasing number of pyridine functions. These results serve as a solid foundation for transient high-resolution hard X-ray spectroscopy on ultrafast timescale to further understand the excited state dynamics in potential Fe^{+II} (poly)pyridine-NHC photosensitizers .

All experiments performed in this work are *proof of principles* studies using solid samples of defined compounds. So far, we could only access feasibility of the methodology under in-situ conditions by theoretical spectroscopy of physical mixtures. Therefore, the next step is the allocation of VtC-XES and HERFD-XANES to real catalytic systems in-situ and transient ultrafast experiments.

6. Supporting Information

6.1 Detection and Characterization of Hydride Ligands in Iron Complexes by High-Resolution Hard X-ray Spectroscopy and Implications for Catalytic Processes

TABLE OF CONTENTS

Section S1 - Structural parameters

Section S2 - Additional Spectra

Section S3 - VtC-XES transitions and donor orbitals

Section S4 - XANES states and acceptor orbitals orbitals

Section S5 - Hydride orbital composition of **1H** and **2H**

Section S6 - XYZ coordinates of all optimized Structures

Section S1 - Structural parameters

Table S1. Atomic distance and dihedral angle between N-Fe-N, P-Fe-P and C-Fe-N planes of **1**, **2**, **1H** and **2H** from DFT optimized structures.

Atomic distance / dihedral angle	Compound			
	1	2	1H	2H
Fe-N1 ^[a]	1.64 Å	1.64 Å	1.64 Å	1.64 Å
Fe-N2 ^[a]	1.64 Å	1.64 Å		
Fe-C ^[a]			1.77 Å	1.77 Å
Fe-P ^{1[a]}	2.20 Å	2.24 Å	2.20 Å	2.19 Å
Fe-P ^{2[a]}	2.20 Å	2.24 Å	2.23 Å	2.19 Å
Fe-H ^[a]			1.52 Å	1.55 Å
Dihedral P-Fe-P ^[b]	87.7°	113.5°	92.4°	142.1°
Dihedral N-Fe-N ^[b]	126.1°	125.8°		
Dihedral N-Fe-C ^[b]			123.7°	121.3°

[a] bond length, [b] dihedral angle.

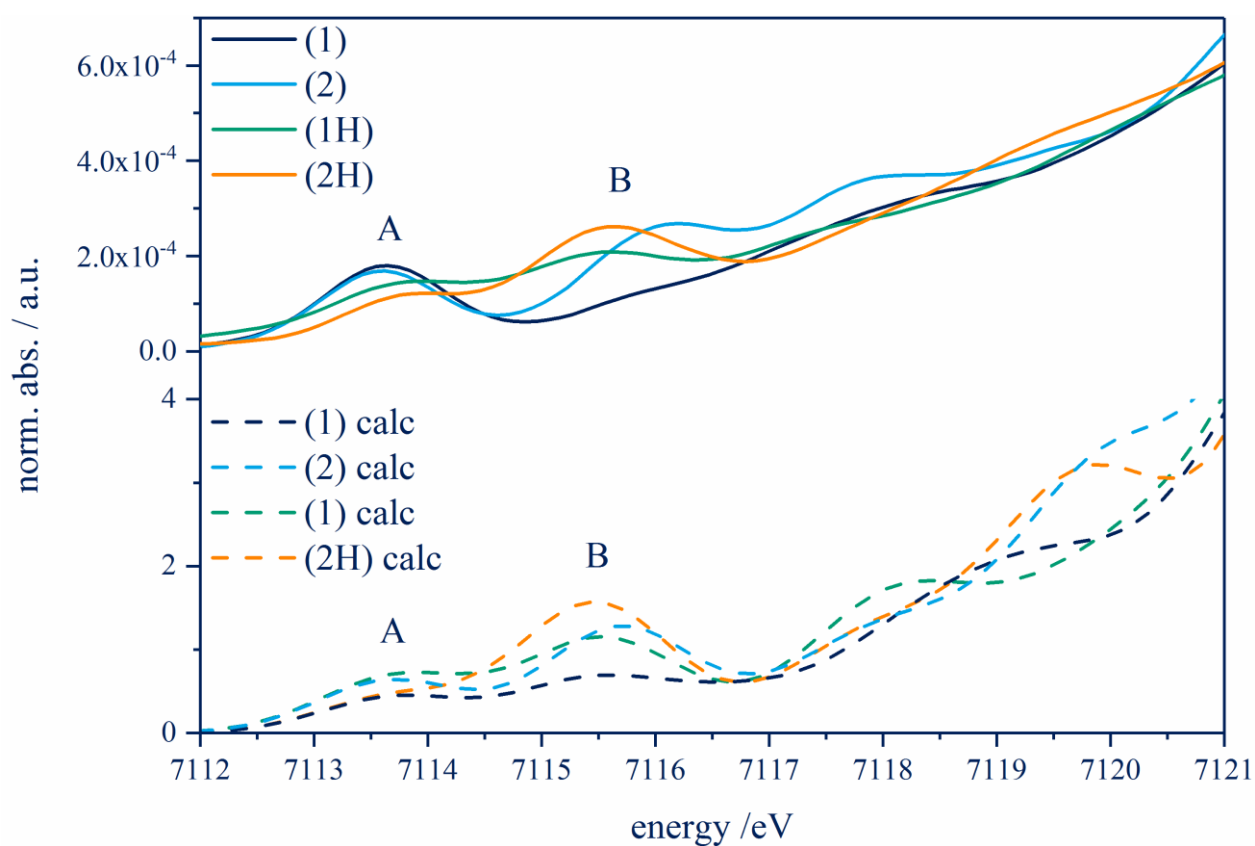
Section S2 - Additional spectra

Figure S1. Comparison of experimental (solid) and theoretical (dashed) Fe K-edge HERFD-XANES spectra of complexes **1**, **2**, **1H** and **2H**.

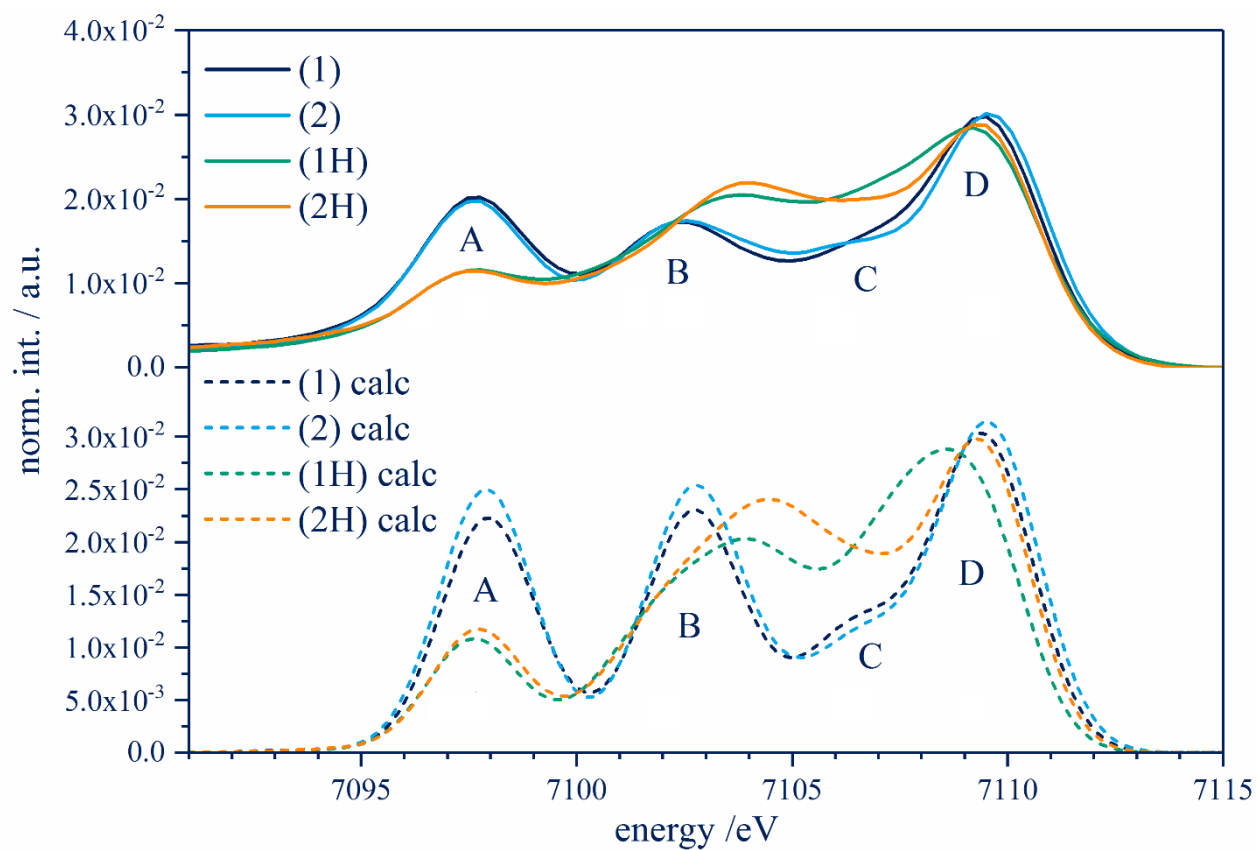


Figure S2. Comparison of experimental (solid) and theoretical (dashed) Fe VtC-XES spectra of complexes **1**, **2**, **1H** and **2H**.

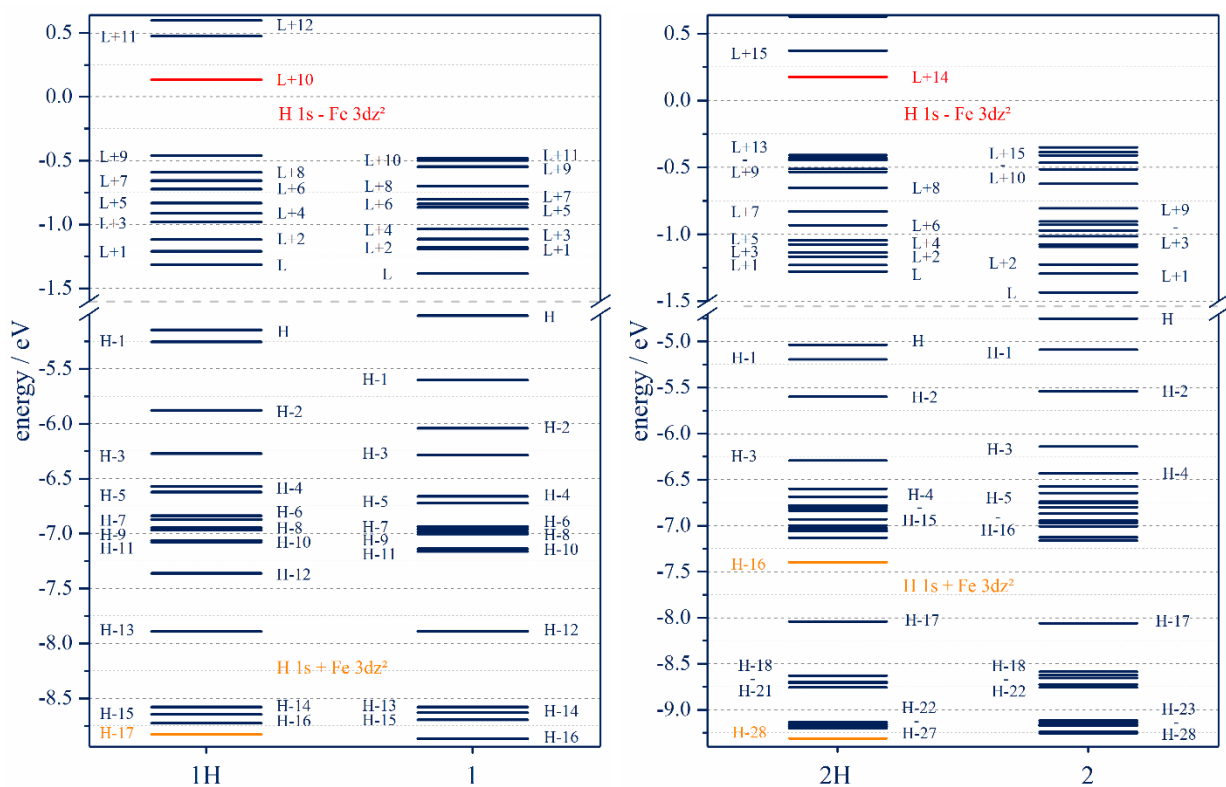


Figure S3. Left: comparison of HOMO (H) and LUMO (L) energies of **1H** and **1**. Right: comparison of

HOMO and LUMO energies of **2** and **2H**. Red: antibonding combination of H 1s and Fe 3d_{z²}, orange: antibonding combination of H 1s and Fe 3d_{z²}

Section S3 - VtC-XES transitions and donor orbitals

Table S2. Comparison of all relevant VtC-XES transitions of **1** and **2** concerning ligand/element populations (donor orbital), energies and normalized intensities.

Complexes								
	1				2			
Ligand / element character	Transition	Popula- tion ^[a] / %	Energy /eV	Norm. Int. ^[b] /a.u.	Transition	Popu- la- tion ^[a] / %	Energy /eV	Norm. Int. ^[b] /a.u.
Fe	HOMO → Fe 1s	64	6940.32	0.44	HOMO → Fe 1s	58.5	6940.63	0.53
	HOMO-1 → Fe 1s	34.7	6940.23	0.60	HOMO-1 → Fe 1s	36.1	6940.11	0.54
	HOMO-2 → Fe 1s	48.7	6939.60	0.50	HOMO-2 → Fe 1s	49.1	6939.74	0.45
	HOMO-3 → Fe 1s	52.5	6939.30	0.22	HOMO-3 → Fe 1s	54.5	6939.28	0.17
	HOMO-4 →	57.6	6939.00	0.01	HOMO-4 →	54.7	6938.91	0.01

	Fe 1s				Fe 1s			
P (PR ₃)	HOMO-13 → Fe 1s	29.7	6937.41	0.28	HOMO-17 → Fe 1s	27.8	6937.32	0.29
	HOMO-14 → Fe 1s	22	6936.79	0.11	HOMO-18 → Fe 1s	16.3	6936.87	0.04
	HOMO-15 → Fe 1s	18	6936.74	0.01	HOMO-19 → Fe 1s	17.9	6936.82	0.06
	HOMO-16 → Fe 1s	22.3	6936.67	0.18	HOMO-20 → Fe 1s	16.9	6936.81	0.04
	HOMO-17 → Fe 1s	15.1	6936.51	0.02				
	HOMO-68 → Fe 1s	15.4	6927.61	0.02				
NO	HOMO-36 → Fe 1s	36.4	6933.83	0.03	HOMO-47 → Fe 1s	33.3	6933.84	0.01
	HOMO-37 → Fe 1s	80.2	6933.75	0.11	HOMO-48 → Fe 1s	77.9	6933.80	0.11

HOMO-39 → Fe 1s	35.5	6933.66	0.05	HOMO-53 → Fe 1s	68.2	6933.62	0.07
HOMO-40 → Fe 1s	85	6933.60	0.09	HOMO-56 → Fe 1s	42.4	6933.58	0.01
HOMO-41 → Fe 1s	57.8	6933.55	0.02	HOMO-63 → Fe 1s	82.5	6933.11	0.76
HOMO-48 → Fe 1s	78.1	6933.11	0.71	HOMO-64 → Fe 1s	82.2	6932.67	0.08
HOMO-51 → Fe 1s	81.1	6932.67	0.07	HOMO-83 → Fe 1s	83.1	6928.48	1.00
HOMO-65 → Fe 1s	83.2	6928.49	0.98	HOMO-86 → Fe 1s	69.8	6927.87	0.17
HOMO-67 → Fe 1s	75.1	6927.91	0.17				

^[a] Population of the given element via Loewdin reduced orbital population analysis, ^[b] normalized to 1 (all values were divided by the overall highest value).

Table S3. Comparison of all relevant VtC-XES transitions of **1H** and **2H** concerning ligand/element populations (donor orbital), energies and normalized intensities.

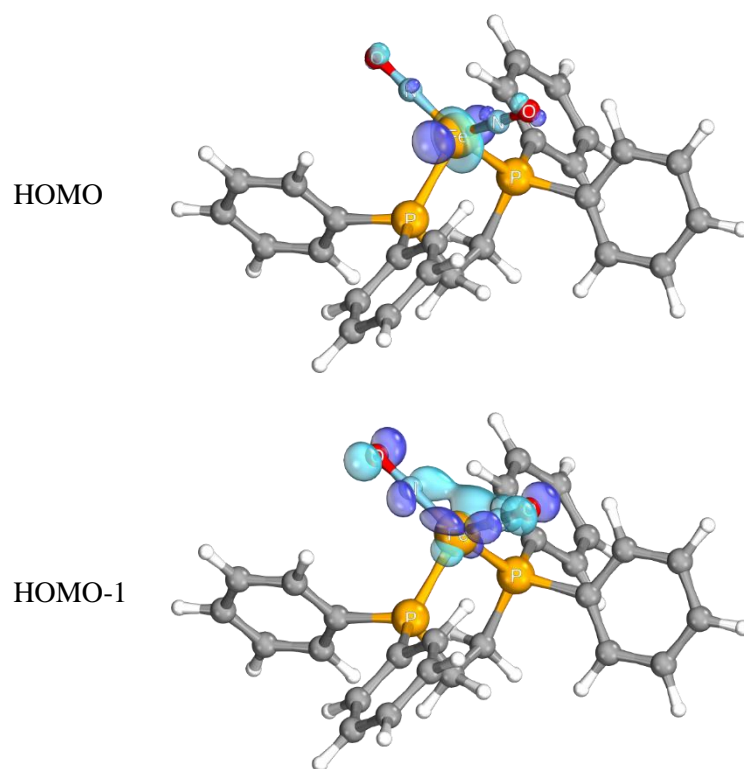
Complexes								
	1H				2H			
Ligand / element character	Transition	Popula- tion ^[a] / %	Energy /eV	Norm. Int. ^[b] /a.u.	Transition	Popula- tion ^[a] / %	Energy /eV	Norm. Int. ^[b] /a.u.
Fe	HOMO → Fe 1s	58.1	6940.10	0.50	HOMO → Fe 1s	61.7	6940.25	0.50
	HOMO-1 → Fe 1s	46.6	6939.91	0.51	HOMO-1 → Fe 1s	35.8	6939.94	0.68
	HOMO-2 → Fe 1s	64.8	6939.51	0.12	HOMO-2 → Fe 1s	58.1	6939.70	0.30
	HOMO-3 → Fe 1s	54.9	6938.94	0.16	HOMO-3 → Fe 1s	51.4	6938.97	0.12
					HOMO-16 → Fe 1s	34.2	6938.97	0.12
P	HOMO-12 →	25.5	6937.34	0.24	HOMO-17 →	27.6	6937.23	0.47

	→ Fe 1s				Fe 1s			
	HOMO-13 → Fe 1s	16.7	6936.67	0.08				
	HOMO-15 → Fe 1s	16.5	6936.49	0.08				
H	HOMO-17 (1Ha) → Fe 1s	10.1	6937.83	0.18	HOMO-16 (2Ha) → Fe 1s	14.4	6938.97	0.12
					HOMO-28 (2Hb) → Fe 1s	8.8	6936.04	0.25
NO	HOMO-45 → Fe 1s	35.1	6933.47	0.03	HOMO-1 → Fe 1s	35.8	6939.94	0.68
	HOMO-49 → Fe 1s	38.7	6933.20	0.06	HOMO-50 → Fe 1s	38.4	6933.70	0.02

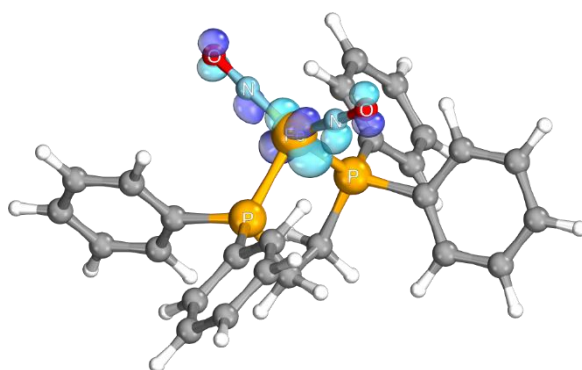
CO	HOMO-53 → Fe 1s	65	6932.71	0.30	HOMO-51 → Fe 1s	59.2	6933.66	0.02
	HOMO-69 → Fe 1s	50.3	6928.13	0.44	HOMO-65 → Fe 1s	71.4	6932.83	0.31
	HOMO-70 → Fe 1s	30.9	6927.91	0.16	HOMO-84 → Fe 1s	51.4	6928.26	0.43
	HOMO-31 → Fe 1s	47.1	6934.74	0.14	HOMO-37 → Fe 1s	70.6	6934.86	0.08
	HOMO-32 → Fe 1s	38.7	6934.70	0.04	HOMO-38 → Fe 1s	67.7	6934.81	0.05
	HOMO-33 → Fe 1s	40	6934.66	0.05	HOMO-39 → Fe 1s	53.7	6934.71	0.35
	HOMO-34 →	53.4	6934.50	0.38	HOMO-67 → Fe 1s	66.5	6931.74	0.17

Fe 1s							
HOMO-56 → Fe 1s	43	6931.65	0.10				

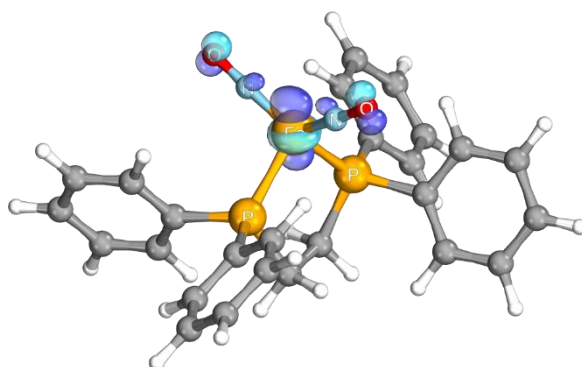
^[a] Population of the given element via Loewdin reduced orbital population analysis, ^[b] normalized to 1 (all values were divided by the overall highest value).

Table S4. Donor orbitals of **1**.

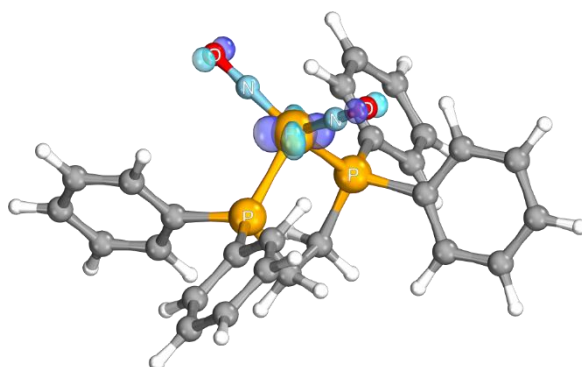
HOMO-2



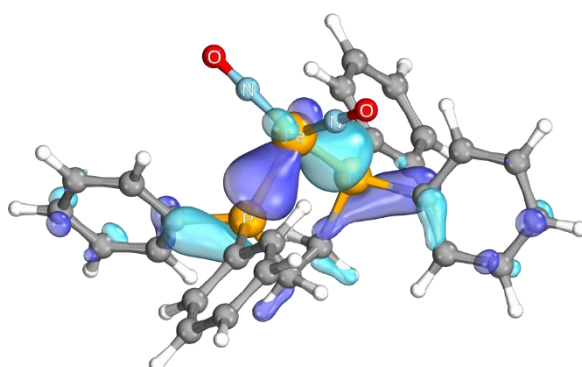
HOMO-3



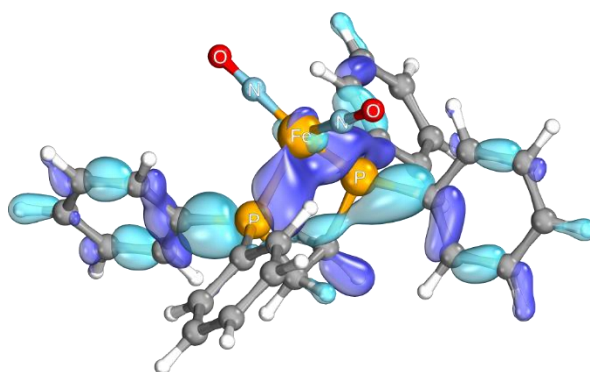
HOMO-4



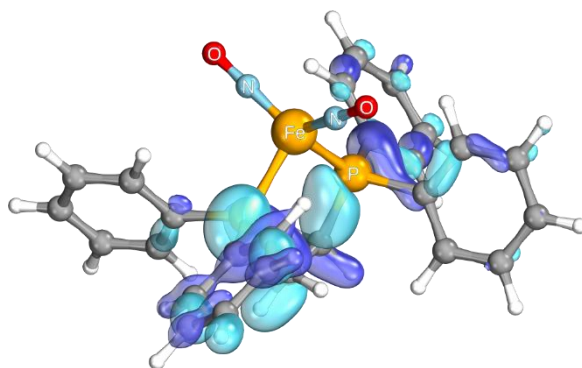
HOMO-13



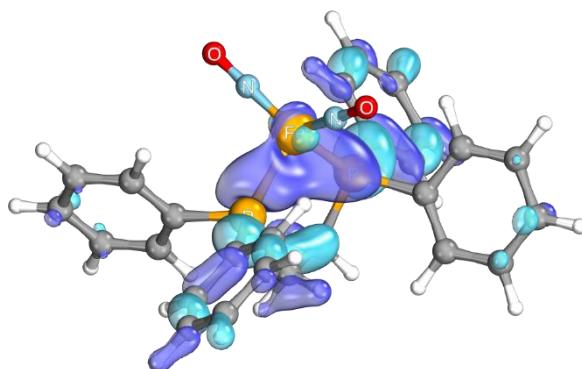
HOMO-14



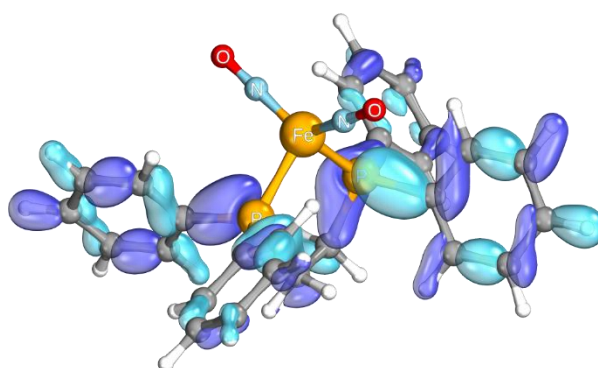
HOMO-15



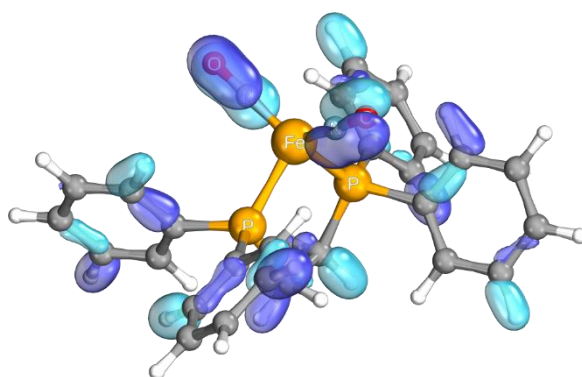
HOMO-16



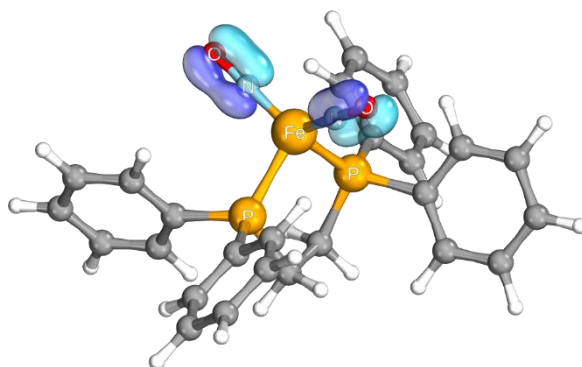
HOMO-17



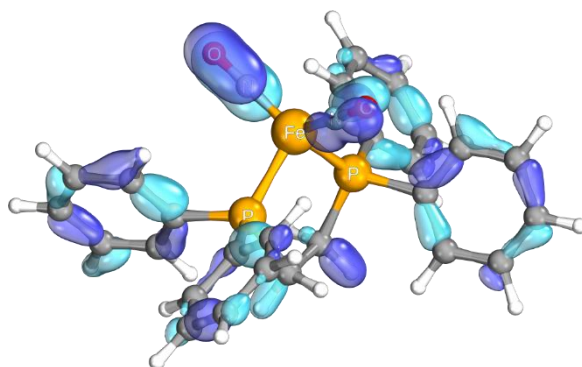
HOMO-36



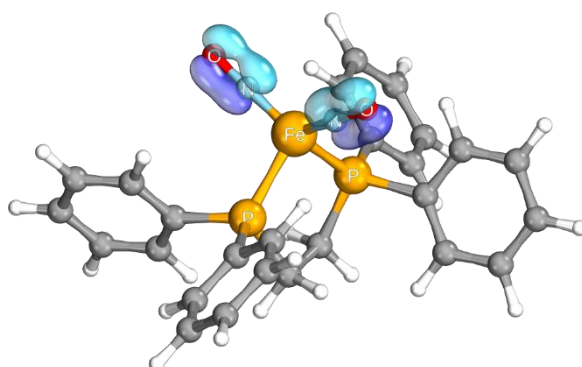
HOMO-37



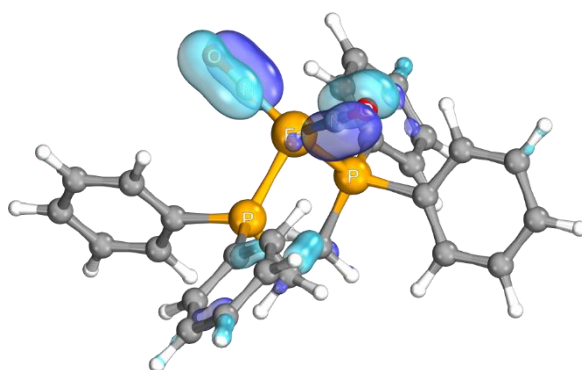
HOMO-39



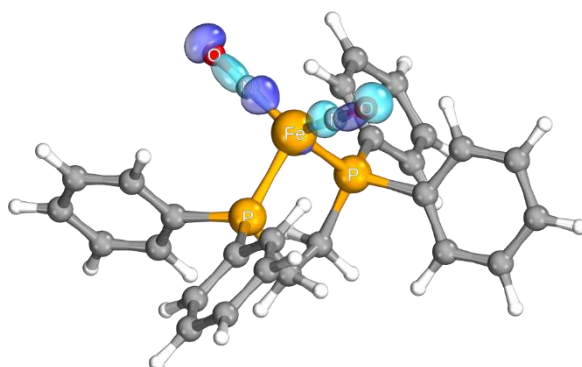
HOMO-40



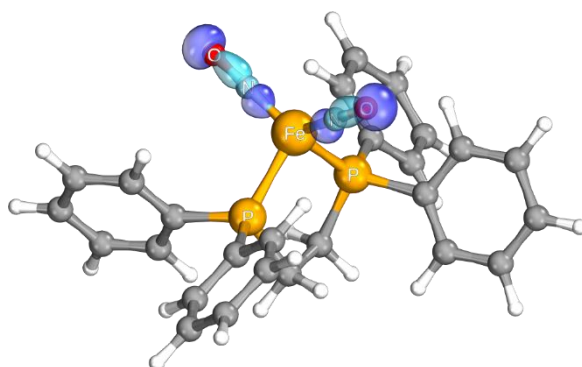
HOMO-41



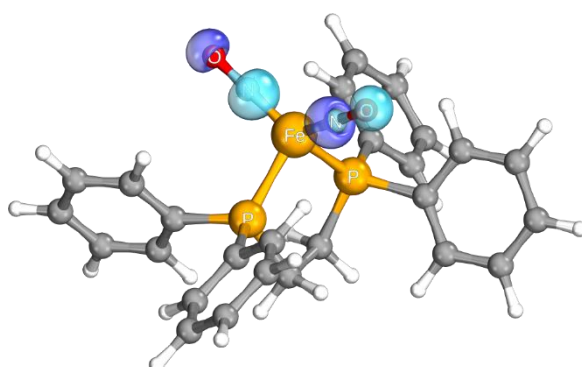
HOMO-48



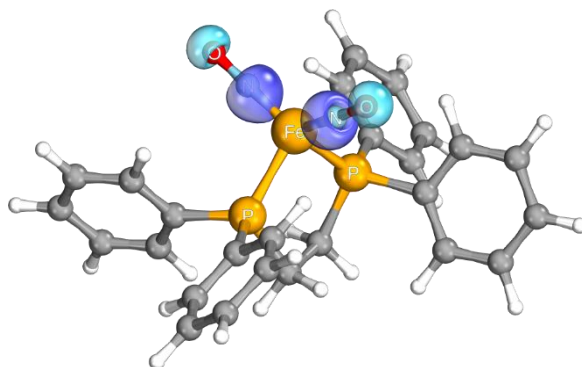
HOMO-51



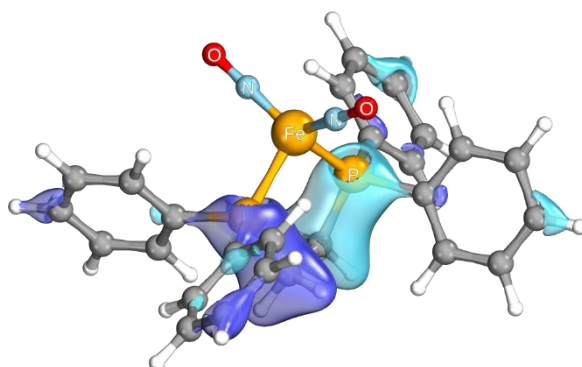
HOMO-65



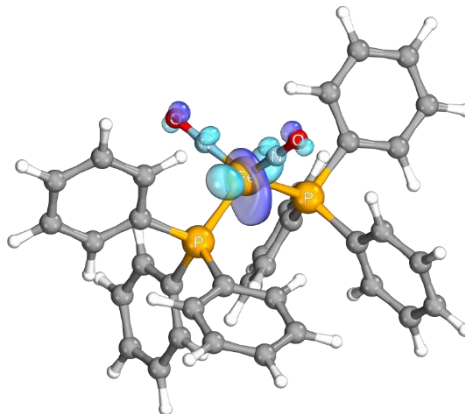
HOMO-67



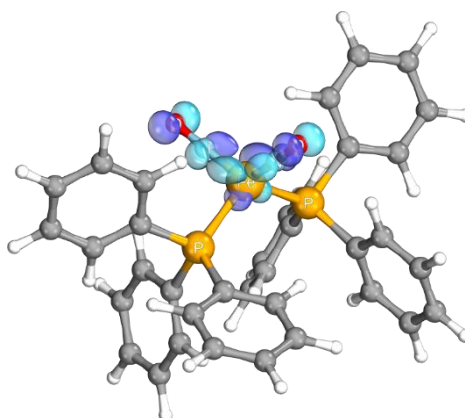
HOMO-68

**Table S5.** Donor orbitals of **2**.

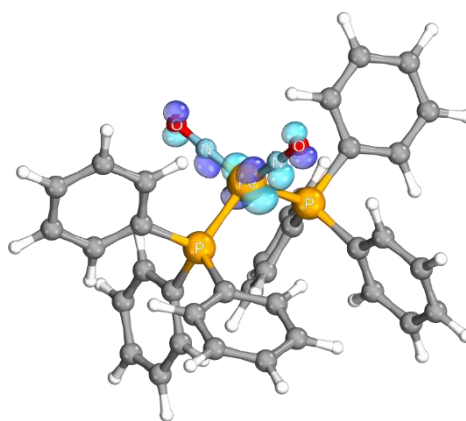
HOMO



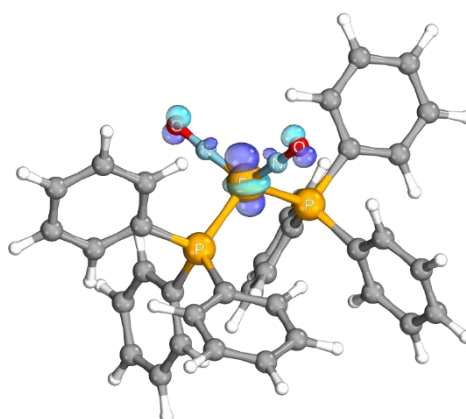
HOMO-1



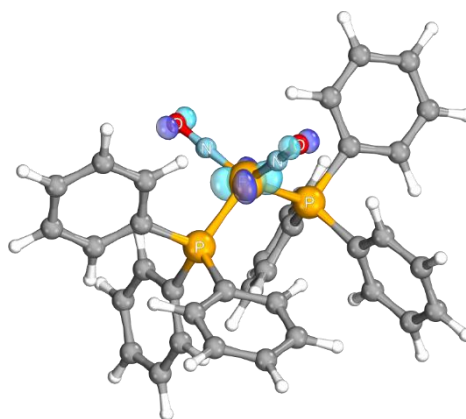
HOMO-2



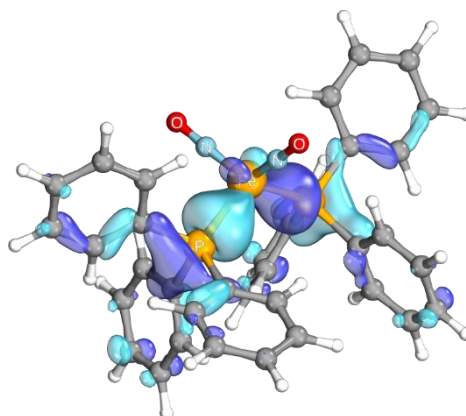
HOMO-3



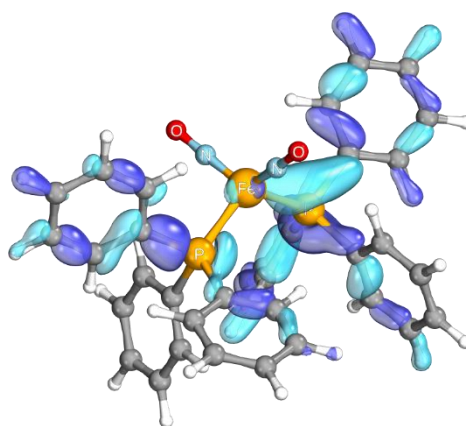
HOMO-4



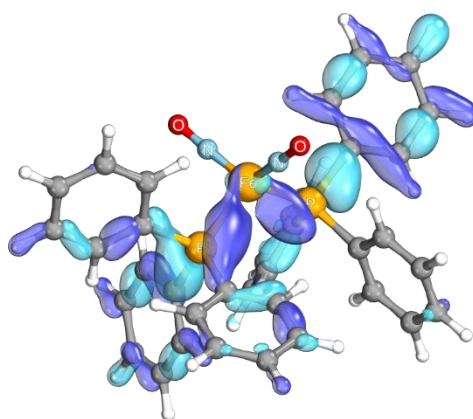
HOMO-17



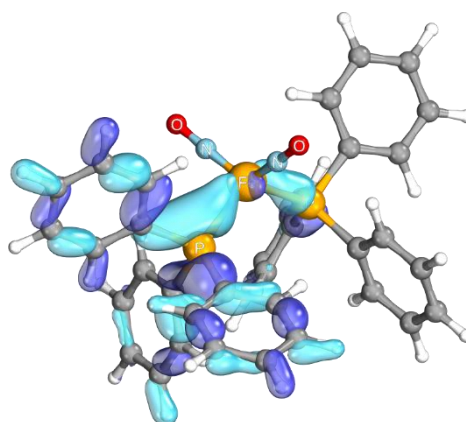
HOMO-18



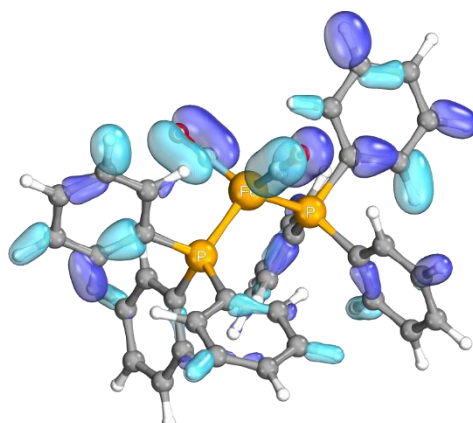
HOMO-19



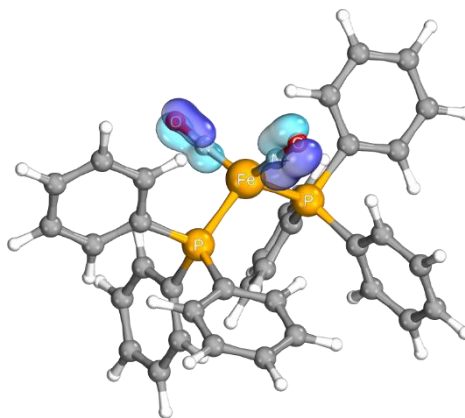
HOMO-20



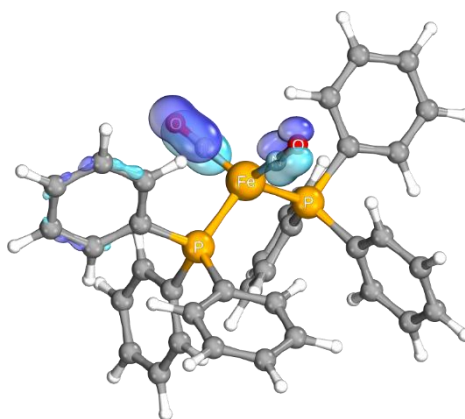
HOMO-47



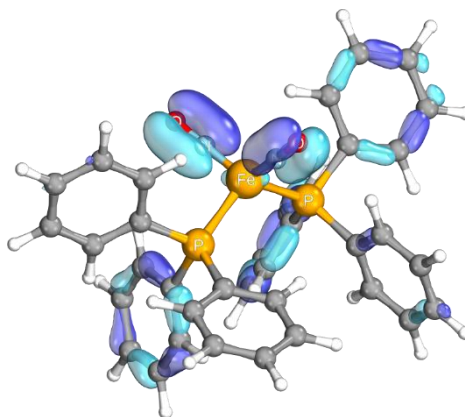
HOMO-48



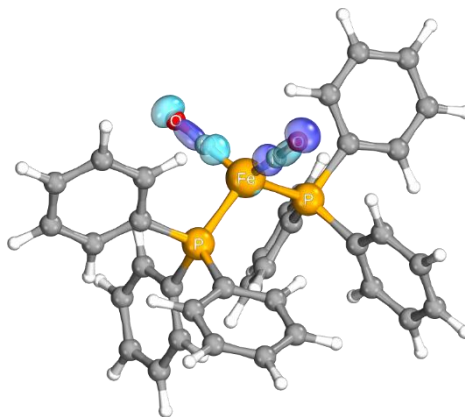
HOMO-53



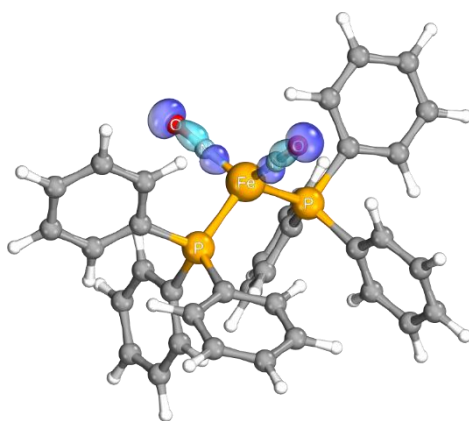
HOMO-56



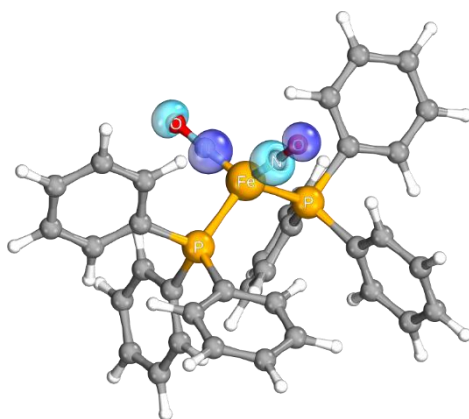
HOMO-63



HOMO-64



HOMO-83



HOMO-86

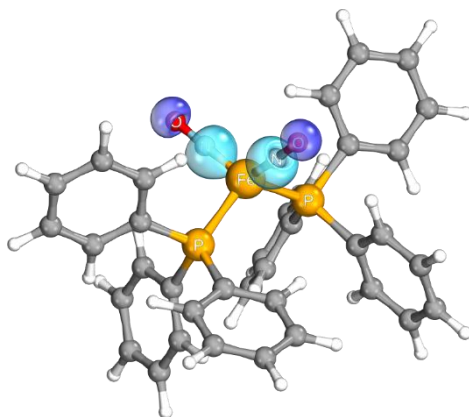
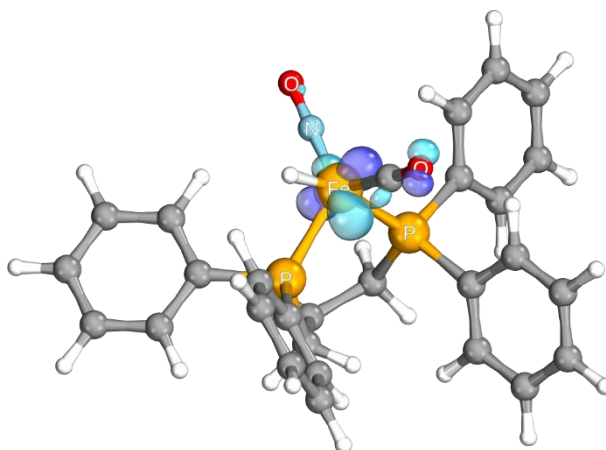
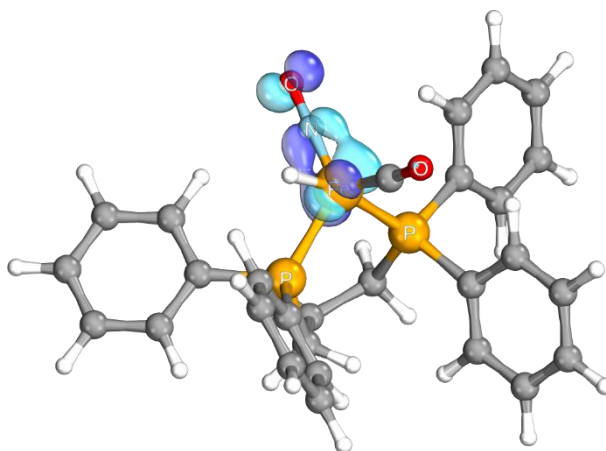


Table S6. Donor orbitals of **1H**.

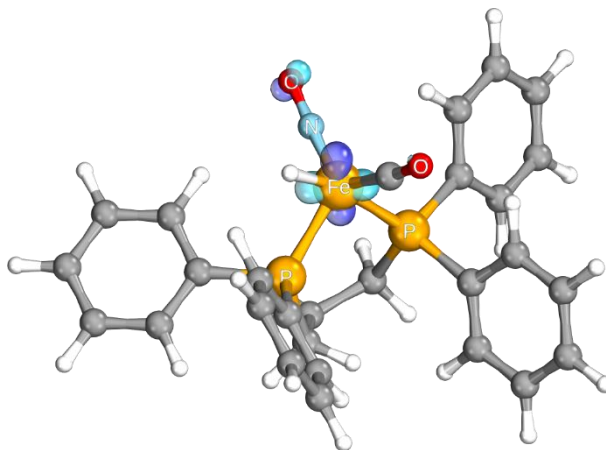
HOMO



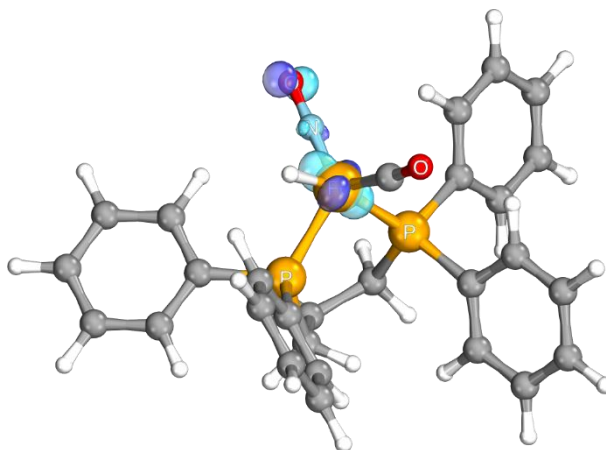
HOMO-1



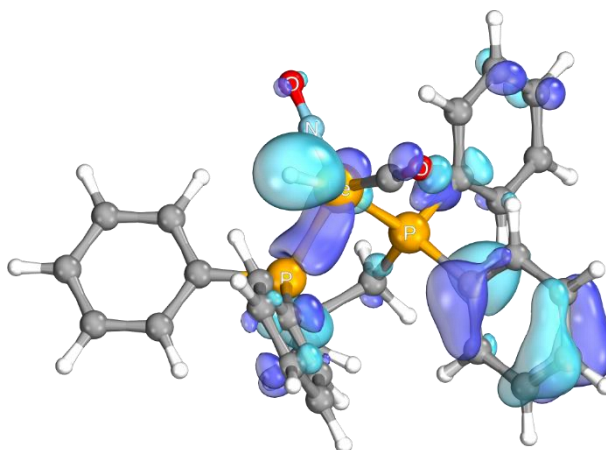
HOMO-2



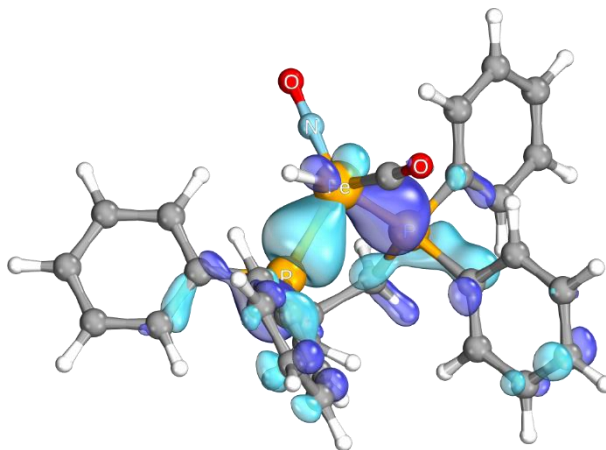
HOMO-3



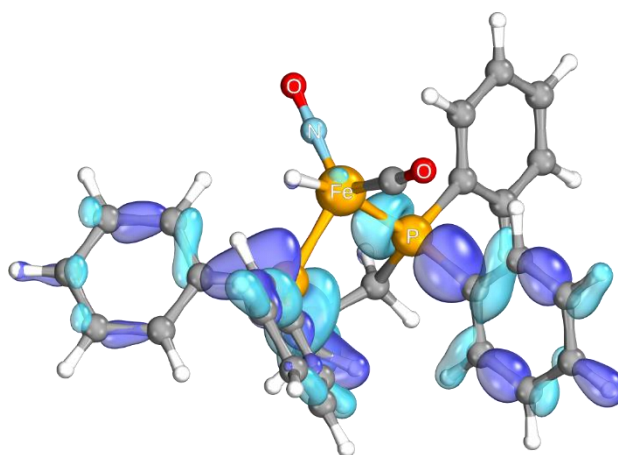
HOMO-12



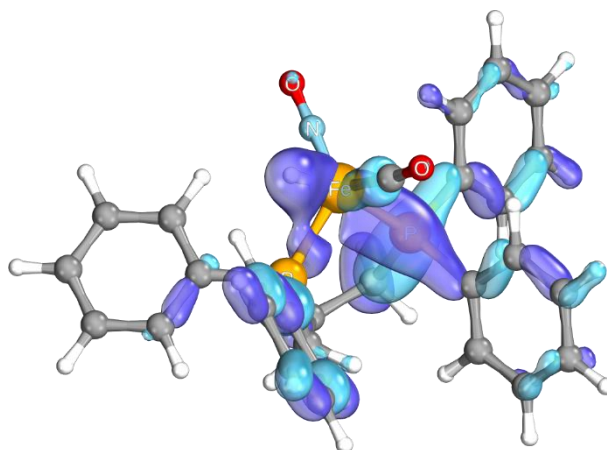
HOMO-13



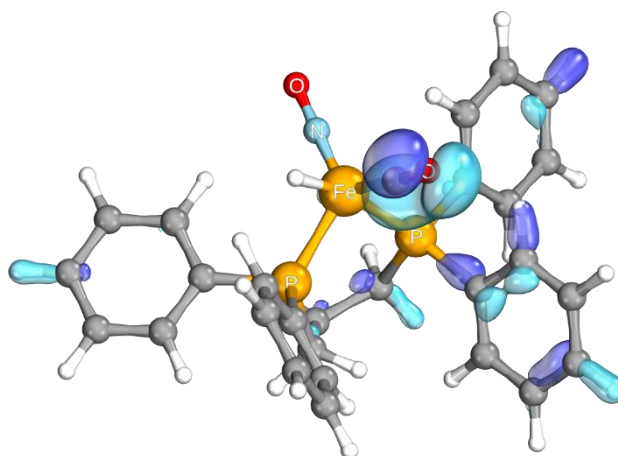
HOMO-15



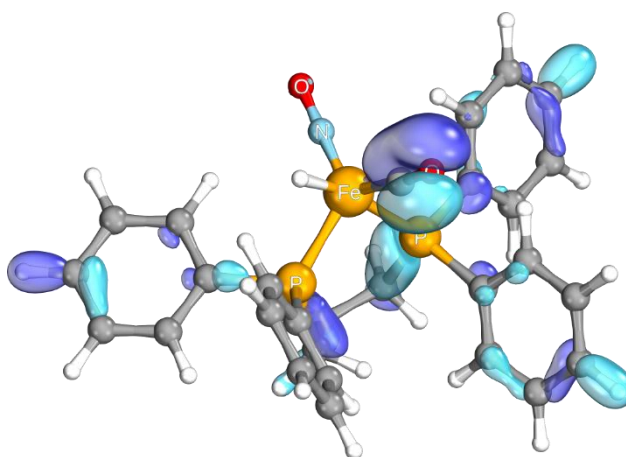
HOMO-17



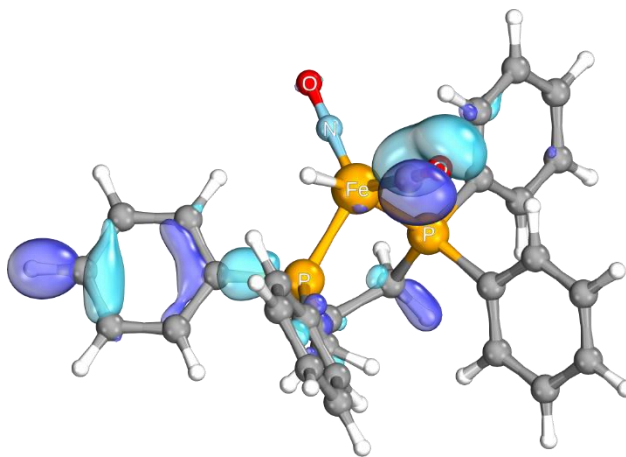
HOMO-31



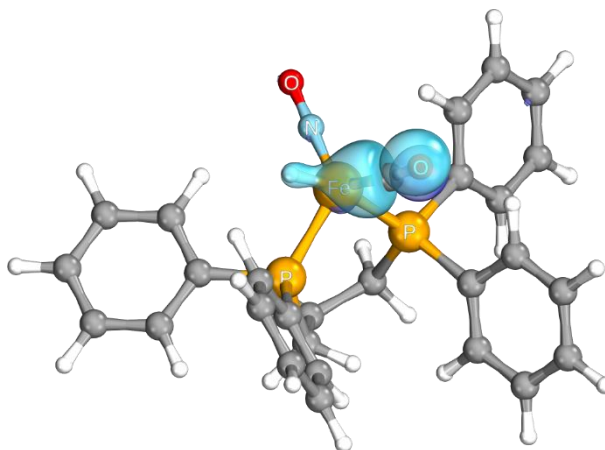
HOMO-32



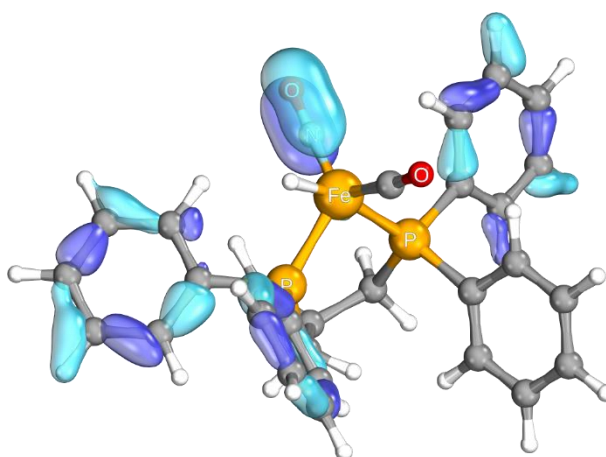
HOMO-33



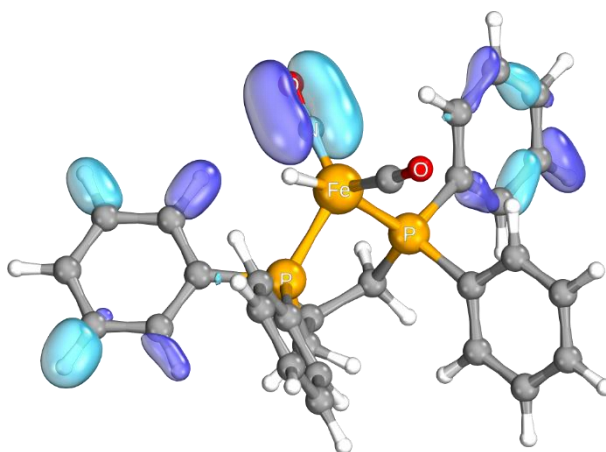
HOMO-34



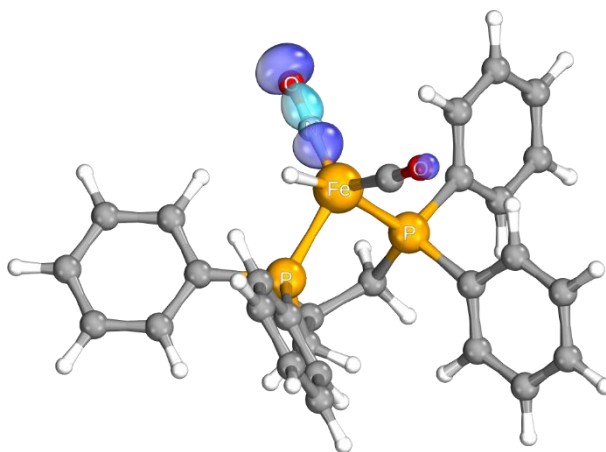
HOMO-45



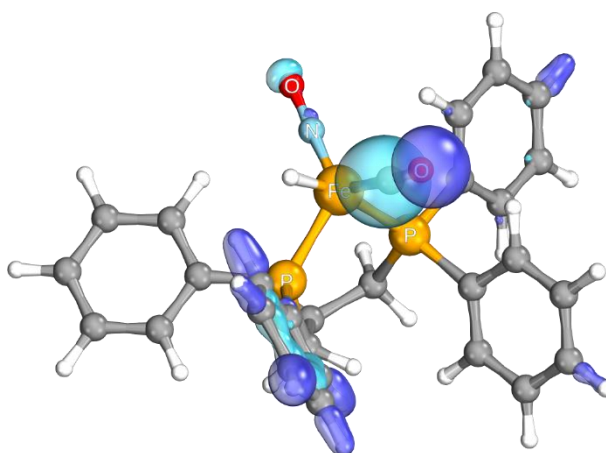
HOMO-49



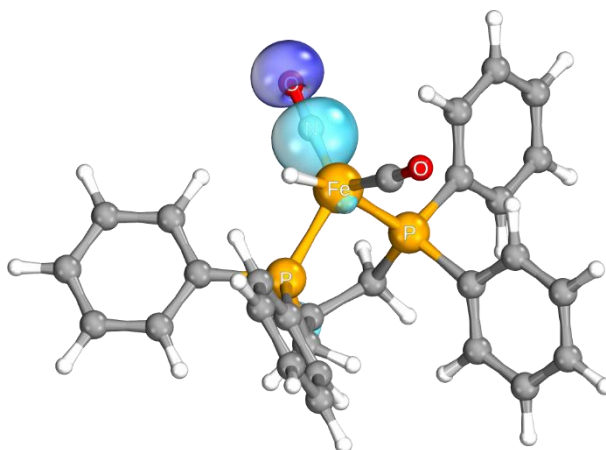
HOMO-53



HOMO-56



HOMO-69



HOMO-70

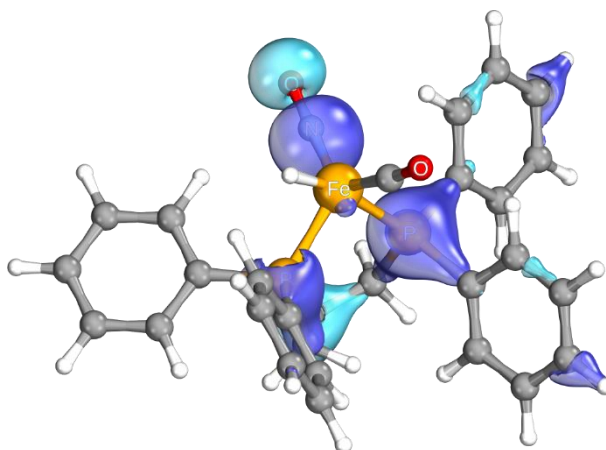
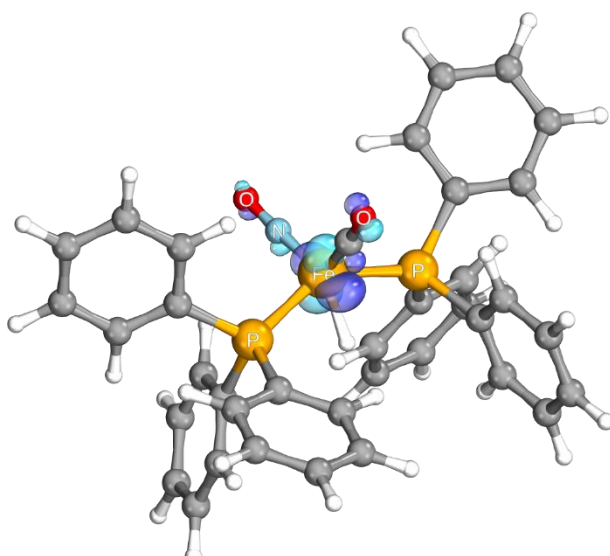
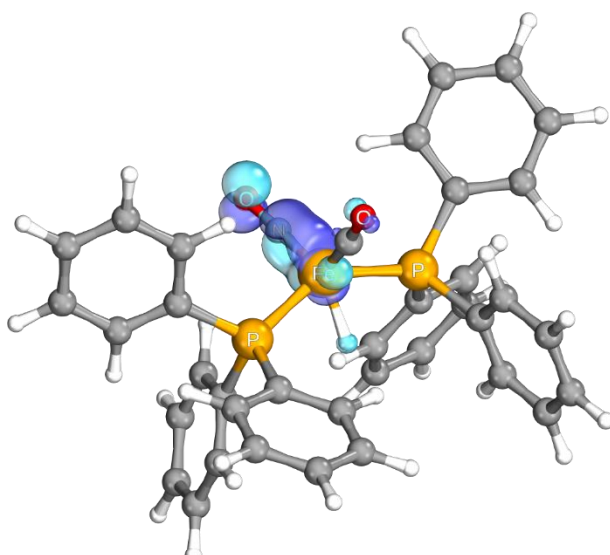


Table S7. Donor orbitals of **2H**.

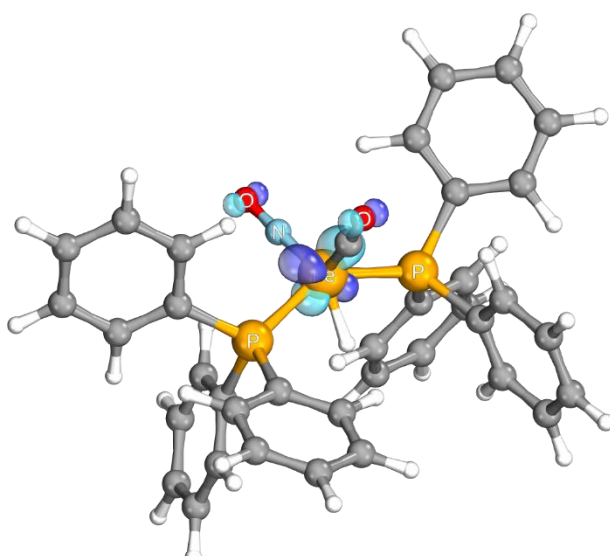
HOMO



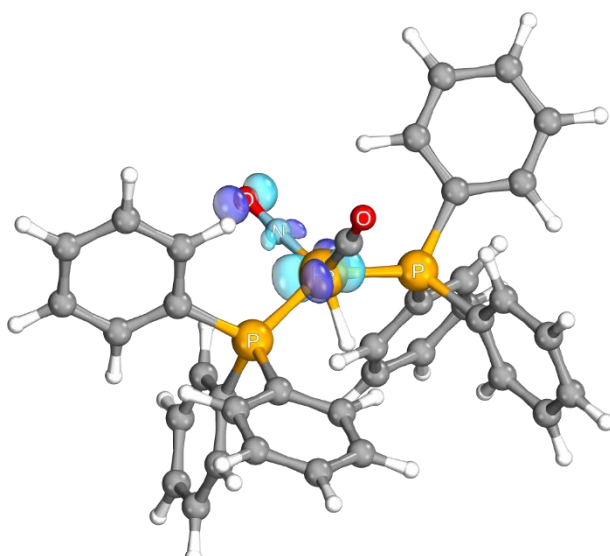
HOMO-1



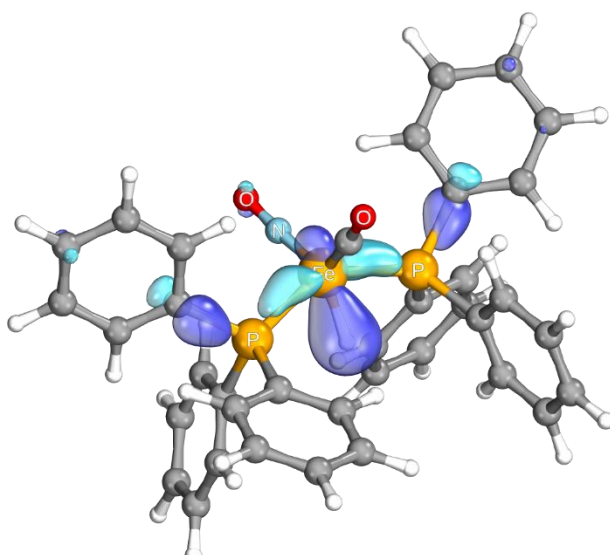
HOMO-2



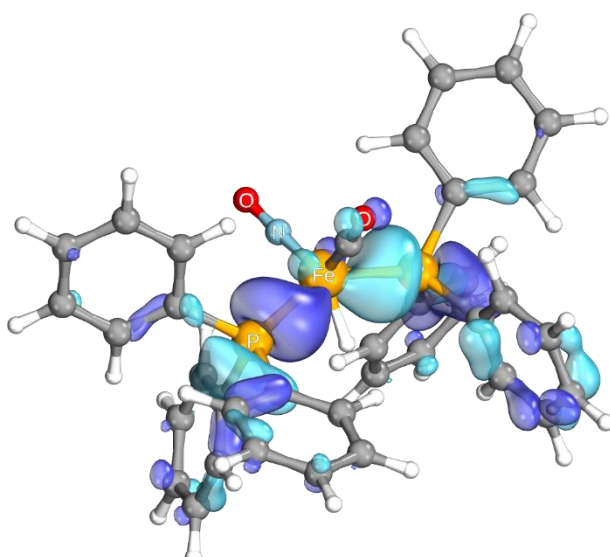
HOMO-3



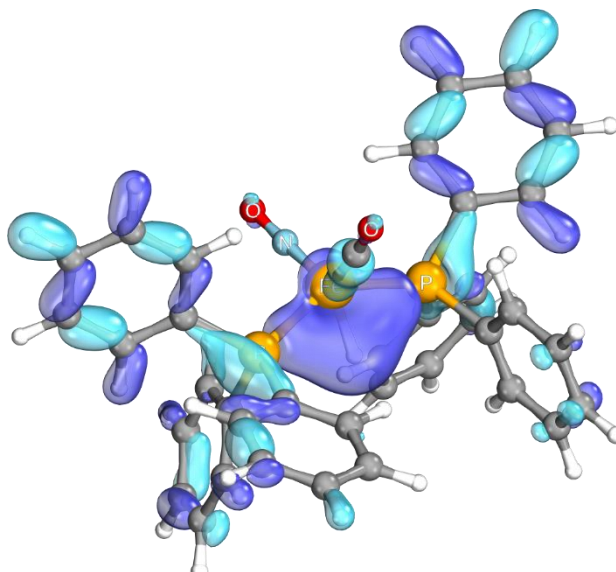
HOMO-16



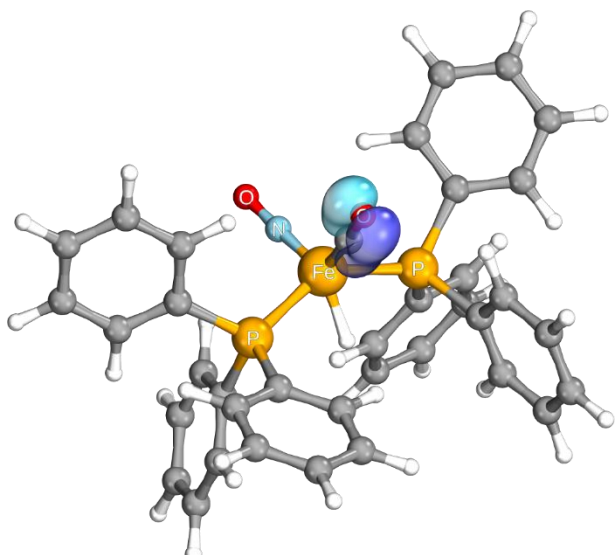
HOMO-17



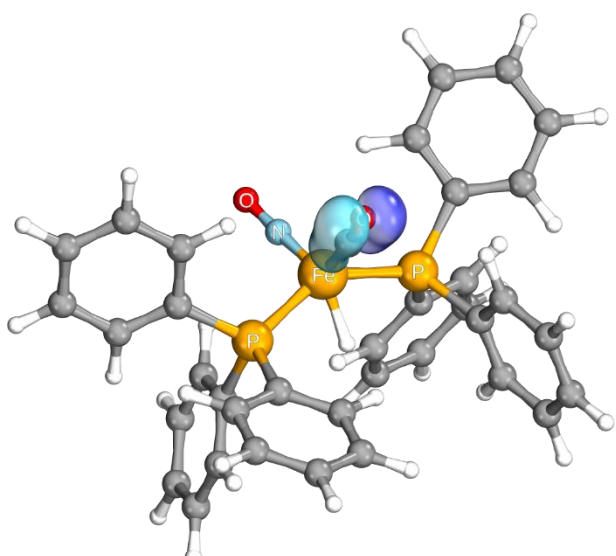
HOMO-28



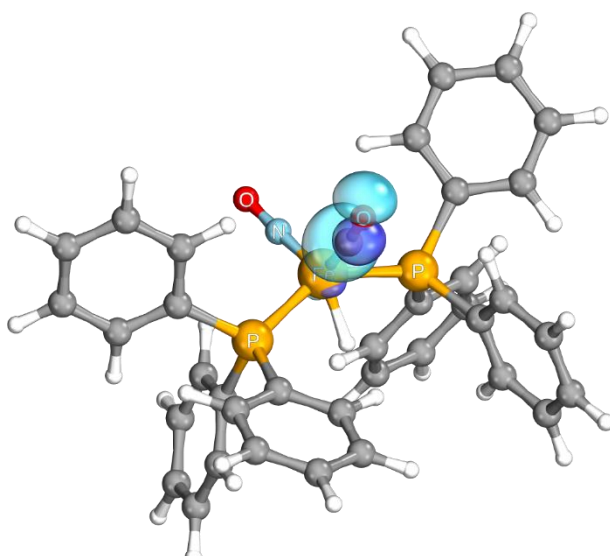
HOMO-37



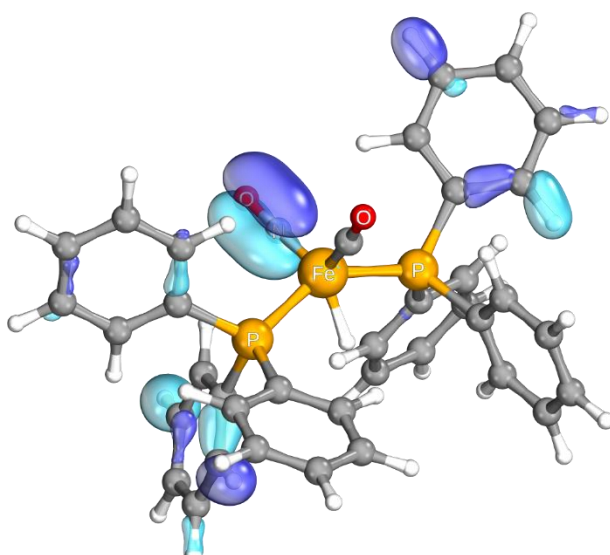
HOMO-38



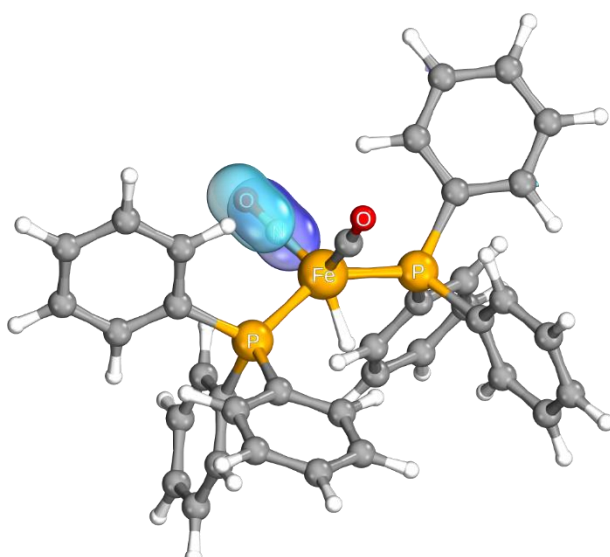
HOMO-39



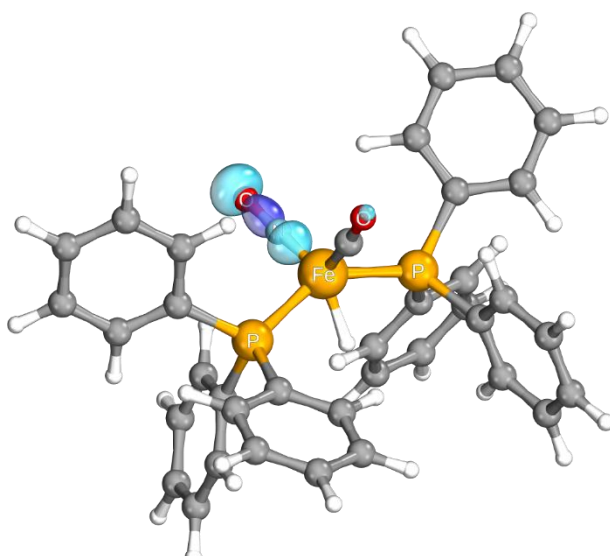
HOMO-50



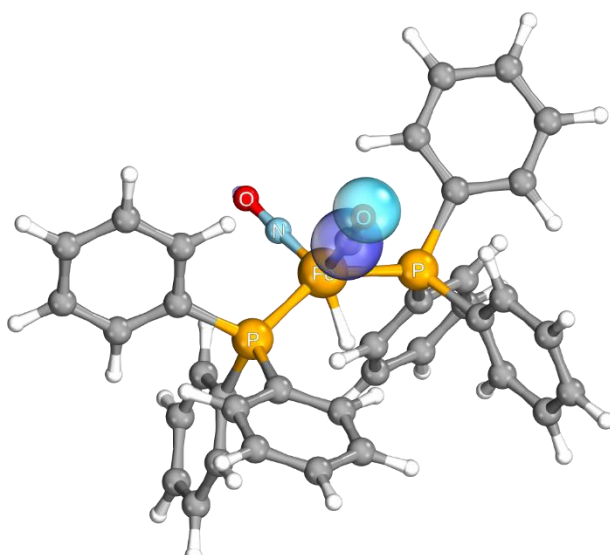
HOMO-51



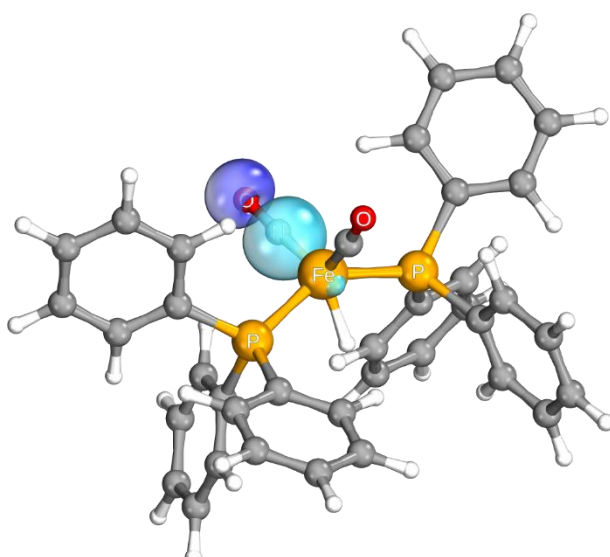
HOMO-65



HOMO-67



HOMO-84



Section S4 - XANES core-excited states and acceptor orbitals**Table S8.** Comparison of all relevant TDDFT XANES core-excited states of **1** and **2** concerning relevant orbital pairs, energies and normalized intensities.

Complexes							
1				2			
Feature	State	Orbital pairs	Energy /eV	Norm. Int. [a] /a.u.	Orbital pairs	Energy /eV	Norm. Int. [a] /a.u.
A	1	0a → LUMO (36 %)	7113.50	0.12	0a → LUMO (74 %)	7113.41	0.18
		0a → LUMO+6 (22 %)			0a → LUMO+1 (35 %)		
	2	0a → LUMO+10 (25 %)	7113.71	0.21		7113.61	0.17
		0a → LUMO (20 %)			0a → LUMO+2 (49 %)		
	3	0a → LUMO+3 (34 %)	7113.72	0.53	0a → LUMO+5 (23 %)	7113.70	0.89
		0a → LUMO+6 (43 %)			0a → LUMO+7 (40 %)		
	4	0a → LUMO+10 (20 %)	7113.84	0.10	0a → LUMO+8 (40 %)	7113.78	0.20
B	5	0a → LUMO+1 (79 %)	7115.12	0.03	0a → LUMO+1 (36 %)	7115.21	0.12

	0a → LUMO+2			0a → LUMO+2		
	(45 %)			(42 %)		
6	0a → LUMO+3	7115.18	0.25	0a → LUMO+3	7115.30	0.01
	(30 %)			(31 %)		
	0a → LUMO			0a → LUMO+5		
	(23 %)			(35 %)		
7	0a → LUMO+2	7115.32	0.26		7115.33	0.11
	(23 %)					
	0a → LUMO+8					
	(32 %)					
8	0a → LUMO+4	7115.41	0.54	0a → LUMO+4	7115.38	0.09
	(76 %)			(49 %)		
9	0a → LUMO+5	7115.53	0.07	0a → LUMO+7	7115.49	0.15
	(74 %)			(38 %)		
10	0a → LUMO+7	7115.62	0.05	0a → LUMO+9	7115.61	0.45
	(80 %)			(51 %)		
	0a → LUMO+8			0a → LUMO+6		
	(29 %)			(22 %)		
11	0a → LUMO+10	7115.84	0.19	0a → LUMO+11	7115.68	0.86
	(28 %)			(23 %)		
	0a → LUMO+11					
	(30 %)					
	0a → LUMO+9			0a → LUMO+10		
12	(78 %)	7115.87	0.10	(31 %)	7115.79	0.70
				0a → LUMO+11		

		(20 %)		
		0a → LUMO+10	7115.90	0.33
13		(57 %)		
		0a → LUMO+12		
		(39 %)		
14		0a → LUMO+14	7116.03	0.08
		(39 %)		
		0a → LUMO+13		
		(38 %)		
15		0a → LUMO+14	7116.06	0.05
		(24 %)		
		0a → LUMO+15		
16		(91 %)	7116.13	0.01

^[a] normalized to 1 (all values were divided by the overall highest value).

Table S9. Comparison of all relevant TDDFT XANES core-excited states of **1H** and **2H** concerning relevant orbital pairs, energies and normalized intensities.

Complexes							
1H				2H			
Feature	State	Orbital pairs	Energy /eV	Norm. Int. [a] /a.u.	Orbital pairs	Energy /eV	Norm. Int. [a] /a.u.
A	1	0a → LUMO (53 %)	7113.47	0.39	0a → LUMO (46 %)	7113.60	0.33

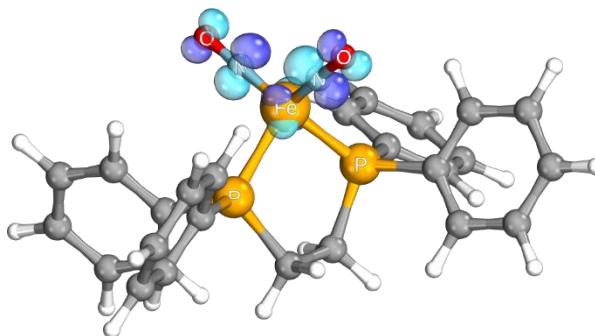
A (Hydride)	2	0a → LUMO+1 (26 %)	7113.63	0.63	0a → LUMO (27 %)	7113.62	0.30
		0a → LUMO+4 (21 %)			0a → LUMO+1 (20 %)		
	3	0a → LUMO+7 (46 %)	7114.03	0.62	0a → LUMO +14 (20 %)	7113.86	0.35
		0a → LUMO+10 (48 %)					
	4	0a → LUMO (24 %)	7115.02	0.29	0a → LUMO+1 (25 %)	7114.88	0.21
		0a → LUMO+1 (30 %)			0a → LUMO+3 (51 %)		
	5	0a → LUMO+2 (54 %)	7115.14	0.12	0a → LUMO+1 (25 %)	7115.11	0.21
					0a → LUMO+2 (42 %)		
	6	0a → LUMO+1 (23 %)	7115.24	0.14	LUMO+4 (66 %)	7115.24	0.08
		0a → LUMO+3 (56 %)			LUMO+5 (25 %)		
B	7	0a → LUMO+5 (37 %)	7115.43	0.16	LUMO+5 (45 %)	7115.30	0.93
		0a → LUMO+6 (24 %)					
	8	0a → LUMO+4 (21 %)	7115.47	0.17	LUMO+6 (17 %)	7115.41	0.09
		0a → LUMO+5 (30 %)					

9	0a → LUMO+7 (27 %)	7115.53	1.00	LUMO+6 (65 %)	7115.43	0.44
	LUMO+11 (29 %)					
10	0a → LUMO+6 (59 %)	7115.7	0.29	0a → LUMO+7 (65 %)	7115.52	0.33
	0a → LUMO+10 (20 %)					
11	0a → LUMO+8 (52 %)	7115.82	0.09	0a → LUMO+8 (40 %)	7115.62	0.88
	0a → LUMO+11 (22 %)					
12	0a → LUMO+9 (75 %)	7115.86	0.33	0a → LUMO+10 (41 %)	7115.77	0.22
13	0a → LUMO+12 (54 %)	7116.06	0.16	0a → LUMO+14 (22 %)	7115.83	0.19
14				0a → LUMO+9 (55 %)	7115.85	0.05
15				0a → LUMO+11 (77 %)	7115.93	0.06
				0a → LUMO+12 (20 %)		
16				0a → LUMO+13 (67 %)	7116.01	0.03
				0a → LUMO+15 (22 %)		
17				0a → LUMO+10 (33 %)	7117.40	0.10
				0a → LUMO+16 (53 %)		

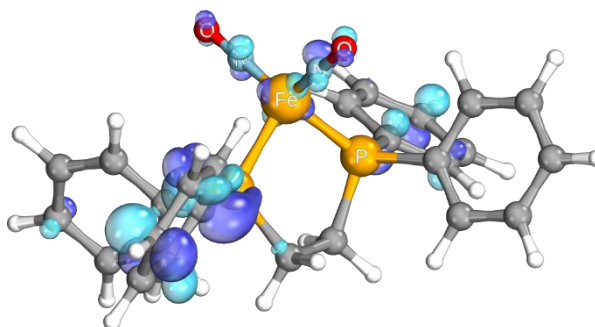
^[a] normalized to 1 (all values were divided by the overall highest value).

Table S10. Acceptor orbitals of **1**.

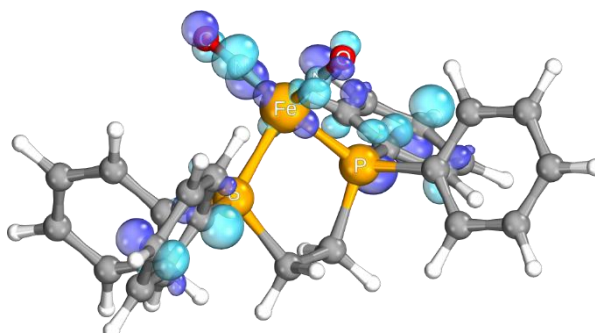
LUMO



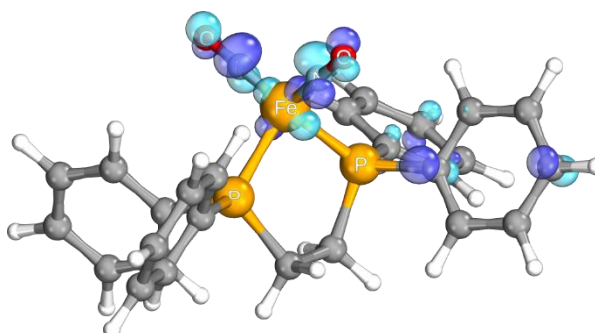
LUMO+1



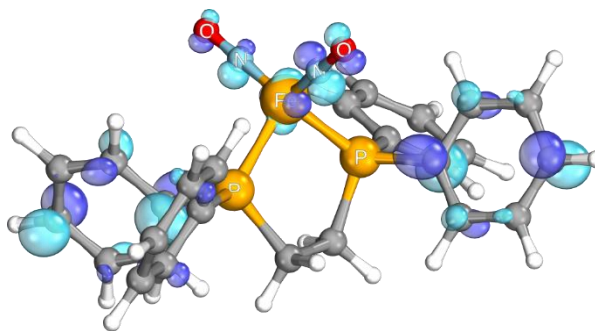
LUMO+2



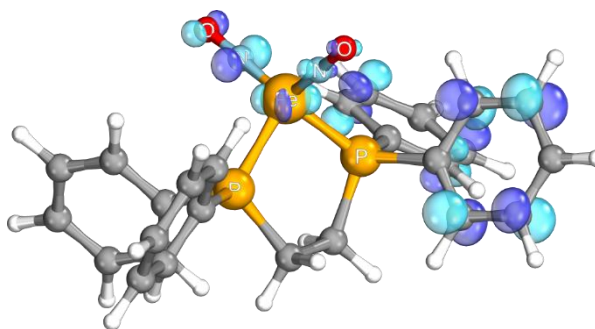
LUMO+3



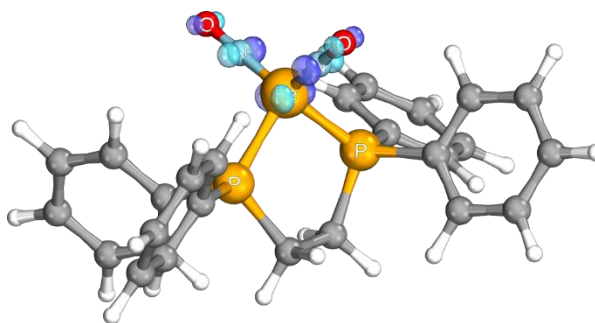
LUMO+4



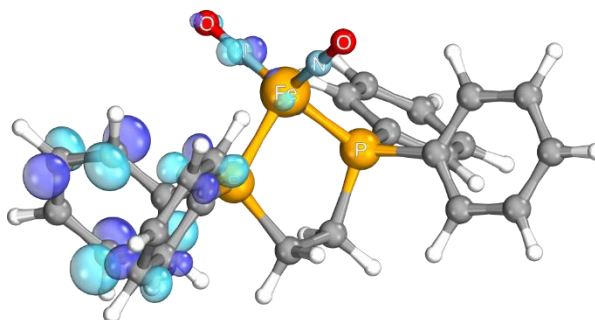
LUMO+5



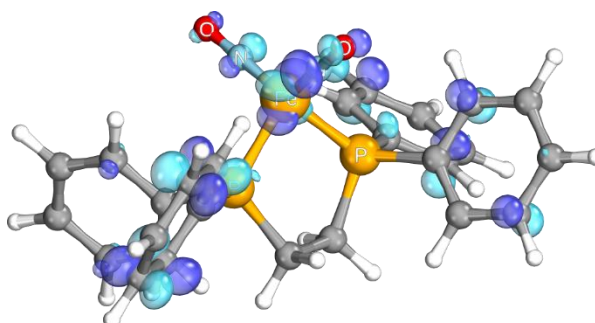
LUMO+6



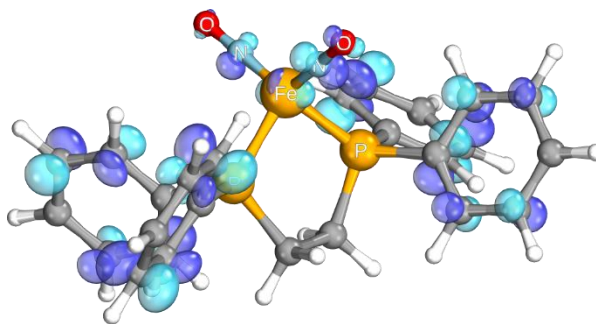
LUMO+7



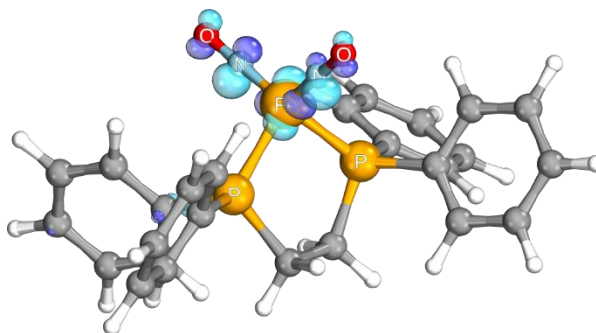
LUMO+8



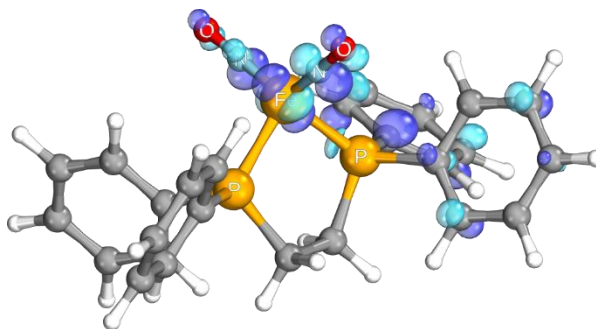
LUMO+9



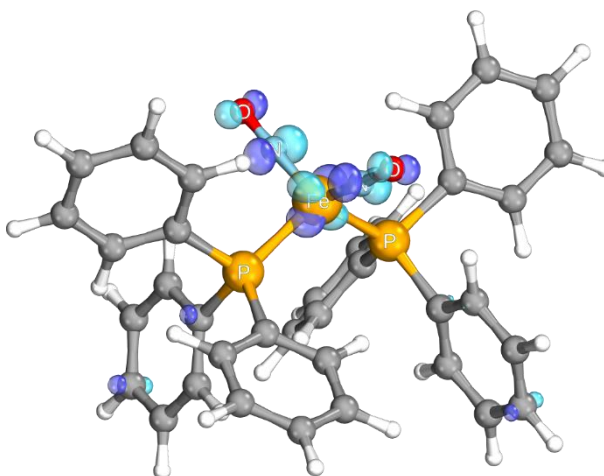
LUMO+10



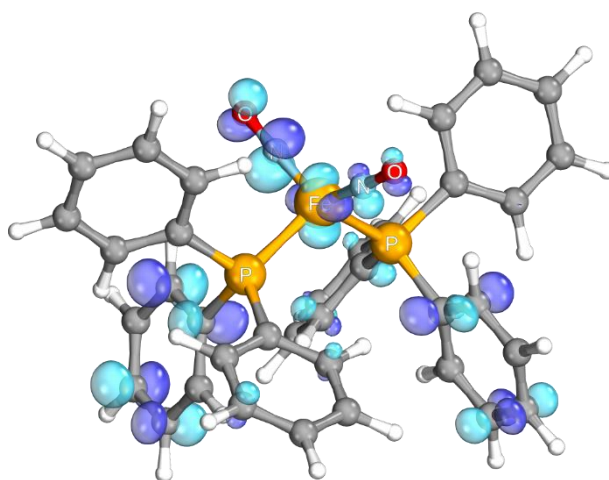
LUMO+11

**Table S11.** Acceptor orbitals of **2**.

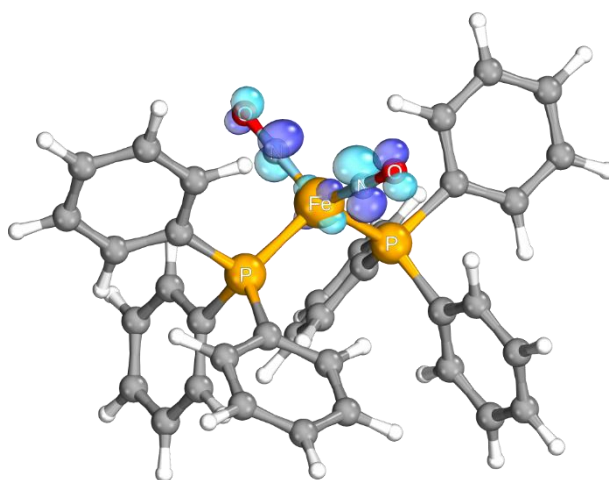
LUMO



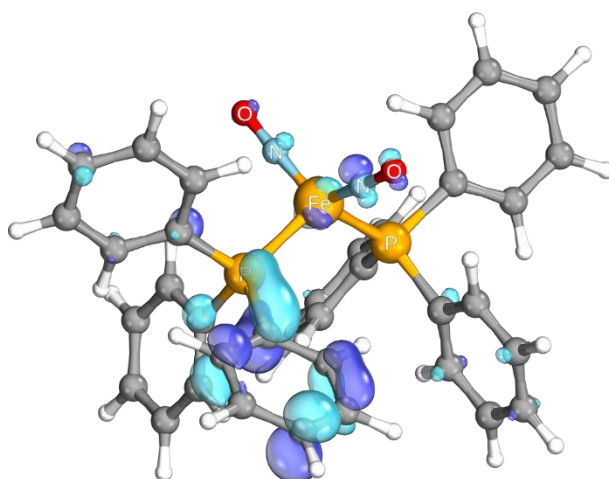
LUMO+1



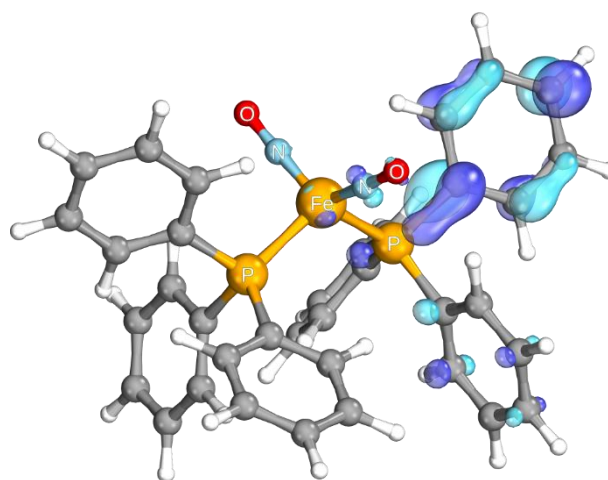
LUMO+2



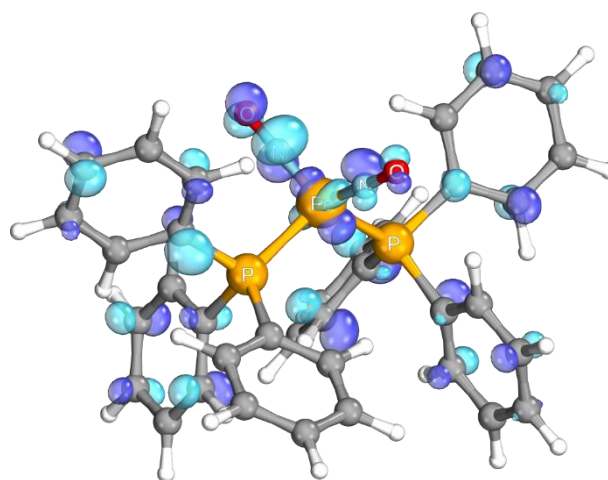
LUMO+3



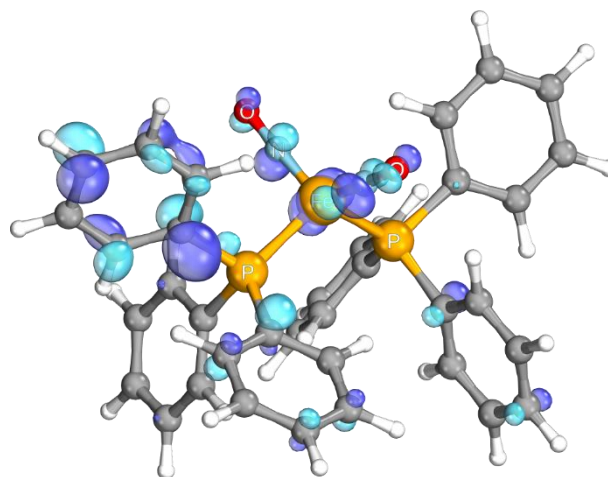
LUMO+4



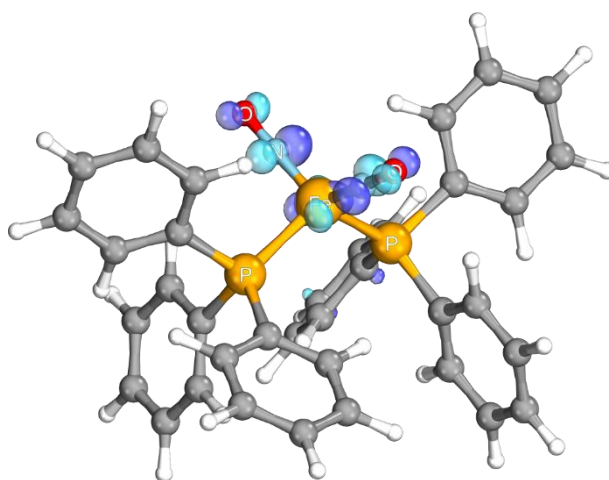
LUMO+5



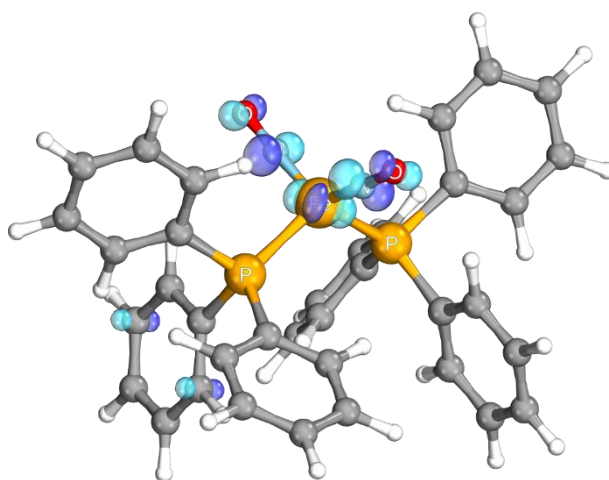
LUMO+6



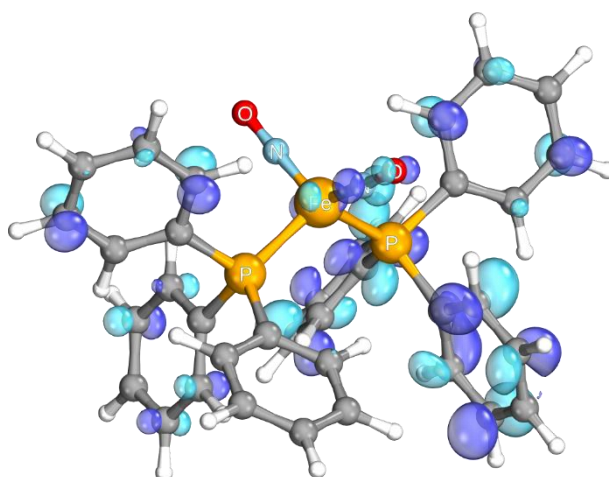
LUMO+7



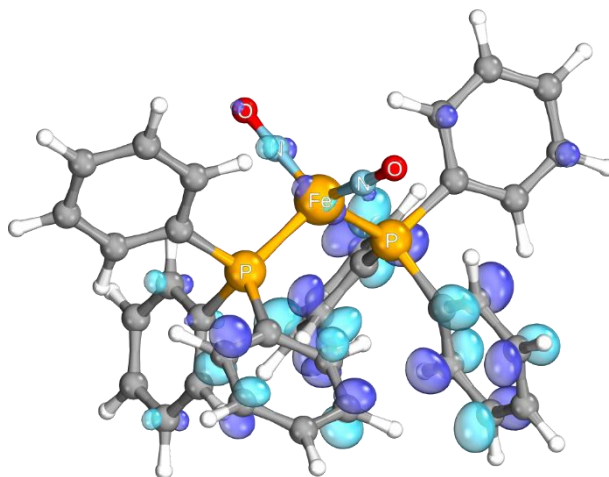
LUMO+8



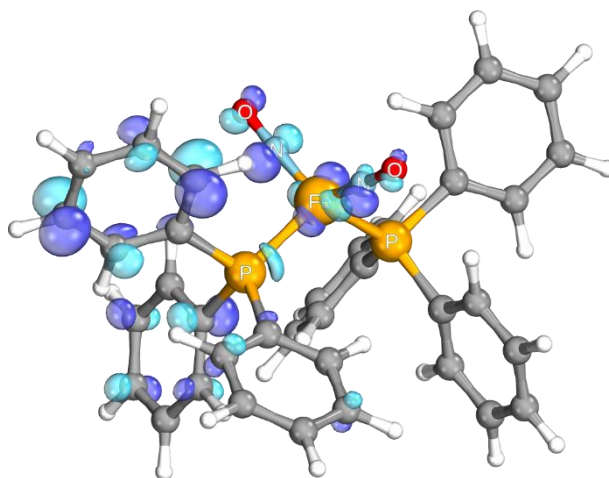
LUMO+9



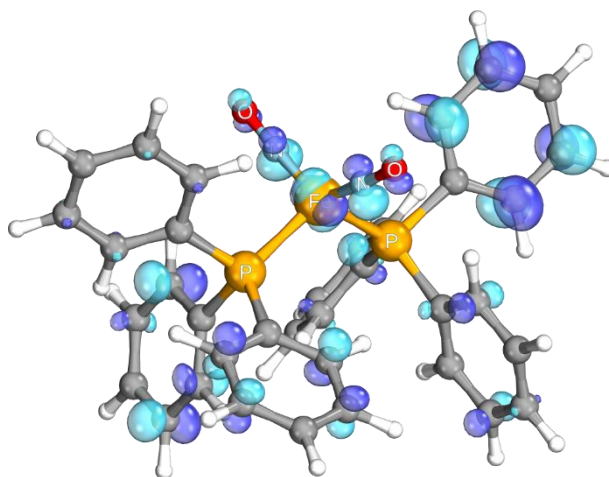
LUMO+10



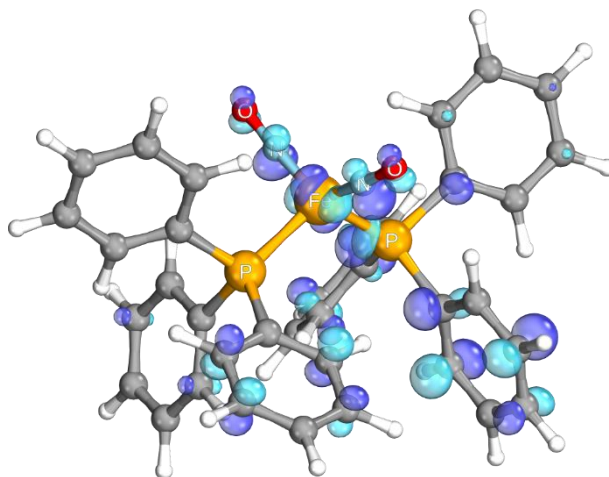
LUMO+11



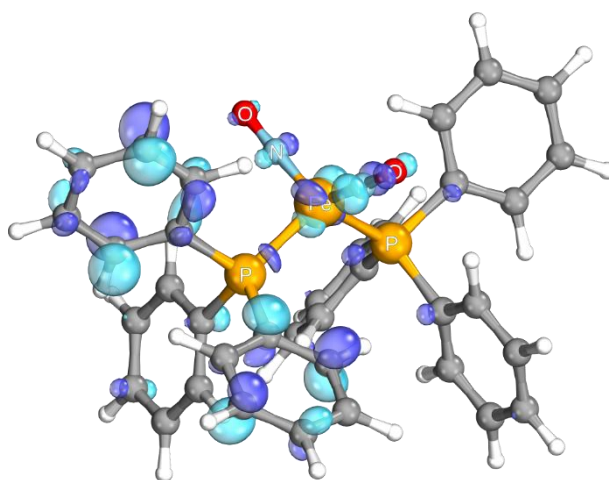
LUMO+12



LUMO+13



LUMO+14



LUMO+15

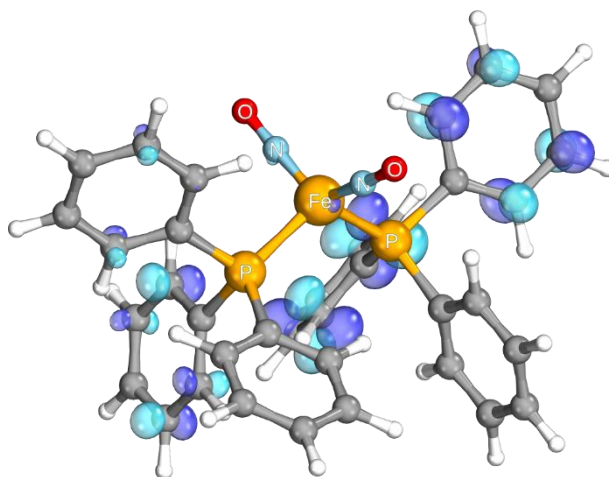
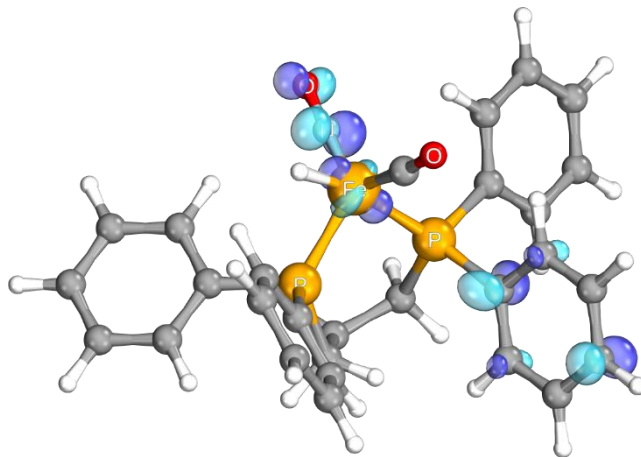
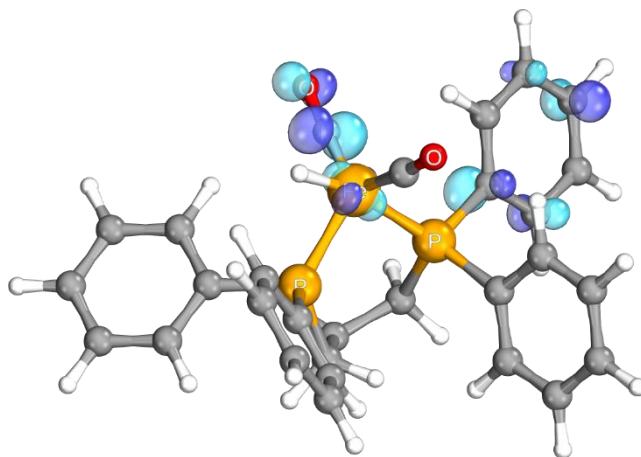


Table S12. Acceptor orbitals of **1H**.

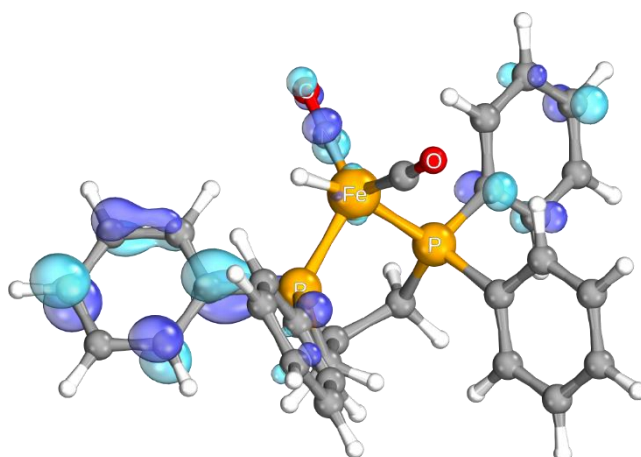
LUMO



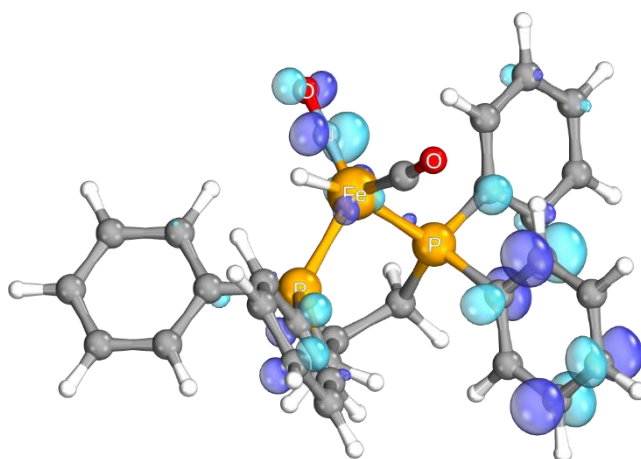
LUMO+1



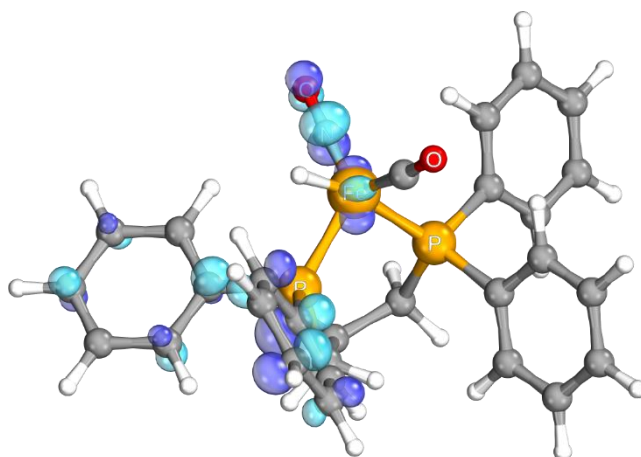
LUMO+2



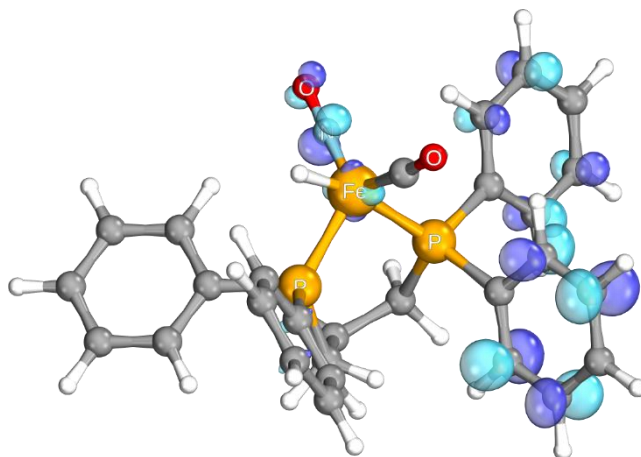
LUMO+3



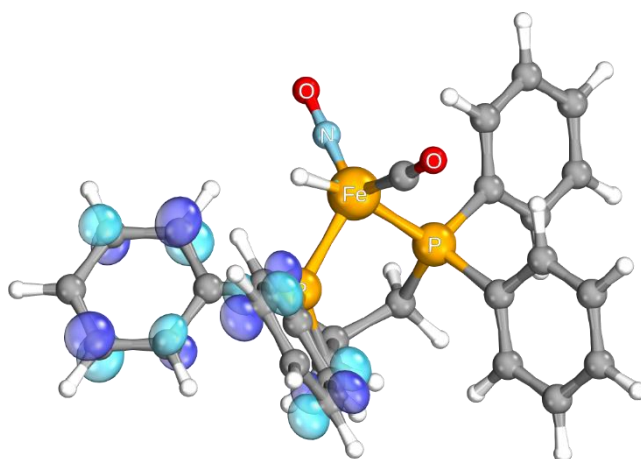
LUMO+4



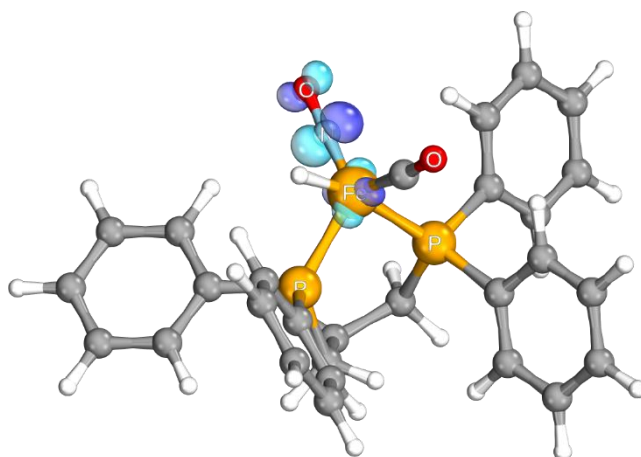
LUMO+5



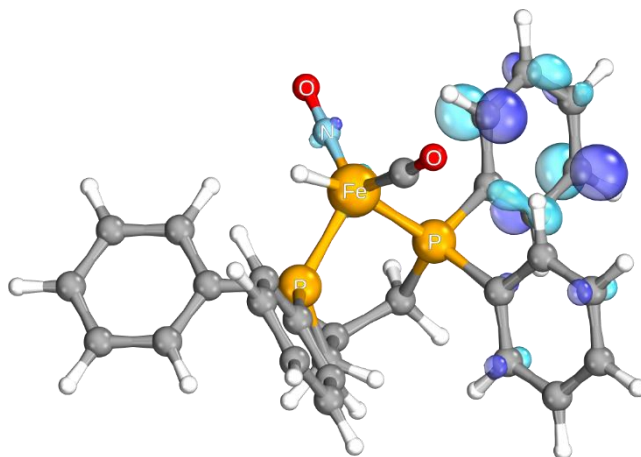
LUMO+6



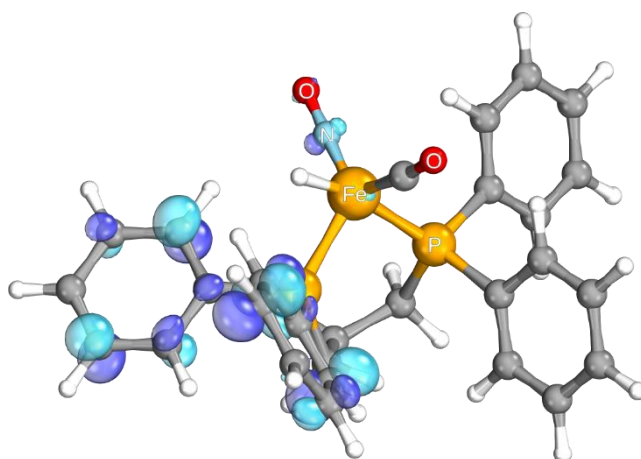
LUMO+7



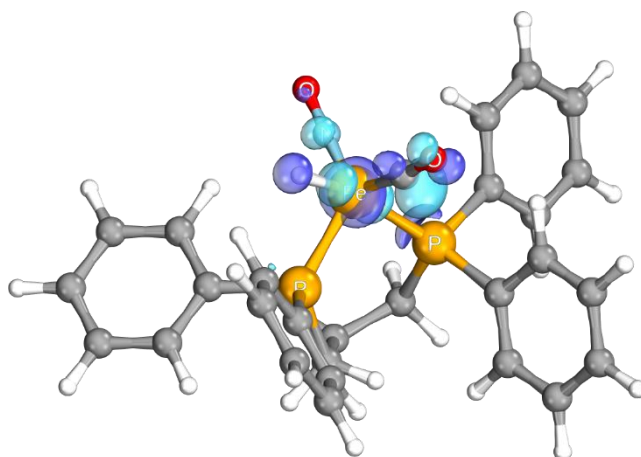
LUMO+8



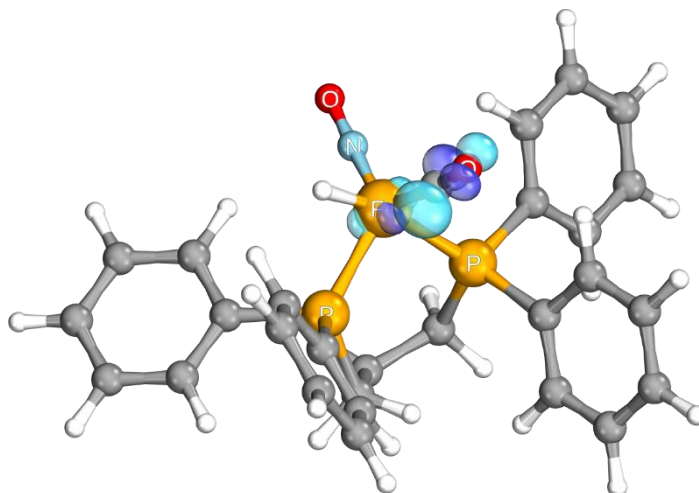
LUMO+9



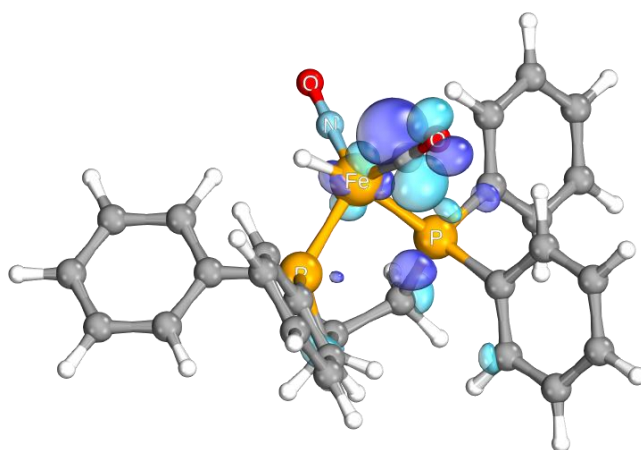
LUMO+10



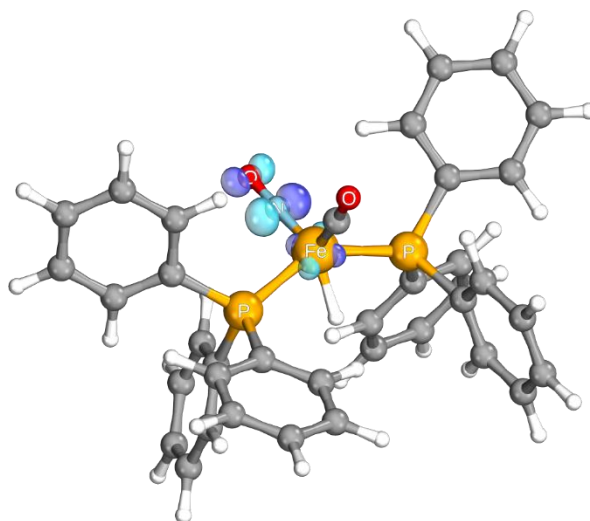
LUMO+11



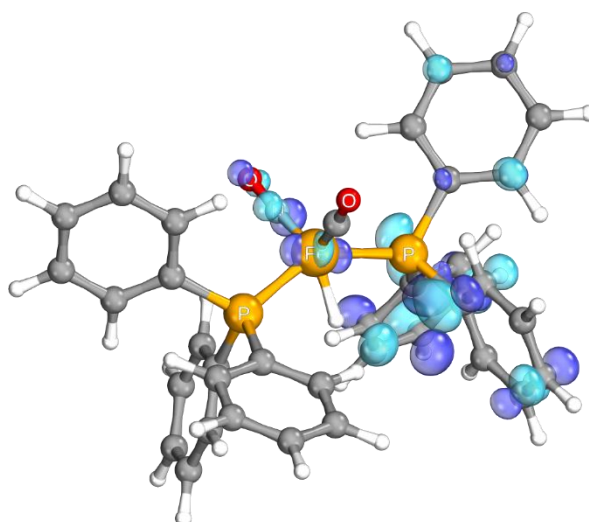
LUMO+12

**Table S13.** Acceptor orbitals of **2H**.

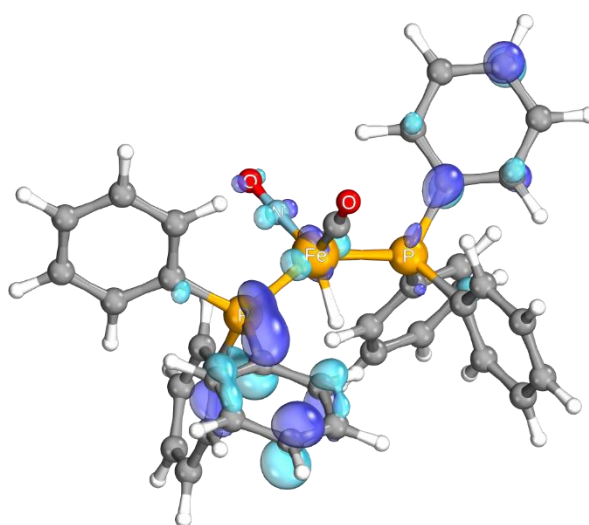
LUMO



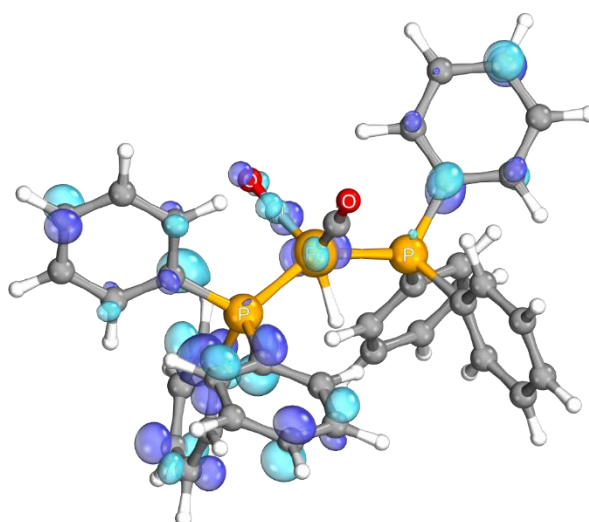
LUMO+1



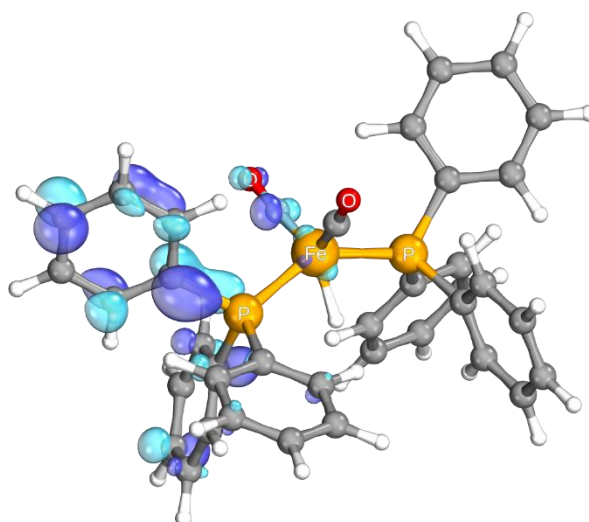
LUMO+2



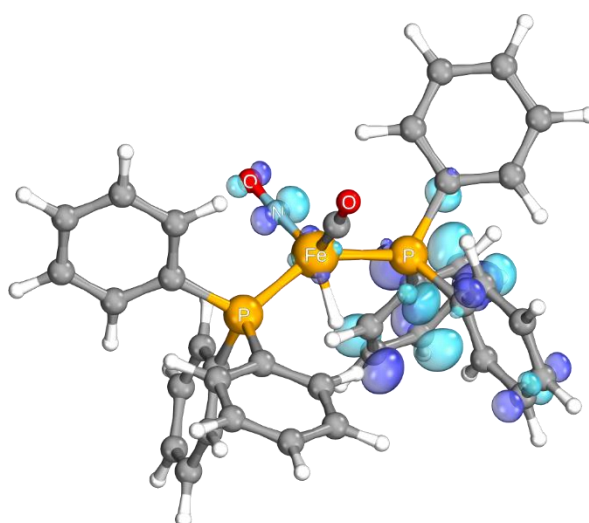
LUMO+3



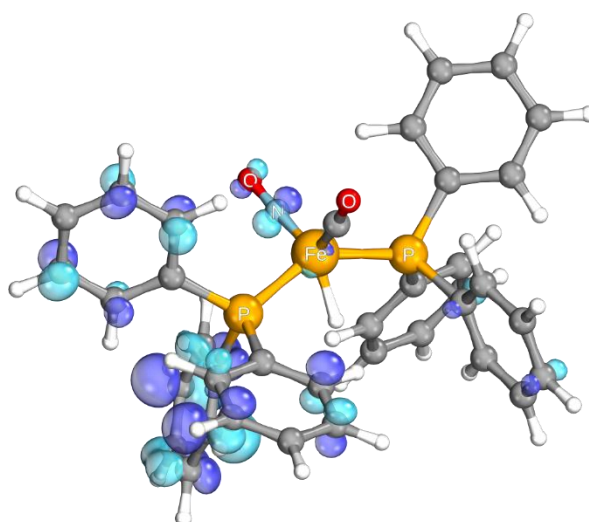
LUMO+4



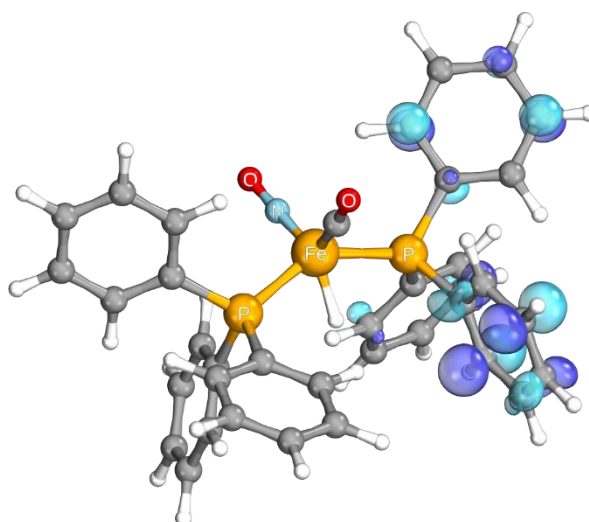
LUMO+5



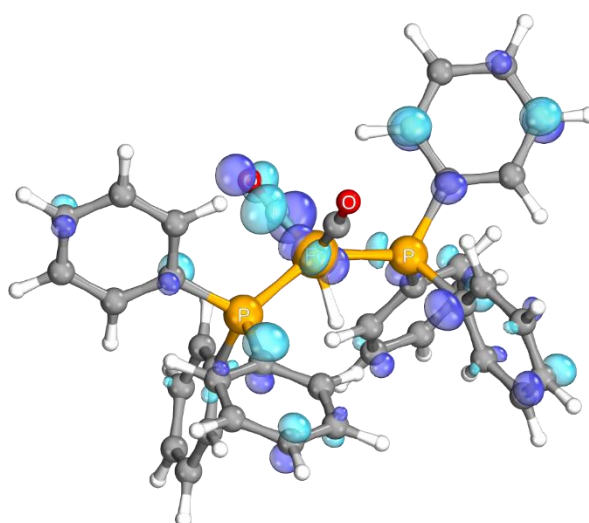
LUMO+6



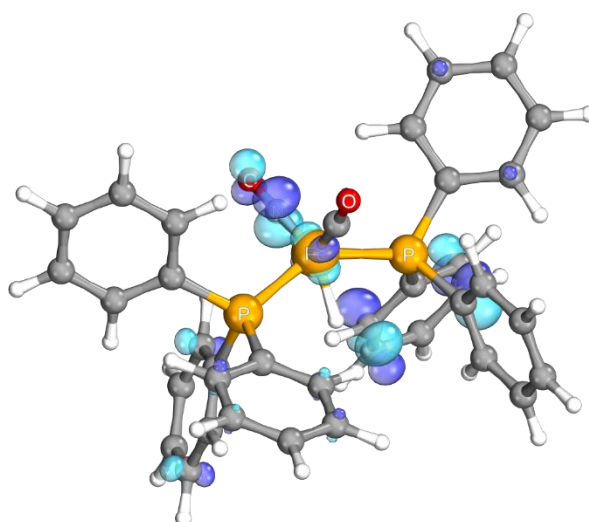
LUMO+7



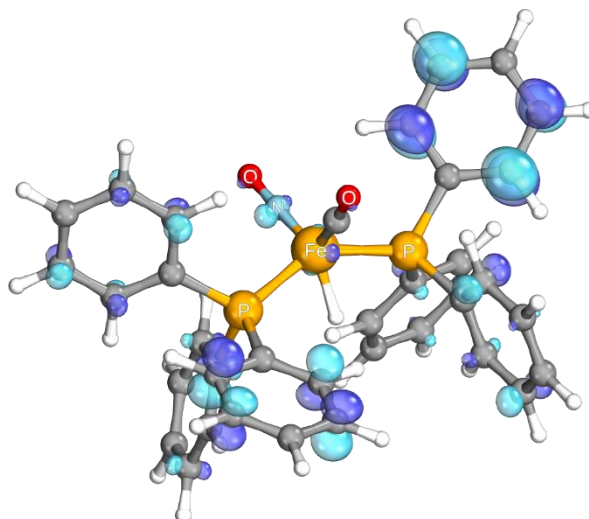
LUMO+8



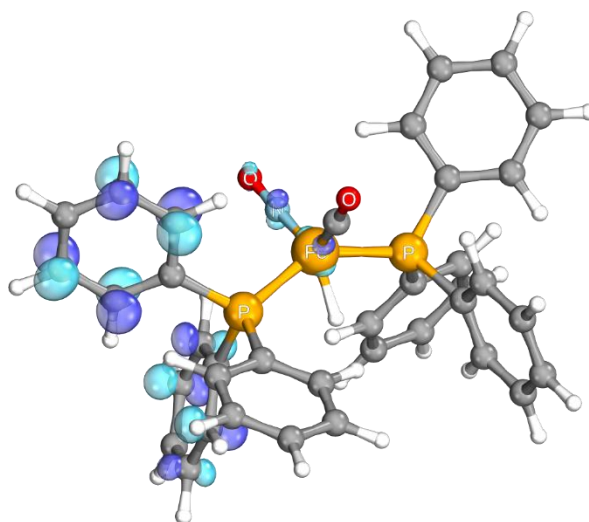
LUMO+9



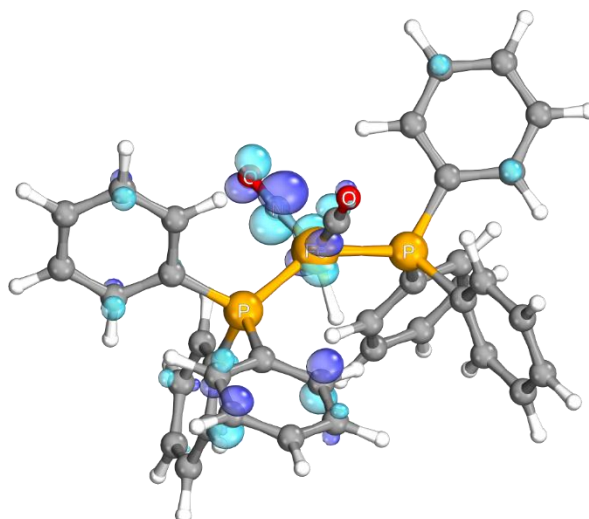
LUMO+10



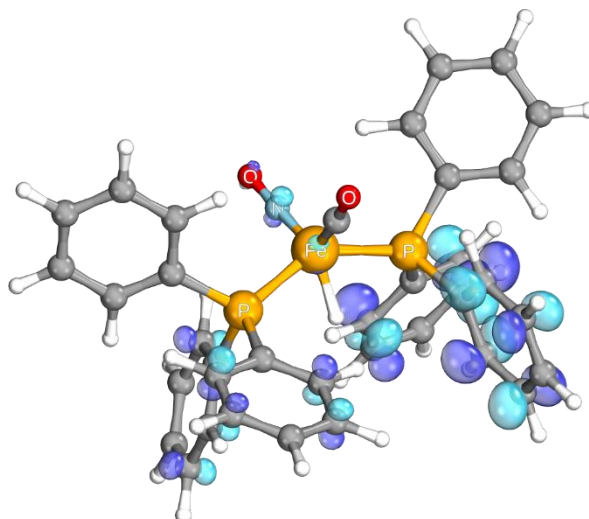
LUMO+11



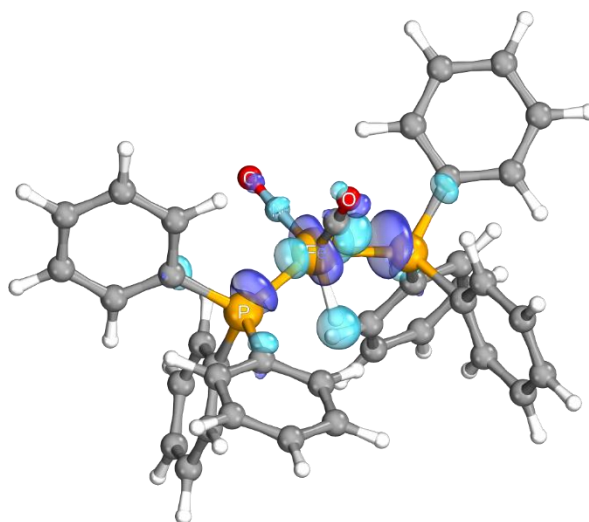
LUMO+12



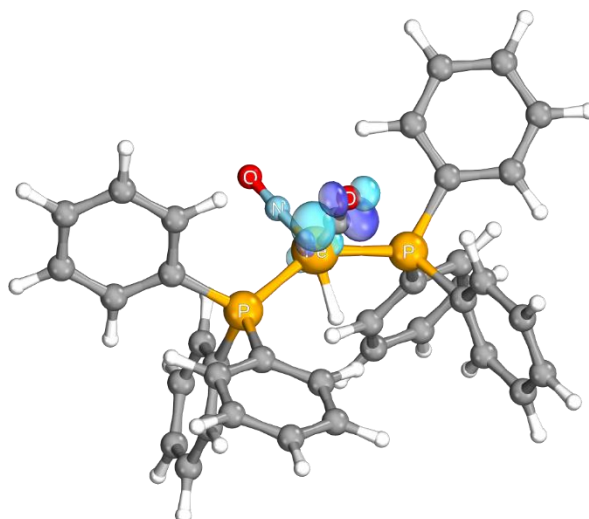
LUMO+13



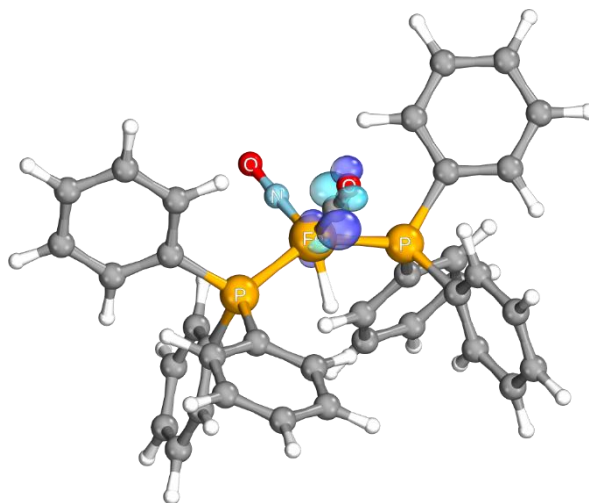
LUMO+14



LUMO+15



LUMO+16



Section S5 - Hydride orbital composition of 1H and 2H**Table S14.** AO populations of orbitals with significant hydride density.

Element / Fragment	Population ^[a] / %				
	1H		2H		
	HOMO-17	LUMO+10	HOMO-28	HOMO-16	LUMO+14
Fe (s, p, d)	16.7	34.1	9.0	35.4	29.5
Fe (p)	2.9	2.7	2.4	1.3	0.5
Fe (d)	13.8	31.2	5.5	34.1	28.6
NO (s, p)	0.5	3.1	0.5	1.4	2.1
CO (s, p)	2.9	15.1	1.7	0.3	5.7
P (s, p, d)	8.6	10.2	10.3	13.0	14.7
P (p)	5.2	4.7	9.6	5.6	7.5
P (d)	3.1	1.7	0.6	6.7	0.8
Ph (s, p)	42.4	12.1	43.8	26.2	29.5
H (s, p)	10.1	6.8	8.8	14.4	5.8
^[a] Population of the given element via Loewdin reduced orbital population analysis. All given values are the sum over all atom orbitals of a given element or fragment.					

Section S6 - XYZ coordinates of all optimized StructuresOptimized Structure of **1**:

57

Fe	-0.24205425010571	-0.17587197602648	0.06890389174928
P	0.35209171215591	-0.54455110665651	2.15934950163762
P	-1.04765037951954	1.75958585482198	0.73226519337858
N	1.16659866221367	-0.02259060814030	-0.76424414572385
N	-1.55148822144044	-1.05030004796810	-0.39807008048686
O	2.17803032259837	0.05540790235943	-1.35843560247648
O	-2.49850588443608	-1.64006854295887	-0.77001877930740
C	-0.18629352759319	-2.04729824527424	3.06795043165888
C	0.44856601772899	-2.45826117626654	4.24563089232075
C	-0.02109368631293	-3.56185667265818	4.94875889614762
C	-1.13106175526819	-4.26474597031323	4.48730727080630
C	-1.76381654827337	-3.86637808062730	3.31458639004548
C	-1.29167974632529	-2.76562361212039	2.60617492666267
C	-2.87485599210052	1.84113608246171	0.87699299104283
C	-3.55672613331817	2.02022002138907	2.08363203788114
C	-4.94968131815528	2.03896817805008	2.11556638984473
C	-5.67879877686674	1.88772442180446	0.94199570534910
C	-5.00911209637016	1.70831626331571	-0.26637582093884
C	-3.62151290612493	1.67617351625916	-0.29710262287845
C	-0.66702756974043	3.31227411835417	-0.16722178712994
C	-1.27145048787743	4.52166722654922	0.19589253942286
C	-0.94304215178657	5.69790938181815	-0.46607990032089
C	-0.01387246663069	5.67808656237457	-1.50449086040498

C	0.58118641560455	4.47886659265694	-1.87928755575100
C	0.25551435512988	3.29927613140379	-1.21453793365752
C	2.15928243122258	-0.51900002850457	2.46286429633541
C	2.81021460352812	0.46786938476292	3.20732197777108
C	4.19527005740494	0.44540929291902	3.35729470410852
C	4.94555507147131	-0.56813728625909	2.77328771976385
C	4.30710871985843	-1.55376252305259	2.02334387335704
C	2.92838091697477	-1.52468776600733	1.86282053128993
C	-0.41099578352927	2.11934036390693	2.44421260906615
C	-0.34074117546781	0.81100812069016	3.23855337878166
H	1.31876083383098	-1.92195841592397	4.60793879738622
H	0.48121688398152	-3.87510935022772	5.85711417360982
H	-1.49614177018406	-5.12501971093520	5.03705707171318
H	-2.62099442350066	-4.41603309977528	2.94261580204383
H	-1.77605243449879	-2.46571976681579	1.68564724093490
H	-3.01076477944418	2.14943853598819	3.01088004447330
H	-5.46272705617857	2.17598809180200	3.06113105457292
H	-6.76279822554491	1.90445809100620	0.96752547427301
H	-5.56940084042157	1.58287890145598	-1.18599138509737
H	-3.10826373867150	1.51704183611168	-1.23921742470207
H	-2.01062173234054	4.54160929467076	0.99057649512756
H	-1.41583417224889	6.62924480449647	-0.17499613525665
H	0.24112257726807	6.59593376453863	-2.02220108139033
H	1.29835148936461	4.45652356032670	-2.69218771273282
H	0.71155404812097	2.36254224562462	-1.50943010516480
H	2.24629851503563	1.26465125884081	3.67818483060893

H	4.68463711998368	1.22123920171907	3.93584297086415
H	6.02276889519802	-0.58816419037617	2.89650025541700
H	4.88551525199216	-2.34181583612687	1.55461224702909
H	2.43969717522536	-2.28467472461680	1.26241762937498
H	-1.00038536045131	2.88429883800255	2.95756393598244
H	0.59033104841127	2.53073087780886	2.28865716545475
H	0.21750179754286	0.92118889341473	4.17223128097347
H	-1.34491953111896	0.46877112592689	3.50264631515921

Optimized Structure of **2**:

73

C	-3.01625475714063	-0.03084554245382	-1.41141987677092
C	-1.07837114702134	-4.24941972235818	-3.99937485364259
C	-1.66828500215918	-4.65986210263345	-2.80942047850281
C	-1.89460571570701	-3.74181662515068	-1.78592310246198
C	-2.80526931830893	-2.05003680051004	0.60687667269858
C	-4.18991467132515	-2.18815517644621	0.46069148293238
C	-4.92802163548403	-2.91547551059544	1.38837662269305
C	-4.29395920462612	-3.51329614618890	2.47431138562592
C	-2.91825908294121	-3.37888541993508	2.62943908234733
C	-2.17966860720733	-2.64658787399570	1.70494316940660
C	-3.75219841344060	-0.39095934335209	-2.54482890746693
C	-4.69332590882437	0.48159228053117	-3.08426561216956
C	-4.91877263269317	1.72002096048160	-2.49358373653846
C	-4.19645284942089	2.08466778065469	-1.36079931242095
C	-3.24495007046127	1.22138421534722	-0.83070158782538

C	-1.52283610440716	-2.40336668948233	-1.93646690877599
C	-0.90755923734180	-2.00477917865275	-3.13130225246331
C	-0.69684143912433	-2.91812351573519	-4.15561003327194
Fe	-0.03864624970703	0.06187272378438	0.10441651372819
H	-0.91293404054882	-4.96096872855422	-4.80074098780540
H	-1.96826357982187	-5.69345918423280	-2.67656314401928
H	-2.36859977261160	-4.07166670813457	-0.86952490421827
H	-4.69476717548899	-1.72299253932119	-0.37719425614866
H	-6.00072658366664	-3.01410034476946	1.26136888128793
H	-4.87203918542041	-4.07564599697093	3.19919348541775
H	-2.41485444269062	-3.83532355577704	3.47412660211819
H	-1.11119398531418	-2.52981241175562	1.84050891887765
H	-3.58829781645431	-1.35290396514416	-3.01496217118528
H	-5.24759036167117	0.19062514633011	-3.96966487928934
H	-5.64907384573348	2.40069406720174	-2.91676433964670
H	-4.36522572772068	3.04906224043358	-0.89534800356389
H	-2.66536880881752	1.51948068730159	0.03545071858184
H	-0.59329525747040	-0.97512148071853	-3.26140060375207
H	-0.22464052894755	-2.59058270332322	-5.07491108788476
N	0.39177220663294	0.87531288303548	-1.25355239716773
O	0.67485462555847	1.49518834574591	-2.21154259950519
P	-1.77673517095970	-1.14412162079873	-0.61911417769474
N	-0.49045309358374	0.74016573366489	1.52697410749728
P	1.74047052347391	-1.17950630436630	0.66503014935999
O	-0.78940821026791	1.27173427953431	2.53401841713561
C	3.07149825823647	-0.11711968634980	1.38096960102938

C	2.63770947253848	-2.09393428307009	-0.65357426072929
C	1.58309020259315	-2.42380282792371	2.01784738257870
C	4.07816135862102	-0.65628784736182	2.19212981676810
C	3.09712586073883	1.25005610345823	1.09637609237709
C	3.95070867999899	-1.78051738364758	-1.01858084893049
C	1.97558120520363	-3.11644882356597	-1.34478444698234
C	1.96616975875858	-3.76230471265624	1.90489665071874
C	1.06671164263702	-1.97212642303463	3.24057726905383
C	5.08766331061182	0.15294123765522	2.69941844866064
H	4.06998477606074	-1.71251550537219	2.43529585215809
C	4.11305566247604	2.05908311786982	1.59886822626224
H	2.30997458746559	1.67808325497977	0.48676141384599
C	4.58943059258730	-2.48161654319687	-2.03787091135768
H	4.48013979803415	-0.98752321220628	-0.50643029290507
C	2.62071435671689	-3.82620690268002	-2.35100723851406
H	0.94923735716346	-3.35951460519464	-1.09803991684155
C	1.83541224921969	-4.62972575184052	2.98792264396869
H	2.38128859814864	-4.13210025686748	0.97545590637050
C	0.94864554679159	-2.83542396400582	4.32179159122467
H	0.76008980250933	-0.93778185482226	3.34783196647115
C	5.10874611426931	1.51358944619483	2.40193482098862
H	5.85691869761076	-0.27944482044509	3.32994038115770
H	4.12036817753497	3.11770230913727	1.36456741766418
C	3.93031618380022	-3.51021685101597	-2.70189393280024
H	5.60505431009264	-2.21852292131419	-2.31121089920573
H	2.09094765708658	-4.61631560152905	-2.86999680681010

C	1.33141838540866	-4.16973028225398	4.19841489793060
H	2.14182686038885	-5.66462291898594	2.88336095327475
H	0.55594153110071	-2.46420532019356	5.26174897386985
H	5.89414148733102	2.14510854292780	2.80197545765022
H	4.43087713161446	-4.05916428648668	-3.49162136581316
H	1.23885645168825	-4.84374754066591	5.04268820558200

Optimized Structure of **1H**:

61

P	-1.95593446064965	1.17533915892459	-0.10206308179580
C	-2.36785918485239	2.29180139633847	1.31706482720781
C	-2.07088195107722	2.25839360945939	-1.57800102990469
C	-2.05615096125478	3.65454885080558	-1.51934106237816
C	-2.09615901955213	4.41342959727139	-2.68765103039232
C	-2.15615310741492	3.78846939356082	-3.92714319104039
C	-2.17185689278670	2.39691569843241	-3.99609636262336
C	-2.12511111467574	1.64061297115321	-2.83354769607676
C	-3.53811253154664	0.23415202791389	-0.22498903505145
C	-4.73852266154806	0.90077052211949	-0.50085870722646
C	-5.93995876543083	0.20544292470158	-0.54331440109318
C	-5.95892058766081	-1.16926111549260	-0.31420951701631
C	-4.77145591678828	-1.84162734035218	-0.04982755822110
C	-3.56658793420412	-1.14290370871424	-0.00514559899695
P	0.53552745612986	1.08739079116428	1.90041665004687
C	1.86419500983460	0.31688482943252	2.91493073054125
C	2.24986641108692	0.87626203775660	4.13954280763888

C	3.25370797207227	0.28792481480555	4.89755549064517
C	3.89213211135639	-0.86289275931449	4.43901383854869
C	3.52379127358614	-1.41791933090695	3.21963415378744
C	2.51366447843320	-0.83120631957374	2.46072816956348
C	-0.79311683486590	1.34907432323485	3.17140110255938
C	1.25777808227817	2.76352065733959	1.64532620792848
C	2.44996761757164	2.84605256339567	0.91412725377380
C	3.04543146085139	4.07328240547002	0.65754647368399
C	2.45931251604652	5.24742030939279	1.12375016801855
C	1.28381275068535	5.18023416003198	1.86055748110258
C	0.69043158688103	3.94707173672919	2.12374705219927
C	-2.23098496435222	1.50328912887805	2.63352863379379
Fe	-0.13991204777805	-0.04804679345844	0.10284438873344
N	-0.16772795537370	-1.58483138885138	0.67076086817216
O	-0.16722546659447	-2.71491762990480	0.99004926956694
C	1.07612425891496	0.55695911141256	-1.03622287344217
O	1.85768339174222	0.86078808617053	-1.83344624442897
H	-0.74710274200110	-0.46410298441120	-1.22141540509305
H	-3.38561093604855	2.67212059569234	1.20116136051925
H	-1.69091993328845	3.14849267995560	1.30519361653520
H	-2.00742894332415	4.16514129645404	-0.56518760484873
H	-2.08024477905119	5.49612844697793	-2.62360030086918
H	-2.18631478556561	4.37959638788510	-4.83527215150407
H	-2.21518031019394	1.89943328769622	-4.95857438435946
H	-2.12589052548989	0.55722852426619	-2.89645619683102
H	-4.73175260179755	1.96762116630197	-0.70033719163176

H	-6.86150089825683	0.73389991295913	-0.76108840643187
H	-6.89699439043516	-1.71227054368184	-0.34824787974742
H	-4.77862842208584	-2.91168118155025	0.12525856327143
H	-2.63972433992217	-1.66367967800269	0.19862594075815
H	1.77378091701424	1.78158400110560	4.49977033173182
H	3.54421015935279	0.73011635318543	5.84384460259102
H	4.67506908131660	-1.32164157053150	5.03242536070529
H	4.01844851836365	-2.31052185884038	2.85455845962117
H	2.22426851000684	-1.26096924243425	1.50975170794254
H	-0.52144553780713	2.20155713715698	3.79999569179600
H	-0.74540145891080	0.46667356290399	3.81372178491208
H	2.91708594816722	1.94166280125938	0.54347081188843
H	3.96636521310115	4.11249519658388	0.08760189933747
H	2.91950799442087	6.20641692246699	0.91546071971899
H	0.82276913780178	6.08626914908518	2.23787697968818
H	-0.21992870871062	3.92657440050777	2.70972781957673
H	-2.83075524688391	1.99036776521691	3.40805955364014
H	-2.66411574784209	0.50841451428287	2.49363285052757

Optimized Structure of **2H**:

74

Fe	0.08551986555281	-0.02434778119095	0.10937053647766
P	0.88880833158775	2.00956815378971	-0.00654932245296
P	0.34550332447868	-2.03127268233663	-0.71506415098429
C	0.78576956143565	-0.38260431224971	1.69252532176562
O	1.15182033864559	-0.61728125778401	2.76926235595477

N	-1.53127108489839	0.19817086765543	-0.07779379538415
O	-2.69788206350236	0.33829905298247	-0.15927440641908
C	2.72076786301605	2.14559458838729	0.04629318076455
C	3.46987204033137	2.45550703747992	-1.09155537031335
C	4.86143327375724	2.48012757363898	-1.03850194435294
C	5.52157718489766	2.20617067682779	0.15411553643266
C	4.78261265406374	1.89987660921215	1.29464716520897
C	3.39413939771110	1.86365295734788	1.24101780039112
C	0.35807485429228	3.18955428374925	1.30315299936188
C	-0.90006752209026	3.00607806023856	1.88404395146339
C	-1.36826823796257	3.88733948623021	2.85197030212849
C	-0.57900864255083	4.95581318390353	3.26521280691620
C	0.68134929467964	5.14021497709806	2.70440079764007
C	1.14597171801199	4.26594986284765	1.72676667299506
C	0.45525334416323	2.89597586060506	-1.56209162594270
C	0.37813684547879	4.29233899230817	-1.62204055285189
C	0.09541533844904	4.93332859511394	-2.82366029884953
C	-0.10933952414383	4.18979957907727	-3.98252498456455
C	-0.04516325468211	2.80127438968112	-3.93079342049784
C	0.22640128144274	2.15778399770508	-2.72698839785668
C	0.07119548392351	-2.10320202366440	-2.53520802668785
C	0.95378421975447	-2.74428365239252	-3.40774200788868
C	0.70241760882546	-2.76704013377797	-4.77820735702393
C	-0.43608198521090	-2.15721660461275	-5.29224785340162
C	-1.32145720613882	-1.51467349612749	-4.42963817636440
C	-1.06750015276967	-1.48171523945152	-3.06385679826205

C	-0.81576989337222	-3.32537674171819	-0.10481708722362
C	-1.40899264816652	-4.26745620443386	-0.95165958790074
C	-2.28013586564527	-5.22710557537761	-0.44284480672015
C	-2.56310795366263	-5.26201699989835	0.91831402179874
C	-1.97725057644769	-4.32898299449291	1.76922243497188
C	-1.11707908221812	-3.36238377948419	1.26104761074436
C	1.98746120505114	-2.82538406649459	-0.50598999265778
C	3.14330896778143	-2.03799041077320	-0.52022553870494
C	4.39906092131617	-2.62697166152180	-0.41969260711847
C	4.51680925199511	-4.00784419518217	-0.29185230586854
C	3.37217004245942	-4.79777304404289	-0.25943088087439
C	2.11507794267513	-4.21165074130328	-0.36701867742685
H	1.16669008496089	0.02337439238347	-0.99599480760698
H	2.96736352370252	2.67979835305657	-2.02481996811126
H	5.42638017580297	2.72267469338618	-1.93175223987284
H	6.60495409073751	2.23224346894636	0.19687467186376
H	5.28848441971573	1.68249284896541	2.22865461559994
H	2.83202207727894	1.61146265614193	2.13287740354695
H	-1.50775355317649	2.16146006309354	1.58279877525047
H	-2.34680197736908	3.73020476180040	3.29053078826338
H	-0.94041054045342	5.63754988665288	4.02709863098399
H	1.30717120682029	5.96423310021449	3.02888554900437
H	2.13058831636432	4.41747009102614	1.29967683834261
H	0.53236210983869	4.88400828928881	-0.72799436100687
H	0.03128011108349	6.01562516261200	-2.85247559232812
H	-0.32884634557942	4.69161948262664	-4.91843150224812

H	-0.21530686800439	2.21272310529887	-4.82538005833090
H	0.25795728763333	1.07528967382002	-2.68193946306255
H	1.84251713946165	-3.22753562365792	-3.02071154780000
H	1.39997760751578	-3.26605121149603	-5.44175001754176
H	-0.63525284212411	-2.18106722202830	-6.35815028605898
H	-2.21076279297957	-1.03336329771328	-4.82105631835745
H	-1.75657581236633	-0.96800226427591	-2.40443159980214
H	-1.19566928615669	-4.25070895973604	-2.01397410608972
H	-2.73900987377294	-5.94473278337572	-1.11380782247375
H	-3.24297920157362	-6.00810213944531	1.31445799217332
H	-2.20055688127697	-4.34514432164582	2.83012178857625
H	-0.68128201343166	-2.62678745054614	1.92694028306582
H	3.05147120978173	-0.96081281074691	-0.60146296948141
H	5.28538073171771	-2.00301779590681	-0.43454852317581
H	5.49608360065393	-4.46584270087436	-0.20704085599253
H	3.45457620228843	-5.87331912429458	-0.14699694910907
H	1.23061595347633	-4.83602170354044	-0.33714562139926

6.2 The Bonding Situation in the Dinuclear Tetra-Hydrido Complex [$\{^5\text{CpFe}\}_2(\mu\text{-H})_4$] Revisited by Hard X-ray Spectroscopy

TABLE OF CONTENTS

Section S1 - Treatment of experimental data

Section S2 - Structural parameters

Section S3 - Additional figures and charts

Section S4 - Composition of $\{\text{H}_4\}$ and Fe localized orbitals

Section S5 - VtC-XES and XANES transitions

Section S6 - XYZ coordinates of all optimized structures

Section S7 - Crystallographic data

Section S1 - Treatment of experimental data

Since HERFD-XANES filters background photons with high efficiency (in contrast to conventional XANES and TFY XANES), all spectra were only area normalized and smoothed to reduce the white noise (not necessary).

VtC-XES spectra are superimposed by the high-energy slope of the $K\beta_{1,3}$ emission line and therefore need to be background corrected. There are multiple ways to do this, either the $K\beta_{1,3}$ emission line is measured within every VtC-XES scan or the $K\beta_{1,3}$ emission line is measured separately and only a section of the $K\beta_{1,3}$ high-energy slope is recorded within every VtC-XES spectra. The separate $K\beta_{1,3}$ and VtC-XES spectra can be joined together to obtain the whole $K\beta$ -XES spectra. The $K\beta_{1,3}$ high-energy slope is subtracted, by either fitting the whole $K\beta_{1,3}$ line with any suitable function like a pseudo-voigt functions, or only a section of the $K\beta_{1,3}$ high-energy slope is fitted by any suited decay function. The resulting fit is subtracted to obtain the background corrected VtC-XES spectra. All VtC-XES data in this work were corrected by the latter method and area normalized for comparison.

Section S2 - Structural parameters

Table S1: Atomic and centroid distances in **1** and **1H**.

Distances	Compounds			
	1H (cryst.)	1H (DFT)	1 (cryst.)	1 (DFT)
⁵ Cp-Fe	1.67 Å	1.67 Å	1.66 Å	1.67 Å
	1.67 Å	1.67 Å	-	-
Cp-Fe	-	-	1.67 Å	1.69 Å
Fe-Fe	2.21 Å	2.17 Å	-	
Fe-H	1.64 Å	1.62 Å		
	1.66 Å	1.62 Å		
	1.54 Å	1.62 Å		
	1.55 Å	1.62 Å		
H-H	1.73 Å	1.71 Å		
	1.73 Å	1.71 Å		
	1.52 Å	1.71 Å		
	1.52 Å	1.71 Å		

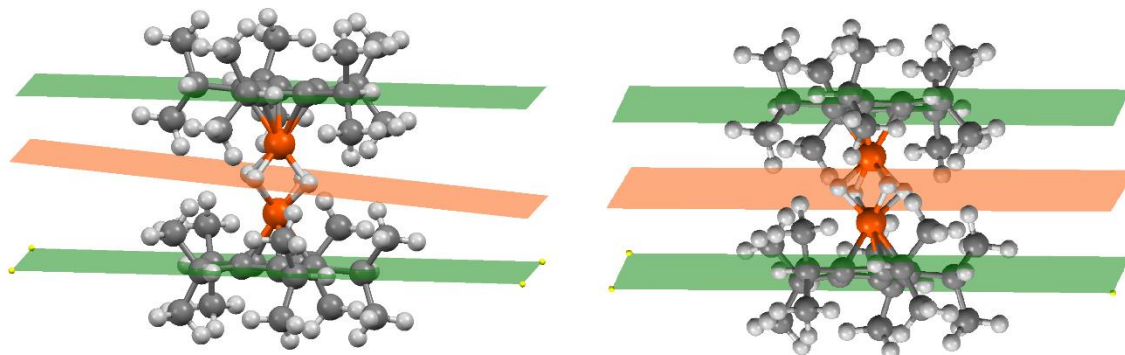
Chart S1. Comparison of crystal (left) and DFT structure (right).

Chart S2. Molecule 1 from the X-ray crystal structure of **1**, distances/Å. Fe1-C1 2.063(3), Fe1-C5 2.056(3), Fe1-C9 2.054(3), Fe1-C13 2.056(3), Fe1-C17 2.065(3), Fe1-⁵Cp_{cent.} 1.661, Fe1-C61 2.062(3), Fe1-C62 2.063(3), Fe1-C63 2.059(3), Fe1-C64 2.066(3), Fe1-C65 2.069(3), Fe1-Cp_{cent.} 1.673. Molecule 2: Fe2-C21 2.049(3), Fe2-C25 2.053(3), Fe2-C29 2.052(3), Fe2-C33 2.053(3), Fe2-C37 2.052(3), Fe2-⁵Cp_{cent.} 1.662, Fe2-C66 2.058(3), Fe2-C67 2.058(3), Fe2-C68 2.054(3), Fe2-C69 2.058(3), Fe2-C70 2.065(3), Fe2-Cp_{cent.} 1.669. Molecule 3: Fe3-C41 2.053(3), Fe3-C45 2.056(3), Fe3-C49 2.063(3), Fe3-C53 2.064(3), Fe3-C57 2.057(3), Fe3-⁵Cp_{cent.} 1.666, Fe3-C71 2.057(3), Fe3-C6 2.053(3), Fe3-C73 2.059(3), Fe3-C74 2.056(3), Fe3-C75 2.063(3), Fe3-Cp_{cent.} 1.667.

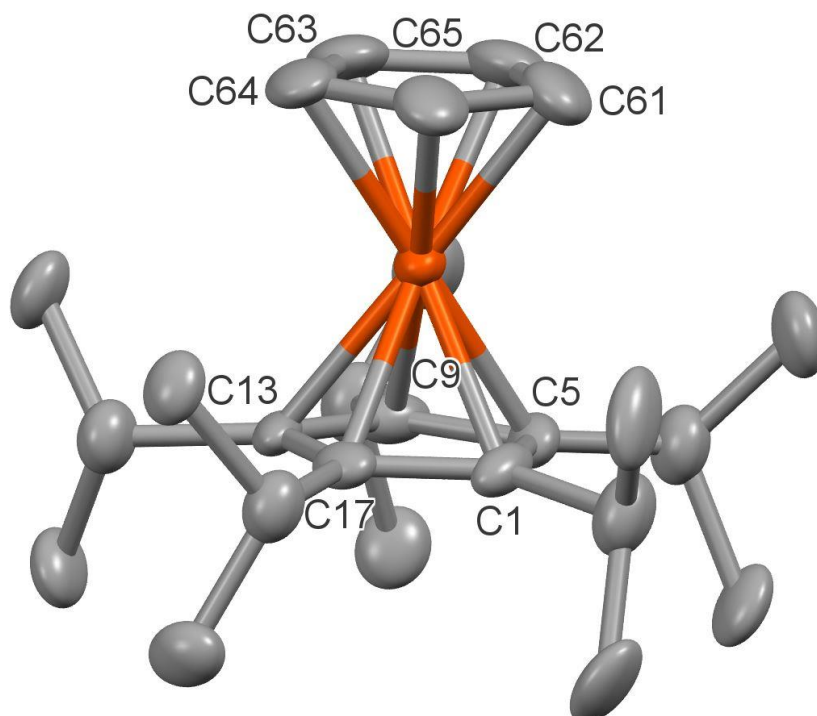
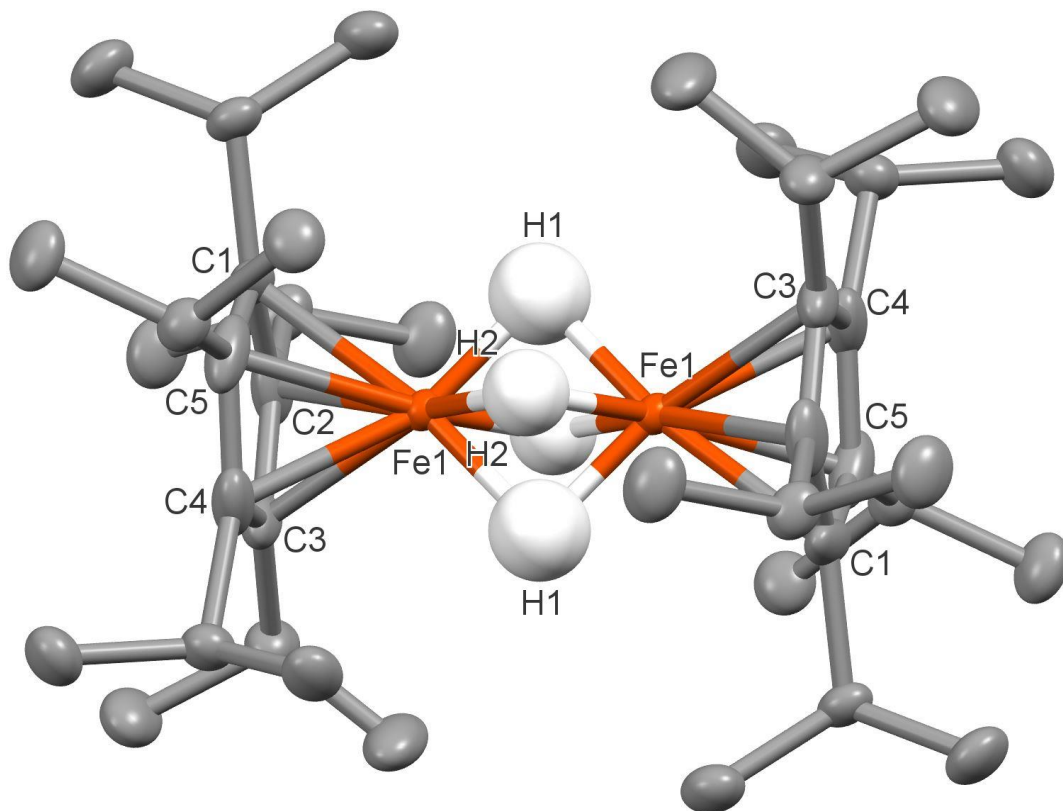


Chart S3. X-ray crystal structure of **1H**, distances/Å. Fe1-Fe1# 2.2145(6), Fe1-C1 2.074(2), Fe1-C2 2.061(2), Fe1-C3 2.048(2), Fe1-C4 2.060(2), Fe1-C5 2.072(2), Fe1-⁵Cp_{cent.} 1.673. The five-membered rings are disordered, only one of two possible orientations of isopropyl groups around the ring is shown for each ⁵Cp ligand.



Section S3 - Additional figures and charts

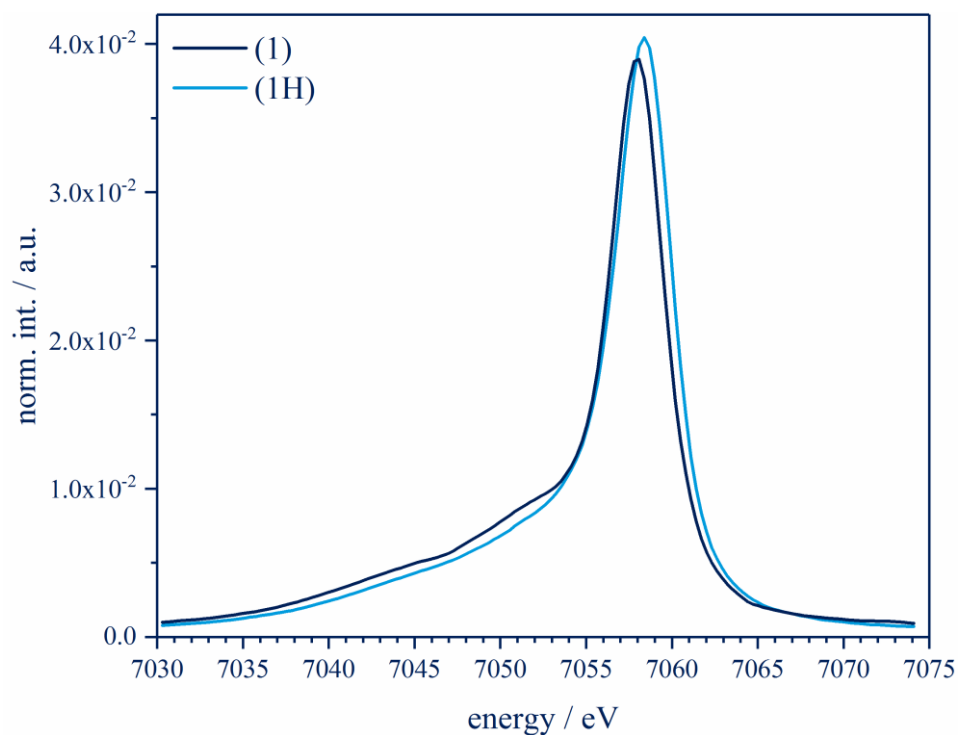


Figure S1. Experimental CtC-XES spectra of complexes **1** and **1H**.

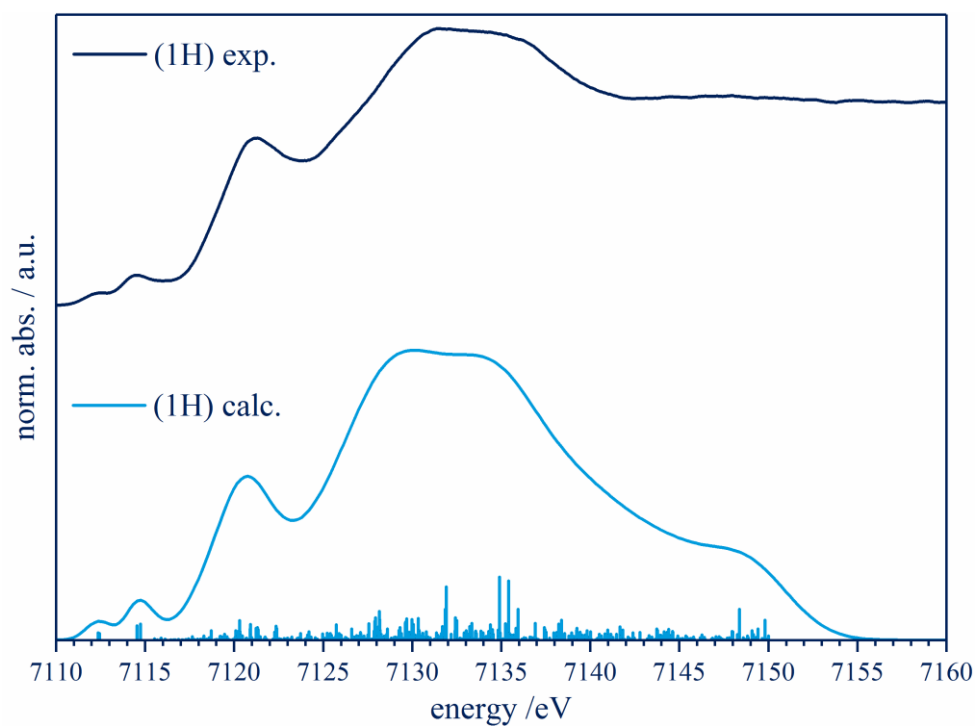


Figure S2. Comparison of experimental (top) and theoretical ($M_S = 1$, bottom) Fe K-edge XANES spectra of **1H**. Transitions were incremental broadened as a function of the absorption energy.

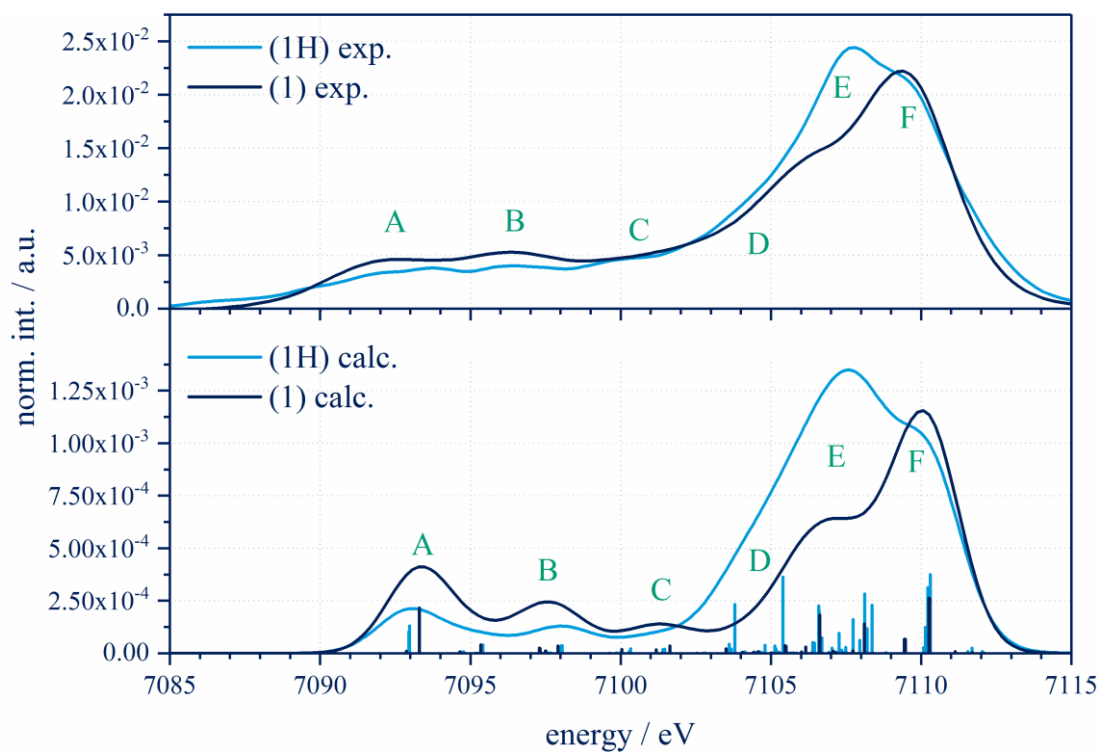


Figure S3. Comparison of experimental (top) and theoretical ($M_S = 1$, bottom) Fe K-edge VtC-XES spectra of **1** and **1H**.

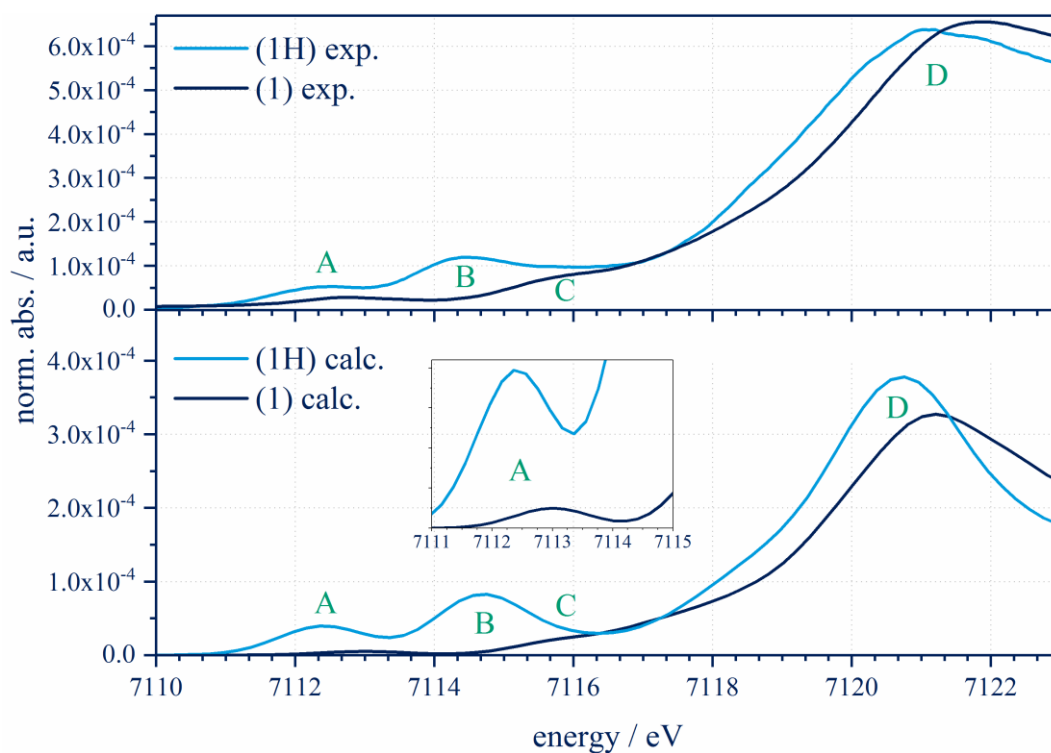


Figure S4. Comparison of experimental (top) and theoretical ($M_S = 1$, bottom) Fe K-edge HERFD-XANES spectra of **1** and **1H**.

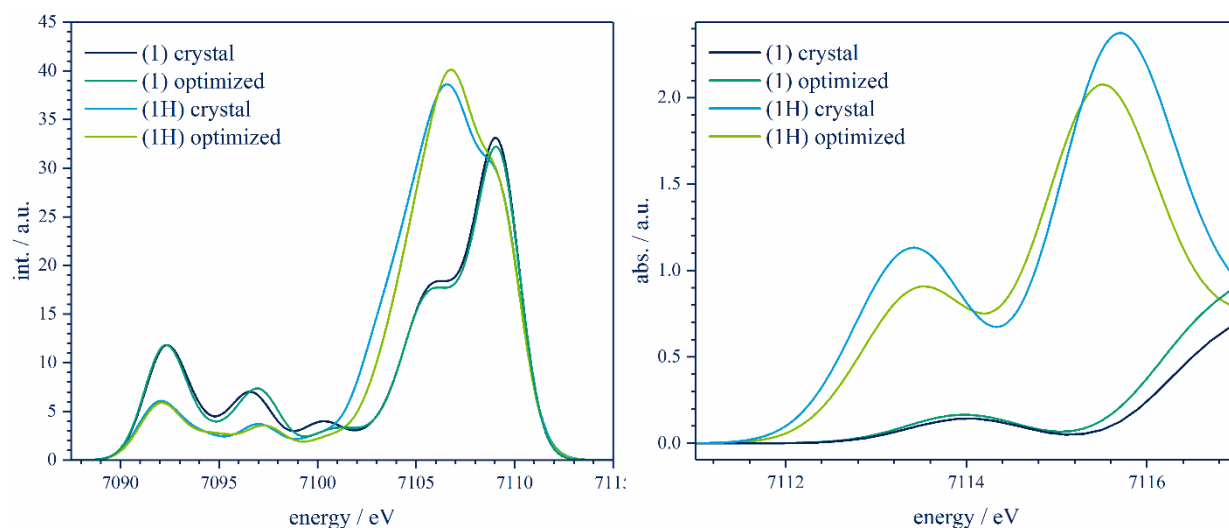


Figure S5. Comparison of calculated VtC-XES (left) and XANES (right) spectra utilizing crystal and optimized structures of **1** and **1H**.

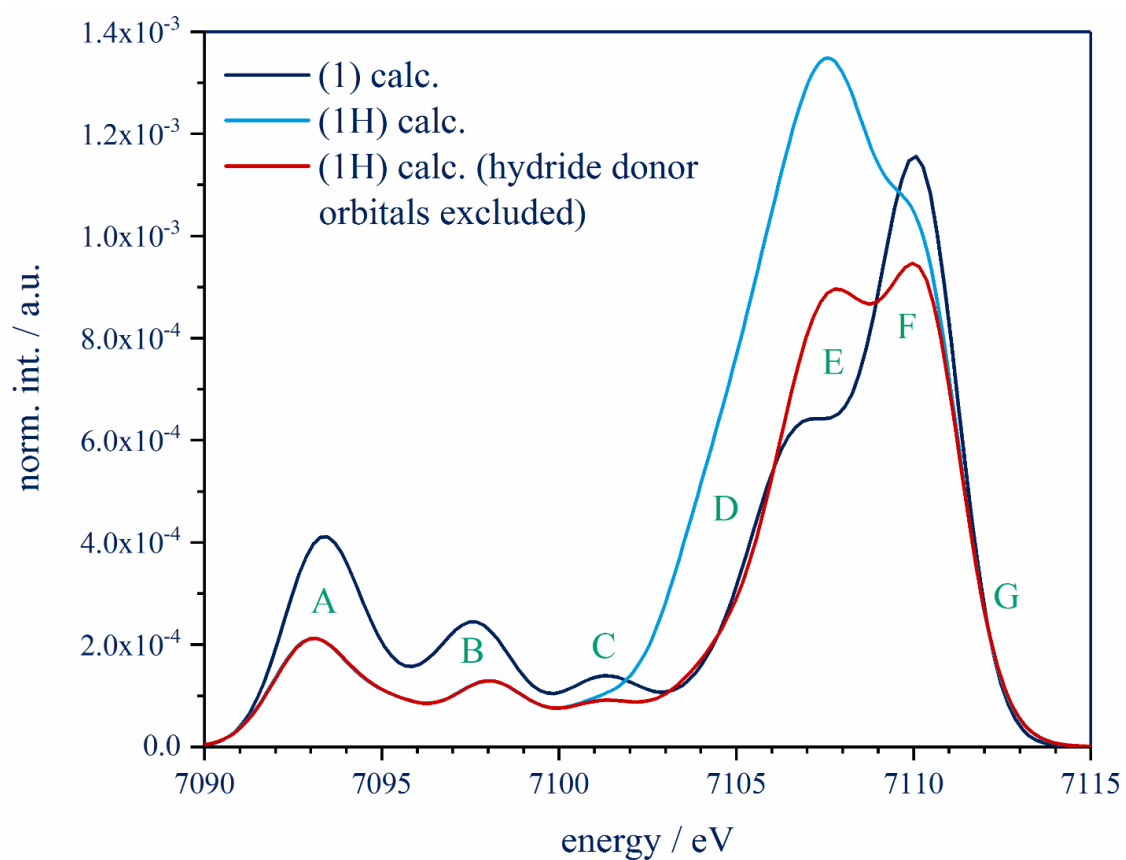
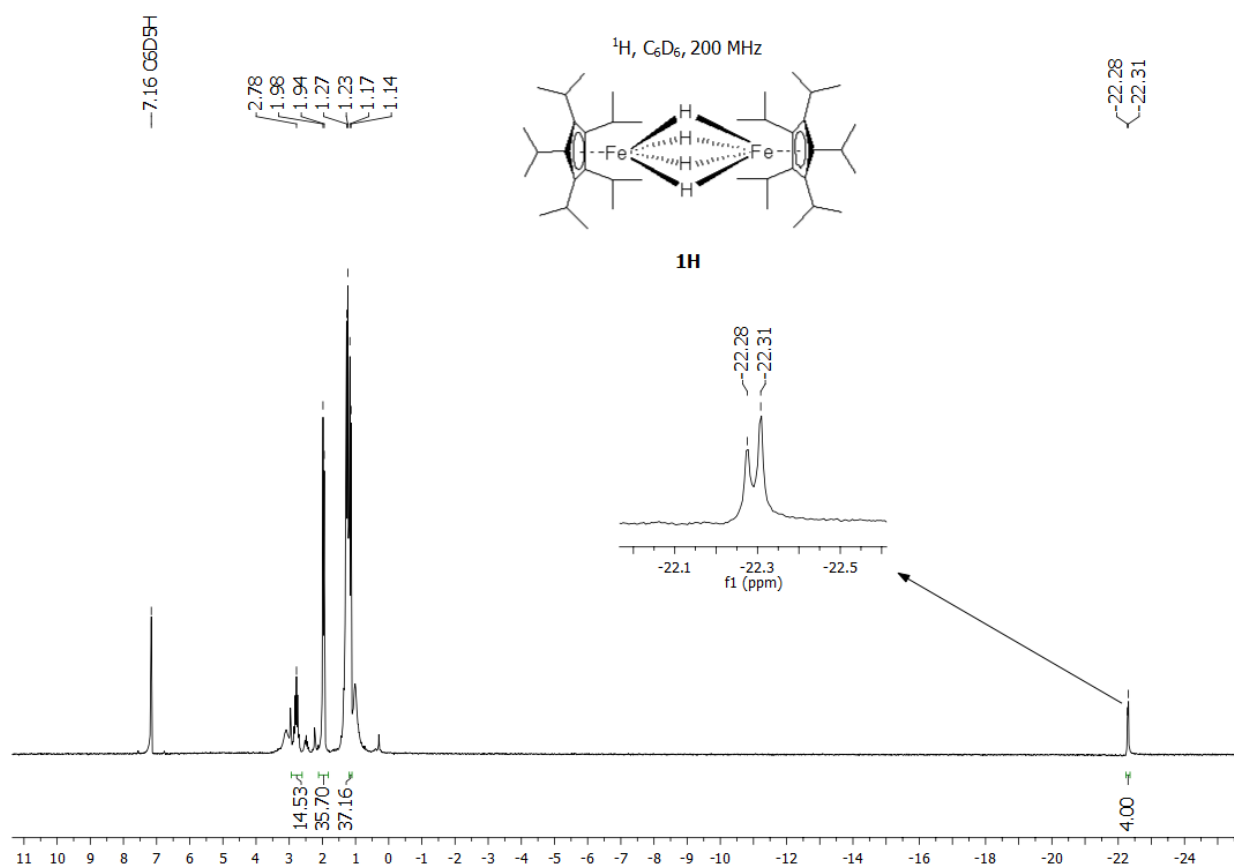
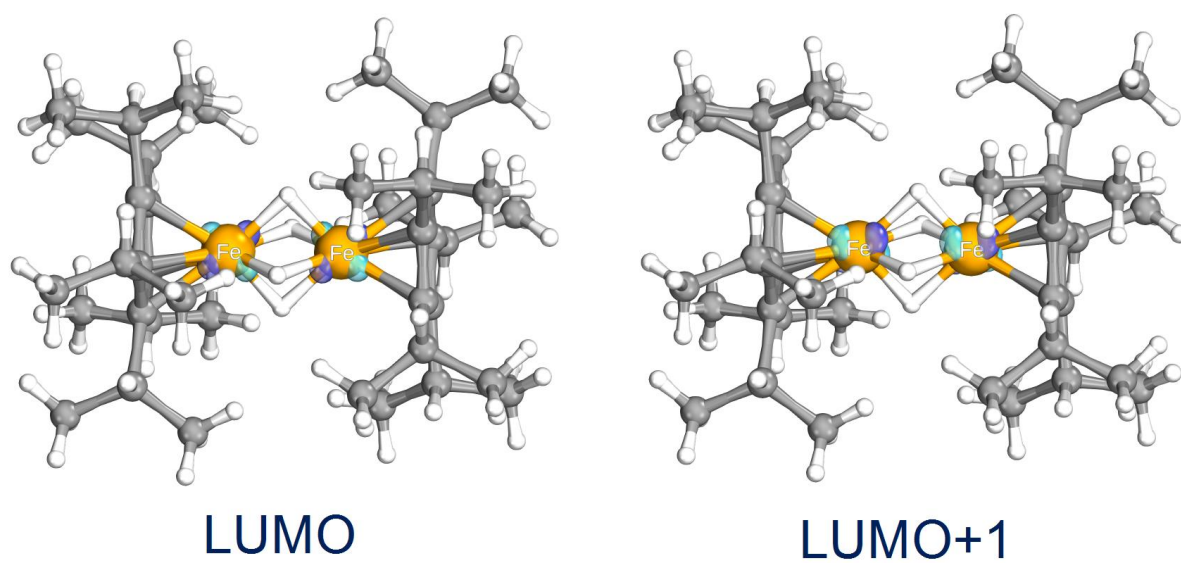


Figure S6. Comparison of theoretical Fe K-edge VtC-XES spectra of complexes **1** (dark blue), **1H** (light blue) and **1H** excluding all transitions of donor orbitals with significant hydride density (red).

Chart S4. LUMO and LUMO+1 of **1H**.Figure S7. ^1H NMR of **1H** in C_6D_6 .

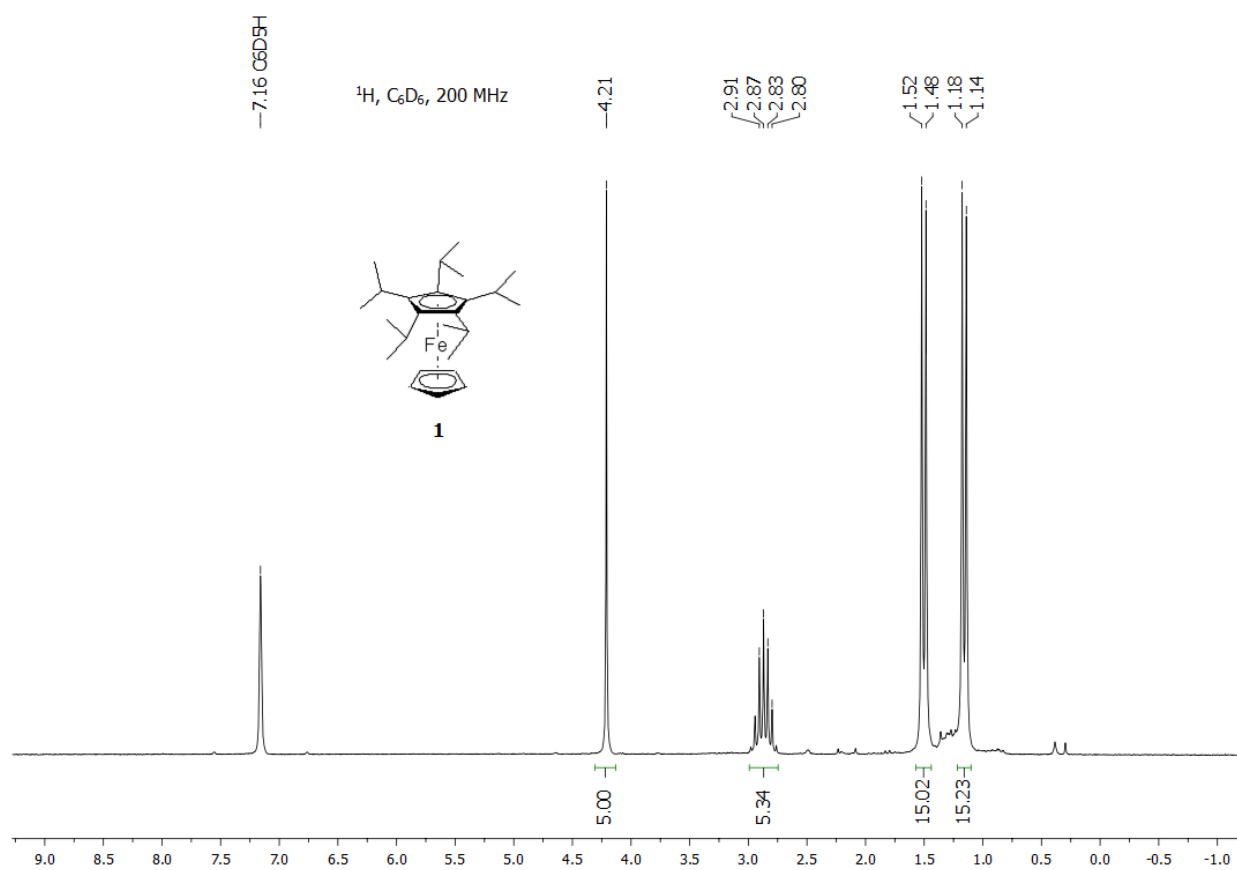


Figure S8. ¹H NMR of **1** in C₆D₆.

Section S4 - Composition of {H₄} and Fe localized orbitals

Table S2. AO populations of hydride localized orbitals of **1H**.

Element / fragment (orbital)	Population ^[a] / %							
	H-82 ^[b]	H-54	H-41	H-20	H-14	H-9	L+2 ^[c]	L+3
	(1 _o)	(2 _o)	(3 _o)	(4 _o)	(5 _o)	(6 _o)	(1 _u)	(2 _u)
Fe (s, p, d)	23.4	13.2	34.8	30.6	10.8	60.8	49.6	46.8
Fe (s)	12.4	3.4	0.2	0	0	0.6	0	0
Fe (p)	8.2	7	7	5.2	5.4	0.2	8	9.8
Fe (d)	2.8	2.8	27.6	25.4	5.4	60	41.6	37
H ₄ (s, p)	29	16.2	26.6	16.4	11.2	13.2	13	12.8
^[a] Population of the given element via Löwdin reduced orbital population analysis. All given values are the sum over all AOs of a given element or fragment. ^[b] H : HOMO, ^[c] L : LUMO								

Table S3. AO populations of Fe localized orbitals of **1H**.

Element (orbital)	Population ^[a] / %									
	H-9 ^[b]	H-7	H-3	H-2	H-1	H	L ^[c]	L+1	L+2	L+3
Fe (s, p, d)	60.8	68	84.8	87.4	87.6	85.8	72.2	72.4	49.6	46.8
Fe (s)	0.6	1.2	0.2	2.4	0	0	0	0	0	0
Fe (p)	0.2	0.8	0.2	1.2	0	0.2	3	2.8	8	9.8
Fe (d)	60	66	84.4	83.8	87.6	85.6	69.2	69.6	41.6	37
^[a] Population of the given element via Löwdin reduced orbital population analysis. All given values are the sum over all AOs of a given element. ^[b] H : HOMO, ^[c] L : LUMO										

Section S5 - VtC-XES and XANES transitions

Table S4. Comparison of all relevant TDDFT core-excited states of complexes **1** and **1H** concerning relevant ligand/element populations (acceptor orbitals), energies and normalized intensities.

Cmpd	Feature	Transition	Calc. energy ^[a] / eV	Norm. Int. ^[b] / a.u.	Element / Ligand character	Core-excited state contribution	LUMOs
------	---------	------------	----------------------------------	----------------------------------	----------------------------	---------------------------------	-------

1	A	1	7113.01	0.031	Fe	0.95	LUMO
		2	7113.02	0.029	Fe	0.95	LUMO+1
1H	A	1	7112.36	0.037	Fe	0.95	LUMO
		2	7112.36	0.452	Fe	0.95	LUMO
		3	7112.45	0.040	Fe	0.96	LUMO+1
		4	7112.45	0.411	Fe	0.96	LUMO+1
	B	5	7114.55	0.891	H	0.95	LUMO+2
		6	7114.55	0.009	H	0.95	LUMO+2
		7	7114.74	1.000	H	0.94	LUMO+3
		8	7114.74	0.008	H	0.94	LUMO+3

^[a] all values were shifted by 151.5 eV, ^[b] normalized to 1 (all values were divided by the overall highest value)

Section S6 - XYZ coordinates of all optimized structuresOptimized structure of **1**:

66

C	-0.69031348669412	0.57916726436960	3.35226642791718
C	-2.02822227933197	-0.11195172502580	3.50369946205010
H	-2.78949493221171	0.66673803313256	3.46743526503396
C	-2.16044294740801	-0.75178920112325	4.88944888143739
H	-3.18621363776691	-1.08363555197968	5.06077362219491
H	-1.90401824809028	-0.04130289331655	5.67584224214847
H	-1.51510765574581	-1.62166848624367	5.01142381656186
C	-2.40821625040898	-1.09291365804791	2.39535202404328
H	-2.48337841449341	-0.58649088970671	1.43488596584003
H	-3.38082937676755	-1.54032954949821	2.60950011444572
H	-1.69555415019484	-1.90873225668506	2.27884153135634
C	-0.50070495904181	1.99476827992464	3.34266379978662
C	-1.57099514619745	3.05587262788961	3.48132728537491
H	-1.06447472508726	4.01967156727870	3.43694676879424
C	-2.22332487042046	2.99724480955863	4.86636186843562
H	-2.85058950271611	3.87534297840647	5.03105079615727
H	-1.47000718521270	2.97264027872101	5.65425744392445
H	-2.85715648160097	2.11954601153845	4.99232787827538
C	-2.61961016944984	3.10501433771316	2.37081881835632
H	-2.16050273136676	3.32741732930430	1.40942159098344
H	-3.34718547087638	3.89213000726988	2.57850908946627
H	-3.17372979431881	2.17373423536562	2.25978037080228
C	0.90416030033973	2.25166351678567	3.33277526394200

C	1.58106204269609	3.59929145570450	3.46069547333384
H	2.65457388743697	3.41614241526454	3.42264859771915
C	1.31717748169555	4.21508924218134	4.83862423401136
H	1.95630640700496	5.08578868736948	4.99684136352778
H	1.52455599745871	3.49969868542559	5.63488188683754
H	0.28548244163912	4.54604978099177	4.95725951700541
C	1.30670744173649	4.60096553283959	2.33970720130831
H	0.25022304456388	4.84140537800468	2.22615216478712
H	1.65915534654700	4.22275996724966	1.38200403071261
H	1.83237031345562	5.53707864796065	2.53823989123397
C	1.58289536786193	0.99503738169314	3.33515898039129
C	3.07350929580845	0.76840122952040	3.46800110174405
H	3.23111257741411	-0.30949822480039	3.43779646644422
C	3.57353225738287	1.21856865078948	4.84442142675621
H	3.56632896037291	2.30270023378768	4.95702629095311
H	4.59960880355479	0.88329008689531	5.00699043246904
H	2.95618259539131	0.80246029852901	5.64107781805204
C	3.94511502552957	1.32994273944355	2.34538986595905
H	3.85209462828064	2.40875122294571	2.22576423362209
H	3.69432077550643	0.87352664423655	1.38972873858118
H	4.99663943803757	1.11620400914903	2.54692747185462
C	0.59725973017274	-0.03872387699632	3.34751046904731
C	0.84134961703321	-1.52520713824850	3.49346129354660
H	-0.13577901528353	-2.00702810908667	3.46945495513323
C	1.42725517413390	-1.85126861214964	4.87097703222035
H	1.42194242522218	-2.92921464750900	5.04304943500132

H	0.84548984617130	-1.38355061609883	5.66575239579989
H	2.45773417368372	-1.51244140433285	4.97716577575862
C	1.64177937965512	-2.18945273820819	2.37396778166792
H	1.12187162463688	-2.10866196324568	1.42129070229326
H	1.77386899391980	-3.25183458831073	2.58829963411451
H	2.63421103728213	-1.76029581467742	2.24100584375627
C	-0.84232987332067	1.18409039598041	-0.00333095568286
H	-1.92131544520422	1.22656904185419	-0.00473503222618
C	0.03187827525934	2.29699114800591	-0.01270358283144
H	-0.26075662493195	3.33631793884980	-0.02334738446791
C	1.36051500029294	1.80949198627114	-0.01595094641128
H	2.25825420662008	2.40936664804779	-0.02902439846449
C	1.30747816917311	0.39525175134754	-0.00886025891824
H	2.15502735922081	-0.27371605771207	-0.01530865865580
C	-0.05393112188583	0.00879953377432	-0.00099895792133
H	-0.42791075816943	-1.00410464541081	-0.00105208736604
Fe	0.36873581200579	1.14733063704288	1.67914942997429

Optimized structure of **1H**:

116

C	21.51928780380988	6.17812288097676	0.84322755088373
C	21.92550736967012	7.43256924032492	0.29807995089237
C	21.50190158032535	8.46013483541147	1.19300362435185
C	20.83215575265969	7.84040563212945	2.29053726297167
C	20.84413089086837	6.42984303610021	2.07443519629508
C	21.84898014085696	4.80389174949904	0.30276256151382

H	21.38233319046510	4.08278392302140	0.97278401852348
C	22.76897053367083	7.60026301054379	-0.94696947316360
H	22.89144486340011	6.60706687119410	-1.37775772557946
C	21.81691912711941	9.93060504623455	1.03163324630250
H	22.33628448164981	10.03609458114317	0.07979432513688
C	20.30258732942430	8.57025559570757	3.50475490170575
H	20.44457336280479	9.63395124747487	3.31605167241902
C	20.33133413475116	5.39962179178807	3.05647761129643
H	19.86576777173837	5.94987047130504	3.87347697095859
C	23.35379434484575	4.52944750295172	0.38731963142962
H	23.73568038402600	4.74121077917978	1.38657473780167
H	23.56287242565723	3.48145459018656	0.16535799178949
H	23.92935617419859	5.12986323121091	-0.31698851064768
C	21.29108479157982	4.48160317559094	-1.08254494816975
H	20.20357347007941	4.53572976941127	-1.08363306013311
H	21.65002061552646	5.15660501440395	-1.85879611666527
H	21.57593366748886	3.46894054615426	-1.37485007166085
C	24.18125993504452	8.07432877160585	-0.59082312319909
H	24.62299446534298	7.44687018142687	0.18394654443720
H	24.83097795709074	8.03030766367414	-1.46675830205848
H	24.19687806294811	9.10209910879611	-0.22802621260572
C	22.15417795858527	8.44509944371932	-2.06158785899856
H	21.19643304263221	8.03445037610006	-2.37627920363958
H	21.98427502264677	9.48148903064772	-1.77157406599234
H	22.81657691960026	8.45651612115932	-2.92942765243026
C	22.80877887192471	10.40353766083400	2.09797607154863

H	23.68265410819139	9.75232711685461	2.13760067743871
H	23.15563877381996	11.41410841611302	1.87499421407512
H	22.37115295779155	10.42481327162024	3.09597220352461
C	20.60469339965250	10.85505635309351	0.93086884660342
H	19.96340362507582	10.56120933006104	0.10174643873613
H	19.99159497384631	10.85605703919534	1.83165073573339
H	20.93010416821331	11.88289851026985	0.75870043452614
C	21.13985665153094	8.25494816343506	4.74741302128963
H	22.20234911963695	8.40605642666378	4.55343806869398
H	20.85578709083494	8.90721130372109	5.57515514156469
H	21.01198878252852	7.22725403626020	5.08716225307340
C	18.80675477618765	8.40656810304601	3.76953543794170
H	18.22411782900931	8.73261649377367	2.90965030582669
H	18.51860166233258	7.37831533217033	3.98632097283487
H	18.50958667783986	9.01326538738113	4.62717546374541
C	21.48941745123578	4.62267055926112	3.68987847668519
H	22.24472272587583	5.30049411891314	4.08902031111068
H	21.12842736308319	4.00338497879418	4.51298813294194
H	21.98613033828302	3.96019252721362	2.98096660679438
C	19.24222910536295	4.46624241138649	2.53094306528691
H	18.37527670635528	5.03341960615496	2.19572237655014
H	19.57042624225813	3.84968262463083	1.69474083462588
H	18.91460682521049	3.78980314488633	3.32279453427188
Fe	19.87173383341726	7.39932791319625	0.52532636893478
H	19.15762689603367	6.46039426605174	-0.58741504956827
H	19.47235044267032	8.11289302379530	-0.87673967114769

C	16.33311496780368	8.79968476327896	-0.84328473426608
C	15.92682144085438	7.54524960312094	-0.29817551228982
C	16.35037424685934	6.51769707772912	-1.19313479985379
C	17.02023503002546	7.13739766784899	-2.29061394371271
C	17.00829349035346	8.54795379482935	-2.07448507138891
C	16.00357593997545	10.17392491052512	-0.30273938976848
H	16.47044786776511	10.89501871560504	-0.97262482104478
C	15.08343870680607	7.37749268422917	0.94691217459961
H	14.96056472916205	8.37072838389223	1.37750046103316
C	16.03537266677280	5.04721844177008	-1.03177932437920
H	15.51686724085257	4.94156362601903	-0.07949082417352
C	17.54991670373235	6.40752645359381	-3.50475940300350
H	17.40646057758165	5.34390836918684	-3.31670197439584
C	17.52103909976698	9.57823304425392	-3.05649104723970
H	17.98695779823536	9.02807426507122	-3.87334353097281
C	14.49882568341193	10.44864551814494	-0.38750226234090
H	14.11706481670742	10.23706229009473	-1.38684368871850
H	14.28989334933179	11.49664985981602	-0.16545485891283
H	13.92304711915376	9.84824882831391	0.31664371818164
C	16.56130082013670	10.49599801685311	1.08268327436402
H	17.64880008871084	10.44163734433558	1.08397252557165
H	16.20207124855425	9.82103324671574	1.85882913544313
H	16.27662477633868	11.50870622653839	1.37499980782682
C	13.67134447190239	6.90277398215747	0.59085510095236
H	13.22932555277941	7.52997476103032	-0.18395977097921
H	13.02162787661080	6.94659516867196	1.46680194912208

H	13.65615952915674	5.87496501535715	0.22813913341798
C	15.69860234940590	6.53315771370864	2.06170767231916
H	16.65614877956205	6.94431149906048	2.37635124571996
H	15.86899806891830	5.49679129765699	1.77190325031016
H	15.03618376471720	6.52159874135484	2.92953035443176
C	15.04243456313794	4.57454760660425	-2.09723406795189
H	14.16861231342510	5.22588758480776	-2.13595660595610
H	14.69563790327640	3.56400780120137	-1.87401424906029
H	15.47909374470317	4.55328772827450	-3.09564634351360
C	17.24764727667538	4.12268087766873	-0.93244904138893
H	17.88981160413037	4.41630057557735	-0.10392489266604
H	17.85981468424518	4.12187898251039	-1.83387259258845
H	16.92236605857818	3.09481092811423	-0.76019737159291
C	16.71412832787431	6.72457138166660	-4.74796957471479
H	15.65128618755192	6.57460576870667	-4.55503905138854
H	16.99817523610834	6.07248702556511	-5.57586089029586
H	16.84350438509146	7.75233674867496	-5.08696001348005
C	19.04621204971813	6.56934336666599	-3.76810596022755
H	19.62763107649644	6.24199708817159	-2.90788207605812
H	19.33595918608345	7.59731782783299	-3.98403844210500
H	19.34333294212452	5.96273490736024	-4.62582355125164
C	16.36289637958959	10.35475191759491	-3.69031895917724
H	15.60792158106105	9.67663823505172	-4.08959491700559
H	16.72394608749883	10.97402986697871	-4.51340815512813
H	15.86576382817328	11.01718102704094	-2.98166137709938
C	18.60965399927665	10.51201895126426	-2.53066844997411

H	19.47670856041000	9.94517302364101	-2.19514792012399
H	18.28095016912831	11.12847987822353	-1.69458671452159
H	18.93728721208089	11.18855046053461	-3.32243709710582
Fe	17.98051944817920	7.57843316933972	-0.52539525776617
H	18.69546506692720	8.51733008289644	0.58770536368641
H	18.38067235780038	6.86495253941716	0.87725561519476

Section S7 - Crystallographic data**Table S5.** Crystallographic data, data collection and refinement.

	1	1H
empirical formula	C ₂₅ H ₄₀ Fe	C ₄₀ H ₇₄ Fe ₂
formula weight	396.42	666.69
crystal size [mm]	0.440x0.201x0.077	0.283x0.183x0.038
<i>T</i> [K]	150(2)	150(2)
a [Å]	1.54184	1.54184
crystal system	Triclinic	Monoclinic
space group	P-1	C2/c
<i>a</i> [Å]	15.7706(8)	25.2350(7)
<i>b</i> [Å]	16.5484(7)	9.9852(2)
<i>c</i> [Å]	16.6794(9)	16.5066(3)
α [°]	61.161(5)	90
β [°]	64.820(7)	112.144(2)
γ [°]	86.338(4)	90
<i>V</i> [Å ³]	3395.5(3)	3852.48(16)
<i>Z</i>	6	4
$\rho_{\text{calcd.}}$ [g cm ⁻³]	1.163	1.149
μ [mm ⁻¹]	5.350	6.193
θ -range [°]	3.241-62.760	3.782-62.745
refl. coll.	25620	12301
indep. refl.	10806	3086
	[<i>R</i> _{int} = 0.0487]	[<i>R</i> _{int} = 0.0360]
data/restr./param.	10806/0/805	3086/0/244
final <i>R</i> indices	0.0451, 0.1046	0.0336, 0.0852
$[I > 2\sigma(I)]^a$		
<i>R</i> indices (all data)	0.0579, 0.1136	0.0364, 0.0872
<i>Goof</i> ^b	1.021	1.073
$\Delta\rho_{\text{max/min}}$ (e·Å ⁻³)	0.815/-0.342	0.307/-0.316

$$^a RI = \sum ||F_o| - |F_c|| / \sum |F_o|, \quad R2 = [\sum (F_o^2 - F_c^2)^2 / \sum F_o^2]^{1/2}, \quad ^b Goof = [\sum (F_o^2 - F_c^2) / (n-p)]^{1/2}.$$

6.3 Revival of the formal description: Fe(-II) identified in the Hieber anion by hard X-ray emission and absorption spectroscopy

TABLE OF CONTENTS

Section S1 – Experimental Section

Section S2 – Treatment of experimental data

Section S3 – XYZ coordinates, single point energies and frequencies of all optimized structures

Section S4 – Analysis of theoretical VtC-XES and XANES spectra of the nitrosyl coordination isomer T_{iso}

Section S5 – FOD analysis of the hieber anion

Section S6 – Comparison of different standard DFT functionals

Section S7 – Additional Figures and Tables

Section S1 – Experimental Section

X-ray Spectroscopy

High-energy-resolution X-ray absorption and emission experiments were performed at beamline ID26 at the European Synchrotron Radiation Facility.^[1] The electron energy was 6.0 GeV, and the ring current varied between 180 and 200 mA. The measurements were carried out using the first harmonic of two u35 undulators. The incident energy was selected using the (311) reflection from a double Si crystal monochromator, leading to a photon flux of approximately 2×10^{13} photons·s⁻¹ on the sample position. Incident energy calibration was performed using a Fe foil. High-energy-resolution fluorescence detection XANES (HERFD-XANES) spectra were measured with a Johann type spectrometer.^[2] Sample, analyzer crystal and photon detector (avalanche photodiode) were arranged in a vertical Rowland geometry.^[3] Fe K-edge HERFD-XANES were obtained by recording the intensity of the Fe K $\beta_{1,3}$ emission line maximum (the energy was changed for each compound to the observed energy maximum) as a function of the incident energy. Emission energy discrimination was performed using the (620) reflection of five spherically bent Ge crystal analyzers (with R = 1 m). The emission was monitored by a photodiode installed at about 90° scattering angle and at 45° to the sample surface. During each XANES scan, the undulator gap was kept at a fixed position and only the monochromator angle was changed. Measurements were carried out at 20 K using a He cryostat under vacuum conditions. Each HERFD-XANES measurement was carried out in 60 seconds. To achieve a satisfying signal to noise ratio four spectra were averaged, each measured at a different spot of the homogeneous sample. To exclude radiation damage, fast measurements over the pre-peak with a scan-time of four seconds were carried out before and after each long HERFD-XANES measurement. Within these time frames, no radiation damage could be detected. VtC-XES and CtC-XES spectra were recorded off resonance at an excitation energy of 7300 eV in the range of 7020-7130 eV, with a step width of 0.3 eV over the K $\beta_{2,5}$ emission line (7080-7130 eV). To observe reasonable data, 30 spectra (60 second per scan) were recorded, utilizing a different sample spot for each scan. Detailed information about the treatment of experimental data is given in the supporting information. Each sample is tested for radiation damage in the beginning by ten fast XANES scans over the pre-edge and whitenline with a scan-time of 10 seconds on one spot, starting with a 100-times attenuated beam and ending with an unattenuated beam. Within these time frames, no radiation damage could be detected (no decrease / increase / shift for all observed pre-edge- / near-edge- / white-line features).

High-energy-resolution X-ray emission and XANES experiments were performed at beamline P64 of Petra III at DESY (Germany).^[4] The electron energy was 6.0 GeV, with a ring current of 100 mA. The measurements were carried out using the first harmonic of a two-meter long U33 undulator. The incident energy was selected using the (311) reflection from a double Si crystal monochromator. Incident energy calibration was performed using a Fe foil. XANES spectra were recorded in transmission mode. XES

spectra were recorded off resonance at an excitation energy of 7500 eV in the range of 6990-7190 eV, with the von Hamos Setup of P64, using eight Si crystals in (440) reflection. To observe reasonable data, 20 spectra (100 second per scan) were recorded, utilizing a different sample spot for each scan. Detailed information about the treatment of experimental data is given in the supporting information. Each sample is tested for radiation damage in the beginning by ten fast XANES scans over the pre-edge and white line with a scan-time of 10 seconds on one spot, starting with a 100-times attenuated beam and ending with an unattenuated beam. Within these time frames, no radiation damage could be detected (no decrease / increase / shift for all observed pre-edge- / near-edge- / white-line features).

Section S2 – Treatment of experimental data

HERFD-XANES is filtering background photons with high efficiency (in contrast to conventional XANES and TFX XANES) and therefore all spectra were only area normalized and smoothed to reduce the white noise (not necessary).

Since, VtC-XES spectra are superimposed by the high-energy slope of the $K\beta_{1,3}$ emission line, these need to be background corrected. There are multiple methods to do this, e.g. the $K\beta_{1,3}$ emission line is measured within every VtC-XES scan or the $K\beta_{1,3}$ emission line is recorded separately and only a part of the $K\beta_{1,3}$ high-energy slope is measured within every VtC-XES scan. Both separate $K\beta_{1,3}$ and VtC-XES spectra can be joined together afterwards to obtain the whole $K\beta$ -XES spectra. The $K\beta_{1,3}$ high-energy slope is subtracted, by either fitting the whole $K\beta_{1,3}$ line with any suitable function like a pseudo-voigt functions or only a section of the $K\beta_{1,3}$ high-energy slope is fitted by any suited decay function and subtracting the resulting fit, to obtain the background corrected VtC-XES spectrum. All VtC-XES data presented in this work were corrected by the latter method and area normalized for comparison.

Section S3 – XYZ coordinates of all optimized structures

[Fe(CO)₃(NO)]⁻, S₀

CARTESIAN COORDINATES (ANGSTROM)

Fe 0.000796 -0.001176 0.004139

N 0.001010 0.001772 1.647258

O 0.000979 0.001256 2.836272

C 0.491055 -1.513346 -0.779929

O 0.819724 -2.519448 -1.264453

C	1.063094	1.173037	-0.793532
C	-1.551281	0.326389	-0.787887
O	1.770730	1.953035	-1.289380
O	-2.583479	0.543942	-1.280017

[Fe(CO)₃(NO)]⁻, T₀

CARTESIAN COORDINATES (ANGSTROEM)

Fe	0.003327	0.000205	0.007377
N	-0.000257	0.001241	1.797664
O	-0.215900	0.768765	2.704962
C	0.478500	-1.685123	-0.453425
O	0.774415	-2.740587	-0.840668
C	1.244882	0.889367	-0.915310
C	-1.511479	0.113916	-0.928989
O	2.067109	1.451043	-1.520026
O	-2.498978	0.167082	-1.544865

[Fe(CO)₃(NO)]⁻, S_{iso}

CARTESIAN COORDINATES (ANGSTROEM)

Fe	0.000753	0.000316	-0.000356
O	0.000063	0.000123	1.720871
N	0.003335	-0.000408	2.902543
C	0.487231	-1.494113	-0.810334
O	0.806555	-2.456807	-1.385651
C	1.058926	1.160777	-0.811077
C	-1.532256	0.334712	-0.817284

O 1.746283 1.907392 -1.385510
O -2.519111 0.554298 -1.398292

[Fe(CO)₃(NO)]⁻, T_{iso}

CARTESIAN COORDINATES (ANGSTROEM)

Fe 0.007696 -0.016954 0.009326
O 0.001746 -0.009763 1.904077
N -0.227964 0.784231 2.821197
C 0.476381 -1.643091 -0.626202
O 0.767223 -2.658657 -1.111804
C 1.177332 0.957834 -0.941006
C -1.495161 0.188241 -0.949951
O 1.904607 1.554230 -1.626273
O -2.423710 0.308548 -1.641044

[Fe(CO)₃(NO)]⁻, S_{side}

CARTESIAN COORDINATES (ANGSTROEM)

Fe 0.008042 0.003320 -0.000762
O 1.299299 0.633339 -1.454212
N 1.575606 0.770716 -0.241804
C -1.567038 0.818252 -0.276636
O -2.582708 1.378917 -0.363919
C -0.002564 0.001182 1.758192
C -0.314038 -1.741467 -0.270803
O -0.050529 -0.023937 2.920873
O -0.493822 -2.887902 -0.354317

[Fe(CO)₃(NO)]⁺, T_{side}

CARTESIAN COORDINATES (ANGSTROM)

Fe	0.000103	0.002312	0.003780
O	-0.078495	-0.244758	1.900678
N	-0.279434	0.997279	1.628812
C	0.420251	-1.568712	-0.734595
O	0.691274	-2.570886	-1.258113
C	1.108042	1.085099	-0.897945
C	-1.488800	0.384457	-0.933181
O	1.806937	1.796040	-1.494496
O	-2.433987	0.650619	-1.552999

Fe(CO)₅

CARTESIAN COORDINATES (ANGSTROM)

Fe	0.002012	-0.001044	0.002148
C	1.807003	-0.039833	0.002111
C	0.003019	0.007517	1.812446
C	-0.945371	-1.537774	0.011952
C	0.000543	-0.016140	-1.808090
C	-0.854507	1.588154	-0.008500
O	2.951195	-0.060915	0.001947
O	0.005289	0.011540	2.953156
O	-1.547152	-2.511192	0.018343
O	-0.000928	-0.026466	-2.948762
O	-1.395664	2.596454	-0.015431



CARTESIAN COORDINATES (ANGSTROM)

Fe 0.051753 -0.299427 0.057089

C -0.212217 1.368270 -0.357648

O -0.392666 2.498175 -0.639083

C 0.310168 -0.239871 1.805386

O 0.472443 -0.145568 2.969820

C 1.475174 -0.736448 -0.897523

C -1.455235 -1.074754 -0.446392

O 2.424461 -0.977329 -1.554786

O -2.479002 -1.544639 -0.796073

Section S4 – Analysis of theoretical VtC-XES and XANES spectra of the nitrosyl coordination isomer T_{iso}

Calculated VtC-XES and XANES spectra of T_{iso} in comparison to S_0 are given in figure S2. The interaction of NO π^* and Fe 3d orbitals in T_{iso} is very similar to T_0 and therefore T_{iso} exhibits more or less the same spectral characteristics as seen in T_0 . The bonding interaction of the NO π_x^* and $3d_{xy}$ orbital (40β) is observed while the remaining NO π_y^* orbital is only weakly interacting with the $3d_{xz}$ orbital, leading to the energetically unfavorable SOMO, 42α . Therefore, a similar blueshift of VtC-XES feature D as seen in T_0 is observed for T_{iso} . The biggest difference between T_{iso} and T_0 is an even further decreasing overlap of NO π^* and Fe 3d orbitals, since the electron-density in NO π^* orbitals is concentrated on the nitrogen atom. Therefore, the SOMO exhibits even less iron density compared to T_0 and bonding interaction of NO π_x^* and $3d_{xy}$ (40β) is even more destabilized in relation to T_0 . The further decreasing Fe density in T_{iso} , leads to a further decreasing intensity of high-energy VtC-XES feature D in relation to T_0 . The $3d_{z^2}$ orbital of T_{iso} is also only semi-occupied, causing the additional pre-edge XANES feature A' as seen for T_0 . However, in contrast to T_0 , the antibonding combination of the NO π_x^* and $3d_{xy}$ orbital (42β) is significantly stabilized, shifting the $42\beta \rightarrow \text{Fe } 1s$ transition into low-energy pre-edge feature A' and leading to a significant intensity increase of A' in relation to T_0 .

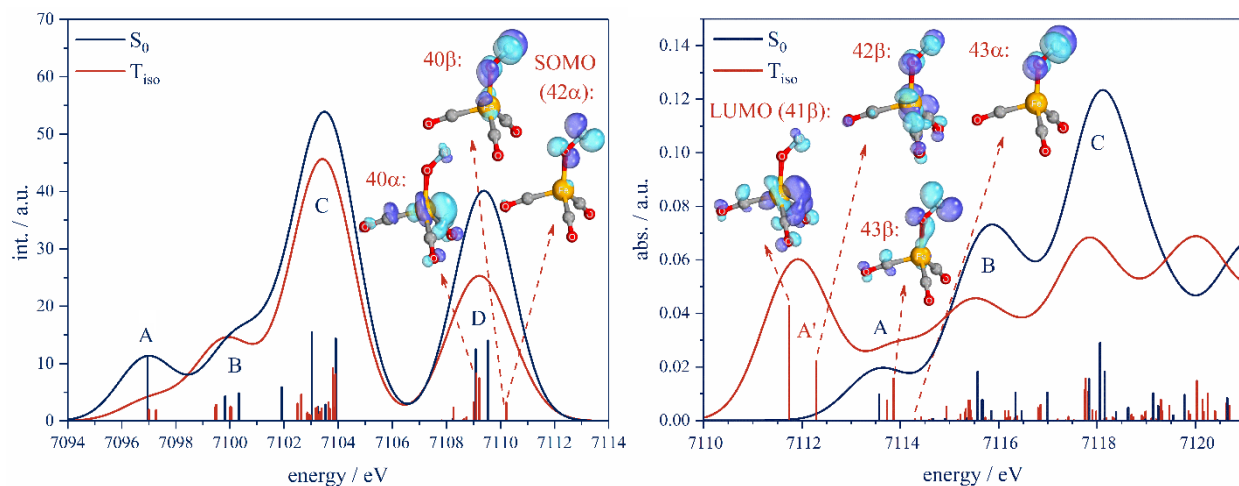


Figure S1: Comparison of calculated VtC-XES spectra (left) and XANES spectra (right) of S_0 and T_{iso} .

Section S5 – FOD analysis of the hieber anion

FOD^[5] calculations were conducted using the TPSSH^[6] functional in conjunction with the ma-def2-QZVPP^[7] basis set at a smearing temperature of 7000 K using the gas phase optimized structure of the hieber anion.

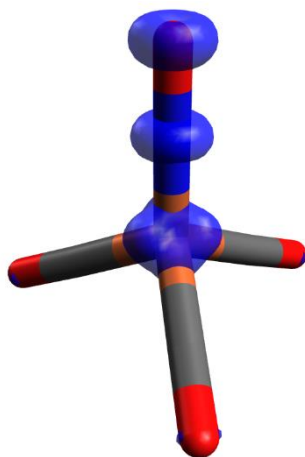


Figure S2: FOD plot of $[\text{Fe}(\text{CO})_3(\text{NO})]^-$ (TPSSH/ma-def2-QZVPP, smear temperature 7000 K, isovalue 0.005 a.u., Avogadro v. 1.2.0)

Table S1. Population of the HOMO to HOMO-4 of the Hieber anion calculated via FOD DFT.

Orbital	Population
HOMO-4	1.98
HOMO-3	1.98
HOMO-2	1.93

HOMO-1	1.86
HOMO	1.86

Section S6 – Comparison of different standard DFT functionals

Table S2. Comparison of Fe 4p/3d and NO 2p contributions to the bonding (HOMO and HOMO-1) and antibonding π Fe-NO interactions (LUMO and LUMO+1) using different standard DFT functionals / ma-def2-QZVPP^[7] (on all atoms except Fe), CP(PPP)^[8] (Fe), CPCM^[9] (ϵ = infinity).

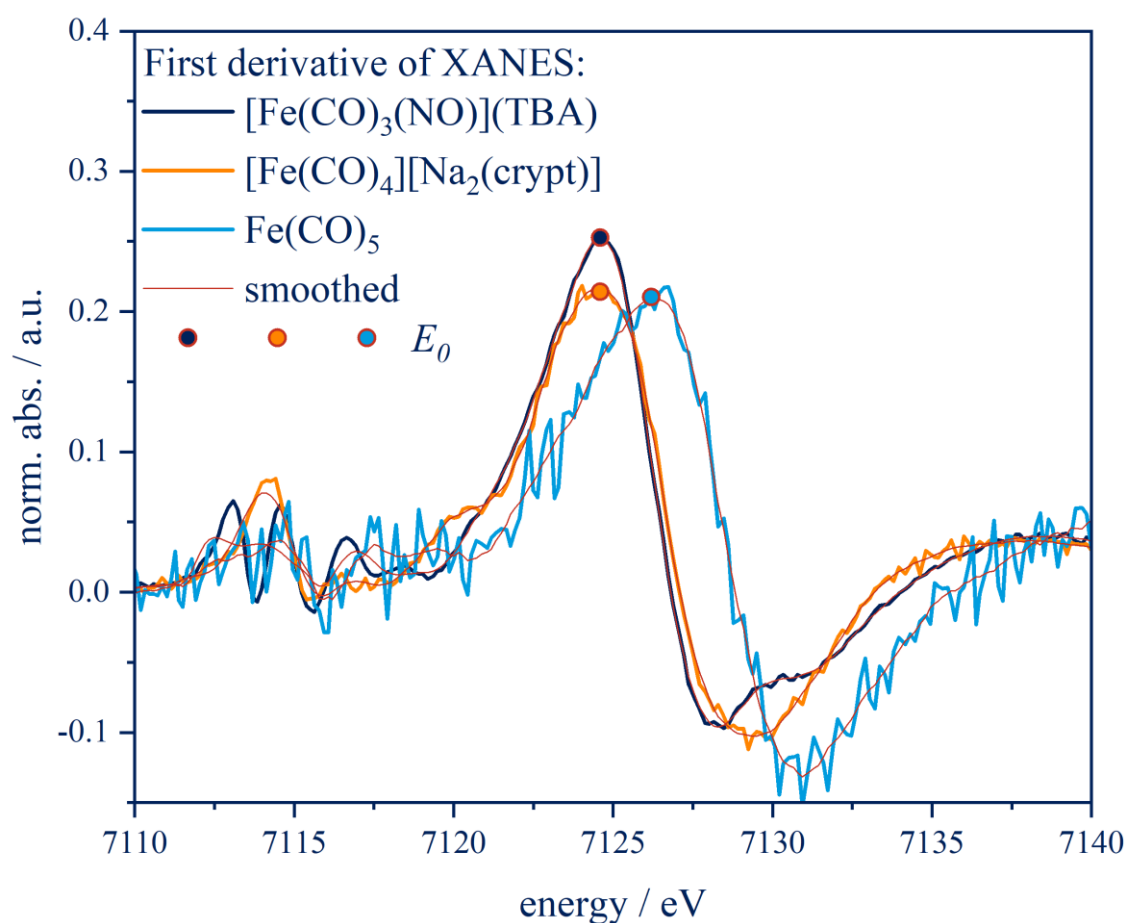
Functional	Parameter	Fe - NO bonding / antibonding			
		HOMO	HOMO-1	LUMO	LUMO+1
BP86 ^[10]	Fe(3d) / %	33.0	33.1	21.4	21.5
	Fe(4p) / %	8.4	8.4	1.0	1.0
	NO(2p) / %	21.3	21.3	47.1	46.9
TPSS ^[11]	Fe(3d) / %	33.5	33.4	21.9	21.9
	Fe(4p) / %	8.3	8.3	1.0	1.0
	NO(2p) / %	21.6	21.7	46.8	46.8
TPSSH ^[11]	Fe(3d) / %	32.3	32.3	20.8	21.0
	Fe(4p) / %	8.6	8.5	1.1	1.1
	NO(2p) / %	23.9	24.1	46.1	45.9
adj. TPSSH ^[12]	Fe(3d) / %	31.9	31.9	16.9	17.0
	Fe(4p) / %	8.5	8.5	0.7	0.7
	NO(2p) / %	24.7	24.7	41.3	41.1
B3LYP ^[13]	Fe(3d) / %	30.7	30.8	18.9	18.9
	Fe(4p) / %	8.8	8.7	1.2	1.2
	NO(2p) / %	26.5	26.5	45.1	45.0

For all functionals identical interactions and symmetry were observed for the respective iron and nitrosyl localized molecular orbitals (HOMO-4 to LUMO+2).

Section S7 – Additional Figures and Tables

Table S3. Comparison of structural parameters of the $[\text{Fe}(\text{CO})_4][\text{Na}(\text{crypt})]_2$ crystal structure and optimized gasphase structure. Additional Figures and Tables.

Compound	C-O bond length / Å	Fe-C bond length / Å	Fe-C-O bond angle / °
$[\text{Fe}(\text{CO})_4]^{2-}$ (DFT)	1.18	1.74	179.92
	1.18	1.77	177.44
	1.18	1.77	177.35
	1.18	1.77	177.30
$[\text{Fe}(\text{CO})_4][\text{Na}(\text{crypt})]_2$ (cryst.) ^[14]	1.20 (2)	1.74 (2)	178.6 (18)
	1.13 (2)	1.81 (2)	176.7 (17)
	1.13 (2)	1.76 (2)	173.7 (15)
	1.16 (2)	1.74 (2)	176.8 (14)

**Figure S3:** First derivative XANES spectra of $[\text{Fe}(\text{CO})_3(\text{NO})](\text{TBA})$, $[\text{Fe}(\text{CO})_4][\text{Na}_2(\text{crypt})]$ and $\text{Fe}(\text{CO})_5$.

REFERENCES

- [1] C. Gauthier, V. A. Solé, R. Signorato, J. Goulon, E. Moguiline, *Journal of synchrotron radiation* **1999**, *6*, 164.
- [2] a) Carra, Fabrizio, Thole, *Physical review letters* **1995**, *74*, 3700; b) Hämäläinen, Siddons, Hastings, Berman, *Physical review letters* **1991**, *67*, 2850.
- [3] P. Glatzel, U. Bergmann, *Coordination Chemistry Reviews* **2005**, *249*, 65.
- [4] Wolfgang A. Caliebe, Vadim Murzin, Aleksandr Kalinko, Marcel Görlitz (Ed.) *AIP Conference Proceedings*, Vol. 2054, AIP Conference Proceedings, **2019**.
- [5] C. A. Bauer, A. Hansen, S. Grimme, *Chemistry (Weinheim an der Bergstrasse, Germany)* **2017**, *23*, 6150.
- [6] a) V. N. Staroverov, G. E. Scuseria, J. Tao, J. P. Perdew, *J. Chem. Phys.* **2003**, *119*, 12129; b) V. N. Staroverov, G. E. Scuseria, J. Tao, J. P. Perdew, *J. Chem. Phys.* **2004**, *121*, 11507.
- [7] J. Zheng, X. Xu, D. G. Truhlar, *Theor Chem Acc* **2011**, *128*, 295.
- [8] F. Neese, *Inorganica Chimica Acta* **2002**, *337*, 181.
- [9] Y. Takano, K. N. Houk, *Journal of chemical theory and computation* **2005**, *1*, 70.
- [10] a) A. D. Becke, *Phys. Rev. A* **1988**, *38*, 3098; b) J. P. Perdew, *Phys. Rev. B* **1986**, *33*, 8822.
- [11] J. Tao, J. P. Perdew, V. N. Staroverov, G. E. Scuseria, *Physical review letters* **2003**, *91*, 146401.
- [12] a) L. Burkhardt, M. Holzwarth, B. Plietker, M. Bauer, *Inorganic chemistry* **2017**, *56*, 13300; b) N. J. Vollmers, P. Müller, A. Hoffmann, S. Herres-Pawlis, M. Rohrmüller, W. G. Schmidt, U. Gerstmann, M. Bauer, *Inorganic chemistry* **2016**, *55*, 11694; c) P. Zimmer, L. Burkhardt, A. Friedrich, J. Steube, A. Neuba, R. Schepper, P. Müller, U. Flörke, M. Huber, S. Lochbrunner et al., *Inorganic chemistry* **2018**, *57*, 360; d) P. Zimmer, L. Burkhardt, R. Schepper, K. Zheng, D. Gosztola, A. Neuba, U. Flörke, C. Wölper, R. Schoch, W. Gawelda et al., *Eur. J. Inorg. Chem.* **2018**, *2018*, 5203.
- [13] a) A. D. Becke, *The Journal of chemical physics* **1993**, *98*, 5648; b) C. Lee, W. Yang, R. G. Parr, *Phys. Rev. B* **1988**, *37*, 785.
- [14] R. G. Teller, R. G. Finke, J. P. Collman, H. B. Chin, R. Bau, *J. Am. Chem. Soc.* **1977**, *99*, 1104.

6.4 The connection between NHC ligand count and photophysical properties in Fe(II) photosensitizers: An experimental study

Spectra

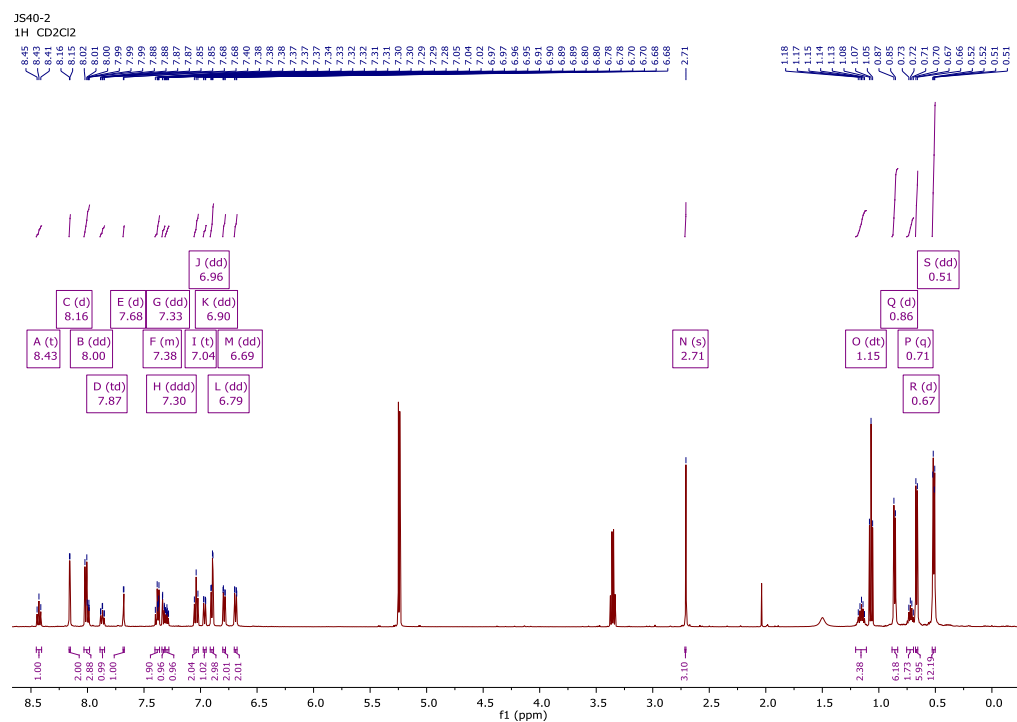


Figure S1. ^1H -NMR of **3** in CD_2Cl_2 .

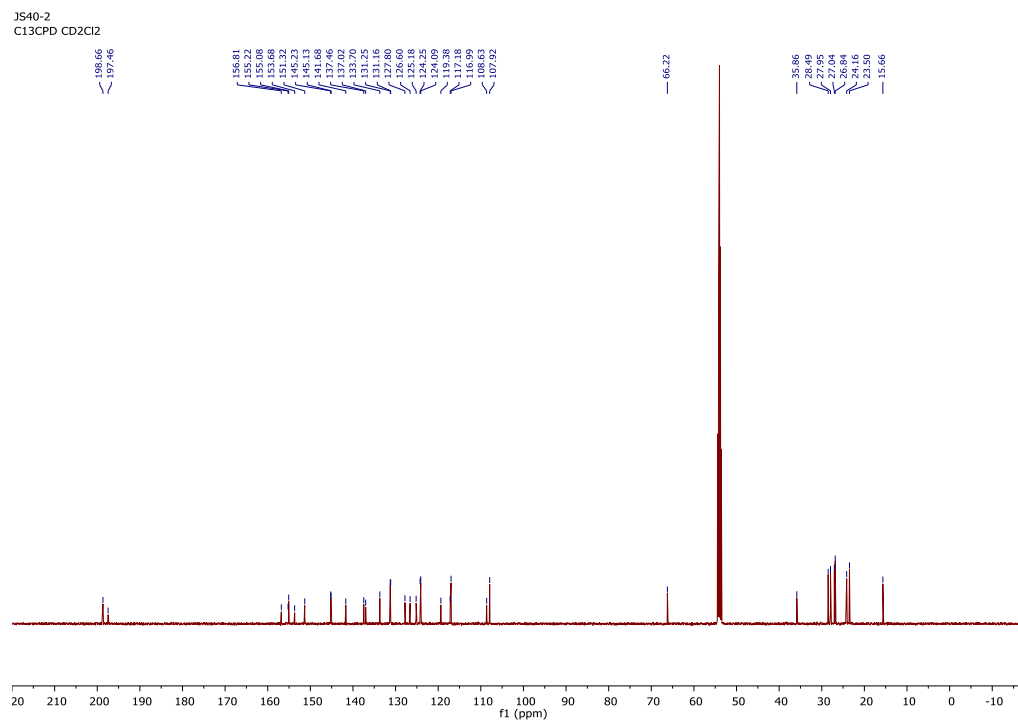


Figure S2. ^{13}C -NMR of **3** in CD_2Cl_2 .

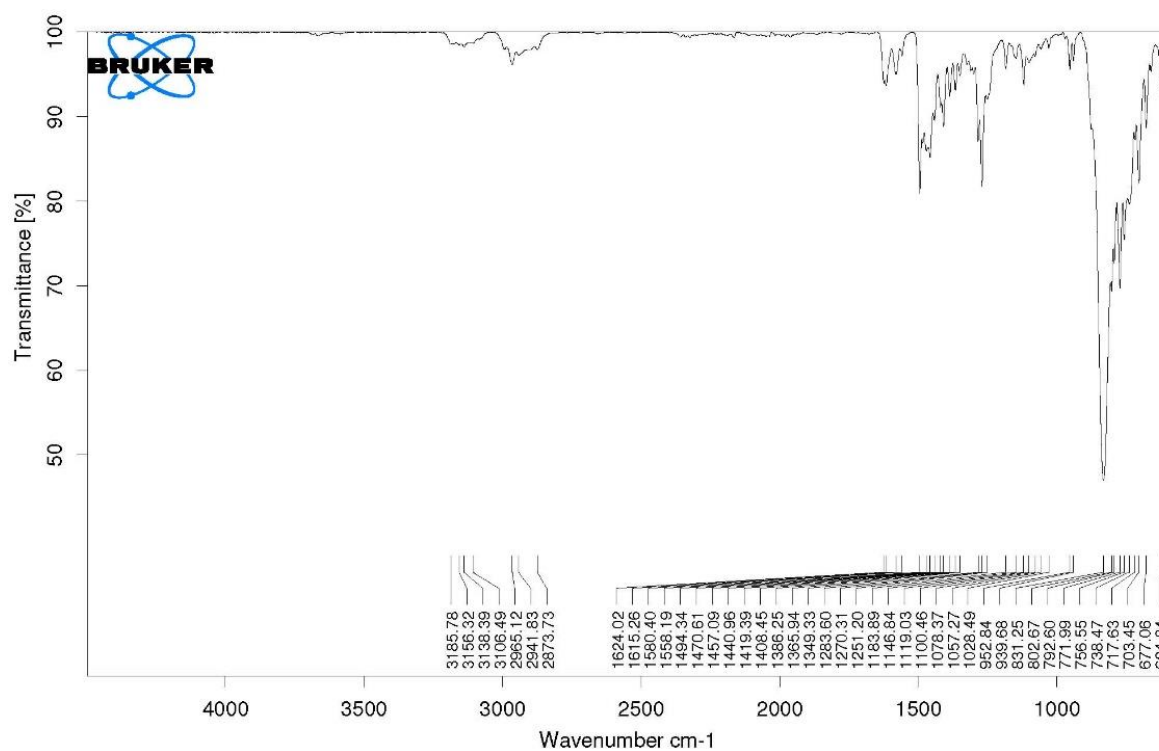


Figure S3. ATR-IR of **3**.

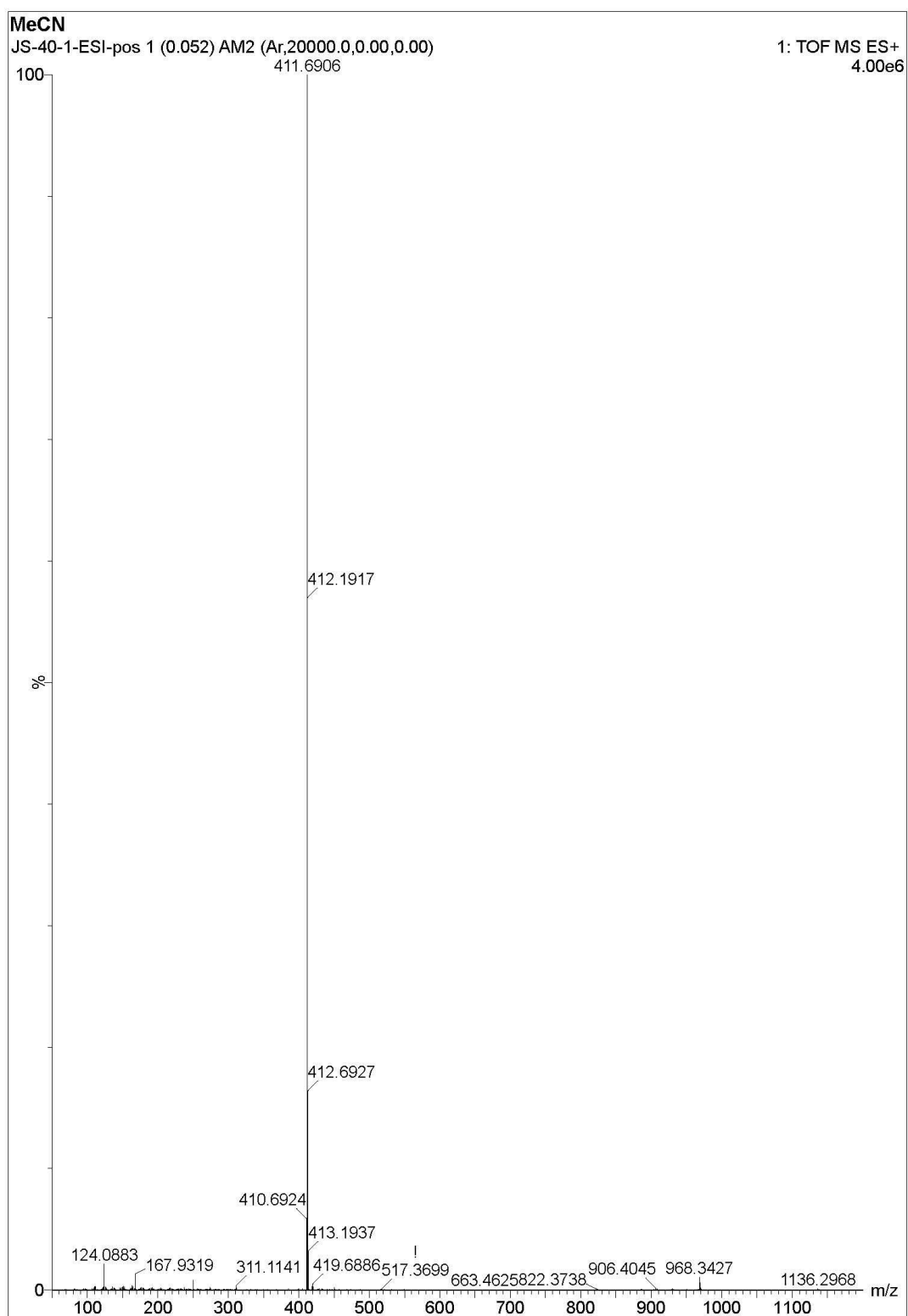


Figure S4. ESI-MS of **3** in CH₃CN.

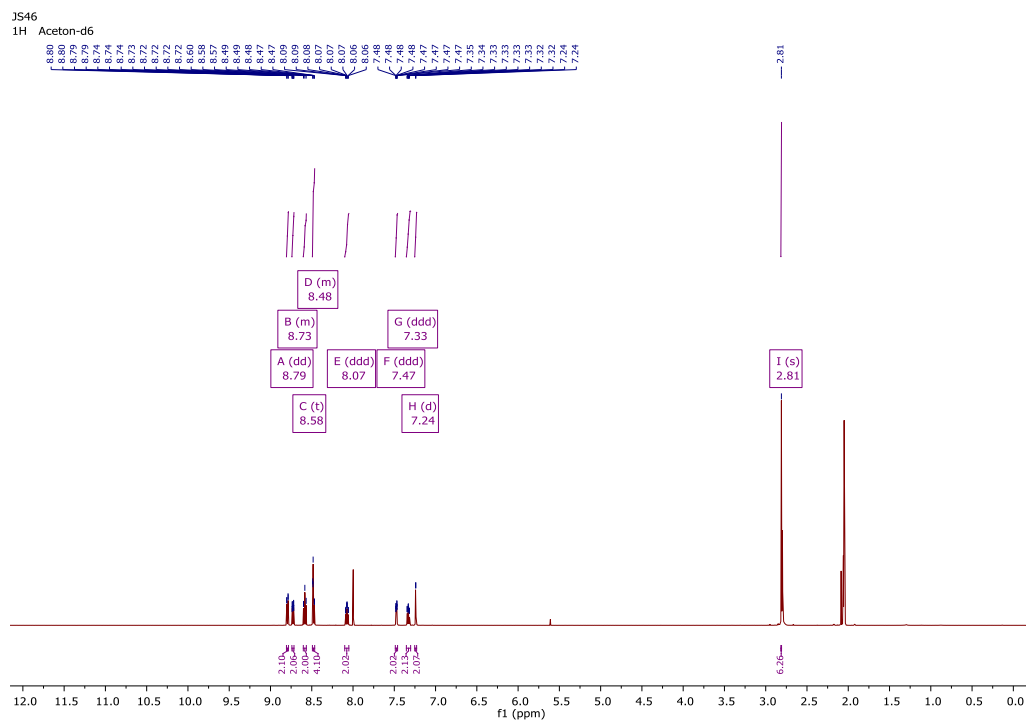


Figure S5. ^1H -NMR of **4** in acetone- d_6 .

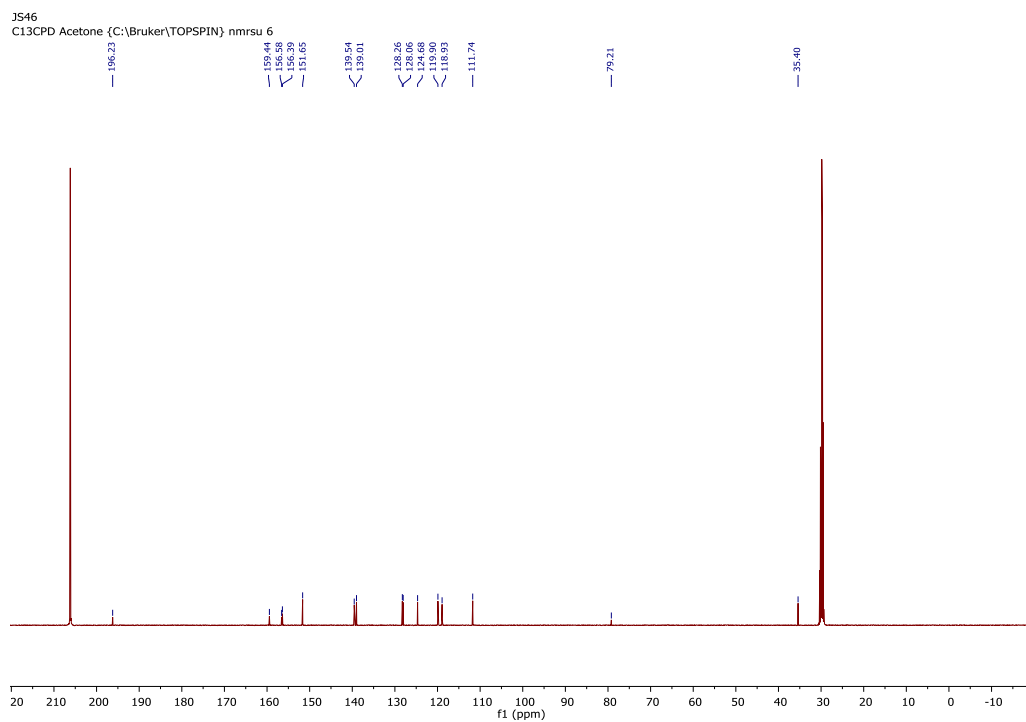


Figure S6. ^{13}C -NMR of **4** in acetone- d_6 .

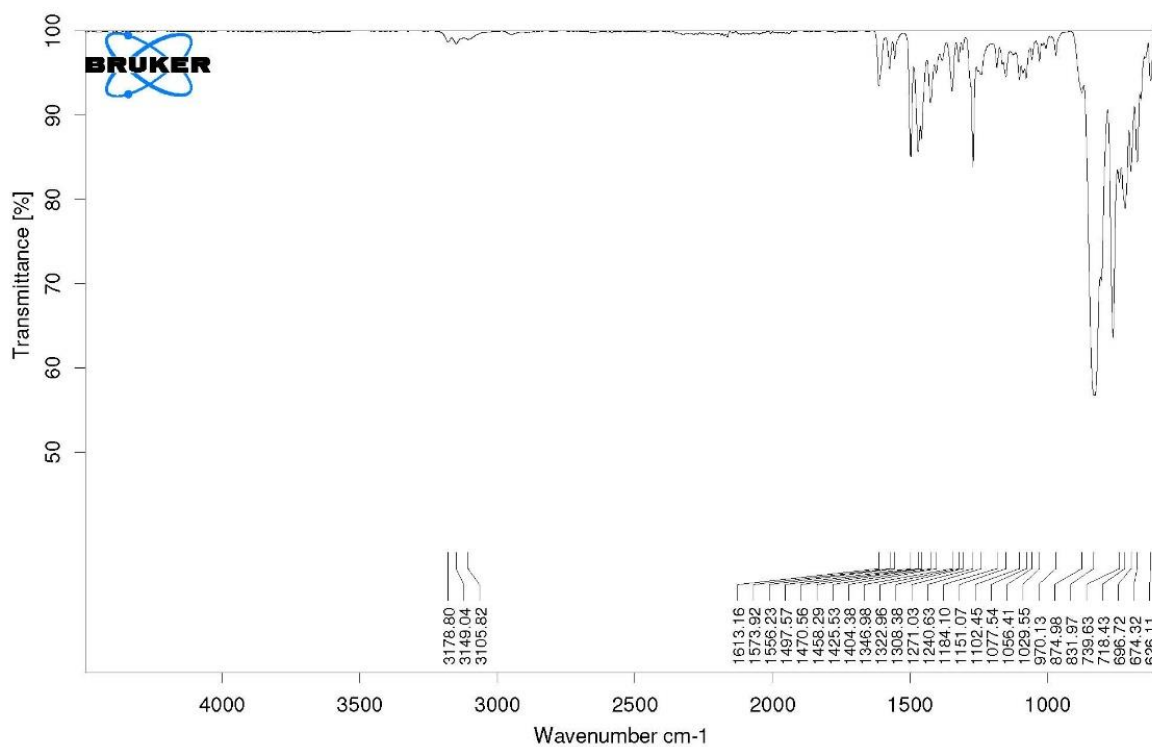


Figure S7. ATR-IR of 4.

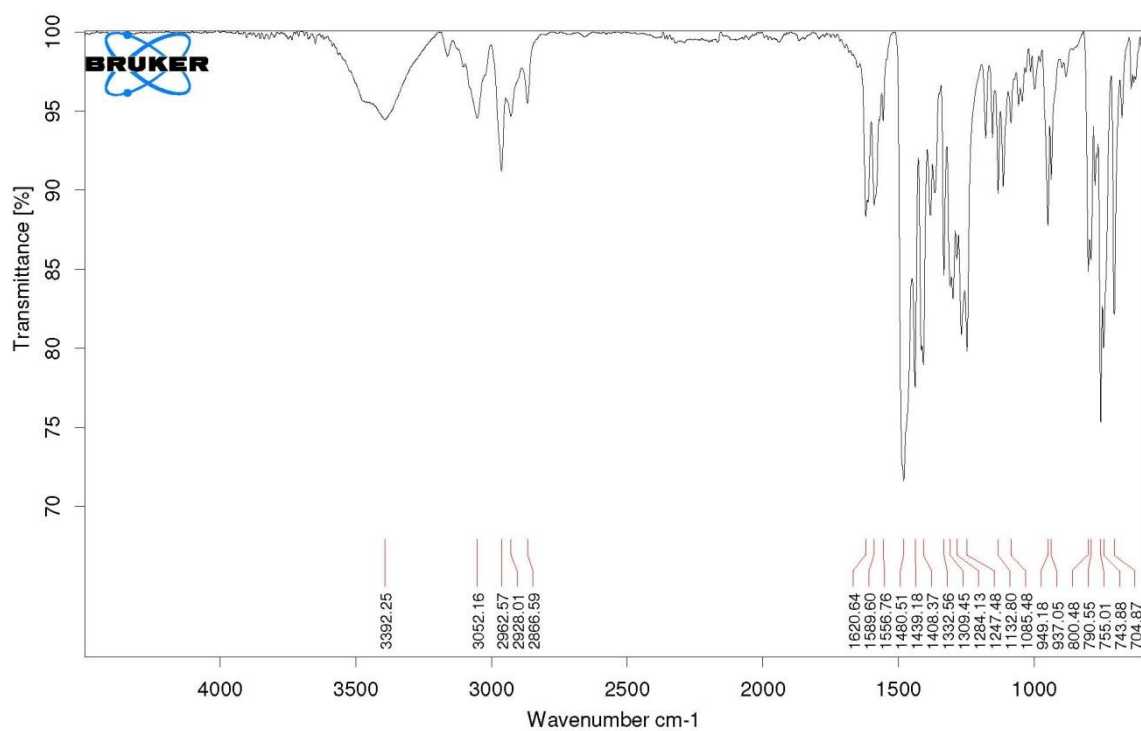


Figure S8. ATR-IR of 6.

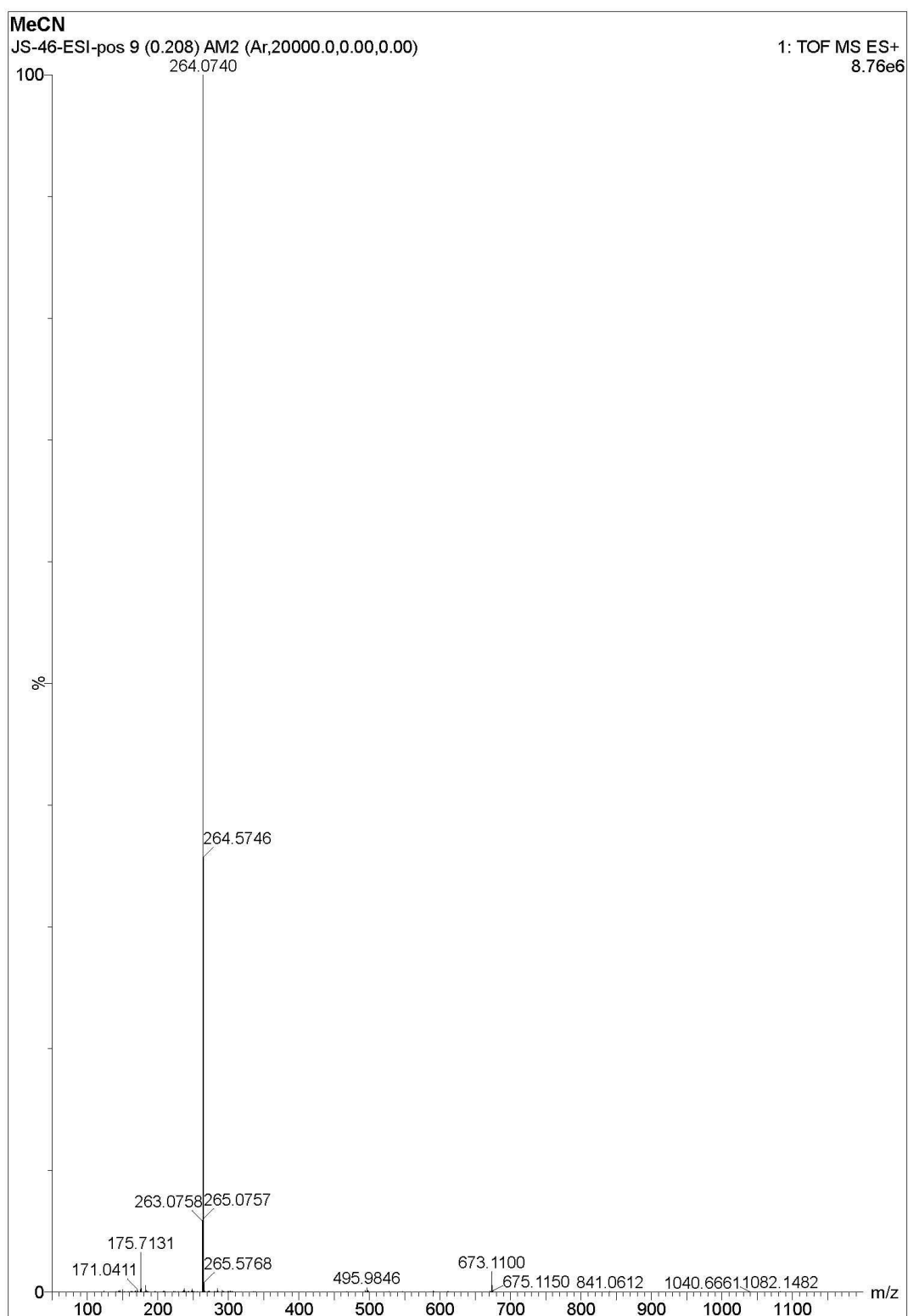


Figure S9. ESI-MS of **4** in CH₃CN.

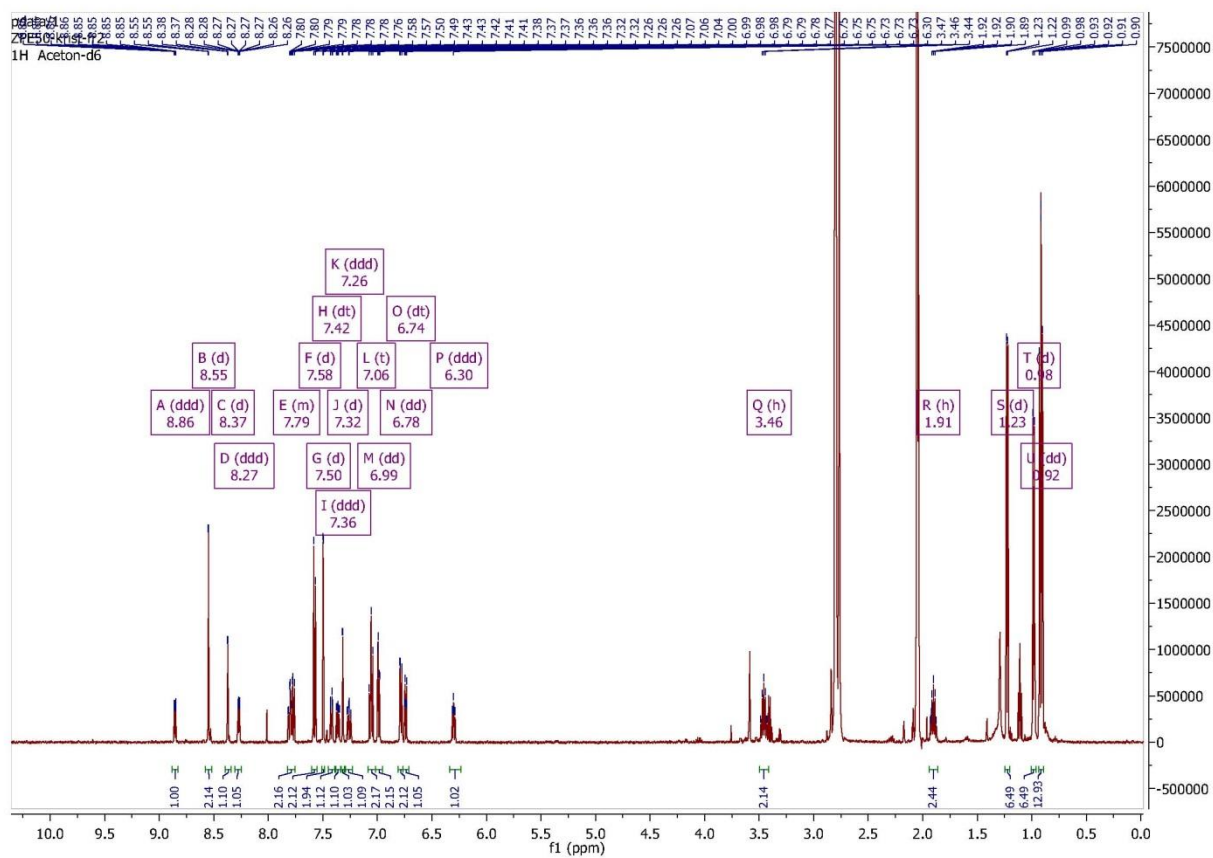


Figure S10. ¹H-NMR of **6** in acetone-d₆.

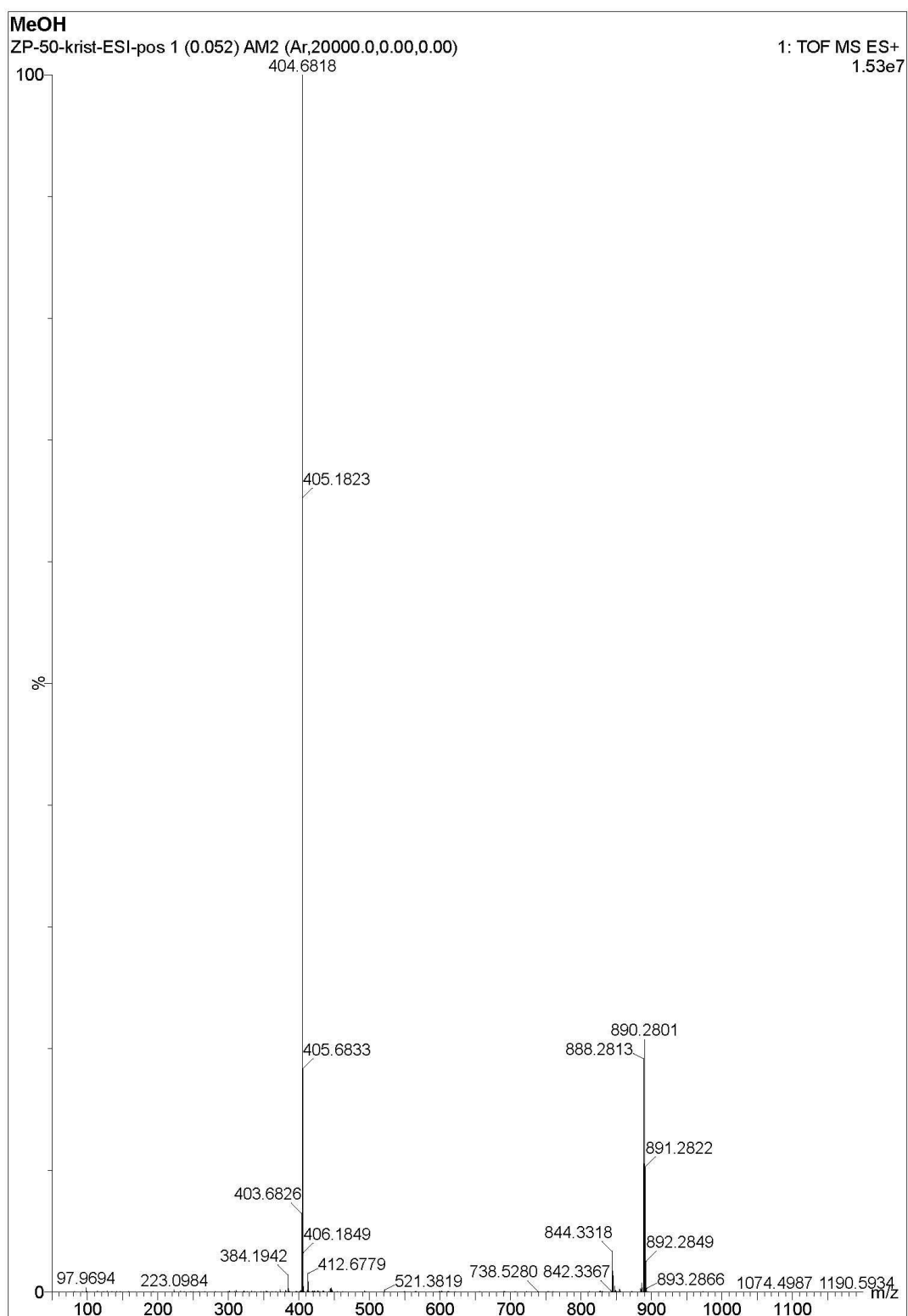


Figure S11. ESI-MS of **6** in CH₃CN.

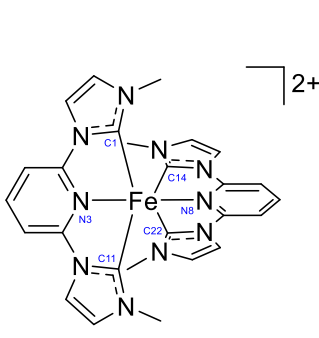
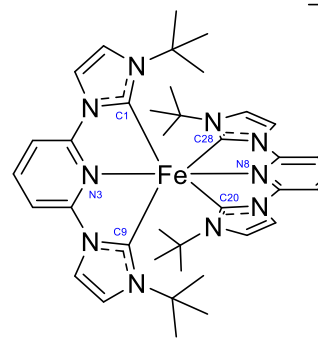
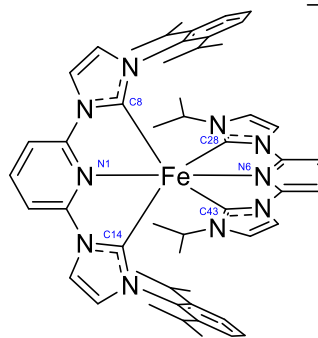
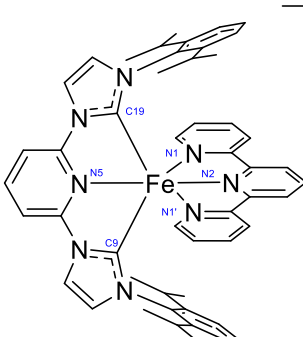
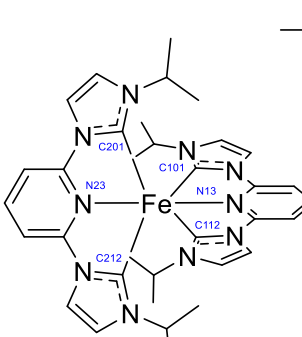
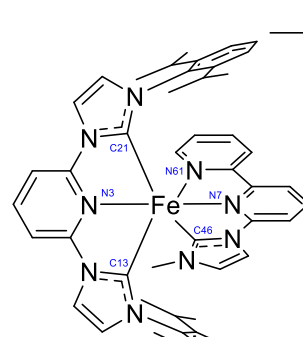
Crystal Structures

Table S1a. Crystallographic data for **3**, **4**, **6**.

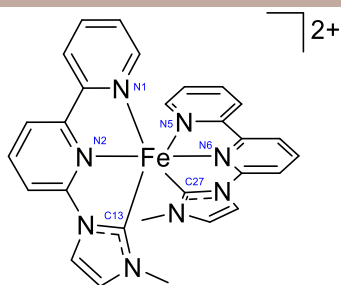
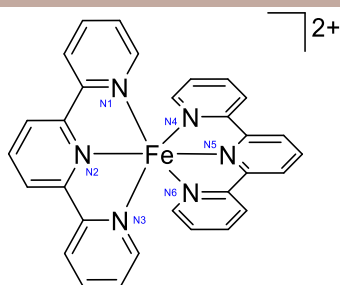
	3		4	6
formula weight	1113.8 [#]	934.5	1143.4	
crystal system	monoclinic		monoclinic	orthorhombic
space group	C 2/c		P 2 ₁ /n	P bca
a [Å]	40.556(6)		11.8308(14)	23.363(3)
b	15.059(2)		25.468(3)	17.913(2)
c	22.295(3)		12.5915(15)	25.657(3)
β [°]	123.282(7)		93.892(3)	
V [Å ³]	11383(3)		3785.2(8)	10737(2)
Z	8		4	8
F(000)	4592 [#]		1904	4694
crystal size [mm ³]	0.47 x 0.38 x 0.10		0.32 x 0.31 x 0.27	0.48 x 0.29 x 0.20

[#] calculated for sum formula without solvent molecules

Table S1b. Selected bond lengths [\AA] and angles [$^\circ$] for reference complexes **A**⁷¹, **B**⁷¹ and **C**⁷², **1**⁷³, **2**⁷³, **3**, **4** and **5**⁷⁴.

					
A		B		C	
Fe-C1	1.966(3)	Fe-C1	2.104(3)	Fe-C8	1.950(3)
Fe-N3	1.919(3)	Fe-N3	1.936(3)	Fe-N1	1.912(2)
Fe-C11	1.965(3)	Fe-C9	2.083(3)	Fe-C14	1.946(3)
Fe-C14	1.965(3)	Fe-C20	2.088(3)	Fe-C28	1.945(3)
Fe-N8	1.930(3)	Fe-N8	1.941(2)	Fe-N6	1.904(2)
Fe-C22	1.970(3)	Fe-C28	2.108(2)	Fe-C43	1.951(3)
C1-Fe-C11	158.6(2)	C1-Fe-C9	158.2(1)	C28-Fe-C43	159.22(13)
C14-Fe-C22	158.0(2)	C20-Fe-C28	157.8(1)	C8-Fe-C14	159.17(13)
					
1		2		3	
Fe-C19	1.993(4)	Fe-C112	1.946(4)	Fe-C21	1.972(4)
Fe-N5	1.922(3)	Fe-N13	1.917(3)	Fe-N3	1.900(3)

Fe-C9	1.997(4)	Fe-C101	1.950(4)	Fe-C13	1.971(4)
Fe-N1	1.952(2)	Fe-C201	1.960(4)	Fe-C46	1.939(4)
Fe-N2	1.866(4)	Fe-N23	1.913(3)	Fe-N7	1.886(3)
Fe-N1'	1.952(2)	Fe-C212	1.951(4)	Fe-N61	1.948(4)
N1-Fe-N1'	162.92(16)	C201-Fe-C212	158.17(17)	C21-Fe-C13	158.63(15)
C19-Fe-C9	158.64(17)	C112-Fe-C101	158.23(16)	C46-Fe-N61	160.89(16)

**4****5**

Fe-N1	1.995(2)	Fe-N1	1.99(1)
Fe-N2	1.892(2)	Fe-N2	1.89(1)
Fe-C13	1.922(3)	Fe-N3	1.95(1)
Fe-N5	1.990(2)	Fe-N4	1.97(1)
Fe-N6	1.895(2)	Fe-N5	1.89(1)
Fe-C27	1.916(3)	Fe-N6	1.97(1)
N1-Fe-C13	160.75(10)	N1-Fe-N3	162.2(5)
N5-Fe-C27	160.62(10)	N4-Fe-N6	160.5(5)

EXAFS Spectroscopy

Data Analysis

Data analysis started with background absorption removal from the experimental absorption spectrum by subtracting a Victoreen-type polynomial.⁷⁵⁻⁷⁸ The first maximum of the first derivative was set as E_0 . Afterwards the smooth part of the spectrum, corrected for pre-edge absorption, was determined by use of a piecewise polynomial which was adapted in a way that the low- R components of the resulting Fourier transform were minimal. The background subtracted spectrum was divided by its smooth part and then the photon energy was converted to photoelectron wavenumbers k . The resulting $\chi(k)$ was weighted with k^3 and Fourier transformed using a Hanning function window. According to the curved wave formalism data analysis was performed in k -space using the EXCURV98^{79,80} program which calculates the EXAFS functions according to a formulation in terms of radial distribution functions:

$$\chi(k) = \sum_j S_0^2(k) F_j(k) \int P_j(r_j) \frac{e^{-2r_j/\lambda}}{kr_j^2} \sin[2kr_j + \delta_j(k)] dr_j \quad (1)$$

To calculate the theoretical spectra XALPHA phase and amplitude functions^{79,80} were used and the mean free path of the scattered electrons was calculated from the imaginary part of the potential (VPI set to -4.00). Additionally a correction for the inner potential E_f was introduced to adjust the phase differences of the experimental and theoretical EXAFS functions.

The quality of the applied least-square fit is determined by the R -factor, which represents the percentage disagreement between experiment and theory and takes into account systematic and random errors according to:^{81,82}

$$R = \sum_i^N \frac{k_i^n}{\sum_j^N k_j^n |\chi_j^{exp}(k_j)|} |\chi_i^{exp}(k_i) - \chi_i^{theo}(k_i)| \cdot 100\% \quad (2)$$

The accuracy of the determined distances is 1 %, of the Debye-Waller-like factor 10 % and of the coordination numbers depending of the distance 5-15 %.⁸³

Results

The XANES (X-ray absorption near edge structure) spectra of the two solid samples **3** and **4** (Figure S12) look almost identical, both spectra show a weak prepeak at 7113.5 eV. Since the prepeak represents a dipole forbidden $1s \rightarrow 3d$ transition, only $3d \rightarrow 4p$ hybridization enables parity allowed transitions. In tetrahedral coordinated systems the prepeak intensity is usually high, whereas in octahedral coordinated systems the prepeak shows only very low intensities. In accordance to the crystal structure data the complexes exist in an octahedral structure, reflected in the low prepeak intensity.

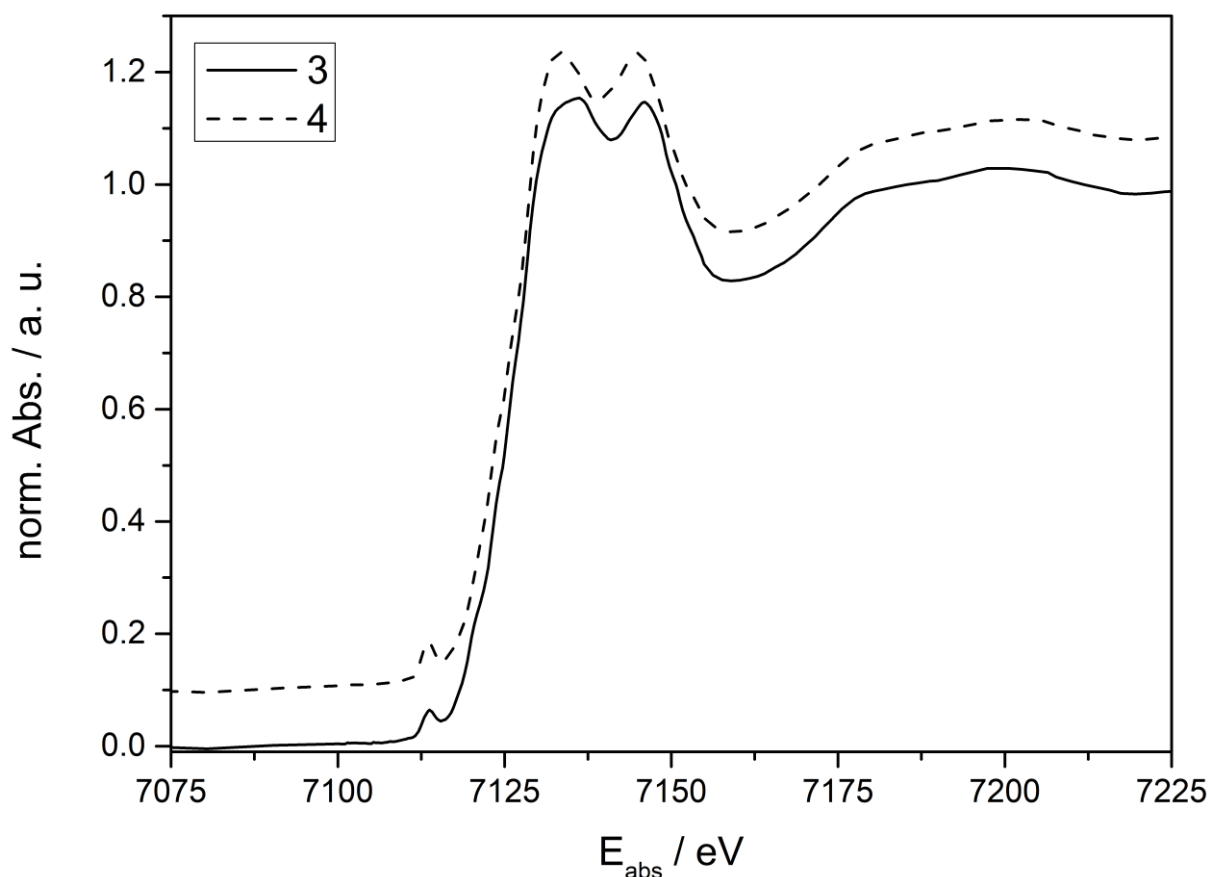


Figure S12. XANES spectra of complexes **3** and **4**.

Based on the crystal structure data the analysis of the EXAFS (extended X-ray absorption fine structure) spectra was performed. The spectra were fitted with two nitrogen shells at around 1.9 Å and 3.2 Å and three carbon shells at 2.8 Å, 3.9 Å and 4.3 Å. Since light atoms like nitrogen and carbon cannot be distinguished by EXAFS spectroscopy the shells were assigned to the predominant atom type at the particular distance. During the fits the distances, coordination numbers, Debye-Waller-like factors σ and the Fermi energy E_f were iterated freely. The amplitude reducing factor was held fix at 0.8000.

Figure S13 shows the resulting fit functions in k-space (top) and R-space (bottom).

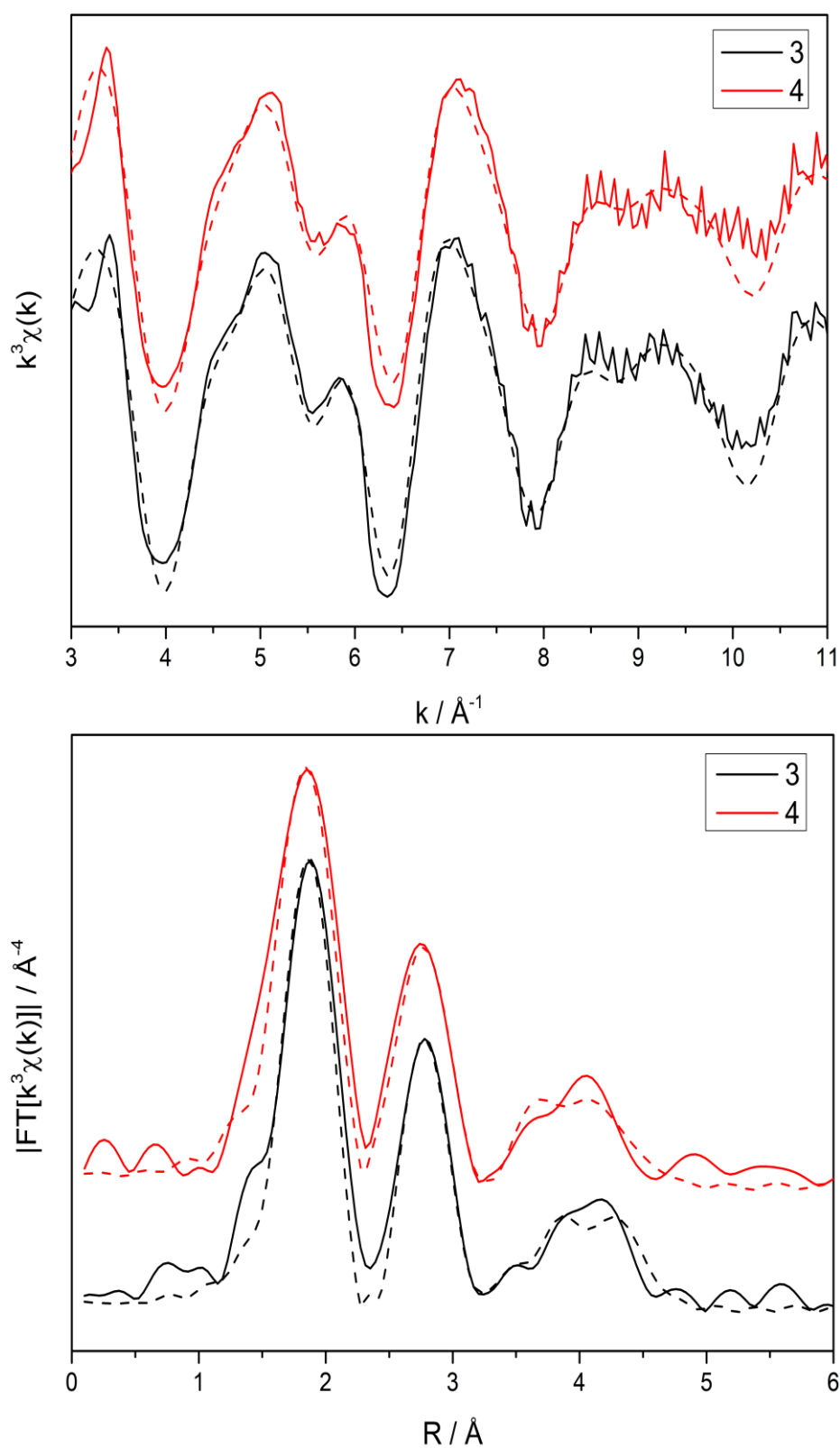


Figure S13. Experimental (solid lines) and theoretical (dashed lines) EXAFS spectra in the k -space (top) and Fourier Transformation (bottom) of **3** and **4**.

The fitting results are displayed in table S2.

Table S2. Neighbor atoms, coordination numbers and distances of EXAFS analysis

Sample	Abs-Bs ^{a)}	N(Bs) ^{b)}	R(Abs-Bs) [Å] ^{c)}	σ [Å ⁻¹] ^{d)}	R [%] ^{e)} E _f [eV] ^{f)} Afac ^{g)}
3	Fe-N	5.8±0.6	1.919±0.019	0.077±0.007	26.48
	Fe-C	7.7±0.8	2.828±0.028	0.059±0.006	1.566
	Fe-N	1.0±0.1	3.297±0.033	0.045±0.005	0.8000
	Fe-C	11.0±1.1	3.849±0.039	0.112±0.011	
	Fe-C	14.8±1.5	4.357±0.044	0.095±0.010	
4	Fe-N	5.7±0.6	1.913±0.019	0.084±0.008	27.82
	Fe-C	8.2±0.8	2.810±0.028	0.074±0.007	2.674
	Fe-N	0.6±0.1	3.262±0.033	0.032±0.003	0.8000
	Fe-C	11.4±1.1	3.825±0.038	0.112±0.011	
	Fe-C	7.6±0.8	4.335±0.044	0.074±0.007	

a) Abs=X-ray absorbing atom, Bs=backscattering atom, b) number of backscattering atoms, c) distance of absorbing atom to backscattering atom, d) Debye-Waller-like factor, e) fit-index, f) Fermi energy, that account for the shift between theory and experiment, g) amplitude reducing factor

X-ray spectroscopy

Each HERFD-XANES measurement was carried out in 60 seconds. Ten spectra with each measured at a different spot of the homogeneous sample were averaged. To exclude radiation damage, fast measurements over the prepeak with a scan-time of four seconds were carried out before and after each long HERFD-XANES measurement. Within these time frames, no radiation damage could be detected.

Since the VtC-XES region is superimposed by the slope of the K β mainline, all four VtC-XES spectra had to be background corrected. For this purpose, the K β mainline slope was fitted by a pseudo-Voigt function and the experiments were subtracted by the resulting fit. Normalization of VtC-XES and HERFD-XANES spectra were achieved by dividing each point by the sum of all intensity values. It should be taken into account that all XES spectra are blue-shifted by 0.63 eV due to a difference in energy calibration of incident- and XES monochromator.

DFT and TDDFT Calculations

Theoretical ligand / element projected XANES spectra were generated by selecting acceptor orbitals with significant Loewdin population values of an given ligand / element (see table S3). Core-excited states with significant percentages of the selected acceptor orbitals were taken into account and transitions to these core-excited states were broadened by a 1.5 eV Gaussian (fwhm) for each ligand / element. Theoretical ligand / element projected VtC-XES spectra were generated by selecting donor orbitals with significant Loewdin population values of a given ligand / element (see table S3) and transitions of these donor orbitals were broadened by a 2.5 eV Gaussian (fwhm) for each ligand / element.

Table S3. Loewdin population limits of the ligand / element project approach

Element and ligand Loewdin population values										
Complex	Donor orbitals					Acceptor orbitals				
	Fe	NHC	terpy	bpy	py	Fe	NHC	terpy	bpy	py
1	50	30	60		50	50	30	35		30
2	50	60			50	50	40			40
3	50	40		50	50	30	30		35	25
4	50	43		70		45	35		60	

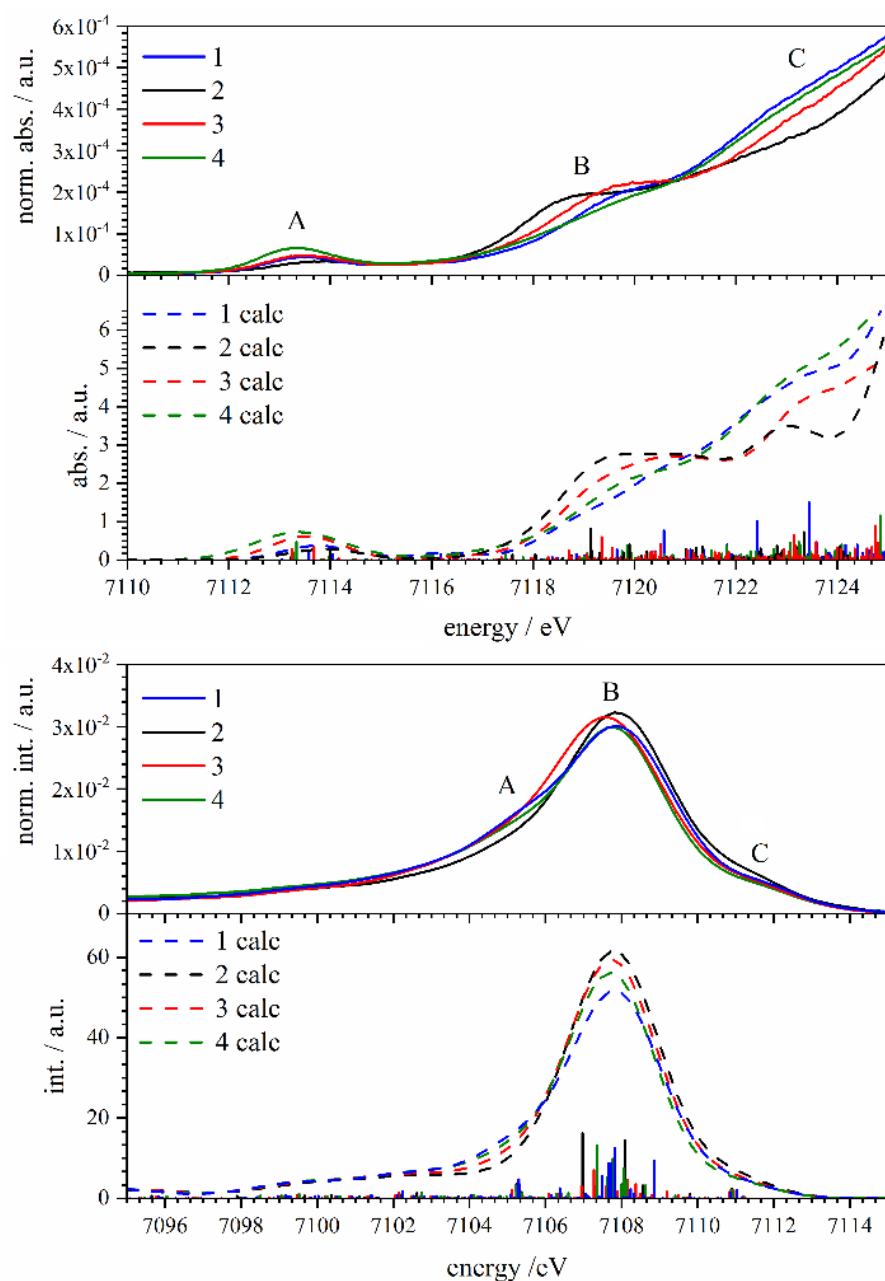


Figure S14. HERFD-XANES spectra of complexes **1-4** (upper half) in comparison to TD-DFT calculations (bottom half) (top). VtC-XES spectra of complexes **1-4** (upper half) in comparison to DFT-calculations (bottom half) (bottom).

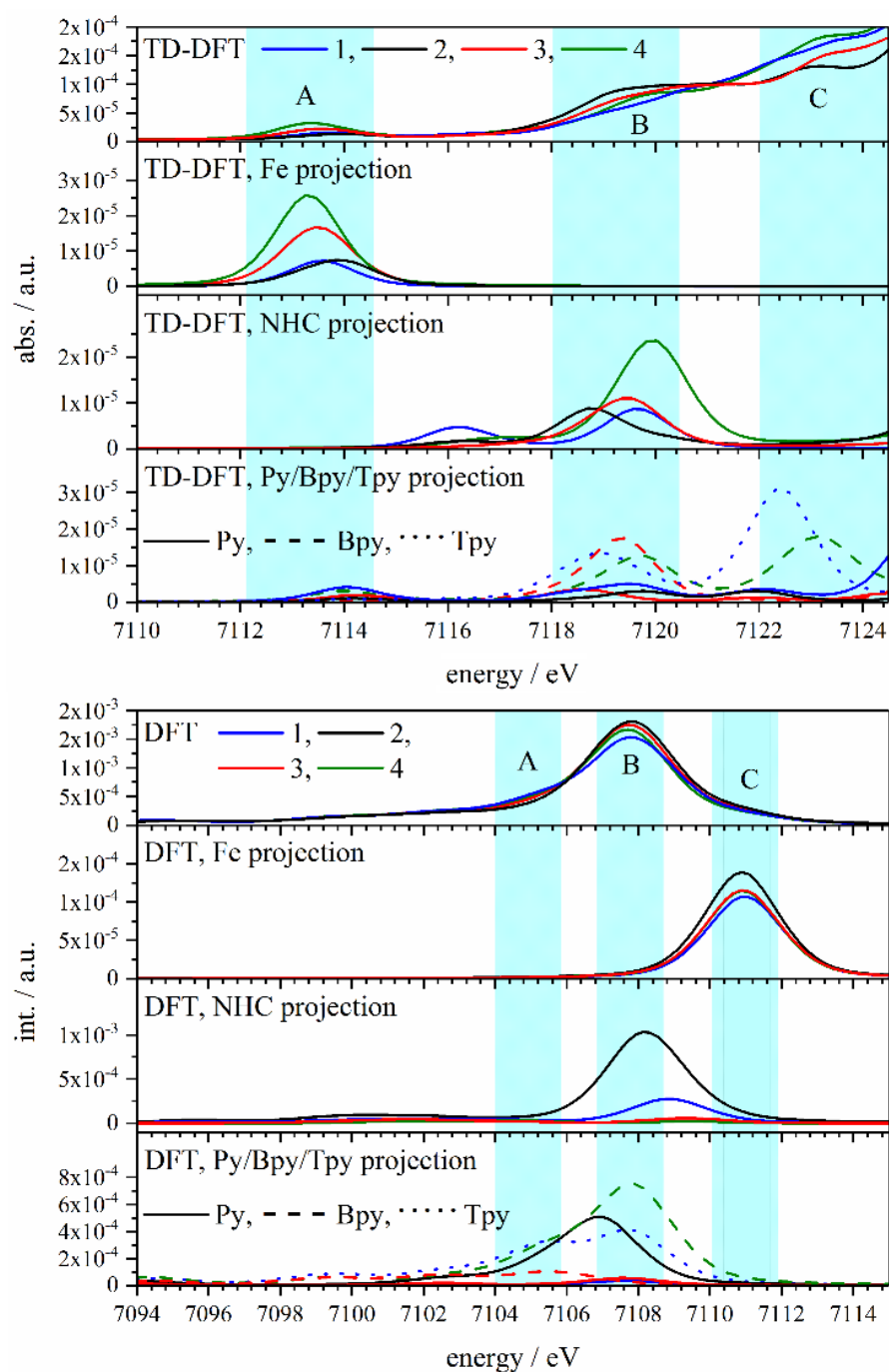


Figure S15. Contributions of Fe, NHC and pyridyl/polypyridyl functions of calculated spectral features in HERFD-XANES (top) and VtC-XES (bottom).

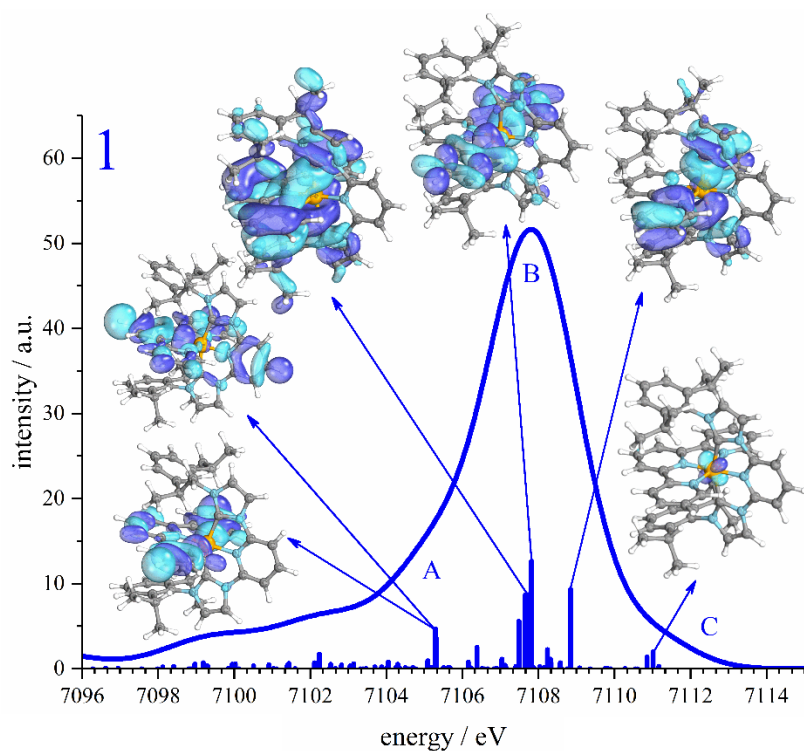


Figure S16. Calculated VtC-XES spectra of complexes **1** and predominant molecular orbitals that contribute to the observed features A, B and C.

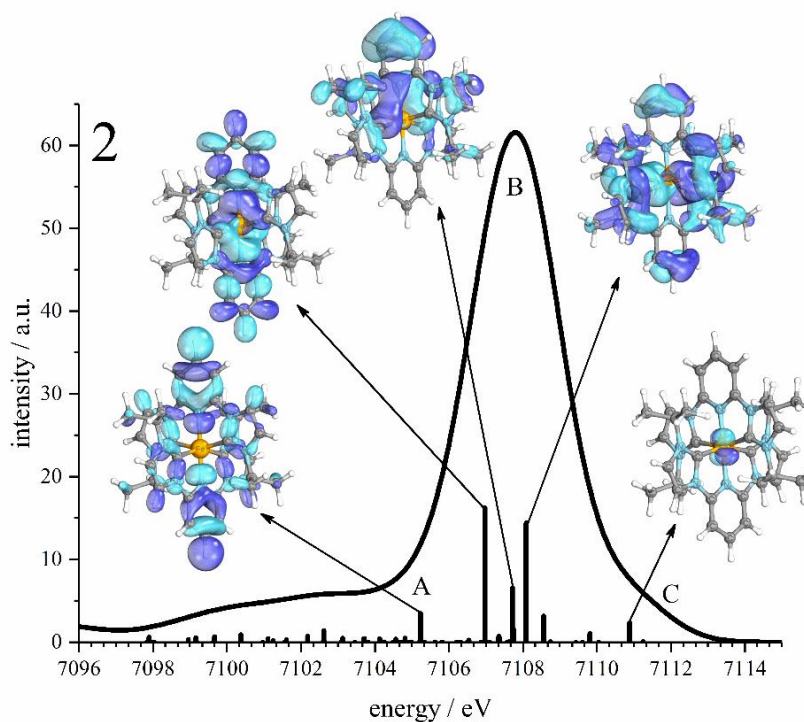


Figure S17. Calculated VtC-XES spectra of complexes **2** and predominant molecular orbitals that contribute to the observed features A, B and C.

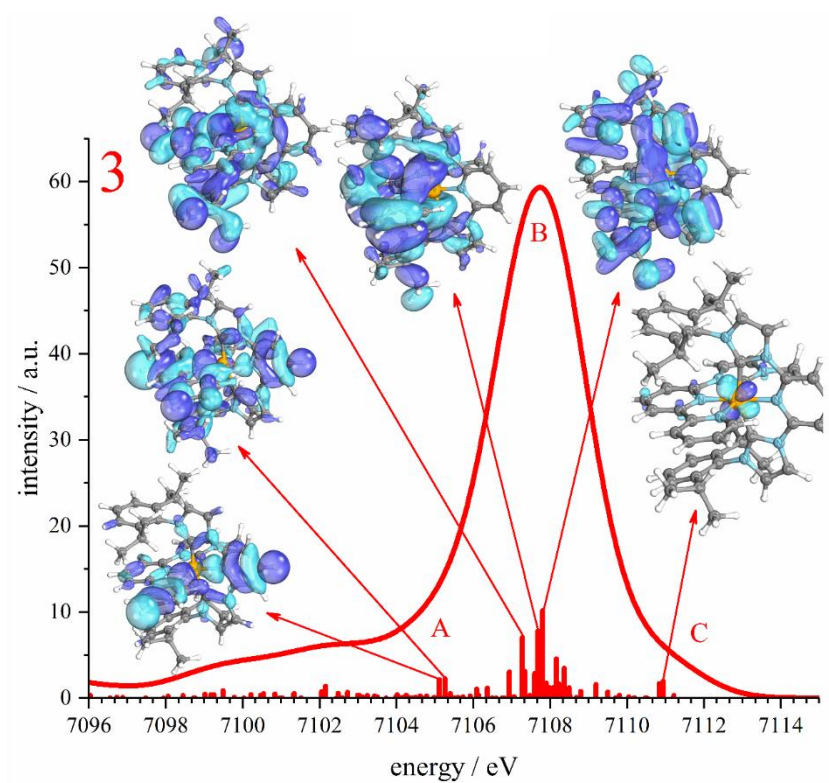


Figure S18. Calculated VtC-XES spectra of complexes **3** and predominant molecular orbitals that contribute to the observed features A, B and C.

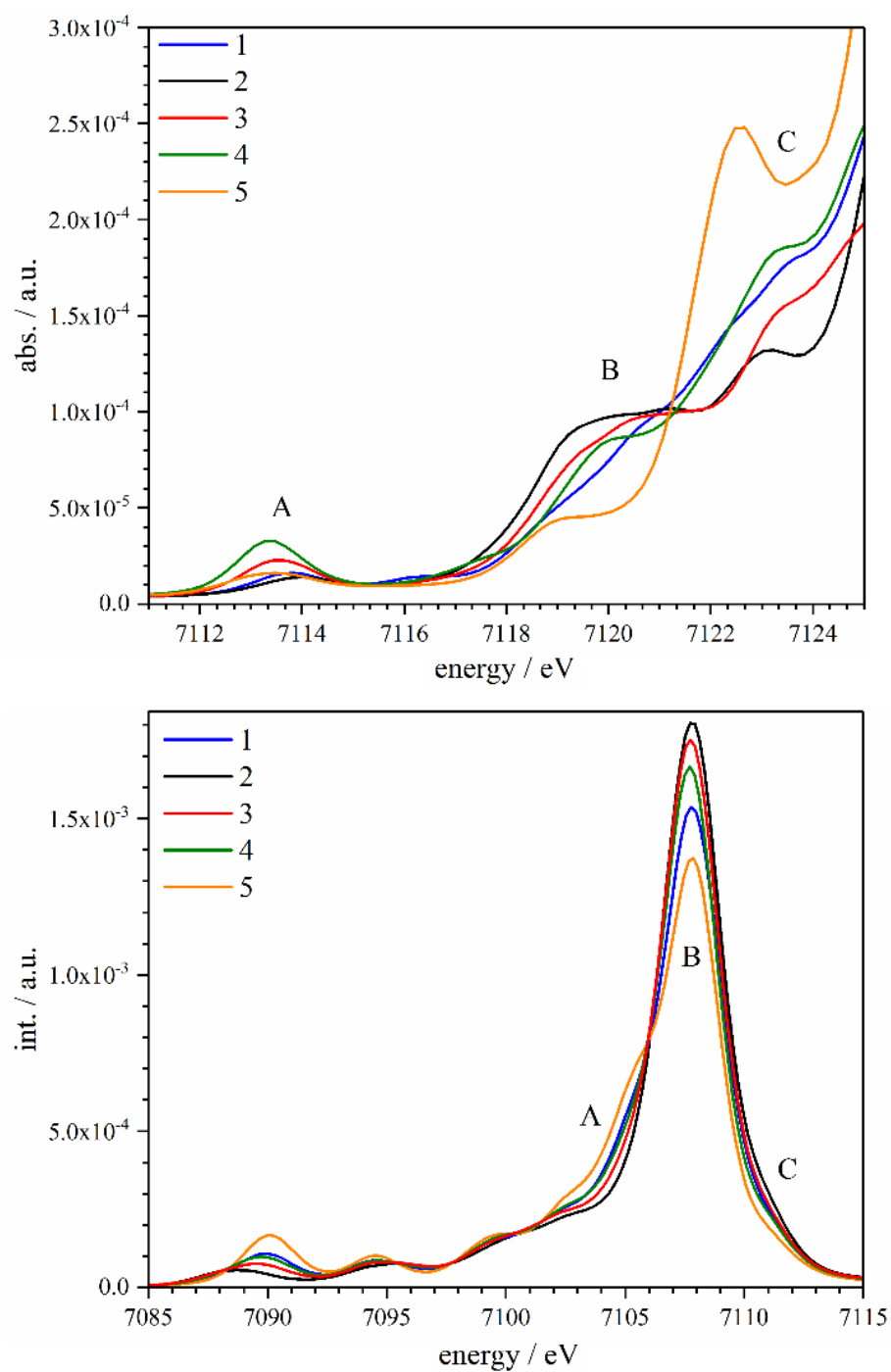


Figure S19. Theoretical Fe K-edge HERFD-XANES spectra of complexes **1 - 5** (top). Theoretical VtC-XES spectra of complexes **1 - 5** (bottom).

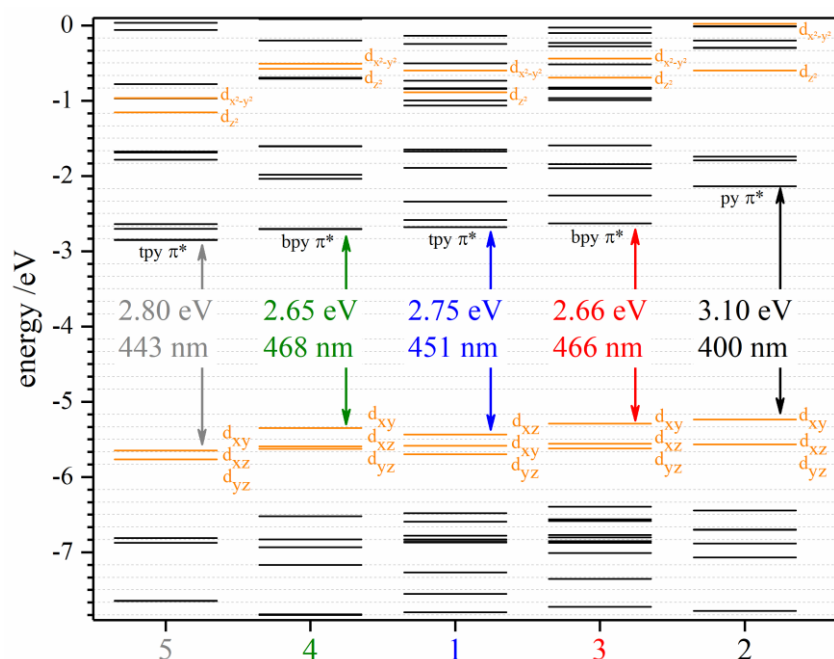


Figure S20. Molecular orbital levels of complexes **1** - **5** with solvation effects included (def2-TZVP / TPSSh, SMD (acetonitrile). Theoretical HOMO - LUMO gaps are given in-between HOMO and LUMO of each complex. Levels with significant Fe 3d contribution are shown in orange. Predominant character of LUMOs are given below each LUMO.

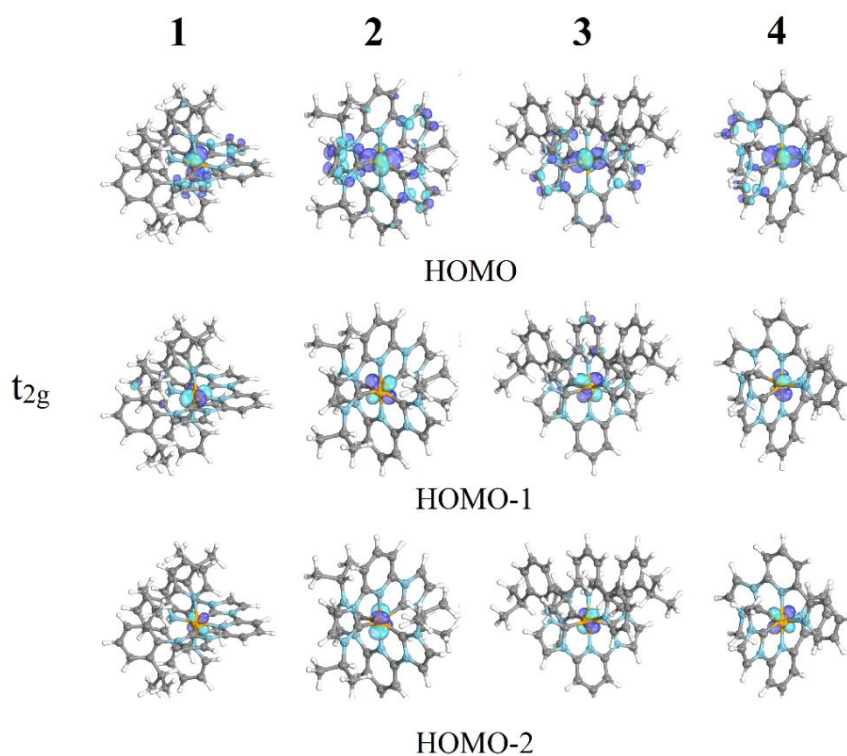


Figure S21. T_{2g} orbitals of Complexes 1 - 4.

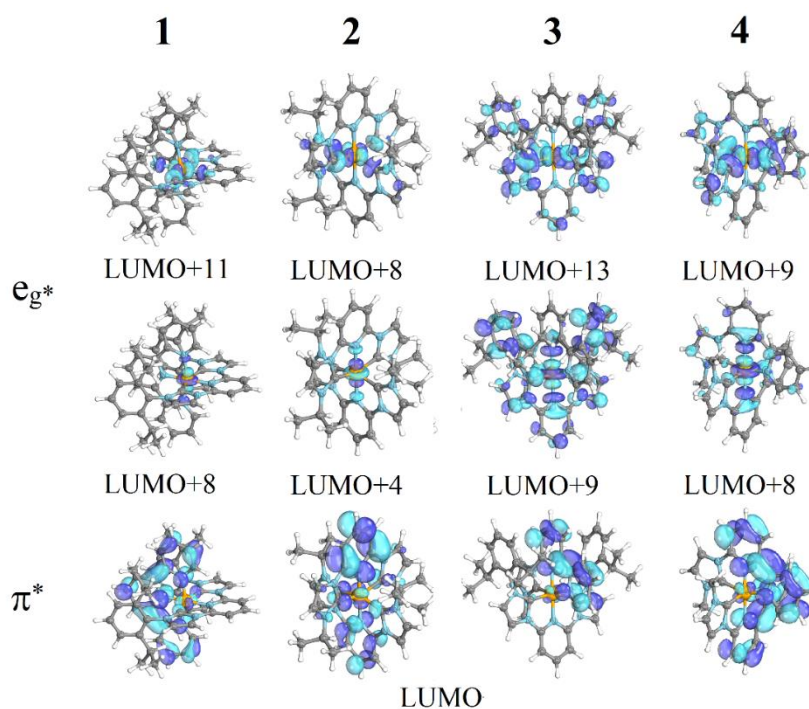


Figure S22. E_g^* orbitals of Complexes **1 - 4**.

Table S4. Comparison of all relevant TDDFT core-excited states of complex **1** concerning relevant ligand/element populations (acceptor orbitals), energies and normalized intensities.

Transition	Calc. energy ^[a] / eV	Norm. Int. ^[b] / a.u.	Element / Ligand character	Core-excited state contribution	LUMOs	Element / Ligand population per LUMO
1	7113.05	0.003	Fe	0.93	7	65.7
2	7113.58	0.164	Fe	0.83	11	54.9
3	7113.82	0.004	Terpy	0.99	0	63.8
4	7114.05	0.090	Py	0.99	2	51.1
5	7114.15	0.006	Terpy	0.87	1	68.9
6	7114.70	0.003	Py	0.83	3	42.5
7	7115.13	0.000	Terpy	0.89	4	64.4
8	7115.21	0.001	Terpy	0.95	5	69.6
9	7115.98	0.005	Terpy	0.99	6	59.6
10	7116.18	0.097	NHC	0.92	8	43.8
11	7116.46	0.007	NHC	0.54	14	53.1
12	7116.52	0.001				

13	7116.59	0.003				
14	7116.72	0.014				
15	7116.75	0.000				
16	7116.92	0.003	NHC	0.96	15	58.2
17	7117.09	0.000	Terpy	0.96	16	50.2
18	7117.48	0.003				
19	7117.48	0.003	NHC	0.53	18	50.9
20	7118.05	0.037	Terpy	0.99	19	62.1
21	7118.16	0.012	Terpy	0.98	20	54.4
22	7118.38	0.039	Py	0.94	21	52.5
23	7118.38	0.044				
24	7118.49	0.028	Terpy	0.75	23	45.9
25	7118.56	0.015	Terpy	0.76	24	38.2
26	7118.70	0.102				
27	7118.85	0.101	Terpy	0.92	26	48.4
28	7118.91	0.009				
29	7119.01	0.078	Terpy	0.95	28	40.4
30	7119.08	0.016				
31	7119.21	0.027				
32	7119.24	0.008				
33	7119.29	0.003				
34	7119.30	0.046				
35	7119.31	0.002				
36	7119.35	0.058	Terpy	0.93	35	62.2
37	7119.56	0.095	Py	0.97	36	31.2
38	7119.61	0.010	Terpy	0.98	37	66.2
39	7119.65	0.188	NHC	0.93	38	31.5
40	7119.70	0.018				
41	7119.73	0.053				
42	7119.84	0.020	Terpy	0.91	41	62.6
43	7119.85	0.009	NHC	0.85	42	30.9
44	7119.91	0.003	Py	0.69	43	43.5
45	7120.08	0.002				
46	7120.10	0.002				
47	7120.14	0.012				

48	7120.20	0.031				
49	7120.20	0.005				
50	7120.22	0.028				
51	7120.30	0.029				
52	7120.35	0.002				
53	7120.40	0.152				
54	7120.41	0.085				
55	7120.46	0.004				
56	7120.58	0.513				
57	7120.65	0.007				
58	7120.68	0.020				
59	7120.71	0.054				
60	7120.77	0.005				
61	7120.79	0.006				
62	7120.86	0.019	Terpy	0.88	62	48.7
63	7120.96	0.008				
64	7120.98	0.013				
65	7121.02	0.073				
66	7121.10	0.180				
67	7121.10	0.011				
68	7121.17	0.009				
69	7121.23	0.014				
70	7121.26	0.013				
71	7121.31	0.008				
72	7121.34	0.038				
73	7121.37	0.177				
74	7121.40	0.053				
75	7121.44	0.013				
76	7121.47	0.037				
77	7121.59	0.004				
78	7121.63	0.064				
79	7121.64	0.008				
80	7121.67	0.091				
81	7121.73	0.021				
82	7121.78	0.006				

83	7121.82	0.265				
84	7121.90	0.033				
85	7121.91	0.099				
86	7122.05	0.066	Py	0.61	85	30.3
87	7122.06	0.053				
88	7122.07	0.065				
89	7122.11	0.048				
90	7122.20	0.004				
91	7122.21	0.050				
92	7122.23	0.018				
93	7122.31	0.033				
94	7122.31	0.030	Terpy	0.55	93	37.6
95	7122.32	0.023				
96	7122.42	0.670	Terpy	0.67	99	40.9
97	7122.49	0.045				
98	7122.50	0.069				
99	7122.51	0.104				
100	7122.57	0.010				
101	7122.64	0.064				
102	7122.66	0.008				
103	7122.67	0.055				
104	7122.74	0.105				
105	7122.76	0.009				
106	7122.81	0.141				
107	7122.87	0.021				
108	7122.93	0.021				
109	7123.01	0.051				
110	7123.07	0.053				
111	7123.14	0.042				
112	7123.19	0.031				
113	7123.22	0.091				
114	7123.25	0.033				
115	7123.30	0.018				
116	7123.41	0.098				
117	7123.43	0.011				

118	7123.44	1.000				
119	7123.51	0.014				
120	7123.59	0.293				
121	7123.68	0.037				
122	7123.69	0.055				
123	7123.76	0.075				
124	7123.82	0.130				
125	7123.84	0.115				
126	7123.88	0.071				
127	7123.94	0.041				
128	7124.03	0.019				
129	7124.05	0.013				
130	7124.16	0.258				
131	7124.18	0.031				
132	7124.24	0.070				
133	7124.32	0.033				
134	7124.36	0.012				
135	7124.39	0.264				
136	7124.39	0.167				
137	7124.49	0.094				
138	7124.50	0.121				
139	7124.60	0.020				
140	7124.62	0.173				
141	7124.71	0.096				
142	7124.80	0.021				
143	7124.87	0.134				
144	7124.93	0.140				
145	7124.94	0.057				
^[a] all values were shifted by 151.5 eV, ^[b] normalized to 1 (all values were divided by the overall highest value)						

Table S5. Comparison of all relevant TDDFT core-excited states of complex **2** concerning relevant ligand/element populations (acceptor orbitals), energies and normalized intensities.

Transition	Calc. energy ^[a] / eV	Norm. Int. ^[b] / a.u.	Element / Ligand character	Core-excited state contribution	LUMOs	Element / Ligand population per LUMO
1	7113.22	0.045	Fe	0.96	4	64.3
2	7113.99	0.149	Fe	0.86	8	50.8
3	7114.17	0.010	Py	0.83	0	53.3
4	7114.17	0.009	Py	0.82	1	53.4
5	7114.49	0.005	Py	0.91	2	44.7
6	7114.96	0.000	Py	1.00	3	49.5
7	7116.10	0.022	NHC	0.88	7	61.7
8	7116.35	0.002	NHC	0.66	5	56.5
9	7116.35	0.001	NHC	0.66	6	56.4
10	7116.81	0.002	NHC	0.88	9	70.5
11	7116.81	0.003	NHC	0.80	10	65.5
12	7116.94	0.001	NHC	0.98	11	68.4
13	7117.32	0.000	NHC	0.70	13	45.1
14	7117.35	0.003				
15	7117.59	0.086				
16	7117.78	0.000	NHC	0.94	15	59.5
17	7118.04	0.094				
18	7118.05	0.089				
19	7118.29	0.001	Py	1.00	18	56.3
20	7118.39	0.011	Py	0.98	19	48.9
21	7118.59	0.029				
22	7118.59	0.029				
23	7118.66	0.001				
24	7118.74	0.039	NHC	0.57	23	41.9
25	7118.75	0.075	NHC	0.57	24	43.3
26	7118.76	0.076	NHC	0.96	25	47.3
27	7118.85	0.005				
28	7118.91	0.004				
29	7119.14	0.543				
30	7119.15	0.167				
31	7119.17	0.122				

32	7119.28	0.001	Py	0.98	31	45.3
33	7119.31	0.125				
34	7119.60	0.001				
35	7119.64	0.003				
36	7119.69	0.006				
37	7119.73	0.020	Py	0.88	38	53.2
38	7119.76	0.042	Py	0.66	39	53.7
39	7119.78	0.001				
40	7119.79	0.127				
41	7119.88	0.007				
42	7119.90	0.266				
43	7120.10	0.024				
44	7120.13	0.073				
45	7120.14	0.032	NHC	0.81	44	41.7
46	7120.14	0.022				
47	7120.19	0.012				
48	7120.24	0.148				
49	7120.25	0.126				
50	7120.32	0.097				
51	7120.33	0.119				
52	7120.38	0.070				
53	7120.53	0.029				
54	7120.63	0.053				
55	7120.64	0.003				
56	7120.71	0.005				
57	7120.71	0.006				
58	7120.76	0.041				
59	7120.87	0.005				
60	7120.89	0.009				
61	7120.89	0.009				
62	7121.01	0.184				
63	7121.14	0.171				
64	7121.15	0.098				
65	7121.21	0.212				
66	7121.24	0.063				

67	7121.33	0.236				
68	7121.33	0.054				
69	7121.49	0.022				
70	7121.50	0.018				
71	7121.55	0.019				
72	7121.58	0.013				
73	7121.66	0.069				
74	7121.69	0.031				
75	7121.79	0.018				
76	7121.85	0.073				
77	7121.92	0.030				
78	7121.93	0.032				
79	7121.95	0.065	Py	0.81	76	54.6
80	7122.09	0.033				
81	7122.12	0.021				
82	7122.16	0.048				
83	7122.21	0.006				
84	7122.25	0.040				
85	7122.38	0.014				
86	7122.46	0.135				
87	7122.48	0.199				
88	7122.57	0.062				
89	7122.64	0.060				
90	7122.65	0.036				
91	7122.71	0.030				
92	7122.77	0.086				
93	7122.81	0.250				
94	7122.83	0.082				
95	7122.88	0.114				
96	7122.91	0.160				
97	7123.00	0.015				
98	7123.19	0.221				
99	7123.20	0.191				
100	7123.34	0.485				
101	7123.35	0.006				

102	7123.53	0.011				
103	7123.56	0.022				
104	7123.57	0.027				
105	7123.60	0.003				
106	7123.67	0.027				
107	7123.74	0.056				
108	7123.83	0.065				
109	7123.91	0.013				
110	7124.04	0.236				
111	7124.10	0.137				
112	7124.11	0.137				
113	7124.20	0.071				
114	7124.36	0.073				
115	7124.39	0.037				
116	7124.55	0.019				
117	7124.56	0.047				
118	7124.58	0.013				
119	7124.67	0.004				
120	7124.77	0.300				
121	7124.77	0.257				
122	7124.94	0.048				
123	7124.97	0.136				
^[a] all values were shifted by 151.5 eV, ^[b] normalized to 1 (all values were divided by the overall highest value)						

Table S6. Comparison of all relevant TDDFT core-excited states of complex **3** concerning relevant ligand/element populations (acceptor orbitals), energies and normalized intensities.

Transition	Calc. energy ^[a] / eV	Norm. Int. ^[b] / a.u.	Element / Ligand character	Core-excited state contribution	LUMOs	Element / Ligand population per LUMO
1	7113.24	0.187	Fe	0.38	9	32.8
2	7113.68	0.224	Fe	0.32	13	33.1
3	7113.87	0.007	Bpy	0.95	0	66
4	7114.16	0.032	Py	0.72	1	50.8

5	7114.49	0.012	Py	0.61	2	44.6
6	7114.81	0.001	Bpy	0.66	3	52.9
7	7115.15	0.001	Bpy	0.90	4	65.2
8	7116.08	0.003				
9	7116.19	0.023				
10	7116.23	0.005				
11	7116.43	0.001				
12	7116.50	0.001				
13	7116.64	0.005				
14	7116.69	0.002				
15	7116.76	0.002	NHC	0.86	15	59.7
16	7116.85	0.003	NHC	0.74	14	59.4
17	7117.27	0.003	NHC	0.97	16	39.8
18	7117.37	0.047				
19	7117.56	0.005	NHC	0.97	18	50.8
20	7117.95	0.028	Bpy	0.85	19	37.4
21	7118.00	0.018				
22	7118.28	0.030	Py	0.97	21	36.4
23	7118.30	0.045				
24	7118.40	0.009	Bpy	0.97	123	37.3
25	7118.45	0.032				
26	7118.70	0.158				
27	7118.75	0.055	NHC	0.93	26	39.3
28	7118.89	0.007				
29	7118.91	0.057				
30	7119.06	0.102				
31	7119.10	0.014				
32	7119.12	0.011	NHC	0.68	31	30.7
33	7119.19	0.006				
34	7119.21	0.023				
35	7119.27	0.003				
36	7119.32	0.001	Bpy	0.85	36	42.5
37	7119.35	0.397	Bpy	0.70	35	44.5
38	7119.44	0.036				
39	7119.52	0.032				

6. Supporting Information

40	7119.56	0.214	NHC	0.97	39	34.1
41	7119.63	0.032				
42	7119.71	0.028				
43	7119.81	0.008				
44	7119.81	0.010				
45	7119.87	0.009				
46	7119.94	0.010				
47	7120.03	0.035				
48	7120.08	0.010				
49	7120.10	0.042				
50	7120.15	0.010				
51	7120.22	0.090				
52	7120.26	0.009				
53	7120.32	0.136				
54	7120.34	0.150				
55	7120.36	0.008				
56	7120.40	0.136				
57	7120.49	0.054				
58	7120.52	0.278				
59	7120.56	0.011				
60	7120.60	0.040				
61	7120.61	0.042				
62	7120.66	0.002				
63	7120.72	0.050				
64	7120.75	0.005				
65	7120.80	0.004				
66	7120.89	0.004				
67	7121.01	0.031				
68	7121.04	0.166				
69	7121.08	0.005				
70	7121.14	0.021				
71	7121.16	0.130				
72	7121.19	0.024				
73	7121.22	0.022				
74	7121.25	0.026				

75	7121.31	0.071				
76	7121.33	0.105				
77	7121.37	0.002				
78	7121.47	0.021				
79	7121.53	0.008				
80	7121.58	0.134				
81	7121.61	0.080				
82	7121.65	0.033				
83	7121.67	0.125				
84	7121.69	0.013				
85	7121.78	0.050				
86	7121.81	0.105				
87	7121.86	0.134				
88	7121.99	0.026	Py	0.82	87	31.7
89	7122.01	0.020				
90	7122.03	0.027				
91	7122.06	0.027				
92	7122.07	0.052				
93	7122.11	0.008				
94	7122.17	0.019				
95	7122.18	0.017				
96	7122.20	0.013				
97	7122.34	0.029				
98	7122.42	0.022				
99	7122.45	0.069				
100	7122.47	0.009				
101	7122.50	0.036				
102	7122.54	0.046				
103	7122.58	0.060				
104	7122.60	0.030				
105	7122.66	0.010				
106	7122.69	0.023				
107	7122.72	0.014				
108	7122.83	0.075				
109	7122.89	0.029				

110	7122.94	0.184				
111	7123.04	0.137				
112	7123.12	0.044				
113	7123.15	0.437				
114	7123.17	0.252				
115	7123.19	0.172				
116	7123.25	0.065				
117	7123.28	0.075				
118	7123.34	0.048				
119	7123.41	0.011				
120	7123.51	0.098				
121	7123.58	0.312				
122	7123.61	0.077				
123	7123.66	0.016				
124	7123.77	0.095				
125	7123.79	0.021				
126	7123.82	0.064				
127	7123.87	0.021				
128	7123.92	0.029				
129	7123.94	0.018				
130	7123.97	0.012				
131	7123.99	0.217				
132	7124.07	0.198				
133	7124.16	0.041				
134	7124.25	0.051				
135	7124.28	0.029				
136	7124.33	0.004				
137	7124.34	0.195				
138	7124.48	0.070				
139	7124.53	0.055	Py	0.93	138	33.2
140	7124.58	0.198				
141	7124.65	0.053				
142	7124.68	0.226				
143	7124.71	0.008				
144	7124.75	0.599				

145	7124.80	0.295				
146	7124.85	0.075				
147	7124.86	0.071				
148	7124.95	0.020				
149	7124.98	0.020				
[a] all values were shifted by 151.5 eV, [b] normalized to 1 (all values were divided by the overall highest value)						

Table S7. Comparison of all relevant TDDFT core-excited states of complex **4** concerning relevant ligand/element populations (acceptor orbitals), energies and normalized intensities.

Transition	Calc. energy ^[a] / eV	Norm. Int. ^[b] / a.u.	Element / Ligand character	Core-excited state contribution	LUMOs	Element / Ligand population per LUMO
1	7113.26	0.133	Fe	0.73	8	53.4
2	7113.33	0.311	Fe	0.51	9	45.0
3	7113.82	0.002	Bpy	0.90	1	66.3
4	7113.96	0.046	Bpy	0.73	0	66.7
5	7114.46	0.015				
6	7114.72	0.006				
7	7115.18	0.003	Bpy	0.88	5	71.3
8	7115.26	0.001	Bpy	0.99	4	71.8
9	7116.07	0.008				
10	7116.22	0.001				
11	7116.43	0.009	NHC	0.67	10	53.9
12	7116.82	0.012	NHC	0.87	11	63.5
13	7117.22	0.003	NHC	0.98	12	43.7
14	7117.41	0.011	NHC	0.91	14	38.6
15	7117.45	0.096				
16	7117.80	0.044				
17	7118.21	0.006				
18	7118.27	0.022				
19	7118.56	0.022	Bpy	0.98	18	64.4
20	7118.58	0.008				
21	7118.92	0.012				

22	7118.96	0.024				
23	7118.97	0.009	Bpy	0.92	21	63.3
24	7119.00	0.055				
25	7119.07	0.118				
26	7119.12	0.078				
27	7119.22	0.031	NHC	0.88	26	41.5
28	7119.34	0.01	Bpy	0.84	27	61.2
29	7119.40	0.006	Bpy	0.93	28	62.1
30	7119.67	0.01				
31	7119.68	0.012				
32	7119.75	0.156	Bpy	0.53	32	67.5
33	7119.78	0.03	Bpy	0.62	31	63.7
34	7119.85	0.258	NHC	0.82	33	54.0
35	7119.93	0.123				
36	7120.02	0.036				
37	7120.07	0.046	NHC	0.91	35	42.1
38	7120.25	0.096	NHC	0.98	37	37.7
39	7120.30	0.015				
40	7120.37	0.015				
41	7120.45	0.014				
42	7120.58	0.019				
43	7120.59	0.109				
44	7120.65	0.03				
45	7120.74	0.088				
46	7120.77	0.066				
47	7120.84	0.006				
48	7121.01	0.117				
49	7121.07	0.01				
50	7121.18	0.095				
51	7121.35	0.013				
52	7121.40	0.048				
53	7121.51	0.162				
54	7121.56	0.033				
55	7121.72	0.106				
56	7121.81	0.244				

57	7121.92	0.013	Bpy	0.90	56	63.1
58	7121.98	0.043				
59	7122.00	0.072				
60	7122.10	0.095				
61	7122.19	0.009				
62	7122.22	0.071				
63	7122.28	0.15				
64	7122.39	0.146				
65	7122.42	0.066				
66	7122.46	0.058				
67	7122.70	0.084	Bpy	0.92	66	61.2
68	7122.74	0.184				
69	7122.89	0.017				
70	7122.95	0.135				
71	7123.00	0.079				
72	7123.07	0.295				
73	7123.19	0.173	Bpy	0.90	72	61.9
74	7123.24	0.313				
75	7123.27	0.26				
76	7123.39	0.058				
77	7123.42	0.057	Bpy	0.47	76	61.6
78	7123.46	0.142				
79	7123.56	0.02				
80	7123.61	0.086				
81	7123.76	0.178				
82	7123.80	0.055				
83	7123.95	0.156				
84	7124.02	0.076				
85	7124.08	0.266				
86	7124.10	0.038				
87	7124.22	0.065				
88	7124.24	0.129				
89	7124.31	0.024				
90	7124.51	0.031				
91	7124.57	0.036				

92	7124.64	0.089				
93	7124.69	0.035	Bpy	0.77	92	66.6
94	7124.75	0.244				
95	7124.83	0.23				
96	7124.85	0.778				
[a] all values were shifted by 151.5 eV, [b] normalized to 1 (all values were divided by the overall highest value)						

Table S8. Comparison of all relevant VtC-XES transitions of complex **1** concerning relevant ligand/element populations (donor orbitals), energies and normalized intensities.

HOMOs	Calc. energy ^[a] / eV	Norm. Int. ^[b] / a.u.	Element / Ligand character	Element / Ligand population per HOMO
-148	7087.77	0.019		
-147	7088.05	0.013		
-146	7089.39	0.025		
-145	7089.58	0.076		
-144	7090.19	0.097		
-143	7090.72	0.020		
-142	7090.73	0.002		
-141	7091.61	0.006		
-140	7093.59	0.001		
-139	7093.78	0.000		
-138	7094.00	0.026		
-137	7094.18	0.001		
-136	7094.29	0.032		
-135	7094.44	0.048		
-134	7094.62	0.016		
-133	7094.77	0.009		
-132	7095.09	0.000		
-131	7095.09	0.000		
-130	7095.32	0.000		
-129	7095.61	0.000		

-128	7095.83	0.031		
-127	7095.89	0.000		
-126	7095.91	0.008		
-125	7096.28	0.000	Terpy	87.3
-124	7096.62	0.004	NHC	36.5
-123	7096.95	0.005		
-122	7097.56	0.000		
-121	7097.57	0.000		
-120	7097.98	0.000	NHC	38.6
-119	7098.12	0.014		
-118	7098.12	0.004	Terpy	93.4
-117	7098.41	0.017	Terpy	93.2
-116	7098.80	0.000		
-115	7098.80	0.000		
-114	7098.85	0.000		
-113	7098.87	0.000		
-112	7098.96	0.035	Terpy	83.9
-111	7099.18	0.045	Terpy	93.4
-110	7099.23	0.025	NHC	44.5
-109	7099.30	0.022	NHC	53.1
-108	7099.84	0.001	NHC	33.9
-107	7099.94	0.033	Terpy	88.9
-106	7100.02	0.037	Terpy	92.8
-105	7100.12	0.000		
-104	7100.12	0.000		
-103	7100.51	0.020	NHC	67.1
-102	7100.91	0.031		
-101	7101.04	0.002		
-100	7101.11	0.000	NHC	41.2
-99	7101.39	0.024		
-98	7101.44	0.040	NHC	38.3
-97	7101.59	0.003		
-96	7102.11	0.045	NHC	49.2
-95	7102.24	0.106	Terpy	83.9
-94	7102.52	0.006	Terpy	75.2

-93	7102.54	0.034	Py	59.3
-92	7102.54	0.002		
-91	7102.56	0.006		
-90	7102.66	0.002		
-89	7102.82	0.028	Terpy	89.4
-88	7103.05	0.021		
-87	7103.09	0.008	NHC	37.8
-86	7103.14	0.037	Terpy	85.3
-85	7103.32	0.000	Terpy	87.7
-84	7103.39	0.000	NHC	49.8
-83	7103.47	0.003		
-82	7103.69	0.013		
-81	7103.88	0.014	Terpy	70.1
-80	7104.01	0.009		
-79	7104.04	0.011	NHC	46.0
-78	7104.05	0.048	Terpy	63.3
-77	7104.25	0.010	NHC	67.0
-76	7104.30	0.031	NHC	53.3
-75	7104.36	0.002		
-74	7104.37	0.002		
-73	7104.50	0.010	NHC	41.4
-72	7104.56	0.000		
-71	7104.59	0.001	Terpy	83.7
-70	7104.69	0.009		
-69	7104.75	0.000		
-68	7104.77	0.001		
-67	7105.07	0.004		
-66	7105.09	0.057		
-65	7105.18	0.011		
-64	7105.19	0.005		
-63	7105.26	0.000		
-62	7105.30	0.287	Terpy	82.0
-61	7105.32	0.215	Terpy	67.2
-60	7105.47	0.001		
-59	7105.51	0.010		

-58	7105.53	0.002		
-57	7105.59	0.000		
-56	7105.60	0.002		
-55	7105.64	0.011	Py	63.2
-54	7105.68	0.008		
-53	7106.16	0.048	Terpy	82.0
-52	7106.19	0.014		
-51	7106.24	0.001		
-50	7106.24	0.001		
-49	7106.39	0.156		
-48	7106.51	0.001	Terpy	79.9
-47	7106.56	0.000		
-46	7106.58	0.000		
-45	7106.67	0.000		
-44	7106.83	0.000		
-43	7106.88	0.002		
-42	7106.90	0.004		
-41	7107.04	0.071		
-40	7107.07	0.002		
-39	7107.12	0.026		
-38	7107.16	0.004		
-37	7107.38	0.003		
-36	7107.39	0.010		
-35	7107.41	0.020		
-34	7107.42	0.004		
-33	7107.49	0.344		
-32	7107.65	0.534		
-31	7107.68	0.071	Py	51.1
-30	7107.71	0.537		
-29	7107.82	0.778	Terpy	69.4
-28	7107.85	0.014		
-27	7107.86	0.010		
-26	7107.89	0.002		
-25	7107.90	0.001		
-24	7108.04	0.016		

-23	7108.11	0.000		
-22	7108.15	0.010		
-21	7108.22	0.018		
-20	7108.24	0.139		
-19	7108.31	0.000		
-18	7108.32	0.069		
-17	7108.34	0.043		
-16	7108.54	0.000		
-15	7108.58	0.045		
-14	7108.60	0.002		
-13	7108.75	0.001		
-12	7108.85	0.576	NHC	30.6
-11	7109.08	0.007	Terpy	75.0
-10	7109.36	0.001	NHC	49.7
-9	7109.76	0.001	NHC	76.5
-8	7109.82	0.004		
-7	7109.91	0.000		
-6	7110.26	0.001		
-5	7110.27	0.002		
-4	7110.55	0.000		
-3	7110.61	0.000		
-2	7110.86	0.085	Fe	78.7
-1	7111.02	0.123	Fe	68.3
0	7111.17	0.018	Fe	68.6
^[a] all values were shifted by 150.9 eV, ^[b] normalized to 1 (all values were divided by the overall highest value)				

Table S9. Comparison of all relevant VtC-XES transitions of complex **2** concerning relevant ligand/element populations (donor orbitals), energies and normalized intensities.

HOMOs	Calc. energy ^[a] / eV	Norm. Int. ^[b] / a.u.	Element / Ligand character	Element / Ligand population per HOMO
-116	7087.73	0.000	NHC	61.9

-115	7087.80	0.041	NHC	63.7
-114	7088.05	0.013	NHC	76.5
-113	7088.05	0.013	NHC	76.3
-112	7089.40	0.066		
-111	7089.42	0.000		
-110	7090.75	0.001	NHC	60.4
-109	7090.75	0.001	NHC	60.4
-108	7091.64	0.000		
-107	7091.68	0.010		
-106	7093.98	0.000	Py	86.6
-105	7094.03	0.063	Py	87.5
-104	7094.23	0.005		
-103	7094.23	0.005		
-102	7094.98	0.002		
-101	7095.00	0.000		
-100	7095.65	0.033		
-99	7095.65	0.033		
-98	7095.74	0.001	NHC	72.3
-97	7095.83	0.001	NHC	72.5
-96	7095.93	0.014		
-95	7095.93	0.014		
-94	7097.83	0.000		
-93	7097.89	0.037		
-92	7097.95	0.000		
-91	7097.95	0.000		
-90	7098.01	0.000		
-89	7098.01	0.001		
-88	7098.03	0.000		
-87	7098.03	0.000		
-86	7098.96	0.020		
-85	7098.96	0.020		
-84	7099.15	0.035	NHC	70.6
-83	7099.19	0.000	NHC	70.7
-82	7099.62	0.000		
-81	7099.66	0.041		

-80	7100.37	0.055	NHC	62.6
-79	7100.37	0.055	NHC	62.5
-78	7100.97	0.000	NHC	75.7
-77	7101.11	0.027		
-76	7101.11	0.027		
-75	7101.24	0.011	NHC	74.5
-74	7101.55	0.000		
-73	7101.61	0.019		
-72	7102.18	0.048		
-71	7102.18	0.047		
-70	7102.58	0.000	Py	64.0
-69	7102.62	0.085	Py	68.7
-68	7102.64	0.002		
-67	7102.64	0.002		
-66	7103.09	0.003		
-65	7103.13	0.031		
-64	7103.14	0.026		
-63	7103.15	0.018		
-62	7103.46	0.000	NHC	76.3
-61	7103.70	0.026		
-60	7103.71	0.028		
-59	7103.81	0.002	NHC	71.6
-58	7104.13	0.026	NHC	67.9
-57	7104.16	0.000	NHC	67.2
-56	7104.25	0.002		
-55	7104.26	0.002		
-54	7104.48	0.000		
-53	7104.52	0.003		
-52	7104.52	0.004		
-51	7104.56	0.023		
-50	7104.68	0.000		
-49	7104.74	0.001		
-48	7104.75	0.002		
-47	7104.81	0.030		
-46	7104.90	0.000		

-45	7104.97	0.000		
-44	7104.98	0.002		
-43	7105.19	0.000		
-42	7105.23	0.213	Py	58.7
-41	7105.35	0.000		
-40	7105.62	0.002	Py	75.5
-39	7105.63	0.002	Py	75.6
-38	7105.80	0.000		
-37	7105.80	0.000		
-36	7105.82	0.000		
-35	7106.20	0.000		
-34	7106.25	0.000		
-33	7106.32	0.001		
-32	7106.32	0.001		
-31	7106.49	0.001		
-30	7106.52	0.009		
-29	7106.54	0.015		
-28	7106.54	0.010		
-27	7106.87	0.000		
-26	7106.90	0.000		
-25	7106.97	1.000	Py	63.7
-24	7107.01	0.003		
-23	7107.10	0.000		
-22	7107.11	0.001		
-21	7107.34	0.006		
-20	7107.34	0.044		
-19	7107.36	0.027		
-18	7107.37	0.031		
-17	7107.57	0.003		
-16	7107.64	0.008		
-15	7107.71	0.371		
-14	7107.72	0.405		
-13	7107.74	0.100		
-12	7108.08	0.882		
-11	7108.09	0.888		

-10	7108.56	0.193		
-9	7108.56	0.196		
-8	7108.75	0.004	NHC	69.7
-7	7109.43	0.000		
-6	7109.61	0.000		
-5	7109.81	0.065	NHC	80.4
-4	7109.81	0.065	NHC	80.6
-3	7110.05	0.000	NHC	62.6
-2	7110.88	0.143	Fe	72.1
-1	7110.89	0.144	Fe	72.0
0	7111.25	0.005	Fe	57.3
[a] all values were shifted by 150.9 eV, [b] normalized to 1 (all values were divided by the overall highest value)				

Table S10. Comparison of all relevant VtC-XES transitions of complex **3** concerning relevant ligand/element populations (donor orbitals), energies and normalized intensities.

HOMOs	Calc. energy ^[a] / eV	Norm. Int. ^[b] / a.u.	Element / Ligand character	Element / Ligand population per HOMO
149	7087.73	0.016	NHC	61.9
148	7087.92	0.023	NHC	72.2
147	7088.01	0.013	NHC	76.6
146	7089.35	0.032		
145	7089.52	0.065	Bpy	66.7
144	7090.28	0.035	Bpy	75.3
143	7090.69	0.002	NHC	59.8
142	7091.37	0.008	NHC	43.2
141	7091.57	0.006	NHC	48.7
140	7093.52	0.001		
139	7093.70	0.000		
138	7093.96	0.026	Py	85.1
137	7094.23	0.040	Bpy	88.8
136	7094.32	0.005	Bpy	63.2

135	7094.47	0.026	Bpy	88.6
134	7094.72	0.009	NHC	41.9
133	7094.99	0.000		
132	7095.00	0.000		
131	7095.37	0.008		
130	7095.56	0.000	NHC	72.7
129	7095.77	0.020		
128	7095.79	0.001		
127	7095.83	0.020		
126	7096.04	0.019	NHC	40.4
125	7096.55	0.003		
124	7096.72	0.007		
123	7096.88	0.005		
122	7097.47	0.000		
121	7097.48	0.000		
120	7097.94	0.000		
119	7098.06	0.014		
118	7098.06	0.002	Bpy	71.5
117	7098.45	0.019	Bpy	65.7
116	7098.72	0.000		
115	7098.73	0.000		
114	7098.74	0.001		
113	7098.77	0.000		
112	7099.02	0.029	Bpy	68.0
111	7099.17	0.026	NHC	44.5
110	7099.25	0.026	NHC	53.7
109	7099.49	0.053	Bpy	75.0
108	7099.79	0.007		
107	7100.03	0.000		
106	7100.04	0.000		
105	7100.21	0.025	Bpy	55.3
104	7100.47	0.021	NHC	66.9
103	7100.54	0.032	NHC	41.0
102	7100.84	0.031		
101	7100.95	0.003		

100	7101.03	0.002	NHC	53.3
99	7101.32	0.025		
98	7101.35	0.032	NHC	69.5
97	7101.52	0.002		
96	7102.05	0.047	NHC	48.7
95	7102.15	0.086	Bpy	62.8
94	7102.44	0.000		
93	7102.46	0.001		
92	7102.48	0.035	Py	62.5
91	7102.59	0.002	Bpy	78.6
90	7102.59	0.003		
89	7102.73	0.042	Bpy	72.9
88	7102.99	0.020		
87	7103.03	0.022		
86	7103.12	0.008	NHC	59.3
85	7103.25	0.019	Bpy	53.1
84	7103.41	0.000		
83	7103.43	0.017	NHC	42.6
82	7103.51	0.010	Bpy	73.1
81	7103.74	0.000		
80	7103.98	0.010	NHC	50.5
79	7104.02	0.026		
78	7104.07	0.008		
77	7104.14	0.003	NHC	57.7
76	7104.20	0.009	NHC	68.6
75	7104.25	0.022	NHC	42.2
74	7104.30	0.008		
73	7104.41	0.003	NHC	41.9
72	7104.44	0.003	Bpy	73.3
71	7104.50	0.006		
70	7104.62	0.017		
69	7104.66	0.003		
68	7104.75	0.001		
67	7104.79	0.016	NHC	46.1
66	7104.97	0.005		

65	7105.08	0.007		
64	7105.10	0.003		
63	7105.12	0.132		
62	7105.16	0.000		
61	7105.26	0.139	Bpy	50.5
60	7105.38	0.003		
59	7105.40	0.034		
58	7105.45	0.005		
57	7105.51	0.000		
56	7105.52	0.003		
55	7105.60	0.005	Py	74.1
54	7105.70	0.003		
53	7105.74	0.010		
52	7105.92	0.017	Bpy	65.3
51	7106.09	0.065		
50	7106.15	0.019		
49	7106.15	0.006		
48	7106.36	0.073	Bpy	70.7
47	7106.48	0.000		
46	7106.50	0.002		
45	7106.59	0.000		
44	7106.75	0.001		
43	7106.80	0.000		
42	7106.81	0.001		
41	7106.94	0.189		
40	7107.00	0.005		
39	7107.04	0.010		
38	7107.07	0.009		
37	7107.27	0.435		
36	7107.29	0.130		
35	7107.32	0.030		
34	7107.32	0.001		
33	7107.34	0.192		
32	7107.48	0.020		
31	7107.60	0.177		

30	7107.61	0.116	Py	53.9
29	7107.69	0.481		
28	7107.79	0.034		
27	7107.80	0.023		
26	7107.80	0.626		
25	7107.90	0.107		
24	7107.99	0.074		
23	7108.07	0.015		
22	7108.09	0.076		
21	7108.16	0.282		
20	7108.17	0.278		
19	7108.22	0.002		
18	7108.23	0.102		
17	7108.37	0.213		
16	7108.45	0.002		
15	7108.49	0.074		
14	7108.52	0.014		
13	7108.68	0.005		
12	7108.80	0.048		
11	7109.19	0.098	NHC	55.6
10	7109.50	0.045		
9	7109.70	0.001	Bpy	54.6
8	7109.80	0.021	NHC	76.4
7	7110.05	0.009	NHC	57.3
6	7110.18	0.001		
5	7110.20	0.002		
4	7110.46	0.000		
3	7110.52	0.000		
2	7110.84	0.104	Fe	75.2
1	7110.94	0.120	Fe	68.1
0	7111.22	0.020	Fe	59.3
^[a] all values were shifted by 150.9 eV, ^[b] normalized to 1 (all values were divided by the overall highest value)				

Table S11. Comparison of all relevant VtC-XES transitions of complex **4** concerning relevant ligand/element populations (donor orbitals), energies and normalized intensities.

HOMOs	Calc. energy ^[a] / eV	Norm. Int. ^[b] / a.u.	Element / Ligand character	Element / Ligand population per HOMO
90	7087.91	0.006		
89	7087.97	0.031		
88	7089.45	0.011		
87	7089.50	0.110		
86	7090.32	0.033		
85	7090.36	0.036		
84	7091.37	0.000		
83	7091.38	0.014		
82	7094.14	0.000		
81	7094.20	0.070		
80	7094.33	0.003		
79	7094.33	0.004		
78	7094.54	0.022		
77	7094.56	0.025		
76	7095.45	0.008		
75	7095.46	0.006		
74	7096.04	0.020		
73	7096.08	0.017		
72	7096.78	0.005		
71	7096.80	0.009		
70	7098.07	0.001		
69	7098.07	0.001		
68	7098.46	0.001		
67	7098.51	0.040		
66	7099.06	0.041		
65	7099.12	0.004		
64	7099.53	0.067		
63	7099.53	0.033		
62	7100.25	0.024		

61	7100.26	0.025		
60	7100.56	0.025		
59	7100.60	0.031		
58	7101.08	0.005		
57	7101.41	0.043		
56	7102.23	0.087		
55	7102.25	0.088		
54	7102.61	0.002		
53	7102.61	0.002		
52	7102.73	0.002		
51	7102.75	0.087		
50	7103.17	0.011		
49	7103.26	0.031		
48	7103.30	0.001		
47	7103.34	0.024		
46	7103.59	0.003		
45	7103.62	0.007		
44	7103.79	0.000		
43	7103.90	0.010		
42	7104.11	0.045		
41	7104.22	0.025		
40	7104.29	0.013	NHC	50.6
39	7104.30	0.008	NHC	57.3
38	7104.49	0.007	Bpy	75.9
37	7104.52	0.002	Bpy	79.9
36	7104.56	0.010		
35	7104.76	0.016		
34	7104.79	0.038	NHC	50.1
33	7104.90	0.007	NHC	53.0
32	7104.98	0.023		
31	7105.24	0.102	Bpy	76.7
30	7105.24	0.192	Bpy	73.0
29	7105.38	0.096	Bpy	82.7
28	7105.57	0.021		
27	7105.61	0.020		

26	7105.88	0.009		
25	7105.91	0.009		
24	7105.94	0.001		
23	7105.96	0.007	Bpy	77.7
22	7106.29	0.064	Bpy	75.6
21	7106.43	0.068	Bpy	82.2
20	7106.60	0.081		
19	7107.10	0.044		
18	7107.35	0.808		
17	7107.38	0.001		
16	7107.49	0.005		
15	7107.62	0.329		
14	7107.76	0.595	Bpy	71.2
13	7107.79	0.533	Bpy	72.0
12	7108.01	0.214	Bpy	70.6
11	7108.06	0.453		
10	7108.12	0.273		
9	7108.64	0.197	Bpy	73.3
8	7108.72	0.009		
7	7108.75	0.009		
6	7109.41	0.041	NHC	60.8
5	7109.65	0.007		
4	7109.75	0.000		
3	7110.04	0.004	NHC	57.2
2	7110.89	0.122	Fe	74.1
1	7110.91	0.107	Fe	74.1
0	7111.19	0.012	Fe	62.9
^[a] all values were shifted by 150.9 eV, ^[b] normalized to 1 (all values were divided by the overall highest value)				

Table S12. XYZ files of all optimized structures.**Optimized gas phase structure of 1:**

111

C	1.01644455548762	1.90672071193329	1.20198856155653
C	-0.57551544561933	2.09814283939512	-0.52038931565645
C	1.10960567227099	3.29008430574261	1.30532435956605
C	-0.52080228886652	3.48560685214069	-0.45558537963224
C	0.33135136512321	4.08100302956115	0.46763527915183
H	1.77568486823520	3.74558255321141	2.02557578054027
H	-1.13092241722675	4.09238309393707	-1.11077812753535
H	0.38918228643552	5.15941725222233	0.53482371755648
Fe	0.08120662272153	-0.51661185623643	0.19024162891576
N	0.18499351535876	1.34594877320225	0.30037602408043
C	-0.86846255706121	-4.50499365321959	0.95724043017192
C	-0.82027470546594	-3.12011911167968	0.92766996712815
C	0.86117439808317	-3.12363296193394	-0.66645988758704
C	0.89001469365537	-4.50875227385209	-0.71019811318323
C	0.00335843032697	-5.19404316533176	0.11719294463250
H	-1.55303458951234	-5.03090788369448	1.60734907873221
H	1.57477067201553	-5.03762486438621	-1.35770955929117
H	-0.00497259184252	-6.27631265370481	0.11083085881631
N	0.01750868152662	-2.44549130586704	0.12585118614971
C	1.48484926785279	-0.88351769221681	-1.16845159624578
C	2.65083171645562	-2.50296925365495	-2.32528147307580
C	3.10195647911573	-1.29542681551959	-2.71274571575808
H	2.93789559030139	-3.49447942524229	-2.62667506127166
H	3.86663615632857	-1.02348824699303	-3.41710076746663
C	-1.37155035362162	-0.87726848161393	1.49348940828968
C	-2.58558857439494	-2.48909496948537	2.60991150507272
C	-3.02058581315016	-1.27837799172469	3.00596516030222
H	-2.89251399412362	-3.47885135953705	2.89716715872562
H	-3.78252455829677	-1.00141529847995	3.71131352863599
N	-1.58350759713714	-2.23398639398685	1.68108039713191
N	-2.28471787690743	-0.31104348275757	2.31606715243140
N	1.66175637379329	-2.24120311317591	-1.38446191542432
N	2.38357265857792	-0.32346756571494	-2.01116491581498

C	-2.54619368226497	1.10486349722828	2.49400543625923
C	-3.54895389135574	1.70139540908876	1.71134500556707
C	-1.85527878034174	1.78498269750536	3.50803779945832
C	-3.81867903858144	3.04968799371685	1.95146777002792
C	-2.16621086491339	3.13214374964269	3.69698834190728
C	-3.13367414350274	3.75901888402013	2.92677957828579
H	-4.58354144026773	3.55038330666329	1.37359269363924
H	-1.65414823638910	3.69486539737592	4.46578242514991
H	-3.37012161185768	4.80193991791572	3.10143751621834
C	2.62653467479598	1.09062338441433	-2.22558336282617
C	1.95709845345145	1.72852817631207	-3.28269979737610
C	3.59494223280712	1.72593035566651	-1.43310303164025
C	2.26221946388997	3.07225772399370	-3.50548072713785
C	3.85437880077751	3.07022149880656	-1.70284960127973
C	3.19473558941992	3.73749417187092	-2.72398742563652
H	1.77005061539451	3.60350622540819	-4.30883482873482
H	4.59235233762628	3.59930268064980	-1.11526609159046
H	3.42314405056111	4.77741765567556	-2.92512081495019
C	-4.35910609462814	0.93205537049575	0.67816966068295
H	-3.68942698793713	0.21758063815624	0.18780162632217
C	-4.96735576766463	1.84218792366913	-0.39406734537295
H	-4.23919921644286	2.53821044660331	-0.81185365926082
H	-5.37010726799385	1.23288479705904	-1.20516104573673
H	-5.79598399312253	2.42490501032129	0.01449994685022
C	-5.51109880018076	0.14154516899328	1.32641346226661
H	-6.10661331008375	-0.34605960260684	0.55121357905787
H	-5.16057072417826	-0.63114516905886	2.00772664074932
H	-6.16460100666971	0.81790176594148	1.88169473267112
C	-0.85624396413918	1.09136738542810	4.41895990310066
H	-0.31954712807459	0.34476069188110	3.82496470904610
C	-1.56539763118194	0.35982441659510	5.57317887563818
H	-0.82654049472016	-0.10070320966209	6.23283567394686
H	-2.15467377472463	1.06641116606561	6.16166435486027
H	-2.23090869184377	-0.42643900112522	5.22002971347051
C	0.16686590889246	2.05966271635174	5.01783885985475
H	0.61481856321576	2.70402395359262	4.25907747034916
H	-0.29477674760556	2.70114048348793	5.77159801395289

H	0.95948617201802	1.49684377868483	5.51387055487972
C	4.38692945220687	0.98849513495149	-0.36570714371724
H	3.71932761133038	0.26203668259003	0.10852546889346
C	4.93113570093234	1.92427348742614	0.71692860266959
H	5.74637194941061	2.53937418252651	0.32993987595430
H	4.16188072382341	2.59413727217223	1.10586798006647
H	5.33423181996496	1.33581410874089	1.54288582912531
C	5.57191024668128	0.21758350941780	-0.97665664296194
H	5.25166167851193	-0.55283457059406	-1.67650088524818
H	6.23524369289296	0.90487805731082	-1.50608956900476
H	6.14655518640423	-0.26957438065891	-0.18558390832501
C	0.97851304548064	1.00612520710504	-4.19627129687249
H	0.42558764657452	0.27925257340987	-3.59184212766261
C	1.70474694565980	0.24195220705318	-5.31864825479752
H	0.97349898759743	-0.21701525175487	-5.98783956455639
H	2.31793541370471	0.92938613460602	-5.90553574551773
H	2.34767393741622	-0.54992991629785	-4.93918320211619
C	-0.02810164227925	1.95655236068050	-4.85235081034260
H	-0.81803374218980	1.37721891277515	-5.33364352619944
H	-0.48504844464385	2.63770602652512	-4.13361371877242
H	0.45139724230588	2.55696573365894	-5.62867252227235
C	-1.39119447570896	1.27223111960868	-1.40608307719332
C	-2.26925978220971	1.75190956437740	-2.37061685434962
C	-1.91477559516573	-0.92328883308108	-1.96907621520219
C	-2.98550439093193	0.85791237415156	-3.15134413952838
H	-2.38974919557206	2.81771163458905	-2.50932116641868
C	-2.80521488261222	-0.50451389797842	-2.94485814081338
H	-1.74432650553234	-1.97412324334446	-1.77759354849488
H	-3.67261781299970	1.21813844664928	-3.90597579541347
H	-3.34333227174491	-1.23926084808256	-3.52894217417231
C	1.73348548067546	0.90122529089166	1.97871387537414
C	2.65879612117730	1.17188265519469	2.98046139142914
C	2.01931456977359	-1.38535565994505	2.28242238036146
C	3.27752130412719	0.12436652963725	3.64446501500776
H	2.89262878687452	2.19565297444128	3.23585094862648
C	2.95100897923089	-1.17861492465929	3.28657705001304
H	1.74023805853962	-2.38492687035726	1.97923138606061

H	4.00097483011220	0.32012088482409	4.42536039369972
H	3.40772947646276	-2.02895530931428	3.77531124198660
N	1.41602182344165	-0.37888201287089	1.63306187848828
N	-1.21714618234651	-0.06569839454077	-1.21144220011809

Optimized gas phase structure of 2:

87

C	0.60323768203182	2.49749123809042	1.03575061508303
C	-1.03789156919294	2.52568449230860	-0.59768566390939
C	0.59026839358430	3.87946798872159	1.14601006359964
C	-1.12489604742885	3.90841372003469	-0.56106898938680
C	-0.29255388676781	4.58175240527884	0.32976167918742
H	1.24107053280146	4.39226395552074	1.83997717337871
H	-1.81332945342182	4.44373593983883	-1.19954841396286
H	-0.33365119489212	5.66159262093709	0.38959598304434
C	2.37948857148202	1.83625641925932	2.69486058437218
C	1.23722359145284	0.25309086369426	1.46734152409985
H	2.65213852131293	2.81719095798758	3.04098990746610
C	2.84472236793686	0.61815932006502	3.03208033991000
H	3.60929294427463	0.34064816352181	3.73558058463358
C	-1.50787900911935	0.29895490478094	-1.26698739347297
C	-2.71524048906961	1.91889018724006	-2.37784545189267
H	-3.04809597032006	2.90917499517290	-2.63278637377910
C	-3.07181174794576	0.71356935696183	-2.86259123213626
H	-3.78220757308215	0.45953314454820	-3.62902669131249
N	1.39693695394633	1.60585357000582	1.73936240566173
N	2.14207776623721	-0.32683519402772	2.28391975945984
N	-1.76009267557985	1.65817173505612	-1.40267165665315
N	-2.33517089890355	-0.25360188506824	-2.17825841566046
Fe	-0.13285152031983	-0.09205278208146	0.09110726557446
N	-0.19452911730815	1.83172792225401	0.18436857544516
C	-0.81481937148328	-4.14097028751291	0.83661890620660
C	-0.84455947892089	-2.75484690590785	0.83164700536488
C	0.78786825996133	-2.63893963258209	-0.80705749341357
C	0.89129565494727	-4.01943460545860	-0.87573964000152
C	0.07094993944035	-4.76837500600347	-0.03571842311678
H	-1.45443608664861	-4.71293606853256	1.49377683178777

H	1.58325790274345	-4.49671639667246	-1.55512833044488
H	0.12387425708971	-5.84909812893776	-0.06035590832501
N	-0.06160846282162	-2.01690046941293	0.02698210512049
C	1.23584222682476	-0.36241876034588	-1.30074965364621
C	2.45327504361960	-1.87924733336904	-2.53864135448307
C	2.79570613541215	-0.63662057989689	-2.93039024871281
H	2.79514627936924	-2.84365525592128	-2.86950714027407
H	3.49940650861358	-0.31688985036529	-3.67807753133709
C	-1.49466539645789	-0.55660675010731	1.44101540841617
C	-2.61155981589404	-2.24015219158428	2.55246962264759
C	-3.08681434152078	-1.05622451827929	2.98411636096378
H	-2.87126150886272	-3.24714374044674	2.82647264773735
H	-3.84823578889336	-0.84119685846238	3.71256715427240
N	-1.63952645912590	-1.92760682518296	1.60936875102929
N	-2.39996328364954	-0.04968284801565	2.30410221519338
N	1.49983214715132	-1.70455431370972	-1.54310908409051
N	2.05300518270861	0.26752350499343	-2.17044251129538
C	-2.43960218224528	-1.69675398288371	-2.48349338078353
H	-1.81355529168786	-2.18074472966484	-1.73647050926506
C	-3.88206055254459	-2.16595472623375	-2.32508048152813
H	-4.54188346563944	-1.67161423632210	-3.04078220152965
H	-3.93964350035865	-3.23849824948153	-2.51631870750076
H	-4.25354063189347	-1.96722567075961	-1.31814875607888
C	2.42793761451233	-1.77527244254304	2.37296766562700
H	1.67201633351086	-2.24526906804931	1.74810693392751
C	3.81632513514724	-2.06276242406989	1.80716772441531
H	3.89680562952644	-1.72584253254958	0.77164651471248
H	4.59019443474785	-1.56268787695076	2.39325404611935
H	4.01310940352524	-3.13525757791081	1.84597121896102
C	2.27122042324481	-2.25581131128680	3.81195752344950
H	1.26921159023530	-2.04692844282843	4.19102487839317
H	2.44819122205571	-3.33137825937421	3.85787945344204
H	2.99724417828461	-1.77800542510983	4.47254437744804
C	-1.88389615115735	-1.96924835683895	-3.87894205785777
H	-0.84639619904079	-1.63843129527154	-3.96066692280877
H	-1.93147309081712	-3.03849517496544	-4.09073499777195
H	-2.47104289693437	-1.45425667765162	-4.64223027129718

C	-2.70382600782108	1.38535520920469	2.49072076166641
H	-1.96029747849598	1.90349290681852	1.88931694231308
C	-4.10108719074770	1.68920842746650	1.95607889207946
H	-4.18814294680634	1.41087717352765	0.90376673289297
H	-4.86338527849884	1.14750593872962	2.51999846400186
H	-4.30917604883824	2.75540539777305	2.05799983615574
C	-2.53833849598027	1.77755459895261	3.95496681274422
H	-1.53013140678449	1.55821055763692	4.31113144501808
H	-2.72745122346431	2.84599486032007	4.06869426099436
H	-3.25185473794704	1.25072925808968	4.59162575245401
C	2.12921887239335	1.72957472374197	-2.38078540539547
H	1.51830734788533	2.15455820774161	-1.58700848410402
C	3.56882443170737	2.21093572395257	-2.23353935229195
H	3.97231481295324	1.95697289496504	-1.25174501198285
H	4.21485114723953	1.77290806920123	-2.99682761380299
H	3.60545510264470	3.29385832301713	-2.35996724650375
C	1.53038364740286	2.08168439572722	-3.74041675829182
H	0.49574066011364	1.74044957946465	-3.81484449809669
H	1.55720232246983	3.16266208508974	-3.88580986165364
H	2.10297475279169	1.62403991093793	-4.54992358661941

Optimized gas phase structure of 3:

112

C	0.71175274033410	2.00489986937210	0.86647540281262
C	-0.86912473033911	1.95305100820464	-0.84949087499127
C	0.73659676954529	3.38877624266991	0.88688415623253
C	-0.89976546436345	3.34210603487626	-0.88733896981690
C	-0.08937004311529	4.05695055329217	-0.01149484947067
H	1.37335909298164	3.92870160966662	1.57365560745460
H	-1.54206888855121	3.86124626563622	-1.58507531792588
H	-0.09897041703916	5.13883901717135	-0.02675259103049
Fe	-0.03334387286240	-0.58229075924317	0.06563179031213
N	-0.06629194767415	1.31183920476311	0.02551662985353
C	-1.07278905292772	-4.55939894642032	0.72937205489672
C	-0.96591080872848	-3.17785158012977	0.76677489168270
C	0.72042530578649	-3.17736350278823	-0.82525723159914
C	0.68919676181341	-4.55875588987778	-0.93502380244054

C	-0.22481084827530	-5.24468352680957	-0.13803523595132
H	-1.78760749448071	-5.08527630819558	1.34618086777581
H	1.34626537293770	-5.08420661291576	-1.61336710802968
H	-0.28087331621041	-6.32386691490720	-0.19779900580881
N	-0.08334906264541	-2.50308123070935	0.01294485122242
C	1.40464206909353	-0.94055572268904	-1.23464138586699
C	2.55959648839892	-2.54299740378036	-2.42751851739680
C	3.06890540034041	-1.33515131733929	-2.73326278929290
H	2.82062185786379	-3.52785104250926	-2.77131076352024
H	3.86182073179395	-1.05618728396476	-3.40289526653705
C	-1.44006236274538	-0.93885540659645	1.40437862882312
C	-2.69105520954542	-2.54574629671303	2.49057356166043
C	-3.05860353652100	-1.33628425735627	2.95231611650931
H	-3.03563085056582	-3.53285984834282	2.74188362287770
H	-3.79532856864215	-1.05754373842685	3.68338035683185
N	-1.70235623812163	-2.29405258991882	1.54568889515201
N	-2.29125481606623	-0.37178577797610	2.29242128675403
N	1.54621512901192	-2.29316455114139	-1.50835544525695
N	2.36873810179614	-0.37383147205994	-1.99828754899786
C	-2.46542864902021	1.04191817302652	2.56522976960320
C	-3.40668456465865	1.75206208219047	1.80328710231667
C	-1.76455376585283	1.60822996967729	3.64263753623700
C	-3.60556209088280	3.09451772377781	2.12771431329850
C	-2.01306585345987	2.95277566607381	3.92370858615974
C	-2.91824113693572	3.68946227902045	3.17462616189941
H	-4.31936887615731	3.67911398973407	1.56335210814206
H	-1.49767331562035	3.42890814113399	4.74673704812786
H	-3.10260449552819	4.72859651595966	3.42014768733020
C	2.68725453985260	1.03716753645689	-2.10464640797125
C	2.02745134219548	1.79006884598157	-3.08791408942519
C	3.70705519988652	1.55962671825580	-1.29124820707322
C	2.38852201765318	3.13220427941039	-3.21285616576374
C	4.03050972348546	2.90587649992094	-1.47022285296223
C	3.37827583231618	3.68452196567062	-2.41481352996638
H	1.89973729437565	3.74897957712351	-3.95484134438942
H	3.65554338284579	4.72433274485807	-2.54127057428991
C	-4.23280788837256	1.09684125566928	0.70848062660674

H	-3.59915657467005	0.36202469018219	0.20202881617352
C	-4.73618844781555	2.10134177147852	-0.33163598464763
H	-3.93933896319533	2.75432225523436	-0.69232083751214
H	-5.16315003272574	1.56624097118864	-1.18150657051199
H	-5.52504944994109	2.73268398774568	0.08290997097929
C	-5.45181776890762	0.35576003792987	1.28909537737687
H	-6.04372624919314	-0.07736217065981	0.47964591949738
H	-5.16800637003369	-0.45226748102171	1.96157517177438
H	-6.08691528868393	1.05169185020411	1.84137517107644
C	-0.80625378795179	0.81034092420226	4.51469181797840
H	-0.27814712400886	0.10030549302376	3.86888619911217
C	-1.54924620278780	0.00893651393837	5.59897969511472
H	-0.82850205130037	-0.49378007019323	6.24818345083438
H	-2.15058125517436	0.67979961185105	6.21656242376579
H	-2.20545720950158	-0.75260082512392	5.18181920650250
C	0.22974689933617	1.69700348806684	5.21374609732505
H	0.70348584587140	2.40106704853819	4.52846022200713
H	-0.23037961187322	2.27039266753472	6.02165636279006
H	1.00614886547460	1.07367861784659	5.66050324586768
C	4.47523105389167	0.71701343564798	-0.28273813399810
H	3.76522142792604	0.02661778581140	0.18575573083830
C	5.13286090248388	1.56259004749212	0.81375104920957
H	5.99352074415050	2.10777632872654	0.41955693788990
H	4.44558123220373	2.28749848588695	1.25107224225193
H	5.49914644894273	0.91186053987928	1.60964596908932
C	5.58224182670527	-0.11851260626241	-0.95194776884884
H	5.18884464487470	-0.86517826988654	-1.63887752102932
H	6.26287236640280	0.53309136434263	-1.50425291973724
H	6.16166464927601	-0.64348600480160	-0.18874291995678
C	1.00592051403907	1.17913473888676	-4.03232814132317
H	0.44041955275914	0.42542393653240	-3.47539857067144
C	1.69094806993039	0.47922812910936	-5.22078614829991
H	0.93735645580564	0.07474338994786	-5.90005058587661
H	2.30287354217501	1.19322899567032	-5.77626000300426
H	2.33064554473526	-0.34396493925165	-4.90650522293736
C	0.02147115945462	2.21271017729367	-4.58569576596938
H	-0.79170082216646	1.70327283771504	-5.10542821069445

H	-0.40169219997007	2.83921645205146	-3.79853365877147
H	0.50833658281985	2.86867315791325	-5.31061842446009
C	-1.62797309390638	1.01749125832628	-1.67207892472326
C	-2.53348245574407	1.38184690130683	-2.66296499827118
C	-2.02360103201043	-1.23268841720500	-2.08257780727140
C	-3.19902749108633	0.39879440318623	-3.37722584844501
H	-2.71490169218192	2.42694243211327	-2.87068499618491
C	-2.93929352836334	-0.93397318761579	-3.07855928916527
H	-1.79633200667744	-2.25839130151638	-1.82644246013000
H	-3.90711582021360	0.66640935463766	-4.15080010984318
H	-3.43478222998728	-1.73711284936418	-3.60768080466506
N	1.44613854872382	1.12982000992840	1.66555903167027
C	2.37377383237365	1.35851603992061	2.67193042965981
N	2.07520473990182	-0.80783224778552	2.34000493266307
C	2.76754748088589	0.14065061303154	3.09500914665411
C	1.24974005319904	-0.22294271279392	1.44777053100891
N	-1.37411294529389	-0.28947490846289	-1.38529443373170
H	3.47312614499180	-0.14096607342788	3.85743006333477
H	4.81193860881909	3.35035217826474	-0.86916456915527
H	2.66629734626380	2.34099342772297	2.99360226425067
C	2.24174405111133	-2.24637476978452	2.50808076170737
H	1.59505658619776	-2.74678783953959	1.79598792617579
H	1.96409401560874	-2.53767285233999	3.52148340470162
H	3.27852897963082	-2.52552961205659	2.31835527575721

Optimized gas phase structure of 4:

61

C	5.22453945622996	3.06504860360554	-4.26613015432588
C	6.27255843872041	2.19259784978714	-3.98541439548493
C	6.47737576772536	1.72830045694869	-2.68825164860837
C	5.59973779292276	2.16688496549137	-1.70902737673374
N	4.58615019937765	3.00516736793219	-1.97381982417431
C	4.38566949494751	3.46284771553288	-3.23023340803413
C	3.22550550934953	4.34943789002252	-3.30499296846440
N	5.59649972372195	1.82300353210074	-0.35819866457632
C	6.43496121737002	0.99268495062893	0.37746340850278
C	5.95828620260592	1.02228624265163	1.63849006085756

N	4.84492693610455	1.86416926754112	1.65032899336491
C	4.59570251132701	2.37183243817157	0.42725130851310
C	1.65269246624056	5.78060656881794	-4.41505081862184
C	2.76850207807646	4.95723533849311	-4.46919779409495
N	2.60142555323622	4.53309314331788	-2.10861122471392
C	1.53188449246889	5.33955238512616	-2.06671580687310
C	1.02764588503259	5.97902947151950	-3.18935067733110
Fe	3.40516269572221	3.52205031225603	-0.57467302823664
C	2.43805096850639	5.23691260743347	1.46060364642035
N	2.19513184566384	4.09610219976510	0.77689843448745
C	1.08534001317810	3.37893696939970	1.01760338856650
C	0.15114434437457	3.75542860796646	1.96961094096481
C	0.39747594101265	4.92901181581615	2.67947277670738
C	1.54336153665674	5.67933979637292	2.43022893652036
N	1.05330780612720	2.25442952432498	0.19370929699451
C	3.69526290009109	5.85802653583575	1.04485603179689
C	2.10038990951210	2.10656922535275	-0.69943897620130
C	0.62363173946431	0.39467532371695	-0.86362645666709
C	0.14224845999798	1.20739679076282	0.09951787762632
C	6.07741470283509	6.82297394820222	0.10065415301410
C	5.49896625414946	5.66772207899823	-0.40305814449807
N	4.33675979273423	5.18127340770118	0.05194329321679
C	4.22244511506653	7.02086069370564	1.59558089465100
C	5.42949437330350	7.51227196474139	1.11929632774378
H	6.93472534422908	1.87177505931162	-4.77921334129976
H	5.06802030739183	3.42595064386636	-5.27326316154002
H	3.27965909758400	4.78422215939237	-5.40689154028968
H	1.27994090104515	6.26026356606736	-5.31110993520910
H	0.15876813206685	6.61711029895391	-3.09757359563340
H	1.06940686468911	5.46990176016057	-1.09758050528796
H	5.97489955339940	5.10363774131643	-1.19421754449315
H	7.01882620719954	7.17108824549076	-0.30342409945242
H	5.85733091005916	8.41474005206572	1.53673563862539
H	3.69269422874188	7.53490904442710	2.38651268775387
H	1.72970868557945	6.59078494058983	2.98091620888230
H	-0.31086846033714	5.25886254760902	3.42840343100989
H	-0.73591991621690	3.16521388553818	2.15336172950475

H	-0.74619611177604	1.13591450482492	0.70117149854802
C	2.64754079554408	0.32348247379841	-2.35504298345834
H	7.28773097840846	1.05107484501174	-2.45688087643657
C	4.06557680730955	2.13587673838906	2.85603006646667
H	3.33800352278275	2.90629133381686	2.62707042263306
H	4.72948526126714	2.48417185814982	3.64658287671960
H	3.55415153801737	1.22922479816142	3.18107210236485
N	1.80896160398021	0.95623851997282	-1.33856776396346
H	0.23109846645918	-0.52532696196417	-1.26178434546362
H	3.07328072877334	1.08782795923693	-2.99843605756760
H	2.02974462535555	-0.34309511529924	-2.95287400637838
H	3.44371654122735	-0.25067415635232	-1.87961549740388
H	6.30758226075874	0.52725551417619	2.52843236256913
H	7.27641000260760	0.47379875324768	-0.04617617350870

Optimized gas phase structure of 5:

59

C	5.02571073491866	2.88217655436653	-4.30742428698149
C	6.09592977871658	2.02777495820893	-4.05850300517686
C	6.37126616490176	1.61022650381437	-2.75951214497268
C	5.55862028595692	2.06298321255244	-1.72420099152470
N	4.52543666687332	2.89161183899355	-1.98333713826197
C	4.24327588765875	3.30379825205828	-3.23682466295892
C	3.07983202622638	4.19255331851159	-3.26902363808910
C	5.65685509242902	1.74554628215908	-0.29768447164876
C	6.63530049341607	0.93917428612589	0.27184139960080
C	6.61544192579138	0.70726398459902	1.64075700591911
C	5.60878473242920	1.28707492845087	2.40345206760091
C	4.66497178158632	2.08641475468887	1.77575687141208
N	4.67888318369255	2.32291447574238	0.45683920710065
C	1.44914578201123	5.60604147434822	-4.31684014856917
C	2.54668696585524	4.76196924846382	-4.41903858861966
N	2.54202386754281	4.43136651775329	-2.03905140603619
C	1.48777008541759	5.25354907454417	-1.95074638674225
C	0.91521731374502	5.86028102428672	-3.05925362196865
Fe	3.43064508850154	3.46742588065979	-0.56134421983176
C	2.64920865130617	5.14762414062520	1.54062735467878

N	2.32914393825892	4.02560848208118	0.86277105437013
C	1.24122088955654	3.29123287023279	1.17806266782137
C	0.40944567876249	3.68387460936029	2.22240120550641
C	0.72198296938154	4.84191640622603	2.92932219663910
C	1.85082295852000	5.58374279192281	2.59388211070544
C	1.10105043345958	2.12244423274573	0.30593898473350
C	3.86755202347766	5.76998511460657	1.01762274949525
N	2.08308424627484	2.02594970857873	-0.63531743031283
C	2.04792281358257	0.99874176264814	-1.49535058137094
C	1.05443649046546	0.03156263692607	-1.46676187317273
C	0.05478423891944	0.12146334218604	-0.50553076715557
C	0.08171172959243	1.18099112977824	0.39149974223820
C	6.14759814179447	6.74335932955990	-0.15082700985930
C	5.53080476363193	5.58310798079132	-0.59489247814476
N	4.41658587310047	5.09566698015098	-0.03268349273803
C	4.44055821131403	6.93485733144747	1.51347490139787
C	5.59514255054303	7.43083806422485	0.92329570665612
H	6.71575151985547	1.68690882056986	-4.87777211017915
H	4.80956245091451	3.21254697383511	-5.31444681452341
H	7.20047324471372	0.94434969275088	-2.56273883537412
H	7.40377654764925	0.49853972014299	-0.34920773508297
H	7.37035588128489	0.08368732777609	2.10208079477116
H	5.54994496811364	1.12777281054497	3.47200393763027
H	3.87036814883015	2.55824568147105	2.33752774694937
H	2.98627813316773	4.54538819283196	-5.38363629716222
H	1.02132368879837	6.05883018698304	-5.20219986950898
H	0.06439759217772	6.51613113006334	-2.93119876333678
H	1.09658982712784	5.42362110540852	-0.95678682339058
H	5.93280481102256	5.01832570425937	-1.42510657504989
H	7.04508043206497	7.09500732009491	-0.64223401547119
H	6.05476250931152	8.33714512768549	1.29649528734928
H	3.98658186403278	7.44946673567343	2.34985268442710
H	2.09803919504103	6.48318365278758	3.14129037390685
H	0.08546673362726	5.16661784629045	3.74237112650275
H	-0.46616645564404	3.10439719086156	2.48154821171943
H	-0.68338124700990	1.27615359868513	1.15055706056925
H	-0.73292621089770	-0.61917757369700	-0.45433858189851

H	1.07244640345196	-0.77556943775368	-2.18695705058378
H	2.84363050275434	0.95969370831482	-2.22680263400325

Optimized structure in solution (SMD) of 1:

111

C	1.02136763246971	1.91021241363040	1.20883400356139
C	-0.56383225725724	2.11144452935327	-0.51802481839604
C	1.12114378952456	3.29291374898077	1.31566476283574
C	-0.50268377241281	3.49878503948671	-0.45250246697577
C	0.34925956783689	4.08804845958075	0.47522626652986
H	1.78660329655545	3.74394281147233	2.03895222564287
H	-1.10752455201036	4.10800666803098	-1.11006418079015
H	0.41266067676875	5.16563233881656	0.54409722407962
Fe	0.07835513234813	-0.50835483472330	0.19076815548049
N	0.19019222865114	1.35336466693000	0.30374716597745
C	-0.87962299589385	-4.49483681968815	0.96421384511740
C	-0.82839015111904	-3.11178637680359	0.92927436441316
C	0.85117662899777	-3.12148721430393	-0.66046823827176
C	0.88046379668902	-4.50500276041895	-0.70206884084951
C	-0.00791554867959	-5.18576010296687	0.12645958067549
H	-1.56542965978489	-5.01345079996292	1.61782580989222
H	1.56763012197266	-5.03150500906948	-1.34789259684424
H	-0.01670275597924	-6.26724878135350	0.12382332350496
N	0.00868886352217	-2.43990450118757	0.12726228206869
C	1.48196726783800	-0.88610890700288	-1.16727197337620
C	2.64212442570207	-2.51515027718504	-2.31256374847500
C	3.10225225696828	-1.31426435887887	-2.70942841401551
H	2.92111482076903	-3.51175189470102	-2.60348916435704
H	3.87034215984621	-1.05646352043494	-3.41470336469045
C	-1.37714522939322	-0.86998186817651	1.49368265508340
C	-2.58490594778679	-2.48331542896934	2.61018889475535
C	-3.02463856830081	-1.27630578227581	3.01198946543527
H	-2.88498730421893	-3.47622680652601	2.89260788746221
H	-3.78689179708185	-1.00831870360720	3.71977718787934
N	-1.58830604993766	-2.22227813273831	1.68259587386053
N	-2.29123450615270	-0.30502114358554	2.32097281686741
N	1.65550646429683	-2.24097743984230	-1.37787342119781

N	2.38624896533025	-0.33333695549470	-2.01376321097947
C	-2.55593099485222	1.10564958214408	2.50144218170865
C	-3.56167132858585	1.70399595004865	1.72371120055130
C	-1.86011395064651	1.79193541372308	3.50825444013248
C	-3.83517823742675	3.05180513088084	1.96442827262899
C	-2.17171771832397	3.13894283045114	3.69993196313476
C	-3.14622279812363	3.76339495329791	2.93594428050204
H	-4.59646964820234	3.55375767599948	1.38252821390706
H	-1.64743913716646	3.70624481915683	4.45734655914714
H	-3.37604230496226	4.80935419473803	3.10389068359882
C	2.63308793821930	1.07427130931649	-2.23838513287532
C	1.96930042949235	1.70940506835932	-3.30113414185450
C	3.59444099368660	1.71912258729801	-1.44460619155609
C	2.27693040117998	3.05123456804446	-3.53424107788569
C	3.85702175070770	3.06191870674719	-1.72052009641658
C	3.20516690556083	3.72211937187240	-2.75171683187655
H	1.78157291332612	3.58015211517856	-4.33746299336977
H	4.58285858985855	3.59816528473879	-1.12401331948920
H	3.42735328994863	4.76404866450389	-2.95184862334625
C	-4.35999952578231	0.93584017016797	0.68101930253859
H	-3.68118553587215	0.23273014735340	0.18961823252922
C	-4.97201452235273	1.84748115338784	-0.38641748802734
H	-4.24858383340576	2.54660015535061	-0.80647581959681
H	-5.37223925651993	1.23847557289538	-1.19965079888285
H	-5.80231814966590	2.42723539473595	0.02626607316567
C	-5.50322240832377	0.12565549937072	1.31679655975371
H	-6.07392977709255	-0.38109349199420	0.53377530468362
H	-5.14673676617045	-0.63400365552053	2.01002318163268
H	-6.18172747018590	0.79119337817797	1.85764660830937
C	-0.83890360581813	1.10491281268907	4.39889342724265
H	-0.30959064657790	0.36502351606945	3.79207751969417
C	-1.51915692104236	0.36225139400748	5.56146303709953
H	-0.76262976073211	-0.11375098047585	6.19109107180285
H	-2.08588578597745	1.06476781113904	6.17876616015324
H	-2.20177020385163	-0.41372516825137	5.21742444208437
C	0.18758043324164	2.07890073631356	4.97996042553406
H	0.62568486268794	2.72261257767610	4.21559440667789

H	-0.26764910940956	2.72175774371463	5.73809034170531
H	0.99039781281995	1.52064433185965	5.46546310770258
C	4.36578107760358	0.99236609340405	-0.35538980615807
H	3.68513096479520	0.27894550865880	0.11746832433039
C	4.90072834306558	1.93849161143693	0.72133077155680
H	5.71941607536496	2.55060200928812	0.33359129034288
H	4.13074741537185	2.61194720369820	1.10121220672834
H	5.29568254559278	1.35777755732597	1.55714339766665
C	5.55016489957341	0.20104817193904	-0.93704934188958
H	5.23422586807091	-0.56193102011210	-1.64737665537847
H	6.24135499647268	0.87679979773036	-1.44812054275708
H	6.09337224940662	-0.29876521415946	-0.13046906837169
C	0.97762268702809	0.98622597722490	-4.19951292896028
H	0.41958924638796	0.27715224392580	-3.58097699239445
C	1.68606200269807	0.19172583407296	-5.30996871636136
H	0.94189837691975	-0.28552267312752	-5.95336226335453
H	2.29094707488928	0.86243088141992	-5.92663598984701
H	2.33540578011616	-0.58967228744243	-4.91924150273287
C	-0.01932525851597	1.93825496164120	-4.86603049072836
H	-0.81461425329711	1.35949720248404	-5.34022696354733
H	-0.47498932014100	2.63059521001047	-4.15776989476412
H	0.46733531537708	2.52695770357026	-5.64860353403785
C	-1.38093906754264	1.29128076611152	-1.40650402287377
C	-2.25211264966341	1.78065365885445	-2.37171590657373
C	-1.91523592012118	-0.90112734800798	-1.97337081279220
C	-2.97063692419592	0.89061508883813	-3.15579597948198
H	-2.36461589864591	2.84755860591550	-2.50693189501761
C	-2.79929271189689	-0.47274779879351	-2.95113626973194
H	-1.75553984848235	-1.95283622588654	-1.78559144231785
H	-3.65268406099097	1.25579693372001	-3.91179516534662
H	-3.33877308680391	-1.20421788321973	-3.53680200450399
C	1.73228598461446	0.90101125295419	1.98491522222181
C	2.65591882590571	1.16953298669470	2.98798521485051
C	2.00916936655594	-1.38756090960365	2.28405639534406
C	3.26976408510549	0.11767579736959	3.65076136984414
H	2.89128143400494	2.19262379451551	3.24395020690041
C	2.93962772324279	-1.18301534328665	3.29001909438436

H	1.72998376057411	-2.38588206461102	1.98220598343453
H	3.99192963719548	0.30957411838532	4.43283797875210
H	3.39121833216524	-2.03664002219711	3.77629651823812
N	1.41089237902675	-0.37792472248713	1.63582348267954
N	-1.21522137056450	-0.04857703980607	-1.21277310169955

Optimized structure in solution (SMD) of 2:

87

C	0.57519520803726	2.50961388225226	0.95759062691040
C	-1.06901744368689	2.50651703159076	-0.68150632741557
C	0.55059831296775	3.89112988079133	1.05288130055774
C	-1.16595071135357	3.88780997723199	-0.66066891594358
C	-0.33779475793225	4.57366700502145	0.22505550571836
H	1.19609091182558	4.41528920175901	1.74288946232560
H	-1.85737898541963	4.40934710761197	-1.30671022702518
H	-0.38569946544671	5.65362118334807	0.27086304675563
C	2.33913534716815	1.85157308319324	2.64200376678951
C	1.21516951625539	0.27442026181335	1.39973194697458
H	2.60312640889110	2.83417774843516	2.99058789620086
C	2.79894939223158	0.63077567878128	2.98514720916567
H	3.55225303007098	0.34980111704229	3.69999807816801
C	-1.51178367620066	0.26859922504402	-1.31098136814187
C	-2.76616862770190	1.83900102392285	-2.43066219783451
H	-3.11592140245953	2.82019395336802	-2.69841695134306
C	-3.11341985783277	0.61544554916133	-2.88021099106112
H	-3.83558443658827	0.33025237051299	-3.62491324243691
N	1.37091635984271	1.62444043611084	1.67144702456093
N	2.10689826399699	-0.31095748849566	2.22271960526021
N	-1.78573547638454	1.61764452540671	-1.47098787061781
N	-2.34346282446072	-0.32206110828260	-2.19082473469997
Fe	-0.13530161248269	-0.08967793838382	0.03120158624700
N	-0.21724660461651	1.83062121383260	0.10966810518369
C	-0.81298799468853	-4.13931897797700	0.74062486870263
C	-0.83976905286979	-2.75464696889542	0.75349763830953
C	0.79666924345826	-2.62085400190593	-0.88766955491618
C	0.89632718194546	-3.99939231706057	-0.97437093162669
C	0.07309575729860	-4.75369564316198	-0.14128845701439

H	-1.45523194047537	-4.71676247728481	1.38991100178963
H	1.58644131933004	-4.46789886508968	-1.66125448678052
H	0.12283013258218	-5.83383279196842	-0.18009331383344
N	-0.05213956160406	-2.01016180703442	-0.04224998087882
C	1.23265495648832	-0.33982941967515	-1.34450828837742
C	2.48024320108007	-1.81729618262892	-2.59129475185234
C	2.82147802305787	-0.56227507693969	-2.94910340168824
H	2.83111701339249	-2.77452787170945	-2.93382261459962
H	3.53673971249220	-0.21982430836529	-3.67611210600118
C	-1.47815636730621	-0.56162165024062	1.37398510555251
C	-2.59722217236299	-2.23303777034454	2.49131090034024
C	-3.05444402168820	-1.04359418467187	2.93359169498734
H	-2.86204288990608	-3.24047411793941	2.75897476944536
H	-3.80375102939212	-0.82154722901431	3.67301332070156
N	-1.63358619501062	-1.92905752698573	1.53749405260998
N	-2.36548948970061	-0.04386547548109	2.24568449379348
N	1.50764320522865	-1.67203656632370	-1.60953255366478
N	2.05587527305082	0.31819513243756	-2.18376195242131
C	-2.43591871406666	-1.77908717573621	-2.40815783318489
H	-1.71038493991064	-2.19866584594792	-1.71703664250839
C	-3.82635724681186	-2.28099350522618	-2.03841252417020
H	-4.58855813298198	-1.86837351368653	-2.70361165716539
H	-3.85412767557345	-3.36883207560201	-2.12442017089742
H	-4.07611667948112	-2.00852224749127	-1.01043994406973
C	2.33910285210263	-1.76605916956387	2.31127228877746
H	1.63721398292024	-2.19333795309717	1.60090235633513
C	3.75954013550651	-2.10065939266269	1.87187161225849
H	3.95455816204447	-1.71980830018214	0.86674719264823
H	4.49789864479853	-1.67499364597059	2.55545840240157
H	3.89058284391790	-3.18432377220819	1.86240737161179
C	2.00578024303189	-2.27084950493530	3.70975432698361
H	0.98286042230751	-2.00477437985114	3.98537981005796
H	2.09908321240606	-3.35817605606150	3.73379514262726
H	2.68707996700623	-1.85525419587317	4.45596913907793
C	-2.02645771324227	-2.12740926564679	-3.83400828128648
H	-1.02646792026435	-1.74678175611766	-4.05416749976400
H	-2.01796106773543	-3.21235903492994	-3.95411812034727

H	-2.72593701866737	-1.71093125486589	-4.56274615727429
C	-2.59505045078214	1.39952124272478	2.45220708318249
H	-1.89735791748823	1.88149050162675	1.77330462790397
C	-4.01788763567780	1.77000512098521	2.05112605961132
H	-4.21996430195092	1.47376316855303	1.01926429393338
H	-4.75284008946675	1.28989506739890	2.70163684490137
H	-4.14784240919702	2.85080824285918	2.13244083176760
C	-2.25140564229694	1.79027660685095	3.88428372636014
H	-1.22733114536615	1.50150289677676	4.13108890463136
H	-2.34289939445432	2.87219857098589	3.99683145866971
H	-2.92860205103778	1.31696259774665	4.59923876728766
C	2.14317908770989	1.78767665020943	-2.29272609617986
H	1.42819423598090	2.15306703605338	-1.56100431590861
C	3.53916377996841	2.26414937802159	-1.91049529979050
H	3.81058634279996	1.91209561931801	-0.91275898004327
H	4.28952174998909	1.90918366329379	-2.62098947457059
H	3.56235617146745	3.35550388987343	-1.91066934958923
C	1.71081257992340	2.24016938729453	-3.68224674223659
H	0.70747837800498	1.87582149400307	-3.91433360607466
H	1.70041736038381	3.33100840918759	-3.72165437684750
H	2.39890482106201	1.87918367908437	-4.45036995599570

Optimized structure in solution (SMD) of 3:

112

C	0.66565579248784	2.02369731587944	0.83810185817931
C	-0.90431334077208	1.92472766006465	-0.88667671257740
C	0.66793720939753	3.40839937594121	0.84168591504135
C	-0.95642485687021	3.31224202612508	-0.94566056311610
C	-0.16288714713781	4.04957782203484	-0.07214775764043
H	1.29113561473935	3.96471422970961	1.52770462504701
H	-1.60075875730978	3.81042465422160	-1.65653561688950
H	-0.18963198142646	5.13084100498629	-0.10189900336351
Fe	-0.03328961868816	-0.58434548733196	0.06535940029544
N	-0.09639958949927	1.30708454636845	0.00118490426239
C	-1.04648611054715	-4.56741485393592	0.73712565925270
C	-0.95265776415527	-3.18615550264417	0.76487376436900
C	0.76434254368361	-3.18004374189104	-0.78887842872383

C	0.75228578111559	-4.56109438039873	-0.88919035074960
C	-0.17054085273636	-5.24868198984794	-0.10463035885911
H	-1.77121223013321	-5.09276896681460	1.34213176449845
H	1.42977535503765	-5.08161095211687	-1.55057655934101
H	-0.21121413485536	-6.32882772571292	-0.15378689501803
N	-0.05784337807499	-2.50827193707006	0.03072054773556
C	1.41951072257456	-0.94022127820063	-1.22321523020742
C	2.59376715728883	-2.54426448735198	-2.39127599687933
C	3.08455172936766	-1.33692368956041	-2.72722884664301
H	2.86255906405930	-3.53478298526381	-2.71200799579466
H	3.86675153619753	-1.06436671652834	-3.41160267500922
C	-1.45013172373098	-0.95117989268131	1.39030578049053
C	-2.72517903274504	-2.56306062768435	2.43521639126357
C	-3.10316686206707	-1.35942199756223	2.90419668460328
H	-3.07259057582992	-3.55499586015417	2.66239971095131
H	-3.85703569898542	-1.09240806008377	3.62173445580636
N	-1.71672668484283	-2.30261123551468	1.51829278221455
N	-2.31745562067214	-0.38909109343440	2.27064152789490
N	1.58408252459113	-2.29072681471632	-1.47382029281941
N	2.37122453573876	-0.37119941693823	-2.00666985319709
C	-2.44749674556890	1.01787807243772	2.58017059289389
C	-3.33220983166766	1.79501566811756	1.81549465210894
C	-1.74136710720706	1.52993006328267	3.68182477155948
C	-3.45724502248343	3.14373685834089	2.15183030353851
C	-1.91059823678121	2.88449212613021	3.97568904346237
C	-2.75143579191425	3.68455415998546	3.21641033012651
H	-4.11765138727909	3.77822238931067	1.57582759183609
H	-1.37518908530879	3.31912015505226	4.80950288869779
H	-2.86103219987683	4.73553235571875	3.45868419561560
C	2.67289598908027	1.03892647153716	-2.12063248148095
C	1.98826809898128	1.79495926894879	-3.08551273736288
C	3.69376831191026	1.57460603830654	-1.31725198831073
C	2.32113444740557	3.14572176165501	-3.19791721486243
C	3.98801326683070	2.93013908466700	-1.47761383643279
C	3.30686678355431	3.70894532872946	-2.40126068348106
H	1.80466258078785	3.76441382768027	-3.91968873360268
H	3.54821103616291	4.76090986791733	-2.50305366690317

C	-4.17211678842852	1.20150440958579	0.69716468250485
H	-3.56567823403170	0.44960223192901	0.18487752707401
C	-4.62172963502843	2.24492370981849	-0.32788354305600
H	-3.79413441124716	2.86193857965295	-0.68064030863040
H	-5.07160952651797	1.74547832977414	-1.18788336663875
H	-5.37869424552945	2.91020462976571	0.09563727586891
C	-5.42017122147473	0.49835285365140	1.25837620426848
H	-6.00800261011307	0.07700772890946	0.43839605693328
H	-5.16912845354111	-0.31264971337799	1.94151185219408
H	-6.04718818671426	1.21484643451515	1.79620079065670
C	-0.85289548601976	0.66617727178166	4.56337356761048
H	-0.36811321963652	-0.07882689736602	3.92569278772538
C	-1.67363348715445	-0.07843762461030	5.63109467477779
H	-1.00576563259828	-0.67322809866143	6.26013916991795
H	-2.19521863573308	0.63919377877286	6.27052056572332
H	-2.41415787255832	-0.75106612101979	5.20123693751895
C	0.23276795141398	1.47276021352795	5.28356214629393
H	0.76150271798074	2.15070547807490	4.61426820337357
H	-0.19682315726218	2.06395386149433	6.09696538260781
H	0.96360517583293	0.79129456497613	5.72396380223980
C	4.49229526623781	0.73463414987677	-0.33247622867427
H	3.81418694837623	-0.00233101067348	0.10792186573033
C	5.10748687354154	1.56789270317467	0.79674703579204
H	5.95505941432102	2.15371752055183	0.43041233232569
H	4.39106158125752	2.25419505129708	1.24754384114953
H	5.48172937446076	0.90441759549004	1.57902107340503
C	5.63267167627457	-0.02349437274471	-1.03442634525066
H	5.27364933061061	-0.71707443248514	-1.79308877110246
H	6.31387672670597	0.68463927129863	-1.51444771610147
H	6.20101041718261	-0.59779564379992	-0.29775442318723
C	0.96053894034675	1.17790277614622	-4.01915073893017
H	0.40251220560830	0.42631499581604	-3.45412272608785
C	1.64333372671738	0.46830078590309	-5.20126830729603
H	0.88631934993839	0.03512075935782	-5.86058516516842
H	2.23335035925698	1.18357802459503	-5.78091338493678
H	2.30513677716590	-0.33492241596173	-4.87848331175969
C	-0.03015092517804	2.20356771130853	-4.57465885463540

H	-0.84192894955917	1.68802648884847	-5.09101214369444
H	-0.46091422192125	2.82911270998865	-3.79158119037917
H	0.45257617892828	2.86169040570983	-5.30192395298240
C	-1.64459645955536	0.96731162834053	-1.69914006679242
C	-2.55417835247405	1.30714645700976	-2.69421239364883
C	-1.99489172342423	-1.29460300804311	-2.08795547683162
C	-3.19768827684899	0.30334733726695	-3.40073151464676
H	-2.75318468230479	2.34716060314425	-2.91043262734361
C	-2.91115120044108	-1.02107423108168	-3.09073729194994
H	-1.75218047021275	-2.31397896656547	-1.82586464803468
H	-3.90827617306714	0.55123552331918	-4.17851863790055
H	-3.38569967492410	-1.84070608550817	-3.61356308177970
N	1.40815115832434	1.17169452604548	1.65073918308327
C	2.32944409020899	1.43180874688835	2.65652136824436
N	2.06107920842218	-0.74487500798590	2.35870289841199
C	2.73781845392041	0.22517587181826	3.09841545429531
C	1.23203757469240	-0.18835662445243	1.45460844836953
N	-1.36745446255735	-0.33208980578923	-1.39767668905285
H	3.44229444782923	-0.04112135676309	3.86695532920998
H	4.75995412824763	3.38307292150769	-0.86975965254180
H	2.60283135840239	2.42636717055111	2.95857667289700
C	2.25226603070436	-2.17521651749295	2.55934988549877
H	1.59695950230177	-2.70749927243706	1.87922800976702
H	2.00368484261911	-2.43855527957754	3.58710735365045
H	3.28865587640049	-2.44125776479712	2.35197951743513

Optimized structure in solution (SMD) of 4:

61

C	5.29301527020470	3.11921560704807	-4.23881045652656
C	6.34323492942287	2.25437428125995	-3.94430649555600
C	6.52126910407633	1.76801359003761	-2.65177356619329
C	5.61316858232284	2.17766961030896	-1.68945105944596
N	4.59355503190540	3.00380222845273	-1.96751416788956
C	4.42361450664418	3.48569398140512	-3.21784521731283
C	3.26373735424804	4.36969013239064	-3.30118016108426
N	5.58129269117008	1.81663135449231	-0.34501660534310
C	6.38634535320262	0.95823363282836	0.39221208083614

C	5.87636251372592	0.97134106374059	1.64235401048393
N	4.78177080359920	1.83375961326866	1.64391956529400
C	4.57365375714161	2.36769427210408	0.42588896880983
C	1.72498990499284	5.83295298290454	-4.40982951883349
C	2.84503320312292	5.01603871654091	-4.45842281115530
N	2.60340421583767	4.51523548434655	-2.11972523793736
C	1.52565808448706	5.30956923366575	-2.08332632818419
C	1.05568380710914	5.98244829777805	-3.20045480461580
Fe	3.39743030663928	3.51641475479826	-0.58291555524913
C	2.46091917511139	5.23316879253168	1.46013456399000
N	2.21010764503321	4.09047247509586	0.78505056583140
C	1.12225058419136	3.35817957266155	1.06751432880769
C	0.22183222053893	3.71619431655218	2.05712142991792
C	0.48170444441194	4.88881509422129	2.76153067108766
C	1.60323880436666	5.65927160121413	2.46776441646906
N	1.07867676333732	2.23359554551544	0.24776446889442
C	3.68764409012147	5.87535816449744	0.99516807038914
C	2.09818332886996	2.09507428398128	-0.67669378751621
C	0.64155365703889	0.36469704768524	-0.78549754521567
C	0.17954443254084	1.17691826631961	0.18919204344393
C	6.00570787895141	6.88441955702953	-0.05092541883283
C	5.45078432274047	5.69756625872066	-0.50377411355833
N	4.31824356806829	5.19150547873834	0.00140822136538
C	4.19153235622445	7.07018932861593	1.49569489311190
C	5.36702095641855	7.58308630758832	0.96725762118262
H	7.03073408730389	1.95644907778853	-4.72503203830149
H	5.15663848234597	3.49677856119165	-5.24249544283436
H	3.39183997656060	4.88075004049743	-5.38184315018935
H	1.38175652637762	6.34405876778255	-5.30009435885609
H	0.17875247672942	6.60997978465631	-3.11347316136896
H	1.02864653546006	5.40472102794048	-1.12802014502190
H	5.92195428031389	5.13020092345543	-1.29417990292956
H	6.92341133506736	7.24607823869473	-0.49517869498426
H	5.77555692582358	8.51223318562773	1.34333745034469
H	3.66769116312597	7.58951054100909	2.28692530766529
H	1.80252011453576	6.57039766477836	3.01421337298261
H	-0.19739722614610	5.20204616864877	3.54360839746171

H	-0.64582977571307	3.10854415999111	2.27218815722278
H	-0.68539053428485	1.10346546674093	0.82407781844428
C	2.61146629717342	0.31595576675414	-2.34258800976871
H	7.33376582872604	1.09830843025459	-2.40730245949709
C	3.94024605638285	2.05730572782018	2.81545629170549
H	3.61684792089325	3.09386986420252	2.83690844273275
H	4.52619051313358	1.84764139261262	3.70730028049765
H	3.07656322573807	1.39213022298682	2.78775664594576
N	1.80147060771573	0.94010786501368	-1.30113901005208
H	0.25576130904893	-0.56448939514905	-1.16755051583576
H	3.00149177127102	1.08209950375278	-3.00634486333501
H	1.97967853632072	-0.36121068061286	-2.91252286183665
H	3.42961309670168	-0.24788099328865	-1.89343008349771
H	6.18940048767376	0.45613617669034	2.53385277862212
H	7.22838733390292	0.43580258181990	-0.02558731478138

Optimized structure in solution (SMD) of 5:

59

C	5.05017958219446	2.92511581224593	-4.29890397329387
C	6.11982801360127	2.07110627350703	-4.04872996930211
C	6.38202514777512	1.63325395518734	-2.75424177687936
C	5.55479998941440	2.06740705778542	-1.72446694967836
N	4.52265864585637	2.89480563766195	-1.98286245621530
C	4.25593226180181	3.32769713521885	-3.23103995667123
C	3.09277613341390	4.21397092983827	-3.26068762237992
C	5.64195938861786	1.73739038763510	-0.30224771381331
C	6.60147908146152	0.90648179693862	0.26120435659566
C	6.57490516391609	0.67130689970048	1.62884730054973
C	5.58652430430434	1.27611526166873	2.39569511189696
C	4.65734067944413	2.09530426963384	1.77262769272928
N	4.67453384215564	2.32812013239596	0.45416686698196
C	1.46993878905678	5.63689294246606	-4.29860088250077
C	2.58409486971729	4.81595225519502	-4.40420080197744
N	2.52708066941878	4.41118632005575	-2.03671818870909
C	1.45230491445257	5.20446141074558	-1.94521638010542
C	0.89535348457970	5.83271580736517	-3.04869886010204
Fe	3.42531530170771	3.46130832813405	-0.56338981505152

C	2.64800216186636	5.15302709703221	1.52437129768973
N	2.32805947830836	4.02682732839696	0.85629600043437
C	1.24367474143957	3.29397397092954	1.17925051655517
C	0.41617054563191	3.68767051454949	2.22495162878560
C	0.73223859532517	4.84849176574068	2.92401978566843
C	1.85502049517541	5.59393351477209	2.57797634346257
C	1.10442852785893	2.12189863869024	0.31519606323638
C	3.86274233797179	5.77122208674401	0.99359023894850
N	2.08868251311512	2.01590064611777	-0.62117526679883
C	2.06187760671937	0.97924480757303	-1.46826541221331
C	1.07007774414647	0.01108502768678	-1.42784876119976
C	0.06381849446365	0.11472403286267	-0.47529873970819
C	0.08272760772596	1.18573934714546	0.40738479149285
C	6.14445290358526	6.72540704283681	-0.18011341217663
C	5.52502783280057	5.56467642290040	-0.61803131183108
N	4.40906466235635	5.08843753186036	-0.05161357259682
C	4.43492212971474	6.93956646634622	1.47947388825888
C	5.59169273403924	7.42501406659921	0.88558804382759
H	6.75145232248155	1.74597823164932	-4.86514748459337
H	4.84131824525638	3.26743798187440	-5.30308087196769
H	7.21228582449070	0.96992816134566	-2.55435425202746
H	7.35749038759060	0.45119573597550	-0.36429119112906
H	7.31411713214809	0.02628075600038	2.08627066843680
H	5.52683215397557	1.12288951710195	3.46491607921254
H	3.87506180464318	2.58106915131276	2.33871685149352
H	3.05572130162071	4.64288987518827	-5.36220745989228
H	1.05776720950480	6.11422816617366	-5.17839247916381
H	0.02605541401874	6.46327967151802	-2.91829383224377
H	1.03114355764005	5.33551508585904	-0.95838571241658
H	5.92779227301644	4.99605478555194	-1.44437677225899
H	7.04454254211166	7.06609847179572	-0.67415056536480
H	6.05212063351268	8.33441530589248	1.24992214035195
H	3.97924218314138	7.46035925372039	2.31089548451689
H	2.10468204203738	6.49673931969890	3.11814258744333
H	0.10123205227836	5.17312257602608	3.74107431709929
H	-0.45509665749536	3.10499224629760	2.49067382236271
H	-0.68579183567807	1.29538785624551	1.16065084106993

H	-0.72444792389120	-0.62503745665671	-0.41934416450892
H	1.09626604812547	-0.80580842528267	-2.13659604121632
H	2.85851691433694	0.92992981054868	-2.19723206911324

Electrochemistry and Spectroelectrochemistry

Analysis of **1**.

Cyclic and square-wave voltammograms and spectroelectrochemistry of the oxidation have already been published.⁷³

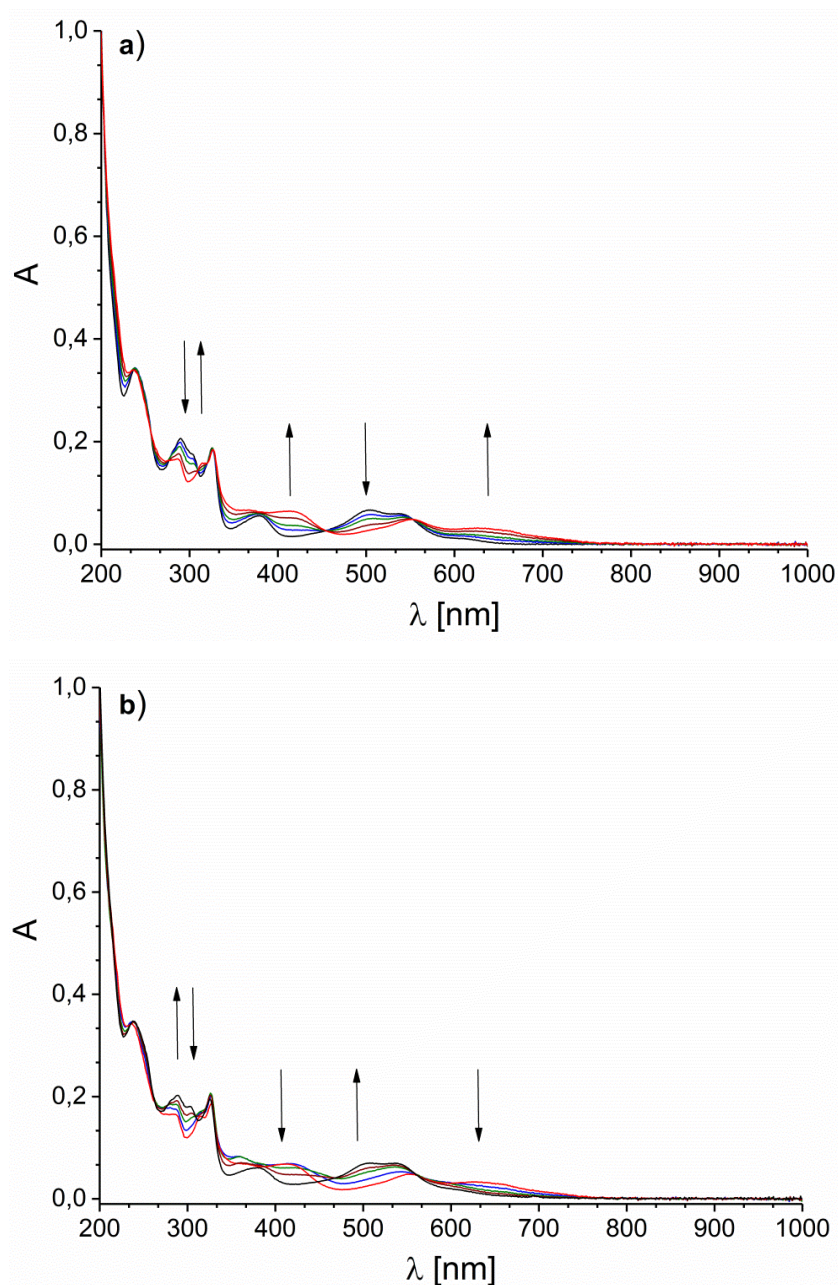


Figure S23. UV-Vis spectra recorded during a chronoamperometric investigation of **1**. Potential controlled reduction a) (start: black line) at -2,0 V. After the reduction was complete, SW analysis of the obtained solution indicates formation of by-products. Re-oxidation b) (start: red line; reference: Ag/AgNO₃) at 0 V was traced with UV-Vis spectroscopy and shows seemingly the regeneration of **1**.

But subsequent SW analysis after the re-oxidation process does not prove the formation of pure **1**. Overall, the species **1**^{red} decomposes over a longer time period.

Analysis of **2**.

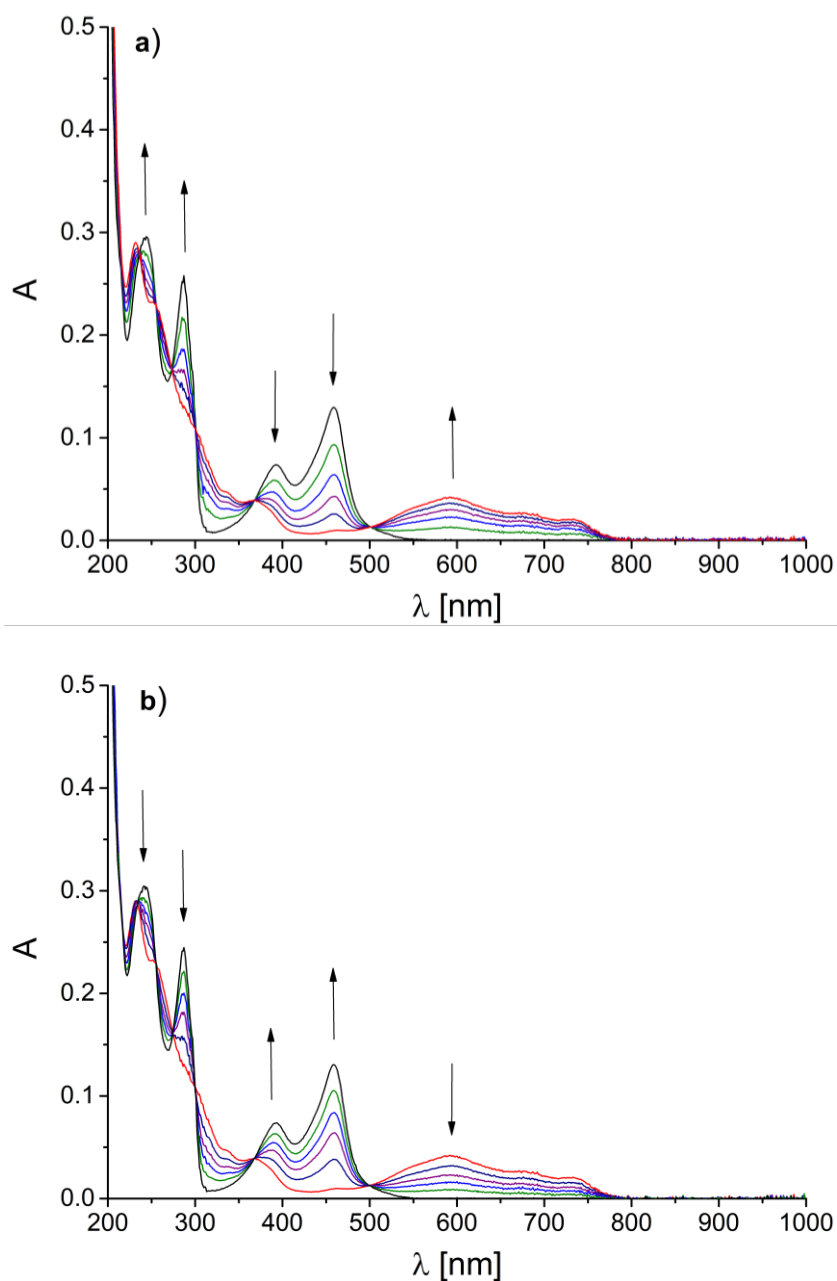


Figure S24. UV-Vis spectra recorded during a chronoamperometric investigation of **2**. Potential controlled oxidation a) (start: black line) at 0,70 V and re-reduction b) at 0,30 V (start: red line, reference: Ag/AgNO₃).

Analysis of 3.

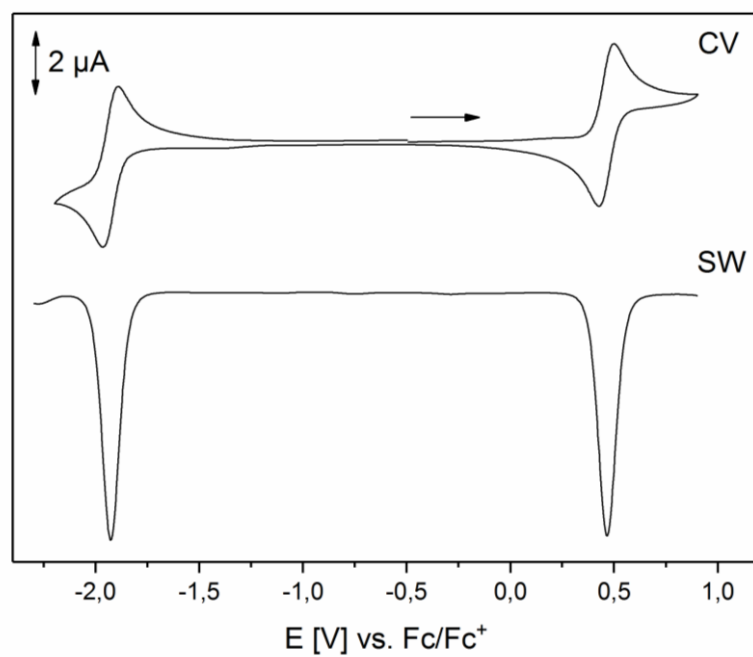


Figure S25. Cyclic voltammograms (scan rate: 100 mV/s) and square-wave voltammogram (Frequency: 25 Hz) of **3** in acetonitrile.

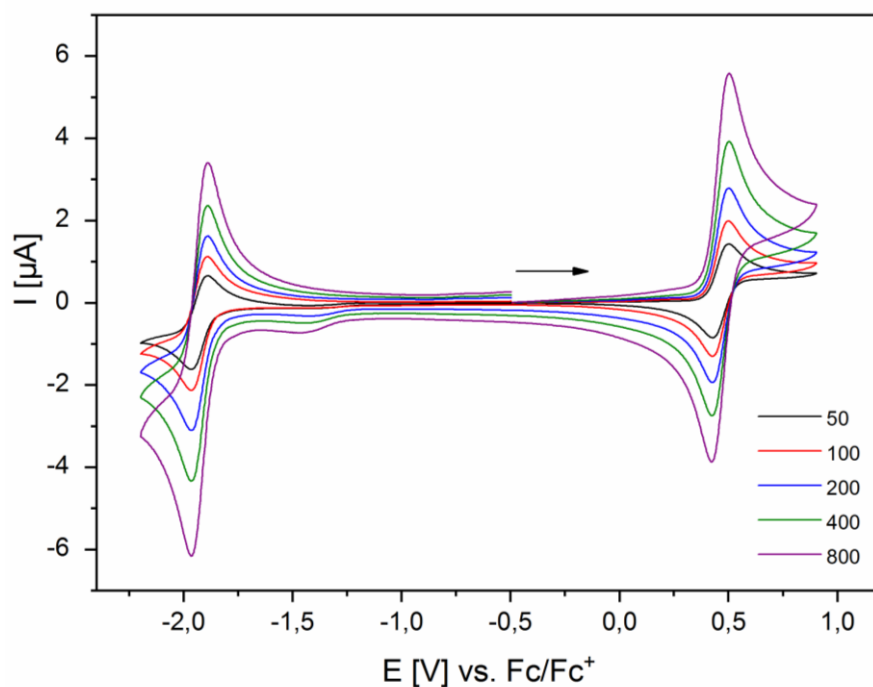


Figure S26. Cyclic voltammograms of **3** in acetonitrile. Scan rates: 50 (black line), 100 (red), 200 (blue), 400 (green), 800 (purple) mV/s.

Table S13. Electrochemical data for the reversible oxidation at $E^0_{1/2} = 0,46$ V vs. Fc/Fc⁺. (*)The ratio was calculated using the empirical method of Nicholson.⁸⁴

ν [mV s ⁻¹]	50	100	200	400	800
E_{pc} [V]	0,43	0,43	0,43	0,42	0,42
E_{pa} [V]	0,50	0,50	0,50	0,50	0,50
$E_{1/2}$ [V]	0,46	0,46	0,46	0,46	0,46
ΔE [V]	68	69	71	74	78
I_{pc} [10 ⁻⁶ A]	-1,31	-1,84	-2,58	-3,47	-4,84
I_{pa} [10 ⁻⁶ A]	1,17	1,64	2,32	3,25	4,56
I_{pa}/I_{pc}	0,89	0,89	0,90	0,94	1,06
I_{pa}/I_{pc} (*)	0,92	0,98	0,99	0,99	0,98
$I_{pc}/\nu^{0.5}$	0,19	0,18	0,18	0,17	0,17

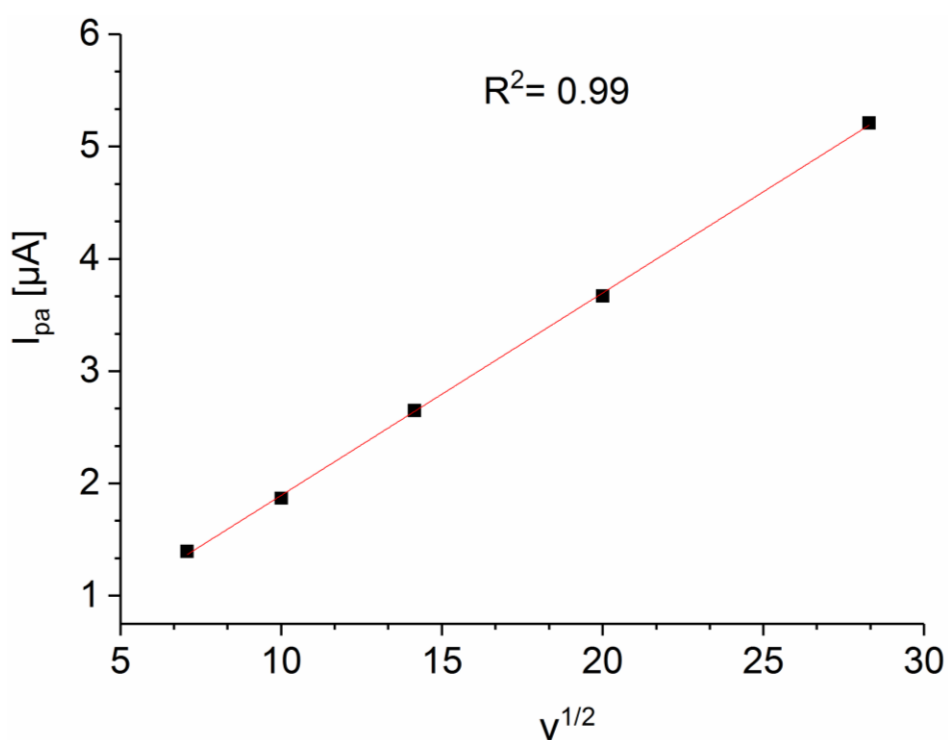


Figure S27. Linear dependence of forward current peak I_{pa} versus square-root of ν (linear fit in red) for the reversible redox processes at $E^0_{1/2} = 0,46$ V vs. Fc/Fc⁺.

Table S14. Electrochemical data for the reversible reduction at $E^0_{1/2} = -1,93$ V vs. Fc/Fc⁺. (*)The ratio was calculated using the empirical method of Nicholson.⁸⁴

v [mV s ⁻¹]	50	100	200	400	800
E_{pc} [V]	-1,96	-1,96	-1,96	-1,96	-1,96
E_{pa} [V]	-1,89	-1,89	-1,89	-1,89	-1,89
$E_{1/2}$ [V]	-1,93	-1,93	-1,93	-1,93	-1,93
ΔE [V]	71	69	68	68	68
I_{pc} [10 ⁻⁶ A]	-1,08	-1,50	-2,16	-3,04	-4,29
I_{pa} [10 ⁻⁶ A]	1,26	1,86	2,65	3,75	5,30
I_{pa}/I_{pc}	1,17	1,24	1,22	1,24	1,23
I_{pa}/I_{pc} (*)	1,21	1,10	1,13	1,11	1,10
$I_{pc}/v^{0.5}$	0,15	0,15	0,15	0,15	0,15

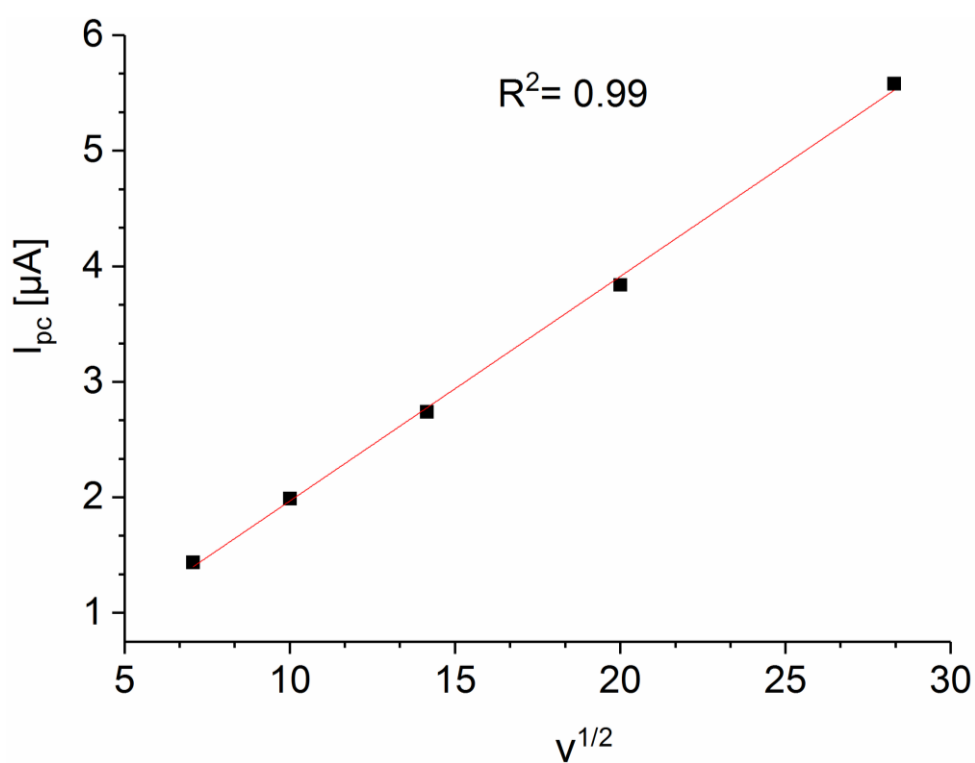


Figure S28. Linear dependence of forward current peak I_{pc} versus square-root of v (linear fit in red) for the reversible redox processes at -1,93 V vs. Fc/Fc⁺.

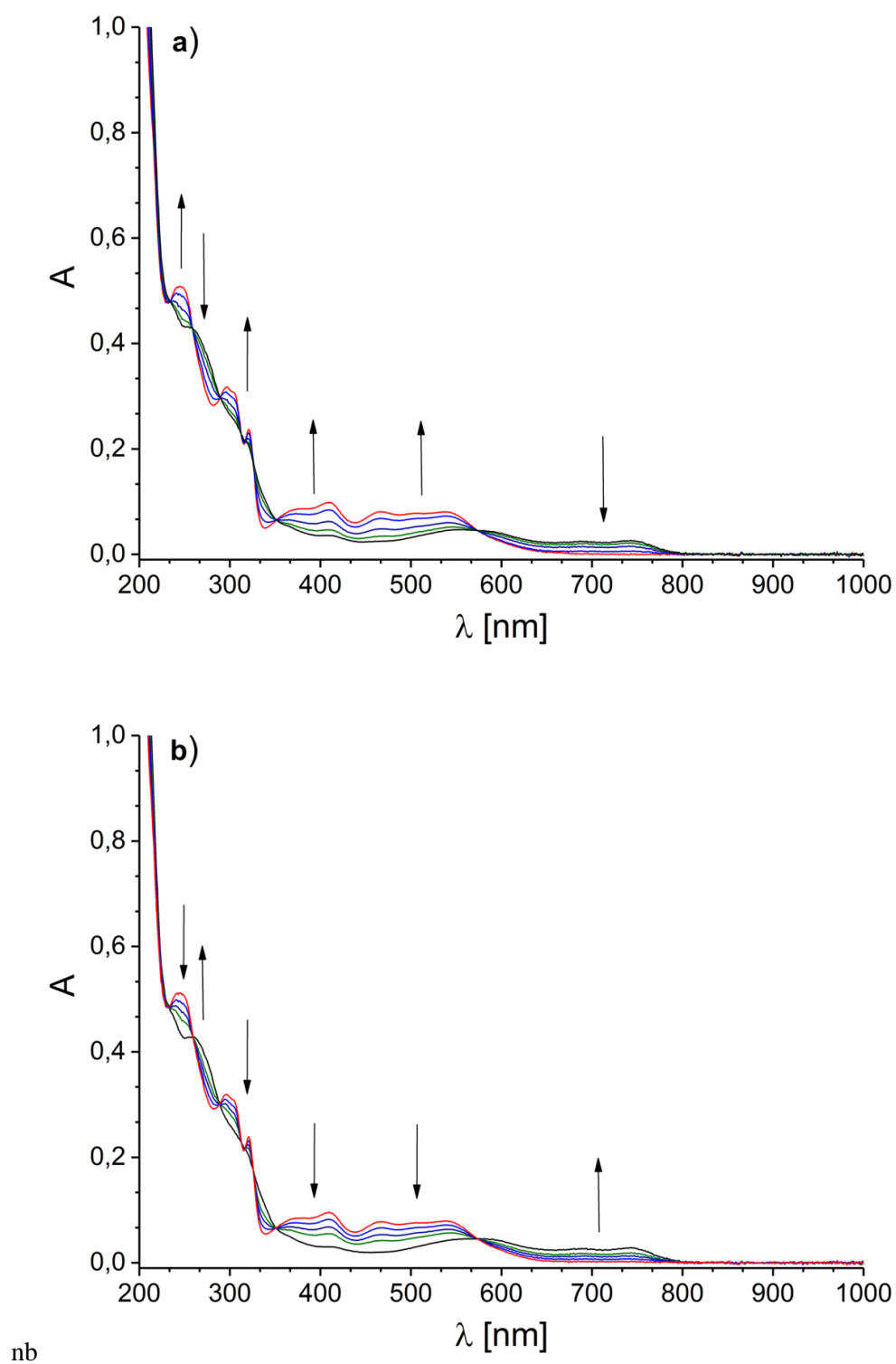


Figure S29. UV-Vis spectra recorded during a chronoamperometric investigation of **3**. Potential controlled oxidation a) (start: black line) at 0,77 V and re-reduction b) at 0,47 V (start: red line, reference: Ag/AgNO₃).

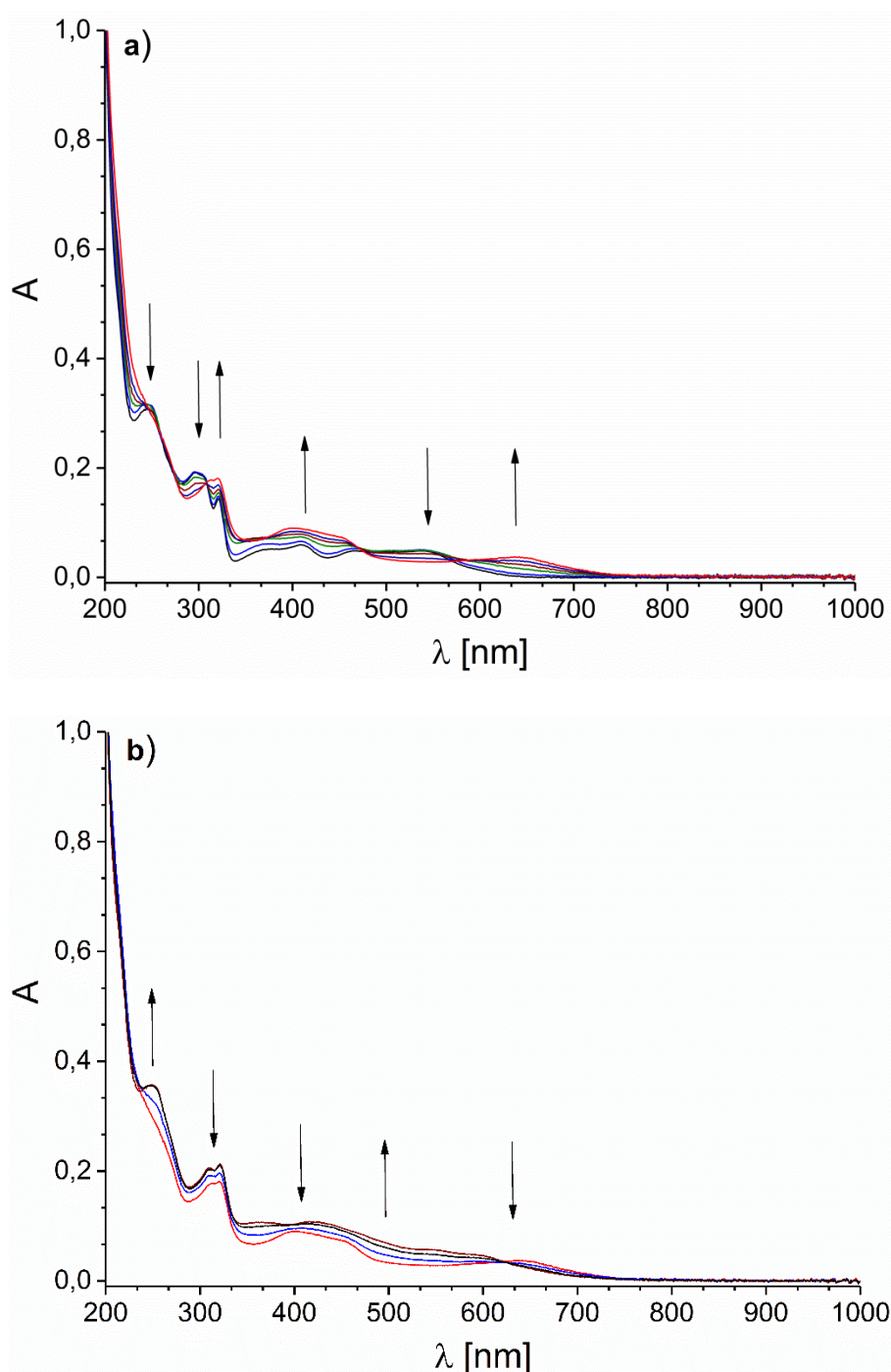


Figure S30. UV-Vis spectra recorded during a chronoamperometric investigation of **3**. Potential controlled reduction a) (start: black line) at -2,0 V. After the reduction was complete, SW analysis of the obtained solution indicates formation of by-products. Re-oxidation b) (start: red line; reference: Ag/AgNO₃) at 0 V was traced with UV-Vis spectroscopy and does not clearly indicates the regeneration of **3**. Subsequent SW analysis after the re-oxidation process does not prove the formation of the original compound **3**. Overall, the species **3**^{red} decomposes over a longer time period.

Analysis of 4.

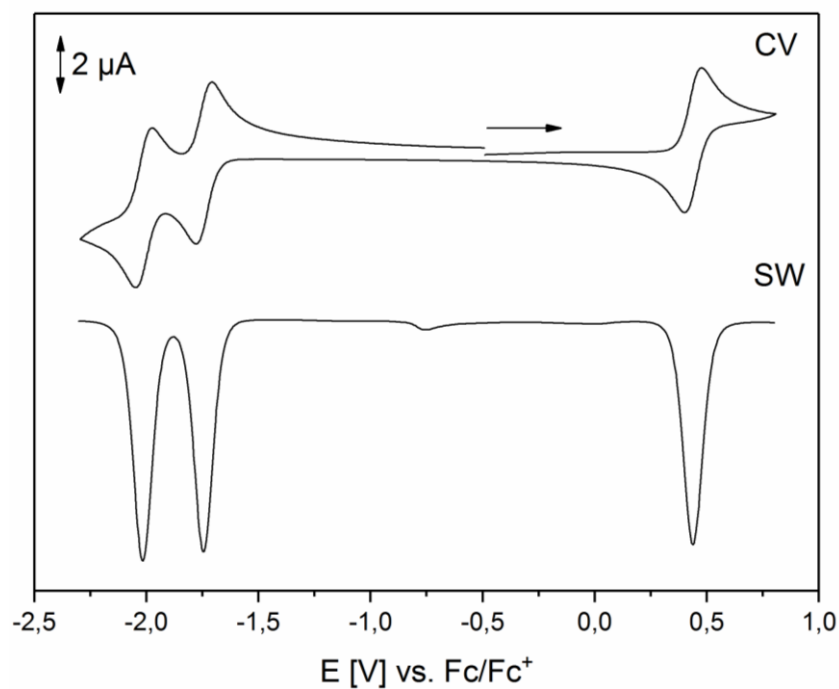


Figure S31. Cyclic voltammograms (scan rate: 100 mV/s) and square-wave voltammogram (Frequency: 25 Hz) of **4** in acetonitrile.

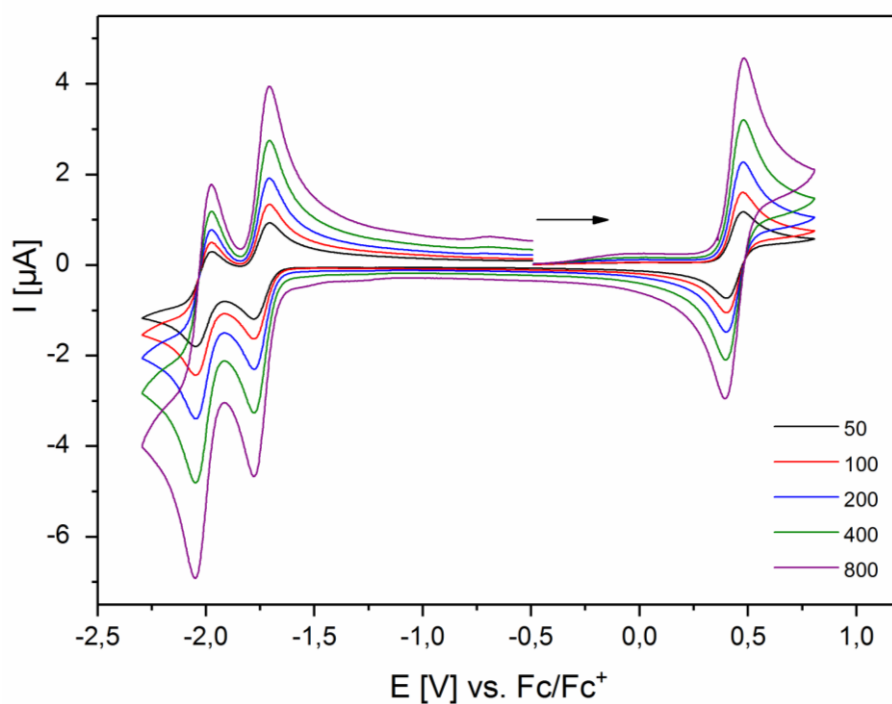


Figure S32. Cyclic voltammograms of **4** in acetonitrile. Scan rates: 50 (black line), 100 (red), 200 (blue), 400 (green), 800 (purple) mV/s.

Table S15. Electrochemical data for the reversible oxidation at $E^0_{1/2} = 0,44$ V vs. Fc/Fc⁺.

ν [mV s ⁻¹]	50	100	200	400	800
E_{pc} [V]	0,40	0,40	0,40	0,40	0,40
E_{pa} [V]	0,48	0,47	0,48	0,48	0,48
$E_{1/2}$ [V]	0,44	0,44	0,44	0,44	0,44
ΔE [V]	73	73	75	81	86
I_{pc} [10 ⁻⁶ A]	-1,08	-1,47	-2,05	-2,78	-3,87
I_{pa} [10 ⁻⁶ A]	1,11	1,54	2,13	2,99	4,25
I_{pa}/I_{pc}	1,02	1,04	1,04	1,08	0,91
$I_{pc}/\nu^{0.5}$	0,15	0,15	0,14	0,14	0,14

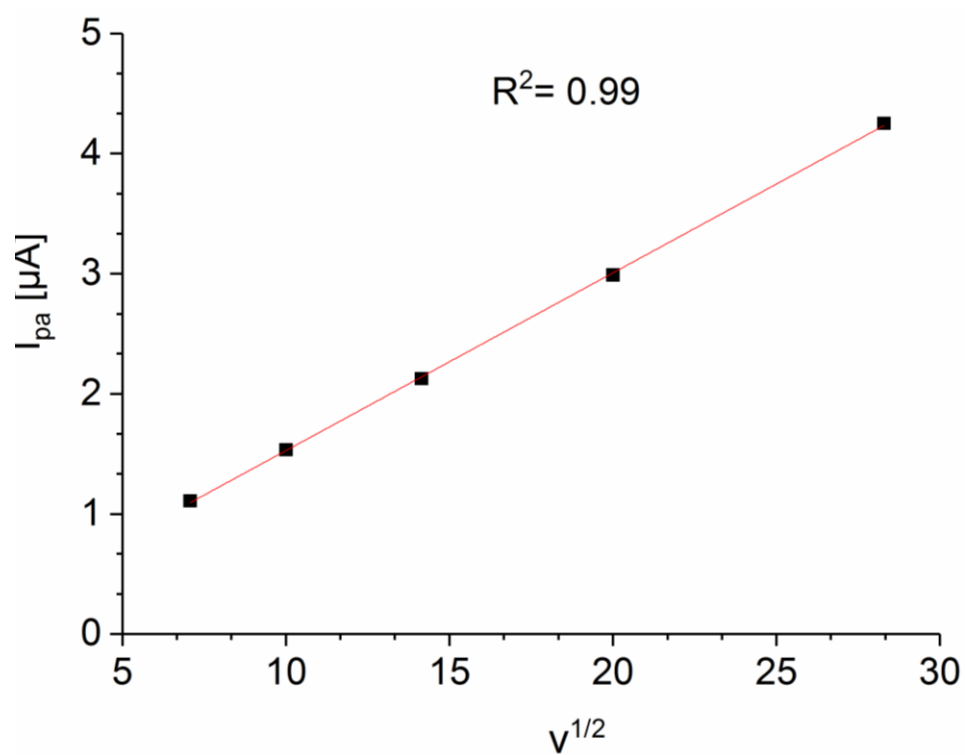


Figure S33. Linear dependence of forward current peak I_{pa} versus square-root of ν (linear fit in red) for the reversible redox processes at $E_{1/2}^0 = 0,44$ V vs. Fc/Fc⁺.

Table S16. Electrochemical data for the reversible oxidation at $E_{1/2}^0 = -1,74$ V vs. Fc/Fc⁺.

v [mV s^{-1}]	50	100	200	400	800
E_{pc} [V]	-1,78	-1,78	-1,78	-1,78	-1,78
E_{pa} [V]	-1,71	-1,71	-1,71	-1,71	-1,71
$E_{1/2}$ [V]	-1,74	-1,74	-1,74	-1,74	-1,75
ΔE [V]	66	61	64	66	68
I_{pc} [10^{-6} A]	-0,93	-1,24	-1,74	-2,39	-3,33
I_{pa} [10^{-6} A]	0,95	1,30	-1,81	2,57	3,62
$I_{\text{pa}}/I_{\text{pc}}$	1,02	1,05	1,04	1,07	1,09
$I_{\text{pc}}/v^{0.5}$	0,13	0,12	0,12	0,12	0,12

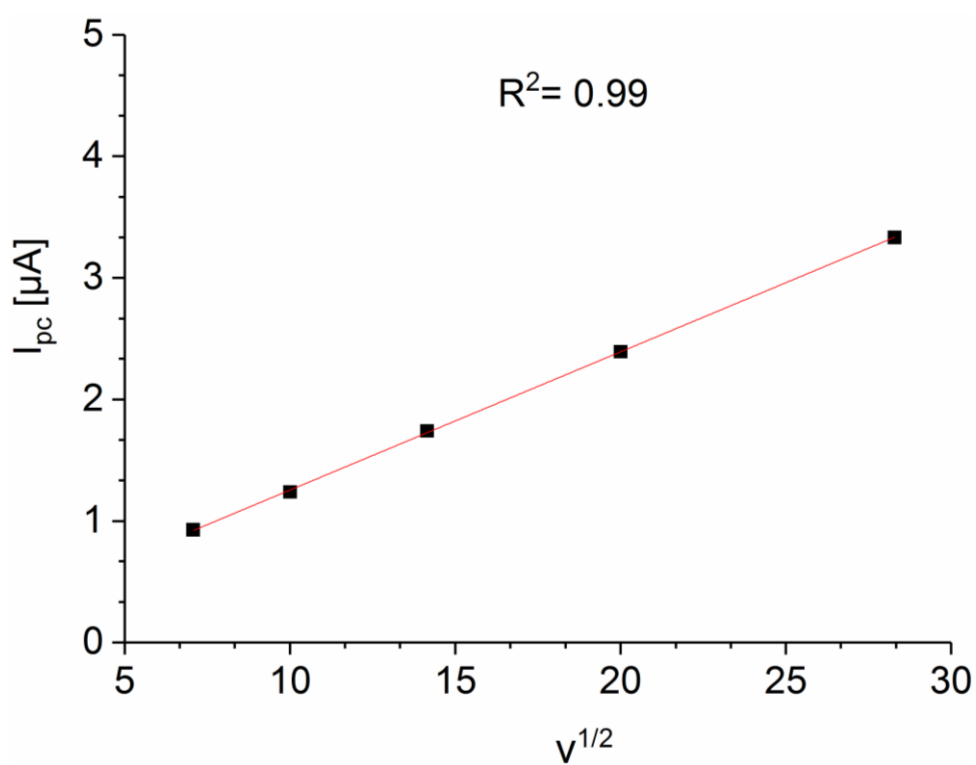


Figure S34. Linear dependence of forward current peak I_{pc} versus square-root of v (linear fit in red) for the reversible redox processes at $E_{1/2}^0 = -1,74$ V vs. Fc/Fc^+ .

Table S17. Electrochemical data for the reversible oxidation at $E_{1/2}^0 = -2,02$ V vs. Fc/Fc^+ .

v [mV s^{-1}]	50	100	200	400	800
E_{pc} [V]	-2,05	-1,99	-2,05	-2,05	-2,05
E_{pa} [V]	-1,99	-2,05	-1,99	-1,99	-1,99
$E_{1/2}$ [V]	-2,02	-2,02	-2,02	-2,02	-2,02
ΔE [V]	63	61	61	66	66
I_{pc} [10^{-6} A]	-0,86	-1,20	-1,69	-2,43	-3,87
I_{pa} [10^{-6} A]	0,84	-1,15	1,64	2,40	4,25
$I_{\text{pa}}/I_{\text{pc}}$	0,97	0,96	0,97	0,99	1,10
$I_{\text{pc}}/v^{0.5}$	0,12	0,12	0,12	0,12	0,14

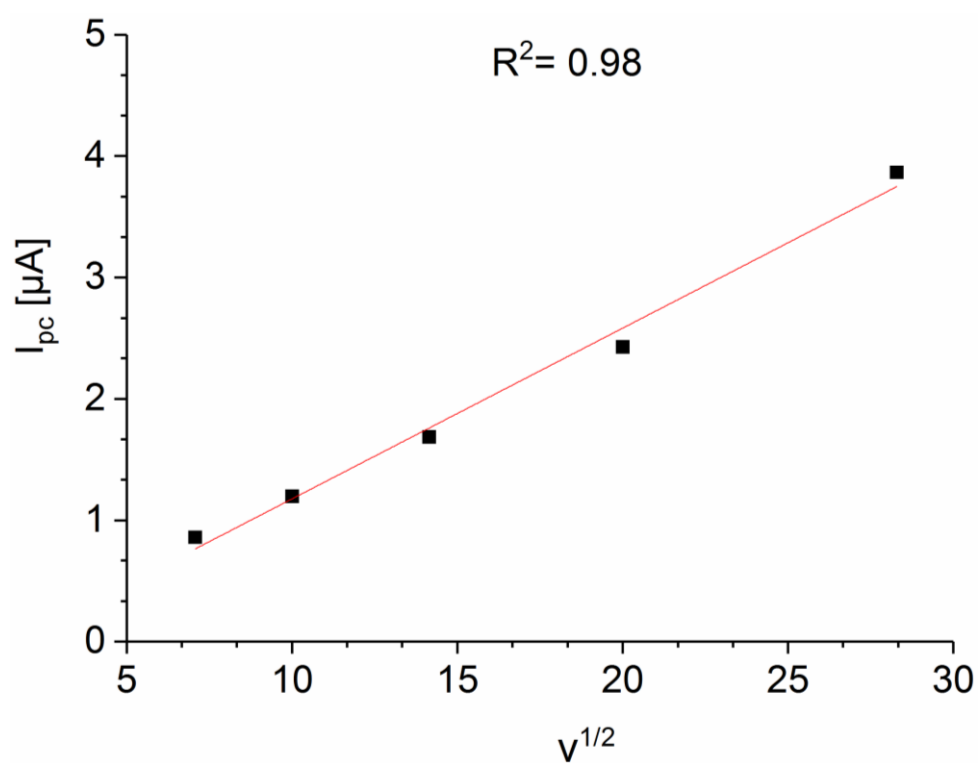


Figure S35. Linear dependence of forward current peak I_{pc} versus square-root of v (linear fit in red) for the reversible redox processes at $E_{1/2}^0 = -2,02$ V vs. Fc/Fc^+ .

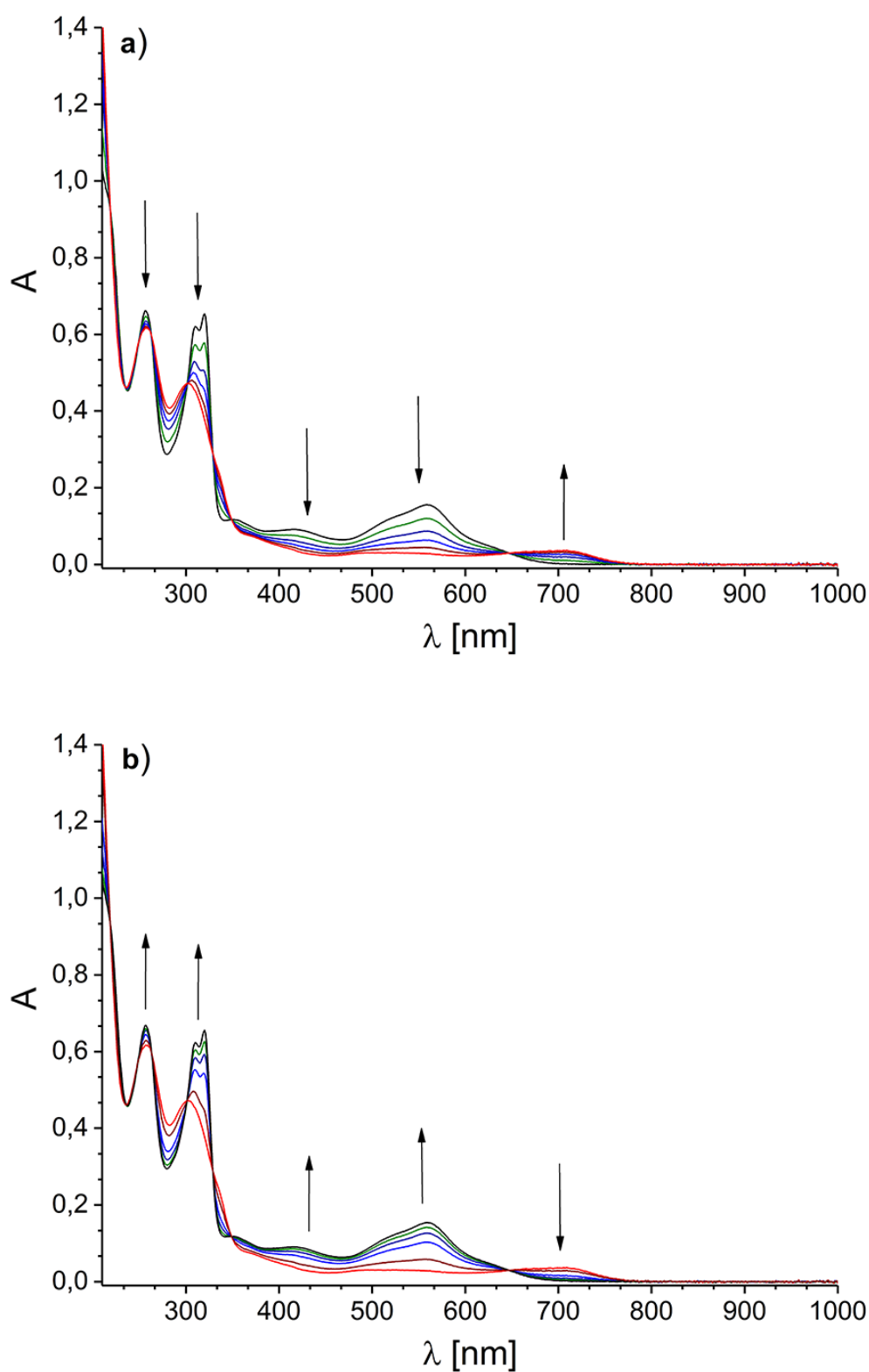


Figure S36. UV-Vis spectra recorded during a chronoamperometric investigation of **4**. Potential controlled oxidation a) (start: black line) at 0,66 V and re-reduction b) at 0,42 V (start: red line, reference: Ag/AgNO₃).

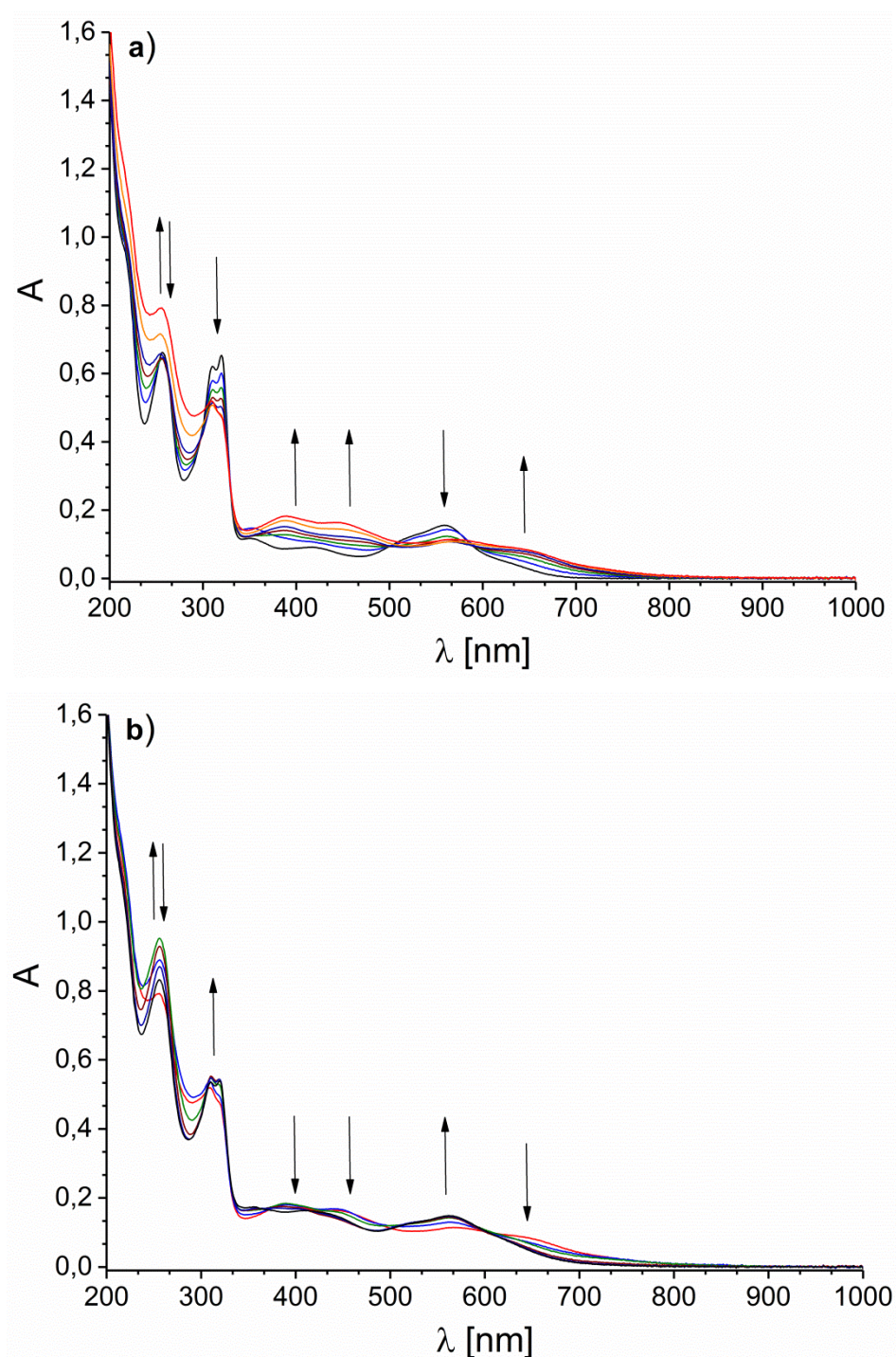


Figure S37. UV-Vis spectra recorded during a chronoamperometric investigation of **4**. Potential controlled reduction a) (start: black line) at -1,8 V. After the reduction was complete, SW analysis of the obtained solution also indicates the formation of by-products. Re-oxidation b) (start: red line; reference: Ag/AgNO₃) at 0 V was traced with UV-Vis spectroscopy and subsequent SW analysis confirm the formation of original compound **4**.

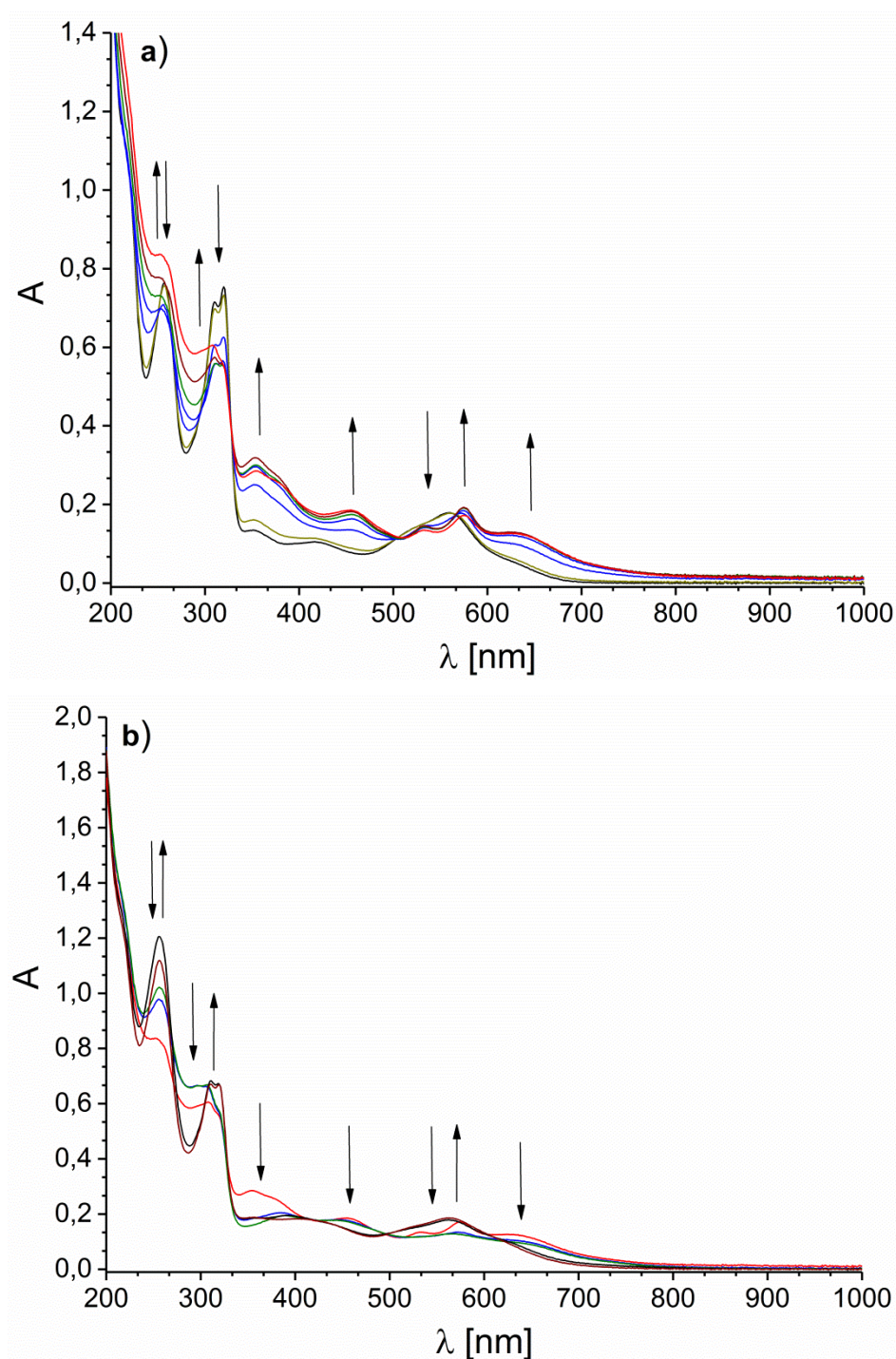


Figure S38. UV-Vis spectra recorded during a chronoamperometric investigation of **4**. Potential controlled reduction a) (start: black line) at -2,3 V. After the reduction was complete, SW analysis of the obtained solution also indicates slight amounts of by-products. Re-oxidation b) at 0 V (start: red line; reference: Ag AgNO₃) was traced with UV-Vis spectroscopy and subsequent SW analysis, which confirm the formation of original compound **4**.

Ultrafast pump-probe spectroscopy

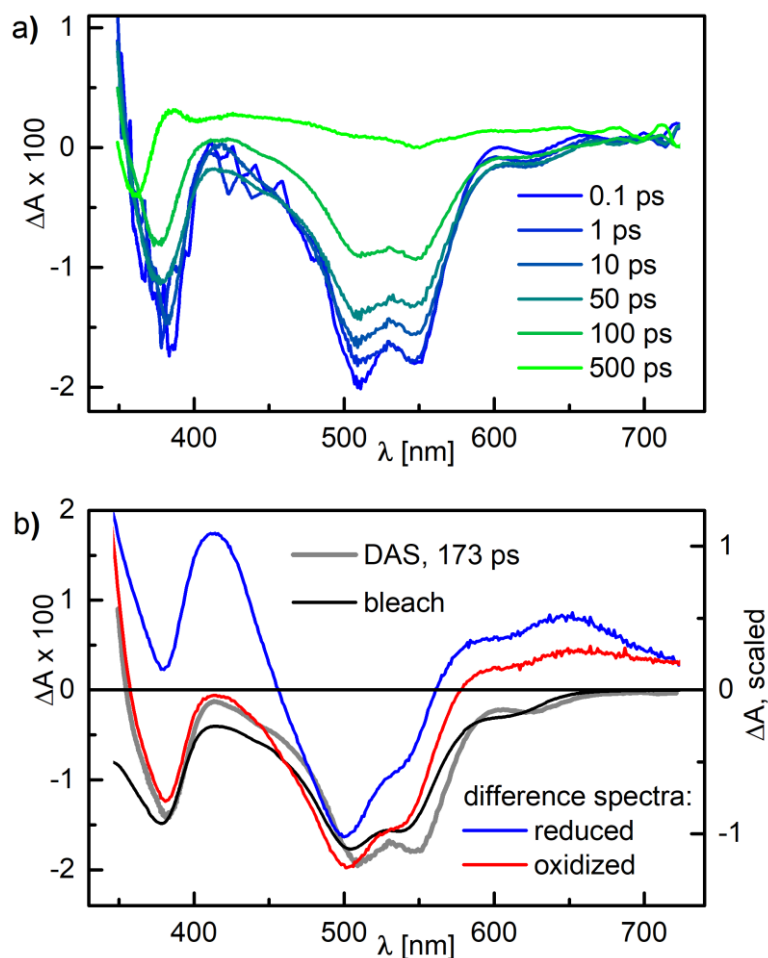
Transient absorption spectra of complexes **1'** and **2'**

Figure S39. a) Transient absorption spectra of complex **1'** in acetonitrile at the specified delay times after optical excitation at 550 nm. This complex is identical to **1** beside of the counter ion. b) Decay associated amplitude spectrum (DAS, grey line, left scale) of the exponential decay with a time constant of 173 ps. The DAS is compared to the inverted ground state absorption reflecting the excitation induced bleach (black line) and to the difference spectra between the reduced respectively oxidized form and the original ground state form of **1**. Bleach and difference spectra are scaled for optimal comparison.

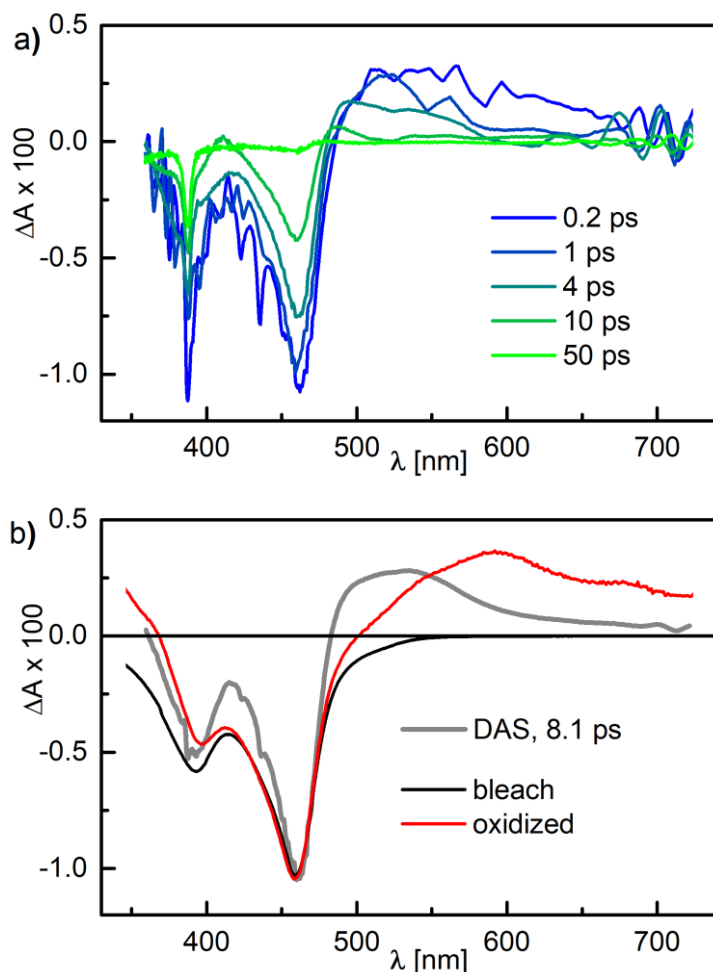


Figure S40. a) Transient absorption spectra of **2'** in acetonitrile at the specified delay times after optical excitation at 388 nm. This complex is identical to **2** beside of the counter ion. Here the second harmonic of the Ti:sapphire laser system was used for excitation since the compound does not absorb at 550 nm. b) Decay associated amplitude spectrum (DAS, grey line) of the exponential decay with a time constant of 8.1 ps. The DAS is compared to the inverted ground state absorption (black line), which reflects the excitation induced bleach, and to the difference spectrum of the oxidized form (red line) of complex **2** with PF_6^- as counter ion. The bleach and the difference spectrum are scaled for optimal comparison. Beside of the bleach contribution the difference spectrum of the oxidized form differs substantially from the DAS. This is expected since the DAS corresponds to a $^3\text{MLCT}$ state which features, as the oxidized form, a hole at the metal center but contrary to it also an excess electron at the ligand.